Heritage in the Crossfire: Developing novel field-based methods for assessing ballistic impact driven deterioration of heritage stone

Oscar Gilbert

A thesis submitted in partial fulfilment of the requirements of the University of the West of England, Bristol for the degree of Doctor of Philosophy

This research programme was carried out in collaboration with the Leverhulme trust

Faculty of the Environment and Technology, University of the West of England, Bristol

September 2023

Word Count: 79,372

I would like to acknowledge the steadfast support and guidance of the many family, friends and colleagues who have provided guidance and help to me on this journey:

My supervisory team and colleagues; Dr Lisa Mol, Professor Tom Blenkinsop, Dr Gary Atkinson and Oliver Campbell, Dr. Andrew Geary, Mahmoud Hadia, Ahmed Masoud and Dr. Charlotte Brassey. Your patience and insights have been invaluable.

My family, particularly my mother and grandmother. It was only with your support throughout my various academic undertakings that I was able to pursue my interests.

My friends, your good humour and empathy has been a constant source of strength.

My partner, Naomi Weeks. Your patience, love, and care have been a light in difficult times; you are more than I deserve.

It is also pertinent to mention the impacts of the COVID-19 pandemic on the work of this PhD project. Due to the global lockdowns caused by the virus, the fieldwork that had been intended to test and refine the findings of this project (planned for Madrid in 2020) became impossible. Further difficulties were presented by a lack of access to laboratory facilities and equipment for almost a year in total that greatly slowed data collection and subsequent processing. Contracting the virus myself twice over the course of the pandemic added to these difficulties. However, throughout this period I endeavoured to ensure that these setbacks did not lower the rigour of my research, or the quality of the outputs. Indeed, as demonstrated by the heroic efforts of the epidemiologists, biologists, pharmacologists and trial volunteers who created the public health measures and vaccines that ultimately ended that dark period, the pursuit of science must continue in the face of adversity.

Contents

Title Image: *The badly scarred Fackeltrager (torch carrier) sculpture at the former Ordensburger Vogelsganf training facility in Germany (now a national park). The monument was damaged by small arms fire during the Second World War and encapsulates many of the difficult ethical issues surrounding conflict damage to heritage stone.*

Source: https://commons.wikimedia.org/wiki/File:NS-Ordensburg_Vogelsang_%E2%80%93_Fackeltr%C3%A4ger.jpg

Abstract

The aim of the PhD was to advance current understanding of the damage caused by ballistic impact into stone-built heritage monuments in arid Middle Eastern and North African climates. Damage was assessed through the development of novel rapid, non-destructive, in-situ techniques for assessing geo-technical metrics of impacted stone across varied impact conditions (target lithology, ammunition type, impact angle). Further to the damage caused by the initial impact, the risk that ballistic impact poses of exacerbating long-term deterioration of impacted stone caused by weathering processes was also studied.

The ultimate application of this research is the creation of a risk matrix and field methods that allow conservation professionals to triage stone-built heritage monuments most at risk of deterioration in the aftermath of armed conflict. This will aid in decision making when seeking to allocate time and resources to the heritage assets most at risk, in order to prevent greater deterioration. To achieve this aim, a variety of methods were developed, including surveys of damaged stone surfaces for rebound hardness and permeability, and Protimeter assessment for the detection of weathering agents. These surveying techniques were coupled with Ultrasonic pulse velocity analysis and photogrammetry to assess aspects of the exterior and interior damage to stone caused by ballistic impact and subsequent weathering. All these methods were portable and non-destructive, and thus well suited to the application of assessing immovable heritage sites damaged in armed conflict. Finally, the data collected using these methods was used to quantify the damaged caused by combinations of various impact conditions (lithology, impact angle, projectile, presence of weathering agents) to construct a risk matrix. This matrix can then be used to assess at-risk heritage stone in situ and prioritise those sites at greatest risk of deterioration.

Results demonstrate that the most important variable in determining ballistic damage to heritage stone is the target lithology and its mechanical properties, whilst impact angle and projectile construction also influence damage levels depending on target lithology. Damage to stone samples was found to be worsened when exposed to subsequent haloclasty weathering processes with lithology again being a key determinant of damage. Laboratory findings were further supported with field studies of damaged heritage sites at risk of weathering deterioration. Results from these show that the methods and risk matrix developed during this project are viable in a field setting, and the methods described here have already begun to be used in active heritage conservation projects. Therefore, this PhD

project represents an original contribution to the field of heritage science, having elucidated a little-understood risk factor which contributes to and exacerbates haloclasty weathering deterioration of heritage stone (namely, conflict driven ballistic impact). Additionally, the research presented here has developed methods to identify and quantitively compare those sites most at risk of haloclasty weathering deterioration in the aftermath of conflict driven ballistic impact.

Chapter 1

Introduction and Background to Research

Chapter 1 Overview: Chapter Structure

This project aims to investigate the ways in which ballistic damage arising from armed conflict affects the weathering of stone-built heritage. The nature of this work necessitates considerations of a number of varied factors. These include the legal and non-governmental structures around cultural property protection, the materials science underpinning ballistic damage, and the chemistry that drives weathering processes. These themes are diverse and their inter-play is complex, therefore a review of the existing literature is necessary to identify the scope and aims of this project within the wider corpus of research. To ensure clarity of this literature review, an overview of its structure and the underlying reasoning are given below. The structure of the literature review was broadly grouped into 4 sections: the background and context of conflict damage to built heritage, the immediate damage caused by ballistic impacts into stone, the long-term deterioration risks of ballistic impact, and the integration of this existing literature into the structure of the research programme of this PhD project.

1.1-1.2: Context and background of conflict damage to built heritage

1.1: Justification of research- the need to protect built heritage

A brief discussion of the cultural and economic benefits of built heritage, outlining why research should be undertaken to preserve and protect it from the threat of armed conflict.

1.2: Armed conflict as a threat to built heritage

An overview of the history and motives of conflict damage to heritage monuments is given, demonstrating that cultural property has been targeted during wars throughout history. Limitations are identified in existing knowledge of how to respond to weathering processes that exacerbate conflict damage and damage caused by small arms fire.

1.3-1.4: Immediate damage caused by ballistic impacts into stone

1.3: Small arms damage to built heritage and stone

As discussed in section 1.2, small arms damage to heritage monuments is poorly understood. Therefore, a review of literature into the ubiquity and increasing power of small arms and the threat they pose to heritage is undertaken. A lack of literature in this area means that a review of ballistic impacts from fields such as meteoritics are identified as useful but limited analogues.

1.4: Ballistic impact fracture formation

An outline of the materials science behind the principal cause of ballistic damage to stone: fracture formation.

1.5: Impact fractures and immediate damage to stone

The initial weakening that ballistic fracture damage causes must be considered when seeking to preserve stone-built heritage. Therefore, an overview of research into damage by impact induced fracture networks is presented here.

1.6-1.11: Long-term deterioration risks of ballistic impact

1.6: Fracture networks and weathering deterioration

In addition to the immediate damage caused by projectiles, fracture networks are a primary driver of weathering processes that degrade built heritage over time. The relationship between fracture networks and accelerated weathering is therefore investigated.

1.7: The state of research into weathering of ballistic damage

Preliminary work into ballistic impact effects on weathering processes is reviewed and results compared with other weathering studies already discussed. Some agreement with field observations on moisture driven deterioration behind hardened stone is identified. Limitations

are highlighted, including the soft lead projectiles used and the lack of research into ballistic damage effects on haloclasty (salt crystallization weathering).

1.8: Weathering processes and stone types in conflict regions

In order to ensure the research is applicable to recent and ongoing conflict damage to heritage, a study area must be defined. This involves identifying the stone types and weathering processes present in conflict regions. The literature suggests that salt, moisture and temperature are key weathering agents in arid regions currently experiencing armed conflict.

1.9: The role of moisture in rock weathering

A discussion of a key weathering agent, and its role in facilitating weathering via solutes such as acidic atmospheric pollutants and salts.

1.10: The role of salt in rock weathering

Reviewing the mechanisms by which salts cause damage to stone in arid regions. The most destructive and most ubiquitous salts, and the means by which they enter stone and crystallise in rock pores are also outlined. Temperature is identified as a key regulator of crystallization behaviour.

1.11: The role of temperature in rock weathering

The role that wide temperature ranges in arid regions play in controlling moisture capillary rise and salt crystallization patterns is explored. Weathering by thermal fatigue stress is also identified as a factor in degrading heritage stone.

1.12-1.14: Integration of existing literature into the structure of this research

1.12: Mitigation- Identifying heritage stone at risk

Having identified risks to built heritage in the previous sections, the methods by which this project may aid in mitigating these risks must be identified. A review of some of the index systems that have previously been proposed for recording and categorising damage to stone and assessing the risk of further deterioration due to weathering is presented. The principle of triaging damaged heritage monuments so that resources are allocated to those most in need of intervention to prevent greater damage is also explored. These concepts are used to develop a proposed application of this research project; developing a risk index that can be used by conservation teams in the field to identify and triage heritage monuments damaged by ballistic impact. This will allow the identification of monuments most at risk of further deterioration that should be a priority for the allocation of resources.

1.13: Conclusions

The ways in which the reviewed literature will influence the focus and methods of the research project are outlined. Limitations in existing research that this project will seek to address are also detailed.

1.14: Research aims and objectives

Based on the conclusions drawn from literature reviewed in previous sections, the specific aims and objectives of this research project are defined.

1.1: Justification of Research- The need to protect built heritage

This research project aims to alleviate conflict damage to heritage monuments through the identification of damaged heritage sites at risk of further deterioration. It is therefore necessary to briefly outline the importance of heritage monuments and why research to protect them is justified.

1.1.1: The importance of built heritage to cultural identity

Many authors have maintained that built heritage sites play a critical role in creating a historical narrative with which an entire community can engage. This gives the community a collective focal point that emphasises the stability and continuity of the nation, and acts to cement societal bonds. Labadi (2007) gives the example of coronation sites that have been used for centuries and thus emphasise the repetition of national traditions throughout history, displaying societal unity and consistency with historical narratives of the nation. Labadi also contends that built heritage acts as a showcase for the values that a given community or nation may associate with and wish to project. Examples of these values include democracy (e.g. the Palace of Westminster, London), Justice (Gerechtigkeitsbrunnen, Bern) or religious devotion (The Great Mosque, Mecca) (Quinalt, 1992, Pulte, 2013).

In addition to their role in cementing societal narratives and presenting communal values, heritage monuments frequently act as areas for modern gatherings, festivities and socializing. These can include festive gatherings at religious sites, such as Diwali at the Golden Temple in Amritsar (Jutla, 2016), or secular events, such as the gathering of crowds outside the U.S. Capitol Building for presidential inaugurations and July 4th celebrations (Baumann, Engelhardt, Matheson, 2010).

Built heritage monuments and landscapes therefore serve to both record and continue historic traditions and values that create communal identity, and to facilitate gatherings and social activity in the modern day. Realising this, it could well be argued that built heritage is integral to both the formation and continuity of communities and nations, and that it is therefore essential that research to mitigate against loss caused by modern armed conflict is undertaken.

1.1.2: The economic importance of built heritage

In addition to the role that built heritage plays in forming the identity of communities, they are equally key to creating economic growth and activity throughout the world. Cultural sites act as a powerful draw for international tourism, which as an industry accounts for over 10% of global GDP, with 40% of international tourists classified as cultural visitors (World Travel and Tourism Council, 2019, Smith, Richards, 2013). The ability of heritage sites to boost economic activity through tourism was explored statistically by Su and Lin (2013) who found that a cultural site that was newly designated a UNESCO World Heritage Site boosted international visitor numbers by almost 400,000 and contributed as much as $21 billion to a country's economy.

The economic benefits of cultural heritage assets can be particularly pronounced in less economically developed countries if managed correctly. For example, as part of its economic reforms of the 1980's and 1990s, Vietnam placed a greater emphasis on tourism to historic sites such as the Imperial city of Hue. As a result, tourism accounts for around 6-7% of GDP in an economy that has seen rapid expansion since the reforms were introduced, and a corresponding increase in standards of living (Hall, Page, 2000, Nguyen, Cheung, 2014, Nguyen *et al,* 2013) .

Thus, in addition to the intangible cultural benefits of built heritage, there are also measurable economic positives that heritage assets confer. It is therefore in the interest of both global economic growth and development in economically disadvantaged areas that research is conducted into protecting such assets from conflict damage.

1.2: Armed conflict as a threat to built heritage

As discussed by Yarwood (2003) in relation to the Balkans War, cultural assets often become targets in times of conflict, as well as victims of inadvertent damage. During the Balkans conflict this was typified by the fighting in Mostar, which saw the deliberate destruction of an iconic Ottoman era bridge, as well as collateral damage to all of the city's historic Mosques.

The deliberate destruction of cultural property is itself a multi-faceted issue with a wide range of motives for combatants, which can include tactical battlefield advantage. This was the case in the destruction of the Parthenon in Athens. The site was used as an ammunition store by Ottoman troops in 1688, and a mortar fired by Venetian besiegers ignited the ammunition and

destroyed the site. This deprived the Ottomans of vital ammunition but destroyed an iconic landmark (Parsons, 2016). Cultural property has also been targeted in punitive expressions of imperial dominance. In response to earlier skirmishes, British troops attacked the African Kingdom of Benin in 1897, razing the city and looting some 2,500 cultural artefacts (Kiwara-Wilson, 2013). Other examples of damage to culturally significant sites are not driven by military reasoning, but by ideological or iconoclastic beliefs, such as the demolition of the Bamiyan Buddhas by the Taliban in 2001 (Flood, 2002).

Arguably, the threat that warfare poses to cultural heritage was not formally acknowledged until after World War II. During that time, looting of artefacts and wholesale destruction of historic city centres such as Warsaw prompted the international community to sign the 1954 Hague convention for the Protection of Cultural Property in the Event of Armed Conflict (Jankowski, 1990, Oyer, 1999). The convention served to create an international legal framework around cultural property in times of conflict. This included the compiling of inventories and contingency planning for conflict during peacetime.

Subsequent updates to the convention have recognised the role of non-governmental organisations (NGO's) in protecting cultural property. Among these NGO's are the International Committee of the Blue Shield, which was recognised as an advisory body to UNESCO on Cultural Property Protection under the 1999 Hague convention second protocol (Shimmon, 2004). In addition to other activities to mitigate damage to cultural property, Blue Shield has partnered with NATO to advise on minimising damage to significant sites during conflict (Rosen, 2017).

The efficacy of preventative measures such as inventories of heritage sites and the integration of NGO expertise into military planning was demonstrated by coalition air strikes in Libya in 2011. During this operation, knowledge of heritage inventories compiled by NGO's such as UNESCO, meant that Libyan government positions were successfully destroyed whilst avoiding damage to nearby Roman ruins (Cunliffe *et al*, 2018).

Other NGO's have highlighted the human impact of conflict damage to heritage sites, with the work of the Getty Institute suggesting that acts of deliberate vandalism often form part of a wider attempt to supress a target group. Such acts seek to destroy collective memories and identities, adding a cultural dynamic to acts of genocide (Luck, 2018, Weiss and Connelly, 2017).

As identified by the Getty report, the risks and consequences of damage to cultural assets are well documented, and a number of preventative and deterrent measures have been introduced since the 1954 Hague convention. These include inventories of significant sites, integration of military decision making with built heritage considerations, and legal penalties against international smuggling and looting of cultural property (Vlasic and Turku, 2016). However, emergency response capability to assess and remedy damage to heritage immediately after a conflict is arguably less well developed. This is illustrated by the first Blue Shield cultural emergency response missions to Iraq in 2003- taking place decades after the signature of the 1954 Hague convention (Van der Plas, 2004).

To support the kind of emergency fieldwork undertaken in Iraq in 2003, training programmes on methods for limiting conflict damage to cultural heritage in the field are being developed. These include courses offered by NGO's such as the International Committee for the Study of the Preservation and Restoration of Cultural Property (ICCROM). ICCROM runs annual training for conservation professionals aimed at securing heritage in the immediate aftermath of crises such as armed conflict. These programmes emphasise rapid response, dealing chiefly with the short-term stabilisation of damaged sites and salvage and rescue of mobile heritage (Lambert and Rockwell 2012). Examples include the evacuation of paintings from government buildings in Belgrade damaged by airstrikes in 1999 (*ibid*), and efforts to rapidly stabilise and re-open the temple of the tooth relic in Sri Lanka after the bombings of 1998 (Wijesuriya, 2000).

Whilst this approach undoubtedly saves invaluable cultural property from immediate destruction, it perhaps risks underestimating the potential for enhanced weathering of the damaged sites over time. Indeed, the ICCROM handbook on first aid to cultural heritage in times of crisis contains no mention of weathering considerations (Tandon, 2018). This is surprising given that deterioration from weathering has been shown to be a considerable risk to heritage monuments damaged by conflict. This is best demonstrated by the Church of St Luke in Liverpool, which was severely damaged by German bombing in 1941. The church was left damaged to commemorate the conflict, but due to enhanced weathering facilitated by bomb damage, portions of stonework were deemed in danger of collapse. As a result, the church was placed on the Heritage at Risk register in 2003. Stabilisation and renovation of the site was necessary to mitigate the weathering damage and the site was re-opened in 2017. This work cost £500,000, illustrating the potentially costly results of ignoring weathering risks posed by conflict damage (Blackett-Ord Engineering, 2014, Architecture Today, 2018).

It is also notable that none of the reports and publications highlighted here have discussed in detail the likely damage effects of the most common weapons on today's battlefields: small arms. This is because damage from explosive weapons often causes more spectacular and complete destruction than firearms. However, as the standard issue infantry weapon of every modern military, military owned small arms number some 133 million, and the total number of small arms globally is over 1 billion (Karp 2018).

With respect to ammunition, the most common cartridges are those that were stockpiled by the major powers during the Cold War. The standard NATO service rifle cartridge is the 5.56 x 45mm, with the US military alone manufacturing over 1 billion rounds a year between 2004-2008. This represented 5-6 times the production of any other NATO small arms cartridge (Siekman, Anderson, Boyce, 2010). The equivalent Warsaw pact ammunition, the 7.62 x 39mm, produced for AK-47 type weapons, was produced in vast quantities by Soviet countries and China. The 7.62 x 39mm cartridge is still widely used today because AK-47 type rifles are the most manufactured firearm in history, with an estimated 150 million units produced worldwide (Jenzen-Jones, 2017). These figures illustrate the sheer quantity of small arms on the battlefield. The lack of literature relating to small arms damage to heritage risks overlooking a key component of modern warfare that could pose a substantial risk to historic fabrics. This project will be focussed on the 5.56 x 45mm and 7.62 x 39mm cartridges, as these are by far the most widely used ammunition types in modern conflicts.

Having reviewed literature relating to conflict damage to cultural property, it is apparent that small arms damage and weathering subsequent to conflict damage have not been fully considered in existing research. Therefore, this project will seek to investigate these threats to built heritage in conflict zones and the relationship between them. It is hoped that this will ultimately enhance future emergency response methods. To this end, the literature review will seek to identify existing publications pertinent to small arms damage and weathering. This approach will identify literature gaps in these areas, allowing the research methods of this project to be tailored to address these gaps and maximise the impact of the research outputs.

1.3: Small arms damage to built heritage and stone

1.3.1: The increasing threat of small arms

As previously mentioned, small arms are the most ubiquitous weapons used in modern warfare, with an estimated 133 million military firearms worldwide. Furthermore, their availability is increasing; overall numbers of firearms increased by 15.7% globally between 2006-2017 (Karp, 2018). The problem of the proliferation of firearms is compounded when one considers that small arms have also greatly increased in their capacity to cause damage, as demonstrated by the work of Krenn *et al* (1995). This work compared early firearms with modern equivalents, some of the key ballistic performance indicators are summarised in table 1.1.

Table 1.1: *A table showing the comparative performance of a 16th century musket and a 20th century assault rifle, demonstrating the improvements in firearm technology (adapted from Krenn et al, 1995).*

Firearm	Projectile Mass (g)	Kinetic Energy at Muzzle (j)	Maximum Range (m)	% Hits at 100m (5010cm^2 target)
German Musket (1580's)	10.84	988	834	54.5
FN FAL Assault Rifle (1958)	9.45	3294	3980	100

Such increases in small arms' capacity for damage has had visible consequences for built heritage. This is exemplified by the defacement of the decorative urn and statuary above the Treasury building at Petra in Jordan. The façade was often targeted with small arms by treasure hunters in the past, who believed that the urn contained gold (Wright, 1998).

However, despite the demonstrable threat posed by small arms to built heritage, much of the literature that has discussed conflict damage to cultural property has been focussed on examples of wholesale destruction of entire sites using explosives. These include the demolition of archaeological sites in Syria and Iraq by the Daesh armed group (Zaradona, *et al*, 2017).

This focus on spectacular acts of demolition arguably obscures the large proportion of heritage monuments exhibiting partial damage caused by small arms impact. Examples of such damage range from 16th century musket ball impacts on English churches through to 20th century machine gun scars on the Fusiliers Memorial Arch in Dublin (English Heritage, 1995, Shiels, 2006).

One of the most prevalent materials used in heritage monuments damaged by conflict is stone, having been used continually for construction since Neolithic times (Gomez-Heras and McCabe 2015, Moffet *et al*, 2003, Becherini *et al*, 2016). Despite this, our understanding of the damage that projectiles can cause to stone is surprisingly limited. For instance, previous studies that have investigated the effects of military ammunition into stone used crushed rock rather than the consolidated blocks of stone used in the built environment (Borvik and Dey, Olovsson, 2015). The findings of this area of research are thus unlikely to be applicable when seeking to understand small arms damage to heritage monuments.

1.3.2: Existing literature on ballistic impacts into stone

The lack of literature on military small arms damage to stone means that we must review analogous publications on ballistic impacts in stone in other fields. For the purposes of this research, "ballistic" is defined as being concerned with free-flight projectiles propelled from a barrel by a gas rather than powered in flight (Carlucci and Jacobson, 2013).

Literature on ballistic impact into consolidated stone is available but consists largely of studies in meteoritics. This research often uses idealised non-military projectiles such as spheres to simulate meteorite impacts (e.g. Kenkmann, *et al.* 2011, Tedeschi, *et al.* 1995). Studies using spherical projectiles should be treated with caution when seeking to draw conclusions about pointed bullet impacts of the type fired by modern small arms, which are conical in shape to facilitate target penetration. This is because Antoun *et al* (2006) demonstrated the importance of projectile geometry in influencing damage to stone using computer modelling. Their work simulated impacts of spherical and long-rod projectiles of equal mass into limestone. The results showed that severe damage (defined as peak pressures > 100MPa) extended to depths 2-3 times greater when cylindrical projectiles were used.

Although the influence of projectile geometry on penetration depth into rock has been confirmed experimentally (e.g. Kumano and Goldsmith, 1995), it is worth noting that many studies on ballistic impact are based on computer simulation. These computer models are often designed to simulate penetrative weapons fired into military targets such as bunkers,

e.g. Fang and Zhang (2013) and Butler (1975). These computer models are chiefly concerned with projectile penetration rather than parameters that affect weathering processes such as fracture morphology. Given that this project is concerned with rock weathering after ballistic impact, such studies based on computer models of damage to military targets will not be applicable when developing methods. Therefore, this research will address this literature gap by ensuring that results are obtained through laboratory testing of ballistic impact in stone and subsequent weathering deterioration, rather than numerical modelling.

1.4: Ballistic impact fracture formation

As discussed, results obtained from spherical projectile impacts should be treated with caution in relation to conflict damage. However, these studies do enhance our understanding of how ballistic impact causes damage to the target stone. French (1998) summarised the findings of a number of laboratory studies involving projectile impact into rock as an approximation of meteorite impacts. Chiefly, damage is caused by two forces; the initial compressive stress wave induced by the projectile hitting the surface of the target, and the tensile rarefaction waves that arise when a compressional wave is reflected off an interface between the rock and a medium with a different wave impedance value. The characteristic impedance of a given medium, wave impedance is defined as: $Z=\rho c$ where ρ is the density of the material and c is the sonic velocity. In addition to density, wave impedance has also been shown by Zhang *et al* (2020), to be positively correlated with compressive strength, tensile strength and porosity. Collectively, these types of waves are referred to in this project as "stress waves", as opposed to shock waves, which are defined as waves that propogate at velocities in excess of the speed of sound in the medium(Housen, Holsapple, 2011, Campbell *et al*, 2022,)

Where stress waves have peak pressures that exceed the ultimate compressive or tensile strength of the rock, the rock fractures. It is also worth noting that in rocks with high wave impedance values, stress waves will propagate less far into the material and thus result in less widespread fracturing.

The typologies of damage caused by impact vary with the location relative to the impact site. Close to the point of impact, waves have sufficient peak pressures to induce shock metamorphism in the impacted stone, such as a change to the refractive index of quartz grains (Stoffler and Langenhorst, 1993, Grieve *et al*, 1995). Further from the impact, the peak

pressure of the compressive wave drops, and this is seen as a zone of fracturing in the areas immediately below the impact crater (French, 1998). Compressive waves that reflect off a free surface (defined as faces that interface with a medium with a different characteristic impedance) as rarefaction waves lead to fracturing and shattering in the near surface areas of the impact site. This induces spallation of the impacted rock, ejecting the sheared fragments from the surface and contributing to the excavation of an impact crater (*ibid*). This model of impact crater formation is depicted in Figure 1.1:

Figure 1.1: *A diagram showing the initial phases of impact crater formation due to compressive wave propagation and ejection of target material due to rarefaction waves. (Source: French, 1998).*

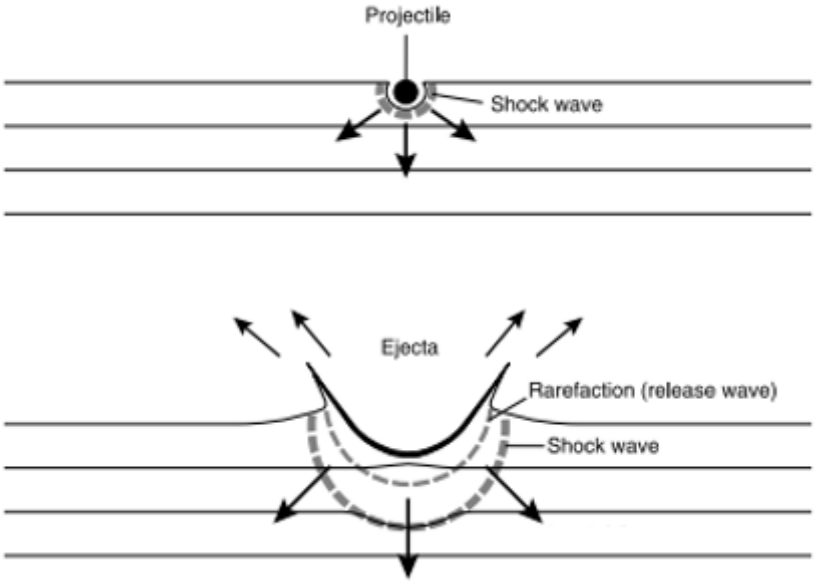

Polanskey and Ahrens (1990) classified the main fracture types that occur under this model by sectioning samples of stone impacted by projectiles. Crushing of the target stone in the area immediately below the impact results in a high density of shear fractures. Spall fractures occur in the near surface area immediately adjacent to the impact crater. Vertical fractures running parallel to the direction of impact arise as rarefaction waves reflect from the sides of the sample. The compressive waves are responsible for concentric fractures in the orientation of the hemi-spherical stress waves, and radial fractures running perpendicular to this. This fracture typology is shown in figure 1.2.

Figure 1.2: *An image showing the fracture morphologies present after projectile impact in stone (Source: Polanskey, Ahrens, 1990).*

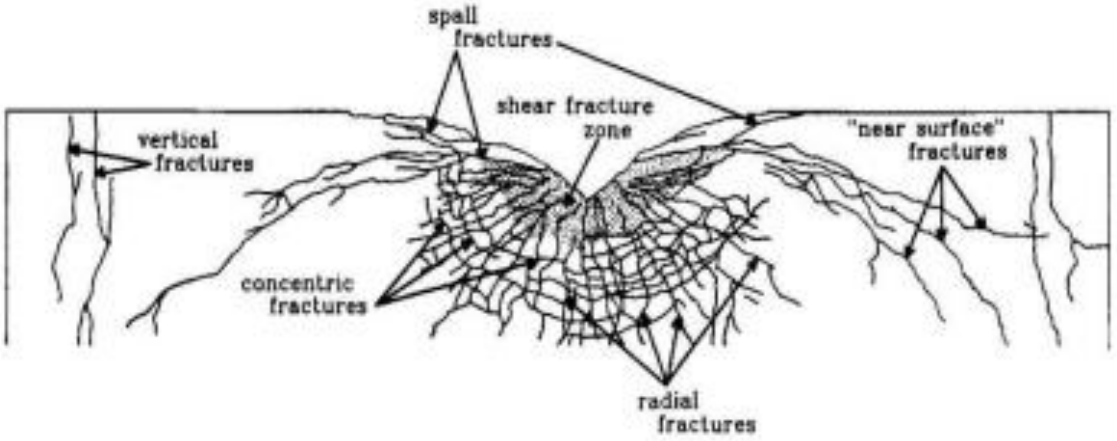

The projectiles utilised in Polanskey and Ahren's work were bullet shaped projectiles fired from a rifle rather than spheres. Therefore, this description of fracture morphology is hypothesised to be representative of the fracture networks that will be generated by the ballistic impacts generated in this research project.

Whilst the models of stone fracture under impact described above are primarily concerned with macroscopic (> 1mm) cracking, it is worth noting that this phenomenon has also been observed on a microscopic scale (<1mm). Scanning Electron Microscopy (SEM) analysis by Siegfried *et al* (1977) of granite impacted by an aluminium projectile showed fractures as narrow as 1µm in width across individual quartz grains. Microscopy also demonstrated that fractures caused by projectile impact are both inter-granular and intra-granular. This multi-scaled fracturing of rock damaged by ballistic impact will have an immediate effect on the mechanical properties of the target stone, as discussed in the next section.

1.5: Impact fractures and immediate damage to stone

The immediate effects of fracture networks on mechanical strength are best described by the Johnson-Holmquist II (JH-2) damage model. The model was created to develop numerical simulations of ballistic damage to brittle materials such as ceramic armour and has subsequently been applied to studies in rock (Johnson and Holmquist, 1999, Ma and An, 2008). The JH-2 model characterises intact, partially damaged and completely fractured materials by comparing their yield stress (σ) against the confining pressure (P) (Grujicic, *et al* 2011). As discussed by Ohnaka (1973), the yield stress of rock increases with increasing pressure. This increase in yield stress will be lower for partially damaged and fractured materials, and the reduction in yield stress is controlled by a damage constant D. Intact and partially damaged materials can withstand negative pressures up to the tensile yield stress of the material (T), whilst completely fractured materials cannot withstand any tensile loading. A schematic diagram of this model is shown below:

Figure 1.3: *A schematic representation of the JH-2 strength model.*

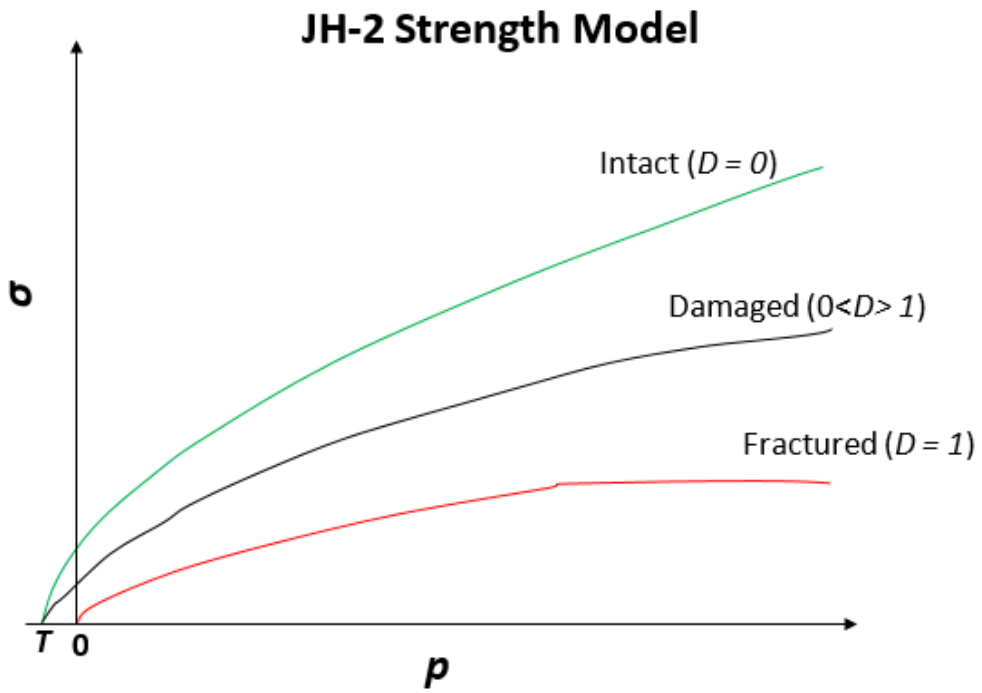

The damage constant *D* is the ratio between total accrued plastic strain and the plastic strain to fracture, such that an intact material will have a *D* of 0, and a fractured material will have a *D* of 1 (Wang *et al*, 2018). When the material undergoes sufficient plastic deformation it will fracture ($D = 1$), resulting in the failure of the material and a corresponding loss of strength.

The validity of the JH-2 model in which fracture networks decrease the mechanical durability of rock was demonstrated experimentally by Ai (2006). The ultrasonic velocity data of granite samples impacted with a lead bullet was found to have a negative correlation with JH2 computed values of peak pressures at impact. Low ultrasonic velocities were also shown to corresponded to fracture networks observed inside the sample after sectioning. This demonstrates the accepted model of fracture formation at impact- that fractures are created where the compressive or tensional pressures produced by a stress wave exceed the ultimate strength of the material (Ai, 2006). The attenuation of ultrasonic velocity in fractured samples observed by Ai also correlates to a lower elastic modulus of the sample, illustrating the ability of fracture networks to lower stone's resistance to deformation. This is termed "crack softening" (Ai, 2006). The significance of Ai's work work to this research project is that it provides direct evidence and an explanatory mechanism for the creation of fracture networks into stone by ballistic impact, which can then be exploited and exacerbated by subsequent weathering processes and resulting in long-term deterioration of the impacted stone, as discussed in section 1.6.

1.6: Fracture networks and weathering deterioration

The weakening that ballistic impact fracturing can cause to stone outlined above poses an obvious risk to heritage targeted in conflict. However, the potential for damage to the target stone is not limited to this immediate mechanical degradation. Fracture networks greatly increase the permeability of a stone sample and thus its susceptibility to the ingress of weathering agents. This increase in permeability was demonstrated by Lamur *et al* (2017) who measured the permeability of a variety of volcanic rocks of varying porosity before and after fracturing.

This work allowed the formation of an equation that describes the effect of a fracture network on the permeability of a given system:

$$\kappa_s = \kappa_\Phi + \frac{\rho_f \bar{l} \bar{w}^3}{A_i}$$

Where:

κ_s is the permeability of a fractured system

κ_Φ is the permeability of the intact system

ρ_f is the bulk fracture density (volume of fracture/volume of host rock)

$\bar{l}$ is average fracture length

$\bar{w}$ is average fracture width

A_i is the area of interest

An increase in permeability caused by fracturing will increase the ability of weathering agents such as water to enter the fractured rock, resulting in greater rates of weathering along fractures. This is exemplified by the observations of Billi *et al,* (2007). In this study it was found that areas of fault damage fracture in carbonate rocks experienced higher rates of dissolution weathering than areas where water flow was only able to exploit more tightly packed bedding planes. This preferential weathering of fracture networks means that the network is expanded further, and further increases the permeability of the fractured network. Worthington *et al* (2016) built upon these findings by showing that enhanced weathering along fracture planes increases permeability in silicate as well as carbonate aquifers.

This preferential weathering of permeable fracture networks and corresponding increase in permeability results in a positive feedback loop, whereby these areas become more likely to experience further increases in the intensity of weathering processes. Navarre-Sitchler *et al* (2013, 2015) described the feedback loop caused by weathering induced fracturing (WIF). The porosity and levels of plagioclase feldspar of quartz-diorite samples were analysed with neutron scattering and transmission electron microscopy techniques. The results showed that rinds from the weathering front of the rock had 9% higher porosity and 32% lower plagioclase levels when compared with un-weathered samples. This suggests that feedback

loops of chemical weathering at the weathering front increase porosity through WIF, and reduce plagioclase levels through dissolution and transport of the mineral due to water action.

The relationship between fracture networks and weathering intensity is further strengthened by fieldwork conducted by Ehlen (1999). This study collected data on the spacing, orientation and length of visible fractures at granite faces exposed to weathering processes and un-weathered granite exposed by tunnelling. This data was then used to construct 3-dimensional models of the sample sites and found that the density of fractures was 62% higher for weathered granite. The critical role that fracture networks play in contributing to the weathering processes of rock has also been demonstrated by Lebedeva and Brantley (2017) using numerical simulation. Using a simplified 2-Dimensional model of weathering front advance into a rock sample, the relationship between advance rate and fracture spacing was found to be non-linear, showing that a greater fracture density accelerates the advance of the weathering front. This is depicted in figure 1.4.

Figure 1.4: *The relationship between weathering advance rate and fracture spacing, as reported by Lebedva and Brantley (2017).*

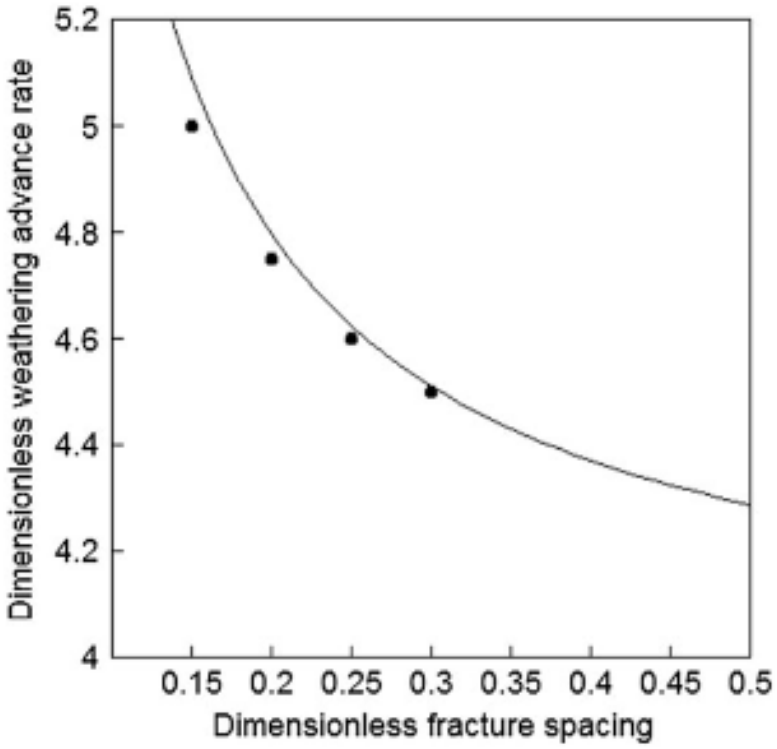

The research reviewed here shows that the fracture networks known to be caused by ballistic impact are likely to exacerbate weathering processes. This interplay between impact induced fracturing and weathering damage is a crucial component in understanding the threat posed to heritage by conflict damage.

1.7: The state of research into weathering of ballistic damage

Having identified a clear link between fracture networks caused by ballistic impact and their potential to enhance weathering, it should be noted that a limited number of pilot studies have begun to explore the relationship between conflict damage and weathering.

A 2017 study by Mol *et al* explored the effects of simulated case hardening weathering with Wacker masonry consolidant. Hardened and non-hardened samples were assessed for Picollo surface hardness before and after impact with a .22 calibre lead bullet. The case-hardened samples exhibited greater loss of surface hardness across the impact face than non-hardened samples after ballistic impact. This was hypothesised to be the result of the reduced plasticity in hardened stone, which facilitated the propagation of fracture networks throughout the surface. By contrast, the non-hardened stone was able to deform locally in the area of the impact via compaction of clay minerals, as observed under optical and SEM microscopy. This compaction resulted in an elevated hardness for the impact site in non-case hardened samples. These results demonstrate the crucial role that weathering processes such as case hardening play in determining the response of heritage stone to projectile impact. Specifically, they demonstrate that the weathering history of a given stone prior to ballistic impact (i.e. case hardening) is important in determining the mechanical response of that stone to ballistic impact, and therefore that weathering is not only an important factor after ballistic impact has occurred, but prior to impact as well.

In addition to hardness measurements, the movement of moisture via capillary action under temperature cycling of 15-65°C (to simulate the effect of groundwater in arid environments) was studied using Electric Resistivity Tomography (ERT). For the hardened samples, moisture was drawn throughout the surface of the stone, possibly due to an increased fracture network. Conversely, moisture was found to accumulate largely behind the impact site in non-case hardened stone. This was due to the compaction of clay minerals in the sample matrix observed at the impact site. Compaction of the matrix altered the moisture flow regimes through this area, resulting in the build-up of water. Higher moisture content and

evaporation though this area caused greater hardness loss to the impact site during weathering cycles than the rest of the non-consolidated sample surface (Mol *et al,* 2017). These results therefore agree with the model of moisture driven deterioration behind hardened areas of stone causing tafoni development as put forward by Mol (2014) and discussed later in this review. Such an agreement indicates that ballistic impacts have the potential to alter and exacerbate weathering processes.

The laboratory findings of Mol *et al* (2017) were partially confirmed with field observations of musket ball impacts on a sandstone church tower inflicted during the English Civil War (Mol and Gomez-Heras, 2018). Sandstone impacted by musket balls were found to have a higher Equotip rebound hardness than surrounding un-impacted stone. It was hypothesised that the lower velocities, rounded shape and soft lead construction of musket balls results in compaction of the clay minerals within the sandstone as previously identified. Although single impact sites were not found to have decreased hardness, blocks that had suffered multiple musket impacts had a greater deterioration in hardness due to exposure to weathering processes.

As well as investigating 17th century musket impacts, this study also showed that modern small arms have a much greater capacity to cause damage to heritage stone. Bullet impacts sustained by sandstone buildings from rifle fire during the 1930's Spanish civil war were found to decrease the hardness of the impacted stone more than individual musket impacts. In addition, Ultrasonic Pulse Velocity readings indicated the presence of fractures and voids behind the impact areas. These results demonstrate that there is a clear difference between musket impacts and modern ammunition. This is important given that Mol *et al*'s 2017 study investigated the effects of deformable .22 lead projectiles not commonly used in armed conflict. Therefore, there is a lack of laboratory research into the effects of impact from high muzzle energy (>1000J) military projectiles on the weathering processes of stone. Military projectiles have constructions designed for penetration (Manes *et al,* 2014), and will have differing damage effects to lead bullets when impacting stone (figure 1.5). The use of military ammunition in weathering experiments may therefore produce substantially different results to existing studies, and be more comparable to real-world damage.

Figure 1.5: *Images showing the differing constructions of military NATO M855 bullet (L) and a pure lead .22 long rifle bullet in cross section (R). (Sources: Campbell et al, 2022, International Ammunition Association)*

These studies have clearly demonstrated a relationship between ballistic impact and deterioration due to weathering in stone used in the built environment. However, many important variables have yet to be explored. Mol *et al* utilised a lead .22 calibre bullet in their 2017 study, which has a significantly lower kinetic energy than modern military grade ammunitions and is significantly more likely to deform on impact (Imperato and Sanchez, 2009). Furthermore, there was no consideration of the angle of impact of the projectile, which is a key factor in determining damage caused by a projectile (Cheon, Choi, 2016). Indeed, in high velocity meteoritic experiments, Gault (1973) observed that the mass of stone ejected after impact, which can be taken to infer levels of damage, is described by the equation:

$$M_e = 10^{-10.061} \, (\rho p / \rho t)^{0.5} \, KE^{1.133} \, (\sin i)^2$$

Where:

M_e is the mass of displaced stone

ρp is the density of the projectile

ρt is the density of the target stone

KE is the projectile kinetic energy

i is the angle of impact, such that $i = 90°$ is an impact with the target stone normal to the projectile trajectory.

As can be inferred from the term $(\sin i)^2$ the angle of impact has a non-linear effect on the mass of ejected stone, and therefore is likely to be a key factor in controlling the levels of damage caused by ballistic impact.

Finally, whilst two weathering variables were explored by Mol *et al* (moisture ingress and temperature cycling) no consideration was given to salt weathering. It is important that we gain an understanding of the interaction between projectile generated fracture networks in stone and haloclasty, as it is a principle means by which heritage stone is weathered (Hamed, *et al.* 2015). Therefore, this project will seek to investigate the effects of military ammunition impacts at differing impact angles on heritage stone, and how the resulting damage alters weathering processes including salt weathering.

The studies discussed here clearly demonstrate that fracture networks caused by ballistic damage are likely to exacerbate weathering issues in heritage stone. In order to address the long-term risks to cultural property posed by ballistic damage, it is therefore necessary that we review the weathering agents and processes likely to be encountered by heritage monuments damaged by conflict, as well as the stone types most commonly affected.

1.8: Weathering processes and stone types in conflict regions

As discussed by Pope *et al* (1995) the weathering processes in a given region will be controlled by a variety of localised climactic, chemical and biological parameters. Thus, it is important to specify the region, environment, and weathering processes we are concerned with in order to define the scope of this research. Identifying an area of interest will also allow the identification of stone types frequently used in heritage monuments in these regions.

Many of the recent examples of conflict damage to heritage monuments have occurred in hot arid regions of the Middle East and North Africa (MENA), such as Syria and Iraq (Danti, 2015). We shall therefore consider the weathering processes and stone types in arid areas to ensure our research is relevant to recent and ongoing conflicts.

Vaughn (2005) defined arid environments as regions where the supply of moisture due to precipitation is exceeded by the potential for evaporation from the soil and transpiration by vegetation (evapotranspiration). Low annual precipitation of 200mm-250mm, and summer temperatures in excess of 40ºC cause high evaporation rates that inhibit the growth of

vegetation. A lack of cloud cover means that arid regions are typified by large diurnal temperature ranges of up to 20ºC. A lack of vegetation can cause desertification in these areas, defined as a reduction in the potential for the land to host biological activity (*ibid*). Cooke *et al* (2006) reviewed the rock weathering mechanisms most prevalent in arid environments, and identified three factors which drive much of the weathering in these climates: moisture, salt and temperature. There is a great deal of interdependence between these weathering processes, as discussed later in this review.

In terms of the lithologies used in heritage monuments in arid regions, this is most easily assessed by determining which stones were quarried in the past. Some studies have investigated the stone types most frequently quarried in arid regions in antiquity. Among the most comprehensive of these are Oxford University's Roman Economies Project (Russel, 2013), and the Quarryscapes survey of Egyptian quarries conducted by the Geological Survey of Norway (Harrel and Storemyr, 2009). These twin sources were analysed to identify quarry types common to both, and the number of each quarry type is presented in figure 1.6.

Figure 1.6*: Stone types by number of quarries in arid regions of the Roman Empire and Egypt (adapted from Russel, 2013, Harrel and Storemyr, 2009). NB: Countries covered in arid regions of the Roman Empire are: Algeria, Egypt, Israel, Jordan, Lebanon, Libya, Morocco, Syria, Tunisia and Turkey.*

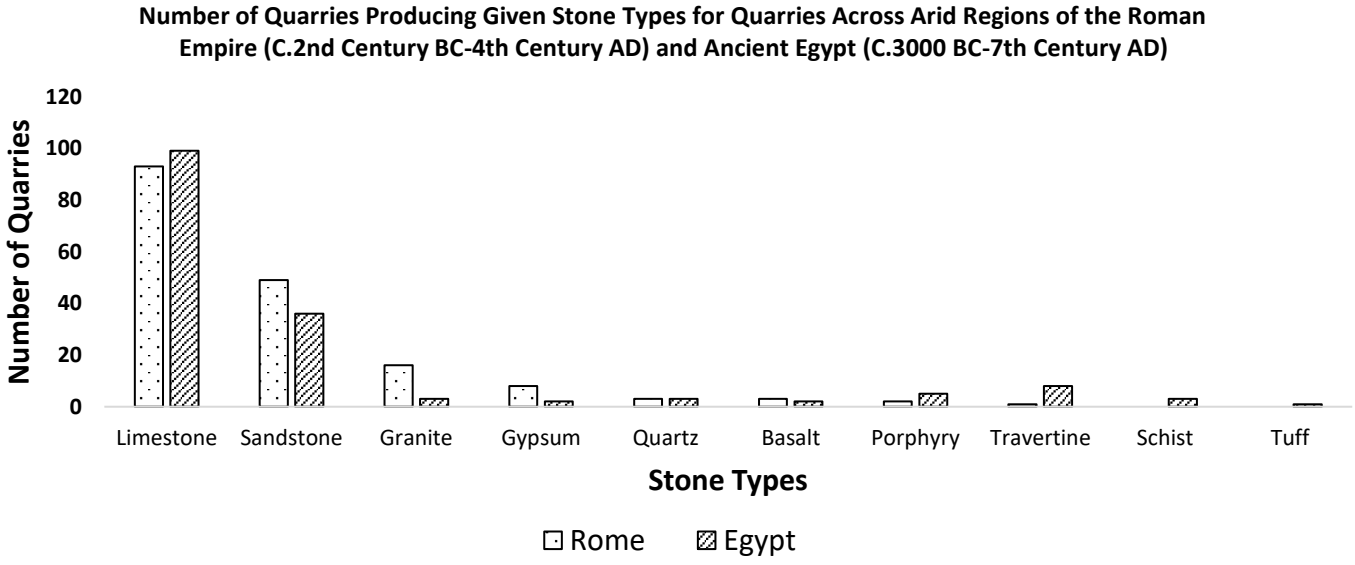

As illustrated in figure 1.6, the majority of quarries active in arid environments under these civilisations quarried either limestone or sandstone. This is confirmed by the fact that these lithologies are frequently used in the monuments constructed during these periods (Fitzner *et al* 2003, Lohmann, 2011). Furthermore, examples of damage to built heritage in these areas include limestone and sandstone monuments, such as Baalbek in Lebanon and the Bamiyan Buddhas (Tahan, 2007, Flood, 2002).

Therefore, the following sections of this review will focus on the weathering processes identified for arid MENA regions: salt, moisture and temperature. Where possible this will be achieved by assessing literature on the effects of these processes on the lithologies most commonly used in MENA built heritage: limestone and sandstone.

1.9: The role of moisture in rock weathering

1.9.1: Moisture as a chemical weathering agent

Water that enters stone causes weathering and degradation through a variety of mechanisms. Amongst these are the dissolution and transportation of the minerals that comprise the rock matrix, which reduces its mechanical strength. This dissolution and transportation can be achieved using de-ionised water under laboratory conditions, indicating that pure water itself acts as a chemical weathering agent. This was demonstrated by Duda and Renner (2013), who tested the triaxial brittle failure strength of saturated sandstone samples using distilled water. The results demonstrated that saturation with pure water could result in a reduction in strength of as much as 23%.

Similar experiments by Shakoor and Barefield (2009) recorded reductions in compressive strength of up to 71.6% for saturated sandstone samples compared to unsaturated rock. Shakoor and Barefield also showed that the largest reduction in strength was observed in samples with the lowest porosity. Duperret *et al,* (2005) suggested that the inverse correlation between porosity and strength reduction is because low porosity rocks have a greater surface area of matrix bridges between grains that can be dissolved and removed in solution by the water (*ibid*). This is supported by the findings of Lin *et al* (2005), who found that the dissolution and leaching away of clay matrix minerals such as illite and kaolinite was chiefly responsible for the weakening of sandstones during saturation.

Experimental studies into the effects of the dissolution and removal of rock matrix by water often make use of distilled water to explore these mechanics and isolate variables. However, weathering by water in nature is often facilitated and accelerated by chemicals dissolved in the water. This is the case for carbonic acid, which is formed when carbon dioxide (CO_2) in the atmosphere combines with water. When carbonic acid reacts with the calcium carbonate which makes up limestone, it forms calcium bicarbonate, which is highly soluble. The calcium bicarbonate is then dissolved by the water, and rapidly transported away in solution. These reactions are outlined below (Thornbush, Viles, 2007, Adamczyk *et al,* 2009):

$$CO_2 + H_2O \rightarrow H_2CO_3$$

Carbon dioxide + water → carbonic acid

$$H_2CO_3 + CaCO3 \rightarrow Ca(HCO_3)_2$$

Carbonic acid + calcium carbonate → calcium bicarbonate

This weathering by carbonation is arguably a lesser issue in arid regions than in cooler regions because the solubility of CO_2 reduces with increasing temperature, meaning that less will be dissolved in rainwater in hotter areas (Wiebe, Gaddy, 1940). However, Bader (2014a) documented the role that weak carbonic acid played in the degradation of the Leptis Magna world heritage site in Libya. The acid was found to contribute to disaggregation of limestone masonry in arches, demonstrating that the process should still be considered a risk in arid environments.

In addition to carbonic acid, weathering rates of stone are also accelerated by other pollutants that alter the pH of water. Water commonly reacts with atmospheric pollutants such as sulphur dioxide (SO_2) and nitrogen oxides (NO_X). This process forms mild acids that react with and dissolve rocks such as limestone. The reaction products are then precipitated as salt weathering crusts (Elgohary 2008):

$$SO_2 \xrightarrow{\text{Oxidation}} SO_3 + H_2O \rightarrow H_2SO_4$$

Sulphur Dioxide → Sulphur Trioxide + Water → Sulphuric Acid

$$H_2SO_4 + CaCO_3 \rightarrow CaSO_4 \cdot 2H_2O$$

Sulphuric Acid + Calcium Carbonate → Gypsum

Elgohary showed the ability of acid rain to dissolve heritage limestone at the ancient Citadel monuments in Amman, Jordan. Using optical emission spectroscopy, rainwater at the site was found to contain high levels of calcium cations, with common solutes being calcium bicarbonate and gypsum. As described in the equations above, the presence of these solutes suggests that weathering by both carbonic and sulphuric acids are a factor at the site. In addition to the structural weakening caused by dissolution weathering, the gypsum salt crusts created through these processes can cause significant aesthetic deterioration to the walls of heritage monuments through blackening, disaggregation, blistering and flaking of stone material (see section 1.10.2).

The problem of acid rain weathering of heritage monuments is a particular issue in urban areas, where levels of atmospheric pollutants are higher due to motor vehicles and industrial production. This was demonstrated by Trudgill *et al* (2001), who took micro-erosion meter (MEM) readings from the limestone of St Paul's cathedral in London over the course of twenty years. Comparing the data with air quality figures over the same period showed that erosion rates decreased from 0.13mm per year in 1981 to 0.05 in 1990, with a corresponding drop in SO_2 levels from 23 ppb to 7ppb over the same period.

Acidic rainwater has also been shown to attack and dissolve the silicate minerals such as mica and feldspar that constitute many sandstones used in heritage monuments. Acidic solutions have been demonstrated to increase the solubility of feldspar, which is the most common mineral in the Earth's crust and a principal constituent of many sandstones (Bevan and Savage, 1989, Nugent *et al,* 1998). The effect of acid rain on heritage sandstones was demonstrated experimentally by Holynska *et al* (2003). This research exposed samples of freshly quarried sandstone, as well as 100 year old samples from a cemetery to baths of saturated aqueous SO_2 solution with a pH of 1.5. X-Ray Diffraction (XRD) measurements of the samples prior to immersion was used to identify the minerals present in the stone. After immersion, samples of the SO_2 solution were analysed with Total Reflectance X-Ray Fluorescence (TXRF) to identify leachates removed from the sandstone by dissolution in the acid. XRD results showed that alumina-silicates, plagioclase feldspar, dolomite and hematite were the constituent minerals of the samples prior to immersion. The presence of these minerals resulted in a significant increase in the concentration of aluminium, magnesium and iron in the analysed solution due to acid attack (*ibid*). Although these results were obtained under laboratory conditions with far higher concentrations of sulphuric acid than are caused by atmospheric pollution, the effect of acid rain on heritage buildings has also been confirmed by field observations. Examples include the work of Nord and Tronner (1995), who attributed the surface deterioration of a sandstone palace and church in Stockholm to the deposition of sulphuric acid.

1.9.2: Moisture as a contributing factor in mechanical weathering

The ability of water and acid rain to dissolve, transport and precipitate mineral components of rock is also a key factor in the development of a weathering process typical of arid environments: case hardening and core softening.

Dorn *et al* (2017) proposed a model of case hardening that is primarily driven by moisture movement in the rock. Dissolution of matrix minerals in the outer layers of rock leads to an increase in porosity, and this porous outer layer is known as a weathering rind (Navarre-Sitchler *et al,* 2013). The porous nature of these rinds allows them to be subsequently infilled with harder indurating agents such as iron and manganese oxides and silica minerals (Figure 1.7). These indurating agents are carried into the pores in solution, and come from a variety of sources, including desert varnish, an Fe-Mn rich layer caused by biological activity on the

surface of the rock (Krinsley *et al,* 2017). Indurating agents are also provided by silica glaze, a surface layer on rocks rich in silica minerals, thought to be produced by winds blowing dust and soil against the surface of the rock (Smith, Whalley, 1988). Induration causes the outer millimetres of rock to become harder than those layers underlying it. This process is known as case hardening (Viles, Goudie, 2004). The difference in mechanical properties between case hardened rock and the un-weathered rock beneath mean that the two layers have differing expansion rates when subjected to heat. This, coupled with the pressures exerted by salt crystals which precipitate between the two layers, can result in the exfoliation and spalling of sheets of the rock's surface (Marszale *et al,* 2014). This surface spalling can result in the loss of surface features with cultural or heritage significance, such as the decay of rock art observed at Wadi Rum in Jordan (Paradise, 2014).

Below case hardened areas, rock unaffected by indurating agents continues to experience matrix dissolution of minerals such as feldspar. This weakens the rock below case hardened areas and is known as core softening. Dorn *et al* (2017) demonstrated this phenomenon with SEM imagery:

Figure 1.7: *SEM images showing case hardening and core softening of sandstones from Utah, USA (adapted from Dorn et al 2017).*

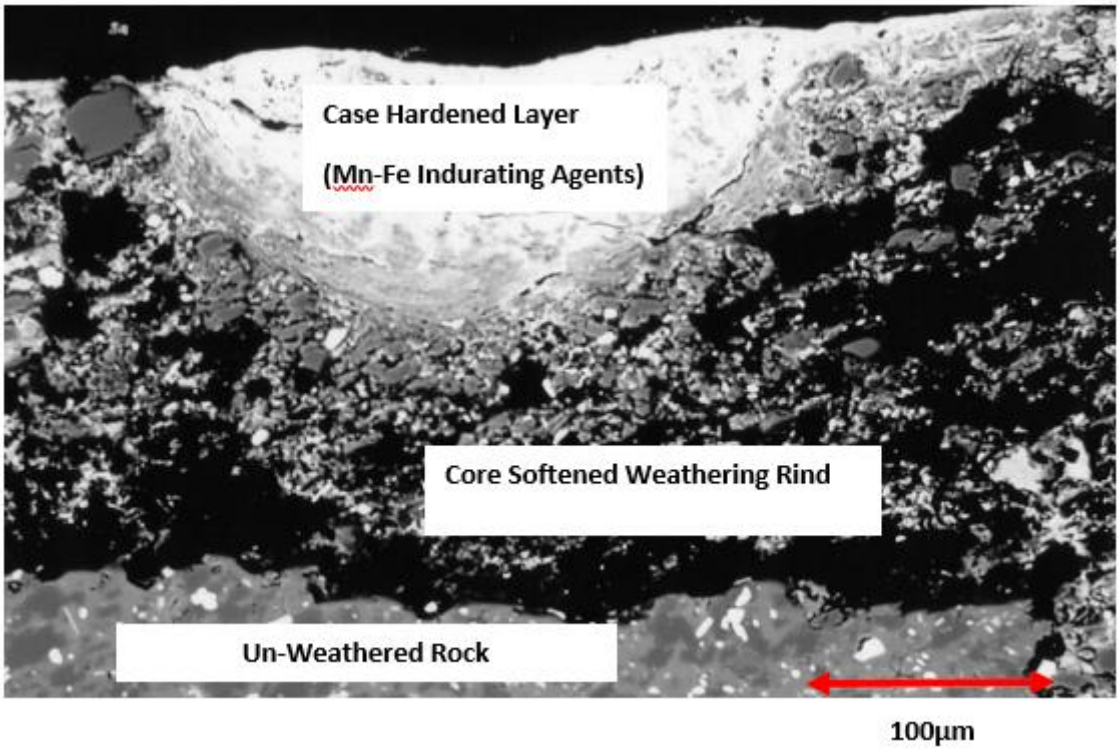

Conca and Rossman (1985) described how core-softening can contribute to weathering of rocks, by analysing samples taken from the exterior and interior of cavernously weathered tonalite boulders. Infrared spectroscopy and hardness testing of the samples suggested that greater moisture flow on the interior of the boulders had resulted in the chemical weathering of feldspar content to form kaolinite. An increase in kaolinite from 0.1% of the un-weathered rock to 2.1% in the weathered interior caused disaggregation of the matrix, making the interior of the boulders friable, and reducing hardness compared to the exterior. The weakening of the interior of the rock resulted in the formation of cave like excavations of the boulder.

Mol (2014) described a model where the interplay between case hardening and core softening is the driving factor in the development of cavernous weathering features. Mol monitored the moisture regimes in mega-tafoni over the course of a year using resistivity, protimeter water mass equivalent (WME) readings and temperature measurements. The results were compared with Equotip readings of rebound hardness at the same sites. Perhaps surprisingly, the results showed that an increase in moisture content was not always accompanied with a decrease in strength, which might be expected due to the weathering caused by moisture flow behind case hardening. Instead, a model was proposed in which a build-up of moisture and associated microbes behind a case hardened area initially acts as an adhesive to hold loose disaggregated grains of rock together. This build-up of moisture continues because the case-hardened surface reduces the evaporation rate, preventing the escape of moisture. This causes an increase in pressure behind the hardened surface that ultimately results in the flaking away of the surface material, and the exposure of the weakened surface. At this point the surface begins to harden due to induration as outlined above, and the cycle begins again, as shown in figure 1.8.

Figure 1.8: *A schematic representation of the cavernous weathering process proposed by Mol (2014).*

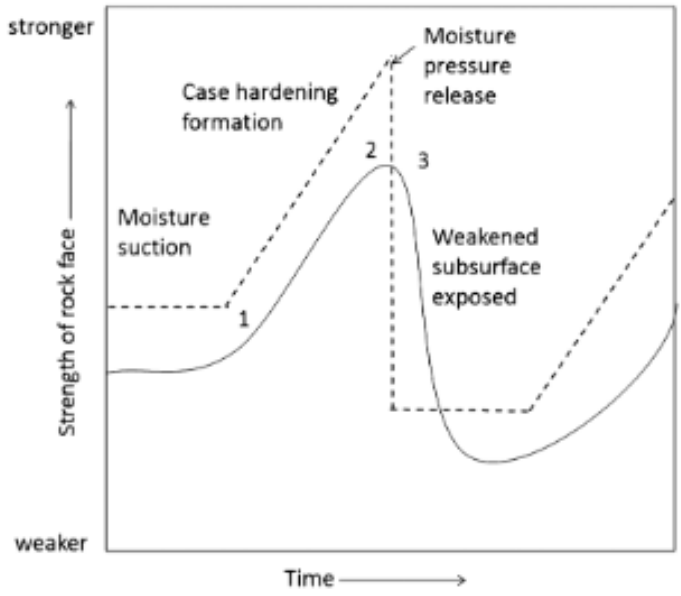

The cyclical nature of the model results in continual erosion, and the development of cavernous weathering is a serious risk to cultural heritage. This is because the build-up of moisture behind case-hardened rock and resultant flaking has been shown to degrade Neolithic rock paintings present at the Golden Gate National Park in South Africa (Mol and Viles, 2010). Furthermore, such cavernous weathering processes can result in the development of tafoni in sandstone (Mol and Viles, 2014). Such tafoni are known to damage the petroglyph rock art present in the Wadi Rum world heritage site in Jordan, and the sandstone tombs at Petra, as seen in figure 1.9, (Paradise, 2014, Franchi *et al*, 2009). It should also be noted that due to the concave, cavernous nature of ballistic impact craters, and the observation by Mol *et al* (2017) that bullet impact can cause hardening at the centre of an impact crater due to matrix compaction, whilst also preventing moisture through-flow and causing an accumulation of moisture (section 1.7), it seems plausible that a ballistic impact may act as a trigger event for the creation of the moisture driven case-hardening model of cavernous weathering outlined in figure 1.8.

Figure 1.9: *An image highlighting cavernous weathering/tafoni of the Obelisk Tomb in Petra, Jordan (Source: Google maps street view)*

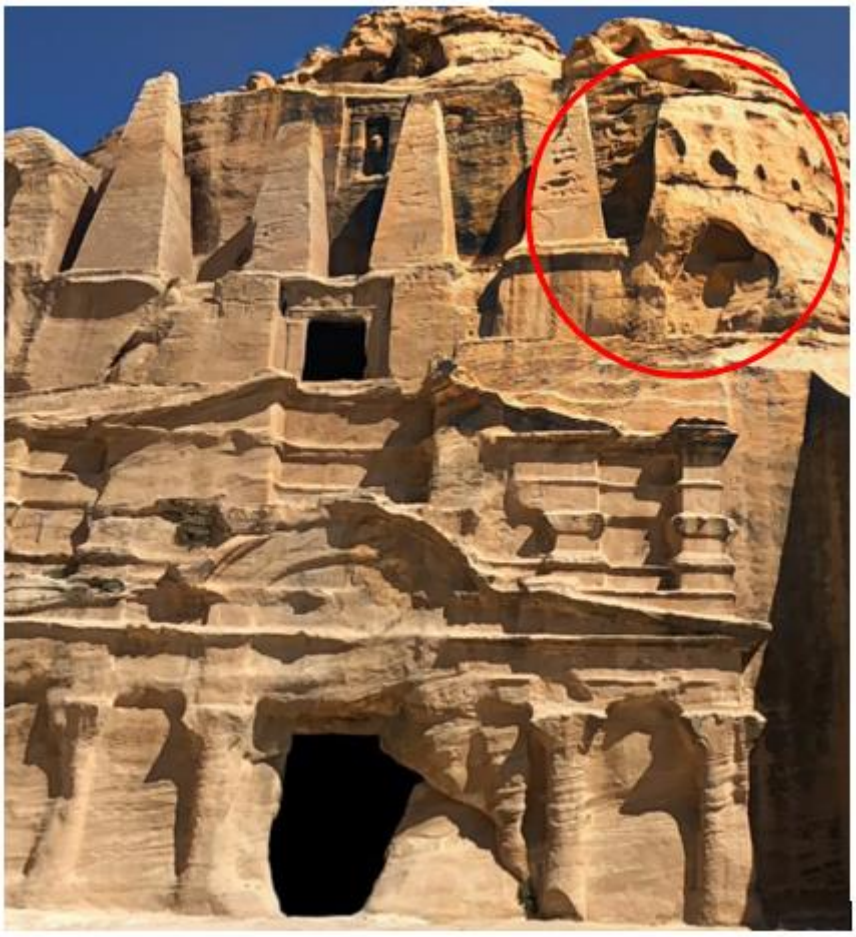

As reported by Young and Young (1992), the moisture flow regimes that result in the creation of tafoni and cavernous weathering formations are thought to be more severe when saline solutions are involved. This is illustrative of the critical role that dissolved salts can play in weathering processes, as will be seen in the following section.

1.9.3 Moisture as a vector for salt weathering

In addition to the transport of minerals and case hardening/core softening, the chemical reactions between water itself and the constituent minerals of rock may weaken the rock. For instance, oxidation of ferrous deposits within the rock by water can convert iron to iron oxide. This may weaken the rock cement and lead to disaggregation (Goudie, 2009). This kind of chemical weathering is characterised by reddish-brown staining on the surface of the

stone, and has been observed to be a contributing factor to the degradation of wall reliefs in the Egyptian Komir Temple complex (Bader, 2014b). Water can also damage stone in the built environment through hydrating minerals present in the rock matrix. This commonly occurs when anhydrite contained in the stone is hydrated to form the salt gypsum (Azam, 2001). As well as hydrating minerals to form salts, it should be noted that water acts as the primary means of transportation of salts into the interior of rocks. This is usually through intake of saline groundwater through capillary action or sea spray at coastal sites (Aly *et al*, 2015). Rise of saline groundwater has been documented to be a major cause of damage to the Karnak Temple complex in Egypt (Mahmoud *et al,* 2010), and salt damage to stone will be the focus of the next section of this review.

1.10: The role of salt in rock weathering

1.10.1: Salt Formation

Salts may occur in the built environment due to natural processes such as sea-spray, human action such as gritting of roads, or be contained in rock deposits themselves. These salts pose a serious threat to cultural heritage. This is demonstrated by the natural salt deposits found in the limestone quarried in the Thebes Mountains. These deposits are known to be a major deterioration factor in tomb wall paintings in the Valley of the Kings, as they are carved from the same formation (Hofman *et al*, 2012, Wust and Schluchter, 2000).

There are a number of different salt types, the chemistry of which it is necessary to understand in order to predict their likely weathering effects on heritage stone. A salt is formed by an acid-base reaction, in which the H(+) cation of the acid combines with the OH(-) anion of the base. The compound formed by the cation of the base and the anion of the acid is a salt (Zumdahl, 1996), e.g:

$$HCl + NaOH \rightarrow NaCl + H_2O$$

Hydrochloric acid + Sodium hydroxide → Sodium chloride + Water

The specific acid and base reacting will affect the morphology of the resulting salt crystals, which in turn affects crystallization pressure. Salt crystallization damage, or haloclasty, is the product of pressure exerted by the growth of salt crystals inside rock pores. This internal pressure serves both to weaken the pores the crystals grow in, and to exploit pre-existing fractures inside the rock (McGreevy, Smith, 1982).

1.10.2: Salt crystallization pressure and damage

Rodiriguez-Navarro and Doehne (1999) showed the role that crystal morphology plays in determining the crystallization pressures developed. Regular cubic crystals of halite (NaCl) caused less damage to limestone than larger, irregular anhedral crystals of sodium sulphate. This is because the monoclinic-prismatic structure of sodium sulphate concentrates growth and stress in a single axis, unlike the cubic structure of halite (Cooke, 1978).

The volume of these differing crystal morphologies will also affect the degree to which they damage stone. The importance of crystal volume is shown in the equation for crystallization pressure given by Charola (2000):

$$P = (RT/Vs)\ ln\ (c/cs)$$

Where:

P is pressure (atm),

R is the gas constant ($cm^3 \cdot atm \cdot K^{-1} \cdot mol^{-1}$)

T the temperature (K),

Vs is the molar volume ($cm^3 \cdot mol^{-1}$) of the crystal substance

(c/cs) is the ratio of actual concentration of saline solution to the super-saturation concentration achieved at high pressures inside pore spaces.

The crystallisation pressure is higher when the molar volume of the salt (Vs) is lower because the greatest pressures are exerted by crystals growing in smaller pores. Salts with a lower molar volume are more likely to crystallise inside these smaller pores and exert a higher pressure (Scherer, 2002).

The saturation ratio is a key term because the source of the outward pressure exerted by salt crystals is the result of repulsive forces between charged ions on the crystal surface and minerals in the pore wall (*ibid*). A super-saturated film between the crystal and the pore serves to grow the salt crystal and exert greater pressure by allowing the addition of extra ions to the crystal lattice (Desarnaud *et al*, 2016). A highly soluble salt will have a high concentration ratio and more ions in solution, and this will result in higher crystallisation pressures. A diagram of this crystallization pressure mechanism is shown in figure 1.10.

Figure 1.10: *Top- A diagram showing the lattice structure of NaCl and the ions which create crystallization pressure (https://commons.wikimedia.org/wiki/File:Ionlattice-fcc.svg).*

Bottom- A simplified diagram showing the development of salt crystallization pressure inside rock pores.

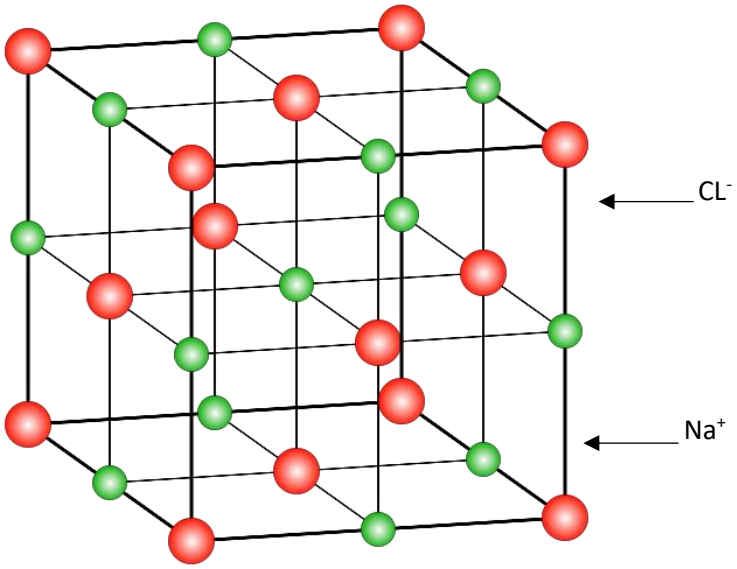

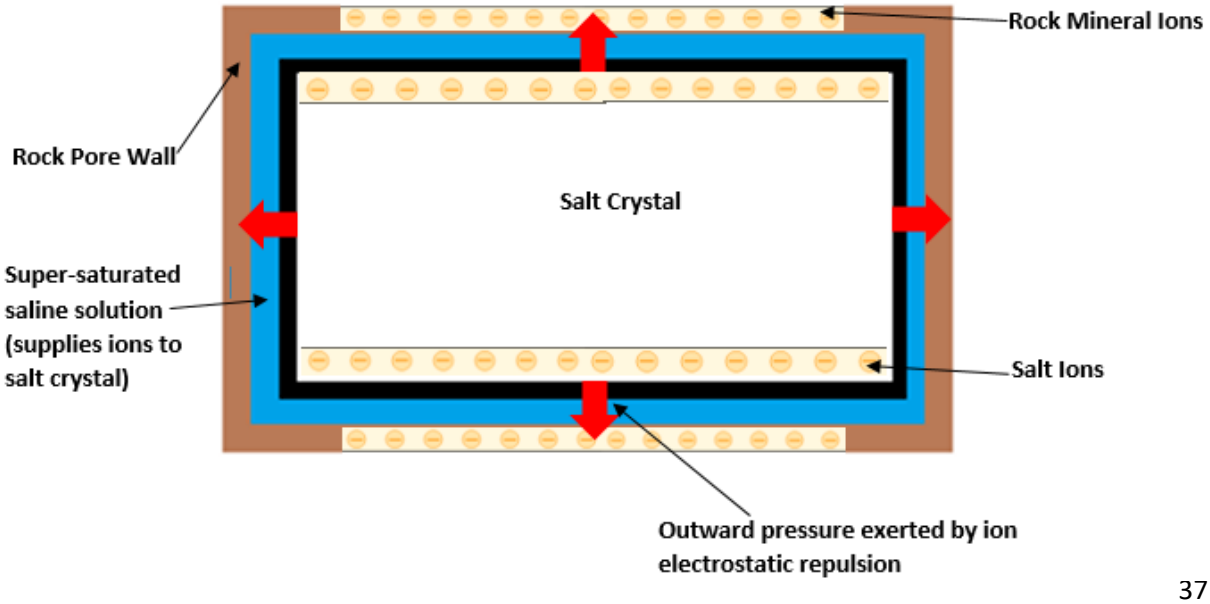

Desarnaud *et al*, (2016) demonstrated the damage induced by salt crystallization in pore space using SEM imagery. The images highlight the fracturing of quartz grains in sandstone affected by haloclasty, as seen in figure 1.11.

Figure 1.11: *A SEM image showing crystallization of NaCl crystals between sandstone pores and inducing fracturing of quartz grains (Desarnaud et al, 2016).*

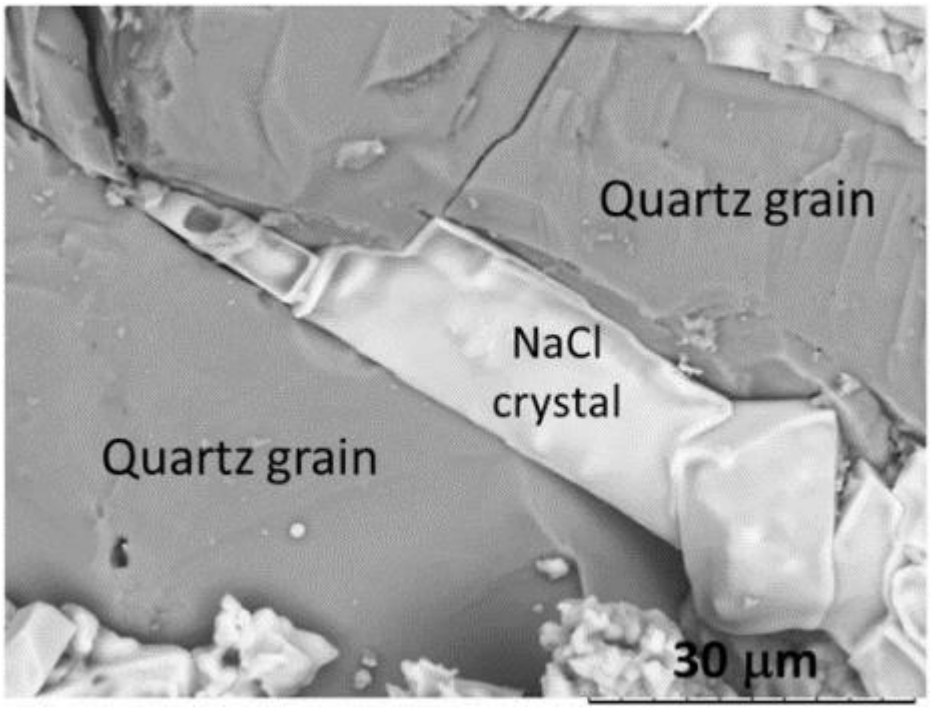

Highly soluble salts will allow for a greater quantity of salt in solution. This more concentrated solution will form crystals with larger sizes than less concentrated solutions. For a given rock pore size, larger crystals with a greater surface area and more repulsive ionic interactions will exert greater pressures than smaller crystals. This was observed for sodium sulphate when compared with sodium chloride crystals (Rodiriguez-Navarro, Doehne, 1999). For these reasons Cooke (1978) identified sodium sulphate as a particularly effective weathering agent of stone under arid conditions. This is because of its high solubility leading to greater amounts of salt available for crystallisation, as well as the fact that it is likely to precipitate out of solution during the wide temperature fluctuations in arid environments. The hydration of salts by moisture also presents a source of internal pressure, as hydrated sodium sulphate (mirabilite) can increase in volume by 314% compared to its anhydrous form, thenardite (Tsui *et al*, 2003). Similarly, anhydrite ($CaSO_4$) expands by 63% when hydrated to form the salt gypsum ($CaSO_4 \cdot 2H_2O$) (Azam, 2001).

1.10.3: Differences in salt damage profiles

The differences in the solubility, morphology and hydration expansion of various salts results in differing capacity for damage. Goudie *et al*, (1970) compared rates of haloclasty in Arden sandstone caused by five salts ($CaCl_2$, $MgSO_4$, NaCl, Na_2CO_3, Na_2SO_4). This was achieved by measuring the loss of mass and splitting of the samples through disaggregation caused by crystallization pressure. Samples were contaminated with salt solutions and mass measured after 40 cycles of temperature cycling between 30-60°C. For both methods of measuring deterioration (mass loss and number of fragments that sample split into) the most destructive salt was Na_2SO_4 (sodium sulphate), followed by $MgSO_4$ and $CaCl_2$. Although NaCl and Na_2CO_3 did not cause mass loss during these experiments, this should not be taken to mean that these salts are not damaging. In fact, samples contaminated with NaCl exhibited a gain in mass after weathering cycles (figure 1.12), this is attributable to a build-up of damaging salt crystals over time increasing the sample's mass (*ibid*).

Figure 1.12: *A chart showing the change in mass of Arden sandstone samples contaminated with different salts (Goudie et al, 1970).*

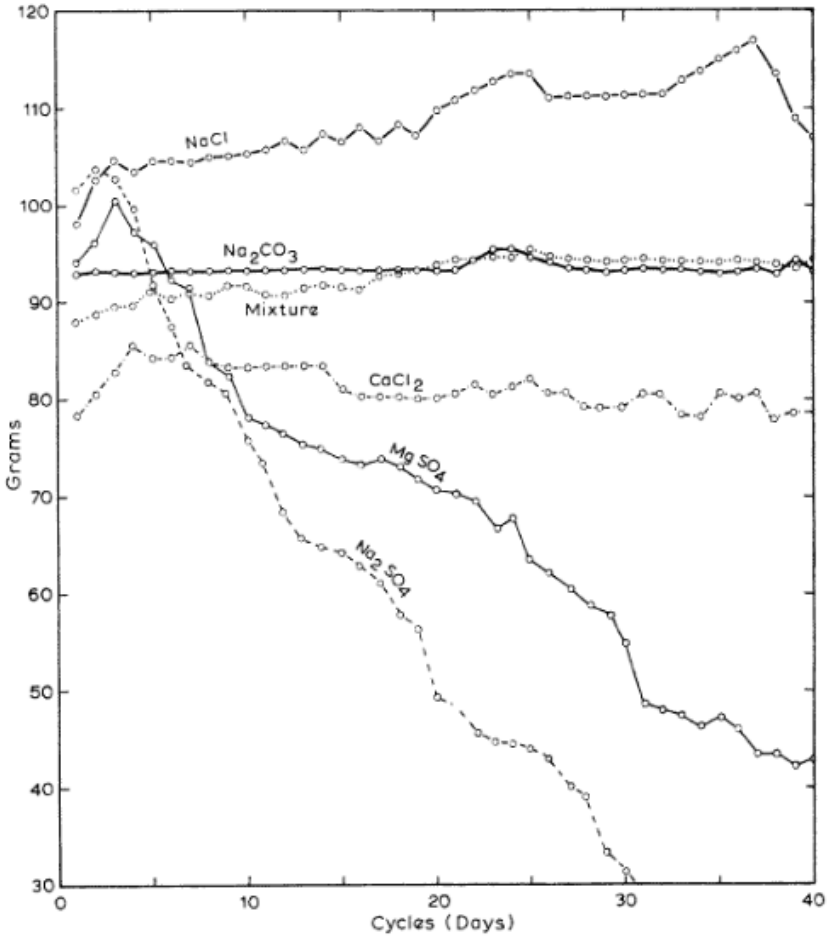

In addition to salt characteristics such as solubility and crystal morphology, Rodiriguez-Navarro and Doehne (1999) highlighted another key factor in the process of haloclasty: the location of crystallisation within the rock. When water containing salt moves to the surface of stone and evaporates there, salt crystals are left behind on the face of the stone. This process is known as efflorescence (Veran-Tissoires, Prat, 2014).

Although it is not considered detrimental to the structural integrity of masonry, it can damage and obscure any surface carvings or paintings present on heritage stone. This has been observed with the loss of hieroglyphs and wall paintings in the Theban necropolis (Wust and Schluchter, 2000). Furthermore, gypsum efflorescences caused by atmospheric pollutant weathering on limestones has been shown to exacerbate weathering on heritage monuments in Budapest and London (Török, 2007, Sabbioni *et al.* 2004). This is caused by detachment of the salt crusts along with the underlying stone, causing blackening, flaking, blistering and disaggregation of the surface of heritage monuments, as shown in figure 1.13:

Figure 1.13: *An image showing gypsum crust weathering morphologies on historic stone in ghent, Belgium (adapted from De Kock et al, 2014).*

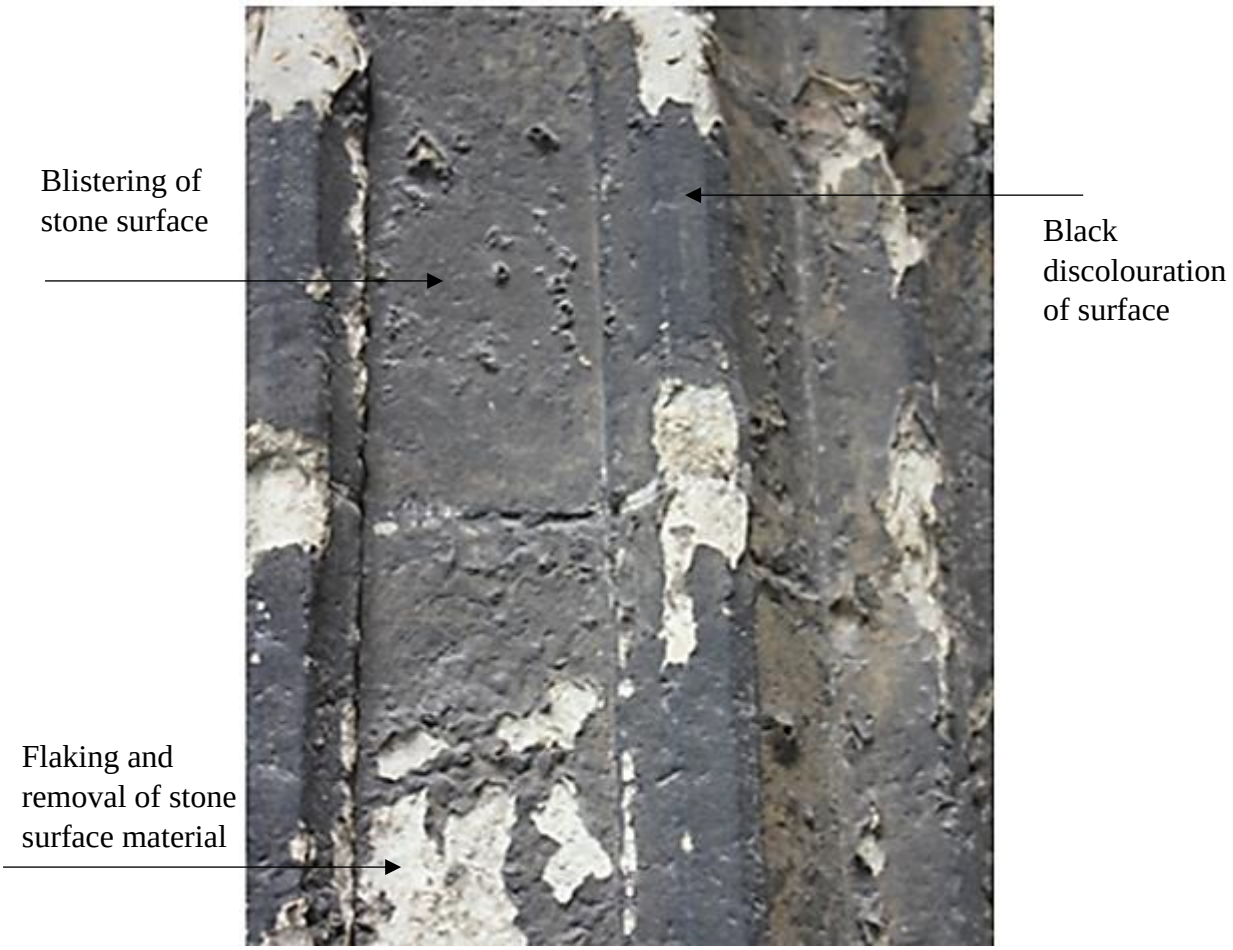

Conversely, Subflorescence occurs when salt crystallises in sub-surface regions of the stone. This results in the damaging build-up of internal pressure inside rock pores already discussed (Espinosa-Marzal *et al*, 2007). Subflorescences can rapidly lead to the degradation of heritage monuments and have been shown to damage structural pillars in historic churches (Giustetto *et al*, 2007). As with crystal morphology, the location of salt crystallisation (efflorescence vs sub-florescence) is controlled by a number of factors. These include the concentration of salt solution, solubility of the salt, temperature, porosity and pore size of the material (*ibid*).

The complex interplay between the parameters controlling salt damage to stone was explored by Sperling and Cooke (1985). This was achieved by comparing the mass loss of Hollington sandstone samples exposed to a sodium sulphate solution. The experiments varied temperature and hydration levels across four samples to determine whether crystallization, temperature or hydration of sodium sulphate crystals caused the greatest deterioration. The results are shown in figure 1.14.

Figure 1.14: *A chart showing the differing deterioration rates of Hollington stone depending on temperature and hydration of salt crystals (Sperling and Cooke, 1985).*

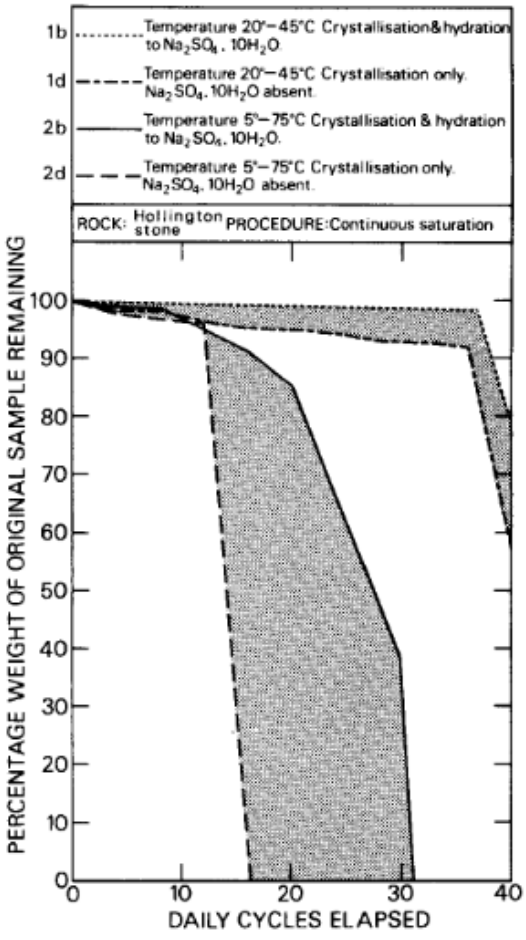

The results presented in figure 1.14 suggest that a wide temperature fluctuation that facilitates the precipitation of salt crystals out of solution is the most influential factor in the rate of haloclasty. It also appears that crystallization pressure alone is more likely to lead to rapid deterioration than the hydration of salt crystals.

This suggests that pressures induced by hydration expansion of salts are significantly lower than those generated by smaller, un-hydrated crystals. This is in agreement with Scherer (2002) who stated that the greatest pressures are created in the smallest rock pores.

1.10.4: Sources of salt in arid regions

Haloclasty is a common weathering process in arid regions because there are many natural sources of salt contamination in these areas, including the natural deposits inside rocks highlighted earlier. Other sources include sodium bicarbonate from the evaporation of saline lakes. Such deposits have been observed in East Africa and are known to increase the Ph of water (Christensen, 2003 Singer and Stoffers, 1980). Alkali aqueous sodium bicarbonate can increase the solubility of rock minerals such as quartz (Crundwell, 2017), and is known to be a factor in rock weathering and breakdown in the rift valley (Goudie and Cooke 1983). Such an availability of natural salts is a serious risk to heritage monuments in arid regions, as described by Bradley and Middleton (1988). Deteriorated Egyptian sculptures in the collection of the British Museum were analysed for salt content and compared with un-deteriorated sculptures. The seriously decayed sculptures exhibited far higher concentrations of soluble salts, and the decay caused by these salts was graphically illustrated with images of the sculptures over time (Figure 1.15).

Figure 1.15: *Images showing the decay of a salt-contaminated Egyptian sculpture over time (Adapted from Bradley and Middleton, 1988)*

1920 **1940** **1983**

The availability of naturally occurring salts and the role of wide temperature variations in transporting and precipitating salt crystals in solution means that heritage in arid environments is particularly at risk from haloclasty. This is exemplified by the extensive salt damage observed at the Carmona Roman necropolis in a semi-arid region of southern Spain (Benavente *et al* 2011). Seasonal precipitations out of solution of naturally occurring salts had resulted in efflorescence that disfigured Roman murals inside the Postumius tomb, whilst subflorescences had contributed to the degradation of structural mortars. Benavente *et al* identified temperature variations at the site as being a key factor in facilitating the degradation of stone at the necropolis due to haloclasty.

In coastal regions of arid countries, saline sea spray provides an abundant source of salts that contribute to haloclasty deterioration of heritage structures, as exemplified by XRF, XRD and microscopic analysis of deterioration at the Anfushi's Necropolis site on the Island of Pharos, Egypt. Study of samples recovered from material lost from the Necropolis walls due to weathering revealed that the proximity of the site to the Mediterranean sea (300m) cause saline sea spray to create large build ups of both halite and gypsum salts which were the chief driver of weathering deterieoration at the site (Fahmy *et al*, 2022).

In order to understand the degradation of built heritage in arid regions, it is now necessary that we review the influence of the extreme temperature regimes typical in these areas on the weathering processes commonly encountered.

1.11: The role of temperature in rock weathering

1.11.1: Temperature variation as a control on water ingress

As discussed previously, diurnal temperatures in arid regions often exhibit wide ranges. Figures for summer temperatures in tropical arid regions typically have daily averages of 31 ºC. Peaks as high as 58 ºC have been recorded in Tripoli, Libya, and daily lows of 15 ºC (El Fadli *et al,* 2013). These extreme temperature regimes play an important role in regulating the rate of weathering by moisture ingress and haloclasty.

The primary mechanism by which salt and other pollutants enter building stone is through capillary rise of contaminated groundwater into the stone. The tendency of a given material to allow moisture movement through capillarity is known as water sorptivity, and is given by the equation (Karagiannis, *et al,* 2016):

$$S = \frac{A_w}{P_w}$$

Where:

S is water sorptivity ($m \cdot s^{-1/2}$)

A_w is the capillary rise coefficient of a given material ($kg \cdot m^{-2} \cdot s^{-1/2}$)

P_w is the density of water ($kg \cdot m^{-3}$)

Experimental studies by Karagiannis *et al* (2016) showed that as air temperature increases, the capillary rise coefficient (A_w) of a given material increases and the density of water ($P_{w)}$ decreases. This results in greater water sorptivity, and more water is taken in through capillary action. For sedimentary stones analysed in this study, an increase in temperature from 20 ºC to 30 ºC resulted in increases of sorptivity of 22-55%. This clearly shows the integral role that temperature plays in regulating moisture ingress into stone-built heritage.

Higher capillary rise will affect the intake of saline groundwater and alter rates of haloclasty. The interplay between increased capillary action due to higher temperatures and corresponding increases to evaporation rates on salts were investigated by Aly *et al* (2015). Cores of Mokattam limestone, of the type used in the construction of the Giza Pyramids, were subjected to continual saline moisture circulation at their base (10% NaCl solution). Temperature was altered between 20 ºC, 30 ºC and 40 ºC to simulate an arid environment over a period of 144 hours. At 20ºC, low capillary rise and low evaporation rates meant that little change was obvious in the cores, as the salts remained in solution.

An increase to 30 ºC allowed more water to evaporate and resulted in efflorescences at the top of the sample. Ion chromatography showed that salt concentrations were highest in the top centimetre of the cores, as capillary action had drawn the saline solution upwards to this area. At 40 º C, salt crystallization primarily took the form of subflorescences at the top end of the cores. High concentrations were reached at the top of the cores within 24 hours for these samples, as opposed to 144 hours for samples kept at 30 ºC. This discrepancy is due to higher capillary rise rates and increased evaporation at 40ºC. These results are shown in figure 1.16 and illustrate the extent to which temperature is responsible for regulating moisture flow and corresponding rates of haloclasty in stone-built heritage.

Figure 1.16: *Charts showing the increase in salt concentration with distance from the base of limestone cores due to temperature-controlled capillary rise over 24 hours (Adapted from Aly et al, 2015).*

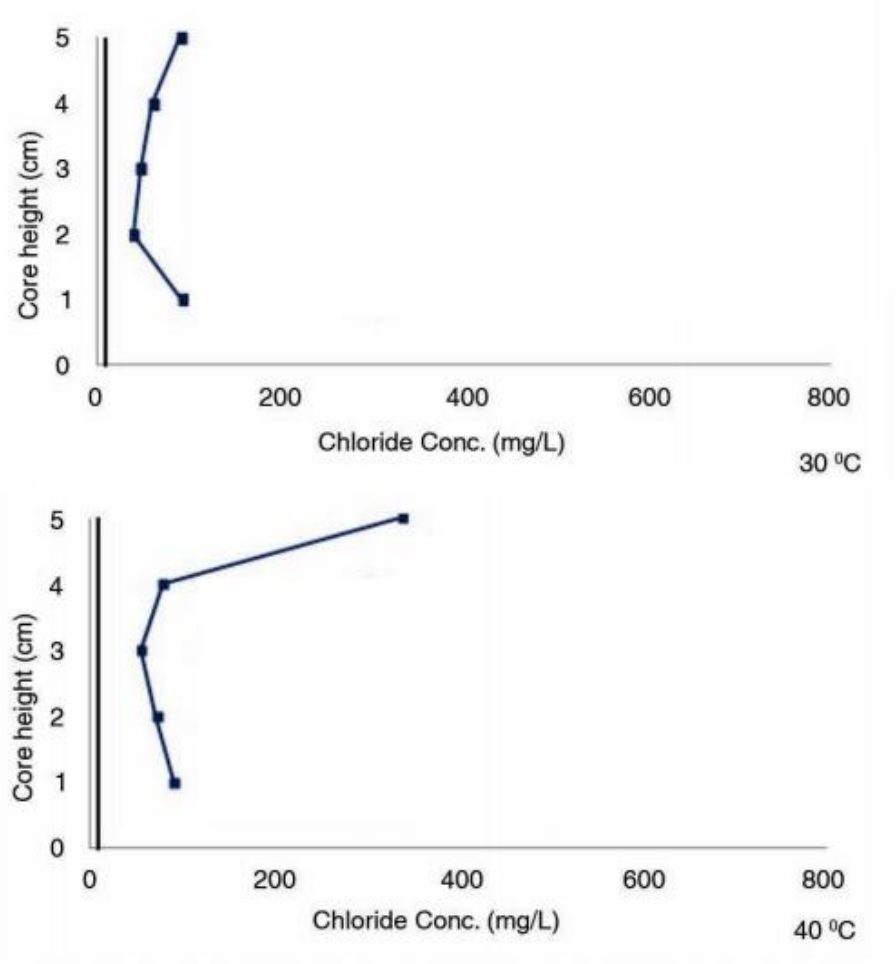

1.11.2 Temperature variation as a control on salt precipitation

Temperature also controls haloclasty by mechanisms other than capillary rise. Firstly, salt solubility is closely related to temperature. Generally, salt solubility increases with temperature (Potter and Clynne, 1978), but there are notable exceptions. At certain concentrations, sodium sulphate decreases in solubility at temperatures both above and below 32.4ºC, and calcium sulphate decreases in solubility with increasing temperature (Rodriguez-Navarro and Doehne, 1999, Klimchouk, 1996). Secondly, high temperatures will increase the evaporation rate of moisture from the rock, and thus precipitate salt crystals out of solution (Smith and McGreevy, 1983). These mechanisms mean that wide temperature variations and high peak temperatures found in arid environments are likely to facilitate

repeated cycles of crystallisation, dissolution and re-crystallisation of soluble salts present within rock.

Shahidazadeh and Desarnaud (2012) investigated the effects of recrystallization cycles of salt by repeatedly saturating and drying sandstone samples contaminated with an NaCl solution. Samples lost 6% of their mass due to disaggregation of the sandstone matrix arising from re-crystallization. Seeking to understand the process that makes re-crystallization destructive to the stone, the researchers investigated the re-crystallization process on a microscopic scale using phase contrast microscopy. The results showed that salt that re-crystallized under slow evaporation rates were significantly larger than crystals precipitated from the original saline solution. This was attributed to the gradual evaporation of the solution resulting in higher concentrations of salt in solution before the nucleation of crystals, ultimately forming a smaller number of larger crystals (Figure 1.17). These larger crystals contained in the same pore size will result in an increased crystallization pressure and a greater level of damage to rock. Therefore, these results show how re-crystallization of salt, facilitated by temperature-controlled solubility and evaporation rates, will increase rock weathering deterioration in arid regions.

Figure 1.17: *Microscopy images showing the increase in size between original NaCl crystals (L), and re-crystallized NaCl due to evaporation (R). (Shahidazadeh and Desarnaud, 2012).*

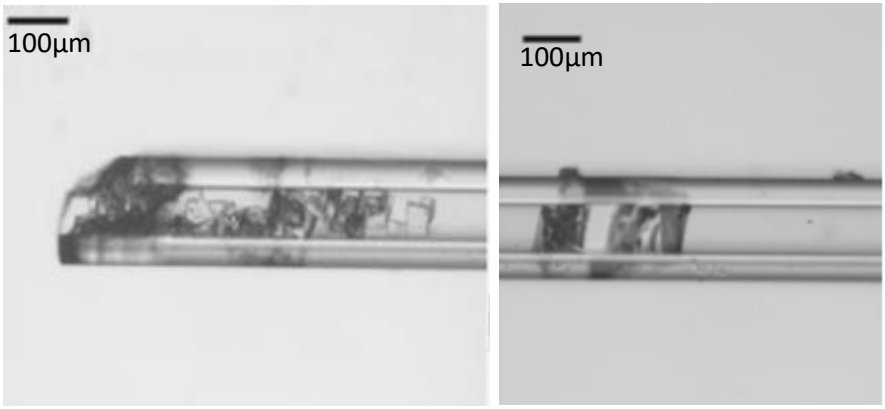

1.11.3: Temperature variation as a factor in mechanical weathering

In addition to accelerating the processes of moisture ingression and haloclasty, extreme temperature cycles also contribute to the weathering of rock through thermal stress weathering. When the surface of a rock is exposed to high temperatures, such as radiative heating from the sun in arid environments (insolation), the outer layers of rock will undergo an amount of thermal expansion (Weiss *et al,* 2004). This thermal expansion will be lower than that of the underlying layers of rock and will therefore establish a tensile stress between the outer and inner layers of the rock. Over time, these repeated daily stresses can weaken the rock and ultimately lead to fracturing (McFadden *et al,* 2005). This process of rock weathering has been observed in the field by Eppes *et al* (2010) who concluded that the orientation of surface fractures in rocks in hot arid deserts could be statistically correlated with seasonal variations in the direction of insolation. The orientation of rocks resulted in preferential heating of certain areas due to exposure to the sun, and these areas exhibited greater fracture densities with similar orientations. Furthermore, orientation of fracture patterns were found to be related to seasonal variations in the path of the sun (*ibid*). It should be noted that there has been some historic debate over whether insolation weathering due to heating by the sun is a significant weathering risk in and of itself, or whether it acts chiefly to exacerbate weathering by chemical agents such as moisture and salt. Turkington and Paradise (2005) point to a number of laboratory studies that suggested that insolation weathering alone had little effect on sandstone. Conversely, Paradise noted a significant variation in weathering rates depending on solar exposure of sandstones in Petra, Jordan.

Thermal stress fatigue weathering is undoubtedly a threat to heritage in field settings, as shown by the degradation of San rock art sites in South Africa (Hoerle, 2006). This is thought to be caused by the differing thermal expansion rates of the pigments used to create the art and the rock, creating stress between the paint and the substrate that leads to deterioration (Hall, 2007). Furthermore, predicative modelling suggests that global warming will mean that thermal stress fatigue is a greater threat to built heritage in the future (Bonazza *et al,* 2009).

Taken together, the availability of saline ground water or sea-spray in arid regions (as discussed in section 1.104, and the controlling factor that the temperature variations found in arid regions have on capillary rise of moisture and precipitation of salt (sections 1.11.1, 1.11.2) lead to the hypothesis that these weathering factors pose the greatest risk to heritage stone damaged by ballistic impact. Therefore, the weathering portions of the experimental work of this PhD project will be dedicated to investigating the links between ballistic impact and the deterioration caused by these mechanisms.

1.12: Mitigation- risk indexes and triaging of damaged monuments

1.12.1: Risk Indices

It is hoped that this research project will ultimately produce outcomes that contribute to conservation and mitigation of conflict damage to heritage monuments damaged by conflict. This research is not concerned with conservation strategies or techniques, but is focussed on creating research outputs that can be used to identify damaged monuments most at risk of future deterioration, so that conservation professionals can make informed decisions about where resources should be allocated and what solutions are appropriate.

Methods for making these decisions should ideally be appropriate for in situ assessment, and not require expert knowledge, so that non-experts can engage with the process and effectively record and assess ballistic damage to heritage assets in the field.

Previous work has demonstrated that it is possible to develop indices based on in-situ observations and measurements that can accurately assess the potential for weathering processes to cause substantial decay to stone monuments. These include the durability index employed by the Building Research Establishment (Inkpen, 2003), or the damage index for stone monuments proposed by Fitzner, Heinrichs and La Bouchardiere (2002). These damage indices categorise weathering deterioration by type and intensity, determined through the absolute scale of the deterioration. This is used to assign the weathering damage a category from 1-5, with 5 indicating very severe damage (*ibid.*). This system is highly versatile and allows for the recording of damage profiles in localised areas of a monument, or across the entire monument surface. Furthermore, case studies have shown such a system can be used to identify specific monument areas most in need of conservation, and to inform targeted intervention to preserve the overall historic structure (*ibid.*). The system developed by Fitzner

et al is comprehensive, listing 75 individual weathering forms, and thus allows detailed and accurate recording of weathering damage.

The comprehensiveness of a damage index must be weighed against the ease of use, and the time taken to train individuals in the system. It is desirable that the system be user-friendly and easy to interpret. This will mean that data can be collected and processed by conservation professionals as well as volunteers or "citizen scientists" who may wish to aid in efforts to preserve built heritage in the aftermath of armed conflict. This principle is at the core of another system for identifying weathering deterioration to stone monuments- the Rock Art Stability Index (RASI) proposed by Dorn *et al* (2008). This is a more concise system than Fitzner *et al*, Identifying 36 weathering forms across six broad categories. These are scored from 0 (not present) to 3 (dominant). When the survey has been completed, the overall score of a rock art panel is used to determine a risk level. Trials conducted showed that volunteers with no training in rock art decay and preservation were able to use the system to categorise and record weathering risks with minimal training across two days. This is clearly advantageous in deploying such a system in the field, as training and implementation by fieldworkers can be rapidly delivered.

It is clear from these previous works that index systems that categorise and score damage type and severity to infer the risk of deterioration to stone heritage are an effective method for ensuring that conservation efforts are appropriately targeted. It is therefore proposed that the findings of this research project are used to develop an index system that will score a number of variables, (angle of ballistic impact, ammunition type, target lithology, presence of weathering agents etc.) to determine the risk of further decay to stone monuments damaged by ballistic impact. This system will be based on measurements of geotechnical indicators of stone deterioration after ballistic impact observed under laboratory conditions and through fieldwork. These include decreases in stone surface rebound hardness, increases in permeability, the likely presence of internal fracture networks and the penetration of moisture and salt. The methods used to assess these geotechnical indicators of deterioration must be both portable and non-destructive, so that findings are reproducible and applicable to in-situ testing of heritage monuments in the field.

1.12.2: Principles of Triaging

Through statistical analysis of the effect of the variables listed above on measurable indicators of stone deterioration, it is hoped that a risk scoring system for every variable can be developed. It will then be possible for the overall risk to a damaged monument to be aggregated, and this information can be used to prioritise the most at risk sites for intervention. It is suggested that the process of using risk scores to prioritise conservation decisions should follow a triaging system. Triaging is used widely in the medical community to determine which patients are most in need of immediate medical intervention to preserve life, and which patients' needs are less urgent. Woo (1991) suggested a means by which this approach could be adapted to the preservation of cultural heritage monuments. Woo describes a four-tiered system of heritage monument triage:

Class I: monuments of significant historic or cultural value and in danger of immediate and substantial degradation without intervention.

Class II: monuments that require some routine restoration or maintenance work but are not in imminent danger of catastrophic decay. Class II designation means that time can be taken to undertake detailed assessment and intervention strategies can be planned.

Class III: monuments that require little or no intervention.

Class IV: monuments that are in such disrepair that expenditure of time and resources to maintain them cannot be justified. Strategies to deal with this class include benign decay or immediate removal. Monuments designated for benign decay are allowed to degrade naturally over time through weathering and other processes, but are guarded against vandalism or demolition. If a monument poses a danger through collapse or other risks, then immediate removal of the monument may have to be undertaken. In these cases, a monument should be extensively recorded prior to removal, and subsequent commemoration is possible.

The principles of triage are also being applied to heritage sites in the face of imminent climate change that will likely lead to significant change or destruction at vulnerable sites. This approach may be successful in allocating resources to sites of greatest significance, and those where resources are most likely to result in a desirable outcome (Perry, 2019, Berenfeld, 2015). Based on these frameworks, it is clearly possible to apply the principles of triage to at risk heritage monuments, and it is hoped that the risk indexing system for

monuments damaged by ballistic impact developed by this research project can be integrated into a triaging system for conflict damage monuments.

1.13: Conclusions

Throughout the various sections of this literature review, a variety of issues facing heritage monuments damaged by conflict, particularly those susceptible to advanced weathering, have been identified. Furthermore, a number of areas in which the existing literature could be improved or supplemented with further research have become apparent. The research outputs of this project will therefore be tailored to take account of the existing theories and methods used in weathering science, and to address gaps in the state of current research. The principal conclusions of this literature review are outlined below, and they have been used to inform the research aims and objectives in the following section.

Conclusion 1: Cultural heritage is frequently a target in warfare, either for tactical advantage or as inadvertent collateral damage. Despite this, small-arms ballistic damage to stone is not well understood. Previous studies on impacts into stone have used non-military projectiles, such as deformable pure lead bullets, spherical projectiles, or numerical simulations of impacts. Angle of impact is also often discounted. Therefore, this research will seek to determine the immediate damage caused by military ammunitions impacting stone.

Conclusion 2: Emergency response procedures to conflict damage to cultural property focus on immediate salvage and stabilisation. Often, they do not consider long-term deterioration such as enhanced weathering potential. This can have damaging and costly consequences for cultural property and understanding how small arms damage affects weathering processes is a principle aim of this research.

Conclusion 3: Many recent and ongoing conflicts that have damaged heritage monuments take place in hot arid environments. The principal weathering processes in these regions are moisture ingress, salt weathering (haloclasty) and temperature cycling. Despite this, the small number of studies on ballistic impact and weathering have not investigated processes such as haloclasty. This project will therefore seek to address all of these weathering parameters in conjunction.

Conclusion 4: The lithologies most commonly used in heritage monuments in these areas are limestone and sandstone. Therefore, weathering processes will be investigated in relation to their effects on these stone types.

Conclusion 5: Previous studies have shown that indexing systems can allow field-based conservation experts and non-expert volunteers to accurately record and assess damage severity and risk to heritage stone. Therefore, this research project will aim to develop findings into a risk index system that will identify which variables (ballistic impact, ammunition type, monument lithology, weathering processes) are likely to cause the most severe deterioration.

Ultimately it is hoped that this risk index can be used to identify monuments most in need of targeted intervention, allowing a triaging system of monuments damaged by conflict to ensure that resources are allocated to sites most in need and where resource expenditure will have the most beneficial outcomes.

1.14: Research aims and objectives

The overall aim of this research is to determine how ballistic impacts from 5.56 x 45mm and 7.62 x 39mm ammunition affect weathering processes on sedimentary stones used in heritage monuments in arid areas (limestone and sandstone). This will be assessed through non-destructive measurements of geotechnical indicators of stone deterioration due to weathering after impact. Findings will be used to develop a risk indexing system and field methodologies that can be used by conservation teams in the field to triage conflict-damaged heritage monuments most in need of conservation intervention.

These aims will be achieved by answering the following research questions. The research questions will be answered by completing specific Research Objectives, as outlined.

Research Question 1: *"How does modern military ammunition affect the investigated stone types in the immediate aftermath of an impact?"*

Research Objective I: To develop field appropriate non-destructive methods to assess exterior and interior damage to limestone and sandstone arising from military projectile damage (7.62 x 39mm and 5.56 x 45mm).

Research Objective II: To use the methods developed under Research Objective I to compare and isolate the effects of changing calibre, angle of impact and target stone type on the damage caused by ballistic impact before weathering using experimental simulations of ballistic impact into heritage stone. This will determine which variables have the greatest effect on damage levels prior to weathering.

Research Question 2: *"How do weathering processes affect the degradation of impacted stone?"*

Research Objective III: To assess the effects of arid environment weathering processes (haloclasty, moisture, temperature change) on the deterioration of stone after ballistic impact and investigate the interaction between ballistic impact and subsequent weathering processes to determine if weathering processes exacerbate damage initiated ˙by ballistic impact.

Research Question 3: *"How do lithology, ballistic impact and weathering conditions combine to deteriorate stone, and which combinations are the most damaging?"*

Research Objective IV: To use statistical analysis of results from weathering experiments on simulated heritage stone samples impacted under differing ballistic and weathering conditions to construct a risk index that can be used to assess the level of risk to damaged stone based on information on target lithology, ammunition, impact angle and weathering conditions.

Research Objective V: To “ground truth” the laboratory based methods that the risk matrix is based on through fieldwork. This will involve identifying and exploring links between weathering risks and exacerbated deterioration of ballistic impacts to ensure that observed links between ballistic damage and weathering behaviours are applicable to real-world situations and can be identified in a field setting using the methods developed in this project.

These Research Objectives have been used to inform and justify the methodological approach to this research. To ensure the clarity of this thesis, at the beginning of each experimental chapter the Research Objectives addressed in that chapter are outlined in the “chapter overview” section along with any other chapter goals. These are then discussed in detail in the introduction section of each chapter.

Chapter 2

Laboratory techniques for surface survey of stone damaged by ballistic impact

Chapter 2 Overview

Chapter 2 aims and hypothesis

The aim of this chapter was to partially address Research Objective I by developing non-destructive techniques of assessing exterior damage to stone that has experienced ballistic impact. It was hypothesised that non-destructive techniques used in other works investigating the integrity and weathering susceptibility of heritage stone, namely surface hardness and permeability survey, would be appropriate and useful in the study of heritage stone damaged by ballistic impact as they would allow quantification of relative damage levels to different areas of an impacted stone sample.

Chapter 2 methods

Systematic rebound hardness and permeability survey was undertaken across the surface of a sandstone sample shot with 7.62 x 39mm ammunition using portable, non-destructive equipment. The data was explored statistically to quantify indicators of damage and spatially to determine patterns of damage distribution.

Chapter 2 principal findings

Findings suggest that the impact surface of shot stone has significantly lower hardness and higher permeability than un-impacted areas of the same stone sample. Spatial analysis of permeability data can also be used to map surface fractures induced by the ballistic impact. These findings demonstrate that these techniques are a viable, non-destructive and portable method of assessing exterior damage to stone caused by ballistic impact and should be considered for future in-situ work on damaged heritage sites as part of this PhD work.

2.1: Introduction

In order to ensure the validity of experiments undertaken during this research, it was first necessary to develop and test experimental methods through a pilot study. This pilot study was conceived with the goal of partially fulfilling Research Objective I : "*To develop non-destructive methods to assess exterior and interior damage to limestone"* (section 1.14). To achieve this, two methods were chosen: Equotip surface hardness survey and Permeability survey. The results were interpreted statistically to determine the overall mechanical effects of ballistic impact on stone as well as spatially using the ArcGis Pro software package. This allowed the exploration of spatial trends across the impacted sample to determine which areas were most damaged by the impact.

2.2: Background

As discussed in section 1.7, hardness testing has been shown to be an appropriate method for assessing the effects of ballistic impact on stone weathering. Work by Mol *et al* (2017) showed that compaction of the impact crater results in a higher hardness in this area and altered moisture ingress and mobility patterns that result in an accumulation of moisture behind the impact area. Fieldwork by Mol and Gomes-Heras (2018) across sites damaged by a variety of historic ammunition types has also shown that rebound hardness testing can demonstrate that differing projectile morphologies and kinetic energies (musket balls vs rifle bullets) result in differing changes in hardness, reflecting differing damage profiles.

However, these previous works have not explored the effects of ballistic impact from military ammunition on rebound hardness profiles immediately after impact. The 2017 study used small calibre .22 deformable lead projectiles not used by military weapons, whilst the 2018 field study explored the effects of Mauser rifle projectiles on limestone after over 80 years of potential weathering since the Spanish Civil war. Therefore, this pilot study was designed with the aim of determining if rebound hardness survey was useful in determining damage patterns to stone immediately after impact.

In addition to changing hardness profiles due to ballistic impact and resultant weakening, knowledge of the fracture networks that will facilitate ingress of weathering agents will be needed to inform conservation strategies. Miao, Yu and Fang (2015) have shown that an increasing fracture density increases the permeability of a fracture network in stone, thus allowing water and associated solutes to penetrate the stone more easily. In addition to contributing to the degradation of the surface of the stone, the presence of surface fractures

caused by projectile impact has been shown to be indicative of a wider fracture network in the interior of the impacted material (Ai and Ahrens, 2014). This interior fracture network will increase the mobility of weathering agents within the stone and exacerbate deterioration (see section 1.6). Therefore, understanding surface fracture networks will aid in identifying likely points of ingress for weathering agents such as moisture and salt that may further degrade the structure. To achieve this goal, permeability survey could identify "areas of interest" on the surface of impacted stone that can then be assessed for interior fracture networks using other techniques. Such permeability survey was trialled in this pilot study by mapping the spatial distribution of areas of high permeability, so that areas at greatest risk of deterioration due to weathering could be easily identified.

This pilot study therefore sought to establish surveying techniques for assessing damage profiles to stone immediately after ballistic impact, and the risk this damage poses for future deterioration. These techniques were developed using two portable, non-destructive instruments appropriate for in-situ testing: The Equotip 550 portable hardness tester and Tiny Perm 3 Air Permeameter. This is in partial fulfilment of Research Objective I. Data from these methods was then analysed quantitatively using statistics packages and mapped spatially using ArcGIS Pro to determine the distribution of damage patterns in stone to identify at risk areas.

2.3: Materials and Methods

2.3.1: Sample Preparation

A sample of well consolidated mesoporous sandstone measuring 14.7cm x 14.7cm 14.7cm was sourced from the Huesca region of Spain. This region is semi-arid and previous works have used samples of this sandstone to explore weathering mechanisms in semi-arid climates, including their implications for built heritage (Micallef, 2003). The stone was freshly quarried to avoid any pre-existing defects caused by exposure to weathering. Selected geotechnical properties for this stone are presented in table 2.1.

Table 2.1: *Selected data geotechnical data on the Huesca Sandstone (Micallef, 2003, Mol et al, 2017).*

Geotechnical Property	**Value**
Density	2450 Kgm^{-3}
Compressive Strength	15.3 x 10^6 Nm^{-2}
Young's Modulus	23 Gpa
Average Pore Size	40-70μm
Water absorption Capacity	1.8%

The sample was shot with a 7.6x39mm cartridge fired from an AK-103 assault rifle at a range of 200m, which is a reasonable combat engagement distance (Erhart 2009). Each side of the sample was then given a number designation. Figure 2.1 shows the allocation of side numbers on the block. Figure 2.2 (A-F) shows the condition of individual sides of the block post-impact. A large portion of the block adjacent to the impact crater was shattered/sheared away due to the ballistic impact. This region was designated as the shattered surface, and a differing sampling regime was designed for this area of the block due to its irregular topography.

N.B: The experimental work of this chapter was conceived as a pilot study for the purposes of developing in-situ techniques for assessing ballistic damage to stone, and not to simulate impact into any particular real-world heritage stone type. The sample was not prepared by the author, and was made available for study after being used in a previous study into ballistic impact by other authors, the results of which were published in a previous study:

Mol, L., Gomez-Heras, M., Brassey, C., Green, O., and Blenkinsop, T. (2017). The benefit of a tough skin: bullet holes, weathering and the preservation of heritage. *Royal Society open science*, *4*(2), 160

Figure 2.1: *A schematic diagram showing the system for assigning side numbers. Side 1 contains the projectile impact crater, sides 2-4 are assigned according to successive 90° clockwise rotations in the same alignment as when the sample was shot. The top of the block is side 5, the bottom of the block side 6.*

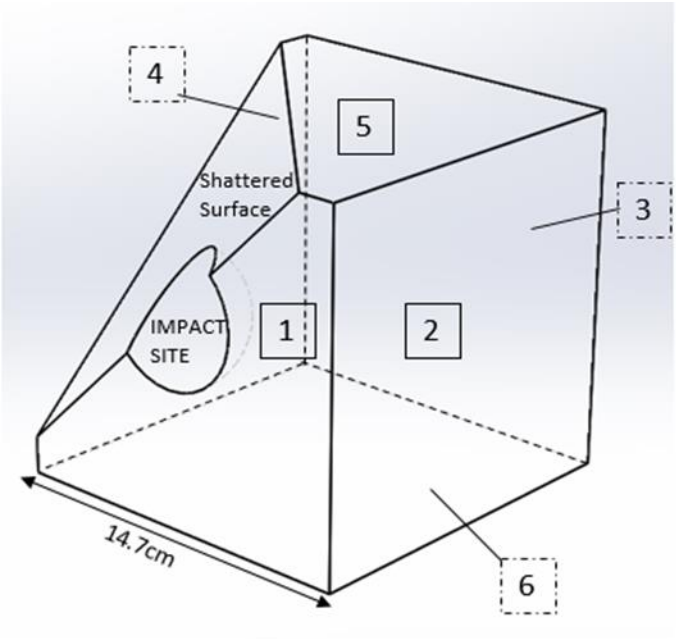

Figure 2.2: *Images showing the extent of damage to each side of the sample. Sides are shown 1-6.*

Side 1

Side 2

Side 3

Side 4

Side 5

Side 6

A grid system was used to ensure consistent sampling of permeability and Equotip surface hardness readings on the individual sample sides. The cell size of the sampling grids was 2cm x 2cm, which was the smallest resolution possible due to the diameter of the Equotip Type D probe support ring D6. This allowed for 49 cells on complete faces, whilst faces damaged by the projectile impact contained less cells. Grid lines were measured using the upper and left-hand edges of each side as the origin. Each cell was assigned an XY alpha-numeric code, such that the lower left cell was A1. This system is depicted in figure 2.3.

Figure 2.3: *Images showing the alphanumeric grid system on an intact side of the sample (side 3) and a side significantly damaged by impact (side 4).*

Side 3 **Side 4**

As seen in figure 2.3, the ballistic damage to some sides of the sample meant that those surfaces had a reduced number of data points. The number of data points for each side is given in table 2.2. Due to the uneven nature of the impact crater and shattered surface, the grid system could not be used in these areas. This heavily damaged area also presented difficulties when attempting to obtain Equotip readings, as the instrument requires relatively flat surfaces of at least 2cm x 2cm for accurate measurements. Therefore, ten points across the impact crater and shattered surface that were flat enough to sample were assessed for both surface hardness and permeability. The points that were sampled were numbered and marked on an image of the surface (figure 2.4).

Table 2.2: *A table showing the number of cells surveyed for each surface.*

Surface	**Number of Cells**
Side 1	22
Side 2	49
Side 3	49
Side 4	30
Side 5	26
Side 6	49
Impact crater/ shattered surface	10

Figure 2.4: *An image showing the various sampling points on the shattered surface of the sample, and assigned numbers:*

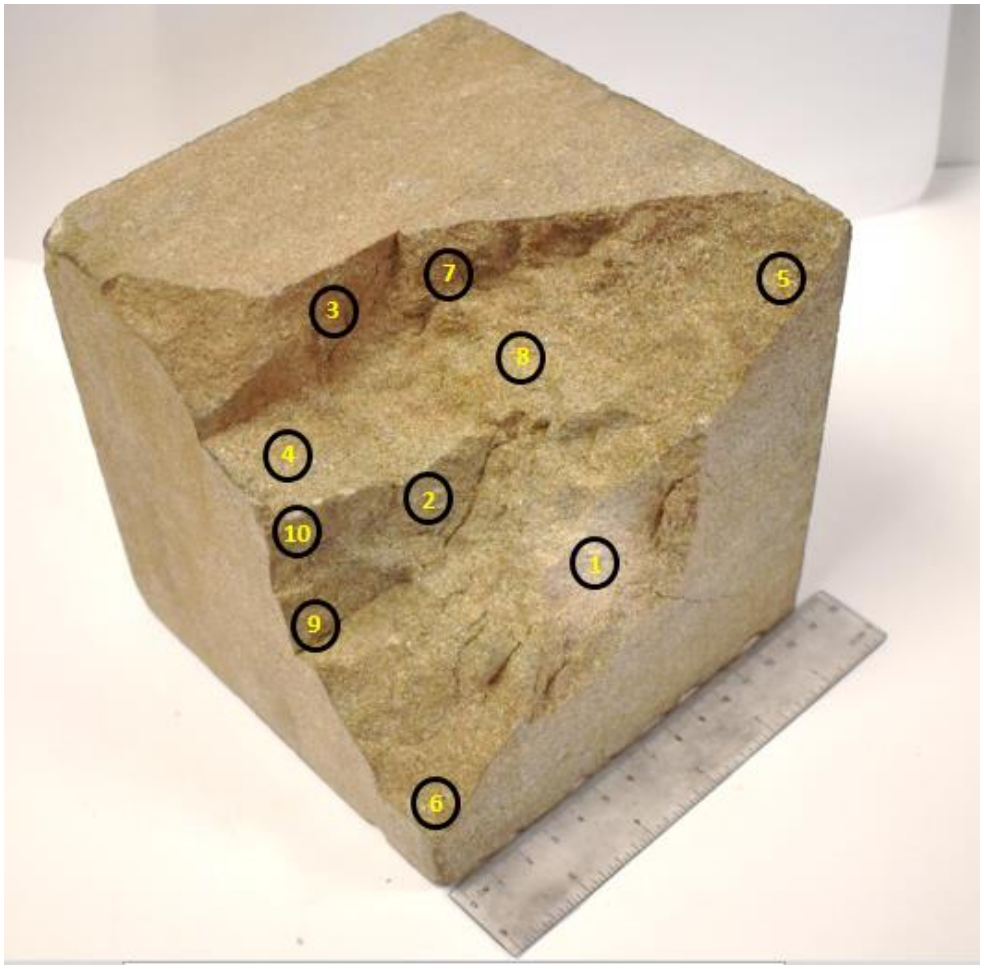

2.3.2: Surface Hardness Survey

The surface hardness survey of the sample was conducted using a Proceq Equotip 550 portable hardness tester with a type D impact device. The Equotip measures surface rebound hardness by firing a 3mm tungsten ball at the target surface. A magnet inside the impact device passes through an induction coil as the impact device is fired and when it rebounds from the surface. The induction signal can then be interpreted by the device to calculate an initial velocity and a rebound velocity. The ratio between the initial and rebound velocities is multiplied by 1000 to give a Leeb hardness (HL): $L = \frac{Vr}{Vi} \times 1000$ (Proceq, 2017a). This principle is demonstrated in figure 2.5.

Figure 2.5: *A diagram showing the operating principle of the Equotip 550 portable rebound hardness tester with type D impact device (Adapted after Procec 2017).*

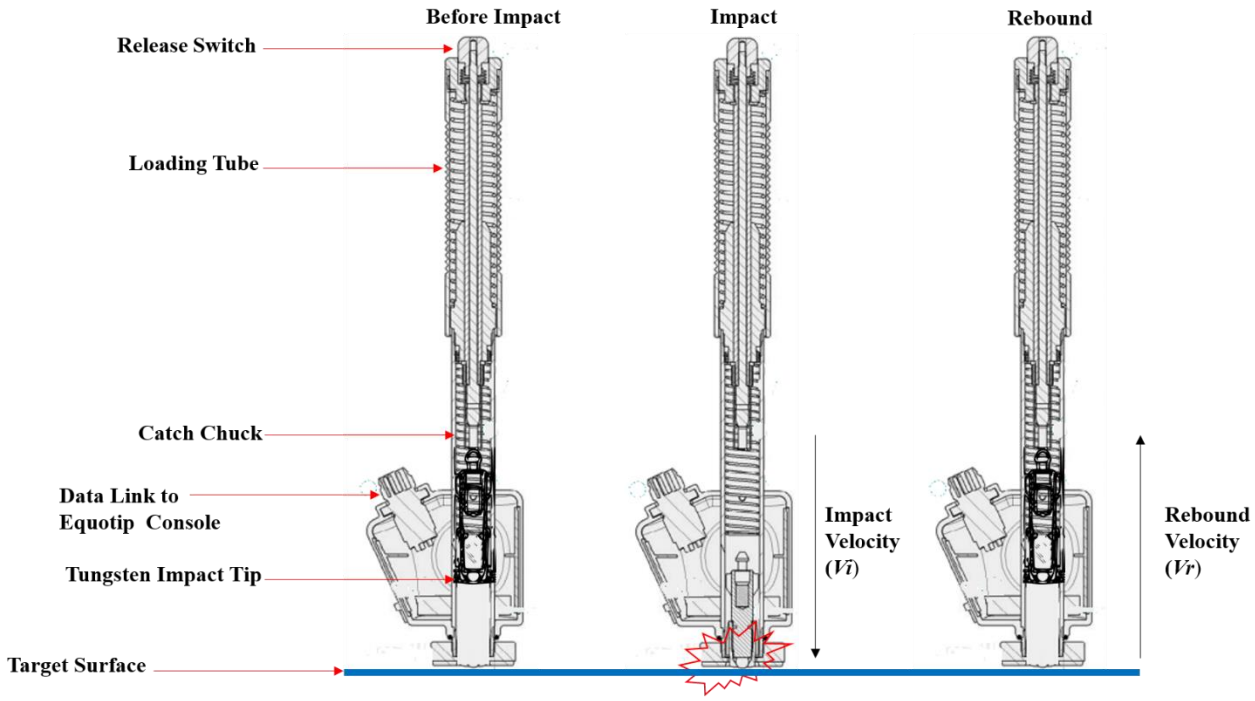

The Equotip was calibrated on an Equotip hardness test block D with a known hardness of 762 Leeb according to standards described under ISO 16859-1 (Annex B) (Proceq, 2019). After calibration, each sampling cell on the sample was measured 3 times and the arithmetic mean for that point calculated.

All measurements were conducted with the test surface horizontal and the Equotip perpendicular to this under the automatic direction setting. Therefore, the influence of gravity on the impact tip is systematically applied to all data points, and so can be disregarded from any conclusions (Aydin, 2009).

Three repeat measurements were used because a single Equotip impact reading can be skewed by the presence of sub-surface fractures (Rodríguez-Rellán 2016). Three repeat measurements for each sampling point is also in keeping with methods used in previous studies into ballistic impact effects on heritage stone, as described by Mol and Gomez-Heras (2018). Given that this study was concerned with determining localised difference in hardness, it was deemed necessary to perform repeat measurements at each point to gain a more reliable figure for individual cells' hardness. However, repeat measurements can cause artificial hardening and disfiguring compaction of a surface when 5+ measurements are performed (Desarnaud *et al*, 2019). Therefore, three measurements were used to ensure that no artificial hardening had taken place due to the repeat measurements, in keeping with previous studies into the hardness of rock subjected to ballistic impact (Mol, Gomes-Heras, 2018). The average hardness of the block was calculated after each run of measurements. No artificial hardening was discovered (run 1:446 Leeb, run 2, 445 leeb, run 3: 445 Leeb, all runs, n=225).

A number of studies have demonstrated the efficacy of Leeb hardness testers in assessing the stability of rock surfaces. This equipment is widely used in characterising rock hardness and can be used to determine the extent of weathering weakening that a rock surface has undergone. This is determined both through the absolute Leeb value, and through the standard deviation of a set of values, with higher variability indicating more severe weathering (Verwaal, Mulder, 1993, Hall *et al*, 2005, Mol, Gomes-heraz, 2018). Other works have demonstrated that the rebound hardness of a rock sample is related to standardized metrics of material integrity, such as compressive strength (Aoki, Matsukura, 2008). Finally, the use of Equotip hardness testers has been shown to be non-destructive, and they are often deployed in the field to assess the stability of heritage buildings without risk to the stone fabric, including monuments such as the Tower of London (Michette, 2021, Aoki, Matsukura, 2007, Wilhelm *et al*, 2016). Previous works have also used equotip to assess damage to heritage stone caused by ballistic impact (Mol *et al*, 2017, Mol, Gomez Heras, 2018).

2.3.3: Permeability Survey

The permeability of the sample's surface was investigated using a New England Research TinyPerm3 air Permeameter. This instrument assesses the permeability to air of the stone by creating a vacuum through a piston stroke, drawing air from the sample (Figure 2.6). The instrument monitors the volume of air withdrawn, and the transient vacuum pulse created at the surface. This data is computed by the instrument and converted into a permeability value in Darcys (D) (Filomena *et al*, 2014) that is displayed on a smartphone via wireless Bluetooth link. The instrument was calibrated according to the manufacturer's automatic standards (New England Research, 2015). The permeability value of the stone is given in darcys or millidarcys, with 1 darcy being equivalent to a flow of 1 cm^3/s of a fluid with viscosity 1 cP (1 mPa.s) under a pressure gradient of 1 atm/cm across an area of 1 cm^2 (Cimini, Bedini, Moresi, 2021).

Figure 2.6: *An image demonstrating the operating principle of the TinyPerm 3 Air Permeameter. (Adapted after New England Research Inc, 2015)*

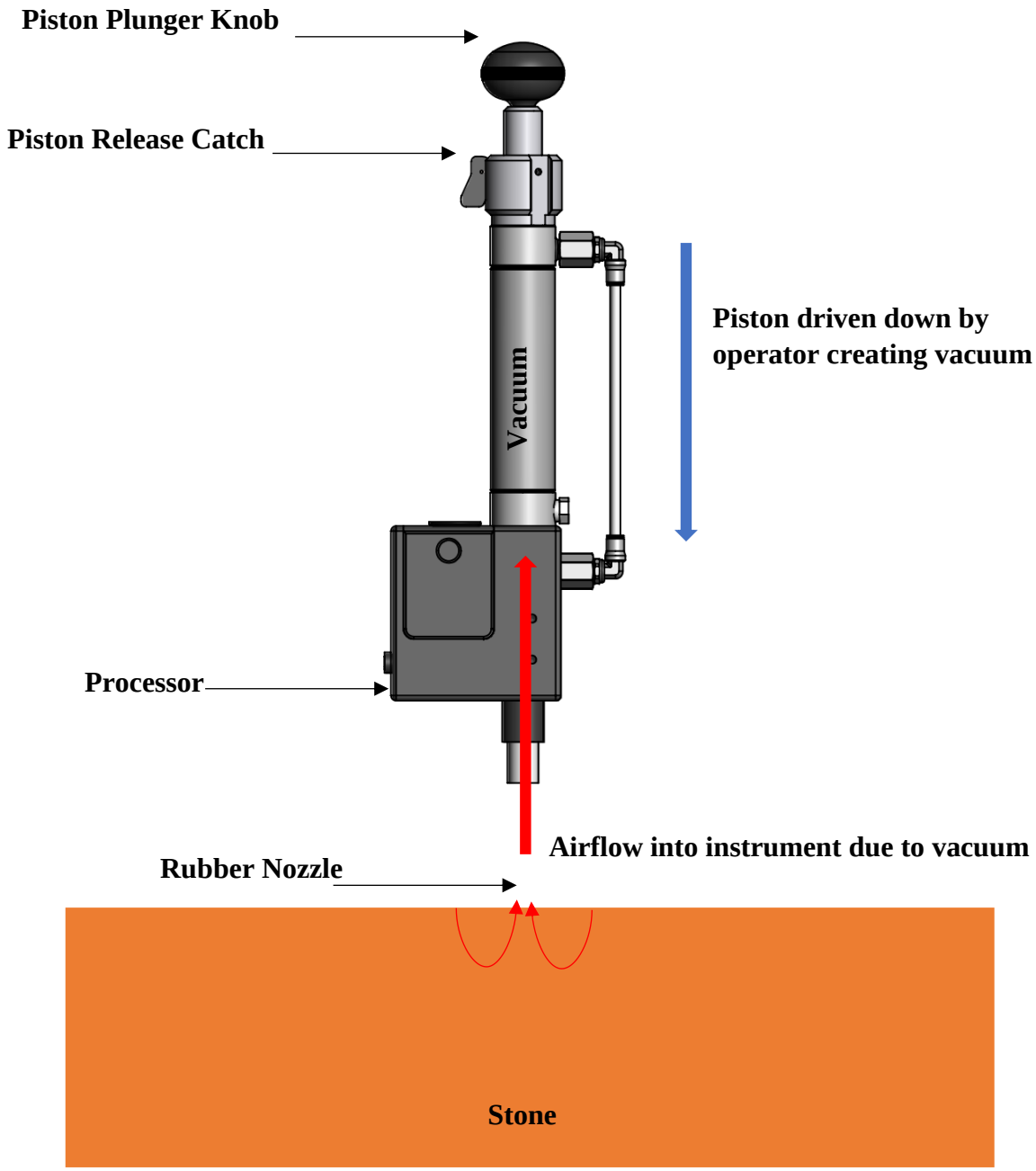

As with the surface hardness readings, the permeability of each cell was measured three times and the mean value calculated. It should be noted that as air permeability values have been shown to differ significantly from water permeability values (McPhee, Arthur, 1991), the permeability results presented here serve only to highlight relative differences across the sample and cannot be used to infer the likely ingress of water as a weathering agent.

This method is portable, non-destructive and allows the permeability of very small areas (c.4cm^2) to be measured. The Tiny Perm equipment has been used to undertake in situ measurements on heritage monuments, such as work undertaken on Strasbourg cathedral by Mertz *et al* (2016) demonstrating the efficacy of using this technique on heritage stone in a non-destructive manner.

2.3.4: Control and Edge Effect Calibration Measurements

As shown in Figure 2.3, the optimal distribution of sample cells across the block surfaces left a margin measuring 5–7 mm on the right and bottom edges that were not sampled. This margin, coupled with the calibration for the edge effect detailed below, which was applied to the upper and left edges of each face (cells A1–A7 and A7–G7) ensured that any observed changes to permeability or hardness could be attributed to ballistic damage rather than damage sustained during the cutting process prior to ballistic impact.

These measures were necessary because it was hypothesised that the cutting process when the samples were quarried could potentially exacerbate the edge effect suggested by Viles *et al* (2011) and lead to an artificial lowering of surface hardness values at the sample edge. It was also hypothesised that a similar edge effect might be witnessed for air permeability readings, whereby permeability is increased towards the edge of the sample surface, as has been discussed in previous works (Turkington, Smith, 2000).

To ascertain the surface hardness and permeability of non-impacted stone and investigate the presence or absence of an edge effect, a control sample of non-impacted Huesca sandstone from the same quarry as the main sample was used. Following the alpha-numerical sampling grid seen in Figure 3, 49 cells were sampled across the face of a non-impacted sample measuring 14 × 14 × 4.5 cm. As with the impacted sample, all cells were measured 3 times for rebound hardness and permeability and the mean calculated. The mean values of cells were used in all statistical analyses. This would allow for the average permeability and

surface hardness of the 24 edge cells to be ascertained and compared with the 25 inner cells (see Figure 2.7) to determine if an edge effect existed. This control sampling would also give an average control value for a non-impacted stone face to compare to the six faces of the impacted sample. All statistical significance analyses were conducted using IBM SPSS 25.

Figure 2.7: *An image showing the control sample and the distinction between inner and edge cells.*

As shown in Figure 2.8, there was a difference in mean rebound hardness of 63 Leeb between the inner and outer cells of the control sample (468 for inner cells vs 405 for outer cell). Analysis using a Shapiro-Wilk test in SPSS Statistics 25 suggests that both data sets are normally distributed (inner cells: n = 25, $\bar{x}$ = 468 Leeb, p = 0.374, edge cells: n = 24, $\bar{x}$ = 405, L p = 0.73).

Therefore, a 2-tail t-test was used to determine whether the difference in means was statistically significant. The results suggest that there is a significant difference between the mean hardness of the inner cells and edge cells ($p = 0.000$).

Figure 2.8: *Mean surface hardness across the control sample, as well as for inner and edge cells of the sample. Error bars are the standard error of the sample population.*

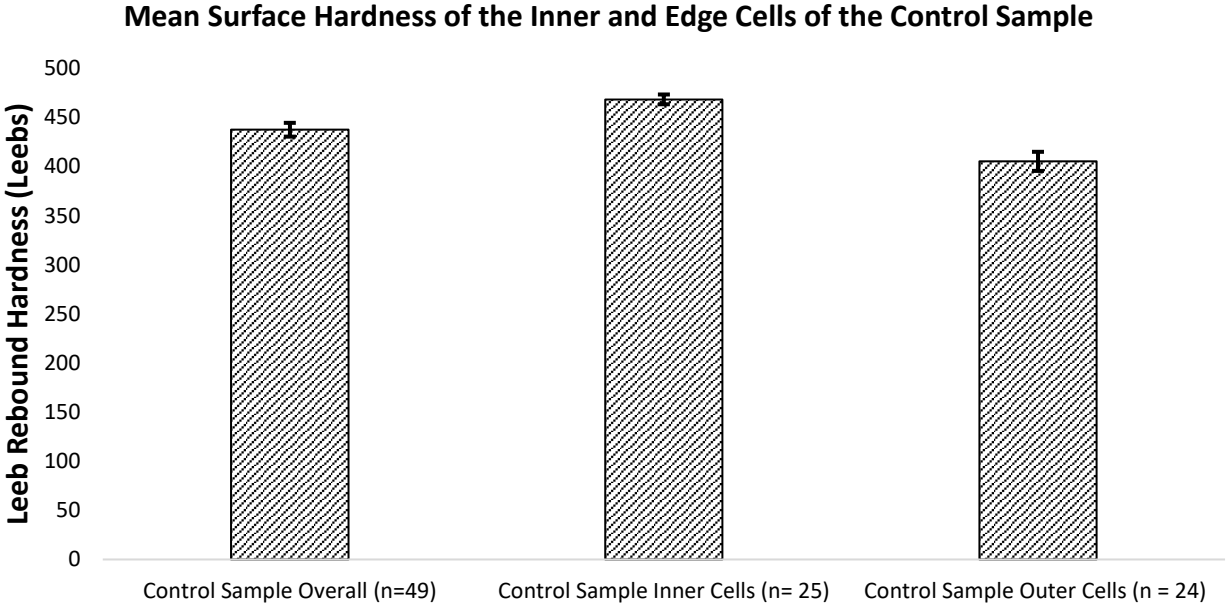

Having established that there is a statistically significant edge effect which lowers surface hardness, the difference in mean surface hardness between the inner cells and the edge cells (63 Leeb) was used as a calibration constant when conducting Inverse Distance Weighted (IDW) heat mapping of surface hardness using ArcGIS Pro (see section 2.3.5). This meant that a 63 Leeb calibration constant was added to the mean values for the cells abutting the edge of the impacted sample (cells A1–A7 and A7–G7). Thus, any lowering of the surface hardness at the edge of the sample compared to the inner cells could be attributed to ballistic damage, as was observed by Mol *et al* (2017), rather than the measured edge effect.

In addition to edge effects for rebound hardness, previous studies have described a discernible edge effect in relation to permeability. This is likely because in a free-standing block, the edges of a face act as an interface between two free surfaces, meaning that permeability readings taken at an edge are higher due to air or water flow through the adjacent free face (Turkington, Smith, 2000). To assess this, the control sample was also surveyed for the average permeability of each of the cells.

The edge effect was found to be responsible for an increase in permeability towards the control sample's edge (Figure 2.9), which was also tested for statistical significance. The permeability readings for the inner cells were found to be non-normally distributed using a Shapiro–Wilk test (n = 25, p = 0.000). Because the permeability data set was not normally distributed, a Mann–Whitney U test was conducted in SPSS to compare the means of the two sample populations. A Mann–Whitney U test is a non-parametric test that assesses the likelihood that the mean of a given sample is significantly different from another. Mann-Whitney-U has been shown to be more accurate when analysing non-normally distributed data sets (Vickers, 2005). The results of this test suggested a statistically significant increase in mean permeability at the edge of the sample (p = 0.000).

The difference in mean permeability between the inner cells and the edge cells was 4.6 Millidarcies (mD) (inner cells: $\bar{x}$ = 2.6 mD, edge cells: $\bar{x}$ = 7.2 mD). Therefore, a value of 4.6 mD was used as a calibration constant when conducting IDW heat mapping of permeability (see section 2.3.5). This means that a 4.6 mD calibration constant was subtracted from the values for the cells abutting the edge of the impacted sample (A1-A7 and A7-G7). Therefore, any increase in permeability at the edge of the sample compared to the inner cells could be attributed to ballistic damage rather than a potential edge effect.

Figure 2.9: *Mean permeability across the control sample, as well as for inner and edge cells of the sample. Error bars are the standard error of the sample population.*

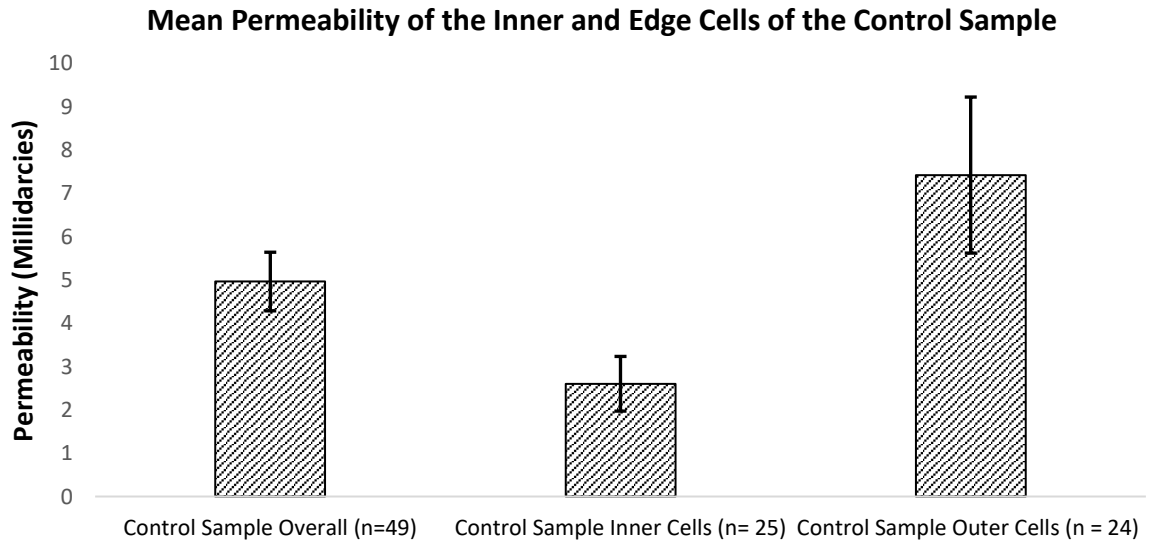

2.3.5: Spatial Distribution Analysis (Heat Mapping) Methods

Images of the sample were processed in the ArcGIS Pro Geographic Information Systems software package. The permeability data was assigned to a point cloud, with each cell shown in Figure 3 given a central point with a permeability value in Darcies. Using this point cloud, and the Inverse Distance Weighted (IDW) interpolation spatial analyst tool in ArcGIS Pro, a series of heat maps of likely permeability across the sampling grid was created with an IDW analysis output cell size of 0.1 × 0.1 cm. This was done under The IDW stretch function, with a custom minimum-maximum data set so that the data range for the whole sample (0.0001-5.34 D) could be assigned to a single temperature colour ramp. This colour scheme allowed the visualisation of differences in permeability across individual sample sides, as well as across the sample overall.

Heat mapping of surface hardness data was conducted using the same parameters as those for permeability but using a bathymetric colour ramp, which better highlighted local differences in hardness and the range of 275–596 L across the whole sample.

2.4: Results and interpretation

2.4.1: Surface Rebound Hardness Survey Results

As shown in figure 2.10 and table 2.3, the average surface hardness of the six numbered faces outside of the impact crater/shattered surface range from 439 to 475 Leeb. The control sample is close to this range with a rebound hardness of 438 Leeb and thus is comparable to the six numbered sides of the impacted sample in terms of hardness.

Figure 2.10: *Surface hardness across the faces of the sample. Error bars are the standard error of the data set for the given surface.*

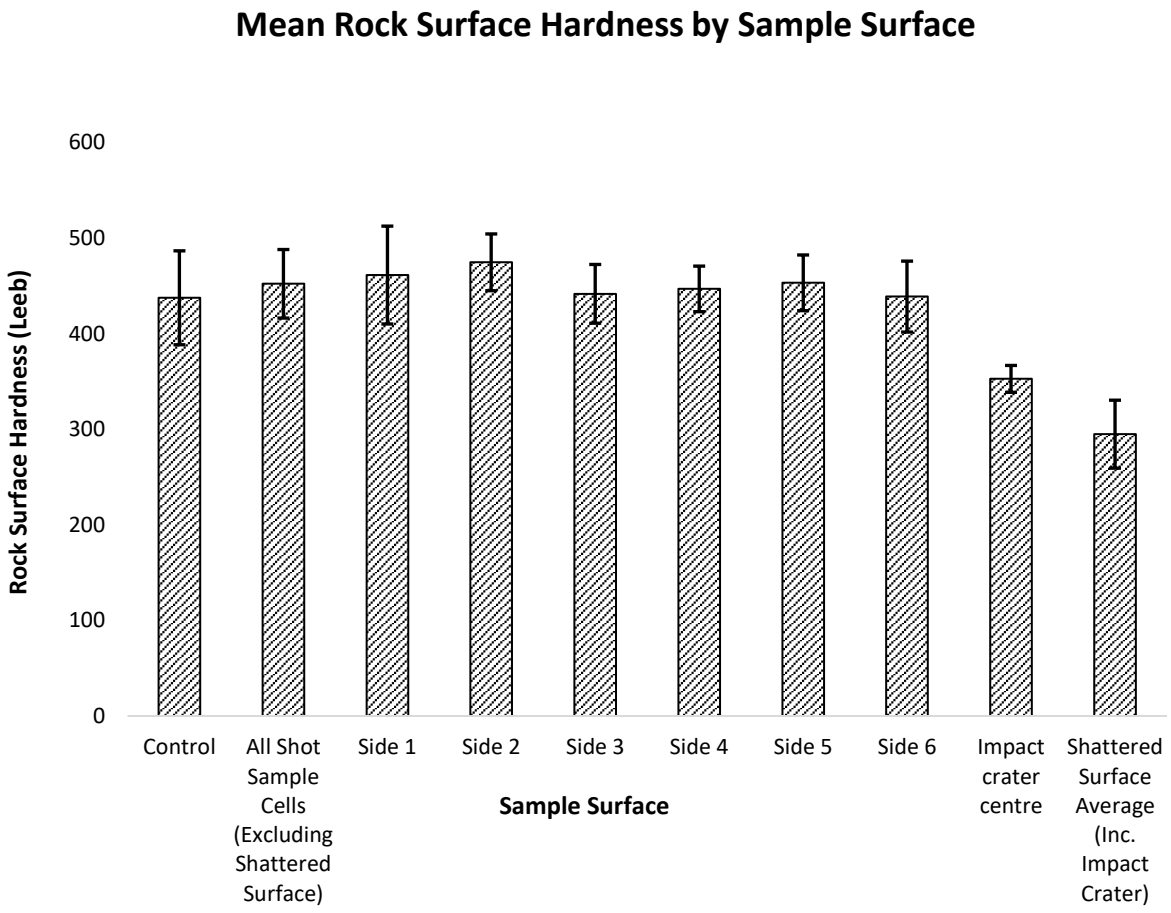

Table 2.3: *Data on the Equotip rebound surface hardness measurements collected for each surface.*

Surface	Number of Cells / Sampling Points	Mean Equotip Rebound Hardness (Leeb)	Maximum Value (Leeb)	Minimum Value (Leeb)	Range (Leeb)	Standard Deviation (Leeb)	Standard Error Leeb)
Control Sample	49	438	528	303	225	49	7
Impacted sample all cells (Outside of impact crater/shattered surface)	225	452	547	275	272	36	2
Impacted Sample Side 1	22	461	533	275	258	51	11
Impacted Sample Side 2	49	475	547	379	168	30	4
Impacted Sample Side 3	49	442	501	374	127	31	4
Impacted Sample Side 4	30	447	489	372	116	24	4
Impacted Sample Side 5	26	453	533	389	143	29	6
Impacted Sample Side 6	49	439	494	318	176	37	5
Impact Crater/Shattered Surface	10	295	353	225	128	36	11

The fact that these sides have an average hardness close to or higher than the control sample suggests that surface hardness survey is not able to detect ballistic damage to impacted stone outside of the impact crater/shattered surface. To demonstrate that no significant change in surface hardness was detectable outside of the impact crater, a comparison of the average hardness values for the control sample ($\bar{x}$ = 438 Leeb) and the 225 sampling cells outside of the crater of the impacted sample ($\bar{x}$ = 452 Leeb) was undertaken using a Mann-Whitney-U test. The significance value (P = 0.116) suggests that the difference in means is not statistically significant.

However, as shown in figure 2.10, the mean hardness for the shattered surface (295 Leeb) was substantially lower than both the mean hardness of the control (438 Leeb), and the non-shattered sides of the sample (452 Leeb). This lower hardness across the damaged surface can be shown to be statistically significant (both tests: $p = 0.000$). Therefore, the Equotip surface survey demonstrates a statistically significant reduction in hardness across the impact crater shattered surface, demonstrating that the technique can be used to quantify the degradation in surface hardness caused by surface shattering/shearing due to ballistic impact.

Furthermore, in Figure table 2.3, side 1 exhibits a larger standard deviation than the surfaces that were not directly impacted by the bullet: 51 L for side 1 vs. an average of 30 L for the other numbered sides of the impacted sample. A higher standard deviation of Equotip readings can be indicative of advanced weathering or weakening of a rock surface (Hall *et al*, 2005, Mol, Gomez-Heras, 2018).

Analysis of the Equotip results from across the impact crater reveals interesting trends in the localisation of damage. Figure 2.11 demonstrates that the impact point (sampling point 1) has a lower hardness than un-impacted cells and the control sample, but higher average hardness than the rest of the shattered surface (353 L mean for the impact point vs. 286 L mean for the rest of the shattered surface).

Figure 2.11: *A chart showing the differing hardness values for the impact point and the wider shattered surface. Error bars are the standard error of the data set for the given sampling point.*

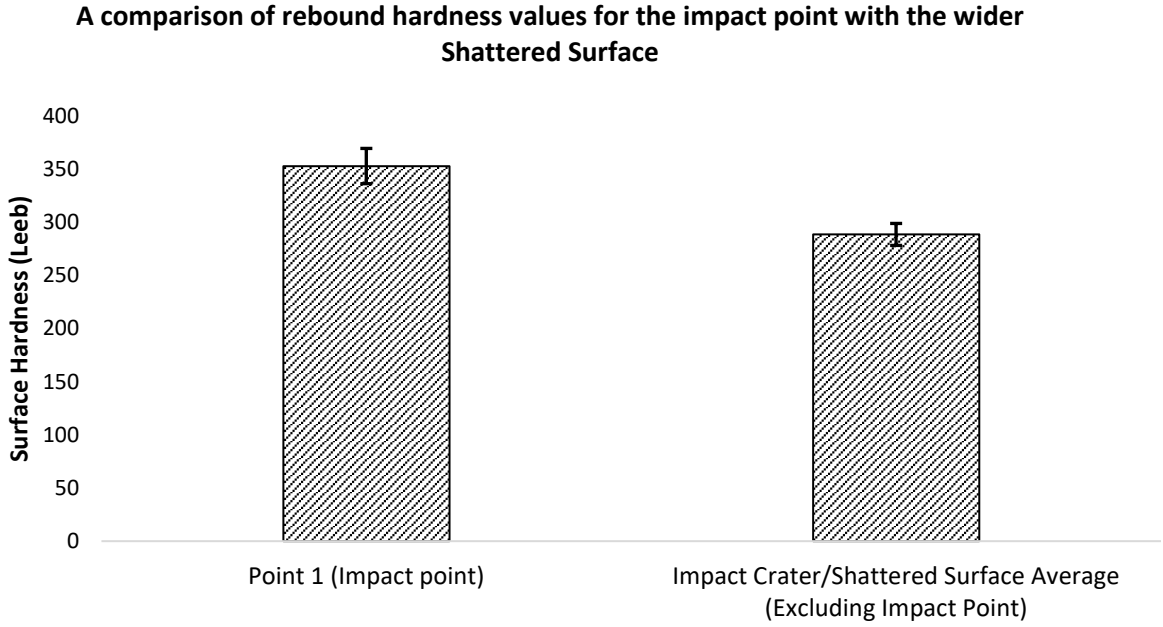

This higher mean hardness at the impact point is likely indicative of compaction and realignment of clay minerals within the matrix, as observed using optical microscopy by Mol *et al* (2017) on samples of the same Huesca sandstone after ballistic impact. X-ray diffraction analysis (XRD) conducted by Mol *et al*. on the Huesca sandstone identifies the relatively high proportion of clay minerals (13% muscovite, 6% kaolinite), which facilitate compaction as a response to impact shock at the impact site (*ibid.*).

This compaction would not happen across the wider shattered surface because the projectile did not directly impact these areas, and thus hardness is reduced to a greater extent in these areas. Increased surface hardness of stone due to ballistic impact has also been observed in field observations of musket ball impacts Mol and Gomez, (2018).

2.4.2: Permeability Survey Results

In contrast to the data obtained from the rebound hardness survey, the permeability survey data for all 225 non-shattered cells was found to be significantly different from the control sample (Mann–Whitney U test, $p = 0.000$). There is also a great deal of variation between the individual sample sides. These observations suggest that ballistic impact has a notable effect both on the permeability of the sample as a whole, and on the individual sample sides. This is demonstrated in in figure 2.12 and table 2.4.

Figure 2.12: *A chart showing the differing permeability profiles of the sample sides. Error bars are the standard error of the data set for the given sampling point.*

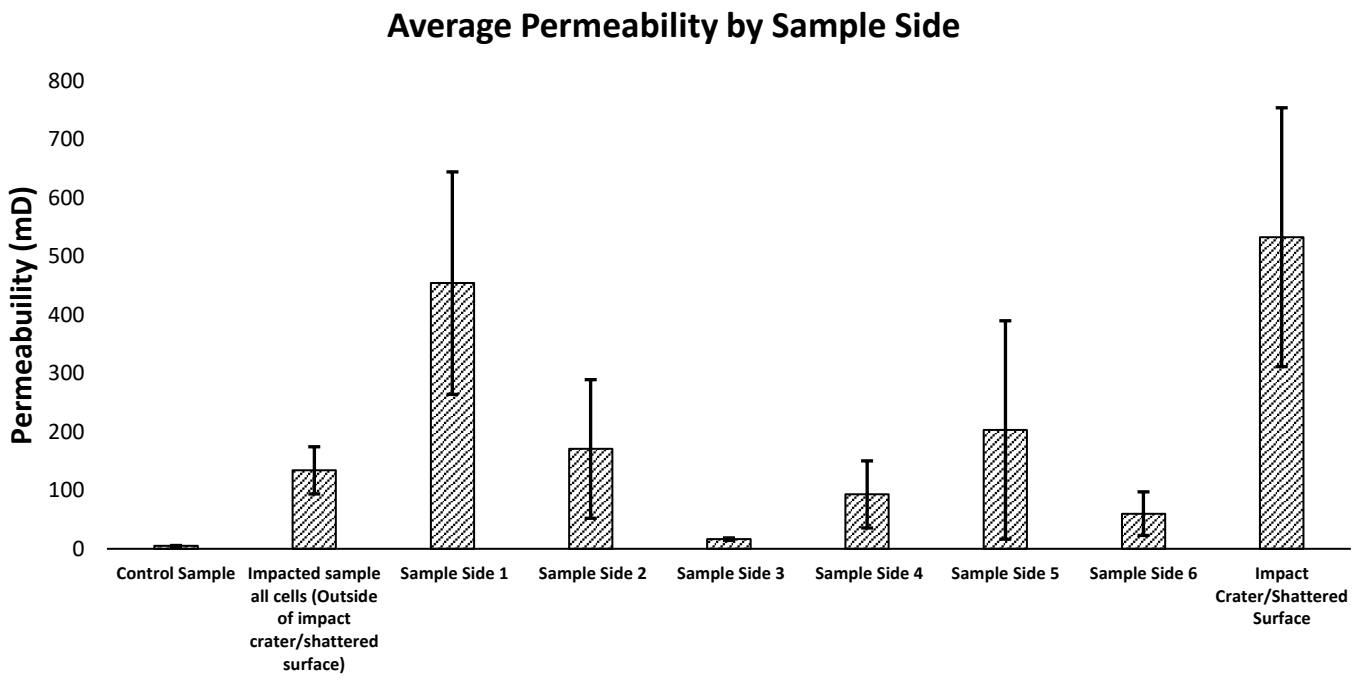

Table 2.4: *Data on the permeability values recorded for each side.*

Surface	Number of Cells/Sampling Points	Mean Permeability (mD)	Maximum Value (mD)	Minimum Value (mD)	Range (mD)	Standard Deviation (mD)	Standard Error (mD)
Control Sample	49.0	5.0	16.4	0.2	16.2	4.7	0.7
Impacted sample all cells (Outside of impact crater/shattered surface)	225.0	134.1	5333.3	0.3	5333.0	604.6	40.3
Impacted Sample Side 1	22.0	454.0	2933.3	0.6	2932.8	891.6	190.1
Impacted Sample Side 2	49.0	170.6	5333.3	0.3	5333.0	828.9	118.4
Impacted Sample Side 3	49.0	16.4	55.5	1.4	54.1	15.2	2.2
Impacted Sample Side 4	30.0	92.9	1600.0	0.6	1599.4	314.0	57.3
Impacted Sample Side 5	26.0	203.1	4866.7	0.4	4866.3	951.4	186.6
Impacted Sample Side 6	49.0	60.1	1600.0	0.8	1599.2	260.8	37.3
Impact Crater/Shattered Surface	10.0	532.5	2033.3	14.9	2018.5	699.4	221.2

Side 1 and the shattered surface show the highest permeability, reflecting the large number of visible fractures across these areas of the sample. The increased permeability seen across side 1 and the shattered surface are due to the fact that the projectile impacted side 1 directly, leading to greater damage in this area and across the adjacent shattered surface.

The sides with the lowest permeability readings were sides 3 and 6. This is likely because side 3 is the antipode of side 1, and thus furthest away from the impact. Therefore, the reduced damage exhibited by side 3 corresponds well with known models of impact damage in rock, in which fracture-inducing stress wave energy reduces with distance from the point of impact (Thoma, *et al*, 2005). Side 6 probably experienced less damage because, at the time of shooting, this side was facing downwards on the target area. This meant that it was the only side with compression/containment, i.e., the mass of the block above it pushing it downward onto the target structure on the firing range. It is worth noting in 2.4 that the sides previously hypothesised to be least damaged by the projectile impact, sides 3 and 6, have the lowest standard deviations. This suggests that, as with the Equotip measurements, the standard deviation of a permeability data set for a given surface of an impacted sample may be related to the damage sustained by it during impact.

This is supported by statistical reasoning, as a lower standard deviation would imply a largely homogenous surface without surface fractures that increase the range and standard deviation of the data set for that side. This is indeed the case with side 3. This notion is also supported by the fact that the non-impacted control sample had both the lowest average permeability and the lowest standard deviation.

The hypothesised compaction at the impact site (point 1 of the shattered surface), which is thought to result in a lower reduction of surface hardness, may also be responsible for a reduction in permeability. The shock generated upon impact can realign clay minerals and reduce moisture flow, as discussed by Mol *et al* (2017). This phenomenon might be expected to influence our permeability measurements at the impact site. As seen in Figure 2.13, the impact point does have a lower average permeability (191mD) than the rest of the shattered surface (570mD), which shows areas of flaking and fracturing due to impact visible in figure 2.4. This is consistent with the findings of the rebound hardness survey, which suggest a compaction of the mineral matrix at the point of impact relative to the wider shattered surface:

Figure 2.13: *Differing permeability values for the impact point and the wider shattered surface. Error bars are the standard error of the data set for the given sampling point.*

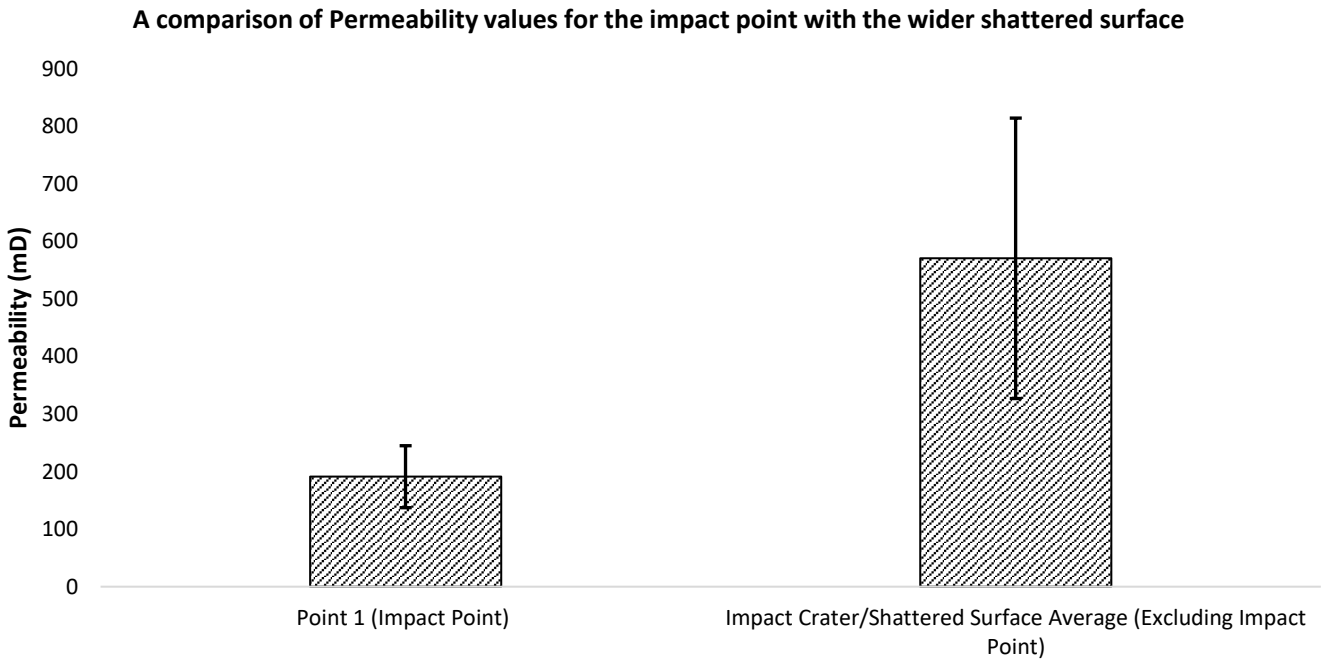

Despite figure 2.13 clearly demonstrating that the impact point has a lower permeability than the shattered surface as a whole, table 2.5 shows that the permeability of the impact point is higher than that for other distal points of the shattered surface (2,5,6,7,10). This is possibly due to the generation of micro-fracture networks across quartz grains at the impact point. Creation of such fracture networks at the impact point has been observed using optical microscopy (*ibid.*) and scanning electron microscopy (SEM) in previous studies (Mol, 2017), creating connected networks that may act to increase permeability. Micro fractures immediately below the point of projectile impact have also been reported by Polanskey and Ahrens (1990), as discussed in section 1.4.

Table 2.5: *Average permeability measurements from the shattered surface sampling points. Impact points listed are the same as those shown in figure 2.4.*

Sample Area	**Average Permeability (mD)**
Control Sample	5
Impact point 1	191
Impact point 2	39
Impact point 3	760
Impact point 4	647
Impact point 5	78
Impact point 6	52
Impact point 7	77
Impact point 8	2033
Impact point 9	1433
Impact point 10	15

These observations suggest that compaction at the impact point results in a permeability value that is lower than the wider shattered surface overall, which experiences widespread fracture formation, but that micro-fractures at the impact point may result in an average permeability higher than intact stone or areas distal from the point of impact. More work would be required to test this theory.

2.4.3. Spatial Distribution Analysis ("Heat Mapping") of Sample Permeability Data

In addition to distinguishing between the levels of damage across the sample surfaces, permeability survey is effective at identifying the areas of a given surface that have been significantly fractured as a result of projectile impact. This is best demonstrated by presenting the permeability survey data in relation to its spatial distribution across the sample surface, as seen in Figure 2.14. Fractures have been highlighted in black. With the exception of side 1, which was impacted face on (indicated by a red '⊗'), the direction of projectile impact is indicated with a red arrow. As discussed previously, a calibration constant of −0.0046 D was applied to the cells contacting the sample edge to remove any edge effect when visualising ballistic damage at the sample's edge.

Figure 2.14. *A series of Inverse Distance Weighted (IDW) permeability heat maps generated for the impacted sample (sides 1–6, A–F). Visible surface fractures are highlighted in black.*

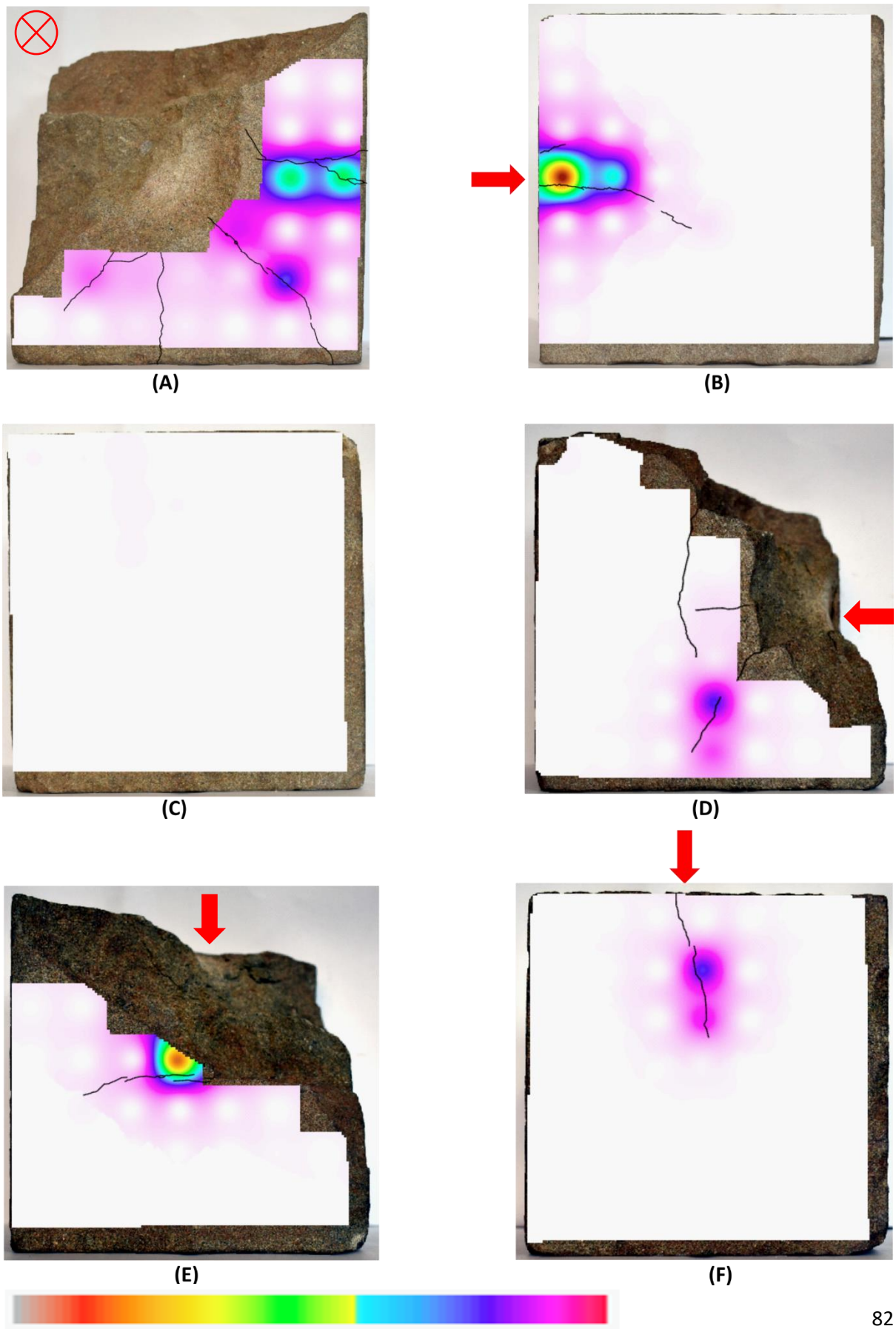

A number of important trends become evident from the visualisation of the spatial distribution of the permeability data. Most obvious of these is that for every surface displaying a fracture network, the areas of highest permeability correspond directly to the position of the fractures. This is perhaps an obvious observation, as a visible fracture will drastically increase the permeability of the local surface it runs through. However, this clearly demonstrates the efficacy of permeability survey analysis in quantifying the increase in permeability and associated risk of exacerbated weathering degradation caused by visible surface fracture. Some areas with surface fractures appear to have higher permeability that other areas exhibiting surface fracture. This is possibly due to differences in the sub-surface extent of the fractures, i.e., that those fractures which extend further into the sample or connect with a fracture network of greater density will give higher permeability readings, but further work will be necessary to confirm this (Miao, Yu, Fang, 2015).

The heat map for side 3 demonstrates that there are no detectable fractures on this side. This supports the earlier analysis of permeability data that suggested that this side was least damaged by the ballistic impact because it was furthest away (see figure 2.12). The area of increased permeability to the upper left corner of side 3 of the sample is notable and although it is markedly lower than the permeability averages for surface fractures on other sides (the highest reading for a side 3 cell is 0.056 D) it could be indicative of sub-surface micro-fractures or defects. This could be the result of natural variation in the stone or could be related to residual stress wave damage towards the rear of the sample. Further work would be necessary to determine the cause of this area of increased permeability.

Overall, the heat maps in figure 2.14 suggest that cells exhibiting large increases in permeability directly correspond with visible fracture networks caused by ballistic damage. Further evidence of the link between increased permeability and visual evidence of ballistic damage can be seen when one considers the area of each sample side left intact after the ballistic impact. As shown in figure 2.15, there is a strong negative correlation (-0.72) between the permeability of a given sample side and the area of that surface as measured using the number of intact sampling cells (i.e. those areas not destroyed/removed from the surface during the ejection of stone material following ballistic impact).

Figure 2.15: *The relationship between surface permeability and the intact area of a sample surface.N.B. due to the large variability of permeability readings, the standard error of the mean is not plotted here as they would make the data unreadable. Stadard deviation data for these data points are collected in table 2.4.*

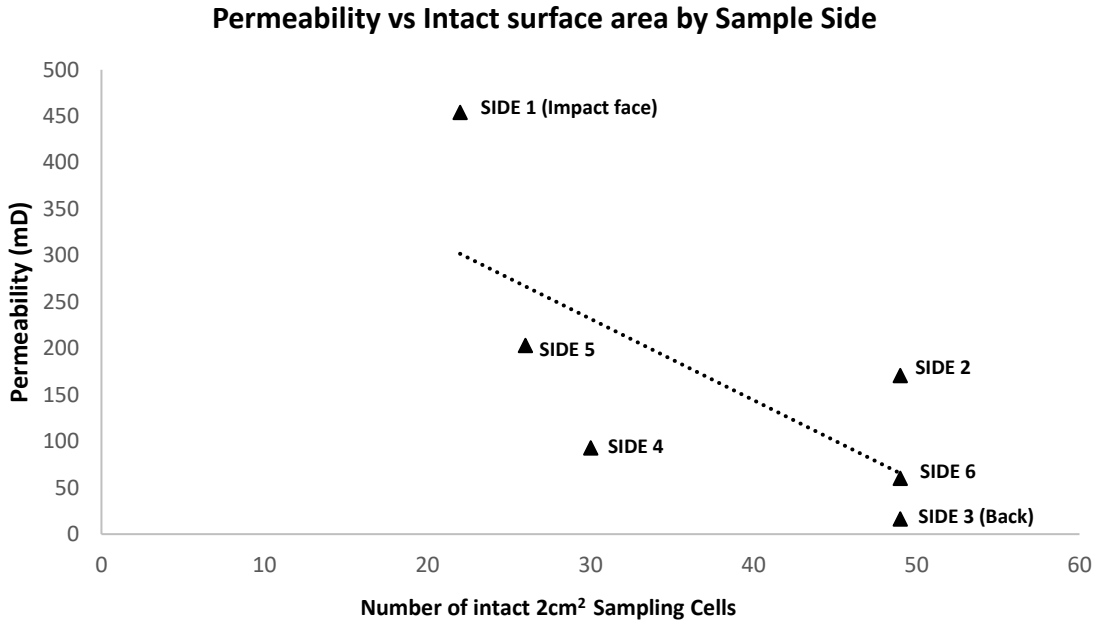

This strong negative correlation demonstrates that as the area of a sample surface destroyed due to ballistic impact increases, so does the permeability of that surface. This suggests that surfaces more intensely damaged by the impact event are also likely to have increased permeability in the stone surface that has not been lost due to impact, placing these surfaces at greater risk of more rapid deterioration as weathering agents exploit this increased permeability.

2.4.4: Spatial Distribution Analysis ("Heat Mapping") of Sample Surface Hardness Data

As can be seen in figure 2.16 (overleaf), spatial analysis of the distribution of Equotip surface hardness readings corresponded less directly with identifiable surface fractures than similar analysis for permeability data. This can be seen in figure 2.16, and although there is some agreement between those areas exhibiting surface fractures and areas of lower hardness, (sides 1,5, 6 in Figure 2.16) other areas of lower hardness appear to be unrelated to the presence of surface fractures, such as sides 2 and 4.

Figure 2.16: *A series of IDW Equotip surface hardness heat maps generated for the impacted sample (sides 1–6, A–F).*

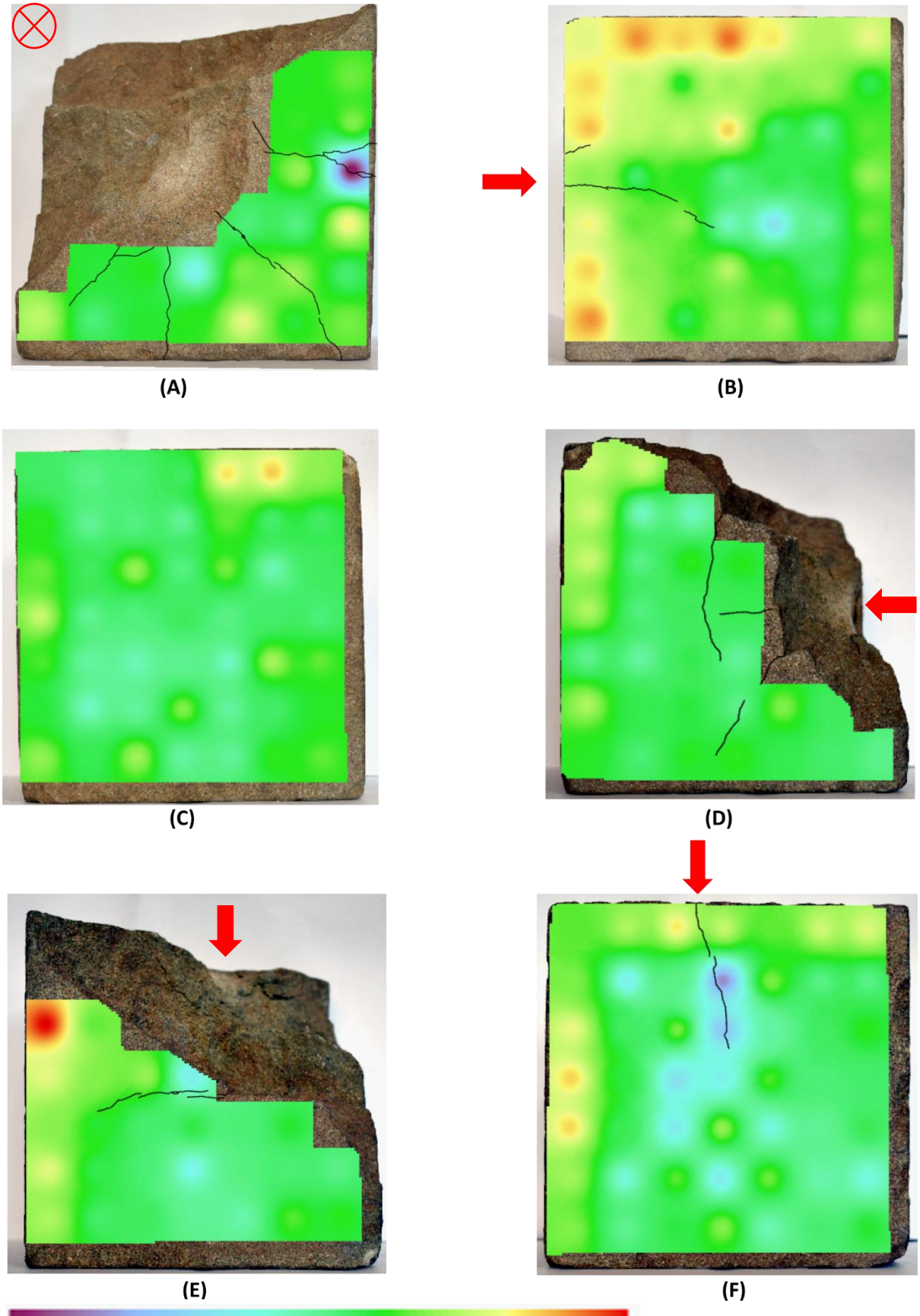

Furthermore, some large fractures visible on the sample surface do not affect the hardness of the surrounding cell, as is the case for the heat map of side 1, and are in direct contrast to the permeability heat map for that side. The addition of the 63 L calibration constant appears to have been successful in creating a broadly homogenous surface hardness independent of the edge effect for many of the sample sides, as seen on sides 3, 4 and 6. However, the left and upper edges for side 2 do appear to be significantly harder than the rest of that surface, indicating that further work may be required to properly investigate the edge effect and to calibrate for its effects when investigating ballistic damage in stone.

2.5: Discussion of significance of results

2.5.1: Discussion of Rebound Hardness Survey Results

The clearest trend in the data from the rebound hardness survey is the differing hardness values between the impact crater/shattered surface and the intact regions of the sample. The damaged area that resulted from ballistic impact has an average hardness of 295 Leeb compared to 452 Leeb for the un-impacted and undamaged regions of the sample. This is in keeping with the model of mechanical strength and hardness loss after impact described by Mitani (2003) and Kato *et al* (2001), where loss of strength and hardness decreases with distance from the impact point as a result of stress wave attenuation in the target material. The substantial difference in surface hardness across damaged and undamaged areas found in this study indicates that Equotip rebound hardness survey is a useful method in identifying regions of impacted stone most damaged by ballistic impact in a single, relatively small sample of stone, and in quantifying the loss in hardness across the damaged areas arising from impact.

Rebound hardness survey has also been useful in determining damage patterns across the impact crater and shattered surface. As shown in Figure 2.4, there is a discoloured area of lighter stone in the centre of the shattered surface. This is the impact point of the projectile (point 1 on the damaged surface) and as shown in Figure 2.11, it has a noticeably higher average hardness than the rest of the shattered surface (353 L for the impact point vs. 288 L average for the rest of the shattered surface). The fact that the impact crater has experienced less weakening than the rest of the shattered surface could indicate compaction of the stone matrix at the impact point, as found in previous studies (Mol *et al*, 2017, Mol, Gomez-Heras, 2018). Although the impact crater has a reduced hardness when compared with the cells sampled on non-shattered sides (353 L compared with an average of 452 L for non-shattered

cells), the fact that it is harder than the surrounding shattered stone is an important finding when seeking to model impact damage to stone. It is notable because it suggests that the most damaged areas may not be the point of direct impact, but rather the wider shattered surface adjacent to the impact point that has sheared away during the ballistic event.

The variability in hardness readings from side 1 is higher than for other sides of the block, with a range of 258 L compared to an average range of 146 L for sides 2-6. The greater variability in rebound hardness for side 1 is also reflected in the higher standard deviation of Equotip readings for this side (Figure 8). Previous work has shown that a high standard deviation of rebound hardness values can be used to detect areas of increased weathering deterioration. Therefore, the standard deviation of Equotip readings for side 1 presented in table 2.3 may indicate that ballistic impact has the capacity to degrade stone to a comparable extent to weathering processes, but much more rapidly (Viles *et al,* 2011, Hall *et al*, 2005).

Equotip surface hardness survey is only partially predictive of the presence of visible surface fractures on an otherwise undamaged surface. This can be seen in the heat maps presented in Figure 2.16; although there is some agreement between surface fractures and areas of reduced surface hardness (sides 1 and 6), for many surface fractures, there is no corresponding reduction in surface hardness (sides 2 and 4). It is possible that fractures resulting in a discernible reduction of hardness in the stone have denser micro-fracture networks associated with them. Investigations using Schmidt hammer by Young and Frowell (1974) demonstrated a decrease in surface hardness with smaller discontinuity spacing. Decreased surface hardness proximal to a visible fracture may therefore indicate a network of micro-fractures associated with it that are unobservable on the surface. If a correlation between lower surface hardness and denser subsurface fracturing could be confirmed it may allow the use of Equotip to aid the findings of permeability survey in highlighting areas of damaged heritage stone most likely to allow ingress of deleterious weathering agents. More studies, including microscopy work outside of the scope of this PhD project would be necessary to confirm this.

When taken together then, the results of the Equotip surface hardness survey demonstrate the efficacy of this method in rapidly assessing areas of a stone sample most damaged by ballistic impact. This suggests this surveying technique will be appropriate when seeking to determine which areas of heritage stone monuments are most in need of targeted conservation intervention in the aftermath of an armed conflict.

2.5.2: Discussion of Permeability Survey Results

Mirroring the Equotip findings, permeability at the impact crater was found to be lower than the average for the wider shattered surface, supporting the notion that there is compaction at this point that causes a smaller reduction in hardness and a smaller increase in permeability compared to the rest of the shattered surface (figure 2.13). However, whilst the impact point has the highest hardness across the shattered surface when measured with the Equotip, it does not have the lowest permeability. This can be seen in table 2.5, which shows that many of the sampling points further from the impact crater have a lower permeability than the centre (points 2,5,6,7,10). The fact that the impact crater has an increased permeability relative to these points is possibly due to the fracturing of quartz grains at the impact site. The fracturing of quartz grains at the site of ballistic damage has been observed under scanning electron microscope (SEM) by Mol after impact by .22 lead projectiles (Mol, 2017). The increase in permeability at the point of impact in this study is evidence of the same phenomenon being present with larger calibre projectile impacts and highlights that ballistic damage to stone causes both macroscopic (observable surface fractures) and microscopic changes (the fracturing of quartz grains).

Another clearly identifiable spatial trend is that permeability (which can be taken to infer damage to the sample due to its correlation with fracture presence) corresponds strongly with the direction of impact. In the heat map for side 1, the fractures and areas of increased permeability can be seen to radiate outwards from the point of impact. Radial fracturing is a classic sign of ballistic impact in brittle materials (Johnson *et al.* 1998) and shows that permeability survey accurately reflects known projectile damage patterns. On sides 2, 4, 5 and 6, it is clear that the side of the surface closest the impact (indicated by the red arrow) experiences a far greater increase in permeability than the side furthest from the impact. This trend is especially clear in the heat map for side 2, where the direction of impact and the orientation of surface fractures are strongly reflected in the areas of highest permeability across the surface.

In the sides that did not experience direct impact (2,4,5,6), the fractures often run parallel to the direction of impact, and this is especially true on sides 2 and 6. However, some surface fractures run perpendicular to the direction of projectile impact, as can be seen on sides 4 and 5. This is perhaps evidence that the tensile stress waves generated by the projectile impact are exploiting pre-existing defects in the stone, resulting in these fracture patterns. This would

support previous findings, which illustrated through computed tomography analysis that internal fracturing of stone arising from bullet impact exploited bedding planes within the sample (Mol *et al*, 2017). The results of the heat mapping process therefore suggest that the spatial distribution of fracture damage in an impacted stone block, which can be mapped using permeability survey, is dependent both on the relative orientation of the projectile and target, as well as the lithology of the target and internal defects such as bedding planes.

In areas distant from the surface fractures, the permeability heat maps are broadly homogenous, indicating that increases in permeability are mostly associated with visible surface fractures. Further studies with more samples will be required to confirm whether substantial permeability increase only occurs with visible surface fracturing or surface disaggregation, as seen in the impact crater and shattered surface. If such a relationship can be established it could allow the development of conservation techniques based on rapid visual identification of fractures likely to increase permeability and allow ingress of weathering agents, reducing data collection time and allowing faster conservation intervention. This hypothesis is supported by the findings of Freire-Lista and Fort (2017), which demonstrated that permeability to air is not significantly increased by micro-cracking in stone. Similar micro-cracking might be caused at distances further from the impact crater but would not be visible with the naked eye, but would not alter the surface permeability of the shot stone. Finally, the heat maps show that the edges of the sample have similar permeability values central regions of the sample surface. This suggests that there has been no notable artificial reduction in permeability due to the calibration constant.

Principally, the permeability results suggest that permeability survey is a potentially useful field technique when seeking to quantify increases to target lithology caused by surface fracturing and allowing mapping of those permeability increases. Perhaps most significantly, results suggest that large increases in permeability that are likely to drastically increase weathering deterioration are only associated with visually identifiable surface fractures and damage. Further chapters of this project will seek to explore this hypothesis. If it can be confirmed it will mean that stone-built heritage most at risk of moisture and salt ingress can be visually identified in a field setting, allowing faster conservation intervention. The potential for visual analysis of surface damage to infer areas of most increased permeability is further supported by the results presented in figure 2.15, which suggest that the permeability of a surface is correlated with the area of that surface lost due to ballistic damage.

One notable limitation of the permeability survey was its time-consuming nature. Each reading of intact stone took approximately 150 seconds, This means a full survey of an intact 15cm x 15cm x 15cm block with 3 repeat measurements would take over 36 hours for an area of 0.135m^2. This may be prohibitively time intensive in a field context under conflict conditions, and therefore the next pilot study of this PhD work trialled a reduced sampling regime (see section 3.2.8).

Statistical analysis undertaken here supports the likely presence of an edge effect for both Equotip surface hardness and permeability for these samples of cut stone. Whilst Viles *et al* (2011), did not record this edge effect on natural stone blocks, this does appear to be an issue for blocks subjected to the strain of cutting equipment. This is worth considering when informing conservation strategies for ballistic damage to stone, as impacts that cause damage and fracturing to the edge of a block may be exacerbated by the edge effect. However, further work is necessary to understand the edge effect, both to confirm its presence for cut stone, and to understand how to effectively calibrate for it during ballistic investigations. It is also worth noting that whilst removal of the edge effect is important for understanding distribution of damage caused by ballistic impact in a scientific sense, in a field setting such as conservation teams triaging damage buildings and planning interventions it is un-important whether damage of an impacted surface is due to the impact itself or other factors. Therefore, it is not advocated that when visualising damage distribution in a field setting that the edge effect be considered.

2.6: Conclusions

The data presented here supports previous work on ballistic damage to stone, confirming previous observations that ballistic impact can lead to higher Equotip surface hardness for the impact crater relative to some areas of the surrounding stone (Mol *et al*, 2017), whilst also demonstrating that these conclusions hold true for higher calibre, more damaging ammunition than previously studied. Furthermore, the significantly lower hardness values of the shattered surface compared with the non-shattered cells illustrate the efficacy of using Equotip surface hardness to identify those surfaces that have been sheared or shattered due to ballistic impact. Therefore, Equotip rebound surface hardness survey has been shown here to be a useful method in distinguishing between less-damaged sides and the impact crater and wider shattered surfaces arising from ballistic impact.

On sides distant from the impacted side of the sample, permeability surveys have been shown in this study to be an effective method for quantifying and mapping surface fracture networks. Results also suggest that visible fractures are largely responsible for increases in permeability. This could aid targeted conservation of damaged heritage sites by rapidly identifying points of ingress for weathering agents that are susceptible to weathering damage.

The principal findings of this chapter are that an integrated dual survey using surface hardness and permeability data provides informative, quantitative insights into the degree of damage caused to stone subject to ballistic impact. Critically, these methods can be utilised rapidly in the field and are non-destructive, pointing to a viable method for assessing damage to built heritage in conflict zones, as outlined in Research Objective I: "*To develop field appropriate non-destructive methods to assess exterior damage to limestone and sandstone arising from military projectile damage (7.62 x 39mm and 5.56 x 45mm)".*

The conclusions of this exploratory pilot study will inform the subsequent methodological approach of this research, and the principal findings that will be carried forward are outlined below:

- Equotip rebound hardness survey and Tiny Perm 3 permeability survey have been shown to be effective, portable and non-destructive methods of assessing exterior damage to stone damaged by ballistic impact. This partially fulfils Research Objective I, and these techniques will be used in future experimental work throughout this project.

- Permeability survey is effective at assessing increases in permeability due to visible fracturing caused by ballistic impact. However, the methodology is time intensive and may not be appropriate to time constraints in a conflict zone. Therefore, other permeability sampling regimes were trialled in the pilot study in chapter 3.

- Spatial analysis of the data generated by these research methods can reveal patterns of ballistic damage to stone. Thus, a spatial approach will be adopted in future

experimental analyses in order to identify regions of damaged stone most at risk of deterioration after impact.

- The 3375cm³ sample size used in this study is large enough to withstand projectile damage without being fully perforated or destroyed, whilst being small enough to be stored and moved in a laboratory environment, and this sample size will be used in future laboratory investigations.

N.B. This thesis chapter, with some minor edits, was published in the journal *Heritage:*

Gilbert, O., Mol, L., Campbell, O., and Blenkinsop, T. (2019). Permeability and surface hardness surveying of stone damaged by ballistic impact. *Heritage*, *2*(2), pp.1369-1389.

Chapter 3

Field testing of Rebound Hardness and Permeability Surveying Techniques

Chapter 3 Overview

Chapter 3 aims and hypothesis

It was hypothesised that the techniques deployed to analyse ballistic damage to stone developed in chapter 2 (rebound surface hardness and permeability survey) would be appropriate for assessing ballistic damage to stone-built heritage assets in a field setting. Furthermore, it was also hypothesised that the hardness and permeability data from a field survey of a heritage site damaged by ballistic impact would reveal that areas damaged by impact would experience exacerbated weathering, as discussed in section 1.6. Therefore, the study described in this chapter aimed to partially address Research Objective I by assessing the suitability of hardness and permeability surveying techniques for field-based assessment of ballistic damage and its interaction with weathering processes.

Chapter 3 methods

Systematic rebound hardness and permeability survey was undertaken across damaged surfaces of a heritage church exposed to weathering by salt and moisture and exhibiting ballistic impact damage arising from shrapnel scarring caused by a bombing raid during World War II. The presence of salt and moisture was identified and recorded using handheld Protimeter resistivity meters.

Chapter 3 principal findings

Findings suggest that ballistic impact interacts with weathering process by facilitating the movement of moisture through the surface fracture networks and the accumulation of moisture behind impact craters, leading to the presence of efflorescences of gypsum salts. This is evidenced by lower surface hardness readings for surfaces exhibiting ballistic impact and higher permeability readings caused by fracture networks caused by preferential weathering of ballistic-induced fracture networks. These results also demonstrate that these methods, originally developed in a laboratory in chapter 2, are appropriate for assessing damage to heritage sites in a fieldwork context. Finally, the results presented here vindicate

they hypothesis that ballistic impact exacerbates deterioration and weakening caused by haloclasty weathering processes.

3.1: Introduction

Chapter 2 served to demonstrate that survey of permeability and rebound hardness could be used to assess exterior deterioration in stone damaged by ballistic impact under laboratory conditions. However, in order to fulfil the stated goals of this project, it was necessary to ascertain the efficacy of these methods in a field setting.

Assessing ballistic damage to stone in the field would likely be more complex than under laboratory conditions because a number of variables that could be discounted in the laboratory pilot study would be present in a field environment. These include determining if deterioration in the impacted stone could be attributed to ballistic damage or was caused by other factors, such as weathering. Furthermore, it would be necessary to determine whether those areas that have been impacted suffer greater weathering deterioration than un-impacted areas. Assessing the ability of rebound hardness survey and permeability survey techniques to distinguish the effects of ballistic impact on the level of weathering deterioration in a field setting was therefore a key aim of this research.

Finally, a field-based study was necessary to determine whether these techniques were effective in a field setting with a wide spatial distribution of impacts into potentially uneven and irregular stone surfaces. This study thus aimed to create systematic sampling regimes that facilitated informative data collection in the field, and to integrate hardness and permeability survey into this sampling regime in order to demonstrate their suitability for in-situ analysis of conflict damage to heritage stone.

To address these issues, a field survey was undertaken at the Royal Garrison Church, Portsmouth. The site is a building of significant historic value, which was damaged by German bombing in 1941. The site exhibits a large number of ballistic impacts in the interior of the church, caused by high velocity metallic shrapnel caused by the fragmentation of the explosive device after detonation. In addition to this impact damage, the site is also highly vulnerable to weathering deterioration due to its lack of roofing and immediate exposure to saline sea spray. These conditions meant that the site was uniquely suited to being a field site

for research as part of this project, combining ballistic damage with high risk of weathering damage by moisture ingress and haloclasty.

3.2: Background to the Site

3.2.1: Site History

The Royal Garrison Church building was constructed in the early 13th century, as part of the medieval *Domus Dei* hospital with an attached chapel. This complex had been constructed by the Bishop of Winchester, and after the dissolution of the monasteries and the stripping of their assets, the site was repurposed as an ammunition store (Wright, 1873, pp.19,153). During the Elizabethan period, it was repurposed as the chapel of the Governor's House, the venue for the marriage of Charles II to Catherine of Breganza. Further historic events were hosted at the site, including a visit by George III in 1778 and a formal reception in 1814 attended by allied monarchs and military figures to celebrate victory in the Napoleonic wars. By the mid-19th century, the governor's house had been demolished and the church was in need of restoration work, which took a decade to complete and was finished in 1871, restoring the 13th century aesthetic of the building (English Heritage, 2004). In 1941 a bombing raid ruined the nave and destroyed the roof. However, the chancel was left relatively intact, and has been separated from the nave by a modern wall. The church still serves to memorialise members of the armed forces, with stained glass windows that commemorate events of the Second World War (*ibid*). The church was entered on to the National Heritage List for England in 1999 as a Grade II listed building, which is the lowest designation, but still states that the building is "of special interest, warranting every effort to preserve it" (Historic England, 2020).

3.2.2: Site Layout

The royal garrison church lies south-east of the entrance to Portsmouth harbour at a distance of approximately 60m from an artificial tidal inlet that surrounds the southern edge of the site. The location and surrounds of the site are shown in figures 3.1 and 3.2.

Figure 3.1: *An ordnance survey map showing the location of the Royal Garrison Church within the Portsmouth Harbour area (adapted from www.bing,com/maps).*

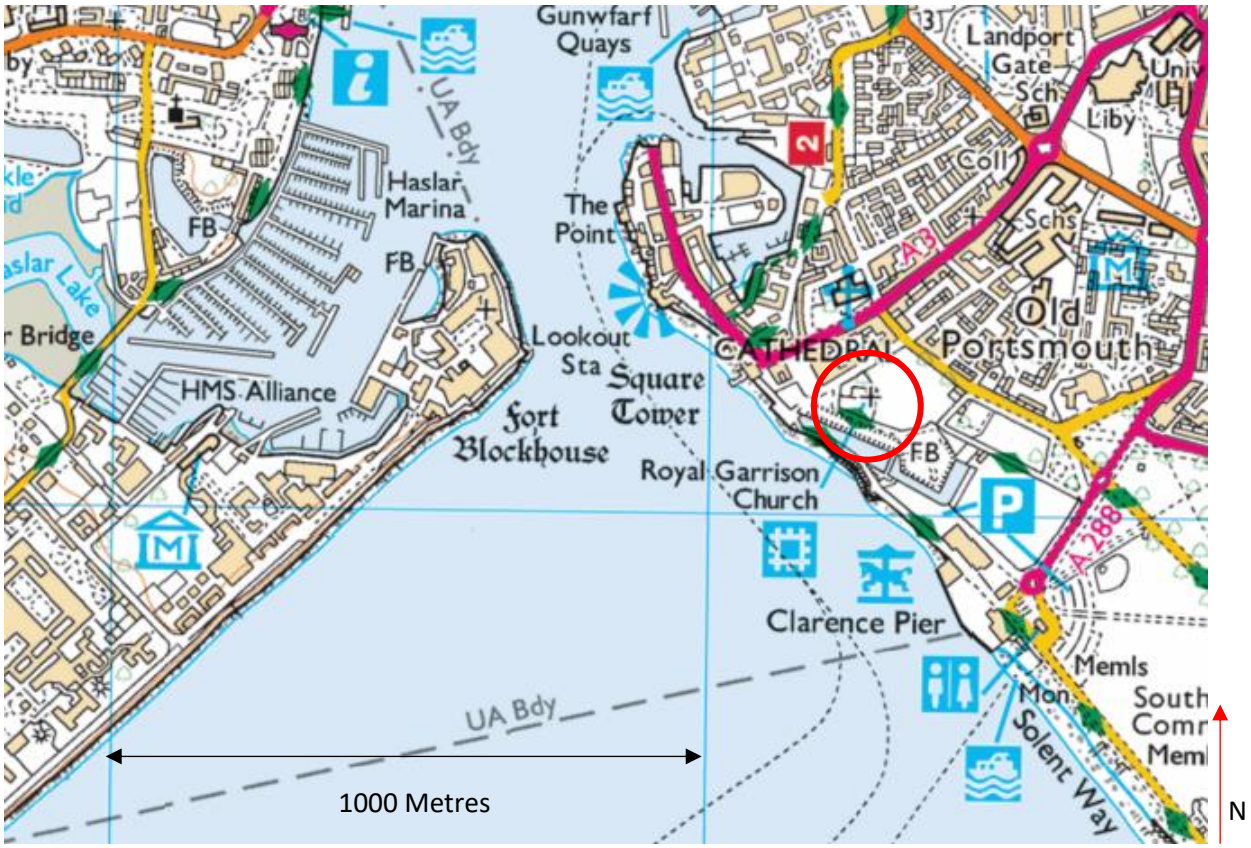

Figure 3.2: *An aerial image showing area of the Royal Garrison Church and the distance to the sea/tidal inle (adapted from www.google.com/maps).*

The bomb damage to the church is chiefly confined to the nave of the building, and resulted in the loss of the church roof, which was partially restored over the adjacent aisles in 1994-1995 (Historic England, 2020). The nave contains eight octagonal columns, many of which exhibit scarring due to shrapnel impact from the bomb blast. The research of this fieldwork was conducted in this area of the church, the layout of which is shown below.

Figure 3.3: *An image showing the central aisle of the nave of the Royal Garrison Church, with the octagonal columns on either side.*

Figure 3.4: *A schematic diagram showing the layout of the nave portion of the Royal Garrison Church.*

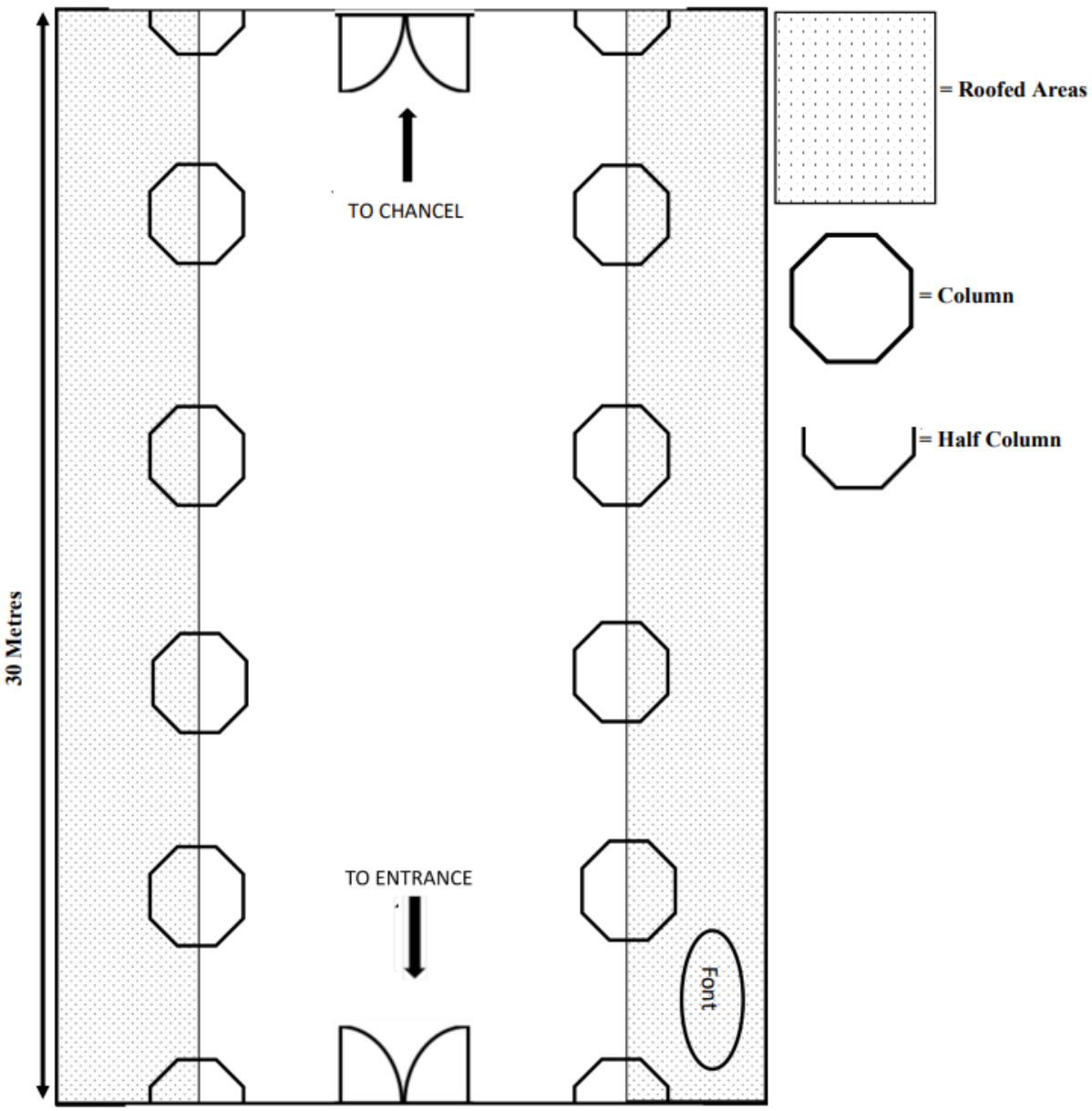

3.2.3: Description of Ballistic Damage at the Site

On the night of January 10th 1941, a large German bombing raid was mounted against the strategically important city of Portsmouth. During the raid, hundreds of high explosive bombs and thousands of incendiary devices were dropped on the city (Hampshire Telegraph, 1945). A mixture of explosive and incendiary weapons was a common tactic of aerial warfare at the time, as the explosions would demolish walls and windows, creating through-flow of air, which would facilitate the rapid growth of fires caused by the incendiary weapons (Taylor, 2011). Images in newspapers after the raid appear to show that the explosion occurred in the centre of the nave, towards the chancel end. The spread of shrapnel from this explosion has caused impact craters on all the octagonal columns except the two nearest the entrance, and impact craters are visible on the walls of the adjacent aisles. In order to ensure that the impacts at the site fit within the scope of this research, it is necessary to outline why these craters can be viewed within the definition of ballistic damage rather than explosive damage.

One of the most frequently used German high explosive bombs of World War II, and a likely candidate for the damage to the church was the SC 50. This weapon had an overall weight of 48-55kg with an explosive charge of 21-25kg of explosive, usually TNT or Amatol (Departments of the Army and Air Force, 1953). Based on parameters of 21kg of Amatol and 35kg of steel casing, the United Nations SaferGuard International Ammunition Technical Guidelines using Gurney equations give an initial shrapnel fragment velocity of 1296ms^{-1} for the SC 50 (U.N. 2020). This is a comparable velocity to those reached by small arms projectiles that exceed 1000ms^{-1}, such as the .338 Lapua magnum sniper cartridge, or the .22-250 remington Swift, which exceeds 1200ms^{-1} (Imperial War Museum, 2020). Therefore, given the velocities and steel construction of the shrapnel fragments that caused the impact damage at the Royal Garrison Church, we can view them as approximately analogous in their likely damage profiles to small arms ammunition, and are thus defined as ballistic impacts.

3.2.4: Description of Weathering Risks at the Site

As previously outlined, the Royal Garrison Church is situated close to the sea at Portsmouth Harbour. As such, the likelihood of saline sea-spray blowing on to the building is high. The building is also situated below an embankment that is immediately adjacent to the sea and could facilitate the collection of saline groundwater around the site. It is also known that salt deposition from marine spray has caused mechanical degradation at other stone-built heritage

sites in the Portsmouth harbour area, such as Portchester castle (May *et al,* 2003). This abundance of saline water means that the risk of haloclasty weathering to the church is substantial, and likely efflorescences are clearly visible on some of the internal columns:

Figure 3.5: *An image showing a likely efflorescence at the base of a column in the Royal Garrison Church. The location of the weathering front suggests that this is the result of capillary rise of saline groundwater.*

Deterioration due to ingress of rainwater is also an issue due to the lack of roofing over the central aisle of the nave, and the Met Office reports an average annual rainfall of 723mm for the area (2022). Clearly these rainfall totals are not consistent with the arid environments which are the principal focus of this project, and therefore this fieldwork served primarily as a pilot study for assessing field-based techniques and sampling regimes in a site with serious haloclasty risks. For example, most of Libya has annual rainfall less than 100mm

(Wheida, Verhoeven, 2006). Mechanical weathering is also likely to play a significant role in the deterioration of stone at the site, especially due to freeze-thaw cycles of moisture within fractures and faults. Clearly, this site cannot be said to be analogous to those in arid environments, chiefly because the maximum temperatures and diurnal ranges are far lower than arid regions. However, some of the weathering processes present at the site are comparable to the weathering processes that are the focus of this research project, particularly the prevalence of moisture ingress and haloclasty weathering. Therefore, this site is well suited to exploring the risks posed to stone-built heritage damaged by ballistic impact and subjected to haloclasty weathering.

3.3: Field Survey Methods

After surveying the interior of the Royal Garrison Church, it was apparent that the majority of impact craters that would be accessible and suitable for analysis were present on the columns of the building. Therefore, a sampling regime was devised that would allow the systematic recording and referencing of this damage. Each of the octagonal columns was assigned a number or letter, and each side of the columns was given a standardised number (figure 3.6).

Figure 3.6: *A schematic diagram showing the sampling scheme and sampling areas within the Royal Garrison Church.*

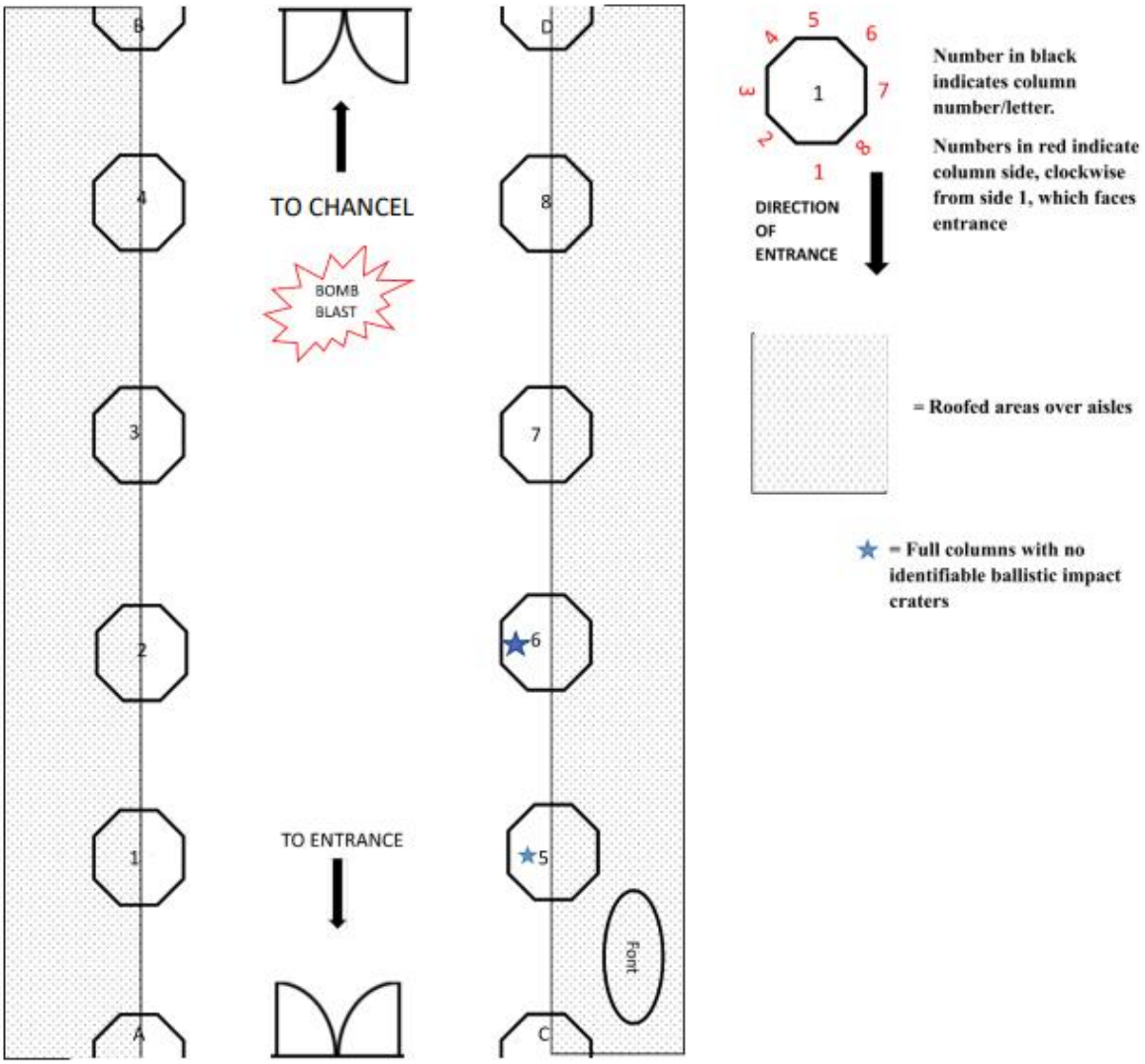

Ballistic impact craters were recorded by their column, side, and height of the centre of the crater. All heights were recorded from the top of the column pediment/base (figure 3.7). Measurements for intact stone (i.e. stone that did not exhibit ballistic damage) were obtained from the same height above the base of each column (10cm, 110cm, 200cm), and from the centre of each side (14.5cm across side) (figure 3.7). This meant that eight sampling points of intact stone were obtained for each column (figure 3.6). Intact stone sampling points were taken at three different heights to account for any reduction of hardness in intact stone caused by capilliary rise of groundwater and a 100cm spacing of sampling points is comparable to previous studies seeking to determine spatial variability in geotechnical properties across large field sites (Bruning, Webster, Teet, 2022).

Figure 3.7: *An Image showing the system for indexing sampling point and impact crater heights.*

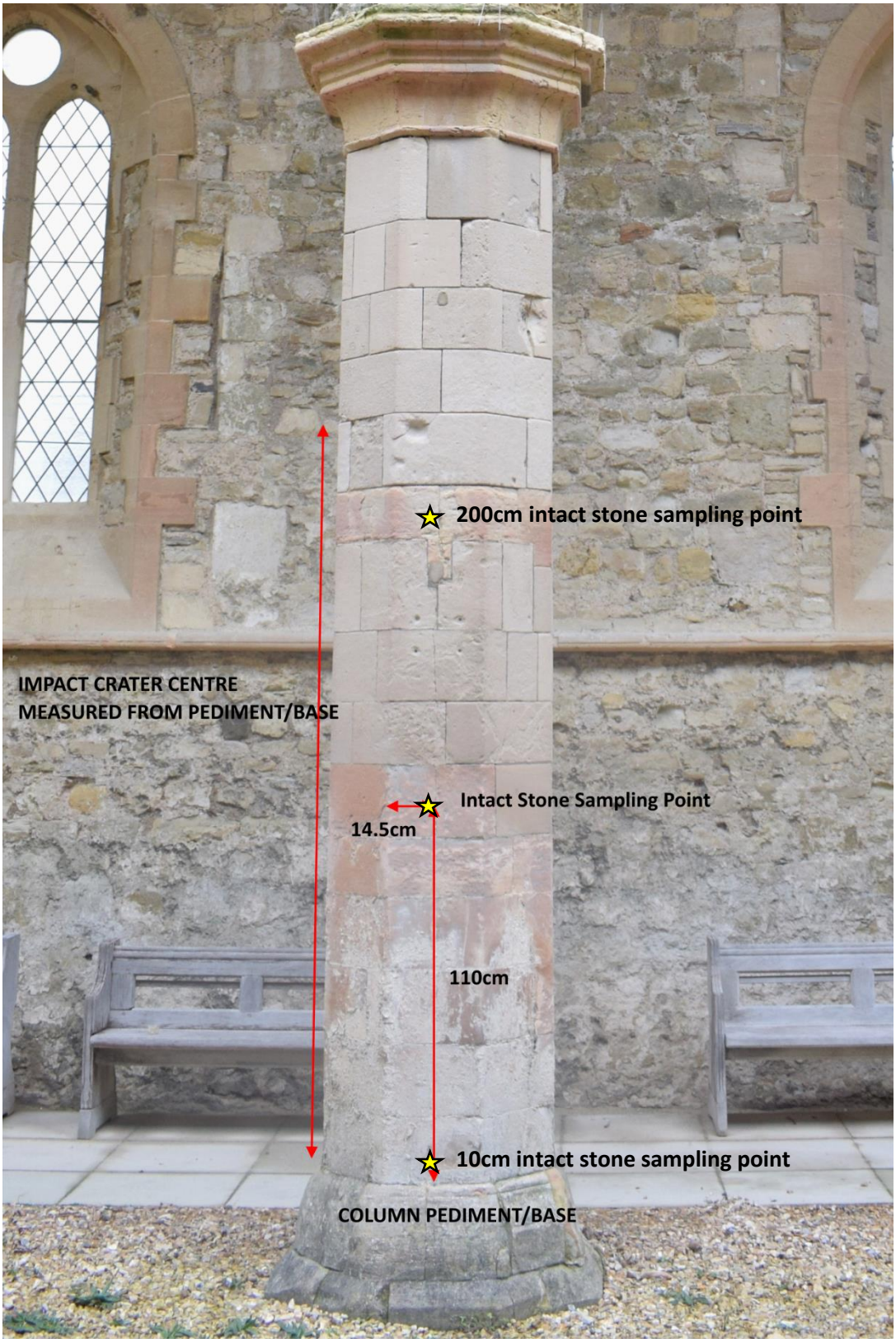

A permeability reading was taken from the intact stone sampling points of each side of each full column using the Tiny Perm 3 Air Permeameter. For every accessible impact crater, a permeability measurement was taken in a cross pattern from the centre, top, left, right and bottom of each impact crater (figure 3.8).

To ensure a representative average of the weathered and variable stone surfaces, ten hardness measurements were taken from the intact point of each side of each full column using an Equotip 550 portable rebound hardness tester with a type D impact device. The repeat impact method was used for each sampling point due to the limited number of areas where readings could be obtained from dry and flat surfaces of intact stone. For every accessible impact crater, ten hardness measurements were taken for every point in a cross pattern from the centre, top, left, right and bottom of each impact crater (fig 3.8).

Figure 3.8: *An Image showing the sampling regime inside the impact craters*

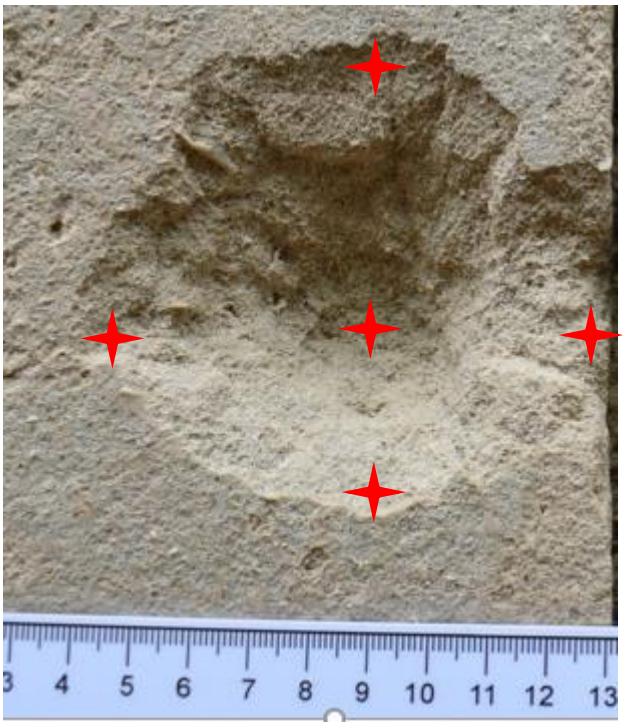

In order to assess the presence of moisture and associated soluble weathering salts in the columns, a Protimeter MMS2 moisture meter was used to survey sides 3 and 8 of each column. In the pinless configuration, the meter emits electro-magnetic waves which induce and electromagnetic field in the surface that is being studied. The signal received by the device from the target surface is then correlated with a moisture content measured as Wood Moisture Equivalent (WME) on a scale of 60-99 (Okai, 2016, Hubner, Kaatze, 2016). The Protimeter MMS2 is entirely non-invasive and non-destructive, and has been used to assess the condition of decorative stone elements of the San Giovanni Baptistry in Florence (Santo *et al*, 2022). The use of this method at the Royal Garrison Church would allow a comparison of the moisture content of surfaces fully sheltered from rain and sea spray by the aisle roofing, and the columns fully exposed to these sources of moisture. In keeping with the protimeter sampling regime used for moisture monitoring at heritage sites by Martinez-Garrido *et al* (2018), readings of moisture were taken every 20cm from the base of the column vertically up to 200cm, as shown in figure 3.9:

Figure 3.9: *The Protimeter sampling regime. Each black asterisk represents a protimeter sampling point. Protimeter sampling points are 20cm apart*

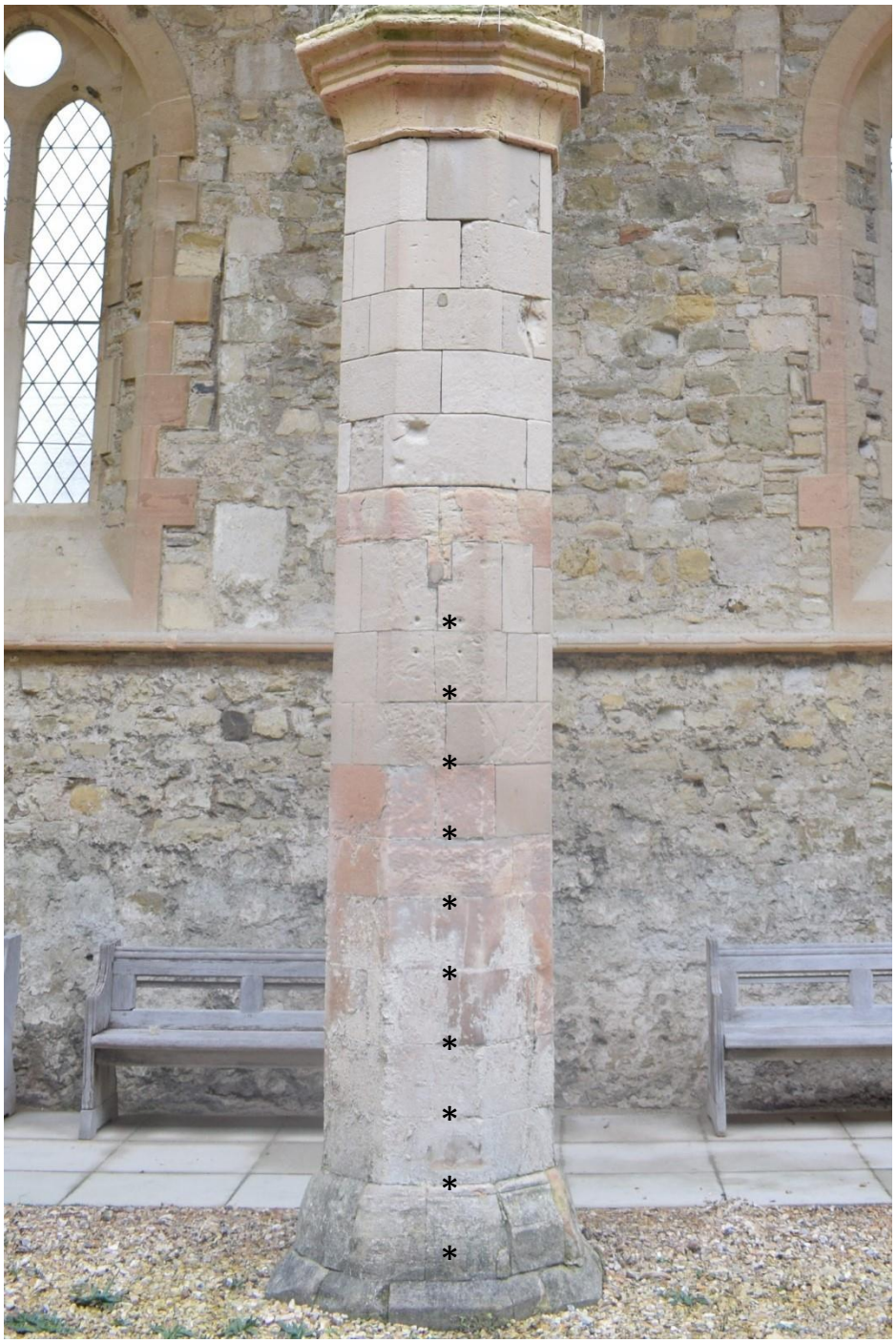

3.4: Results and interpretation

3.4.1: Rebound Hardness Survey Results

Outside of impact craters, the column sides protected from the bomb blast and most shielded from subsequent weathering due to roofing (sample set A) are significantly harder than sides most exposed to the bomb blast and open to weathering due to a lack of roofing (sample set B). The sample sets are depicted in figure 3.10 and the data showing this trend is presented in figure 3.11.

Figure 3.10: *A schematic showing the sides featured in sample sets A and B.*

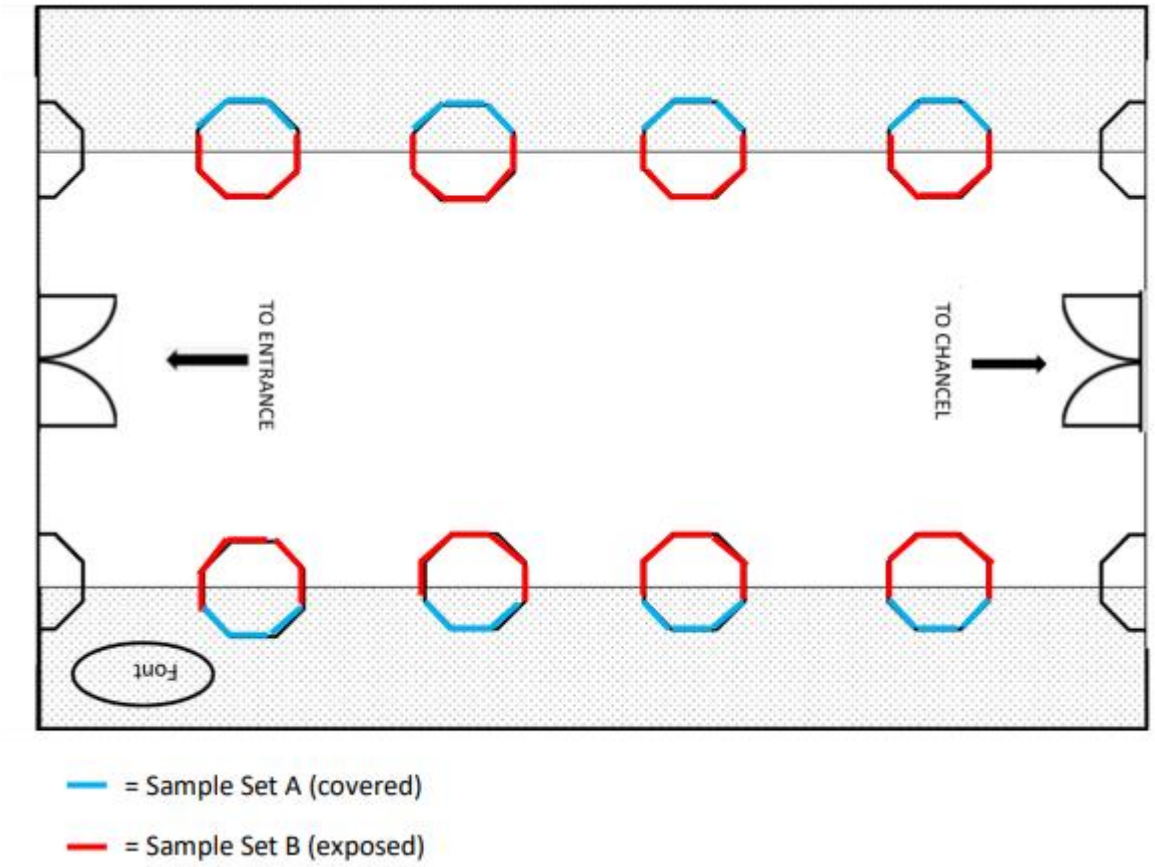

The protected column sides are on average 16 Leeb harder than the exposed surfaces (417 Leeb vs 401 Leeb) and this difference can be shown to be statistically significant based on a significance level of 0.1 (P=0.065) (figure 3.11, table 3.1). This is evidence that exposure to the bomb blast and subsequent weathering has weakened the most exposed surfaces of the columns to a greater extent than those not facing the blast and with the aisle roofing to protect them from weathering. N.B: these results pertain only to un-impacted column

blocks/surfaces, and do not include data from impact craters, which is discussed separately later in this chapter.

Figure 3.11: *The difference in hardness between column sides sheltered from the bomb blast and sheltered by the aisle roofing and the column sides exposed to the blast and weathering. Error bars are the standard error of the given data sets.*

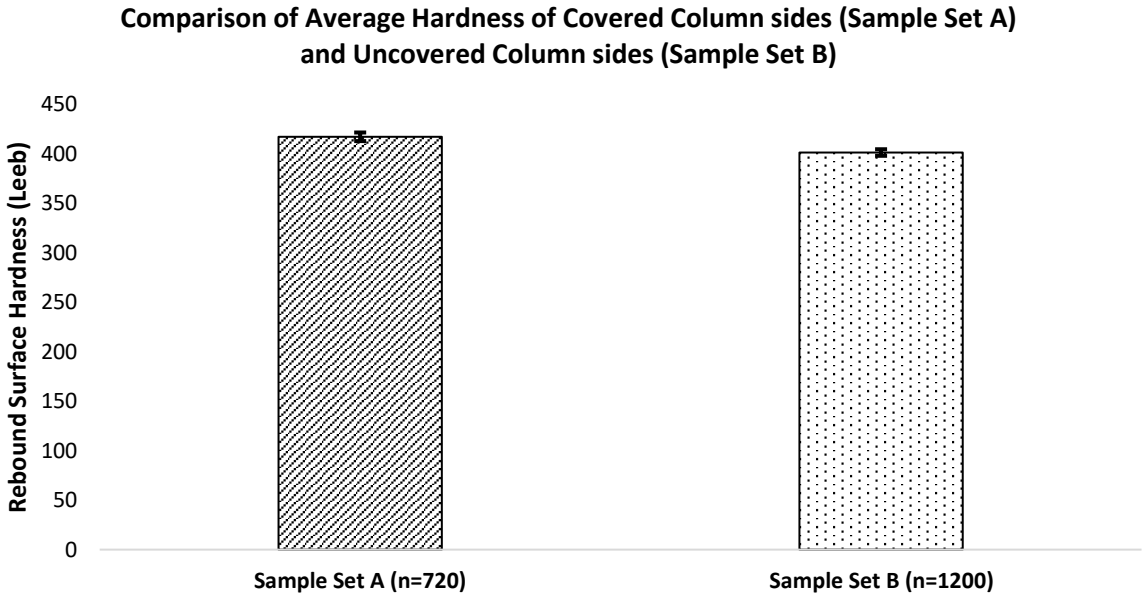

Table 3.1: *Descriptive statistics of sample sets A and B*

	Mean (Leeb)	**n**	**Maximum reading (Leeb)**	**Minimum reading (Leeb)**	**Range**	**Standard deviation**	**Standard error**
Sample Set A	417	720	726	200	526	116	4
Sample Set B	401	1200	703	200	503	114	3

The data presented in figure 3.11 and table 3.1 is evidence that rebound hardness survey is able to distinguish those surfaces that are more exposed to weathering processes and are therefore more likely to deteriorate after ballistic impact. This suggests that rebound hardness survey is appropriate for analysis of weathering deterioration to damaged monuments in the field.

Having shown that hardness survey can identify surfaces most affected by weathering deterioration, it was necessary to determine if the technique could indicate whether ballistic impact has an influence on weathering rates. To test this, the average hardness of the 20 column sides showing an identifiable ballistic impact was compared with the hardness of the 44 column sides containing no impacts. The results of this analysis are presented in figure 3.12 and table 3.2. Again, results pertain to intact column blocks, but on sides of the octagonal columns where impact craters are present elsewhere; impact craters themselves are not discussed in these results.

Figure 3.12: *The difference in hardness between column sides with and without ballistic damage. Error bars are the standard error of the given data set.*

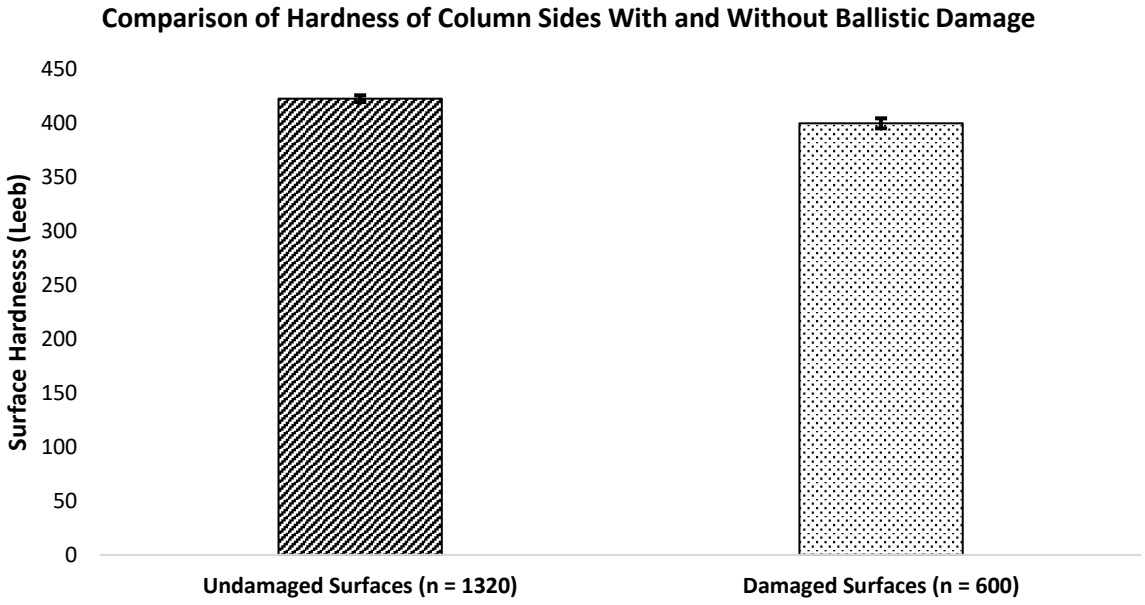

Table 3.2: *Descriptive statistics of the hardness survey of the undamaged and damaged column sides.*

	Mean (Leeb)	n	Maximum reading (Leeb)	Minimum reading (Leeb)	Range	Standard deviation	Standard error
Undamaged Surfaces	422	1320	726	109	617	113	3
Damaged Surfaces	399	600	692	200	492	113	5

The fact that undamaged column sides are harder than those exhibiting ballistic impact (422 leeb vs 399 leeb) suggests that the presence of ballistic impact exacerbates weathering action of stone surfaces that have been damaged by impact. This is explained by ballistic impact creating surface and sub-surface fracture networks in these column sides. These damage induced fracture networks will be less present in column sides without ballistic damage, meaning that moisture and salt are less able to migrate around undamaged surfaces and less weathering induced weakening occurs on these surfaces. This hypothesis is also supported by permeability data and spatial analysis presented in following sections (3.4.2, 3.4.4).

One interesting trend is that there appears to be no difference in hardness between impact craters and un-impacted stone (415 Leeb for unimpacted stone and 416 leeb for the impact craters). This data is presented in figure 3.13 and table 3.3. Figure 3.13 and table 3.3 also show that the centre of impact craters is marginally harder than the wider impact crater (419 Leeb for the impact centres, 415 Leeb for the wider impact crater), but this difference is not statistically significant (P = 0.69). Therefore, whilst this data does not contradict previous findings that centre of an impact crater is harder than the wider crater surface due to compaction of the stone matrix (see chapter 2.1), it can also not be taken as evidence of this phenomenon at this site.

Figure 3.13: *A comparison of the average hardness of the impact craters and the intact stone surfaces. Error bars are the standard error of the given data sets.*

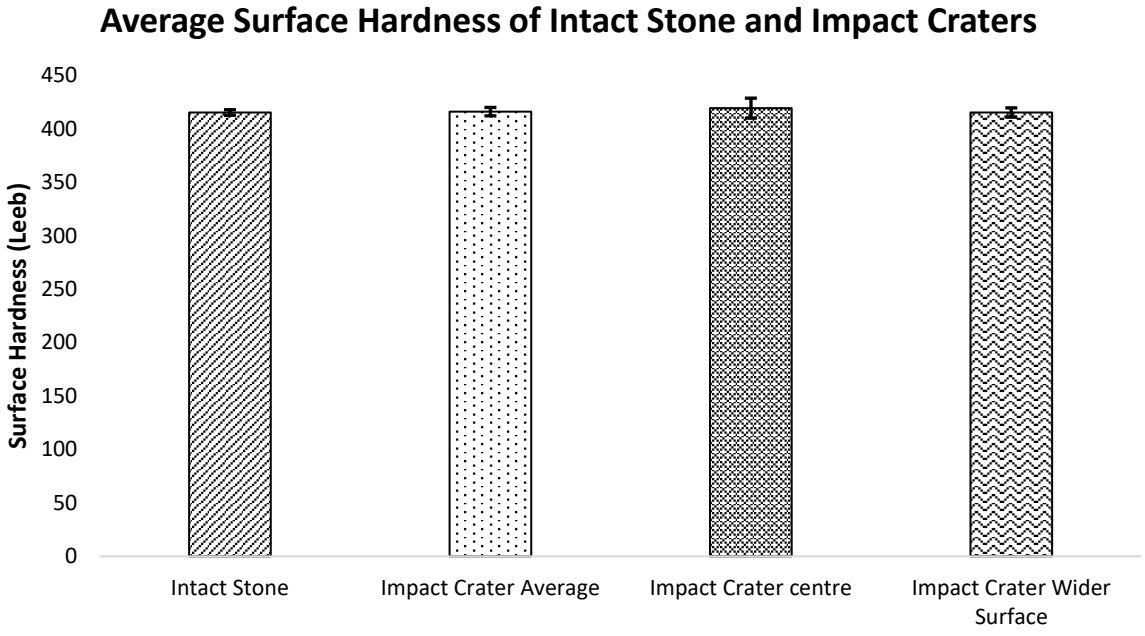

Table 3.3: *Descriptive statistics for the data sets presented in figure 3.13*

	Mean (Leeb)	**n**	**Maximum reading (Leeb)**	**Minimum reading (Leeb)**	**Range**	**Standard deviation**	**Standard error**
Intact Stone	415	1920	726	109	617	114	3
Impact Crater Average	416	600	669	201	468	96	4
Impact Crater Centre	419	120	620	205	415	102	9
Impact Crater Wider Surface	415	480	669	201	468	95	4

The fact that the intact stone and the impact craters have very similar values for hardness is hypothesised to be the result of over 70 years of weathering exposure. Whilst in the immediate aftermath of the bomb blast and shrapnel impact it seems probable that the impact craters would have been weaker than unimpacted stone, over the intervening time this weakened material will have been removed through weathering action. As a result, the stone that has been left has experienced very similar conditions to the unimpacted stone that is also exposed to weathering risks through the open church roof, and as a result there is no difference in hardness between the two data sets. This hypothesis is supported by both the fieldwork undertaken by Knight and Burningham (2020), and laboratory studies simulating weathering in coastal environments by Porter *et al* (2010). These studies demonstrated that in coastal environments erosion caused by weathering action served to remove rock surface material that was substantially weakened, leaving behind stronger fresh rock. It is believed that similar processes are responsible for the lack of hardness reduction observed in the impact craters relative to the rest of the column surfaces.

3.4.2: Permeability Survey Results

The results of the permeability survey support the conclusions drawn from the hardness data that impact craters create fracture networks that facilitate higher mobility of weathering agents that cause greater weathering weakening of the column sides where impact craters are present. This is demonstrated by the data presented in figure 3.14 and table 3.4:

Figure 3.14: *A chart showing differences in permeability between intact stone sampling points and impact craters. Error bars are the standard error of the mean.*

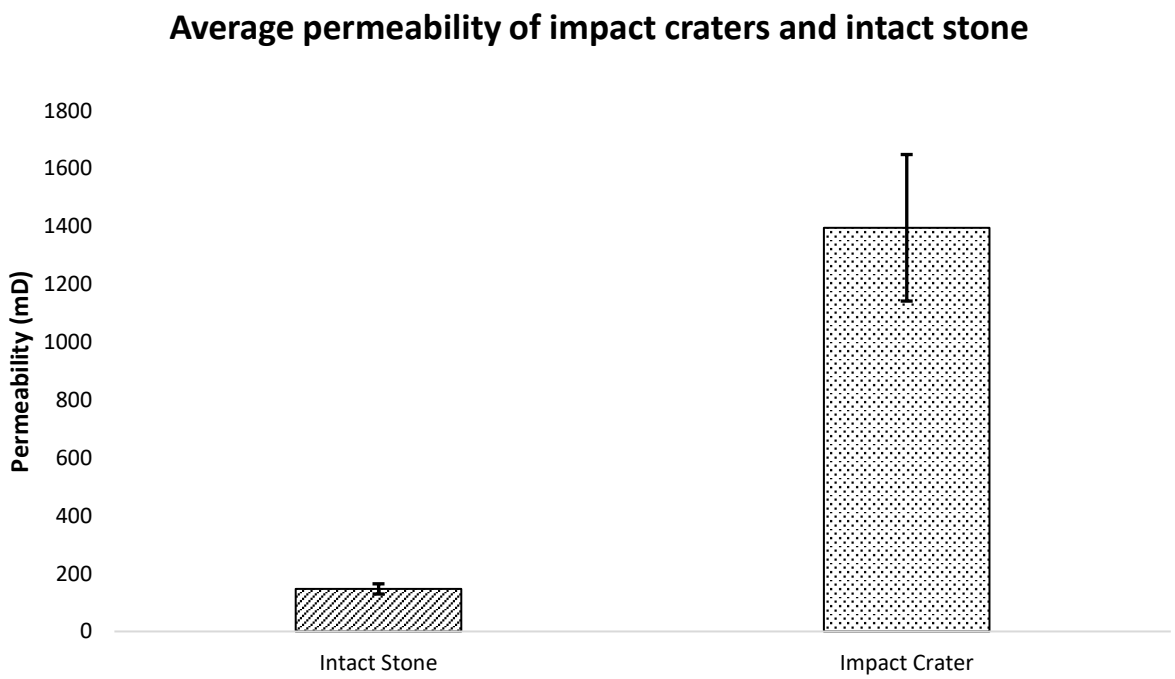

Table 3.4: *Descriptive statistics for permeability measurements of impact craters and intact stone.*

	Mean (Millidarcies)	**n**	**Maximum reading (Millidarcies)**	**Minimum reading (Millidarcies)**	**Range**	**Standard deviation**	**Standard error**
Intact Stone	147.1	192.0	1600.0	0.4	1599.6	244.1	17.6
Impact Crater	1395.4	72.0	9700.0	1.5	9698.5	2149.3	253.3

This large increase in permeability for the impact crater is caused by the dense fracture networks created by ballistic impact. The large increases in permeability caused by fractures present in the impact crater also result in the large standard deviation for the permeability of the impact craters (2149.3) as areas of the impact crater that do not have open fractures will have a much lower permeability. This is consistent with the findings of chapter 2 as discussed in section 2.4.1. This heightened permeability in impact craters acts as a point of ingress for

weathering agents and causes greater weathering on those column sides which exhibit impact craters. Further evidence for the fact that ballistic impact leads to greater weathering and moisture mobility can be seen when one considers the permeability of column sides exhibiting impact craters against those column sides that do not exhibit impact craters:

Figure 3.15: *The difference in permeability between undamaged whole column sides and column sides showing ballistic impact.*

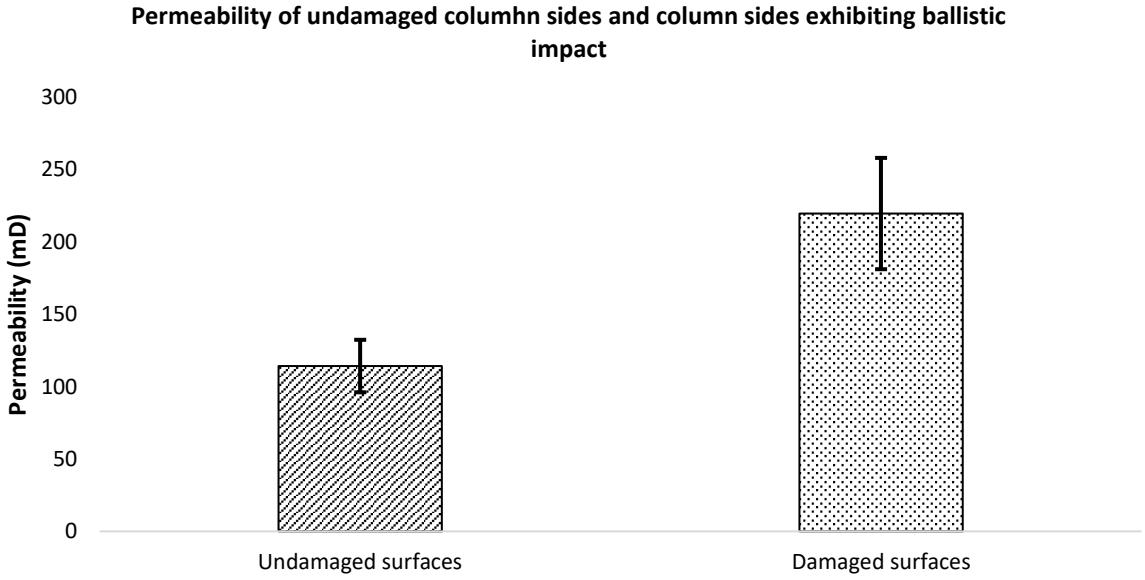

Table 3.5: *Descriptive statistics for the permeability of undamaged column sides and column sides with ballistic damage.*

	Mean (Millidarcies)	**n**	**Maximum reading (Millidarcies)**	**Minimum reading (Millidarcies)**	**Range**	**Standard deviation**	**Standard error**
Undamaged Surfaces	114.2	132.0	1600.0	0.4	1599.6	208.3	18.1
Damaged Surfaces	219.6	60.0	1100.0	4.6	1095.4	297.8	38.4

The fact that column sides with impact craters have a substantially higher permeability than the column sides without impact craters suggests that the fracture networks created by a ballistic impact may cause weathering feedback loops as discussed in section 1.6. As more

moisture and salts enter through the fracture networks created by ballistic impact these fracture networks are extended throughout the impacted surface through preferential weathering as discussed in section 1.6. This will increase permeability across the wider impacted surface, resulting in the increased permeability readings seen in figure 3.15 and table 3.5, as well as the increased moisture mobility suggested by the Protimeter moisture readings outlined in the following section.

Due to the location of the bomb blast, the sides with ballistic damage are also the sides that face the central aisle and are fully or partially exposed to weathering through the open roof of the central aisle. As observed in figures 3.18-3.22 below, these exposed surfaces have a far higher density of fractures than the sides under the cover of roofing. This increased fracture network across exposed sides will facilitate higher levels of weathering due to the ability of moisture and salt to exploit and exacerbate fractures across the exposed surfaces, as well as freeze-thaw processes associated with the greater water present on these surfaces due to rainfall (Noiriel *et al,* 2010, Yu, *et al,* 2015). These larger fracture networks that are more exposed to weathering are likely responsible for the increased permeability readings for the column sides exhibiting ballistic impact craters.

Whilst the increased exposure to weathering on these surfaces will contribute to raising the average permeability, ballistic impact is also instrumental in creating and exacerbating fracture networks (Gilbert *et al,* 2019). To demonstrate how ballistic impact exacerbates permeability increases, the distance from the location of the bomb blast to each of the columns was plotted against the area of positively identified ballistic impact craters and areas of ballistic damaged. The damaged area was calculated using scaled photographs of each column which were analysed in the ImageJ software package. Ballistic damage was categorised as those areas showing hemispherical craters and radial fracturing. Secondly, the permeability of each column outside of the impact craters was plotted against the area of ballistic damage. The results of these analyses are presented in figure 3.16 and 3.17:

Figure 3.16: *Column permeability vs distance from bomb blast*

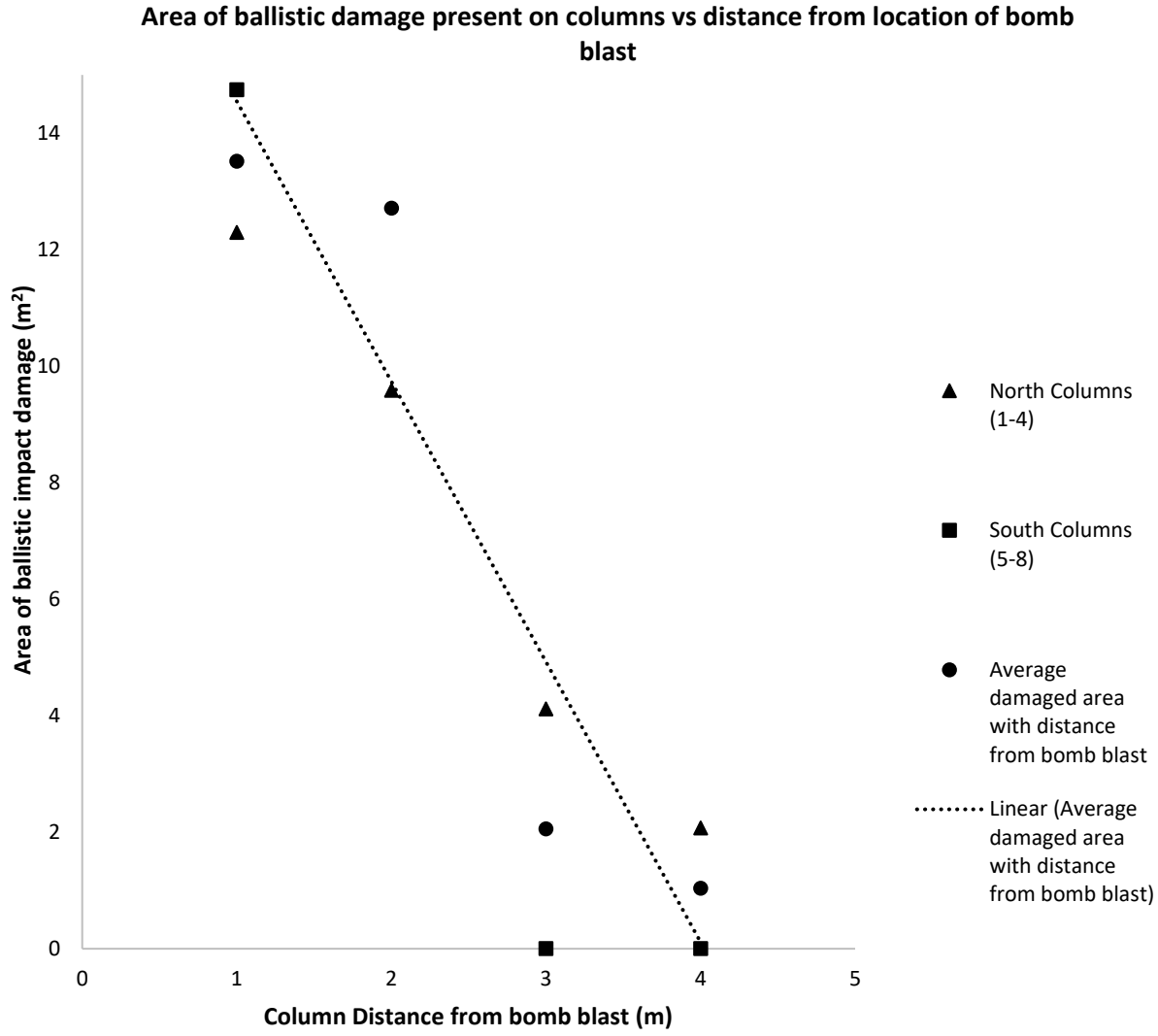

Figure 3.17: *Column permeability outside of impact craters vs distance from bomb blast*

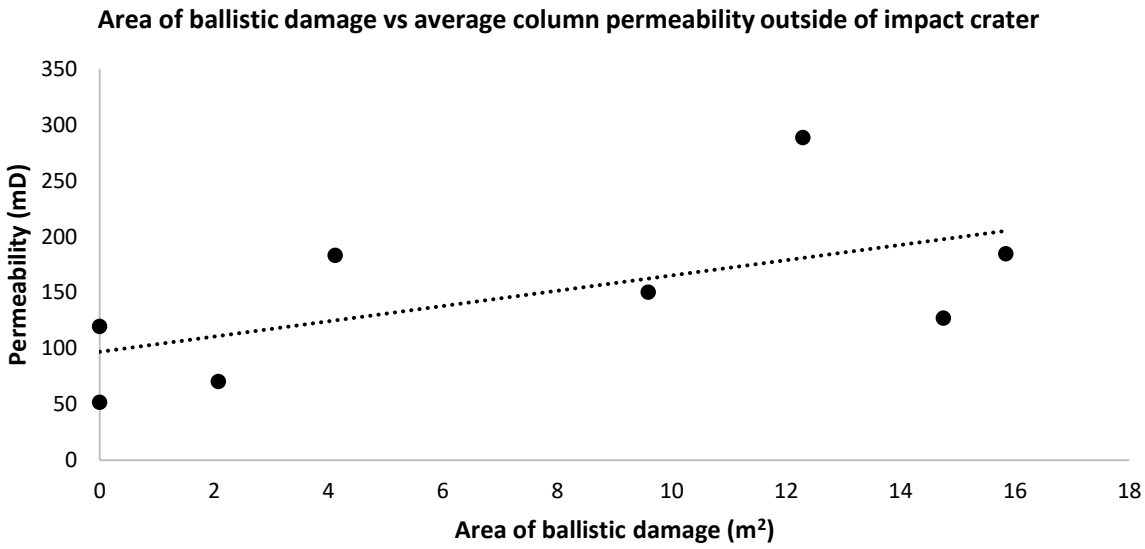

As figure 3.16 and 3.17 show, area of ballistic damage is strongly correlated with distance from the bomb blast (correlation coefficient -0.9) although this correlation was not shown to be statistically significant, possibly due to the small number of data points available as there were only four possible distances from the bomb blast. Area of ballistic damage was moderately correlated with the permeability of the column outside of the impact crater, and this correlation was statistically significant (coefficient co-efficient 0.6, $p = 0.0008$). Taken together, this suggests that areas closer to the blast are likely to be more severely damaged and that that damage will lead to an increased permeability across the column as a whole due to fracture networks initiated at impact craters. This supports the findings of chapter 2, which suggest that visible ballistic damage such as fracture networks can be used to infer increased permeability (section 2.5.2). It is worth noting, that due to the fact that weathering processes have caused impact craters and non-impact areas of the columns to have very similar hardness values (see figure 3.13) that although area of damage is correlated with distance from the blast, no correlation between distance from bomb blast exists.

Impact craters and ballistic damage likely act to connect fractures across separate stone blocks within the column faces, thus increasing the connectivity and overall permeability of the fracture network (Leary, Pogacnik, Malin, 2012). This will increase the mobility of moisture within the fracture network across impacted sides, leading to greater weathering within these fracture networks and an overall increase in permeability for these sides. To demonstrate the way in which impact craters increase the connection of fracture networks

schematic diagrams of each of the column's surfaces were constructed by Oliver Campbell at the University of Cardiff, which showed the locations of impact craters and surface fracture networks. These schematics were created from photographs taken at the church and used in figures 3.18-3.22. These figures are shown below; impact craters where fracture networks across separate stone blocks converge have been circled. The visual analysis of these schematic presented here was undertaken by the author.

Figure 3.18: *A schematic showing greater fracture density on the exposed sides of column 2, and the areas where impact craters allow fracture networks to connect across separate blocks. Image adapted from schematics created by Oliver Campbell.*

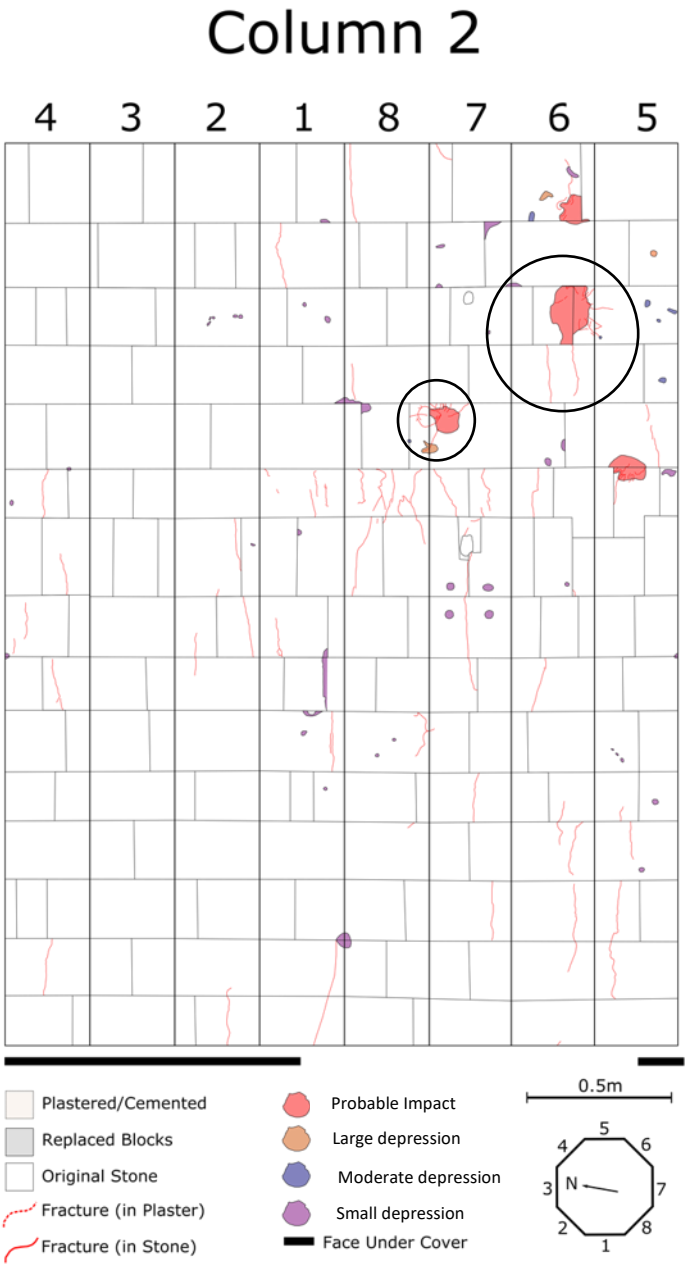

Figure 3.19: *A schematic showing greater fracture density on the exposed sides of column 3, and the areas where impact craters allow fracture networks to connect across separate blocks. Image adapted from schematics created by Oliver Campbell.*

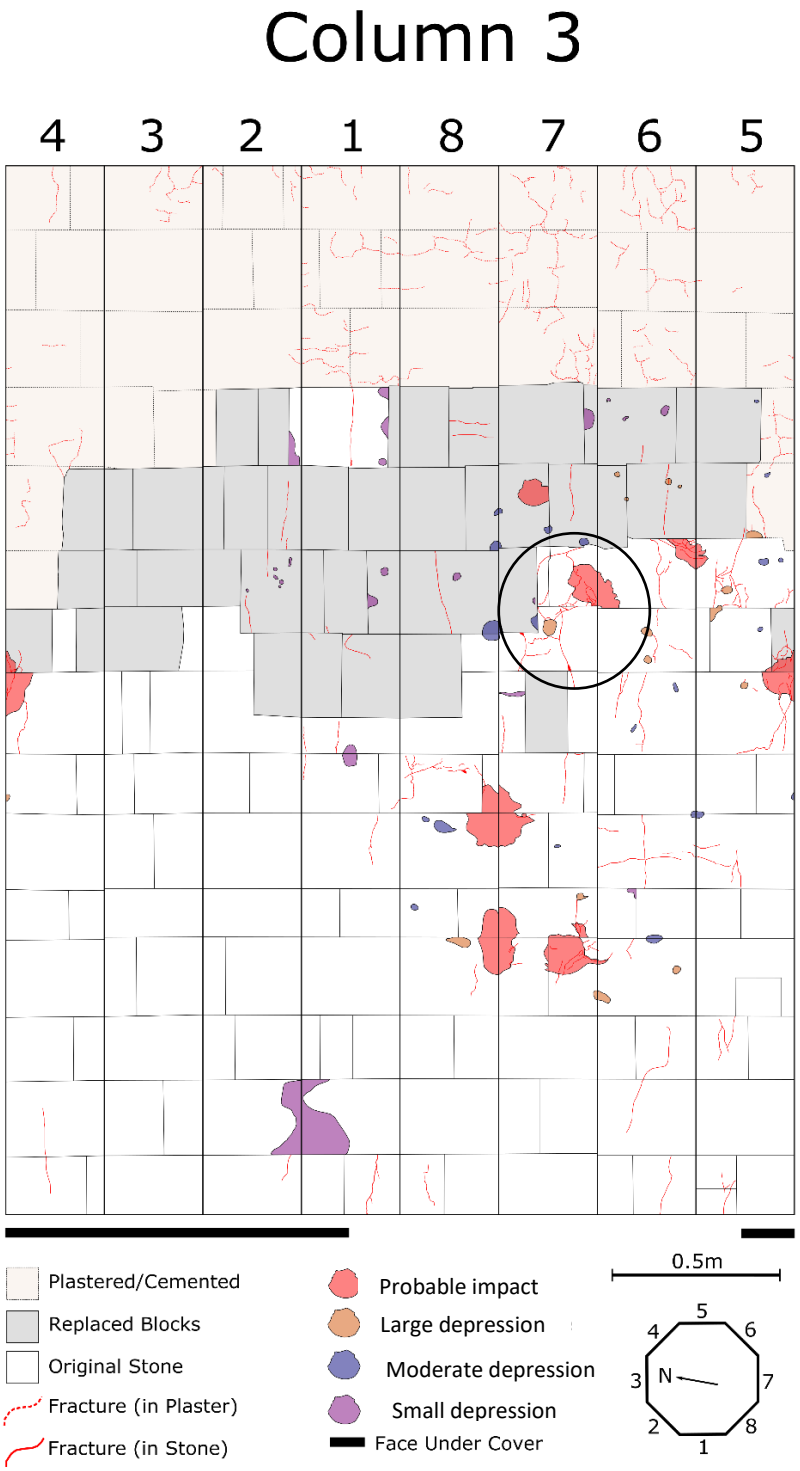

Figure 3.20: *A schematic showing greater fracture density on the exposed sides of column 4, and the areas where impact craters allow fracture networks to connect across separate blocks. Image adapted from schematics created by Oliver Campbell.*

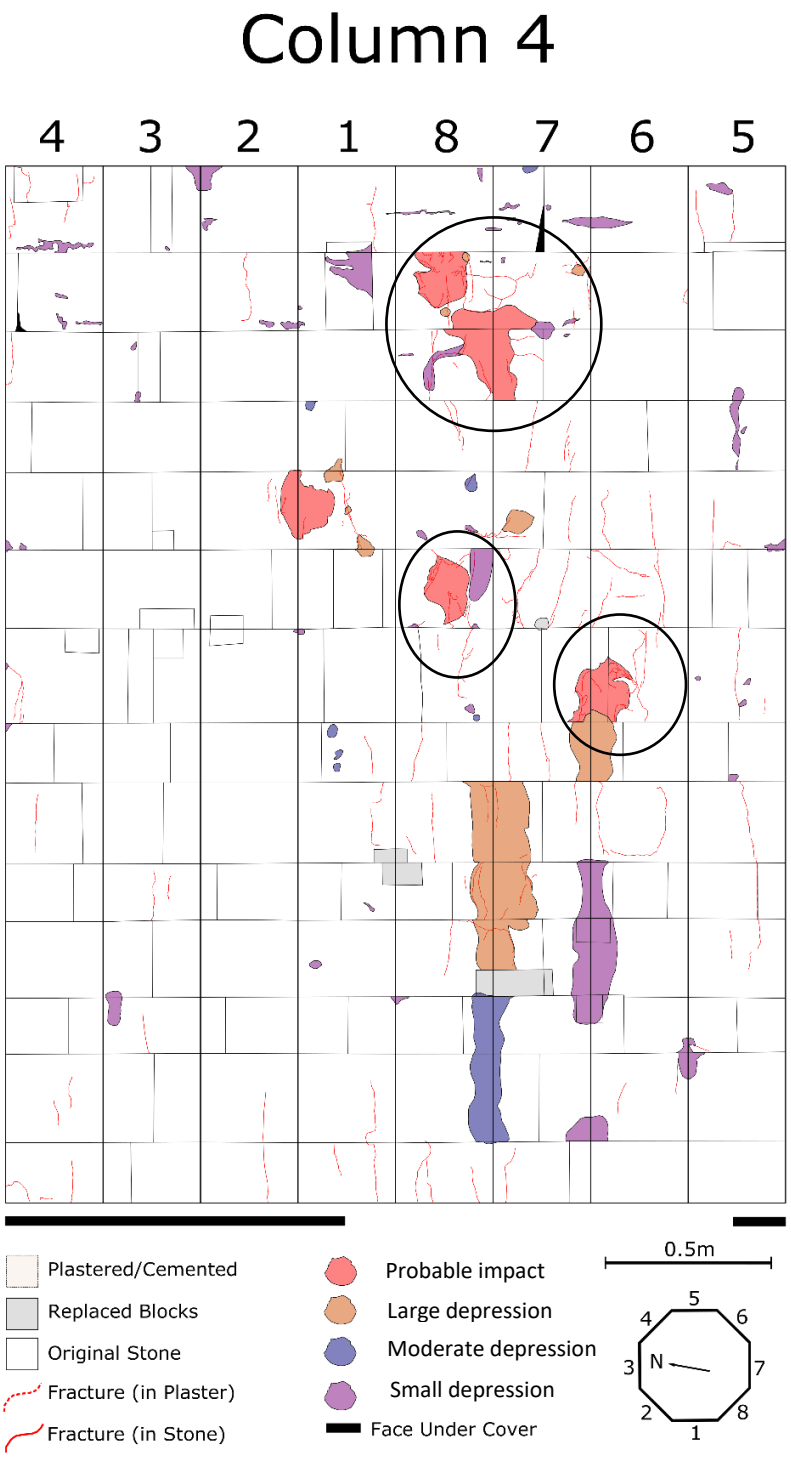

Figure 3.21: *A schematic showing greater fracture density on the exposed sides of column 7, and the areas where impact craters allow fracture networks to connect across separate blocks. Image adapted from schematics created by Oliver Campbell.*

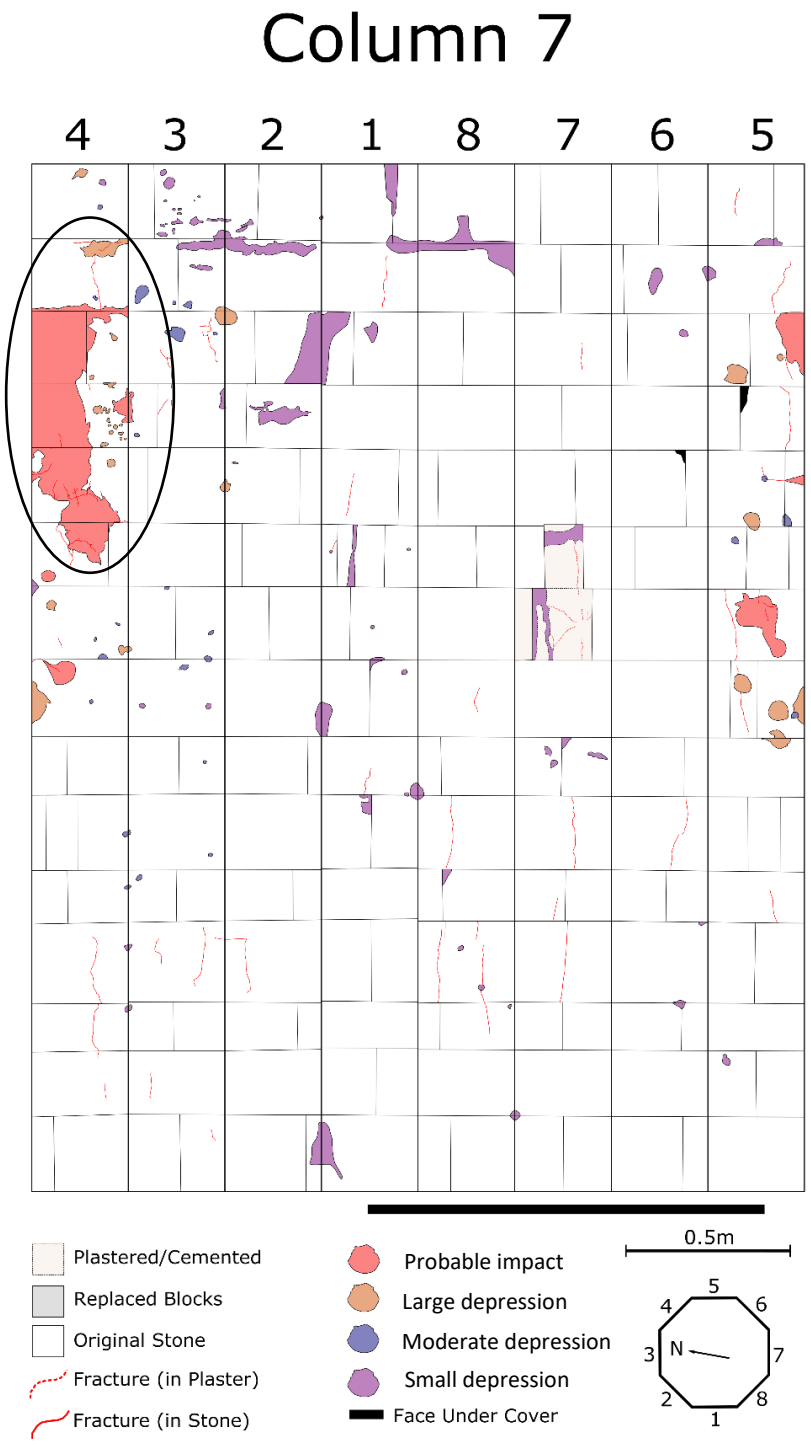

Figure 3.22: *A schematic showing greater fracture density on the exposed sides of column 8, and the areas where impact craters allow fracture networks to connect across separate blocks. Image adapted from schematics created by Oliver Campbell.*

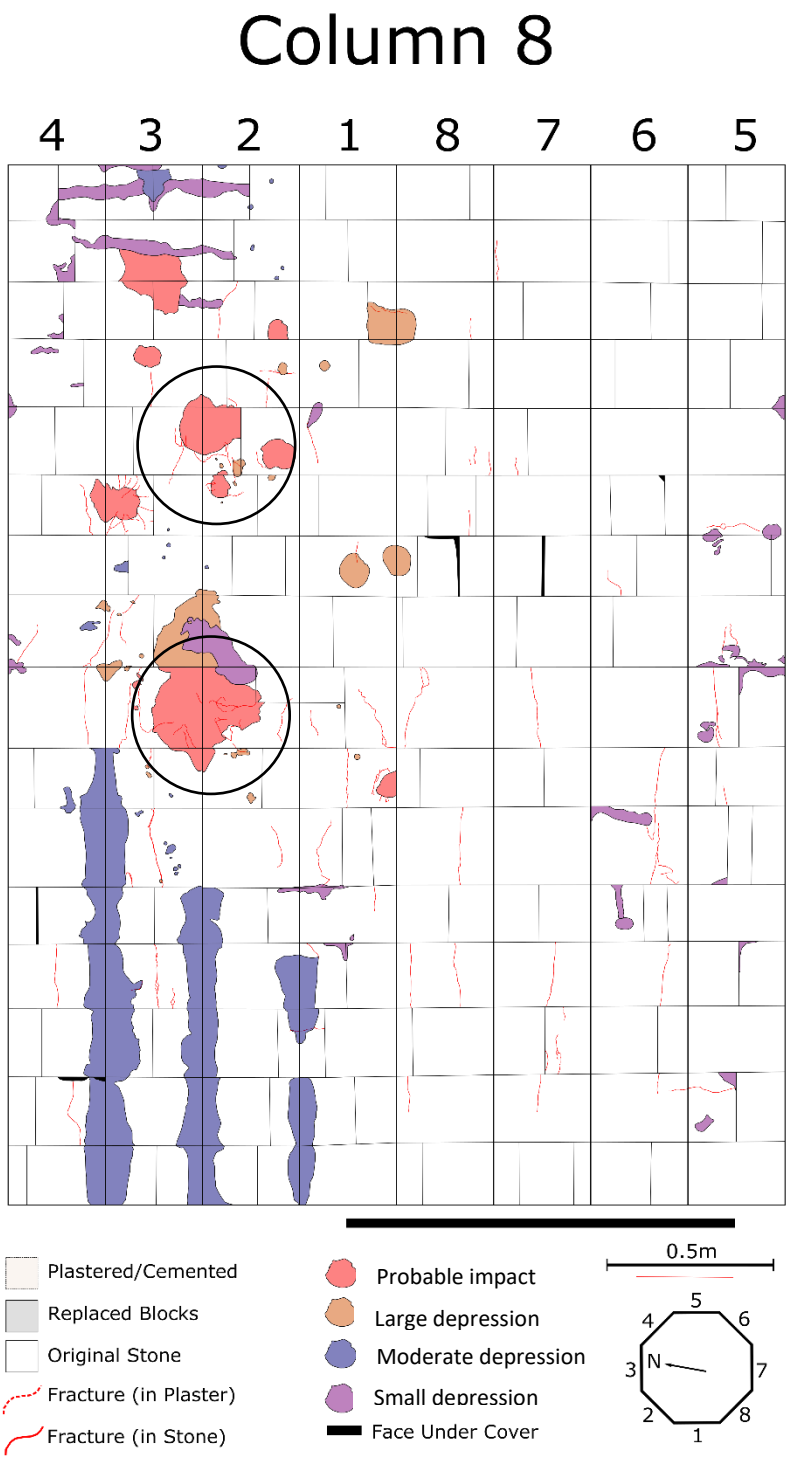

As can be seen above, these figures clearly demonstrate how ballistic damage is likely to exacerbate and extend the fracture networks caused by weathering processes on the exposed column sides as depicted in figure 3.15. This likely causes the increase in average permeability for these sides. It is also worth noting that every individual block exhibiting an identified impact crater in the above figures also contains a visible fracture network. Conversely, many blocks that do not contain an impact crater do not exhibit a fracture network. This is further evidence of the critical role that ballistic impact plays in inducing fracture networks in heritage stone that are responsible for exacerbating weathering deterioration of monuments.

3.4.3: Protimeter Results: Moisture Mobility

The protimeter data was plotted according to the height above the column base and grouped into those column sides exhibiting ballistic impact craters (n=5) and undamaged surfaces without craters (n=11). The data presented in figure 3.23 shows that the damaged surfaces have a much higher moisture content at the base of the columns, which quickly drops after only a 20cm increase in height to 40cm above the column base. Conversely, the undamaged surfaces have a lower moisture content at the base of the column but see increases at 60cm and 100cm above the previous 20cm interval. This indicates that due to a greater fracture network on damaged surfaces caused by ballistic impact (as previously discussed) moisture has high mobility in these surfaces, and rainfall from the open church roof is able to rapidly migrate from the surface's upper region to the base of the column, where it accumulates due to gravity. Surfaces without ballistic impact do not have as widespread fracture networks, meaning that moisture can accumulate in upper regions of the surface without being able to access the base of the column, causing the spikes in moisture content seen at 60cm and 100cm.

Figure 3.23: *Average Protimeter Moisture Content of Sampling Points by Column Surface Type.*

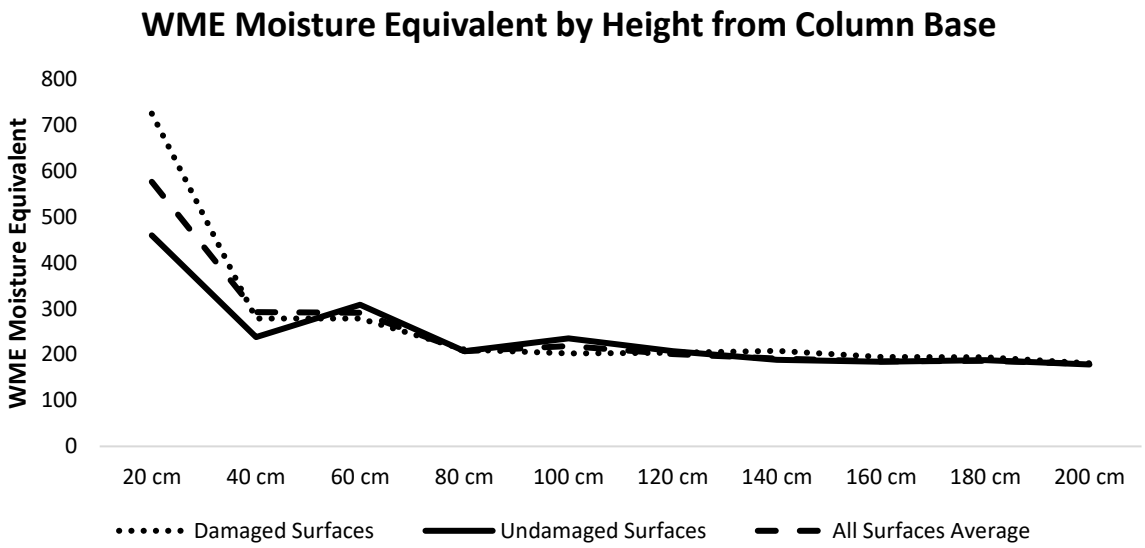

The data presented in figure 3.23 is therefore further evidence that ballistic impact causes increased fracturing in impacted surfaces, which facilitates greater mobility of weathering agents and thus causes greater weakening and reductions in surface hardness as seen in figure 3.15.

The principle that ballistic impact craters facilitate the accumulation of moisture at the base of columns is also supported through visual analysis of the columns. In addition to their contribution to creating and extending fracture networks, it appears that ballistic impact craters and associated radial fractures that are close to or across column edges act to channel rainfall on exposed column faces (those without roofing cover) to the column edges. This preferentially erodes the column edges, flattening them and creating depressions as the moisture is channelled downwards by gravity, clearly demonstrating how ballistic damage can affect weathering behaviours and patterns:

Figure 3.24: *A diagram showing erosion/weathering below ballistic impact along the edges of column 8.*

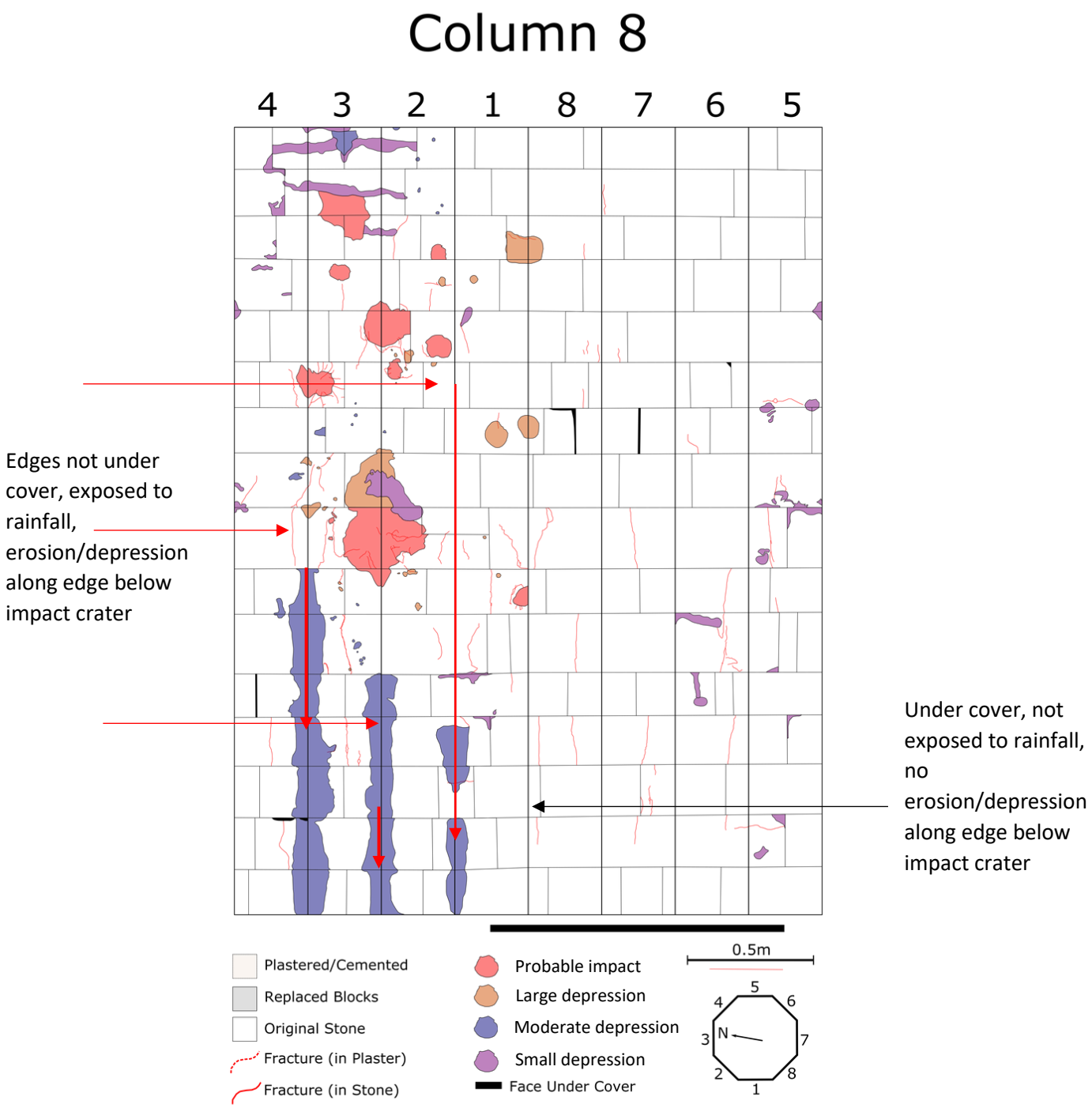

Figure 3.25: *A diagram showing erosion/weathering below ballistic impact along the edges of column 4.*

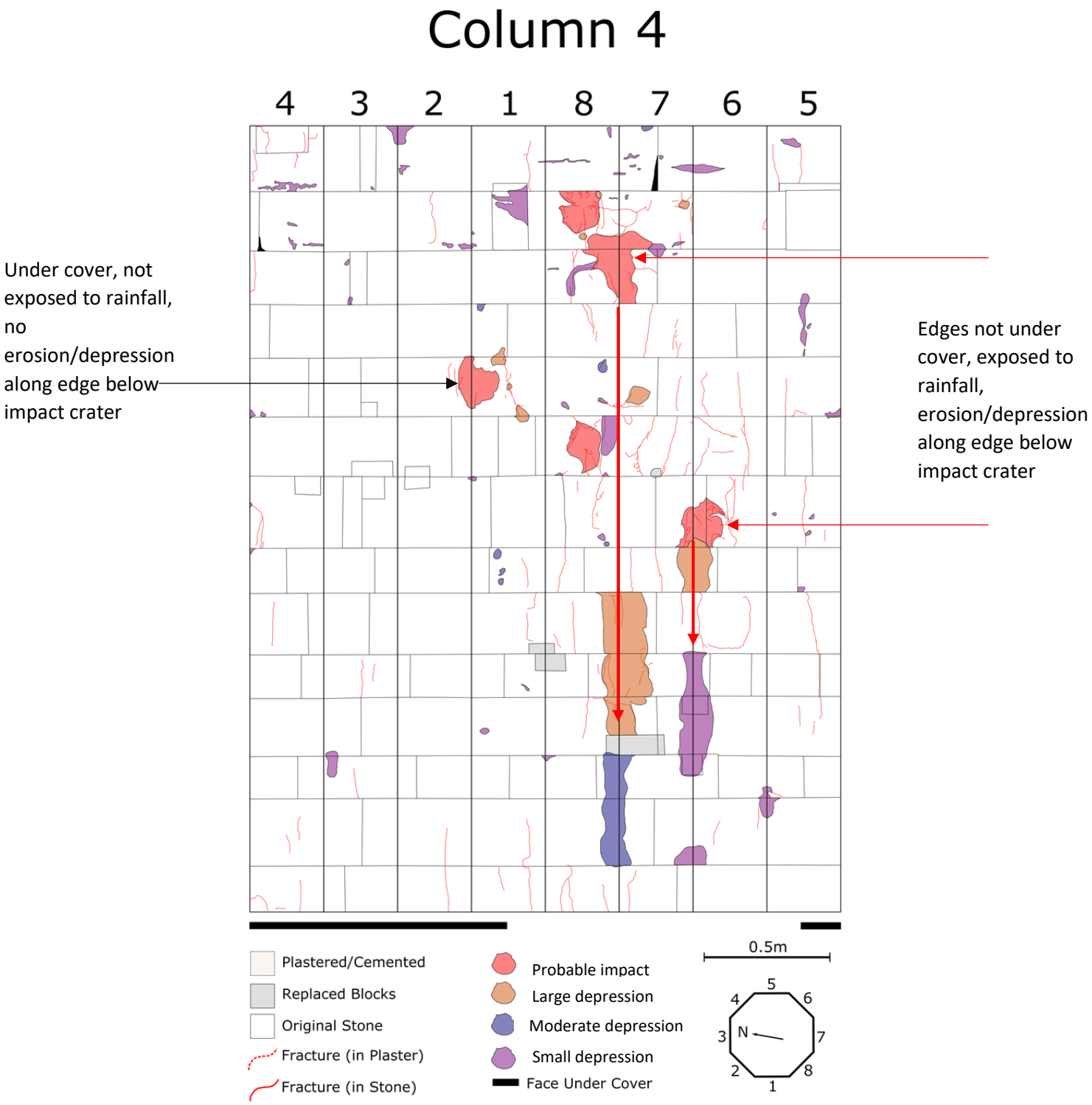

Figure 3.26: *A diagram showing erosion/weathering below ballistic impact along the edges of column 1.*

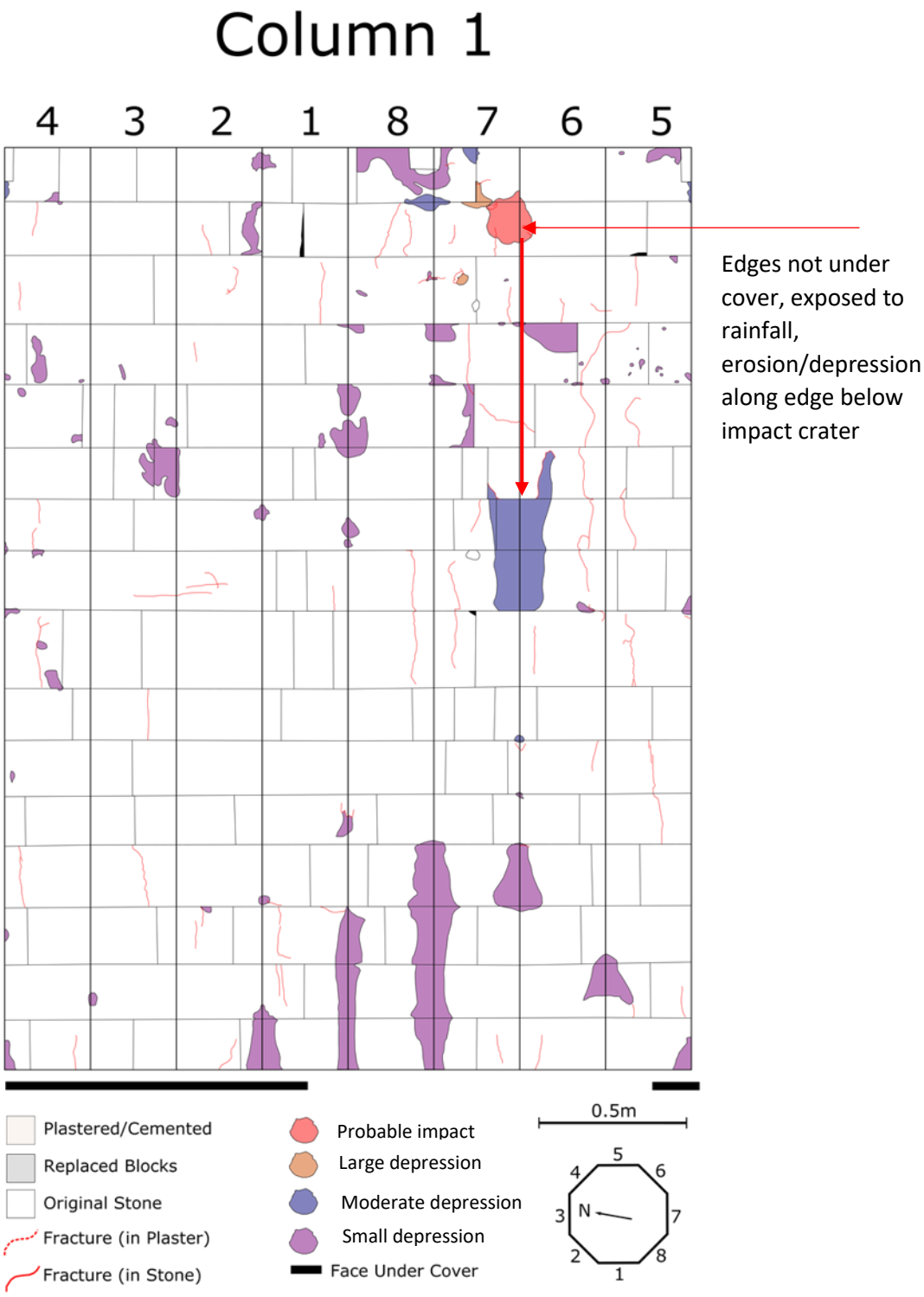

These figures demonstrate that ballistic damage affects precipitation flow and resultant weathering patterns across the surface of the stone, in addition to its probable role in extending and connecting fractures in the sub-surface of the stone demonstrated in previous figures. This will lead to aesthetic deterioration on the surface as well as mechanical deterioration in the sub-surface.

3.4.4: Importance of surface orientation

One interesting spatial pattern is the orientation of column sides with lower surface hardness. The column sides that are aligned north/north-west have a higher average surface hardness than the sides facing south/south-east (sides 6,7,8). This is shown in figure 3.28.

Figure 3.27: *A schematic showing column orientation*

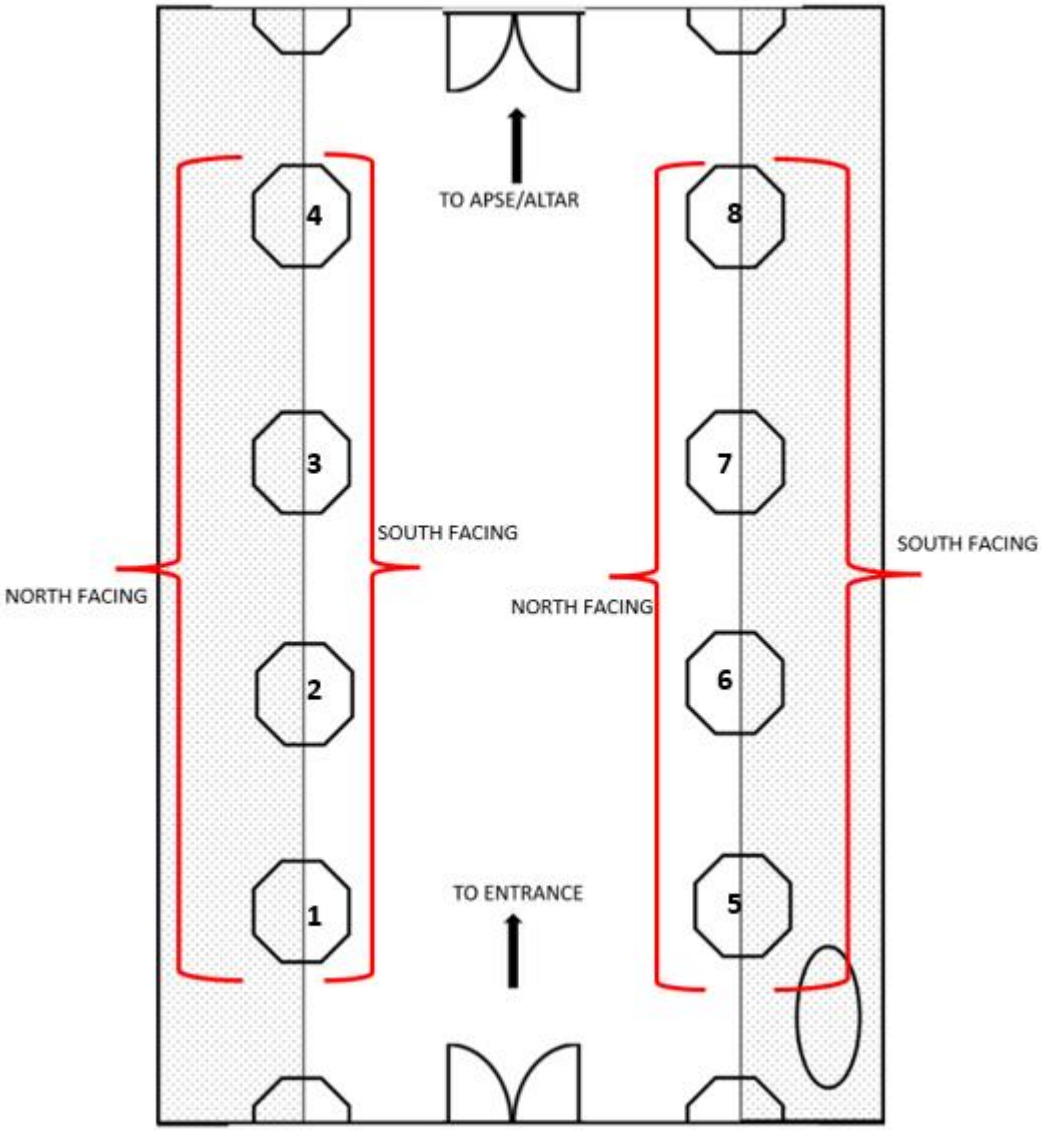

Figure 3.28: *The average hardness of column sides by orientation. Error bars are the standard error of the given data set.*

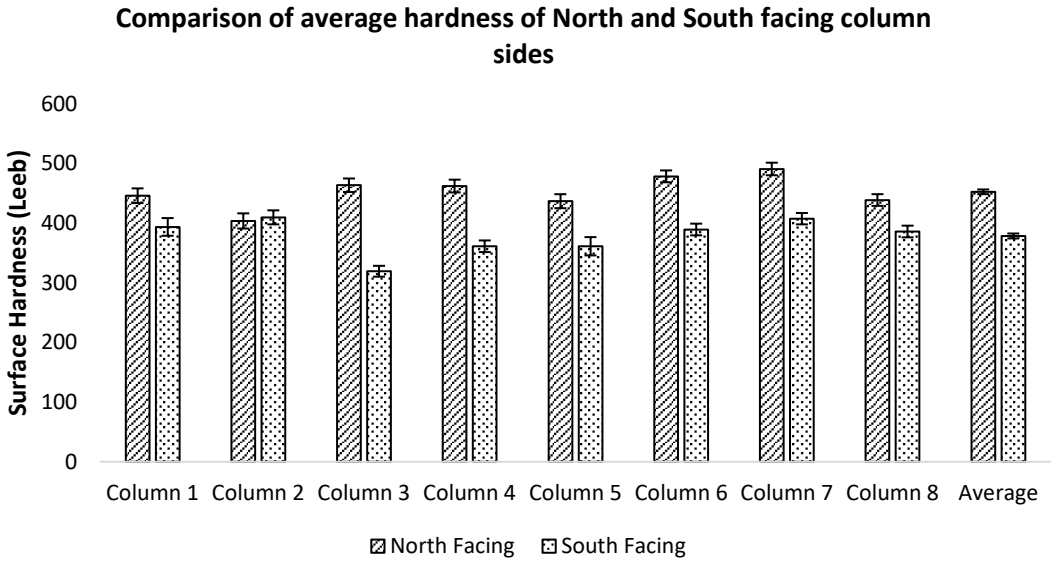

Figure 3.27 shows that for every column except column 2, the north facing surfaces are substantially harder than the south facing surfaces. It is conceivable that column 2 contains stone material more recently restored than the other columns, which would explain the apparent discrepancy from the behaviour of the other columns, but further research would be required to confirm this.

This apparent relationship between the orientation of the column faces and their average surface hardness can be explained when one considers the likely amounts of sunlight and saline sea spray experienced by each part of the building. The course of the sun across the sky relative to the church nave is shown below:

Figure 3.29: *Course of the sun in the sky relative to the nave of the RGC. The path shown is for the 2020 Summer solstice (20/06/2020) in order to demonstrate maximum experienced sun. Calculated using sunearthtools.com.*

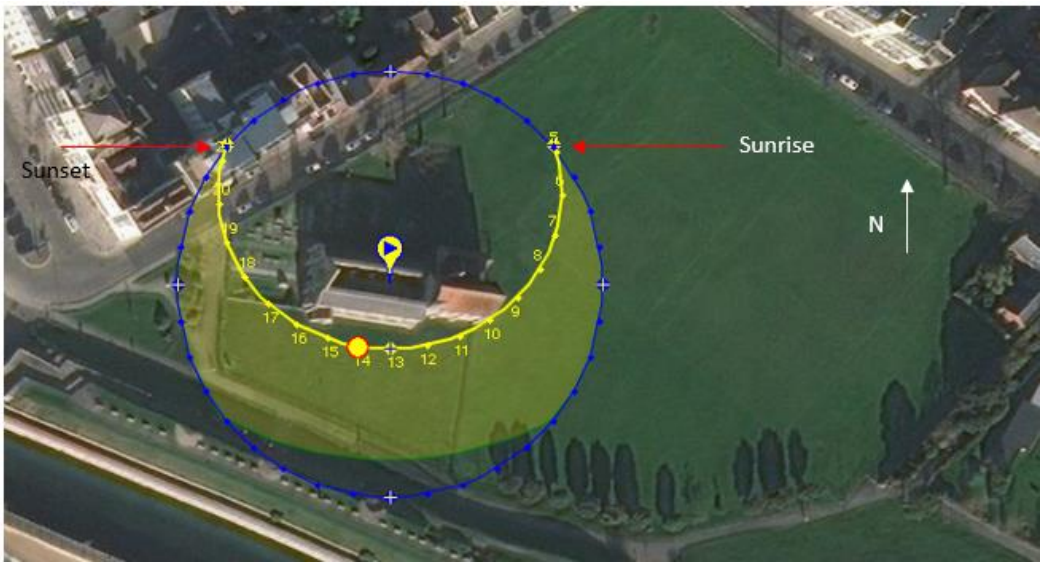

As this figure demonstrates, the northern side of the church, and the northern faces of the columns are in an effective shadow zone, and certainly experiences far less sunlight than the southern faces, which are exposed to the sun both through the south facing windows, and through the open roof in the central nave. South facing column sides are also more likely to be exposed to saline sea spray from the nearby sea front as they face towards the sea and spray carried by the wind is therefore likely to land on south facing columns. Therefore, saline sea spray is likely to be deposited on south-facing column sides. The greater sun exposure of these south-facing surfaces will then lead to higher temperatures on these surfaces, and thus greater capillary rise and evaporation of moisture, causing greater precipitation of NaCl crystals in pore spaces on south facing column sides. In turn this will cause weathering weakening on these surfaces and reduce rebound hardness for these sides (Ludovico-Marques, Chastre, 2012).

This theory regarding the role played by exposure to direct sunlight for weathering behaviours is supported by the differing behaviours of north and south facing impact craters. North facing impact craters often exhibit a black weathering surface that causes the stone within the impact crater to bubble and flake:

Figure 3.30: *Image of the black weathering formation in an impact crater on column 8 side 2, north facing.*

Interestingly, this black weathering crust is frequently present in north facing impact craters, but absent in south facing impact craters:

Figure 3.31: *Images showing the different weathering formations dependant on face orientation.*

North facing, black discolouration present in impact craters

Column 8

Column 7

South Facing, No black discolouration present in impact craters:

Column 2

Column 3

Column 4

This disparity in the presence of weathering crusts in craters is possibly attributable to the lack of sunlight drying the north facing impact craters through evaporation of moisture. This is supported by the hypothesis for the formation of black gypsum crusts put forward by Rodriguez-Navarro and Sebastian (1996): A lack of solar heating and corresponding drying will allow the accumulation of greater moisture levels on North facing surfaces, which will then hydrate sulphur ions present on the columns due to air pollution and saline groundwater rise. This creates sulphuric acid, which then oxidizes to produce black gypsum crusts. These weathering agents will then precipitate as discoloured weathering crusts (Mol *et al*, 2017). Török (2007) notes that bubble or "framboidal" weathering crusts of black gypsum often form on stone surfaces under cover due to a lack of exposure to remove them. Macaluso and Sauro (1996) also record bubbling/blistering weathering formations associated with gypsum. Based on these observations, it seems likely that the black framboidal weathering crusts at the RGC are caused by precipitation of gypsum. The general scaling and flaking of the stone surfaces at the RGC are also highly consistent with the images of gypsum weathering presented by Farkas *et al* (2018) (figure 3.32). Gypsum weathering crusts are commonly associated with limestone buildings and could be due to atmospheric pollution, or to gypsum containing building materials present at the site, such as mortars (Kloppmann *et al*, 2011). Sulphates contained in sea-spray from the nearby coast at the RGC site will also contribute to the formation of these gypsum crusts (Montana *et al*, 2008). This is a notable observation because it demonstrates the interplay between ballistic impact and weathering processes. The impact craters act to allow the accumulation of weathering agents on north facing columns, causing the growth of gypsum efflorescence and leading to obvious damage to the aesthetic value of these regions of the church. This is clear evidence that ballistic impacts can exacerbate some aspects of weathering processes.

Figure 3.32: *Similarities between efflorescences seen at the Royal Garrison Church (A) and efflorescence on historic buildings confirmed by Farkas et al (2018) as Gypsum using X-Ray Diffraction analyses (B, C).*

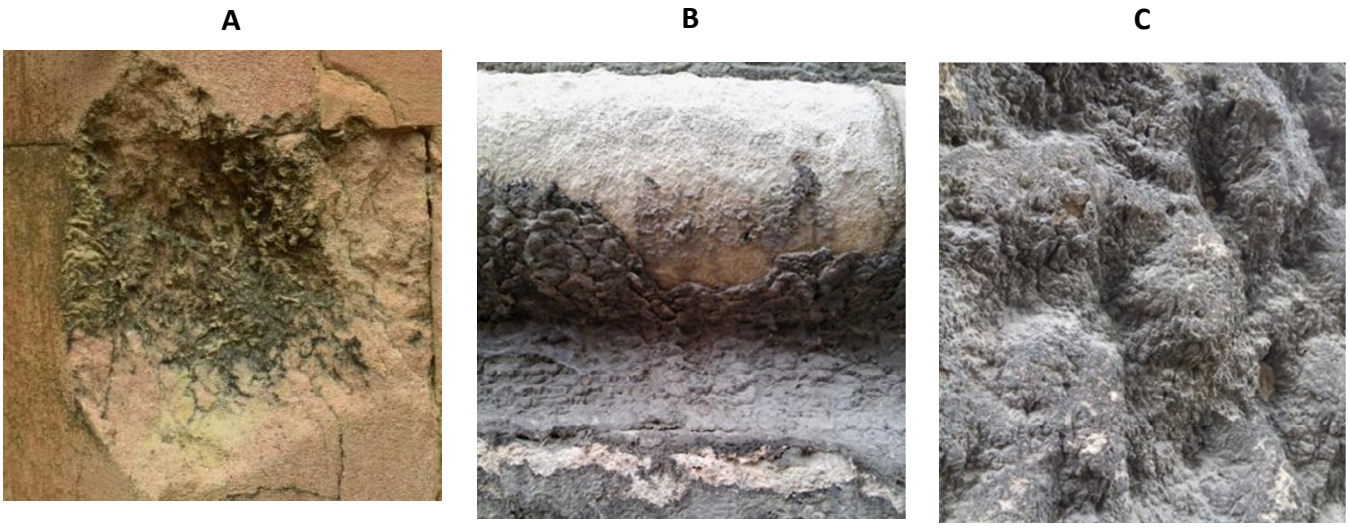

Further evidence of differing weathering behaviour being related to surface orientation can be seen when protimeter data is plotted according to the surface orientation, as seen in figure 3.33:

Figure 3.33: *The difference in moisture presence by height above column base by surface orientation.*

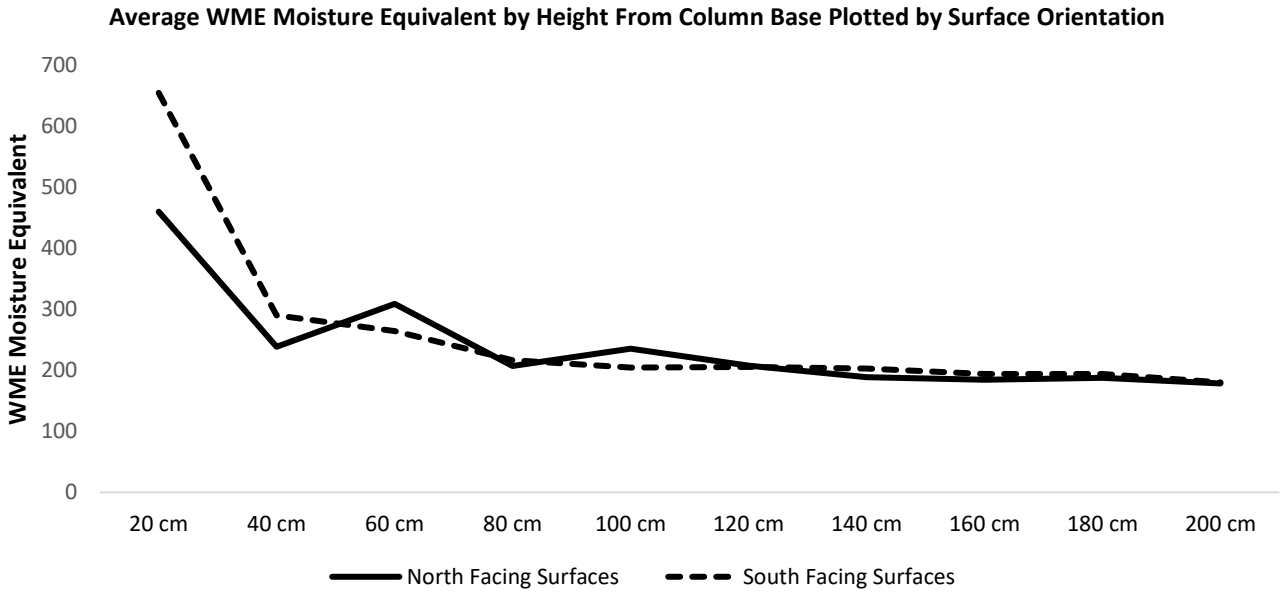

Figure 3.33 shows that south facing columns have a higher moisture content at their base, which rapidly declines with height from the column base. This is consistent with a ready supply of sea spray supplied to these columns, which is rapidly dried off on the upper regions of the column most exposed to the sun (as outlined above), leading to high moisture levels at the column base which decline rapidly further up the column. Conversely, north facing columns are not dried by exposure to the sun on upper regions of the column, leading to accumulations of moisture at various heights above the column base, and causing the spikes in moisture seen at 60cm and 100cm. This accumulation of moisture above the column bases would in turn contribute to the accumulation of soluble salt efflorescences, including gypsum seen in north facing impact craters and supporting the hypothesis regarding the importance of moisture in the formation of these crusts (figures 3.29, 3.30). This is therefore further evidence that there is close interplay between the specific weathering conditions at a heritage site (exposure to moisture and soluble salts, exposure to sunshine) and the specific behaviour of ballistic damage (accumulation of gypsum efflorescence in north facing ballistic impact craters).

3.5: Discussion of significance of results

The fieldwork at the Royal Garrison Church has served to demonstrate a clear link between ballistic impacts and weathering processes. The surfaces that have been exposed to both weathering and ballistic impact have a lower hardness than the surfaces which were not subjected to ballistic impact and have been protected from weathering processes by the aisle roofing (figure 3.11). Furthermore, surfaces that exhibit ballistic impact craters are weaker than those which do not exhibit ballistic impact (figure 3.12).

The area of damaged caused by the ballistic damage present on a column is also correlated with the average permeability, and thus weathering susceptibility of that column (figures 3.16, 3.17). Furthermore, impact craters have substantially increased the permeability of surfaces where they are present, acting to connect surface fracture networks across stone blocks which facilitate greater moisture mobility and weathering feedback loops, as demonstrated in figures 3.18-3.22). This is in agreement with the model of weathering induced fracturing cycles put forward by Navarre-Sitchler, Brantley and Rother (2015). Protimeter data supports this hypothesis, showing that the greater moisture mobility facilitated by ballistic damage induced fracture networks causes the accumulation of greater moisture levels at the base of surfaces with ballistic impact (figure 3.21).

The presence of saline sea spray and rainwater from the open church roof are not the only weathering factors present at the site; spatial analysis of the column sides supports the theory that directional exposure to solar heating affects weathering processes at the Royal Garrison Church. South facing column sides are exposed both to greater levels of saline sea spray, and solar heating. This will cause the rapid precipitation of salt crystals on south facing sides and this has led to south facing surfaces having substantially lower surface hardness than north facing surfaces (figure 3.28). This agrees well with the observations of Rothert *et al* (2007), who observed exacerbated salt crystallization and associated decay of Maltese heritage buildings on surfaces with most exposure to sunlight and corresponding increases in salt precipitation.

The orientation and position of column sides displaying ballistic impact craters influences weathering process. South facing impact craters do not accumulate high levels of saline moisture due to solar drying, whilst north facing ballistic impact craters act to collect high concentrations of moisture containing salts such as gypsum. This results in the formation of black weathering crusts on north facing impact craters that contribute to the aesthetic deterioration of the church. Interestingly, this finding agrees with the field observations of Matsukura and Tanaka (2000) who observed the concentration of gypsum efflorescence in cavernous weathering features such as tafone, which are morphologically similar to ballistic impact craters. Finally, the presence of impact craters across column edges channels the downward travel of rainwater and sea spray, causing substantial weathering depressions immediately below impact craters (figures 3.24-3.26).

The survey at the Royal Garrison Church has aptly demonstrated that the methods first developed in chapter 2 for the laboratory-based elements of this PhD are capable of obtaining sufficient data in a field setting to provide insightful information on ballistic impacts and their interaction with weathering factors. The methods used in this field study were also completely non-destructive and non-invasive and caused no damage to the site.

Taken together, these findings demonstrate that there is a great deal of interplay between ballistic impact and weathering processes. Ballistic impacts directly contribute to exacerbated weathering processes that lower the hardness of stone surfaces, increase their permeability and control moisture flow regimes. Ballistic impact also contributes to aesthetic deterioration, causing the accumulation of disfiguring weathering crusts and channelling of surface moisture to create surface depressions.

Therefore, these results provide real-world data and validation for the subject matter of this PhD, as it demonstrates that ballistic impact alters and exacerbates weathering by haloclasty in heritage buildings, whilst also demonstrating the validity of the proposed methods for identifying these risks in a field work setting.

3.6: Conclusions

The principle achievements of this chapter have been to demonstrate both that ballistic impact interacts with weathering processes in a "real-world" field setting, as well as showing that the methods deployed in the previous chapters of this PhD are appropriate for fieldwork and can identify interactions between ballistic impact and weathering action, and could therefore be used by conservation professionals in a post-conflict setting. Therefore, this chapter has progressed the work of this project by fulfilling the following Research Objectives:

Research Objective I: "*To develop field appropriate non-destructive methods to assess exterior and interior damage to limestone and sandstone arising from military projectile damage (7.62 x 39mm and 5.56 x 45mm).*"

Research Objective III: *"To assess the effects of arid environment weathering processes (haloclasty, moisture, temperature change) on the deterioration of stone after ballistic impact and the interaction between ballistic impact and subsequent weathering processes."*

Research Objective V: *"... ensure that observed links between ballistic damage and weathering behaviours are applicable to real-world situations and can be identified in a field setting using the methods developed in this project."*

Chapter 4

Thesis Chapter 4: Pilot study of laboratory techniques and analysis of the effects of angle of ballistic impact

Chapter 4 Overview

Chapter 4 aims and hypothesis

To develop techniques for simulating weathering conditions in arid environments, as well as further refining techniques for assessing interior and exterior damage to stone damaged by ballistic impact and weathering. Finally, to collect preliminary data on how angle of ballistic impact controls damage levels to the target stone, in keeping with Research Objective II, and explore the effects of weathering after ballistic impact, as dictated by Research Objective III. It was hypothesised that ballistic impact perpendicular to the impact face would cause more damage than oblique impact due to greater transference of kinetic energy to the target. It was also hypothesised that direct impact would cause a denser fracture network that would result in greater ingress of weathering agents and exacerbated haloclasty weakening of the samples.

Chapter 4 methods

Measurements of rebound hardness, permeability and ultrasonic velocity were undertaken across two limestone samples impacted with 7.62 x 39mm ammunition at varying angles (90◦ and 45◦) and subjected to a haloclasty weathering regime designed to simulate ingress of saline groundwater in arid environments. This process was used to track the deterioration of the samples after both ballistic impact and subsequent weathering. Three-dimensional models of the samples were created to collect quantitative data on changes in sample volume and surface area.

Chapter 4 principal findings

Findings suggest that angle of impact is important in determining the distribution of mechanical deterioration due to ballistic impact and subsequent weathering. Contrary to the hypothesis, direct perpendicular impact appears to cause greater deterioration and weakening in the impact crater of the samples and shattered surface of the samples, but oblique impact appears to cause greater damage across the wider surface of the samples outside of the impact crater, and potential reasons for this are discussed. Areas of methodological refinement were identified for future experiments within this PhD project. In particular, improved methods for permeability survey are discussed.

4.1: Introduction

The literature discussed in sections 1.9-1.11 illustrates that weathering processes, including haloclasty, can cause significant deterioration to heritage sites damaged by conflict. This includes aesthetic deterioration through prominent NaCl efflorescence and black gypsum deposits, as well as exacerbating physical deterioration through reductions in hardness of damaged surfaces and increased permeability.

To explore the effects of weathering processes on shot stone, it was necessary to replicate the effects of weathering processes in a laboratory setting. This would allow weathered samples to be systematically analysed. To achieve this, a study was undertaken that would subject samples to a weathering regime that replicated haloclasty weathering through capillary rise of saline groundwater into impacted samples under a heating regime that replicated diurnal temperature cycles in a hot arid environment. Undertaking this preliminary work would ensure that the efficacy of the weathering regime could be assessed, and the methodology refined and optimised before a larger experimental run later in the work of this PhD project.

This pilot study also provided an opportunity to collect preliminary data on one of the questions posed in Research Objective II and III:

RO II: "*To compare and isolate the effects of changing angle of impact on the damage caused by ballistic impact before weathering".*

RO III: "*To assess the effects of arid environment weathering processes (haloclasty, moisture, temperature change) on the deterioration of stone after ballistic impact".*

Finally, the pilot study served to determine whether experimental parameters such as impact angle and velocity could be controlled within the limits required for a full experimental run. This would allow any methodological problems to be addressed before the main experiments and ensure the range set-up could be optimised prior to the main experiments.

To achieve these goals, the study was undertaken with two 15cm x 15cm x 15cm cubic samples of limestone, in keeping with the sample size determined in chapter 2. The samples were shot with 7.62 x 39mm (AK-47) ammunition at a velocity corresponding to the impact

velocity at a range of 200m. This ammunition was chosen due to it being one of the most common cartridges used in modern conflicts (see section 1.2). One sample was orientated so that the projectile was normal (90°) to the target face, and the other sample was rotated so that it was impacted at 45°. In keeping with the methods developed in chapter 2, measurements of sample mass, rebound hardness, and permeability were taken after impact and compared with control measurements to determine the damage caused immediately after impact at the respective angles. The samples were then subjected to a weathering regime designed to approximate the ingress of NaCl contaminated groundwater under diurnal heating conditions experienced in hot arid environments. After weathering, mass, surface hardness, and permeability measurements of the samples were taken again to determine the deterioration caused by the weathering regime, and whether this was affected by the angle of impact. It should be noted that the use of only two samples meant that the data collected in this pilot study was limited preliminary data. This data can then be used to develop and refine methods for assessing damage profiles caused by alternating impact angles in the future experiments of this project using a larger number of samples that will yield more extensive data sets.

This pilot study also allowed the exploration of two additional techniques for the non-destructive analysis of impacted stone as discussed in chapter 1: three-dimensional photogrammetric modelling of the samples and Ultrasonic Pulse Velocity (UPV) analysis.

Photogrammetric models could be used to quantify and compare damage to the samples through two methods:

(1) Changes in sample volume detected on the models would indicate the loss of stone material due to ejection of stone after impact as well as weakening and disaggregation after weathering, and;

(2) Changes in surface area detected on the models could be used to measure the accumulation of salt efflorescence on the samples' surface.

UPV analysis was used in this study to assess the density of the samples' internal fracture network after shooting and after weathering. This would indicate whether the angle of ballistic impact affected the extent of internal fracturing, and how those fracture networks were affected by weathering processes. The analysis of fracture networks is key to predicting

weathering behaviour after impact because larger internal fracture networks will facilitate greater mobility of weathering agents inside the impacted stone, as outlined in section 1.6.

4.2: Methods

4.2.1: Sample Preparation- Stone selection

As discussed in section 1.8, one of the most commonly used stone types for heritage in arid MENA regions is limestone. To ensure that the results of this study were applicable to lithologies present in arid regions, it was necessary to find a limestone that could be sourced in the U.K. and was a good approximation for limestones found in arid areas. This decision was made because it was deemed not feasible to import large amounts of stone for future studies from the MENA region.

A limestone used extensively in heritage buildings in an arid environment is Mokattam limestone, a Middle Eocene Egyptian limestone group frequently used in the construction and restoration of many heritage monuments in Cairo, and in the construction of the Pyramids at Giza (Fitzner, Heinrichs, La Bouchardiere, 2002, Harrell, 2012). As described by El-Azabi (2006), the petrographic properties of the Mokattam limestone group can be variable in grain size, porosity, size of bioclasts, porosity and mineral content. Many formations of this group have been used in heritage construction and restoration across Cairo, often in the same building (*ibid.*). To account for this variability, it was decided to cross-reference literature on the geotechnical characteristics of the Mokattam limestone group in order to identify a comparable limestone. This could then be used as a proxy for a heritage limestone frequently used in an arid environment. Note, that as discussed in section 1.7, it is important that the limestone used as an experimental analogue has technical properties comparable to the weathered Mokattam present on heritage buildings, rather than freshly quarried Mokattam. Therefore, the data used in this cross-referencing process was taken from sources analysing Mokoattam samples from heritage buildings. This process identified Cotswold Hill Cream limestone as an approximate geotechnical match for Mokattam limestone (Table 4.1).

Table 4.1: *A comparison of the geotechnical properties of Cotswold Hill Cream limestone and Mokattam limestone. N.B.: Technical details for Cotswold Hill Cream Limestone are taken from Building Research Establishment testing (1999a).*

	Cotswold Hill White Guiting	Cotswold Hill Honey Limestone	Oathill Limestone	Upper Lawn Bath Limestone	Bath Stone (Top Bed)	Bath Stone (Lower Bed)	Cotswold Hill Cream Limestone	Mokattam formation Middle Eocene Limestone	Source of Mokattam Geotechnical data
Compressive Strength (MPa)	15.9	22.6	8.16-16.52	16.4	14.8	22.5	36.6	40	El Nahhas *et al*, 1990
Porosity (%)	27.7	21.8	25.56	27.2	22.95	15.32	20.6	18.6-26.8, average of 24.2	Fitzner *et al*, 2002
Water absorption (wt %)	11.14	7.7	9.2	8.03	11.16	7.4	8.5	6.12-10.75	Park and Shin, 2009
Density ($Kgcm^{-3}$)	1965	2200	2002	1982	1988	2260	2158	2100	Ahmed, Török, Locsei, 2006

4.2.2: Sample preparation- Shooting

Two samples of Cotswold Hill Cream limestone were used for this study, measuring 15 cm x 15 cm x 15 cm with a mass of 7.4kg and a density of 2.2gcm$^{-4.}$ In order to facilitate methodical data collection, each of the sample faces was given a number, the designation of face numbers is outlined in Figure 4.1.

Figure 4.1: *The number designation of each sampling surface on the cubic samples.*

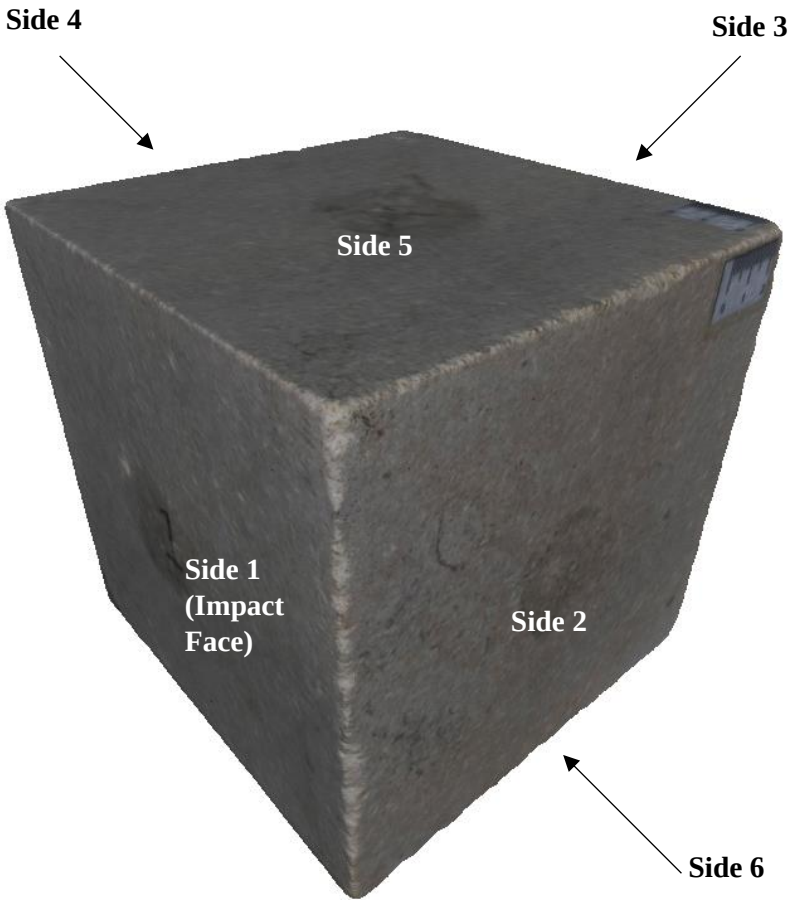

The samples were shot at the Cranfield Ordnance, Testing and Evaluation Centre (COTEC), at a distance of 200m as this is a plausible engagement distance of the AK-47 as the guns full range is 400 m (Rottman, 2011). The velocity of the projectile at a distance of 200 metres was calculated using a COTEC in-house point-mass external ballistics model created using

coefficient of drag data provided by the Ministry of Defence, as communicated by Champion (2020). The propellant charge inside the ammunition cartridges was then reduced from 1.6g to 1.15g in order to reduce their velocity to approximately 540 ms^{-1} over the 14m distance on the range.

Reducing the propellant charge in this way will inevitably result in some variation in the velocity of the projectile. As a result, the muzzle velocity for the projectile impacting sample 1 was 518ms^{-1} and 526ms^{-1} for sample 2. Given that the 7.62 x 39mm cartridge is known to have muzzle velocity variations of ±20ms^{-1} (Wen *et al,* 2017), this represents an acceptable degree of accuracy in relation to the target velocity of 540ms^{-1}.

As discussed in sections 1.4 to 1.6, one of the principle causes of projectile damage to stone is through the creation of fracture networks (Antoun et al, 2002). These fracture networks are caused by waves reflected back into the target block when the waves meet a material boundary with a different stress wave impedance value, which is a function of density and module of elasticity (Concu, De Nicolo, Valdes, 2014, Jones, 1972, Fernando *et al,* 2020, Sawangsuriya, 2012, Erkman, Christensen, Fowles, 1966).

For any given block in a "real life" wall, stress wave reflection will be created at the edges and faces of the blocks, either by a difference in stress wave impedance between the stone and the surrounding mortar, or the difference in stress wave impedance of surrounding air in a dry stone wall. Mortars at heritage sites will vary widely in density and module of elasticity (Middendorf, Knofel, 1998), and therefore it would not be possible to accurately approximate a mortar in a heritage wall for these experiments. Furthermore, it was not feasible to construct a full-scale mortared wall during the single day shooting session at COTEC. The use of mortar on the samples would also have made subsequent permeability measurements on non-impact surfaces of the samples impossible. This would have seriously reduced the amount of data available to assess damage to the blocks through surface fractures causing increases to permeability. Finally, it was also not possible to buy enough Cotswold Hill limestone blocks to construct a full scale dry-wall within budgetary constraints.

Therefore, it was decided to use un-mortared concrete to surround the samples to approximate a dry-stone wall. Dry stonewalls are found at a number of heritage sites in arid regions, such as ancient Egyptian settlements at Wadi el Hudi, Iron age fortifications in Cappadocia, Turkey, and the walls of Great Zimbabwe (Liszka, 2017 Summers, 2001, Walker, Dickens, 1995, Pikirayi, 2016). Heritage structures can also have their mortar

dissolved and removed over time due to weathering processes such as haloclasty, resulting in air gaps between stone blocks, as observed in Petra, Jordan (Mtani, 2016, Eklund, 2008). During firing, the samples were placed on a concrete platform, between two 60 x 60 x 60 cm concrete blocks, with a concrete block placed on top and two 1000cm^3 concrete blocks behind the target sample (Figure 4.2). The density of the concrete corresponded well with the density of the limestone (2.2gcm^{-3} for the limestone, 2.3gcm^{-3} for the concrete).

Figure 4.2: *A schematic and photograph showing the containment of the sample blocks prior to shooting.*

It should be noted that there were limitations to this method. As seen in figure 4.2 the concrete blocks placed on top and behind of the sample did not align exactly with the sample. The top containing block had dimensions of 10cm x 20cm x 25cm and the blocks behind had dimensions of 10cm x 10cm x 10cm. This caused a 2.5cm gap on both sides of the top and rear containing blocks. This would mean that the stress wave impedance and corresponding wave reflection was not representative of a block sitting in a wall with properly sized containment on each side. The containment arrangement of the samples in this experiment was due to properly sized 15cm x 15cm x 15cm concrete cubes being unavailable at the COTEC facility.

Therefore, the containment arrangement described here was designed to prevent the target blocks from moving during projectile impact, rather than simulating “real world” containment of a block in a wall. Although this would not reflect a real-world scenario of a block sitting in a wall, it would ensure consistent containment conditions of the two samples impacted at differing angles, and thus allow preliminary analysis into the effect of impact angle on damage and weathering processes.

This limitation would be factored into future experimental firings, and additional properly sized concrete cubes would be obtained so that the top and rear of the samples could be completely contained by 15cm x 15cm x 15cm cubes in future experiments of this PhD work. This will allow the construction of an approximation of the containment provided to a block by a dry-stone wall, such as are found the heritage sites detailed previously.

Sample 1 was angled so that the impact face was at 90° to the projectile and sample 2 was rotated through 45° to create an angled impact (figure 4.3).

Figure 4.3: *The arrangement of the target sample, weapon mount and velocity radar for both of the impact angles. Note that the sample impacted at 90° was slightly recessed compared to the sample impacted at 45° to ensure that the distance from the barrel to the target was kept constant after the larger blocks were re-arranged to facilitate 45° impact. The distance between barrel and target face was measured before each firing to ensure that a 14m distance was maintained.*

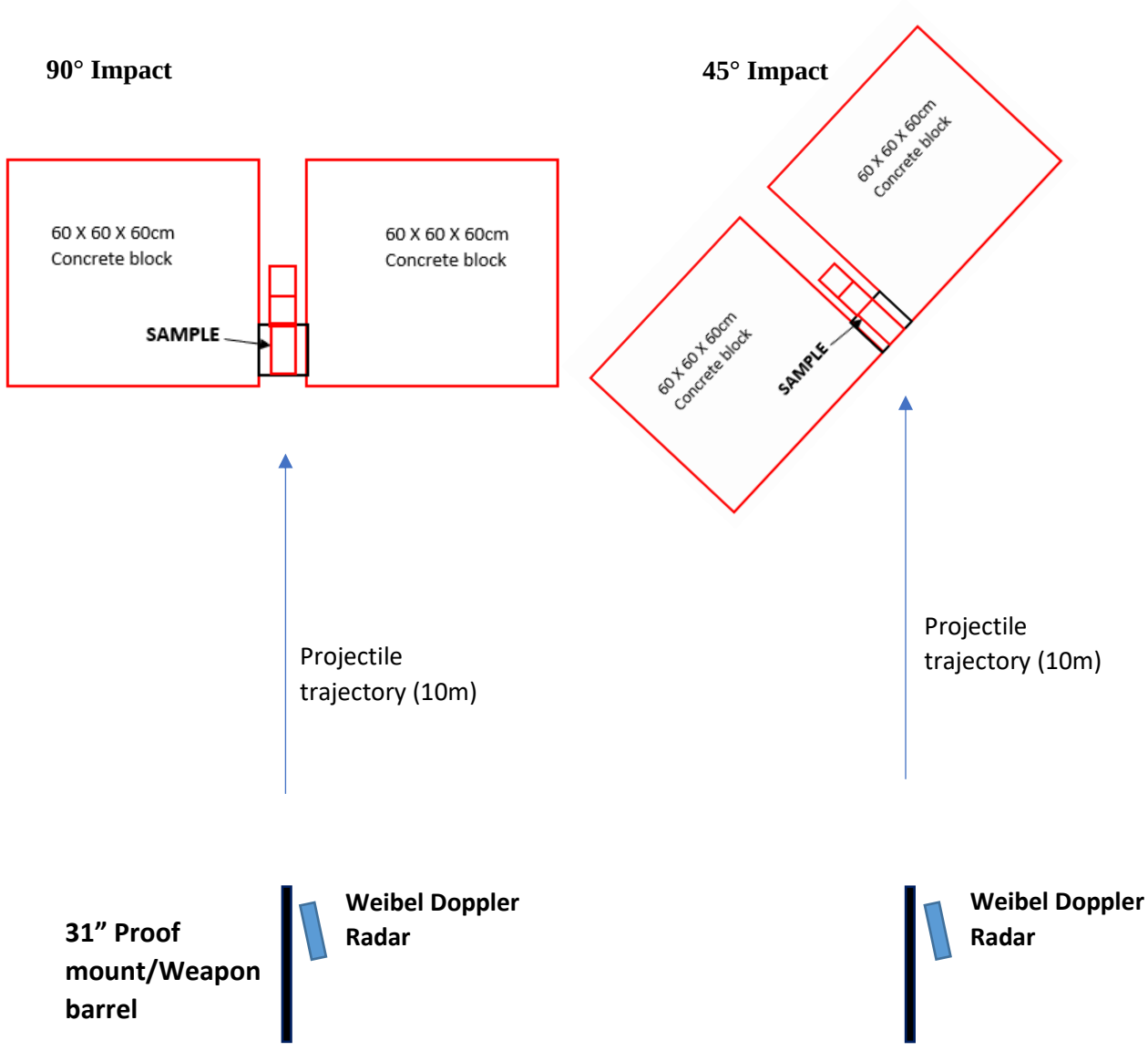

4.2.3: The weathering regime

After shooting, the samples were placed in a Carbolite 201 furnace in trays containing saturated NaCl solution (0.357g/ml) on a five-hour heating cycle from 20 °C to 50 °C at a ramp rate of 0.1 °C/minute. Once the 50 °C set point was reached, it was maintained for two hours. The samples were then cooled for five hours at a ramp down rate of 0.1 °C per minute back to 20 °C (figure 4.4). The samples were then left at 20°C for 12 hours to simulate overnight summer temperatures in hot arid regions. This heating regime was designed to approximate the diurnal heating conditions found in hot arid environments. These temperatures are based on the temperature cycles reported in arid regions of North Africa by Pinker *et al* (2007), who recorded daily maximum surface temperatures of 50°C. Summer temperatures of 50°C have also been recorded in areas of the Middle East, such as south-eastern Iraq, as described by Ahmed and Hassan (2018). The temperature regime featuring equal heating and cooling ramp rates of a constant gradient has also been shown to be effective in work by Sperling and Cooke (1985), who investigated haloclasty weathering of limestone through the ingress of saline water under diurnal temperature cycling. Holmes *et al* (2015), also showed that diurnal temperature ranges follow a similar 12-hour cycle in arid desert regions of North Africa, as determined using infrared and microwave radiometry in Niger , demonstrating that this heating regime approximates real-world diurnal temperature cycling. The heating cycles were continued until the mass change between two consecutive cycles was $\leq 0.1\%$. This is because when no mass change is detected after a weathering cycle, then the sample has not absorbed any further moisture or salt, or lost stone material due to weathering action. This indicates that the weathering process is complete. This point was reached after 8 cycles and the samples were then dried for 24 hours at 50 °C.

Figure 4.4: *The 12-hour heating regime of the samples.*

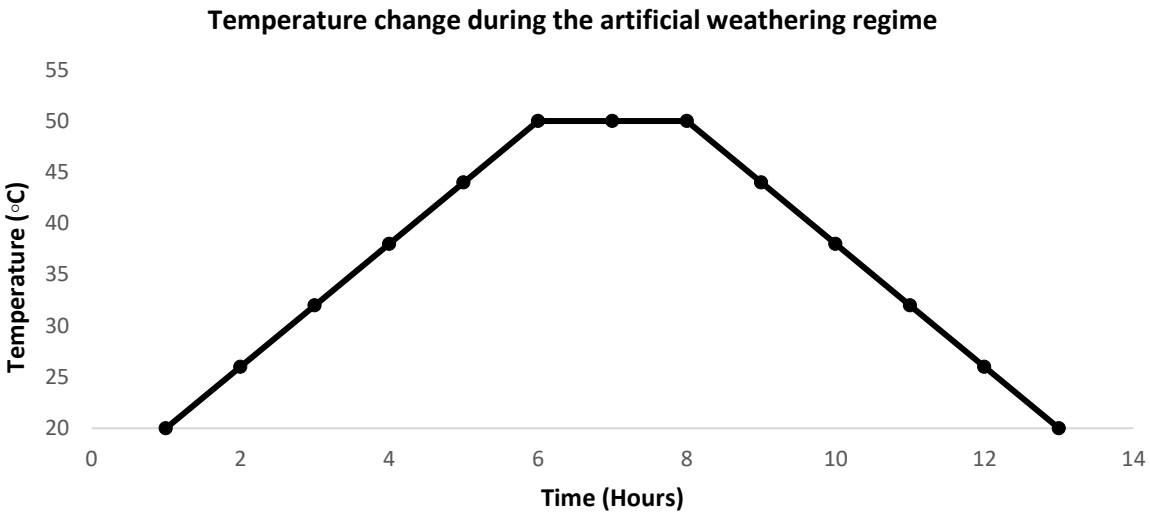

At the beginning of each temperature cycle saturated NaCl solution was introduced to the base of the samples up to a volume of 400 ml to simulate saline groundwater, that is to say that 400ml of liquid present, excepting any volume displacement due to the presence of the stone. As described by Ahmed and Fogg (2014), capillary rise of groundwater containing dissolved salts is a major source of salt weathering damage at archaeological sites, such as Luxor in Egypt. The accumulation of saline groundwater can be the result of human activity, such as increased irrigation to facilitate expanded agriculture, as is the case at Luxor, Egypt. Alternatively, it may be the result of natural processes such as the encroachment of saline seawater into freshwater aquifers in coastal areas of arid regions such as Tunisia and Israel (Paniconi *et al., 2*001, Sivan *et al.*, 2005).

NaCl was selected because it is known to contribute to weathering at heritage sites in arid regions, such as Karnak (Mahmoud, Kantaranis, Stratis, 2010). Aly *et al* (2015) also cite NaCl as one of the most common salts affecting built heritage in arid areas such as Egypt and used NaCl in their experimental work investigating capillary rise of saline solution in Mokattam limestone. Aly *et al's* work produced significant damage in cores of Mokattam limestone due to the growth of NaCl sub-floresceces that resulted in mechanical degradation and loss of volume from the samples (*ibid*). Furthermore, as discussed in section 1.10.3, a great number of studies have shown both the prevalence of NaCl in arid environments and stone heritage, and its ability to cause mechanical degradation (Menendez, Petranova, 2016). The sample orientation in the furnace replicated the orientation when the samples were shot,

so that the side submerged in the NaCl solution was the side that had been facing downwards during shooting.

4.2.4: Mass Monitoring Methods

The mass of both samples was measured prior to shooting, after shooting and after each temperature cycle. This allowed the mass/volume loss due to shooting to be calculated and compared with values calculated using photogrammetric modelling, as well as the mass change due to moisture/salt intake. The mass increase due to salt crystallization would be differentiated from the mass increase due to moisture intake by weighing the samples after they had been dried at 50°C for 24 hours. Mass measurements were taken with Adams Equipment 16kg digital scales.

4.2.5: Photogrammetric Modelling Methods

Varying impact angle was likely to result in differing crater morphologies. Understanding how differing crater morphology influences the damage caused by ballistic impact and subsequent weathering will be important in assessing risk to stone-built heritage damaged by conflict. Therefore, the morphology and dimensions of the impact craters were recorded in three dimensions through photogrammetric techniques. Photogrammetry could then be used in documenting and measuring the scale of visible weathering deterioration throughout the weathering experiments, such as efflorescence. Structure from motion photogrammetry requires no contact with the subject and thus is inherently non-destructive.

As a result, the technique is widely used in heritage science, and has been used to make three-dimensional records of many heritage monuments, including reconstruction of monuments destroyed by war, such as the Great Mosque of Aleppo (Grussenmeyer, Al Khalil, 2017).

In order to assess volume loss, as well as accurately recording surface changes to the samples due to NaCl efflorescence, photogrammetry was used to create three-dimensional models of the samples after shooting and after weathering. These models were created by placing the samples in a black photographic box, on a rotating turntable. The samples were lit using a magnifying lamp facing the sample, and a small LED light on the top interior side of the photographic box. A 2cm scale bar was placed on three orthogonal edges of the samples in order to allow scaling of the 3D models.

The samples were imaged using two cameras, one face on to the sample and a second at a raised angle, looking down on to the top side of the sample (Figure 4.5). The cameras used to image the sample were two Nikon D3500 with the following settings:

Zoom: 5.6

Shutter speed: 1/640

ISO: 1600

Pixel Dimensions: 6000 x 4000

Figure 4.5: *The photogrammetry set up*

The samples were slowly rotated, with 40 overlapping photographs taken on both cameras during each full rotation. Once a rotation was completed, the sample orientation was changed twice, so that the side originally facing downward could also be imaged. This process was repeated three times, meaning that 240 images of each sample was taken. Once these images had been collected, they were processed in the Agisoft Metashape software package to generate a three-dimensional model. This is achieved through the software using recognisable surface features on the sample in the overlapping photographs to calculate the relative positions of each image in relation to the object (Yilmaz, *et al* 2008). This generates a three-dimensional point cloud model of the object. The points in this cloud can be transformed into a series of triangles across the surface of the object that approximate its topology and create a solid three-dimensional surface. This process is known as “meshing” (Curless, 1999).

Finally, the colour and surface details of the object are mapped onto the model in a process known as texture mapping (Weinhaus, Devarajan, 1997) (see figure 4.6).

Figure 4.6: *Various steps in the creation of the 3D models of a cubic control sample of limestone, A: Dense cloud generation, B: Creation of polygon mesh from point cloud, C: Creation of solid mesh from polygon mesh, D: Creation of textured mesh (finished model).*

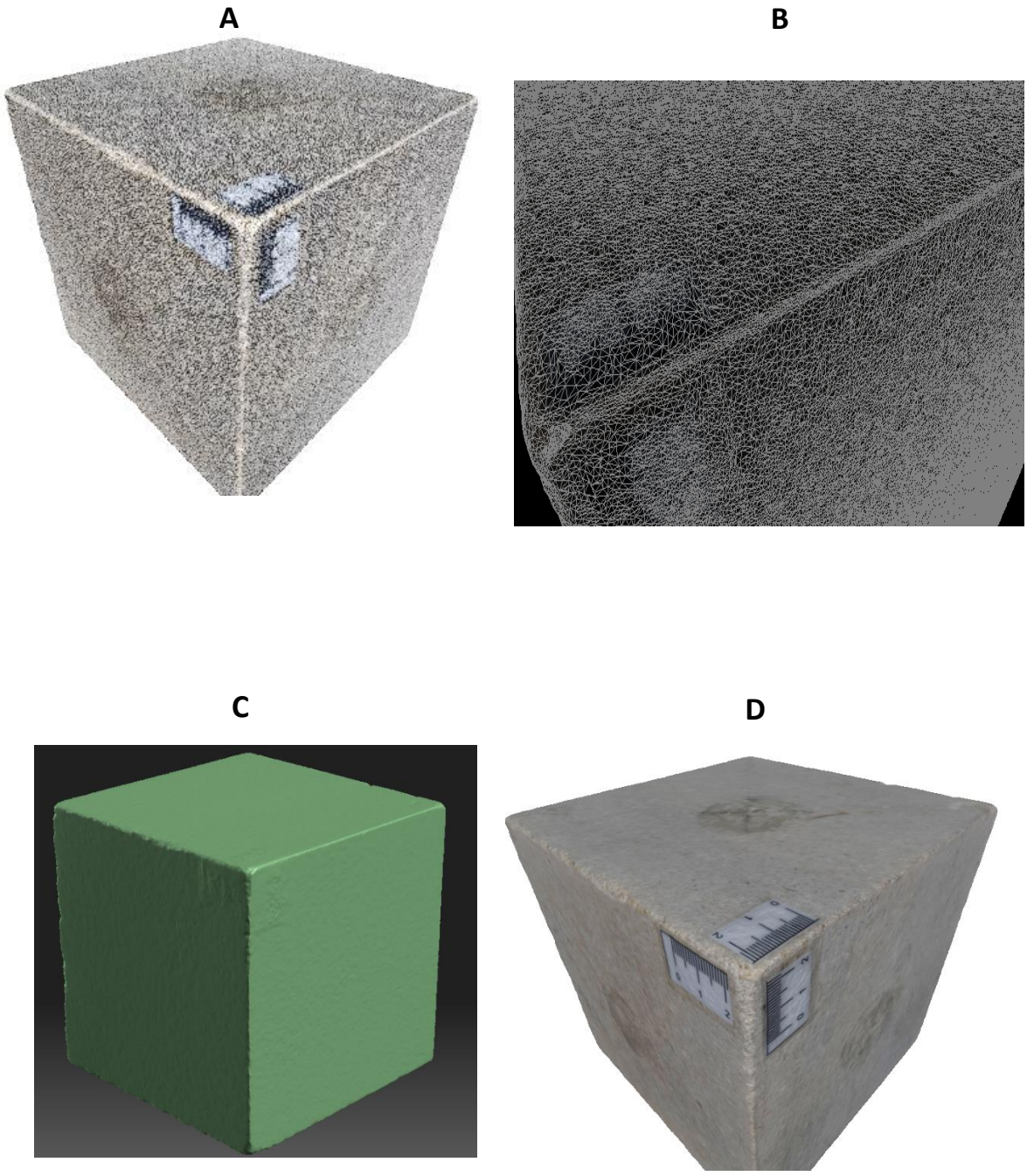

4.2.6: Ultrasonic Pulse Velocity (UPV) Methods

As discussed in section 1.6 and Research Objective I (*To develop non-destructive methods to assess… interior damage to stone after ballistic impact*), understanding to what extent ballistic impact creates fracture networks in the stone interior will be important to understanding weathering behaviours. This is because fracture networks increase the mobility of moisture and dissolved salts throughout the stone, allowing them to access a wider area of the stone and cause greater deterioration (Ehlen, 1999). Chapter 2 outlined methods for detecting and analysing surface facture networks but to fully characterise the threat posed by ballistic impact to heritage stone it is also necessary to develop methods that allow the assessment of interior fracture networks.

The extent of interior fracturing after ballistic damage was demonstrated by Mol *et al*, (2017) using X-ray tomography, whilst work by Mol and Gomez-Heras (2018) showed that UPV analysis could indicate the extent of sub-surface damage in heritage monuments damaged by ballistic impacts. In Mol and Gomes-Heras' work, areas with larger impact craters, which suggested an impact with higher kinetic energy, were found to have lower leeb surface hardness values and reduced UPV values. This suggests that more damaging impacts create a denser fracture network behind the impact crater, which would be susceptible to greater weathering action.

The ability of this type of analysis to determine the extent of fracturing in rock was also demonstrated by El Azhari, and El Hassani (2013) who showed that the velocity of P waves travelling through building stone samples from Morocco was substantially reduced with an increasing number of fractures. Furthermore, the increase in density that a sample undergoes due to moisture and salt filling fracture spaces and pores can be detected as an increase in UPV readings, this was shown in experimental work by Török and Vasarhelyi (2010). Therefore, in order to develop in-situ techniques for assessing how the angle of ballistic impact affects the extent of fracturing in stone, and how these fracture networks are exploited by weathering agents, UPV analysis was deployed in this pilot study. This technique was particularly suitable for this research, as UPV analysis is non-invasive and non-destructive, and therefore poses no risk of damaging heritage assets in a field setting and requires no removal of material for sampling. This is demonstrated by the UPV analysis undertaken on heritage sites such as the Limassol castle in Cyprus by Chrysostomou *et al* (2010).

UPV operates on the principle that compressive waves (P waves) generated by a transducer propagate with a greater velocity through intact stone of a given density and matrix than through the equivalent stone with an interior fracture network. This is because the P wave velocity is reduced by the discontinuities and change in medium created by a fracture network (Leucci, De Giorgi, 2006). Therefore, a lower P wave velocity can be taken to infer a denser interior fracture network (figure 4.7).

Figure 4.7: *The principles of Ultrasonic Velocity detection of fracture network.*

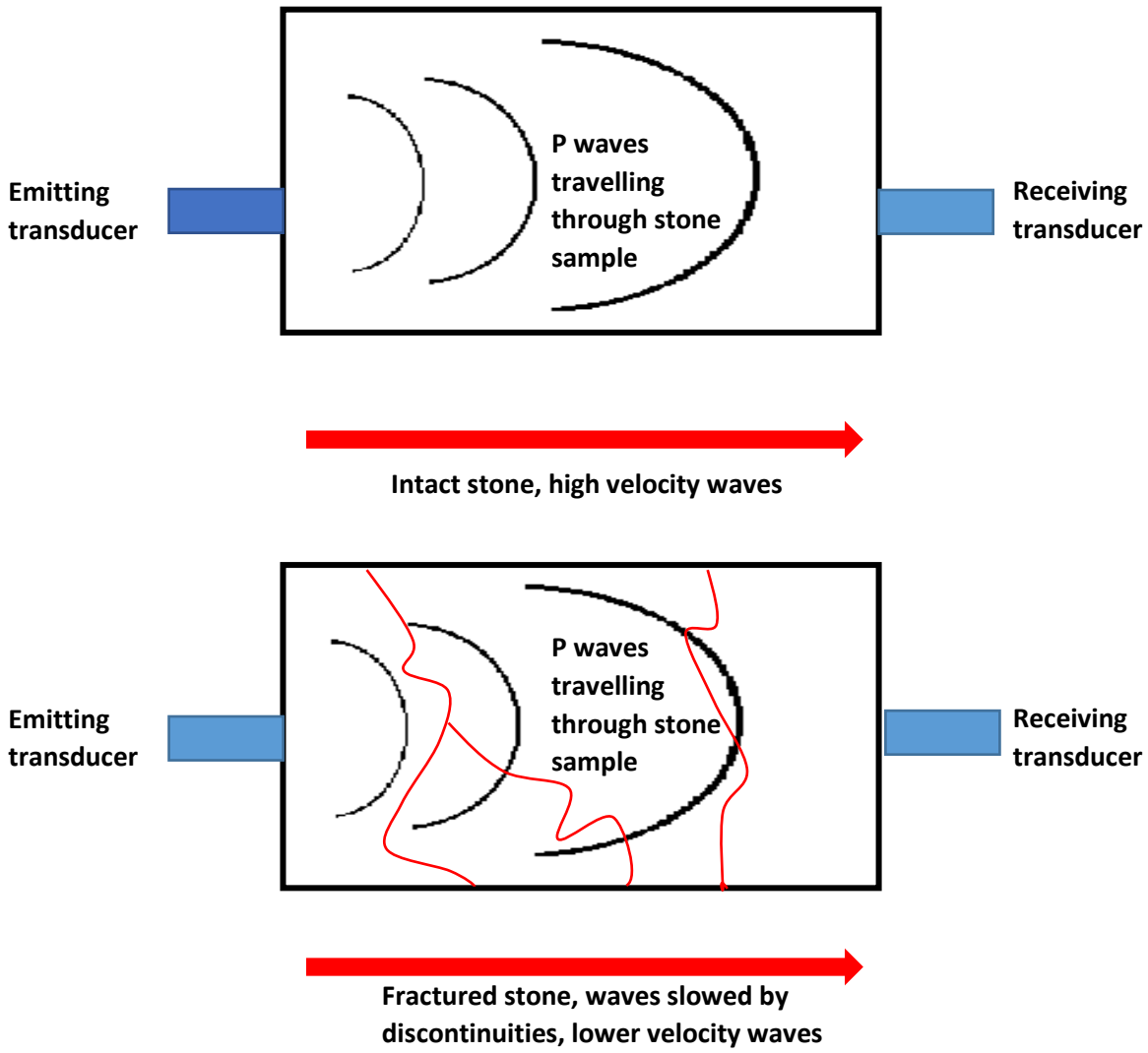

In this study, UPV analysis was conducted using a Proceq Pundit 200 UPV instrument with 54 kHz exponential transducers. This configuration is recommended for use in heritage buildings because it does not require the use of a transducer coupling gel that can stain historic fabrics (Zielinska, 2018, Proceq, 2017b). The aim was to establish if internal fractures caused by ballistic impact could be detected as reduced UPV readings after ballistic impact, and if the angle of impact affected the change in UPV readings after shooting and weathering. N.B: UPV analysis was not used in the pilot study outlined in chapter 2 because control data for the un-shot UPV was not collected in the study undertaken prior to the sample used in chapter 2 being made available to the author.

The intact UPV of the limestone (565 ms^{-1}) was established as the average UPV of 96 readings taken from 32 intact 15cm x 15cm x 15cm samples of Cotswold Hill Cream Limestone. The two samples used for shooting were chosen at random from a population of 34 limestone samples so as not to skew any results based on individual sample defects. Measuring many control samples in this manner meant that an accurate average reading for the limestone could be calculated. After impact, UPV was measured across the centre point of opposing faces of the cubic samples, such that the emitting transducer was at the centre point of sides 1, 2 and 5 whilst the receiving transducer was at the centre point of sides 3, 4 and 6 respectively (Figure 4.1). To ensure that the sampling points were consistently in the same orientation, a rig was constructed that held the transducers at a level height on either side of the sample (figure 4.8). This rig ensured that the distance between the transducers was the same for every reading, and therefore that calculations of velocity over that distance were accurate. The rig also ensured a consistent pressure applied to the transducers for every reading, as increased or reduced pressure applied to the transducers can artificially alter readings

The pulse voltage was 200 V, the receiver gain was x1 and the pulse repetition frequency was 20 Hz. These settings were chosen in accordance with the operating instructions of the device, which recommend the lowest transmitter voltage and gain setting that will achieve a stable velocity reading (Proceq, 2017b). The average UPV for the sample was calculated as the mean of the three readings for that sample, and the results of these readings are detailed in section 4.4.4. The UPV measurements were then repeated after the weathering regimes.

Figure 4.8: *The rig used to ensure consistent positioning of the transducers during UPV measurements.*

4.2.7: Equotip Surface Hardness Measurements

As discussed in sections 1.7 and 1.15 and demonstrated in the pilot study undertaken in chapter 2, surface hardness testing is an effective method for assessing the mechanical deterioration of stone due to ballistic impact and weathering. Therefore, this study measured the hardness of the samples at each stage; before shooting, after shooting and after weathering to determine how detrimental these processes were to the target samples.

The same 49 x 49 hardness ampling grid described in section 2.3.2, was used for this testing but a cardboard grid was used to facilitate faster sampling. As described by Viles *et al* (2011), Equotip rebound hardness survey has been used to survey a variety of lithologies, including both sandstones and limestones, and therefore it was appropriate to deploy the same sampling methodology on the limestone samples used in this experimental work as that developed in the pilot study on a sandstone sample in chapter 2. The Equotip device was fitted with a 14.5mm diameter D6a support ring which was smaller than the 20mm support ring used in chapter 2.

This meant that the three readings taken within each sampling cell could be collected at different points within the cell, in keeping with the Single Impact Method put forward by forward by Aoki and Matsukura, (2007). Given that this study is concerned with the weakening caused by weathering processes, the single impact method is most appropriate for this work because it will minimise any risk of artificial compaction and hardening caused by repeat impacts with the equotip rebound device. Secondly, as discussed in section 2.3.2, minimising the number of impacts on an individual point will also minimise any potential disfiguring of heritage stone surfaces in areas of intricate detailing or rock art etc in a field setting, as discussed by Desarnaud *et al*, (2019).

Five points of the impact crater and wider shattered surface on each sample were also measured for mean hardness (see figure 4.9). These five points were selected because they were flat enough to allow reliable hardness readings to be obtained, which was not possible across much of the shattered surface. Three repeat measurements were conducted at each of these five sampling points and the mean calculated. This was done to ensure that variability of hardness readings due to fracturing of the impacted surface did not result in unreliable data from inside the impact area as only a limited number of sampling points for the impact crater were possible. A single reading from a given point inside the impact crater may result in an unreliable hardness value due to sub-surface fractures, as discussed by Rodríguez-Rellán (2016), and therefore a mean value was deemed to be more reliable.

Figure 4.9: *Equotip/permeability sampling points across the impact crater and shattered surface regions of the two samples. The impact crater is defined as the hemispherical damaged region immediately around the impact point, and the shattered surface is the wider surface that has sheared away. Collectively the crater and shattered surface are referred to as the "impact area". Numbered markers indicate sampling points. Note that for both samples, a small amount of lead residue from the projectile has been retained at the point of impact (the dark marks at the impact point). This neccessitated sampling immediately below the direct point of impact to get accurate measurments of hardness and permeability.*

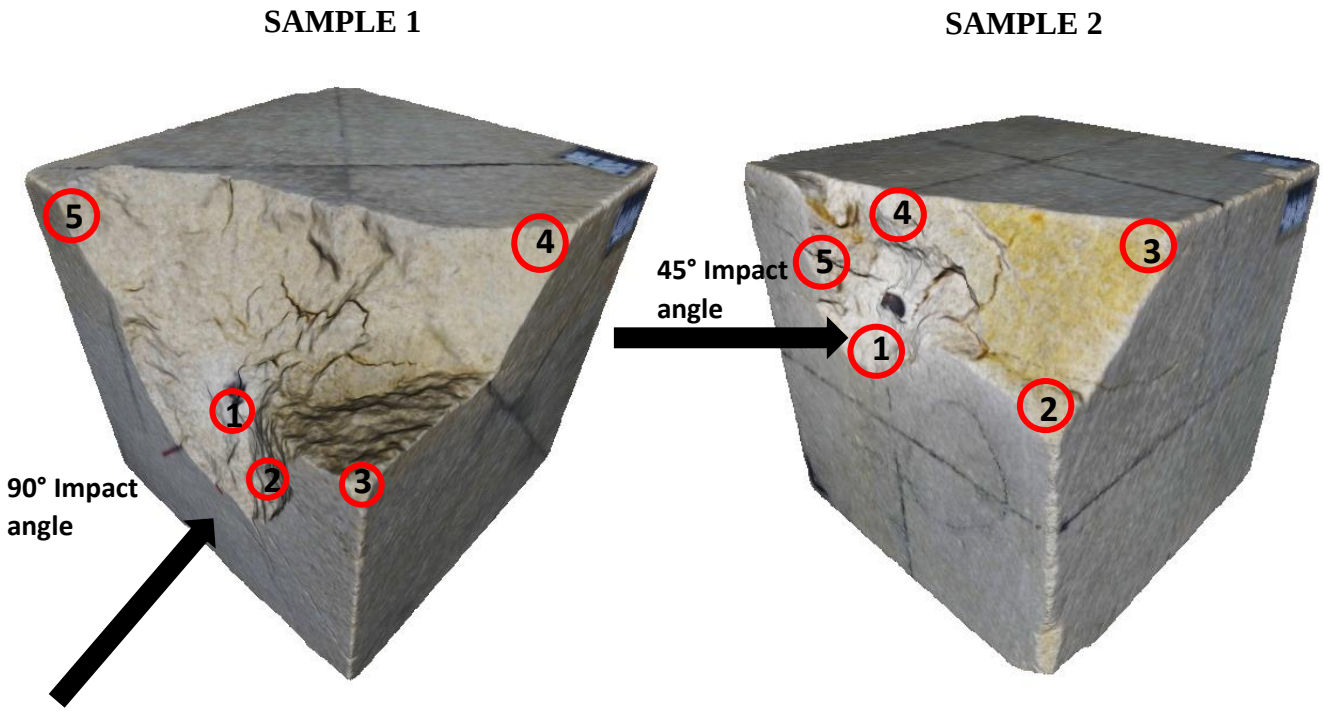

4.2.8: Permeability Measurements

As discussed in section 1.6 and 2.4.2, ballistic impact creates fracture networks in the impacted stone that raise the susceptibility of the stone to ingress and weakening by weathering agents such as saline water. Therefore, changes in the samples' permeability after shooting and weathering were measured, in order to determine how permeability increases caused by ballistic impact affect the weathering process. As was the case with Equotip survey, previous studies have shown that permeability using a Tinyperm permeameter can be deployed across different lithologies such as limestone and sandstone (Grover *et al*, 2016), and therefore the use of a technique first used on a sandstone sample in chapter 2 is valid for the limestone samples of this experimental work. However, as outlined in section 2.5.2, a full

survey of every 2cm x 2cm cell on the sample's surface with three repeat measurements for each cell is a time-intensive methodology that may not be suitable for field situations where access to sites may be time limited. Therefore, it was decided to use this pilot study to test more rapid sampling regimes for determining the effects of ballistic impact and weathering on permeability.

The experimental findings from section 2.4.2 demonstrated that increases in permeability after impact are most pronounced on the impact face which contains the most visible fractures and in the impact crater and shattered surface itself (Gilbert *et al,* 2019). Therefore, permeability sampling in this experiment focussed primarily on this region of the samples. Using the sampling grid, all 49 cells of the impact faces (side 1) were measured once for permeability withgland Research TinyPerm 2 Air Permeameter (see section 2.4.3). On all other faces (2-6) the 4 corner cells and the central cell were measured (figure 4.10). This sampling regime was designed to assess any change to the average permeability of the surfaces outside of the impact face due to the artificial weathering regime.

This sampling process was undertaken after shooting and after the weathering regime and removal of salt efflorescence by gentle brushing. The five areas of the impact crater and shattered surface measured for rebound hardness were also measured for permeability (figure 4.9). The same crater sampling points were used for permeability and hardness readings so that the effects of weathering across the impact area on both surface hardness and permeability could be directly compared through survey of the same area. The intact permeability of the limestone (5.4 millidarcies) was established as the average of 1470 measurements from five 15 cm x 15 cm x 15 cm intact control samples of the same limestone (table 4.2). Five samples were selected at random for these control measurments to ensure that readings were as representative as possible. Given that each reading took around 150 seconds, these control measurements took a total of over 61 hours. Therefore, it was not deemed practical to take permeability measurements from all 32 control samples.

Table 4.2: *Summary of the control data set taken from five 15cm x 15cm x 15cm intact blocks of Cotswold Hill Cream limestone. N.B: As discussed by the manufacturers of the Tinyperm, localised ares of stone may have fairly high ranges in permeability on a milidarcy scale due to localised differences in matrix structure and porosity etc (New England Research, 2016).*

Control Sample	**n**	**Average Permeability (millidarcies**	**Minimum reading (millidarcies)**	**Maximum reading (millidarcies)**	**Range (millidarcies)**	**Standard deviation of readings**
1	294	7.49	0.022	54.37	54.34	10.56
2	294	5.02	0.033	25.33	25.29	6.60
3	294	4.79	0.015	87.84	87.83	8.57
4	294	5.43	0.014	88.93	88.92	9.62
5	294	4.18	0.029	27.00	26.97	5.8
Average for all samples	1470	5.39	0.014	88.93	88.92	8.50

Figure 4.10: *Permeability sampling points on sides 2-6, and the sampling technique with the Tiny Perm 2 air permeameter.*

4.3: Results and interpretation

4.3.1: Visual Analysis

Inspection of the samples after weathering showed that the weathering regime had caused the accumulation of significant salt efflorescence. A notable trend is the obvious exploitation of fractures by the saline solution through the preferential accumulation of salt efflorescence along surface fractures (figure 4.11, overleaf). This lends support to the theory discussed throughout section 1.6 that fractures caused by ballistic impact are likely to exacerbate weathering processes through increased ingress of moisture and dissolved salts.

Figure 4.11: *Progress of the weathering front and the growth of salt efflorescence on sample 1 side 4. Note that efflorescence can be clearly seen to occur preferentially along the fracture running from the centre to the bottom left of the block (highlighted in black), indicating greater penetration of saline solution into this fracture.*

0 Weathering Cycles

1 Weathering Cycle

2 Weathering Cycles

3 Weathering Cycles

4 Weathering Cycles

5 Weathering Cycles

6 Weathering Cycles

7 Weathering Cycles

8 Weathering Cycles

Figure 4.12: Composite image showing the spread of the NaCl efflorescence weathering front after each cycle of the weathering regime on sample 1 side 4.

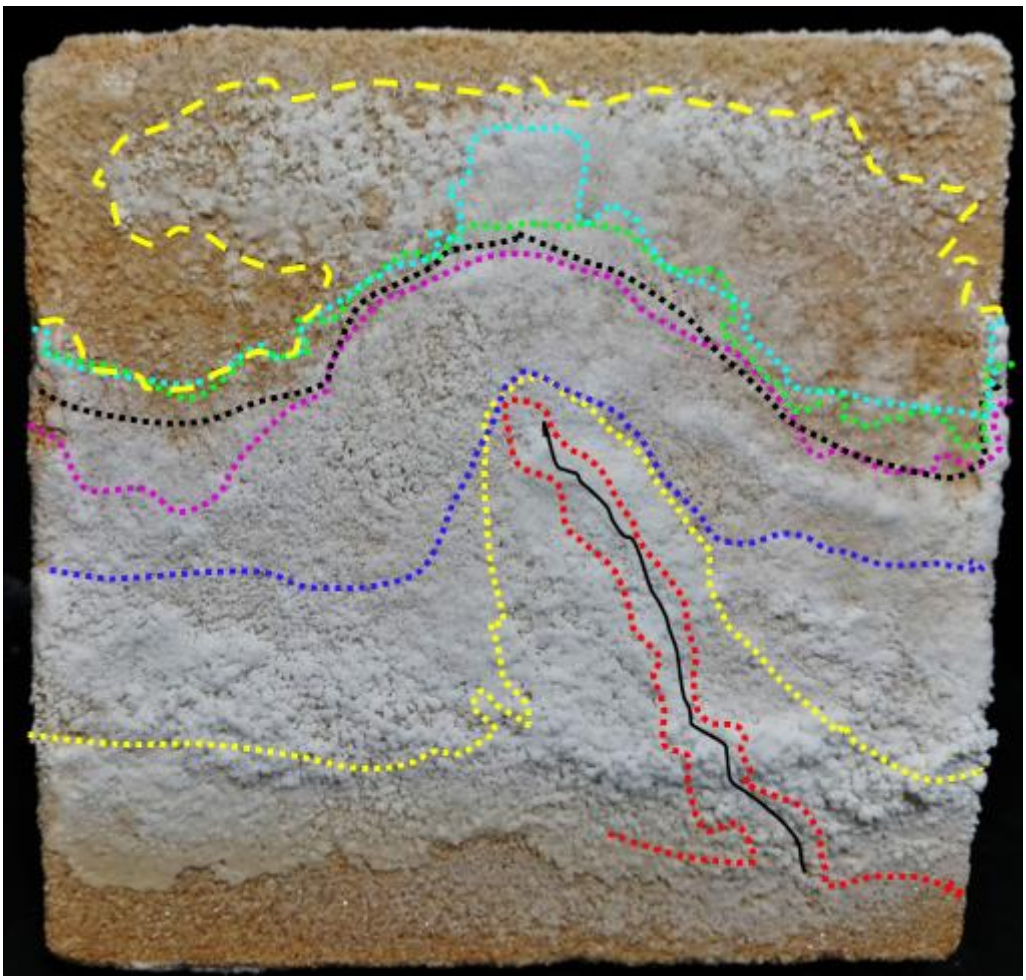

Figure 4.12 shows that after eight weathering cycles the efflorescence has spread from the base of side 4 to the top of the block, preferentially exploiting the large fracture. This demonstrates that capillary rise of saline solution along ballistic impact fractures facilitates rapid accumulations of salt efflorescence, which in a heritage context could deteriorate surface features such as carved detail or painted rock art. Furthermore, the widespread occurrence of efflorescence on the samples suggests that the weathering regimes designed for this study are a viable method of simulating haloclasty processes observed in arid environments. This is an important finding, because it shows that the weathering simulation methodology is effective and can be carried forward into the future experiments of this project.

4.3.2: 3D Modelling Results

4.3.2.1: Error calculation

Before the 3D models of the samples could be used to conduct quantitative analysis of the samples, it was first necessary to ensure that they were properly scaled and yielding accurate dimensional data. To correctly scale the models of the weathered samples, a scaling factor was applied based on the discrepancy between known distances on the sample's surfaces (a 2cm scale bar) and the arbitrary distance applied between the same two points by the Meshlab software. The models were then scaled by applying a scaling factor to each of the model's dimensions to compensate for any discrepancy between the known distance and the arbitrary distance given by the model. This was done using the "compute geometric measurements" and "scaling" tools in the Meshlab software package.

To estimate the error of the 3D models, the density of the intact samples and the mass of the shot samples could be used to calculate the volume loss due to shooting. The largest difference between the volume of the sample calculated using mass loss and the volume calculated by the Meshlab software was then used as the error figure for the 3D models. This approach to calculating error in photogrammetry models using known volumes has been used in previous work by Yilmaz (2010) and Bjorn, Lundqvist and Hjelmstrom (1954). Based on these measurements, the volume error of the 3D models was 0.3%. The data used in this error calculation process is detailed in table 4.3.

Table 4.3: *Mass and volume loss of the samples after shooting and calculated error of the Meshlab models of the sample volume.*

Sample	Impact angle (°)	Mass Before Shooting (g)	Volume before shooting (cm^3)	Density (gcm^{-3})	Mass after shooting (g)	Mass Lost (g)	Volume lost (%)	Volume after shooting based on sample mass (cm^3)	Volume after shooting Meshlab 3D model (cm^3)	% error of 3D model
1	90	7431	3375	2.20	6998	433	6%	3178	3168	0.3%
2	45	7399	3375	2.20	7250	149	2%	3307	3316	0.3%

Once the volume error of the models was known, it could be used to calculate that error of the Meshlab calculation of the samples' surface area would be 0.2% as outlined below:

For a + 0.1% error on a distance measurement of 10cm:

0.1% error on distance

0.2% error on area

$$10.01cm \times 10.01cm = 100.2cm^2$$

$$100.2cm^2 \times 10.01cm = 1003cm^3$$

0.3% error on volume

4.3.2.2: Sample volume loss

Table 4.3 demonstrates that the volume of stone lost due to ballistic impact is higher for a sample impacted at 90° (6 %) than for a sample impacted at 45° (2 %) (Figure 4.13). As discussed in section 1.7 and demonstrated by the work of Gault (1973), a projectile impact at 90° has been shown to cause higher volume loss to the target stone than an oblique impact. This difference in volume lost is due to the higher amount of ejecta from a 90° impact, caused by higher rarefaction wave pressures as more of the projectile's kinetic energy is

transferred to the target (Schultz, 1996, Melosh, 2013). This raises the interesting possibility that the volume of stone lost due to ballistic impact may be related to the impact angle, with lower volume loss being correlated with a shallower angle of impact. The fact that only two samples were used in this preliminary study means that there is insufficient data to confirm this correlation, and a greater number of samples will be analysed in the future experimental work of this project in order to ascertain the relationship between angle of impact and crater volume loss.

Based on the observation that volume can be indicative of the level of ballistic damage to a block, it was decided to explore the relationship between other spatial data and the level of damage. The 3D models were used to assess if ballistic impact and the subsequent weathering regimes resulted in significant changes to the samples' volume and surface area. The reasoning behind this was that a significant reduction in volume for either sample would be indicative of stone material loss due to projectile impact or haloclasty, whilst an increase in surface area may indicate the accumulation of irregular NaCl efflorescence that altered the sample's topography.

The results of the analysis of changes in sample volume are shown in figure 4.13 and table 4.4.

Figure 4.13: *Change in sample volume due to shooting and salt efflorescence accumulation. Error bars are 0.3% of the calculated volume, as calculated in section 4.4.2.*

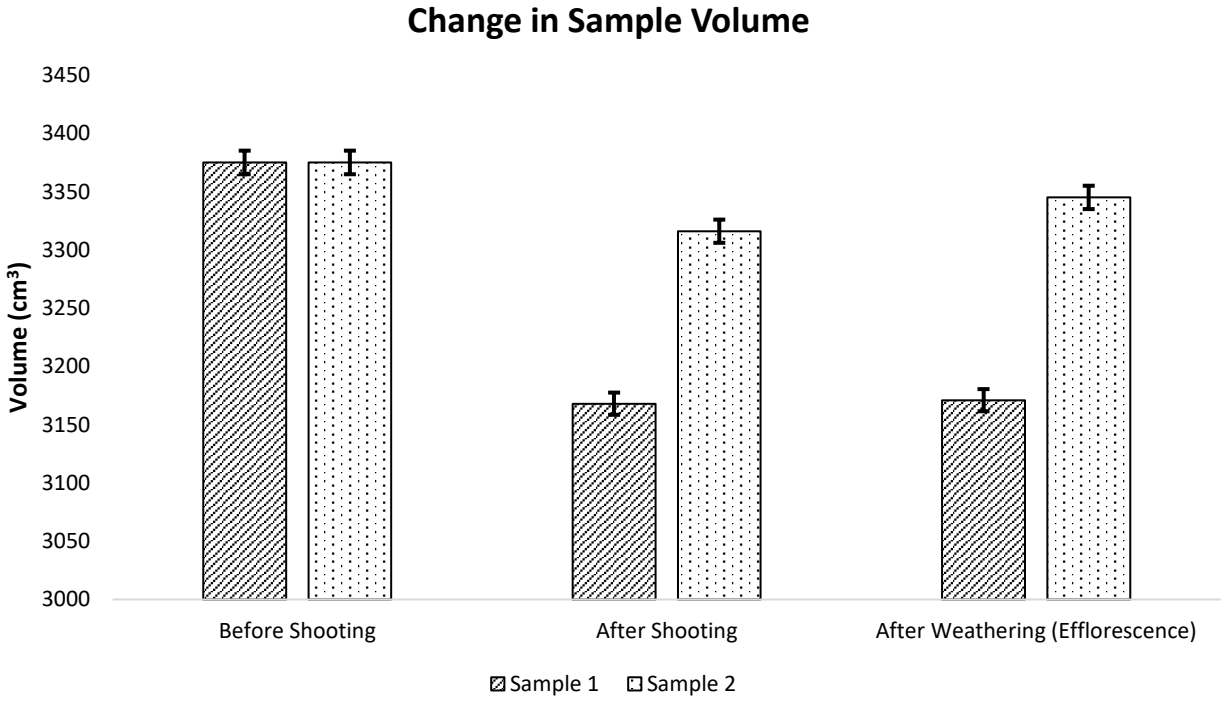

Table 4.4: *Data on the change in sample volume after shooting and after weathering based on the 3D models.*

Sample	Impact Angle (°)	Intact Volume (cm^3)	Volume change after shooting (cm^3)	Volume Change After Shooting (%)	Volume Change of Shot Samples Due to Salt Weathering/Efflorescence accumulation (cm^3)	Volume Change of Shot Samples Due to Salt Weathering/Efflorescence accumulation (%)
1	90	3375	-207	-6	+3	+0.1
2	45	3375	-59	-1.7	+29	+0.9

As figure 4.13 and table 4.4 demonstrate, both samples undergo a notable reduction in volume due to the ballistic impact, whilst sample 1 loses a greater proportion of its volume due to the direct 90° angle of the impact (see above). After weathering, both samples see a small increase in volume. Sample 1 increases in volume by 0.1%, whilst sample 2 increases by 0.8%. The increases in volume for sample 2 is above the 0.3% error threshold, which suggests that the substantial NaCl efflorescence accumulation seen in figures 4.14 and 4.15 (overleaf) does lead to a detectable increase in sample volume. The increase in sample 1's volume is smaller than that for sample 2 because sample 1 lost a small amount of stone material on one of its corners, as shown in in figure 4.16. This was the only loss of stone material noticeable with the naked eye on either sample and would offset any substantial increases in volume due to efflorescence on sample 1, resulting in a negligible overall change in volume.

The increase in volume of sample 2 outside the margin of error suggests that photogrammetry can detect changes in volume due to efflorescence. However, the small relative increases in volume for both samples (<1%) suggests that further experimentation and data collection will be necessary to determine whether photogrammetry can reliably and consistently quantify increases in volume of stone samples due to weathering after ballistic impact. Furthermore, the use of only two samples in this preliminary study limits the reliability of these conclusions, and future weathering experiments of this project will analyse a greater number of impacted samples in order to assess the reliability of this preliminary finding.

Figure 4.14: *Textured and un-textured 3D models of the sample 1 showing how salt efflorescence is likely to alter the sample volume and surface area.*

Sample 1 before weathering (textured)

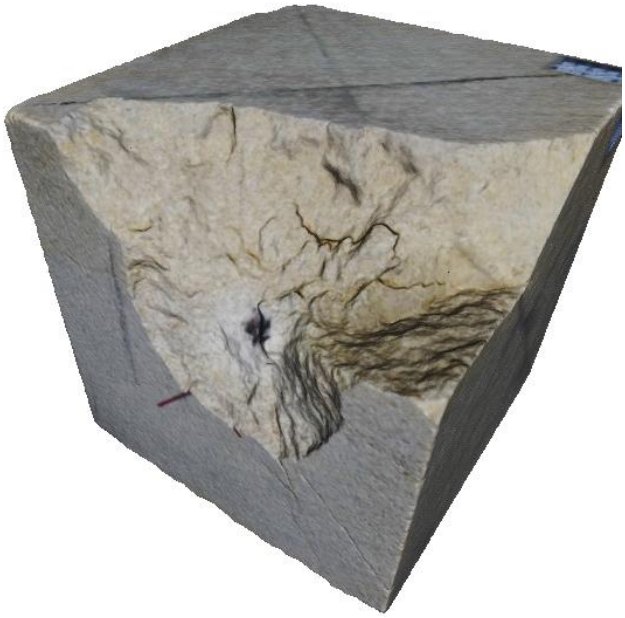

Sample 1 after weathering (textured)

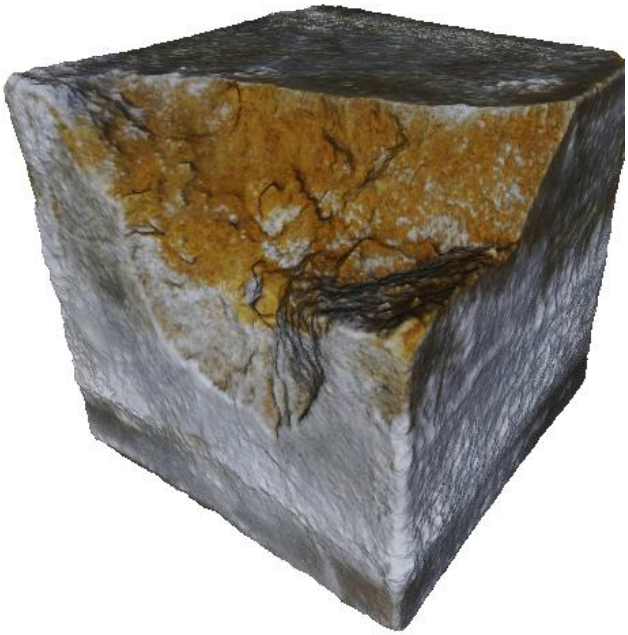

Sample 1 before weathering (not textured)

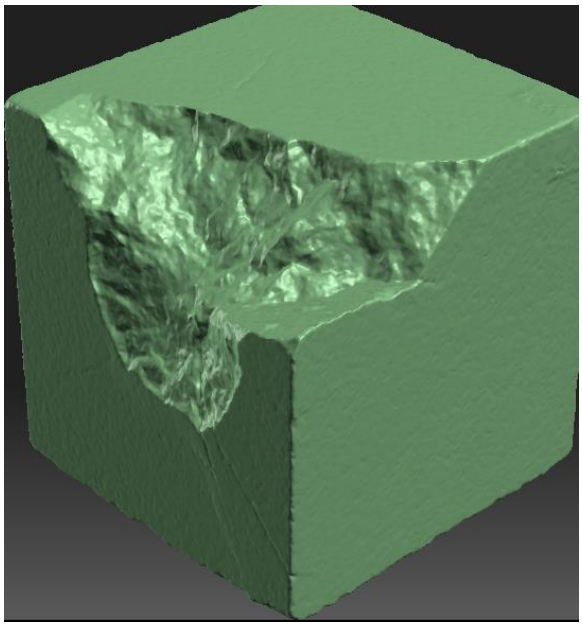

Sample 1 after weathering (not textured)

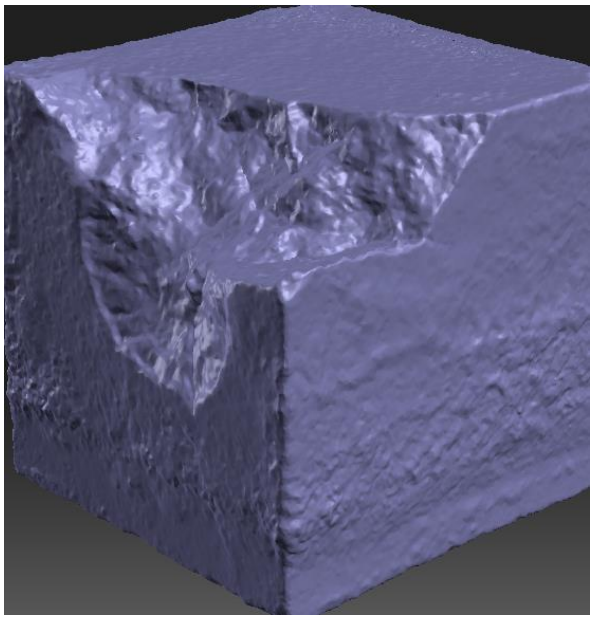

Figure 4.15: *Textured and un-textured 3D models of sample 2 showing how salt efflorescence is likely to alter the sample volume and surface area.*

Sample 2 before weathering (textured)

Sample 2 after weathering (textured)

Sample 2 before weathering (not textured)

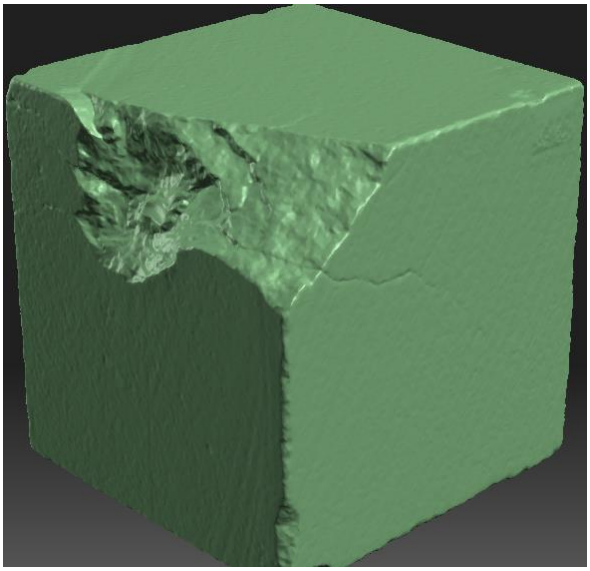

Sample 2 after weathering (not textured)

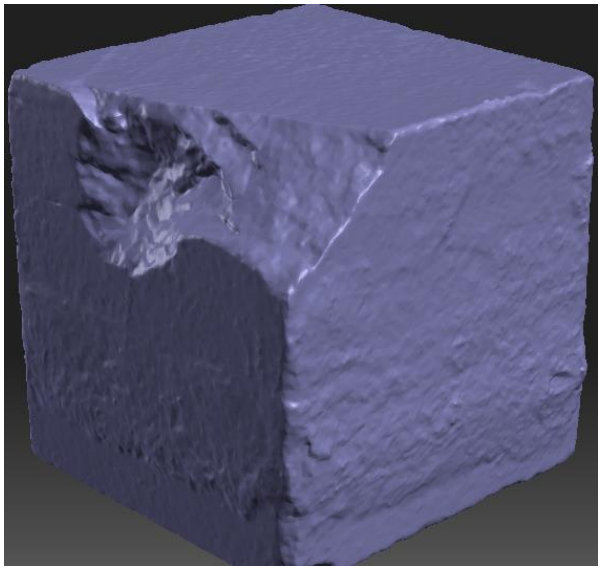

Figure 4.16: *3D models showing the small loss of stone matrix on sample 1's corner after weathering.*

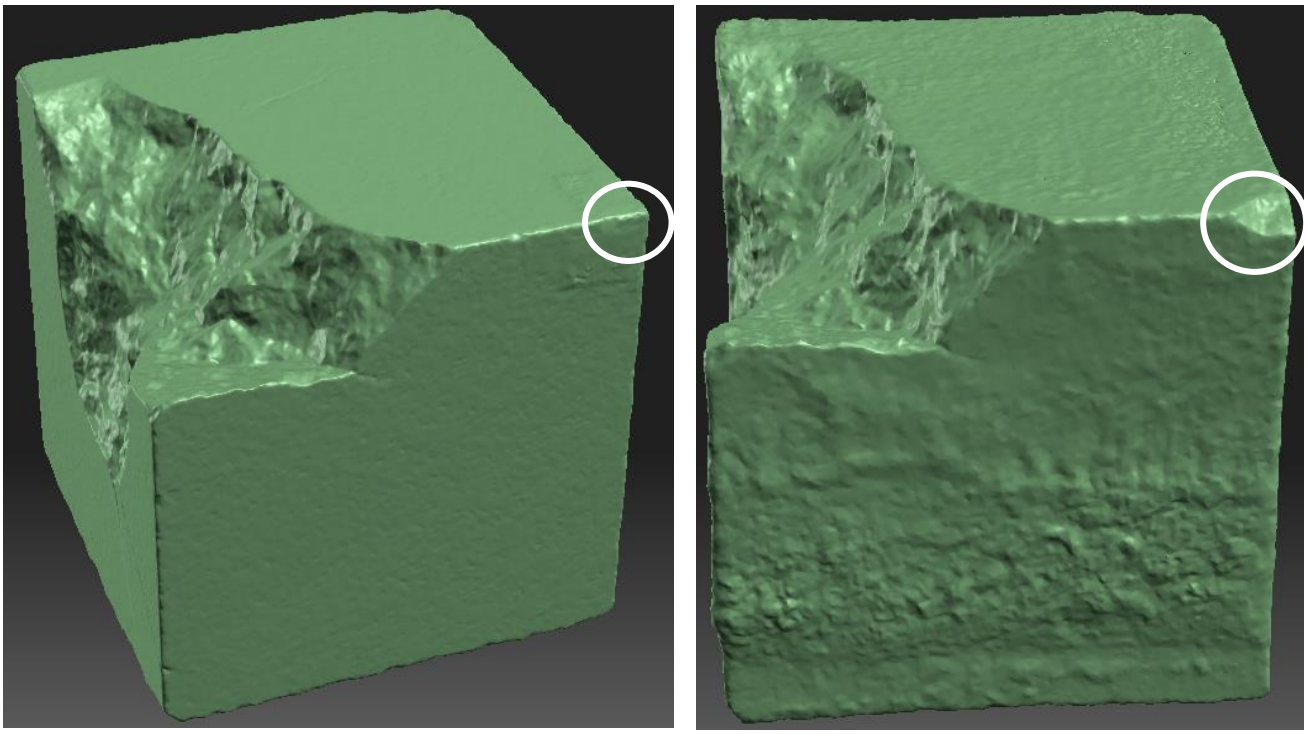

4.3.2.3: Changes in sample surface area

Visual analysis of the changes in surface morphology due to efflorescence seen on the 3D models in figures 4.14 and figure 4.15 suggested that efflorescence was likely to alter sample surface area. As described in the introduction to this section, it was hypothesised that photogrammetric analysis of changes in surface area of the 3D models before and after weathering could be used to quantify the growth of irregular salt efflorescence that accumulated on the samples. This was tested using the "compute geometric measures" tool in Meshlab, and the results are presented in figure 4.17.

Figure 4.17: *Change in overall sample surface area due to shooting and salt efflorescence accumulation. N.B. Error bars are 0.2% of the calculated surface area as outlined in section 4.4.2.*

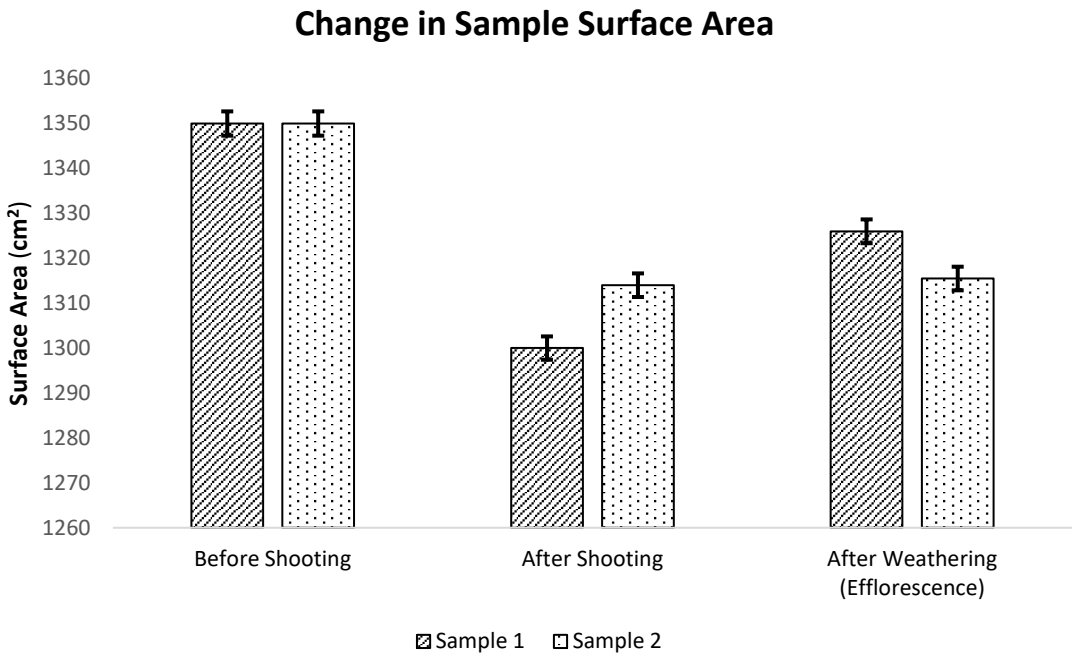

Table 4.5: *Data on the change in sample volume after shooting and after weathering based on the 3D models.*

Sample	Impact Angle (°)	Intact Surface area (cm^2)	Surface areas change after shooting (cm^3)	Surface area Change After Shooting (%)	Surface area Change of Shot Samples Due to Salt Weathering/Efflorescence accumulation (cm^3)	Surface area change of Shot Samples Due to Salt Weathering/Efflorescence accumulation (%)
1	90	1350	-50	-4.7	+26	+2
2	45	1350	-68	-2.7	+1	+0.08

Figure 4.17 demonstrates that ballistic impact results in a reduction in surface area for both samples. As with the change in volume, the 90° impact experienced by sample 1 results in a greater reduction in surface area (-4.7% for sample 1 vs -2.7% for sample 2). The most notable result is that the change in surface area for sample 1 after weathering is substantially larger than for sample 2 (sample 1 =2 %, sample 2 = 0.08%. The increase in the surface area is indicative of a greater accumulation of efflorescence on sample 1 that sample 2. This conclusion is supported by visual analysis of the samples, which shows a much greater coverage of salt deposits on intact sides of sample 1 than sample 2:

Figure 4.18: *Salt efflorescence coverage is greater on intact surfaces of sample 1 than the same face of sample 2:*

Sample 1 side 4 **Sample 2 side 4**

The fact that the increase in surface area due to salt efflorescence is greater for sample 1 than sample 2 suggests that the 90° impact experienced by sample 1 results in a more connected fracture network. Given that the samples were subjected to identical weathering regimes, (volume of saline solution, temperature of heating regime, orientation and location in furnace) the differing fracture networks are likely to be a controlling factor in the spread of efflorescence, rather than differing exposure to weathering agents. A more connected fracture network would increase the mobility of the saline solution inside sample 1 when compared

with sample 2. This would result in greater precipitation of salt crystals in surface pores for sample 1, as seen in figure 4.18. Efflorescence exploiting fracture networks in sample 1 is also visible in the accumulation of salt crystals along fractures seen in figure 4.11. The model of NaCl depositions exploiting pre-existing fracture networks is also described in work by Warke, Smith and Lehane (2011).

Further evidence for the influence of fractures on the accumulation of efflorescence comes from the analysis of individual surfaces of sample 1. Using the "compute area of selection" tool in Meshlab, the surface area of each of sample 1's surfaces was calculated after shooting and after weathering. As table 4.6 demonstrates, the largest increases in surface area for sample 1 are observed on side 4 and side 1:

Table 4.6: *Changes of surface area on individual surfaces of side 1 due to efflorescence accumulation:*

Sample 1 Surface	Surface area before weathering (cm^2)	Surface area after weathering (cm^2)	Increase in surface area (cm^2)
1	146	152	6
2	198	200	2
3	224	224	0
4	219	230	11
5	157	159	2
6	222	225	3
Impact crater/shattered surface	134	136	2

As can be seen in table 4.6, sides 1 and 4 exhibited the largest increase in surface area due to efflorescence after the salt weathering regime. This is notable because these are the only surfaces on either sample that have surface fractures that extend into the lower portions of the block and would thus allow faster capillary rise of the saline solution. This contrasts with sample 2, which due to the 45° impact only exhibits horizontal fractures, which would not aid capillary rise of salt water as quickly, as shown in figure 4.19.

Figure 4.19: *Contrasting the vertical fractures on sample 1 that will facilitate rapid capillary rise with the horizontal fractures on sample 2. Red lines indicate fractures, blue lines indicate level of saline solution at samples base.*

Sample 1 side 1

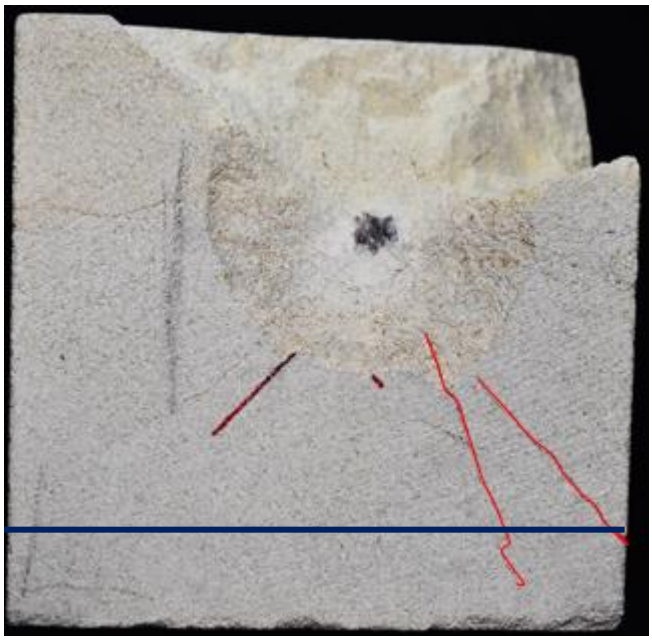

Sample 1 side 4

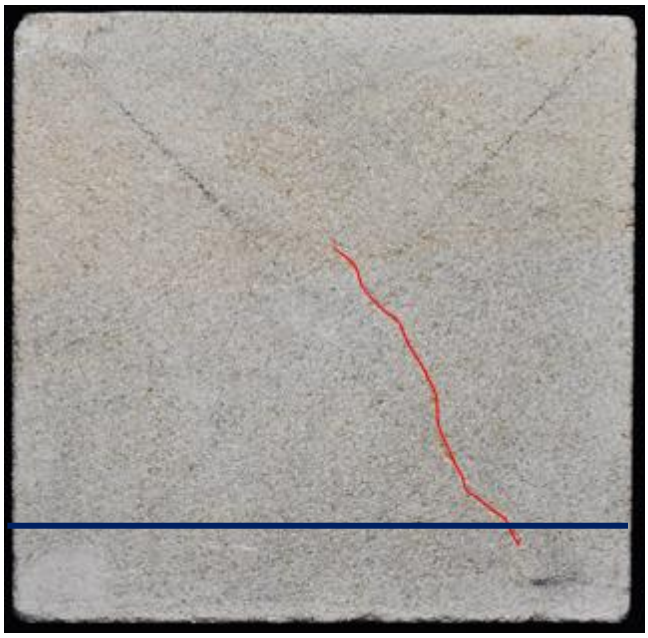

Sample 2 side 1

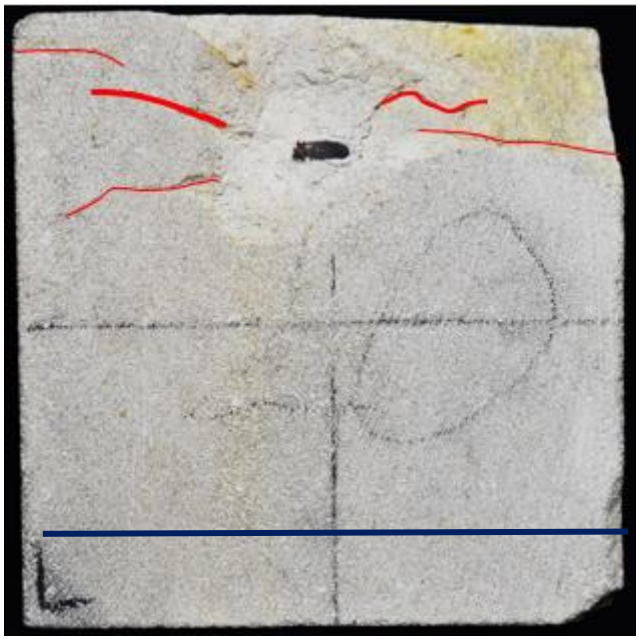

Sample 2 side 2

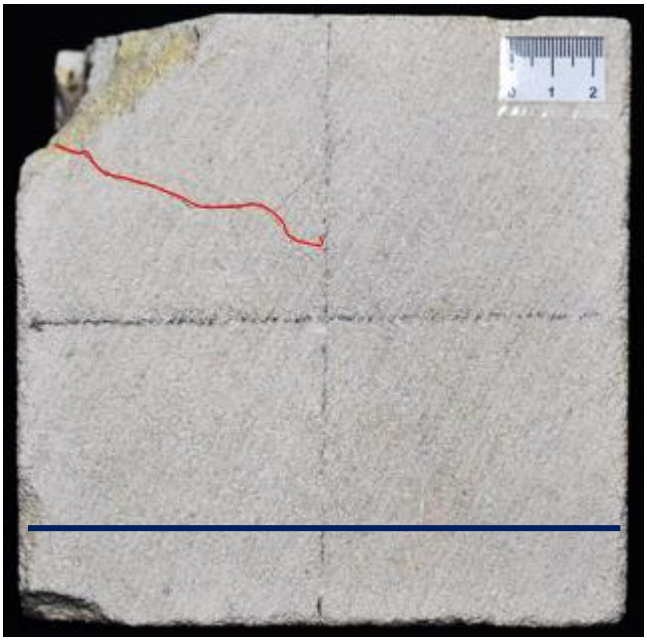

Taken together, the data in table 4.6, and the images of fracture orientation in figure 4.19 suggest that the angle of impact is an important factor in controlling the spread and orientation of surface fractures in impacted stone. In turn, surface fractures, and their position relative to any ground water and soluble weathering agents such as salt, are controlling factors in the level of efflorescence that accumulates on shot stone after weathering.

4.3.3: Mass monitoring results

The postulation that sample 1 developed a denser and more connected fracture network during impact than sample 2 is also supported by data from mass monitoring.

After shooting, sample 1 reduced in mass from 7.4kg to 6.988 (-6%), whilst sample 2 dropped from 7.4kg to 7.25kg (-2%).This difference is likely because more of the projectile's kinetic energy is transferred to the impact face of sample 1 during the 90° impact, resulting in larger rarefaction wave pressures that eject more material as discussed in sections 1.4 and 4.4.2.2.

After 8 weathering cycles, both samples increase in mass. Sample 1 increased from 6.998 to 7.75kg (+10.7%) and sample 2 increased from 7.25kg to 8.025kg (also +10.7%). This is shown in figure 4.20. This suggests that there is an upper limit on the relative mass change for the samples that occurs when accessible pore spaces are saturated and fracture voids are sealed with NaCl crystals, as observed by Flatt *et al* (2014) and Noiriel *et al*, (2010). The fact that the relative mass changes are the same does not affect the results showing that volume and surface area of efflorescence are different between the two samples, as these metrics are independent of the total mass of the salt taken on by the samples, which is a product of both efflorescence and subflorescence.

Figure 4.20: *Relative mass change of the samples during the weathering cycles.*

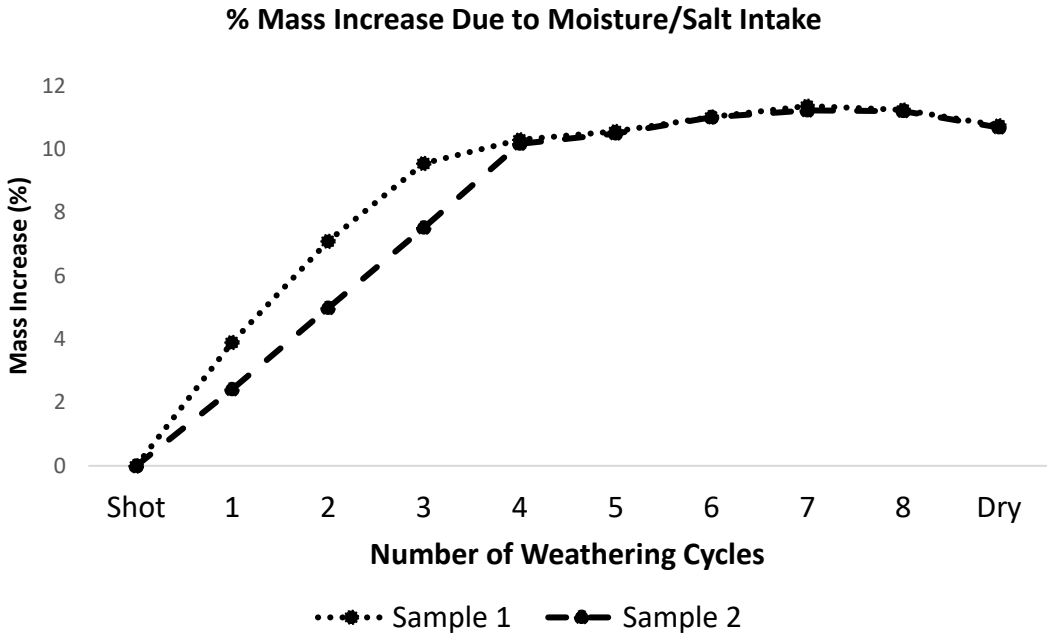

Figure 4.20 shows that sample 1 undergoes a greater relative mass change in the initial three cycles, suggesting that the NaCl solution permeates sample 1 more rapidly than sample 2. The faster uptake of water by sample 1 is hypothesised to be due to a higher fracture density inside sample 1 resulting from the 90° impact, supporting the conclusion in section 4.4.2.3 that the greater accumulation of salt efflorescence across the surface of sample 1 is the result of higher moisture mobility through a denser internal fracture network. This is in agreement with previous experimental work, which demonstrated that large accumulations of efflorescence occur when the rate of capillary rise into a stone sample is faster than the rate of evaporation due to heating (Aly *et al*, 2015, Rodriguez-Navarro, Doehne, 1999). This is because a high rate of capillary intake allows saline solution to quickly reach surface pores of the stone before evaporation then causes crystallization of the salts on the sample's surface. This is likely to be the case for sample 1, which sees a rapid uptake of saline solution due to its denser fracture network (figure 4.20). This in turn leads to a greater coverage of efflorescence and corresponding increase in surface area (figure 4.17) as intake of solution is faster than the rate of evaporation. UPV analysis results also indicate a denser fracture network inside sample 1, as discussed in the following section.

4.3.4: Ultrasonic Velocity Results

The UPV results in figure 4.21 show that sample 1 experienced a greater decline in UPV after shooting than sample 2. Sample 1 had an average UPV of 395ms^{-1} after shooting (-170ms^{-1}/ -30% from the control average of 565ms^{-1}), and sample 2 saw a reducition in UPV to 498ms^{-1} (-67ms^{-1}/ -12%) This is consistent with sample 1 having a higher internal fracture density than sample 2, because the P waves take longer to pass through the voids associated with a fracture network than they take to travel through intact rock (see section 4.2.6).

Sample 1 likely has a denser fracture network than sample 2 because the 90° impact creates higher tensile wave pressures that lead to a larger internal fracture network (Wang, Konietzky, 2009). It is worth noting the large standard error bar for sample 1 after weathering seen in figure 4.21 reflects the fact that the impact crater on this sample reduced the number of orientations across the block where UPV could be measured (n=2, as opposed to n=3 for the 45° impact). This was because it was not possible to obtain UPV readings from inside the impact crater for sample 1 because the uneven surface of the impact face, and retention of the lead projectile in the impact crater would make reliable calibration of distance and density between the UPV sampling points impossible. This increases uncertainty for the mean value. Therefore, conclusions drawn from this small data set should be treated with caution. Steps that will be taken to address the issue of ballistic impact reducing the number of UPV readings possible after ballistic impact in future experimental design are discussed in section 4.4.5.

Figure 4.21: *Changes in sample UPV after shooting and after weathering. Error bars represent the standard error of the given data set.*

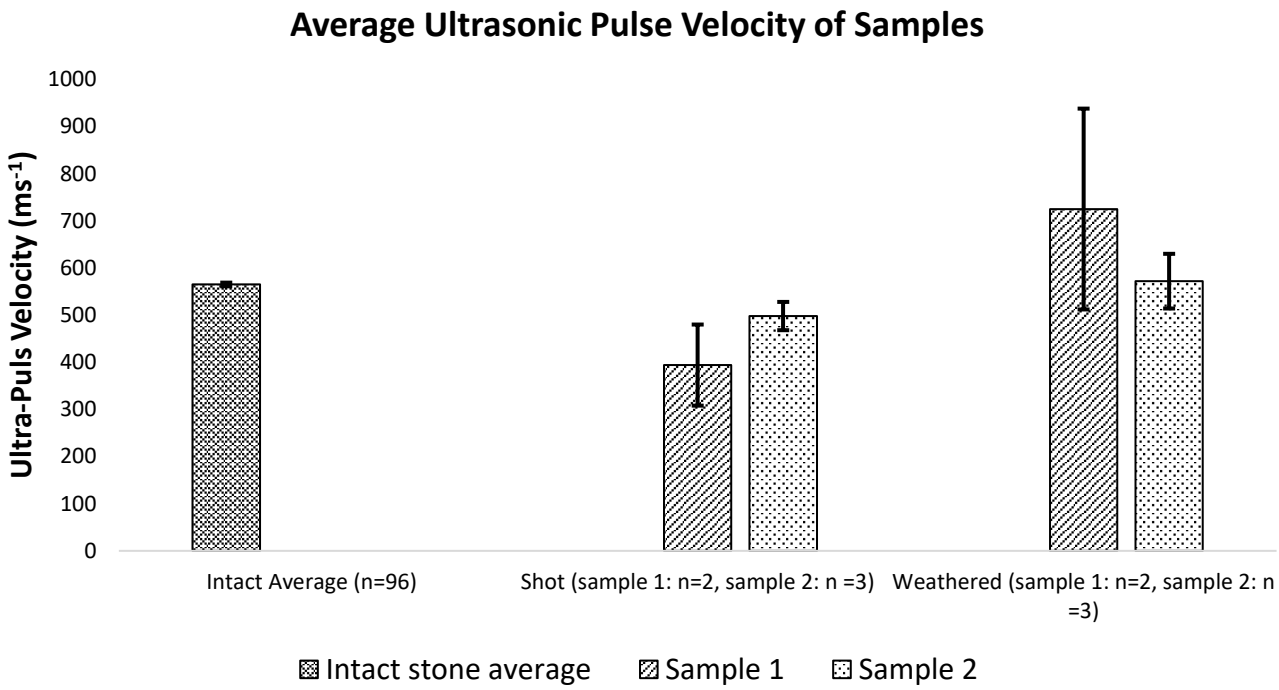

After the weathering cycles and removal of efflorescences, the mass (and therefore density) of both samples increased above their intact levels after shooting (table 4.7). This increase in density is reflected in the increase in UPV above intact levels seen in figure 4.21, and is caused by NaCl crystals filling accessible pores and fracture spaces, as previously observed in UPV analysis by Aly, (2016).

Table 4.7: *Changes to the samples' volume, mass, density and UPV after shooting and weathering.*

Sample	Impact angle (°)	Sample Volume before shooting (cm^3)	Sample Mass before shooting (kg)	Sample Density before shooting (gcm^{-3})	Sample Volume after shooting, weathering and efflorescence removal (cm^3)	Sample Mass after shooting, weathering and efflorescence removal (kg)	Sample density after shooting,weathering and efflorescence removal (gcm^{-3})	Average Sample UPV after shooting, weathering and efflorescence removal (ms^{-1})
1	90	3375	7.40	29	3166	7.63	2.4	725
2	45	3375	7.39	29	3316	7.91	2.4	572

The higher UPV readings after weathering for sample 1 seen in table 4.7 are caused by the NaCl solution exploiting a denser fracture network inside the central portion of sample 1. This denser fracture network is a result of the 90° impact and allows more NaCl precipitation in the central region of block 1 than block 2. This is in keeping with experimental observations of NaCl precipitatipon sealing fracture networks in limestone and increasing UPV readings after salt crystallsation (Noiriel *et al*, 2010, Aly *et al*, 2016). Despite the two samples having similar densities, the orientation of fractures and associated NaCl precipitation in sample 1 results in higher UPV readings for this sample, as UPV measurments were taken across the centre point of the sample block faces. This is explained in figure 4.22.

Figure 4.22: *Schematic of the effect of ballistic impact and salt precipitation on UPV readings. Not to scale.*

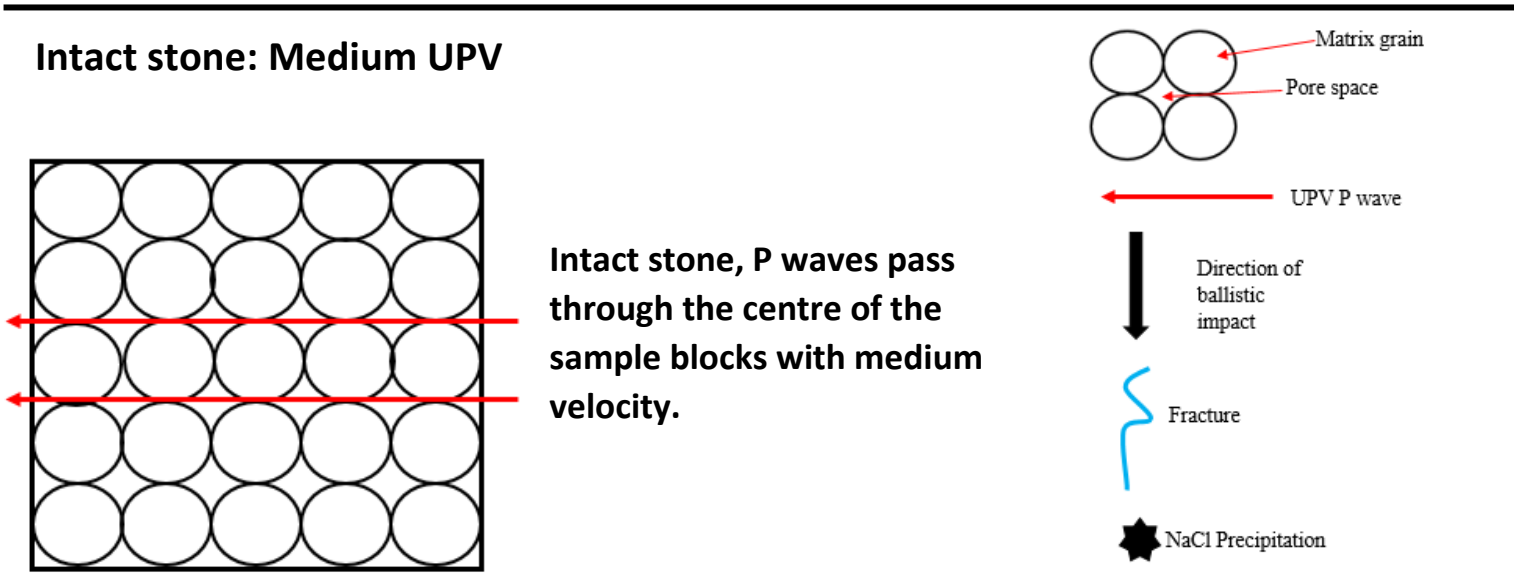

This figure, supported by the UPV results presented above, outlines the causal mechanism by which 90° ballistic impact creates a denser internal fracture network. This greater fracture density is responsible for faster uptake of saline solution observed through mass monitoring measurements, as discussed in section 4.4.4. It is worth noting that in a field setting, that an increase in UPV readings for weathered heritage stone above a known control value (i.e. for freshly quarried samples of a lithology known to be used in heritage buildings) could be used to infer a fractur network infilled with salt crystals. Contextual information would be necessary to assess whether this infilled fracture network was caused by ballistic impact, i.e. by recording the presence or absence of visible impact craters.

4.3.5: Rebound hardness results

4.3.5.1: Hardness results from outside the impact areas

Unlike the hardness survey results for the Huesca Sandstone in chapter 2, the results of the Equotip rebound hardness survey of the limestone samples in figure 4.23 and table 4.8 show that ballistic impact results in a noticeable reduction in rock surface hardness (RSH) outside of the impact area. The fact that the Huesca sandstone used in chapter 2 does not undergo a reduction in hardness outside of the impact area, whilst the Cotswold Hill Cream limestone does, is presumed to be a result of the differing mechanical responses of the two lithologies The Huesca sandstone is denser than The Cotswold Hill cream limestone used in this study (sandstone: 2.45gcm^{-3}, limestone: 2.2gcm^{-3}), and previous studies have shown that the penetration and damage to a granular porous target such as stone is inversely proportional to the target density (Ringl, Bringa, Urbassek, 2012). Therefore, the denser Huesca sandstone is likely to be less damaged by the ballistic impact. The difference in lithology response to ballistic impact will be explored further in subsequent sections.

Figure 4.23 and table 4.8 show that after both shooting and weathering, sample 2 exhibits the greatest weakening across the wider sample surface with a -7.1% (27 leeb) loss after shooting, and -14.8% (57 Leeb) after weathering compared to intact hardness. This is compared with a -4.3% reduction (17 leeb) for sample 1 after shooting, and a -10.9% loss (42 leeb) after weathering.

Figure 4.23: *Change in hardness outside of the impact areas. Error bars represent the standard error of the given data set.*

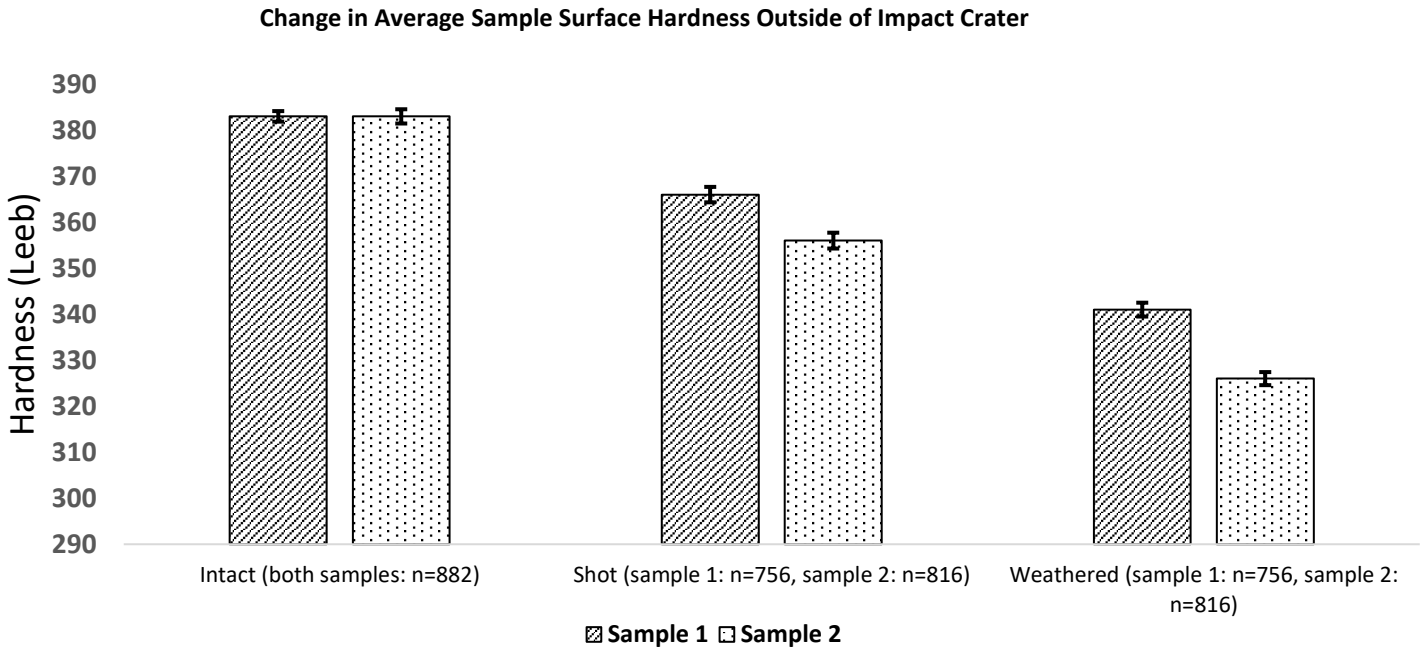

Table 4.8: *Data on the change in surface hardness after shooting and after weathering outside of the impact area.*

	Impact angle (◦)	Hardness before shooting (Leeb)	Hardness after shooting (Leeb)	Reduction in hardness after shooting (%)	Hardness after weathering (Leeb)	Reduction in hardness after weathering compared to intact hardness (%)
Sample 1	90	383	366	7.1	341	14.8
Sample 2	45	383	356	4.3	329	10.9

The fact that sample 2 experiences the greatest reduction in hardness after both shooting and weathering may be because the projectile impact was above the centre of side 1 and at a 45° angle. This trajectory means the projectile impact on sample 2 was closer to sides 2 and 5 (figure 4.9), causing loss of stone material on both of these faces. Therefore, the magnitude of stress waves experienced by these faces would be higher for sample 2 than sample 1, leading to a higher reduction in RSH across sides 1, 2 and 5. Compressive stress waves with high magnitudes reflecting off these faces as rarefaction waves will result in sub-surface spallation fractures, which lower the hardness of these non-impact faces more than in sample 1 (Antoun *et al*, 2002; Aydin, 2009).

This is in contrast to sample 1, where stress waves primarily lead to fracturing and ejection of matrix on the impact face (side 1). After weathering, NaCl precipitation within this sub-surface spallation fracture network is hypothesised to be the cause of greater haloclasty weakening across sample 2's non-impact faces. This is supported by microscopy analysis by Lopez-Acre *et al* (2010) which demonstrated that salt crystallisation inside pre-existing fractures in stone creates inter and intra-granular micro-fractures across a stone's surface. This micro-fracturing across the surface will weaken the surface and reduce RSH values, as seen for sample 2. To test this, the hardness reduction for each of the sample's sides was plotted individually after shooting and after weathering. The changes in hardness for each side after shooting are shown in figure 4.24:

Figure 4.24: *Data on the level of surface hardness loss of each sample surface after shooting. N.B. samples do not have a standard error bar as it is not possible to calculate standard error for relative change on a single sample surface.*

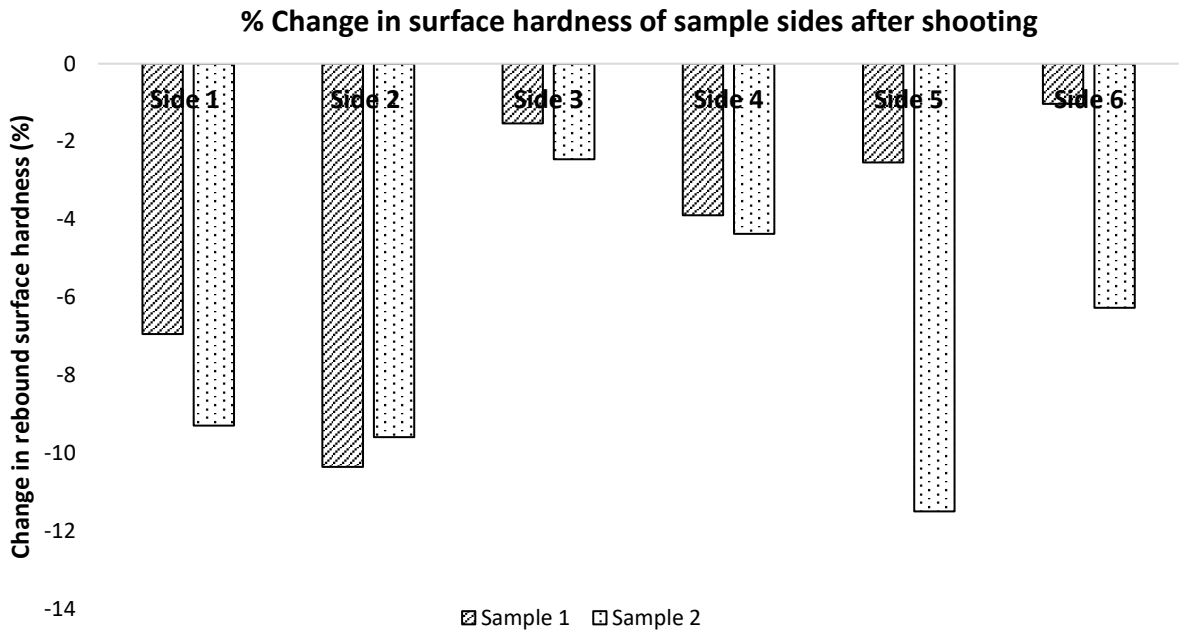

As figure 4.24 shows, for sample 1 the sides that saw notable reductions in hardness were sides 1 (-6.9%) and 2 (-10.3%). This is an interesting trend because these are the surfaces with large visible surface fractures directly connected to the impact crater. This is also true of sample 2, where sides 1, 2, and 5, which all show surface fractures connected to the impact crater, have the greatest reduction in hardness (-9.3%, -9.6%, and -11.5% respectively).

For both samples, side 3 saw a very small decrease in hardness (-1.5% for sample 1, -2.4% for sample 2). This is in keeping with previous findings in chapter 2, which show that this surface is least affected by ballistic impact because it is the antipode of the impact face and therefore experiences stress waves with the lowest magnitude.

It is notable that all surfaces of sample 2 except for side 2 saw a larger reduction in hardness than the equivalent side of sample 1, including side 3, which is most distant from the impact. This is thought to be the result of projectile impact on sample 2's corner. Forquin and Hild (2011) demonstrated that brittle materials subjected to edge-on projectile impact show fracturing perpendicular to the impacted edge. The fact that the projectile trajectory for sample 2 resulted in the projectile impacting the top right corner of side 1 could have resulted in the propagation of fractures across a wider area. This is because this corner is at the

confluence of three edges. Previous research has demonstrated that flexural “edge waves” can propagate in brittle materials like stone, transmitted along the edge of the medium and causing fracturing (Nobili, Radi, Lanzoni, 2017, Norris, Krylov, Abrahams, 2000). Work by Nakazawa *et al*, (2002) demonstrated that high-speed impact induces edge waves in rock.

It is therefore plausible that the impact across the sample’s corner resulted in the greater weakening of all of sample 2’s surfaces due to more extensive micro-fracturing caused by edge wave propagation to sides distant from the impact.

It is also possible that the fact that sample 2 experiences greater loss of hardness on every surface is due to inhomogeneity or internal defects such as bedding planes inside sample 2 that are exploited by stress waves, as discussed by Kumar and Kring (2008). As only two samples were used in this study, further experimentation would be required to determine whether impact on a sample’s edges or corners results in weakening of a greater area than 90° impact due to edge wave propagation. This could be addressed by investigation into a greater number of samples impacted at differing angles, and this will be considered in future experimental design, as discussed in section 4.4.5.

Figure 4.25 shows the change in hardness of the various sample surfaces after weathering compared to their intact hardness. All surfaces experience further loss in hardness when compared with their hardness after shooting, suggesting that NaCl crystallisation is producing mechanical degradation of the stone. This validates the methodology of simulating salt ingress and weathering used in this study.

Figure 4.25: *Changes in surface hardness for each sample surface after weathering. N.B. samples do not have a standard error bar as it is not possible to calculate standard error for relative change on a single sample.*

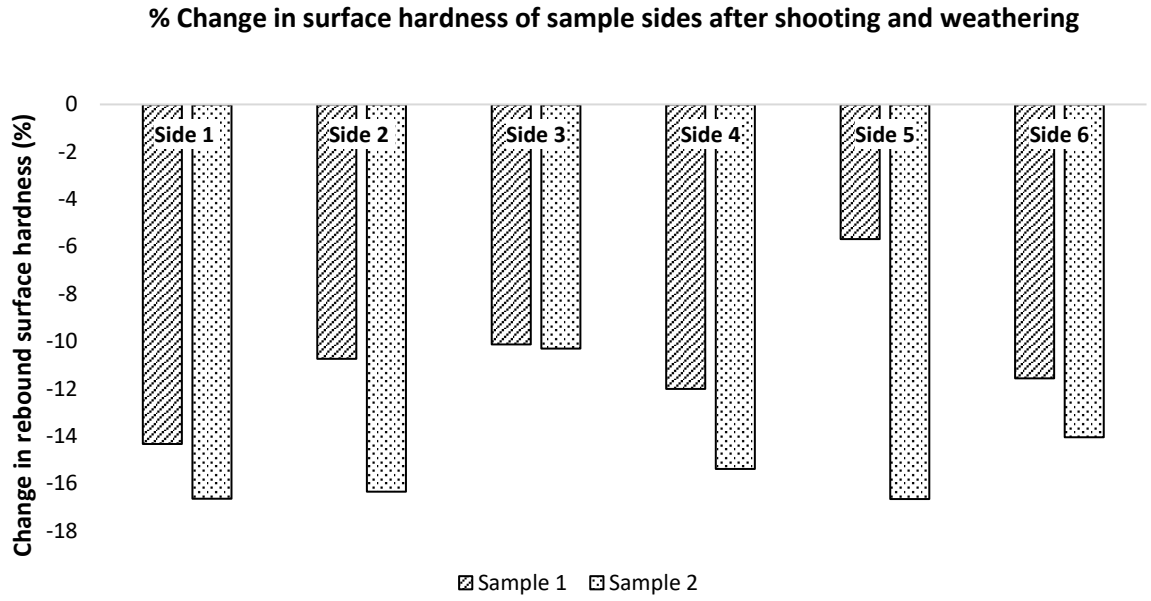

Some of the greatest reductions in hardness after weathering for both samples are seen on the impact face (side 1). This suggests that for both samples, the fracture network created on the impact face is highly susceptible to further degradation after salt weathering. This denser fracture network is caused by the impact face experiencing the highest wave pressures during impact (Nakazawa *et al,* 2002).

As was the case after shooting, side 3 on both samples is also less reduced in hardness after weathering than sides directly damaged by projectile impact. This surface underwent the lowest reduction in RSH due to shooting, and the fact that it also experiences the smallest deterioration due to weathering suggests that damage and fracturing caused by ballistic impact is an important factor in determining subsequent weathering damage. This is because surfaces furthest from an impact event will be most protected from the damage caused by ballistic impact, meaning that they experience less fracturing that can then be exacerbated by weathering through salt crystallisation.

Furthermore, sides exhibiting surface fractures connected to the impact crater in sample 2 that underwent substantial reductions in hardness after shooting also see the greatest decline in hardness after weathering. Sides 1, 2 and 5 see reductions in hardness of 16.6%, 16.4% and

16.7% respectively. This is further evidence that weakening and fracturing caused by ballistic impact influences subsequent deterioration due to weathering through salt crystallisation.

4.3.5.2: ***Hardness results from across the impact area.***

A complex pattern of behaviours emerges when analysing the hardness measurements from the impact area after shooting and after weathering, as seen in figure 4.26.

Figure 4.26: *Changes in hardness from the samples' impact craters and shattered regions. Error bars represent the standard error of the given data set.*

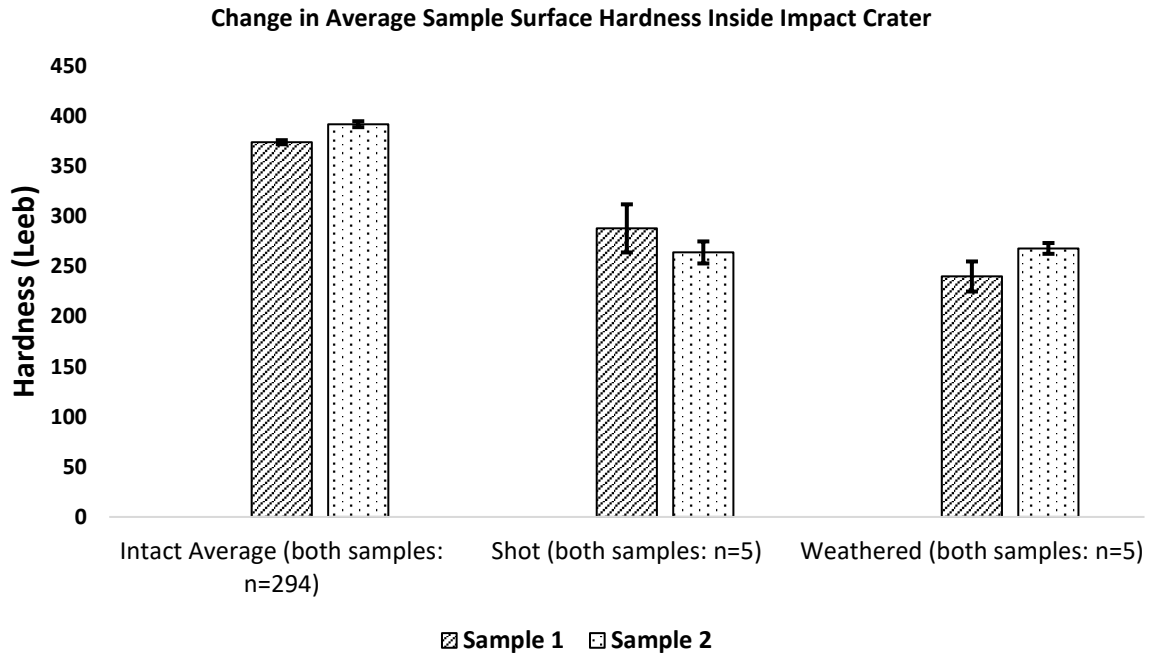

Table 4.9: *Data on the changes in hardness from the impact crater and shattered region after shooting and after weathering.*

	Impact angle (°)	Intact Hardness Average (Leeb)	Shot hardness average (Leeb)	Change in hardness after shooting (%)	Weathered hardness average (Leeb)	Change in hardness after weathering compared to intact hardness (%)
Sample 1	90	383	288	-23	240	-36
Sample 2	45	383	264	-33	268	-32

As shown in figure 4.26, immediately after impact, sample 1's crater experiences less weakening than sample 2. This is likely due to the compaction of the stone matrix in the impact crater that results from a 90° impact angle. Compaction has previously been shown to result in less weakening in directly impacted areas (Gilbert *et al*, 2019, Mol *et al,* 2017, see chapter 2). However, this compaction is unlikely to happen during a 45° impact, and hence the impact area for sample 2 experiences a larger reduction in hardness.

To demonstrate that 90° impact causes compaction of the stone matrix, the distance from the impact point to each sampling point can be plotted against the measured hardness for that point:

Figure 4.27: *Data on surface hardness of sampling points with increasing distance from the impact crater centre.*

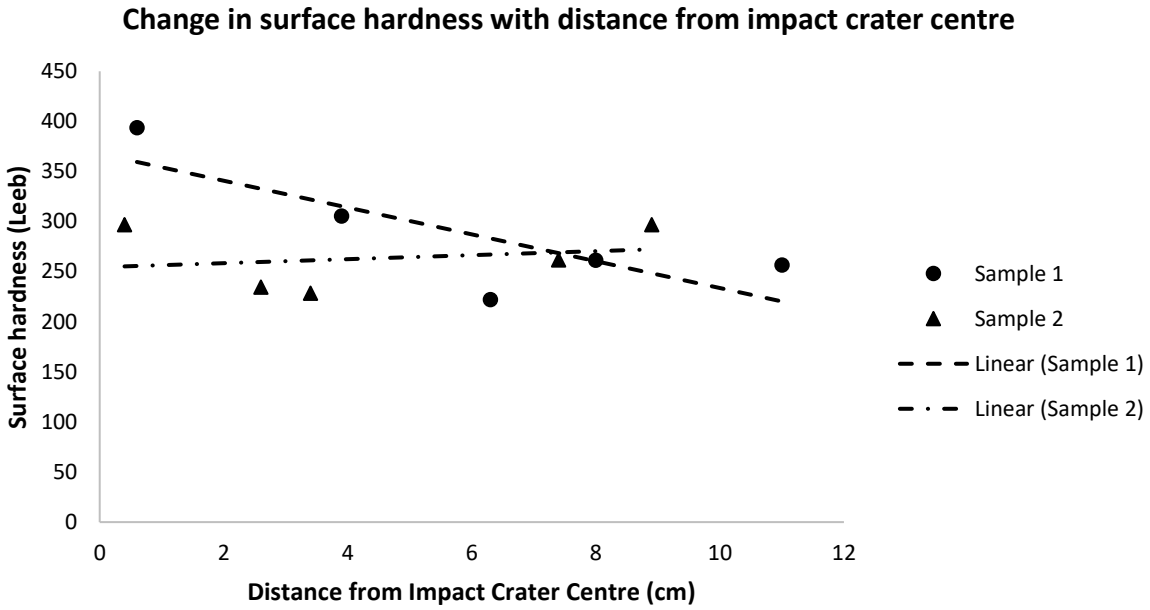

As figure 4.27 shows, for sample 1 there is a clear negative correlation (correlation coefficient: -0.8) between distance from impact crater centre and the hardness of a sampling point. Furthermore, the hardness of the sampling point just below the impact centre has a hardness value higher than the average of the intact stone for sample 1 (394 Leeb for sample 1 impact crater centre vs 383 Leeb average for sample 1 before shooting). Such a trend of increased hardness at the impact centre with decreasing hardness further from the impact crater is strong evidence of the matrix compaction at the impact centre after 90° impact suggested by Mol *et al,* (2017) and Gilbert *et al,* (2019).

Conversely, sample 2 shows no such relationship between distance from impact centre and hardness, with a slight positive correlation (correlation coefficient: 0.21). Sampling points for sample 2 were either inside the impact crater or taken in the same direction as the projectile trajectory to ensure that only areas directly affected by the projectile impact were sampled (figure 4.9). This suggests that a 45° impact does not cause notable compaction and hardness increase because the trajectory of the projectile across the sample's surface does not allow compressive waves to crush the stone matrix. As with all the findings in this limited pilot study, analysis of the effects of impact angle on crater hardness variation using a greater number of samples will be part of the future work of this project, to ensure that these results are not simply caused by random inhomogeneity of the stone matrix in these two samples.

Figure 4.26 also shows that after weathering, the impact area of sample 1 experiences further loss of hardness (288 leeb to 240 Leeb), whilst sample 2 shows a very small increase from 264 Leeb to 268. This difference is thought to be the result of a denser fracture network in sample 1 originating from the impact crater.

A denser fracture network connected to the impact crater in sample is evidenced by the UPV measurements and mass monitoring results in sections 4.4.4 and 4.4.3, which demonstrate that the denser fracture network in sample 1 originating from the impact crater facilities higher moisture mobility throughout the sample. This greater moisture mobility causes more haloclasty deterioration in the crater area. Conversely, the 45° impact of sample 2 results in a less dense fracture network connected to the impact crater, as suggested by the UPV results. A less dense fracture network causes lower moisture movement and haloclasty which results in a minimal degree of weathering of the impact crater in sample 2 and no significant change in hardness.

Furthermore, the compaction of the stone matrix in the impact crater of sample 1 shown in figure 4.27 will reduce moisture flow through this region. This will cause the accumulation of saline solution in this region, and result in a greater level of salt crystallisation in the impact area for sample 1 than sample 2, which does not undergo matrix compaction. This will cause a greater degree of hardness loss after weathering in the 90° impact sample than the 45° sample, as seen in figure 4.26. This is in agreement with Mol *et al* (2017) who demonstrated that weathering weakening is increased in regions of stone compacted by 90° ballistic impact.

The hypothesis that the impact crater of sample 1 experiences more weakening due to haloclasty is supported by the level of salt efflorescence exhibited in the impact craters of the two samples (figure 4.28). More efflorescence is present in the impact crater of sample 1 indicating that saline solution is more able to access this crater and cause mechanical degradation.

Figure 4.28: *Images showing the greater level of salt efflorescence (white areas) in the impact crater (black circle) of sample 1 than sample 2. This is indicative of greater haloclasty in the impact area of sample 1, caused by a denser fracture network facilitating higher mobility of saline solution.*

Sample 1

Sample 2

In addition to the greater salt efflorescence coverage in sample 1's impact crater shown in figure 4.28 an increased level of haloclasty weathering in the impact crater of sample 1 is also evidenced by data from permeability analysis, as will be explored in the following section.

4.3.6: Permeability results

4.3.6.1: Permeability results from across the impact area

As table 4.10 shows, the average permeability of the impact crater and wider damaged region after shooting was well above the 5.4mD of the control readings. Furthermore, sample 1's crater average permeability is substantially less than sample 2's (Sample 1: 211.4 mD, Sample 2: 1301.9 mD). This difference is likely due to the compaction of the stone matrix at the impact point after 90° impact in sample 1, which reduces the ability of air to flow through this region. This is supported by the findings of Mol *et al*, (2017) which showed that impact crater compaction reduced moisture through flow. During a 45° impact, any compaction of the stone matrix would be significantly less than for a 90° impact, because shock pressures decrease with decreasing angle of impact (Rubin, Swindle, 2011). A lack of substantial compression in sample 2 due to the 45° impact results in a notable increase in permeability due to the creation of fracture networks and absence of compaction.

Table 4.10: *Permeability data and changes at each of the impact area sampling points depicted in figure 4.9.*

Impact area Sampling Point (Fig. 4.10)	Sample 1 crater permeability after shooting (Millidarcies)	Sample 1 permeability after weathering (Millidarcies)	Change in permeability (Millidarcies)	Sample 2 permeability after shooting (Millidarcies)	Sample 2 permeability after weathering (Millidarcies)	Change in permeability (Millidarcies)
1	214.9	448.5	+234.6	74.5	74.3	+0.8
2	91.3	235.1	+144.8	5000	908	-4092
3	257.5	216.7	-40.8	801	330.7	-470.3
4	254.2	194.1	-60.1	330	389	+59
5	240.3	860	+619.7	305	510.4	+205.4
Average	**211.44**	**390.68**	**+179.24**	**1301.9**	**442.48**	**-859.42**

As discussed by McKinley and Warke (2007), salt crystallization inside pores will result in a localised reduction in permeability, whilst salt crystallisation in fractures will widen fracture networks and result in localised increases in permeability. This is why in table 4.10, for both samples some points increase in permeability whilst others decrease.

This difference in observed permeability between the two samples impact areas after impact and after weathering is thought to be the result of the interplay between matrix compaction, fracturing and NaCl crystallisation behaviours controlled by impact angle. This theorised dynamic is outlined here:

1) Impact- 90° impact with higher shock pressures (Rubin and Swindle, 2011) creates compaction in regions of the impact crater as seen in hardness readings from the impact crater (figure 4.27), and a denser fracture network radiating from the impact crater into the block. Compaction in the impact crater lowers permeability relative to the 45° impact as crushed matrix grains reduce pore space (Okubo, Schultz, 2007). 45° impact causes no compaction as shown in the hardness results (figure 4.27) and a less connected fracture network, as evidenced by UPV results (figure 4.21).

2) Ingress of weathering agents- saline solution permeates the blocks. This happens more quickly in the block impacted at 90°, as evidenced by the mass monitoring results that show a more rapid increase in mass due to uptake of saline solution (figure 4.20).

3) Salt crystallisation- The growth of NaCl crystals inside the denser fracture network of the 90° impact sample expands the fracture network and increases permeability (Celik and Aygun, 2019). NaCl crystals also expand the region of compacted matrix created during 90° impact, which further increases permeability. With a less dense fracture network, and no compacted region to expand, NaCl crystallisation in the 45° impact sample takes place primarily in pore spaces, which reduces the average permeability in the impact crater area.

The hypothesis that angle of impact and resultant fracture network is the cause of the differing permeability results between the two samples is supported by McKinley and Warke (2007). This research reported that depending on the condition of the weathered stone, salt crystals can increase permeability through exploitation of micro-fractures or decrease permeability by filling rock pores with salt crystals. Therefore, the permeability readings from the impact crater and shattered surface mirror the trend of the hardness results in suggesting that the angle of impact controls the damage to the impact area both after shooting and after weathering.

When considering both data sets for the impact area, the sample impacted at 90° experiences an average decrease in hardness of -48 Leeb and an average increase in permeability after weathering of 179 mD, whilst the sample impacted at 45° sees no significant change in hardness (+ 4 Leeb) and a drastic decrease in permeability (-859 mD). This is shown in figure 4.29.

Figure 4.29: *Data on changes in hardness and permeability across the impact areas of both samples. Error bars are not included because the data presented is a single calculation of the difference in the average of hardness and permeability across the impact area before and after weathering. All data on hardness and permeability of individual sampling points across the impact area are included in tables 4.9 and 4.10.*

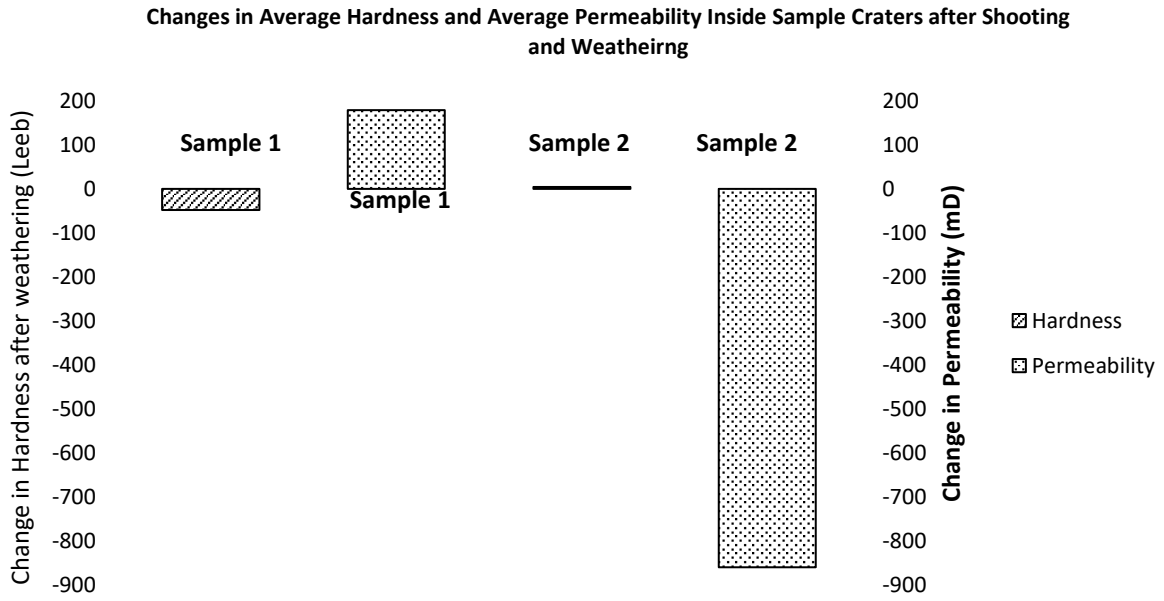

The data presented in figure 4.29 suggests that weathering causes greater mechanical deterioration across the impact area after 90° impact, as the stone is made both weaker and more susceptible to further ingress of weathering agents through increased permeability associated with a denser fracture network. Conversely, sample 2 sees a negligible increase in hardness, and a substantial reduction in permeability. This suggests that the impact area is most at risk of weathering deterioration after a 90° impact rather than a 45° impact, and this could be an important consideration when seeking to prioritise which areas of ballistic damage to focus conservation efforts on in the field.

However, the small sampling numbers from the impact areas for both permeability and rebound surface hardness survey (n = 5) mean that further experimental work will be required to confirm these findings. The small number of sampling points used across the impact areas was due to the need to find flat points across these uneven surfaces that would give reliable rebound hardness readings. These sampling points were used for permeability readings as well so that the effects of weathering on hardness and permeability could be compared directly across the same areas. The issue of small sampling numbers across the impact areas will be addressed in future experimental designs through the inclusion of a greater number of samples as discussed in section 4.4.5.

4.3.6.2: Permeability results from outside the impact area

To determine the effect of surface fractures outside of the impact area on the permeability of the samples, all of the permeability readings taken from the intact portions of sides 1-6 for both samples were analysed (Figs. 4.9 and 4.11). As figure 4.30 shows, outside of the impact area sample 1 saw a much larger increase in permeability than sample 2 after shooting (sample 1: 383mD, Sample 2: 31mD). Sample 1 also saw a greater reduction in permeability after weathering relative to its permeability after shooting (sample 1: 54 mD, sample 2: 22mD). Note that the data for permeability “after weathering” is the absolute value of permeability and represents a decrease in permeability relative to the permeability values obtained after shooting. This reduction is attributed to NaCl precipitation inside the fracture network, this blocks the fracture network and lowers its permeability. The large error bar presented for sample 1 after shooting is a result of the variation in the data set caused by the high permeability of cells with large fractures and the low permeability of un-fractured cells.

Sample 2 exhibits a much lower permeability after impact than sample 1, which suggests that the 45° impact creates a less connected and less permeable internal fracture network due to lower rarefaction wave pressures inside the block (Melosh, 2013, Leary, Pogacnik, Malin, 2012). This is supported by UPV analysis, which demonstrated that the fracturing caused by impact was less dense after 45° impact (figure 4.21), and the slower ingress of saline solution into sample 2's fracture network (figure 4.20). Because sample 2 sees a much smaller increase in permeability after impact than sample 2, it also sees a smaller reduction in permeability after NaCl crystallisation, as there is a less extensive fracture network for the crystallisation process to saturate and fill.

Figure 4.30: *Permeability changes outside the impact area (including undamaged cells of the impact face) relative to intact permeability average. Error bars represent the standard error of the given data set. Error bars are the standard error of the given data set.*

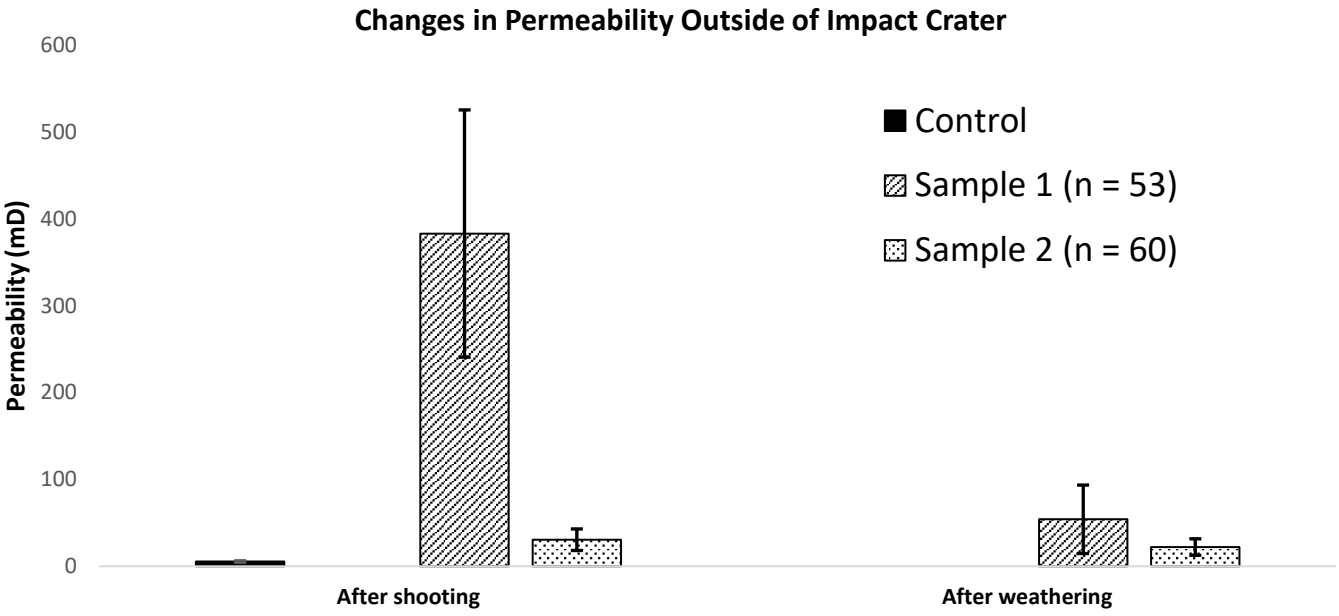

The fact that sample 1 sees such a pronounced reduction in permeability outside of the impact crater supports evidence from the results of mass measurements and UPV, which suggest that 90° impact creates a denser and more permeable internal fracture network that facilitates a higher quantity of NaCl crystal precipitation that in turn clogs stone pores and fractures and reduces permeability.

However, whilst the permeability readings reveal broad trends about the average changes in permeability across the two samples as a whole, more detailed analysis is required to determine whether the reduced sampling regime outside of the impact face yields informative data (figure 4.10).

As was the case in section 2.4.2, the most significant increase in permeability was observed on the impact face of both samples, whilst the the non-impact faces saw a smaller increase in permeability after shooting. This is because the greatest density of visible surface fractures is found on the impact face. Because of the higher increase in permeability on the impact face after shooting, this area also sees a greater reduction in permeability after weathering due to NaCl crystallisation in existing fractures. This data is shown in table 4.11:

Table 4.11: *Data on changes in permeability after shooting and after weathering on different faces of the samples outside of the impact areas.*

	Side 1 average permeability after shooting (mD), Sample 1: n = 30, Sample 2: n = 37	Side 1 average permeability after weathering (mD), Sample 1: n = 30, Sample 2: n = 37	Change in permeability on impact face after weathering (mD)	Average permeability of sides 2-6 sampling points after shooting (mD), Both samples: n = 23	Average permeability of sides 2-6 sampling points after weathering (mD), Both samples: n = 23	Change in permeability of non-impact face sampling points after weathering (mD)
Sample 1	509.8	19.9	-489.9	218.3	98.6	-119.7
Sample 2	34.8	15.6	-18.2	7.1	10.8	+4.7

Whilst the data presented in figure 4.30 and table 4.11 appears to show large differences in the changes in permeability due to weathering between the two samples, this does not demonstrate the effect of the variability of the data set on the average values of these data sets. The permeability data is likely to be highly variable, as cells containing visible fractures will have much higher changes in permeability than cells not containing fractures (Gilbert *et al,* 2019). To determine whether the difference in average values was a consistent trend, or a

result of variability skewing the average, the data for changes in permeability was plotted using the values for the change in permeability of individual cells after weathering.

Cells were assigned an individual alpha-numeric code according to the numbering system outlined in section 2.4.1, such that the bottom left cell was A1 and the top right cell was G7. Side 1 was designated S1, and side 2 was designated S2 etc., such that the top right cell on side 2 would be designated S2G7. The results of plotting the change in permeability for individual cells of the impact face (side 1) are shown in figure 4.31:

Figure 4.31: *Changes in permeability for individual cells on the samples' impact faces after weathering.*

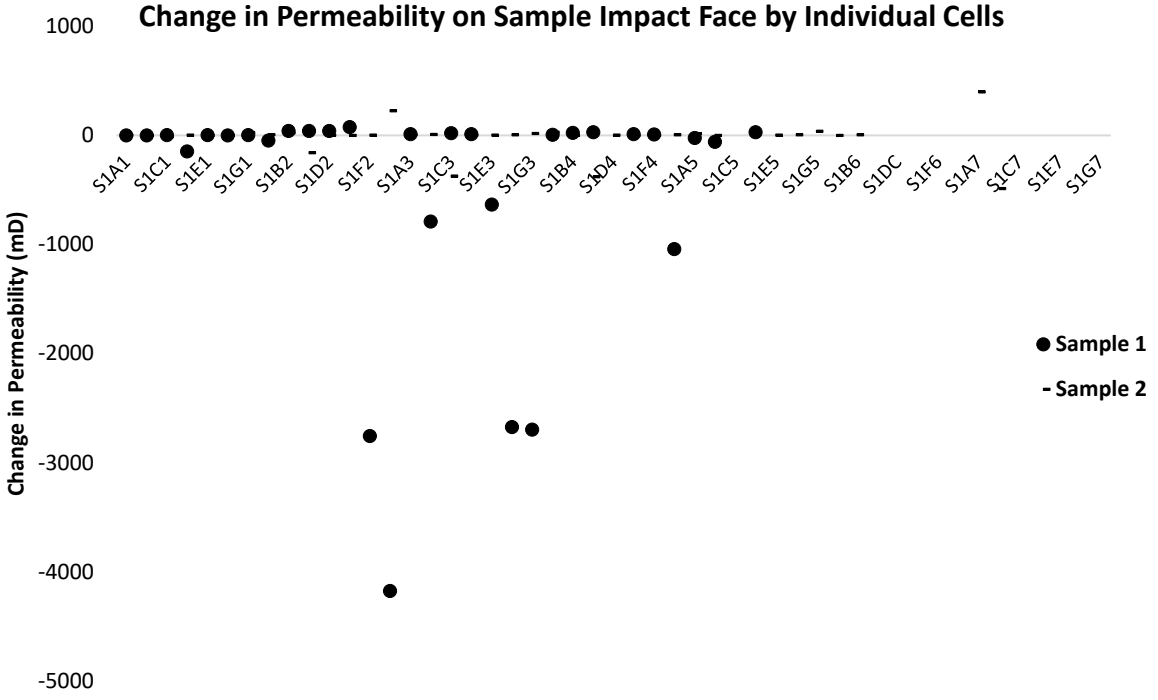

As figure 4.31 shows, a number of cells on sample 1's impact face see a reduction in permeability of over 1000 mD, whereas the greatest reduction for a cell on the impact face of sample 2 is -489mD. This suggests there is a trend of localised reductions in permeability on sample 1 that are substantially greater than for sample 2. This is because 90° impact causes a denser visible surface fracture network associated with the impact face than 45° impact, and this leads to a greater frequency of localised areas of increased permeability. During weathering, this denser fracture network becomes saturated with NaCl crystals, which results

in a greater average reduction in permeability after weathering for sample 1 than sample 2, as is recorded in table 4.11.

When the data from the 5-point sampling on non-impact faces is plotted in a similar way, it becomes apparent that individual cells have skewed the averages of the data set for sample 1 outside of the impact face:

Figure 4.32: *Changes in permeability of individual sampling points on non-impact faces.*

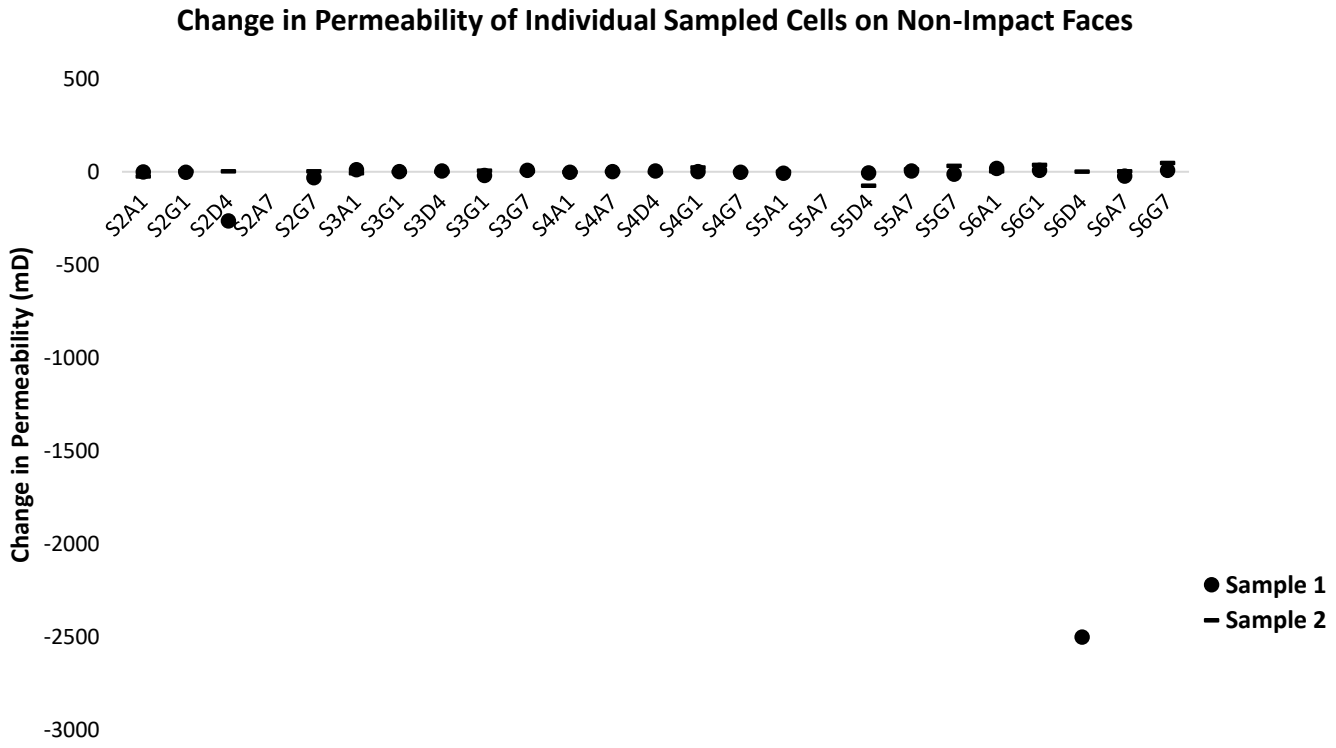

Figure 4.32 shows that only two cells on either of the samples sees a change in permeability in excess of 100mD (cell 1 S2D4 and cell S6D4). These two cells exhibit visible surface fracture, and their increased permeability skews the average permeability of the non-impact face sampling points of sample 1, resulting in a much larger average change in permeability than sample 2 on non-impact faces. (-119.7mD for sample 1, +4.7mD for sample 2). If these two cells were disregarded from sample 1, the average change in permeability would be much smaller (-1.3mD). This demonstrates that a small number of cells with visible surface

fracture can skew a data set of permeability readings and further supports the conclusion from section 2.5.2 that visible surface fractures are the principal cause of changes in permeability.

Given a larger number of samples shot under replicate conditions, the skewing effect of single cells containing visible fracturing would be reduced due to a larger number of data points. Therefore, further experimental work seeking to refine permeability survey will continue to seek a permeability regime with a reduced number of data points on non-impact sides, but with replicate samples to prevent the skewing effects discussed here. Finally, given that visible fractures are the primary cause of large increases in permeability, and surface fractures propagate from the impact crater towards non-impact faces (see figure 4.19) future permeability sampling regimes would also be designed to evaluate how surface fractures initiated at the impact crater propagate to non-impact faces of the samples.

4.4: Discussion of significance of results

4.4.1: Effects of impact angle outside impact craters prior to weathering

As stipulated by Research Objective II: "*To compare and isolate the effects of changing angle of impact on the damage caused by ballistic impact before weathering"*, understanding how ballistic variables such as angle of impact control damage levels immediately after impact is integral to understanding which factors pose the greatest risk of subsequent weathering deterioration.

One of the clearest indicators of the differing damage profiles caused by the impact angle is the mass/volume loss revealed by the mass monitory and 3D modelling of the samples. As shown in table 4.3, 90° impact results in a mass/volume loss of almost 6%, whilst 45° impact causes 2% of the sample to be lost. This is due to lower kinetic energies delivered to the sample at a more oblique angle of impact. As previously discussed by Gault (1973), for a projectile of given mass and kinetic energy impacting a rock target of given density, the mass of ejected material is reduced as the angle of impact decreases. This is an important finding as it suggests that aesthetic deterioration due to removal of stone material from the surface of an impacted stone monument is exacerbated by 90° impact. The finding that 90° impact causes the ejection and loss of more stone material is an important finding with respect to heritage conservation, because it suggests that a 90° impact will cause more severe scarring

of heritage stone, with the potential for larger impact craters and loss of aesthetic value through the greater destruction of decorative features such as carvings.

90° impact is also responsible for an increased fracture network within the impacted stone. Data from UPV measurements showed that P wave velocities were reduced by 30% (-170ms^{-1} in the directly impacted sample, and 12% (-67ms^{-1}) in the sample impacted at 45° (section 4.4.4, figure 4.17). This indicates that 90° impact and associated high tensile wave pressures result in the creation of denser fracture networks in the interior of the impacted samples. This is supported by the findings of Wang *et al* (2019) who demonstrated that fracturing under impact loading is more extensive after a direct impact than angled impact.

The denser fracture network created by a 90° impact is evidenced by the far greater increase in permeability for the sample impacted at 90° (+378mD) above the permeabilty of the 45° impact sample (+50mD) (see section 4.4.6.2, figure 4.31). This is in keeping with work by Collins, who reported that impact into rock raises permeability and alters fluid flow patterns (2014). The creation of a denser fracture network by 90° impact is likely to be an important factor in determining the deterioration of stone due to weathering after ballistic impact. This is because a denser and more connected internal fracture network will make the stone more permeable and thus allow the ingress and mobility of moisture and salt (Kubeyev, 2013). This is an important finding for field-based applications, as identifying which impacted regions of a damaged monument are most exposed to weathering processes will be critical in assisting conservation proffessionals to develop conservation strategies.

Despite 90° impact causing greater volume loss and a denser fracture network, sample 2 exhibits signs of greater damage when surface rebound hardness is considered. The results presented in figure 4.23 demonstrate that sample 2 underwent a 7.1% (-27 Leeb) reduction in hardness after shooting compared with a 4.3% (-17 Leeb) reduction for sample 1.
As discussed in section 4.2.5.1, the trajectory of a 45° impacted closer to sides 2 and 5 and across the sample's corner. This is thought to cause tensile waves and edge waves to create near-surface spallation micro-fractures across a wider area of the sample's surface than for 90° impact, reducing the overall hardness (Siegfried *et al*, 1977, Nakazawa *et al*, 2002, Nobili, Radi, Lanzoni, 2017) . It is also possible that sample 2 has a weaker wider surface because less of the stone matrix was ejected from the sample than after 90°. This may mean that the stone matrix for sample 2 is weakened through fracturing, but is not imparted with

sufficient kinetic energy to be ejected from the sample, as is the case for sample 1. This could cause more weakend material to remain on sample 2, resulting in a lower overall hardness. Further analysis involving a greater number of impacts at different angles will be required to determine whether angle impact has a verifiable weakening effect on the wider sample surface. If this could be confirmed, it would be an important finding as it would suggest that whilst 90° impact causes the most damage through ejection of stone material and crater formation, an angled impact causes less visible deterioration over a wider area that may be susceptible to deterioration over time. This might inform conservation stratgies in the field by allowing the identification of large areas of stone weakened by an angled impact that are likely to face future deterioration.

4.4.2: Effects of impact angle inside impact area prior to weathering

Surface hardness results from the impact areas suggest that 90° impact results in compaction of the stone matrix. This is demonstrated in figure 4.27, which shows that in the 90° sample there is a relative hardening of points closer to the impact centre due to crushing caused by the projectile impact. This is in agreement with the findings of previous works which suggest the compaction of the stone matrix at the point of 90° impact (Mol *et al*, 2017, Mol, Gomez Heras, 2018 Gilbert *et al*, 2019). Conversley, 45° impact does not appear to result in any notable matrix compaction. This means that after impact the sample that was impacted at 45° sees a larger overall reduction in hardness than sample 1 (90°) across the impact crater and shattered surface, as observed in figure 4.26. This suggests that in the immediate aftermath of a ballistic impact, a crater arising from 45° impact may be weaker and more at risk of short-term mechanical deterioration due to disaggregation, as the relationship between surface hardness and mechanical weakening and deterioration has been demonstrated in previous works, such as Coombes *et al* (2013).

The process of matrix compaction by 90° impact also has implications for the permeability across the impact area. Okubo and Schultz (2007) demonstrated that 90° impact into rock results in a reduction in pore space due to the compaction and crusing of the stone matrix which will reduce permeability. As a result of this process, whilst both impact areas see an increase in permeability, there is a lower increase in permeability across the impact area of the 90° impact than sample than the 45° (figure 4.27). This differing change in permeability between the two samples is notable, because alterations to permeability inside the impact

crater will result in the alteration of moisture flow regimes, which can cause the accumulation of moisture and increase weathering, as reported by Mol *et al*, (2017). This would suggest that the impact crater of stone undergoing 90° impact is likely to undergo greater weathering driven deterioration than after an angled impact, as is demonstrated in section 4.4.4.

4.4.3: Effects of impact angle on weathering behaviour outside the impact area

The effect of the increased permeability of sample 1 outside of the impact area on the weathering processes was a much faster uptake of saline solution experienced by sample 1 when compared with sample 2 (section 4.4.3, figure 4.20). This highlights the fact that 90° impact creates a denser fracture network that facilitates higher moisture mobility inside the impacted sample. This phenomenon has also been observed in work by Nia and Jessen (2015), who modelled capilliary rise in porous media and recorded that ingress of liquids through capilliay action was faster in fractured systems, and exploited fractures preferentially. This is a valuable insight in the context of conflict damage to heritage because it demonstrates that stone subjected to 90° is at risk of faster ingress of weathering agents, and thus a more rapid deterioration due to weathering.

Despite the faster uptake of saline solution into sample 1 than sample 2, the reduction in surface hardness due to weathering outside of the impact crater is more pronounced in sample 2 (section 4.4.5.1, figure 4.23.). This is thought to be the result of a wider area of spallation micro-fracturing across sample 2 caused by the wider propagation of rarefaction waves and edge waves discussed in section 4.4.5.1. The creation of near-surface spallation micro-fractures by ballistic impact was demonstrated by Siegfried *et al* (1977). Micro-fractures are exploited by the saline solution and result in NaCl precipitation during the weathering regime (Nia, Jessen, 2015, Warke, Smith, Lehane, 2011). This would explain why sample 2 experiences a greater reduction in hardness after both impact and weathering. As with the damage caused immediately after impact, these findings suggest that 45° impact results in greater weathering damage and weakening to the stone surface outside of the impact area than is the case for 90° impact.

Whilst sample 2 likely has a wider area of near-surface micro-fracturing, sample 1 undoubtedly has a denser, more permeable and more connected internal fracture network.

This is supported by the greater increase in surface area caused by efflorescence on sample 1 than sample 2 after weathering. This is due to the rate of saline solution intake through fractures being higher than the rate of evaporation, which causes the development of efflorescence, as discussed by Aly e*t al,* (2015). This is reflected in the spatial analysis undertaken using the 3D models in section 4.4.2.3 and figure 4.17. The tendency of salt efflorescence to be exacerbated by fracture networks is also demonstrated in figure 4.11, which clearly demonstrates a fracture facilitating the ingress of the saline solution.

Further evidence of increased salt precipitation throughout sample 1's internal fracture network comes from the significant increases in UPV and reductions permeability for the block after weathering (figures 4.22, 4.30). This is caused by NaCl crystals filling the space created by the fracture networks and thus decreasing permeability and increasing the UPV velocity in these regions, (Noiriel *et al,* 2010, Aly, *et al,* 2016). The realisation that 90° impact results in a denser internal fracture network with greater moisture mobility is notable, because it may result in much greater levels of stone deterioration when the saline solution contains salts known to be more destructive to stone heritage, such as sodium sulphate (Menendez, 2018).

4.4.4: Effects of impact angle on weathering behaviour inside the impact area

After weathering, the impact area of sample 1 sees a greater reduction in hardness than sample 2 (section 4.4.5.2, figure 4.26). This is because the impact area in sample 1 is connected to a denser internal fracture network that results from its 90°, as evidenced by the UPV results previously discussed. This facilitates greater moisture mobility and allows the saline solution to access the impact crater of sample 1 more easily, causing greater levels of haloclasty than in sample 2.

Furthermore, the compacted region of sample 1's impact area (figure 4.27) will reduce moisture through-flow and cause the accumulation of saline water in the compacted region, which will further increase the deterioration due to weathering. This is in keeping with the findings of Mol *et al* (2017). This compacted region is not present in the impact area of sample 2 after 45° impact, and therefore it does not undergo a notable reduction in hardness inside the impact area due to weathering weakening.

The denser fracture network connected to sample 1's impact area quickly becomes saturated with NaCl crystals after weathering that expand the fracture network further and reverse the compaction of the impacted area (McKinely, Warke, 2007). This results in an overall increase in permeability for the 90° impact. Conversely, sample 2 has a smaller fracture network connected to the impact area after 45° that is not extended by NaCl crystallisation. The result is that NaCl crystallisation in the impact area of sample 2 acts to seal pores and fractures and results in a large overall reduction in permeability (figure 4.31).

Therefore, weathering in the impact region of the two samples leads to decreasing hardness and increasing permeability after a 90° impact, whilst weathering of the impact area after 45° has no notable effect on hardness and reduces permeability. This is evidence that weathering leads to a much more severe deterioration of the impact area after 90° impact. This could be a valuable finding when seeking to minimise the deterioration of weathering processes to a heritage monument after conflict damage. As with all of the findings in this preliminary pilot study, the future experimental work of this project will investigate these processes in a greater number of samples in order to confirm or refute these findings.

4.4.5: Methodological refinements

This pilot study resulted in the validation of a number of the techniques deployed, as well as the identification of a number of areas where the methodology could be improved. Therefore, the work presented in this chapter will be used to inform experimental design in future chapters. The principal findings that will be carried forward are outlined below:

- Cotswold Hill Cream limestone is an approximate geotechnical match for limestones used in built heritage in arid environments such as Mokattam limestone, and can be sourced in the U.K. Therefore, samples of this limestone will be used in the future experiments of this research when investigating the ballistic damage and weathering deterioration of limestones in arid environments.

- Methods used at COTEC to control projectile velocity and angle of impact were effective in producing the desired conditions, and these will be used in the future experiments of this project. Properly sized containment blocks will be used when shooting samples in future experiments.

- The weathering regime was proven effective at simulating haloclasty weathering and weakening by ingress of saline groundwater under diurnal temperature changes, and demonstrated that ballistic impact creates fracture networks in stone that cause capillary rise of saline solution. This is direct evidence of the interplay between ballistic impact and weathering factors, and demonstrates that this study has been useful in fulfilling Research Objective III: "*... investigate the interaction between ballistic impact and subsequent weathering processes*".

- 3D models of the samples created using photogrammetry appear to be effective at detecting changes in surface area and volume due to ballistic impact and weathering, although the changes in volume and surface area are very small (0.1%).

- Photogrammetry is also an effective method for visually recording the results of weathering regimes, such as the accumulation of salt efflorescence, and the technique will be used to record and analyse damage in future experiments. This compliments the techniques described in section 2.3 in developing techniques for assessing exterior damage to stone subjected to ballistic impact. This helps to fulfil Research Objective I: "*To develop non-destructive methods to assess exterior and interior damage to limestone and sandstone arising from military projectile damage (7.62 x 39mm and 5.56 x 45mm)".*

- Angle of ballistic impact is clearly an important factor in determining the extent of ballistic damage and subsequent weathering deterioration. Therefore, this variable will be included in future experiments exploring damage to impacted stone. This is in partial fulfilment of Research Objective II: "*compare and isolate the effects of changing calibre, angle of impact and target stone type on the damage caused by ballistic impact before weathering*".

- UPV analysis is able to detect the increased fracture network inside the samples due to ballistic impact. This is in partial fulfilment of Research Objective I: "*To develop field appropriate non-destructive methods to assess interior ballistic damage"*. UPV analysis will be used in future experimental works to assess interior damage to the impacted samples. However, the creation of the impact crater reduces the number of

orientations in which UPV readings can be taken as discussed in section 4.4.4. This will mean that in future experiments only two UPV measurements will be taken for each sample after shooting to ensure a reliable and consistent methodology.

- The reduced permeability sampling regime used outside of the impact face was prone to skewing of the data set. Therefore, a permeability sampling regime for non-impact faces that balances the need for an approach that is rapid enough for field use whilst still providing quality and representative data through a larger number of replicate samples would be utilised in future experimental work. This regime would also be designed to further explore how visible surface fractures propagate from the impact crater to non-impact surfaces of the sample.

- Many of the conclusions reached in this study, such as the suggestion that angled impact leads to weakening of a wider surface area, are limited by the small number of samples and will require further investigation to confirm. Therefore, future experimental runs in this project will include a greater number of samples with differing impact angles to ensure conclusions can be stated with confidence. This will also overcome the issue of a small number of sampling points in the impact area caused by the uneven surface being difficult to obtain readings from, as more samples will yield more data from a greater number of impact areas.

4.5: Conclusions

The work undertaken in this pilot study has yielded a number of important experimental findings and aided in refining the methodological approach of this research.

Firstly, this pilot study has been valuable in determining a number of viable methods for future experimental work, including the stone type used, the weathering regime design, and the analytical methods deployed such as UPV analysis and 3D photogrammetric modelling. This work has also allowed for the refinement and improvement of a number of methodological aspects, such as the frequency of permeability sampling used, and the use of a larger number of replicate samples

The pilot study demonstrated that the angle of ballistic impact plays an important role in determining damage to stone both after impact and after weathering. This is because 90° impact results in a larger impact crater and the loss of more stone material due to ejection of debris. 90° impact also creates a denser and more connected internal fracture network that facilitates greater weathering agent mobility, weakening the impact crater and causing higher levels of salt efflorescence. Conversely, 45° impact weakens the wider surface of the stone away from the impact crater and causes greater weathering weakening in these areas. Furthermore, 45° impact results in less compaction of the stone matrix at the point of impact and this causes greater reduction in hardness inside the impact crater immediately after impact.

The differing responses of the two samples to the weathering regimes are significant because they suggest that there is no "worst case scenario" in terms of weathering of stone damaged by ballistic impact. 90° impact results in greater material loss, weathering deterioration and hardness loss inside the impact crater, whilst an 45° impact causes greater weathering and reduces hardness across the wider target surface. If confirmed in the future experiments of this project, these findings may prove invaluable in assessing damage to heritage monuments in conflict regions and devising appropriate conservation strategies.

N.B: An abridged version of this thesis chapter was published in the peer-reviewed proceedings of the 14th international congress on stone deterioration*:*

Gilbert, O., Mol, L., Campbell, O., and Blenkinsop, T. (2020). The influence of angle of ballistic impact on stone weathering. In *Proceedings of the 14th International Congress on the Deterioration and Conservation of Stone, Göttingen, Germany* (pp. 309-315).

Chapter 5

Effects of ballistic variables on damage to target stone

Chapter 5 Overview

Chapter 5 aims and hypotheses

To assess the effects of changing the following variables on the extent of immediate damage (prior to weathering) caused by ballistic impact into stone:

- Lithology
- Ammunition
- Angle of Impact

It was hypothesised that impact by the steel-cored 5.56 x 45mm ammunition at 90° would transfer the most kinetic energy to the target stone, resulting in higher pressure stress waves and thus the most damage. It was also hypothesised that the sandstone used in these experiments would be less damaged than the limestone due to its higher wave attenuation properties.

Chapter 5 methods

To assess the effects of lithology on damage sustained by an impacted sample, an initial study using three limestone and three sandstone samples shot with 7.62 x 39mm ammunition at 90° and a constant velocity was used. Sample damage was assessed using surface hardness survey, permeability survey and photogrammetric assessment of material loss and surface area change. The massive amounts of damage sustained by limestone samples in this initial study then necessitated reducing the impact velocity for the remaining experiments that assessed the effect of ammunition type and impact angle in order to ensure that samples would be usable for the future weathering experiments of this thesis (see section 5.2).

In the main experimental run, the effect of impact angle and ammunition type on damage sustained was investigated using measurements of rebound hardness, permeability and ultrasonic velocity. 24 stone samples were used (12 limestone, 12 sandstone), generating three repeat samples for each impact condition (lithology, ammunition and impact angle). Photogrammetric models were also created for each sample before and after shooting. Two common military ammunition types were used (7.62 x 39mm and 5.56 x 45mm). Impacts were conducted at two angles: 90 ◦ and 45◦.

Chapter 5 principal findings

Findings suggest that the single most important variable is the target lithology, with limestone samples of lower initial hardness, strength and density being substantially more damaged than the sandstone samples. Results also demonstrate that 5.56 x 45 ammunition is more damaging than 7.62 x 39mm ammunition due to its construction featuring a steel penetrator. Finally, results show that impacts at 90◦ are usually (but not invariably) more damaging than impacts at 45◦. Analysis of these variables and their effects on damage sustained allowed the construction of a simple risk matrix which will allow rapid field-based assessment of the risk posed to stone built heritage damaged by ballistic impact.

5.1: Study into influence of target lithology

5.1.1: Introduction

As discussed in section 1.4, mechanical properties of a given lithology such as the compressive strength and tensile strength are controlling factors in determining fracturing and ejection of material from a stone surface subjected to ballistic impact. Accordingly, the fracture density of an impacted rock sample is related to the rate at which the rock impedes and attenuates the stress waves caused by impact. Zhang, Hou and Aladejare (2020) and Xu *et al.* (2016) demonstrated that rock samples with higher wave impedance had higher values for mechanical properties such as density and compressive strength, and a lower porosity. A higher wave impedance reduces the amount of fracturing and damage sustained when a given lithology is subjected to impact. This is because stress waves propagating through the rock attenuate more quickly and thus cause less damage (*ibid,* see section 1.4). This raises the possibility that field measurements of mechanical properties, or reference data sets, could be used to identify stone-built heritage most at risk of serious fracture damage due to ballistic impact. It should be noted that such data sets would have to consider the geotechnical properties of the heritage stone after weathering in-situ, rather than the fresh stone after quarrying, as long-term weathering processes will alter properties such as the compressive strength of the rock.

To assess this, three samples of limestone and three samples of sandstone with differing mechanical properties were shot with 7.62 x 39mm ammunition at a constant range and velocity. Measurements of mechanical properties and photogrammetric analysis were used to determine the relative damage caused to each of the sample lithologies. This would allow a direct comparison of the effects of target lithology on the damage sustained.

5.1.2: Methods

5.1.2.1: Sample Generation

As outlined in section 4.2.1 the selection of lithologies for this project was governed both by the need to find stone types that are broadly analogous in geotechnical properties with those used in heritage sites in arid MENA regions, whilst also sourcing them within budgetary constraints. The limestone selected was Cotswold Hill Cream Limestone, as an approximate match for Mokattam limestone used in heritage buildings in Egypt (see chapter 4). The sandstone used was Stoneraise Red Sandstone, as this broadly matched many of the geotechnical properties of the middle part of the Umm Ishrin sandstone formation. As reported by Delmonaco, *et al* (2013), as well as Migon and Goudie (2014), many of the heritage structures at the Petra World Heritage Site in Jordan are hewn from the Middle Umm Ishrin formation, and the stone is also widespread throughout the Wadi Rum World Heritage Site. Therefore, identifying a broad geotechnical match for the Umm Ishrin Sanstone will ensure that results obtained from the sandstone samples are broadly analogous to what might be expected for ballistic impacts into heritage stones found in arid areas of the MENA region.

To summarise how these matches were identified, the geotechnical properties of the sample stones and the heritage stones they are matched to are given in tables 5.1 and 5.2. The properties of the two stone types are compared in table 5.3 and microscopic images of the lithologies' matrix are shown in figure 5.1.

Table 5.1.: *Geotechnical Properties of Cotswold Hill Cream Limestone and Mokattam heritage limestone.*

Geotechnical Properties	Cotswold Hill Cream Limestone (Source: Building Research Establishment 1999)	Mokattam formation Middle Eocene Limestone	Source of Mokattam geotechnical data
Uniaxial Compressive Strength (MPa)	36.6	40	El Nahhas *et al*, 1990
Porosity (%)	20.6	18.6-26.8, average of 23.2	Fitzner *et al*, 2002
Density ($Kgcm^{-3}$)	2158	2100	Ahmed *et al*, 2006
Water absorption (wt %)	8.5	6.12-10.75	Park and Shin, 2009

Table 5.2: *Geotechnical Properties of Stoneraise Red Sandstone and Umm Ishrin heritage sandstone.*

Geotechnical Properties	Stoneraise Red Sandstone (Source: Building Research Establishment 1999b)	Middle Umm Ishrin Sandstone Average	Source of Umm Ishrin Geotechnical Property Information
Uniaxial Compressive Strength (MPa)	75-84	105	Delmonaco *et al*, 2014
Porosity (%)	11	13.5	Heinrichs, Fitzner, 2000
Density (Kgm^{-3})	2272	2300	Heinrichs, Fitzner, 2000

Table 5.3: *Comparison of the geotechnical properties of Cotswold Hill Cream Limestone and Stoneraise Red Sandstone*

Geotechnical Properties (Sources: Building Research Establishment 1999a and b, Campbell *et al*, 2022)	Stoneraise Red Sandstone	Cotswold Hill Cream Limestone
Compressive Strength	75-84	36.6
Porosity (%)	11	20.6
Density (Kgm^{-3})	2272	2158
Water absorption (wt %)	2.32	5.4
Tensile strength (MPa)	5	2.2

Figure 5.1: *Cross polarised photomicrograph of Cotswold Hill Cream Limestone (A). Cross polarised photomicrograph of Stoneraise Red Sandstone (B). Campbell et al, 2022.*

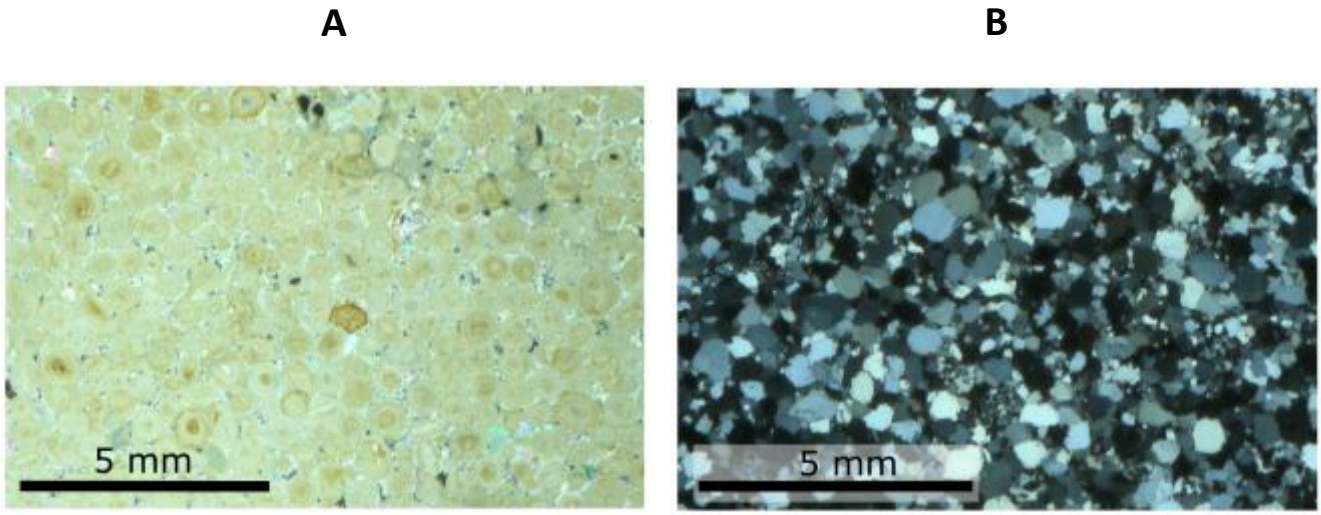

Three 15cm x 15cm x15cm samples of each of these lithologies were used in this study. Each of the samples was given a unique code based on the lithology and sample number. The Stoneraise Red sandstone samples were designated "SRS_X" and the Cotswold Hill Cream Limestone were designated "CHCL_X" ("X" being the sample number). Samples were shot with lead cored South African 7.62 x 39mm ammunition at an average velocity of $537.3ms^{-1}$ (measured with Weibel Doppler radar) and an impact angle of 90°. As outlined in section 4.2.2 these are plausible conditions for an impact during combat conditions.

As discussed in sections 4.2.2 and 4.4.5, the methodology for this set of experiments was refined to more fully confine the target samples during shooting to approximate the containment they would experience when sitting in a dry-stone wall as part of a heritage structure, and therefore a more accurate reflection of reality. Such a confining arrangement of blocks was likely to result in a different pattern of fracturing and matrix ejection than was exhibited by the samples in chapter 4, due to a different configuration of free surfaces with different wave impedances resulting in different rarefaction wave pressures than seen in chapter 4 (French, 1998, see section 1.4). To generate confinement on all sides of the target, concrete blocks (density = 2300kgm^{-3}, dimensions = 15 x 15 x 15 cm) were placed above, below and behind, with large 60 x 60 x 60 cm placed on either side for lateral confinement:

Figure 5.2: *The containment arrangement for the samples and range set up.*

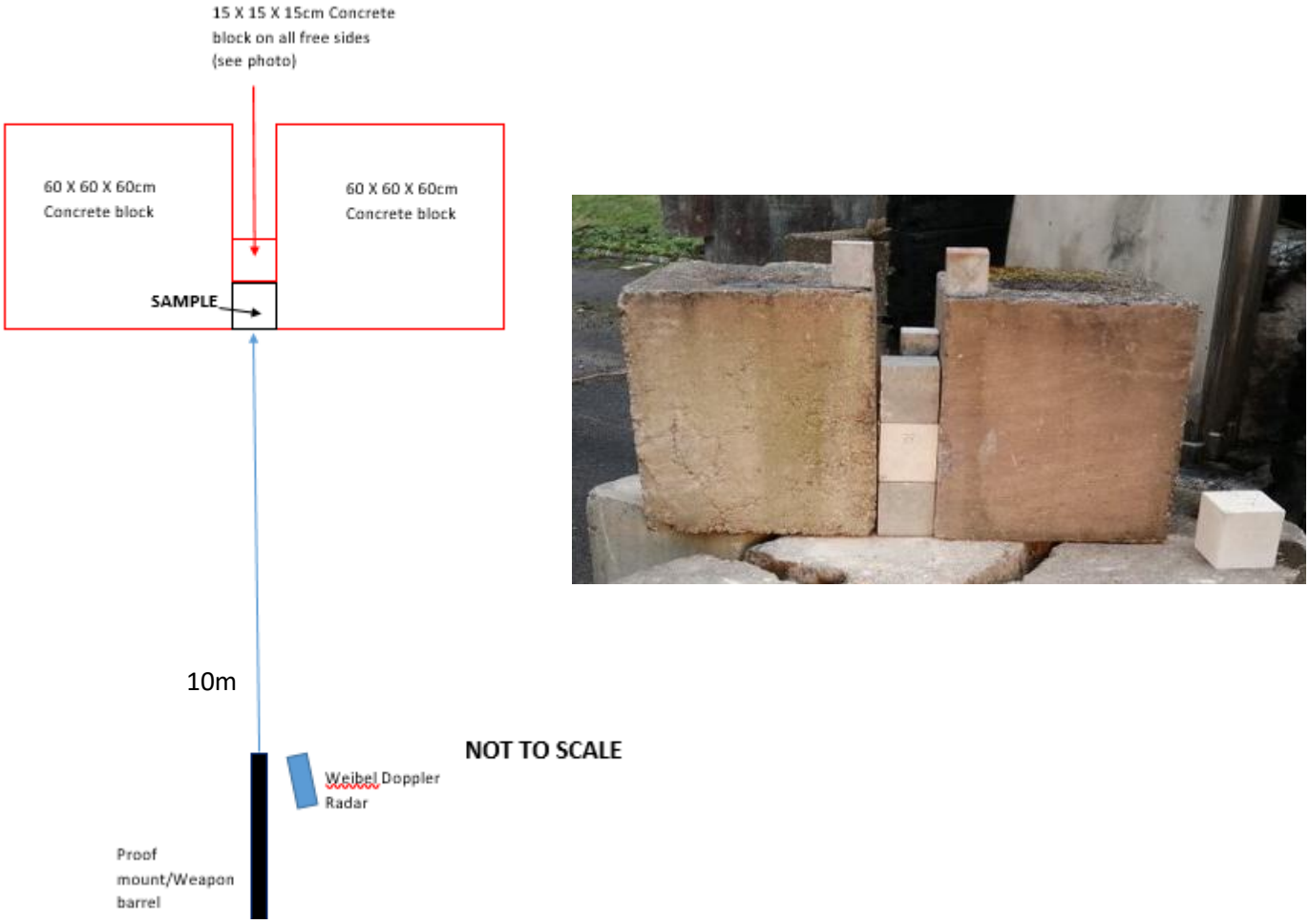

5.1.2.2: Data collection

Surface hardness data collection

As outlined in section 4.2.7, prior to shooting, a 7 x 7 sample grid was laid over each of the 6 faces of each of the samples with three readings from each cell giving 882 readings per sample. Sample surfaces were numbered 1-6 in accordance with the numbering scheme shown in figure 3.1. After shooting, only data on the impact faces was collected because sampling non-impact faces of the limestone samples was likely to cause artificial damage to the samples because this would require turning the heavily damaged impact face down on to the sampling bench or balancing the sample on a face with a reduced area whilst measurements were taken, which may cause the sample to topple over under the pressure of the instruments, again causing artificial damage. For sampling, evenly spaced sampling points were marked across the impact faces of the limestone samples that were then sampled for rebound surface hardness using an Proceq Equotip 550. Impact faces of the sandstone samples were sampled using the same 7 x 7 grid seen in section 4.2.7.

Figure 5.3: *Sampling points on heavily damaged limestone impact faces.*

Permeability data collection

As outlined in section 4.2.8 a New England Research Tinyperm 3 Permeameter was used to obtain control permeability readings from five intact samples of both lithologies (1470 control readings for each lithology). After shooting, permeability readings were taken at the same sampling points used for Equotip data collection outlined above.

Photogrammetry Data Collection and Mass Monitoring

Following the methods laid out in section 4.2.5 a 3D photogrammetric model was created for each of the six samples before and after shooting, and the volume and surface area of the models calculated in Meshlab. This was coupled with measurements of the samples mass before and after shooting using an Adams Equipment 16kg scales to assess changes to mass, volume and surface area caused by ballistic impact.

UPV Data collection

Although control UPV data was collected for all of the samples in this study, the ballistic impact caused sufficient destruction to the limestone samples to remove the UPV sampling points and change the volume of the samples to such an extent as to make comparative UPV measurements after shooting impossible. Therefore, UPV analysis of shot samples is explored more fully in section 5.2, once measures had been taken to mitigate the destruction of the limestone samples.

5.1.3: Results and interpretation

5.1.3.1: Visual analysis of sample damage

An initial visual inspection revealed that the limestone samples had suffered substantially more damage than the sandstone samples, as evidenced by the largest surviving intact portion of each sample, these are depicted in figure 5.4:

Figure 5.4: *Un-textured 3D models of each of the shot samples. All samples are in the same orientation as when they were shot.*

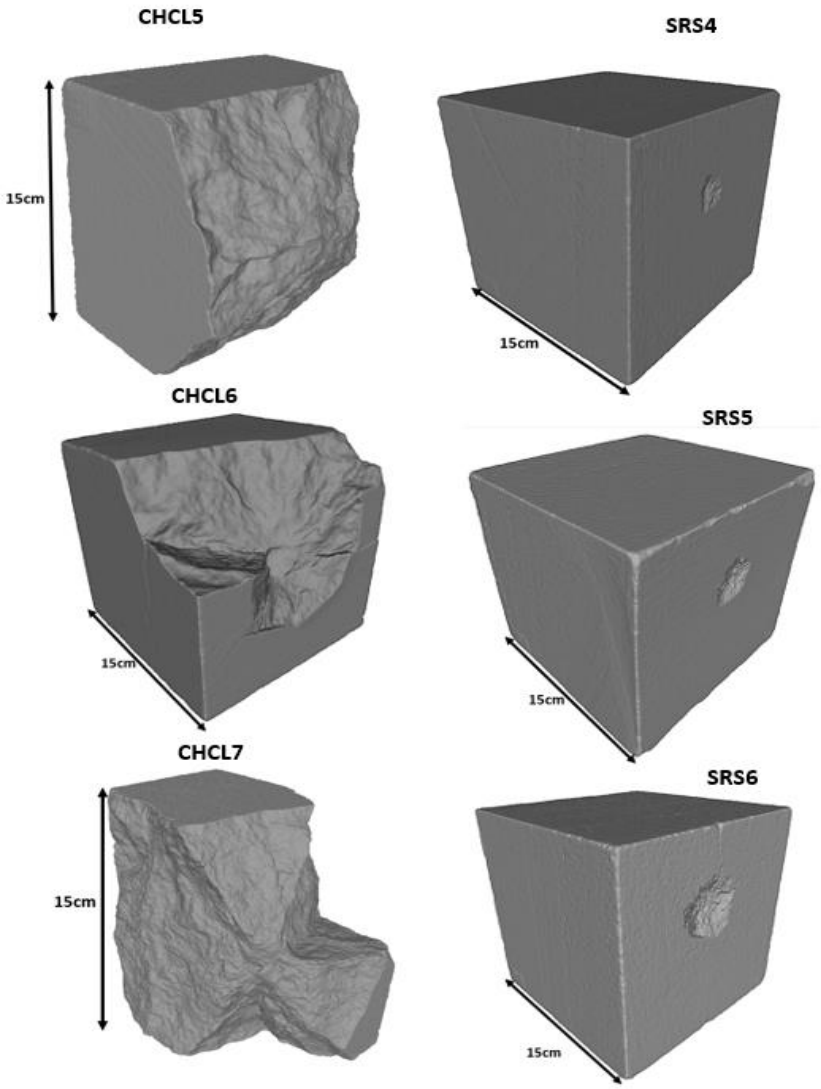

As figure 5.4 demonstrates, all limestone samples exhibit large scale fragmentation of the block and a large proportion of mass loss. Conversely, relatively little mass was lost from the sandstone, resulting in minimal impact craters on the target face of each sandstone sample. The next step was to quantify and compare the changes to sample mass and volume.

5.1.3.2: Changes to Sample Volume and Surface Area

Samples were weighed to quantify the loss of mass/volume from fragmentation and material ejection from the impact crater. In the cases where the block had fragmented into multiple pieces, the largest remaining piece was used as the value for "remaining mass". The results are detailed in figure 5.5:

Figure 5.5: *A comparison of sample volume before and after shooting. As discussed in section 3.3.2.1, the error on photogrammetry calculations will be 0.3% of the calculated area value. Therefore, error bars are not visible in this chart.*

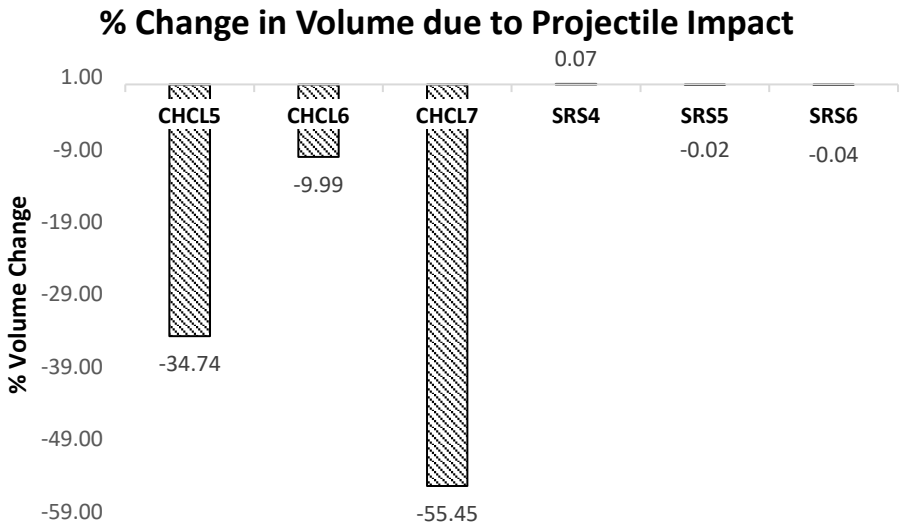

As figure 5.5 demonstrates, the limestone (CHCL) samples lose a much greater proportion of their intact mass than the sandstone (SRS) samples, with the limestone samples losing 10-56% of their original volume, whereas the sandstone samples witness negligible changes in volume, all well below 1% (the small increase of + 0.07% in volume for sample SRS 04 is an artefact due to the volume loss from that sample being negligible, and therefore undetectable

using the photogrammetry models with a 0.3% error as outlined in section 4.4.2.1). This suggests that the limestone, which has lower compressive strength, lower density and higher porosity than the sandstone, suffers much more substantial damage than the sandstone. One possible explanation for this is that the wave impedance value (which is controlled by density, compressive strength and porosity, see section 1.4) of the limestone is much lower than for the sandstone, which allows stress waves from the projectile impact to propagate with higher energies to a deeper depth through the limestone, as Cheng *et al* (2019) showed that wave energy dissipates in an exponential function with distance from the impact. This means that rarefaction waves reach the free surfaces of the limestone with more energy and thus cause greater spallation fracture and ejection of material (section 1.4).

In keeping with the results from the volume loss analysis, data from the surface area of the impact crater and damaged regions of the samples suggests that the limestone samples are more adversely affected than the sandstone samples (figures 5.6, 5.7). This is demonstrated by the fact that the damaged region on the limestone samples ranges from 185cm² to 370cm², whilst the values for the sandstone samples are much lower (4cm²-16cm²). This larger region of weakening and deterioration can be related to the differing mechanical properties of the sample types as previously discussed, as the lower wave impedance of the limestone allows higher amplitude waves to cause greater spallation and ejection of material and thus create a damaged region of greater area (Melosh, Ivanov, 1999, Maurer, Rhinehart, 1960).

Figure 5.6: *Showing the contrast of the damaged surface created by ballistic impact between limestone (CHCL_5) and sandstone (SRS_4) samples*

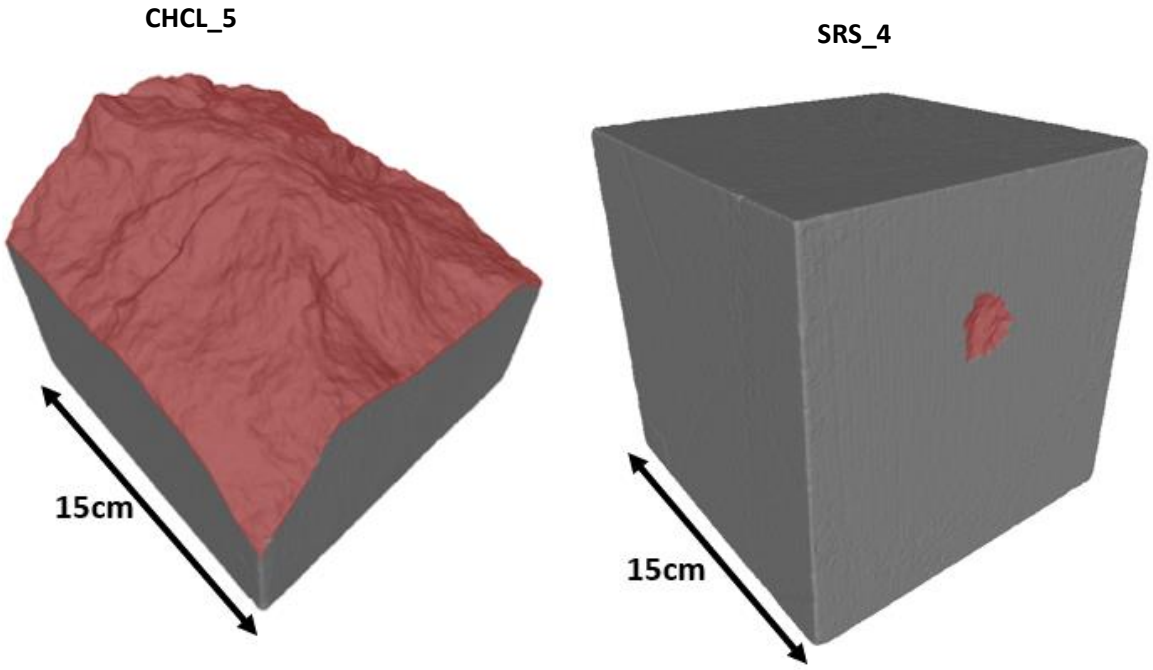

Figure 5.7: *Results showing the difference in impact crater/damaged region surface area according to lithology type. As discussed in section 3.3.2.1, the error on photogrammetry calculations will be 0.2% of the calculated area value. Therefore, error bars are not visible in this chart.*

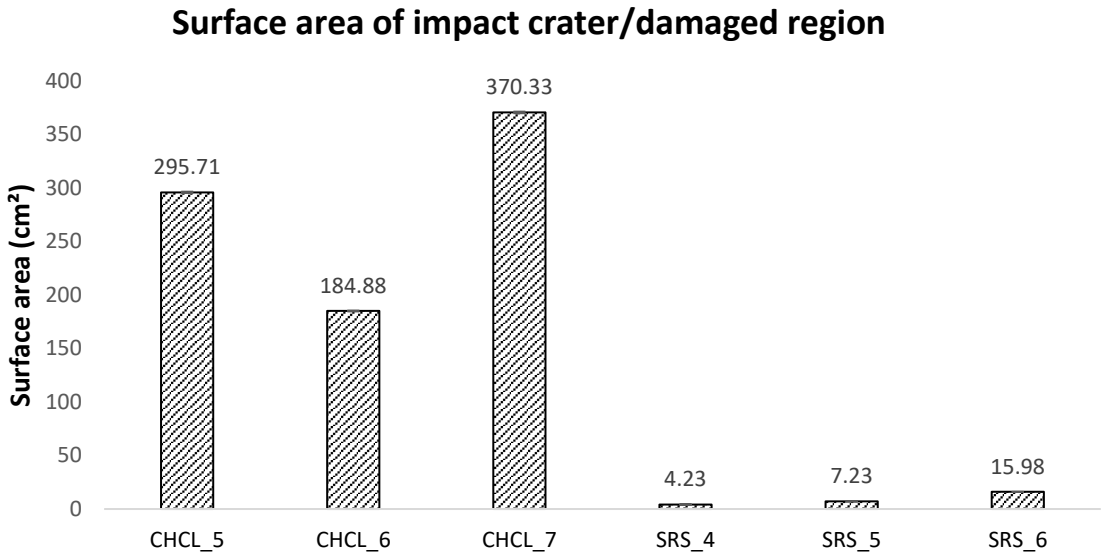

The results in figure 5.7 suggest that in a heritage context, monuments built from stones with lower stress wave impedance will suffer a larger area of impact crater and surface deterioration. In turn this will cause a greater loss of aesthetic value of the heritage asset, such as scarring to the building and a loss of surface decoration features. Loss of aesthetic value over an extended region of damaged heritage stone is another reason for considering both the area of impact crater as well as sample volume loss. Furthermore, a larger impact crater area is likely to be associated with a larger internal fracture network, as observed by Ahrens *et al*, (2002).

5.1.3.3: Permeability Results

The average increase in permeability was much higher for the limestone (7857 %) than the sandstone samples (1003 %). This is shown in figure 5.8 and table 5.4. The results demonstrate the strong relationship between surface fracturing and increasing permeability. Samples CHCL_5, CHCL 6, CHCL_7 and SRS_6 all exhibit large surface fractures connected to the impact crater, or complete disaggregation of the target face. These samples also see increases in permeability ranging from 249.8 mD to 598.1 mD. Conversely, the two sandstone samples that do not exhibit surface fracture (SRS_4 and SRS_5) have much lower permeabilities (4.8 and 30.4 mD). SRS_6 exhibited one large fracture on its surface, proceeding across side 1 to side 6, and as a result has an increased permeability average of 587.24mD. This fracturing is likely related to random defects such as bedding panes in this sample causing pre-existing weakness that are exploited by the stress wave cause by ballistic impact to create a fracture.

Figure 5.8: *Average increase in permeability increase of shot samples above control average. Error bars are the standard error of the measurements for the given sample type.*

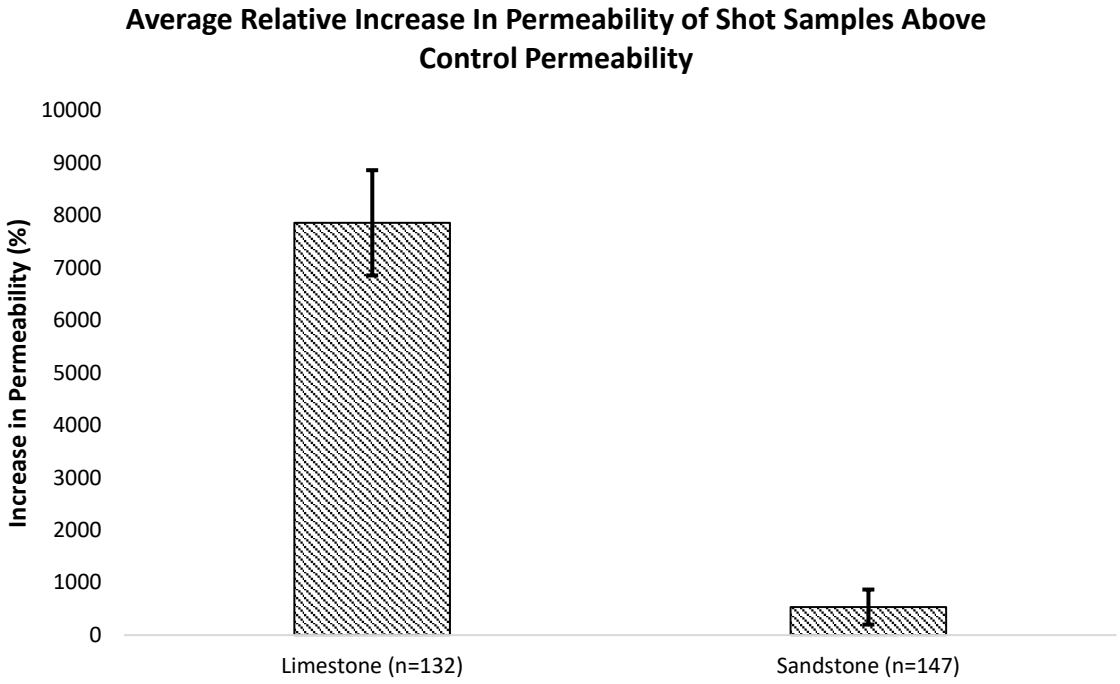

Table 5.4: *Descriptive statistics relating to the permeability of individual samples and control sample data sets.*

Sample	**Average Permeability (mD)**	**Maximum (mD)**	**Minimum (mD)**	**Range (mD)**	**Standard Deviation (mD)**	**Standard Error (mD)**
Limestone Intact Control (n = 1470)	5.39	89	0.01	89	8.50	0.22
CHCL_5 (n= 49)	249.80	1300	9	1291	279.50	39.93
CHCL_6 (n=46)	482.17	2400	0.69	2399	701.52	103.43
CHCL_7 (n=37)	598.12	3300	7	3293	779.21	128.10
Shot limestone average	428.74	3300	1.1	3299	620.98	54.05
Sandstone Intact Control (n = 1470)	10.11					
SRS_4 (n = 49)	4.80	61	0.08	61	11.66	1.67
SRS_5 (n = 49)	30.36	652	0.09	652	113.09	16.16
SRS_6 (n = 49)	587.24	2700	15.50	2685	525.18	75.03
Shot sandstone average	207.47	2700	0.08	2700	409.45	33.77

The results in figure 5.8 and table 5.4 show that limestone samples undergo a substantially larger increase in permeability (<7000%) due to surface fractures induced by ballistic impact than the sandstone samples (c. 1000 %). Figure 5.9 demonstrates the relationship between visible surface fracture and increased permeability. As previously discussed, the differing levels of permeability increase caused by surface fracturing is a product of the differing mechanical properties of the two lithologies. Rarefaction waves with peak stresses in excess of the tensile strength of the rock will propagate to a greater depth in the limestone due to its lower wave impedance (Cheng *et al*, 2019). This causes more fracturing across the surface of the limestone than the sandstone as in the regions where peak wave pressure exceeds tensile strength a spallation fracture is formed (section 1.4). The greater level of surface fracturing on limestone samples can be observed in figure 5.4.

Figure 5.9: *Permeability map of the impact face of samples CHCL 6 (A) and SRS X (B) demonstrating the relationship between visible surface fracture and increased permeability of cells (high permeability = red, low = green). The number in each cell is the permeability of that cell. Visible surface fractures on the impact face of each sample are highlighted in blue/black. Note that the most permeable cells (>1000mD) for both samples are those containing visible surface fractures, and that those cells with permeability below 10mD contain no visible surface fracture and are on the sample regions where there has been no loss of matrix. Cells with low permeabilities that do feature surface fracture are those cells where the fracture did not intersect the centre of the cell and was therefore not sampled by the permeameter nozzle. Cells without a value are those where no reading was possible due to sample topography.*

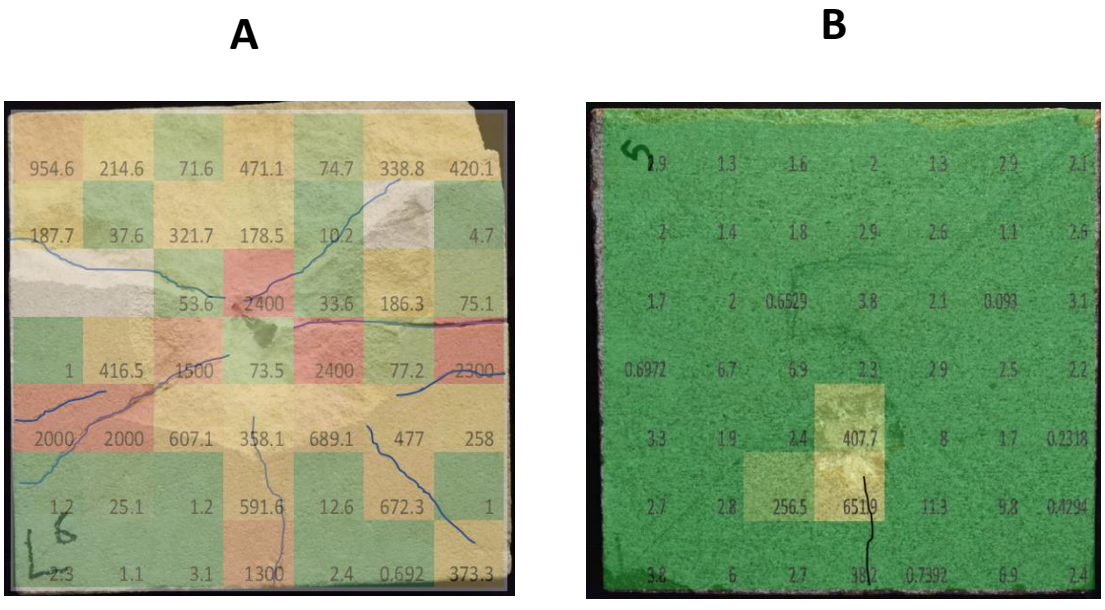

5.1.3.4: Rebound Surface Hardness Survey Results

After shooting all samples exhibit a reduction in surface hardness. The limestone samples experience an average reduction in hardness of 24.3%, whilst the sandstone samples only experience an average reduction of 9.3%. This is shown in figure 5.10, which shows the hardness of the shot samples as a percentage of their mean intact hardness. The data on average surface hardness used to create figure 5.9 is contained in table 5.5, along with other descriptive statistics.

Figure 5.10: *The shot samples' hardness as a percentage of their intact hardness. N.B. samples do not have a standard error bar as it is not possible to calculate standard error for relative change on a single sample.*

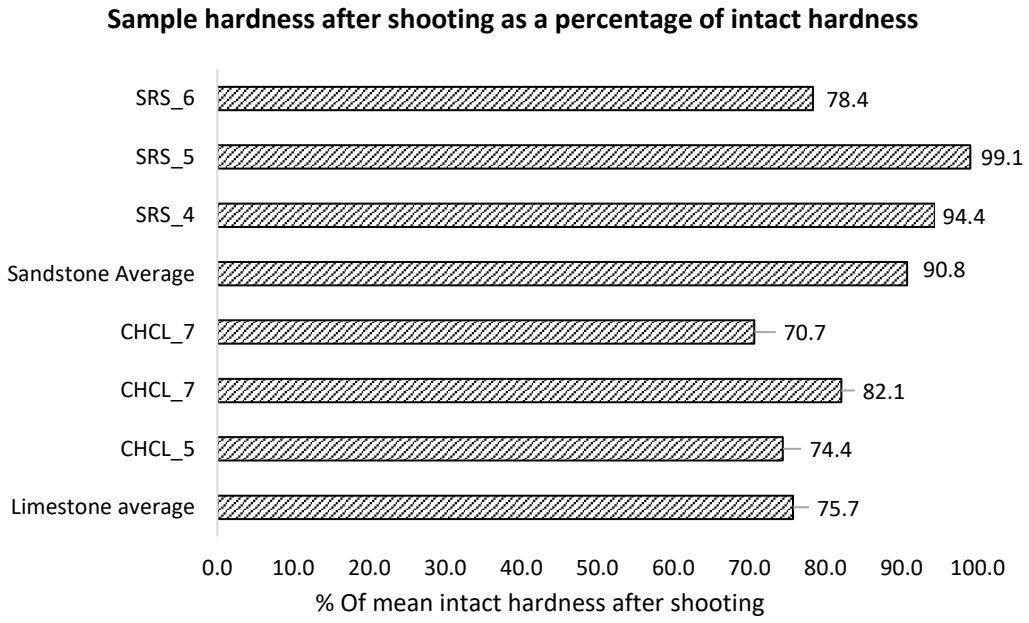

Table 5.5: *Descriptive statistics relating to the hardness survey data.*

	Mean (Leeb)	Maximum (Leeb)	Minimum (Leeb)	Range (Leeb)	Standard Deviation	Standard Error
Limestone average intact (n=447)	370	517	200	317	44	1
Limestone average shot (n=396)	281	434	201	233	53	3
CHCL_5 intact (n=147)	366	498	224	274	42	1
CHCL_5 shot (n=147)	272	417	201	216	46	4
CHCL_6 intact (n=138)	362	517	210	307	45	2
CHCL_6 shot (n=138)	297	419	201	218	59	5
CHCL_7 intact (n=111)	384	513	200	313	43	1
CHCL_7 shot (n=111)	271	434	204	230	50	5
Sandstone average intact (n=447)	688	895	216	679	123	2
Sandstone average shot (n=447)	625	810	213	597	130	6
SRS_4 intact (n=147)	712	895	233	662	96	3
SRS_4 shot (n=147)	672	802	301	501	85	7
SRS_5 intact (n=147)	684	895	222	673	135	5
SRS_5 shot (n=147)	678	810	240	570	97	8
SRS_6 intact (n=147)	669	895	216	679	123	2
SRS_6 shot (n=147)	524	735	213	522	138	11

The finding that the sandstone samples experience a lower reduction in hardness is in agreement with findings from the analysis of the surface area of the impact crater and damaged region. Because the sandstone samples have a much smaller area that has been observably damaged by the projectile (figure 5.6), less of the sample's surface has been weakened by the impact to the point of surface matrix disaggregation. When surveyed for rebound hardness, this results in the overall surface hardness reduction being greater for the limestone samples than for the sandstone because a larger area of the limestone samples is disaggregated and experiences hardness loss, as shown in figure 5.6 and demonstrated in the data displayed for the impact faces shown in figure 5.10. The fact the limestone samples have a lower initial surface hardness and see a greater relative reduction in surface hardness is to be expected given the relationship between surface hardness, compressive strength and stress wave impedance. As discussed by Aoki, Matsukura (2008), rebound hardness increases with compressive strength of the sample tested, and Zhang, Hou and Aladejare (2020) showed that higher compressive strength increases wave impedance. Therefore, it can be inferred that a lower rock surface hardness of undamaged rock can be used as an indicator that a given lithology may be more at risk of increased damage from ballistic impact.

To understand the spatial distribution of hardness loss into the two lithologies after impact, the average hardness loss of each cell across the triplicate samples was calculated after shooting. This was then plotted spatially using a three-colour traffic light gradient in an Excel matrix containing the average hardness loss values for each cell of the impact face of each of the shooting conditions (three measurements for each cell, three triplicate samples for each shooting condition, nine measurements total for each cell). The bottom of the colour gradient (red) was calibrated to be the cell with the greatest hardness loss on each surface, and the top (green) was the cell that had seen the smallest reduction in hardness. The colour gradient is equally distributed across the data range, such that yellow is the mid-point of the range between the cell with the largest and smallest reduction in hardness. It was hypothesised that this method would show the spatial distribution of weakening caused by each shooting condition, and was used in preference to the GIS based approach outlined in chapter 2 because this method could be easily used by conservation professionals in a field setting without access to specialist software or training in order to spatially visualise areas of stone damaged by ballistic damage that could be targeted for intervention. Furthermore, it is a more accurate representation of this data set than the Inverse Distance Weighting (IDW) method of representing spatial data used in chapter 2 for an average of multiple readings taken within a cell. This is because IDW assumes a value assigned to a single point, rather than the average of multiple values obtained within a given cell (see section 2.3.5). The results reveal that for limestone samples, large hardness losses are seen across the impact surface. This is due to the disaggregation across the wider sample surface as shown in figure 5.4. conversely, hardness loss for the sandstone samples is focussed on the cells closest to the impact crater centre, with outlying cells often seeing no hardness reduction. This pattern is shown in figure 5.11:

Figure 5.11: Spatial distribution of average hardness loss by cell on the impact face for limestone samples (A) and sandstone samples (B). All values are the average Leeb rebound surface hardness loss for the given cell.

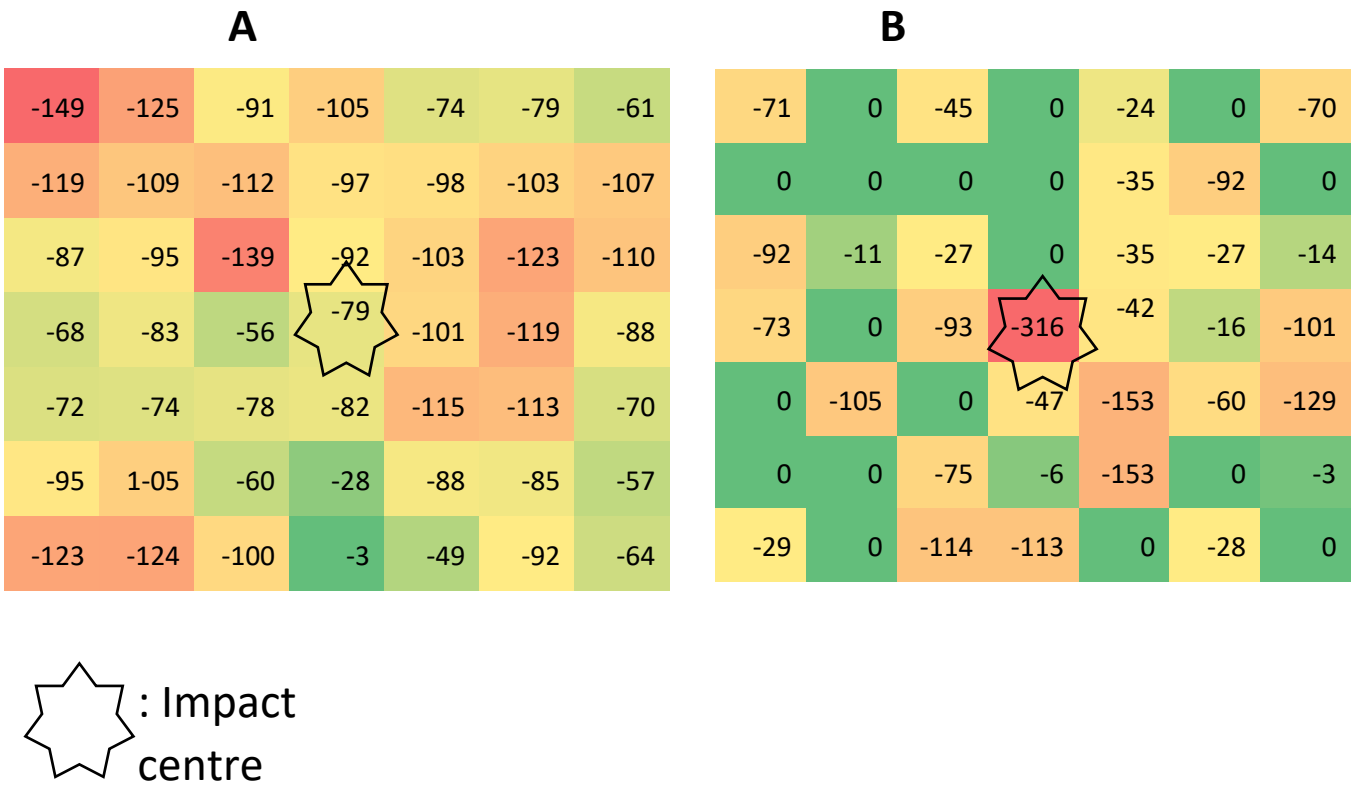

The results in figure 5.11 demonstrate the different responses of the two lithologies, with limestone samples seeing much greater hardness loss across the impact face than sandstone samples. This suggests that lithology, and associated mechanical properties, is a key determinant of the distribution of hardness loss. Therefore, when assessing heritage damaged by ballistic impact in a field setting, it will be imperative to consider how the lithology of the damaged site may determine the distribution and extent of damage across the impacted surface.

It should be noted that the data presented in figure 5.9 does not consider hardness reductions on non-impact faces of the samples. These surfaces were not surveyed for hardness due to the destruction of non-impact faces on the limestone samples, as discussed in section 5.1.2.2. Therefore, in order to understand patterns of hardness reduction on non-impact faces, the sample generation methods were modified in future experiments of this project, as discussed in section 5.2.2.1.

5.1.4: Discussion of significance of results

The results presented here strongly suggest that mechanical properties of the target lithology play a key role in determining the level of damage sustained by a rock sample subjected to ballistic impact. The Cotswold Hill Cream Limestone has a lower compressive strength and lower density than the Stoneraise Red Sandstone, and a higher porosity (table 5.3). As outlined in section 1.4, these mechanical properties are known to reduce the wave impedance value for a given lithology, and therefore stress waves arising from ballistic impact propagate with higher energies/ peak pressures to a greater depth in the limestone, resulting in more widespread fracturing and damage to the limestone. Limestone samples thus see a greater reduction in volume and a larger surface area of impacted/damaged stone (figures 5.4-5.6). This is caused by propagating stress waves with peak pressures in excess of the compressive/tensile strengths of the impacted rock (section 1.4). Stress waves with pressures sufficient to induce fracturing will propagate further in the limestone samples due to their low wave impedance, and as a result the limestone samples see more material loss to spallation fracture end ejection of the stone matrix. This is consistent with the findings of Guldemeister *et al* (2015) who utilised both numerical modelling and laboratory measurements to demonstrate that for a projectile of given velocity, impact crater size is controlled by the tensile yield strength of the rock which is impacted, because as shown in table 5.3, the tensile strength of the sandstone samples is higher than that of the limestone samples (5 MPa vs 2.2 MPa).

The ability of stress waves to propagate easily through the limestone samples also results in a greater average loss of rebound hardness across the impact face (figure 5.10. 5.11). This greater loss of hardness of the limestone samples is a product of the far larger damaged area of limestone samples compared with sandstone samples. The larger damaged area is due to matrix spallation fracture and ejection due to lower tensile strength as discussed above (French, 1998). In turn, this larger damaged area is characterised by disaggregation and fractures across the surface as described by Polanskey and Ahrens (1990) and shown in figure 5.6. Therefore, limestone samples exhibit a larger area of hardness loss across the impact face than sandstone samples, and this disparity is controlled by the mechanical properties of the two lithologies.

Permeability increase is also far higher for limestone samples than for sandstone samples. As shown in figure 5.8, this is chiefly due to the presence of a greater extent of visible surface

fracturing on the impact face of the limestone samples than on sandstone samples. As demonstrated experimentally by Ai and Ahrens (2006), the extent of fracturing initiated at the impact crater will be dictated by the mechanical properties of the target lithology, principally the tensile yield strength, which as discussed above is significantly higher for the sandstone samples. The permeability results therefore supplement the evidence from both photogrammetry and hardness analysis by demonstrating that the mechanical properties of the target lithology can cause large disparities in the damage suffered by impacted stone.

The results of this chapter thus show that mechanical properties that lower the wave impedance of a lithology will make that lithology more susceptible both to mechanical degradation (loss of surface hardness which is related to compressive strength) as well as increasing the exposure of the impacted rock to ingress by weathering agents such as moisture and salt (increase in permeability).

The fact that surface hardness is correlated with compressive strength (Aoki, Matsukura, 2008) means that field measurements of heritage stone hardness can be used to infer relative compressive strength. This could then be used as a rapid way of assessing likely wave impedance of a given heritage stone, and therefore the relative risk posed to heritage monuments composed of different lithologies by ballistic impact could be assessed in the field. These findings could then be used to inform conservation strategies and restoration interventions by helping to prioritise appropriate use of resources.

Another interesting finding of these experiments is that the limestone samples are significantly more damaged than the limestone samples used in chapter 4. Unlike samples 1 and 2 in chapter 4, the samples used in this study (CHCL_5 and CHCL_6) experience the complete destruction and removal of the impact face. This was unexpected, as it was at first thought that the greater confinement arrangements used in this experiment would result in less damage to the samples because there would be less reflection of rarefaction waves from exposed free surfaces. However, recent research has highlighted than increased containment pressure can actually increase the extent of spallation fracture by reducing the spallation strength of the confined rock (Li *et al.* 2017). More confining blocks were used in this experiment than in chapter 4, which would increase the confining pressure and therefore increase the fracturing and damage to the limestone samples. It was the massively increased damage to the limestone samples, which would have rendered useful data from weathering experiments impossible due to the loss of the impact face, which necessitated that the

remaining limestone samples be shot at a reduced velocity/increased range when investigating the effects of changing ammunition type and impact angle (section 4.2).

5.1.5: Conclusions

The findings from this section demonstrate that lithology, and specifically the mechanical properties of a given lithology, are a critical parameter in determining the damage caused by ballistic impact. Lithologies with lower compressive strength and density and higher porosity will have a lower wave impedance. This will allow stress waves caused by ballistic impact to retain sufficient pressures to cause fracturing and ejection of stone material, increasing loss of stone material, reductions in surface hardness and permeability caused by surface fracturing. This conclusion demonstrates that when dealing with ballistic impact to heritage stone and designing possible intervention strategies, proper consideration must be given to the mechanical properties of the heritage stone affected.

The results also provide insight into the potential for rapid in-situ assessment of the relative vulnerability of heritage monuments of differing stone monuments to exacerbated deterioration caused by ballistic impact, either through the use of rebound surface hardness survey as a proxy indicator for compressive strength and therefore wave impedance, and also the visual identification of surface fracturing which will cause increased sample permeability and corresponding susceptibility to ingress of weathering agents likely to exacerbate weathering deterioration.

Finally, as discussed in section 5.1.3.4, the limestone samples generated in this section of the project were largely destroyed by the ballistic impact and exhibited such large loss of volume that hardness and permeability readings could not be obtained from non-impact faces. This observation was used to refine the sample generation methods in future experimental sections of this project to ensure that limestone samples with well-define craters confined to the impact face of the limestone samples were obtained, ensuring that weathering behaviour of classic impact craters could be observed, and so that data could be obtained from non-impact faces. These methodological refinements are outlined in section 5.2.2.1.

5.2: Study into ammunition type and impact angle

5.2.1: Introduction

Section 1.7 and the pilot study presented in chapter 4 have discussed and demonstrated that the angle of ballistic impact is a key variable that controls both the extent and distribution of damage sustained by stone samples subjected to ballistic impact, and section 5.1 showed that target lithology is another key determinant of the level of damage sustained after ballistic impact. However, as section 1.7 also discussed, there is a lack of published research into how the different construction materials and ballistic characteristics of modern small arms ammunition may alter the damage profile of impacted stone. A larger number of replicate samples would also allow for more representative data collection for permeability from non-impact surfaces, an issue identified for the permeability data collection methods used in chapter 4 (see section 4.4.5).

To address these issues and allow for larger, more representative data sets, 12 samples of each of the two sample lithologies used in section 4.1 were obtained and shot with two ammunition types (7.62 x 39mm and 5.56 x 45mm) at two differing impact angles (90◦ and 45◦).

Damage to the samples was assessed through photogrammetry, mass measurements, Ultrasonic Pulse velocity, Equotip surface hardness survey and permeability survey to gain a comprehensive insight into the damage caused by altering these variables (lithology, impact angle, bullet type).

5.2.2: Methods

5.2.2.1: Sample Generation

As previously discussed, in section 5.1 it was discovered that limestone samples were largely destroyed by 7.62 x 39mm impact at an average velocity of 540ms^{-1} (corresponding to a range of 200m), whilst sandstone samples were almost unscathed. It was necessary to ensure that the range methods produced samples that would be useful in future weathering experiments of a reasonably consistent size, and with an impact face which could be assessed for weathering damage as might be found on a damaged heritage building rather than disaggregated rubble, as well as a defined impact craters and sufficient material remaining on non-impact faces to obtain data. To achieve this, limestone samples for the study into ammunition/impact angle were shot at a velocity corresponding to a range of 400m instead. This velocity would vary according to the ammunition used as 5.56 x 45mm bullets travel faster than 7.62 x 39mm. The reduced velocities to simulate impact at 400m were calculated using the ballistic model used by COTEC staff described in section 4.2.2. Sandstone samples were shot at velocities corresponding to 200m because reducing the velocity would not produce sufficient damage/cratering to assess the effect of ballistic impact on weathering behaviour in future experiments. In remaining discussion, these samples will be described as "the cratered samples" to differentiate them from the largely destroyed limestone samples generated in section 5.1, which were too badly damaged to exhibit conventional impact craters as may be observed in a conflict scenario.

To ensure that interpretations of the data are valid, statistical analysis for limestone and sandstone samples was conducted separately to isolate the effects of the remaining variables (impact angle and bullet construction). The differing responses of the two lithologies to identical impact conditions (bullet, angle, range) have already been explored in section 5.1. Table 5.6 summarises the shooting condition of each of the samples used. The containment used for each impact was the same as that described in section 5.1, with the samples and containment blocks rotated relative to the firing mount to create 45◦ impacts (as in figure 3.3).

Table 5.6: *Shooting conditions for each of the target samples:*

Sample	Simulated Impact Range (m)	Ammunition	Velocity to simulate impact range (ms^{-1})	Impact Angle (◦)
SRS_4	200	7.62 x 39mm	540	90
SRS_5	200	7.62 x 39mm	540	90
SRS_6	200	7.62 x 39mm	540	90
SRS_16	200	7.62 x 39mm	540	45
SRS_19	200	7.62 x 39mm	540	45
SRS_20	200	7.62 x 39mm	540	45
SRS_10	200	5.56 x 45mm	700	90
SRS_12	200	5.56 x 45mm	700	90
SRS_14	200	5.56 x 45mm	700	90
SRS_17	200	5.56 x 45mm	700	45
SRS _18	200	5.56 x 45mm	700	45
SRS_21	200	5.56 x 45mm	700	45
CHCL_12	400	7.62 x 39mm	430	90
CHCL_13	400	7.62 x 39mm	430	90
CHCL_14	400	7.62 x 39mm	430	90
CHCL_26	400	7.62 x 39mm	430	45
CHCL_28	400	7.62 x 39mm	430	45
CHCL_34	400	7.62 x 39mm	430	45
CHCL_18	400	5.56 x 45mm	600	90
CHCL_35	400	5.56 x 45mm	600	90
CHCL_36	400	5.56 x 45mm	600	90
CHCL_30	400	5.56 x 45mm	600	45
CHCL_31	400	5.56 x 45mm	600	45
CHCL_33	400	5.56 x 45mm	600	45

5.2.2.2: Bullet Characteristics

As outlined in the introduction, the construction and ballistic parameters of the bullets used in this study are key parameters. The characteristics of these projectiles are given in table 5.7 and figure 5.10:

Table 5.7: *Technical details for the two ammunition types used in this study. Velocity Data is Taken from experimental measurements using the Weibel Doppler Radar*

Bullet	Mass (g)	Bullet Volume (cm^3)	Muzzle velocity (ms^{-1})	Muzzle Kinetic Energy (J)	Construction materials	Cartridge Stamp	Country of Origin
7.62 x 39mm	7.95 g		740	1729.8	Lead core, brass jacket	13 88,	South Africa
5.56 x 45mm	4 g	0.5	930	2176.1	Steel penetrator, lead plug, gilding metal jacket (95% copper, 5% zinc)	L17A2 RG 15 +	United Kingdom

Figure 5.10: *Illustration of the differing construction and materials of the bullets used in this study. Adapted from Campbell et al (2022).*

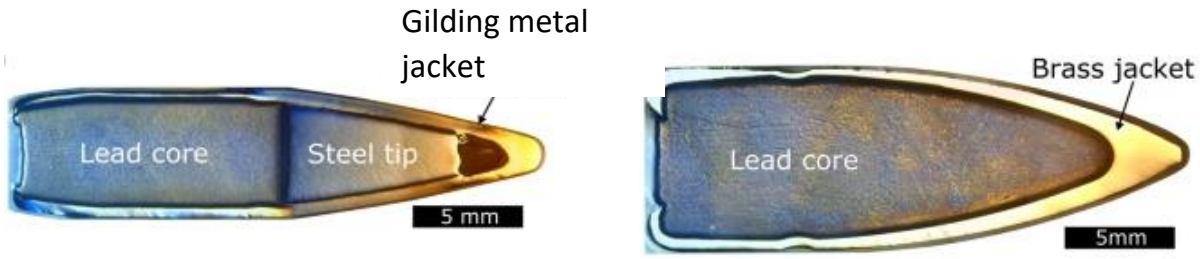

5.2.2.3: Data collection

Rock Surface Hardness Survey

For each sample, control readings for rebound surface hardness were taken following the methods outlined in section 4.1.1.2. The same measurements were taken after the samples had been shot.

Permeability Survey

Control measurements were taken using the methods outlined in section 4.1.1.2. Results from chapters 2,3,4 and 5 consistently show that increases in permeability are caused primarily by visible ballistic damage such as disaggregation and visible surface fracture networks, and also that surface fracture networks are initiated at the impact crater and propagate to non-impact surfaces from the impact face. If this hypothesis could be proven, it would allow faster assessment of the effect of ballistic damage on impacted stones' permeability by allowing survey to focus on the surfaces where impact occurred, and fracturing is most intense. Furthermore, Sections 2.6 and 3.4.5 highlighted the need to find a method of collecting permeability data that was rapid enough to be used in the field, but still produced data sets with a sufficient number of data points to give meaningful results. Therefore, the permeability survey needed to balance testing the hypothesis that surface fracture on non-impact faces is initiated at the impact face, and expedited data collection. To achieve this, after shooting, all 49 cells of the impact face were measured for permeability. On non-impact sides, permeability measurements were taken from the columns and rows of cells that would intersect any surface fractures proceeding from the impact face. This sampling regime gave 189 permeability measurements per sample, whilst still ensuring that any increases in permeability due to surface fracturing propagating from the impact face were identified and facilitating faster data collection. This permeability sampling regime is shown in figure 5.12:

Figure 5.12: *The permeability sampling regime on non-impact sides, showing the 28 cells sampled and how they successfully intercept and detect fractures initiated on the impact face from the impact crater.*

Photogrammetry data collection

Following the methods laid out in section 4.2.5 a 3D photogrammetric model was created for each of the samples before and after shooting, and the volume and surface area of the models calculated in Meshlab. This was coupled with measurements of the samples mass before and after shooting using an Adams Equipment 16kg scales to assess changes to mass, volume and surface area caused by ballistic impact.

Ultrasonic Velocity (UPV) data collection

The method for collecting UPV data was similar to that outlined in section 4.2.6. Before shooting, a Proceq Pundit 200 was used to measure the UPV for each of the samples in 3 different orientations (measured across sides 1 and 3, sides 2 and 4 and sides 5 and 6). The pulse voltage was 200 V, the receiver gain was x1 and the pulse repetition frequency was 20Hz. The same rig outlined in section 4.3.6 was used to hold the transducers steady to gain a constant reading. After shooting the UPV measurements were repeated in the same fashion. Where an impact crater was present, readings were taken from an intact region immediately above the impact crater on side 1 to avoid changing the distance between transducers which would produce erroneous figures for UPV.

5.2.3: Results and interpretation

N.B: To ensure a concise presentation of results, descriptive statistics for Equotip, Permeability and UPV are given in the tables contained in appendix A.

5.2.3.1: Hardness Survey Results

In chapters 2 and 3 of this thesis, results suggested that the weakening experienced by sides distant from the impact point would see relatively less weakening. To explore this further, the average hardness loss of each sample surface was determined and averaged according to the angle at which the samples were shot. The sample surfaces were divided into three "zones"; the impact face (side 1) sides adjoining the impact face (sides 2, 4, 5 and 6) and the side opposite the impact face (side 3). This was done to prevent skewing of the data by inhomogeneities on a single surface of a single sample of the replicate sample sets and to aid understanding of the spatial distribution of damage in a way that could inform field-based rapid assessment of ballistic damage. That is to say, conservation professionals in a field setting could be trained to prioritise survey in these three zones depending on the likelihood of damage in each. The results of this analysis are presented in figure 5.18.

Figure 5.13: *Charts showing hardness reduction by sample surface and impact angle for both lithologies. Error bars are the standard error of the mean for the given data set.*

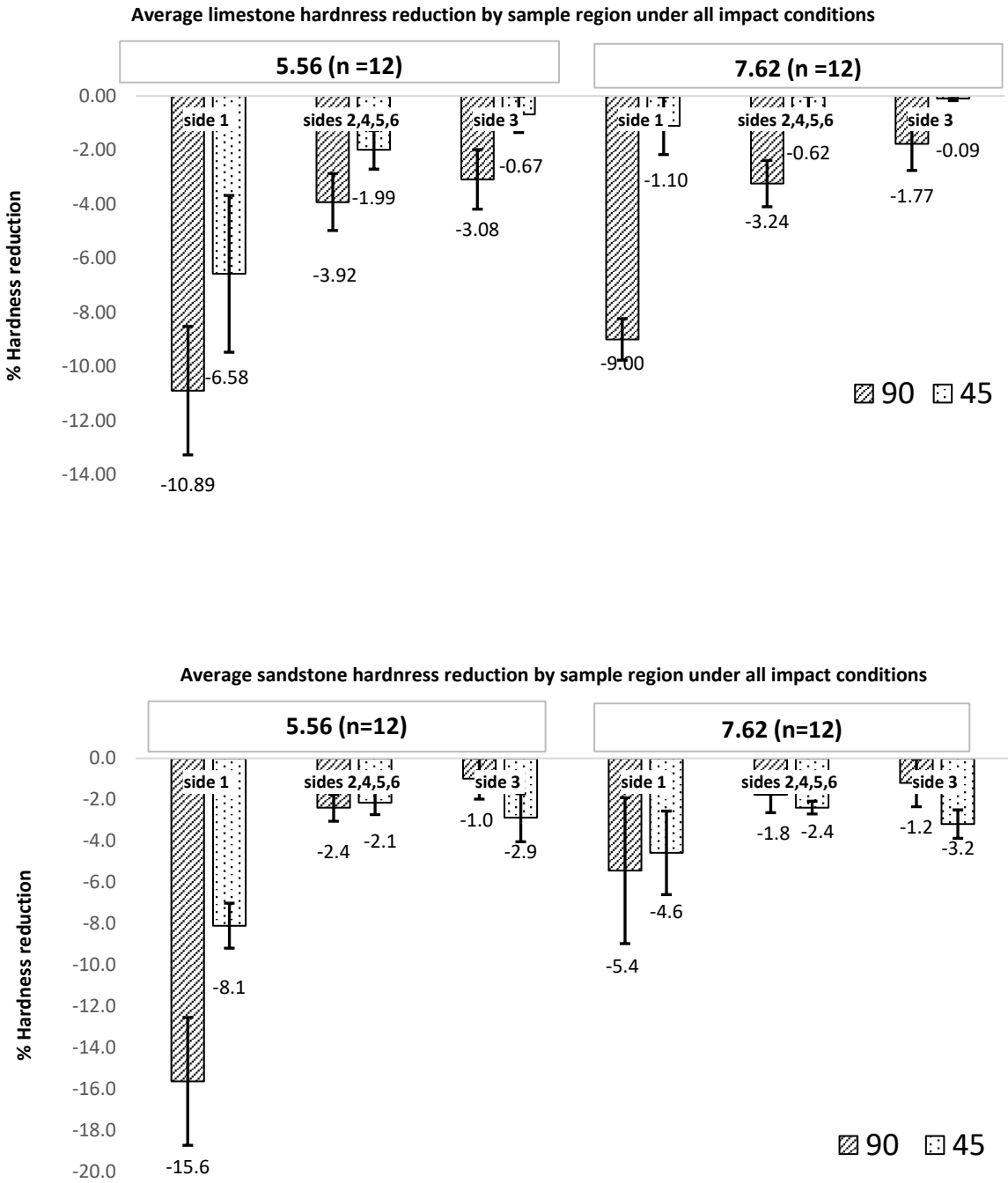

As would be expected, the impact face (side 1, see figure 4.1) sees the greatest reduction in hardness for under all impact conditions. This is because the kinetic energy and corresponding stress wave pressures will be highest on the impact face. Conversely, under most impact conditions, side 3 experiences the lowest loss of hardness. For instance, for sandstone samples impacted by 5.56 ammunition at 90°, the impact face sees a reduction of 15.6%, vs a loss of only 1% for side 3. This is in keeping with the findings presented in the results of chapters 1 and 3, which consistently found that the face opposite the impact surface experiences the lowest loss of hardness due to stress waves reaching this surface being attenuated by the intervening rock matrix and thus having lower peak pressures (Thoma *et al,* 2005).

It should be noted that this observation is not always true, as for sandstone samples impacted at 45°, side 3 experiences a greater average hardness reduction (c. 3%) than the average for sides 2,4,5 and 6 (c. 2%). Although this observation should be treated with caution due to the uncertainty represented by the overlapping error bars for these surfaces shown in figure 5.12, one possible explanation is the differing reflection patterns of rarefaction waves propagating after 90° and 45° impact. After 90°, hemispherical stress waves induced by the impact will propagate to sides 2,4,5 and 6 with greater peak pressures than experienced by side 3 as previously discussed. However, after 45°, stress waves will propagate with greater stresses to side 3 than after 90°, due to compressive stress waves reflecting from the free surface of side 2 to side 3 as rarefaction waves that induce micro-fracturing and corresponding weakening. This finding suggests that oblique impact (45°) is capable of inducing greater weakening on the surface opposite the impact face than 90° impact, and this should be considered when devising survey regimes for damaged stone after conflict damage. That said, these results are within the margin of error represented by the error bars present on figure 5.13, and thus should be treated with caution.

Although across all impacts, 7.62 x 39mm ammunition had a slightly higher kinetic energy at impact than 5.56 x 45mm ammunition (898J vs 850 J), figure 5.13 demonstrates that impact by 5.56 x 45mm projectile often produces greater loss of hardness than 7.62 x 39mm ammunition under equivalent impact conditions, particularly on the impact face. The cause of this is that the construction of the respective projectiles. The 7.62 x 39mm ammunition contains only a soft lead core, whilst the 5.56 x 45mm ammunition contains a harder steel penetrator (figure 5.10). This difference in construction means that on impact with the harder sandstone blocks, the kinetic energy of the 7.62 x 39mm projectile is partially spent on

deforming the projectile itself. Conversely, the steel core of the 5.56 x 45mm ammunition is too hard to be deformed by impact with the sandstone surface, and thus more of the kinetic energy of the projectile is used in penetrating the samples and causing sub-surface fractures which lead to a detectable reduction in surface hardness. The difference in damage profiles caused by the construction materials of the projectile and their tendency to deform was previously discussed by Khan *et al*, who demonstrated that during impact, harder projectiles deform less and penetrate target materials to a much greater depth. This variability in projectile interactions with the sandstone samples is also illustrated in figure 5.14, which shows that impact by steel cored 5.56 x 45mm projectile causes greater penetration and a larger impact crater than impact by lead cored 7.62 x 39mm ammunition:

Figure 5.14: *The difference in the size of impact crater and depth of penetration after impact by 7.62 x 39mm lead cored ammunition (A) and 5.56 x 45mm steel cored ammunition at 90◦ (B).*

A **B**

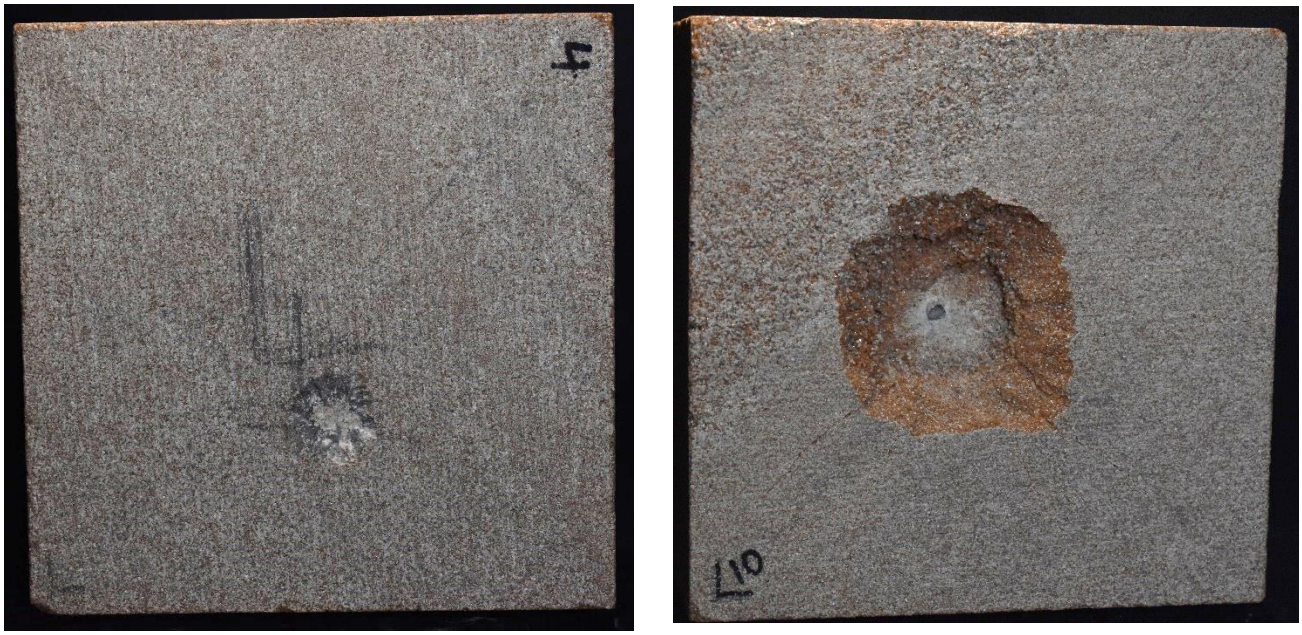

Based on the data presented in figure 5.13, it seems likely that in most instances, 90◦ impact causes greater overall weakening to the impacted samples than 45◦ impact, which manifests particularly as large reductions of hardness on the impact face, where hardness reduction is always greater after 90° than after 45°. This is to be expected as previous numerical modelling by Fawaz, Zheng and Behidan (2004) have shown that oblique angles of impact

result in lower stresses in the region of the projectile-target interface than 90◦ impact, as much of the kinetic energy of the projectile will not be imparted to the target surface as the projectile ricochets away from the target surface. This would suggest that the higher stresses experienced at the impact surface for 90◦ are the cause of the greater weakening and loss of hardness seen across the 90◦ impact samples.

To further investigate the effects of individual variables, ANOVA tests were conducted across both lithology types by ballistic variable (angle of impact and projectile) to determine which variables had statistically significant effects on hardness loss when altered. This analysis was conducted on the impact face, where hardness loss was greatest (see figure 5.12) The results of these ANOVA tests for mean hardness loss are shown in table 5.8.

Table 5.8: *Results of ANOVA tests grouped by target lithology to determine which ballistic variables have a significant effect on relative hardness loss on impact face. Limestone: A. Sandstone: B.*

A

Tests of Between-Subjects Effects

Source	Type III Sum of Squares	df	Mean Square	F	Sig.
Corrected Model	152.218[a]	3	50.739	4.125	.048
Intercept	550.874	1	550.874	44.790	<.001
Bullet	42.259	1	42.259	3.436	.101
Angle	102.254	1	102.254	8.314	.020
Bullet * Angle	7.706	1	7.706	.627	.451
Error	98.393	8	12.299		
Total	801.485	12			
Corrected Total	250.611	11			

a. R Squared = .607 (Adjusted R Squared = .460)

B

Tests of Between-Subjects Effects

Source	Type III Sum of Squares	df	Mean Square	F	Sig.
Corrected Model	227.666[a]	3	75.889	3.705	.061
Intercept	853.398	1	853.398	41.668	<.001
Bullet	141.347	1	141.347	6.901	.030
Angle	53.001	1	53.001	2.588	.146
Bullet * Angle	33.319	1	33.319	1.627	.238
Error	163.847	8	20.481		
Total	1244.911	12			
Corrected Total	391.513	11			

a. R Squared = .582 (Adjusted R Squared = .425)

The results presented in table 5.8 show that for limestone, impact angle is more significant than bullet type, with angle having a *P* value of 0.02. This is hypothesised to be because the limestone is weak enough that impact by either projectile causes loss of hardness, However, 90◦ impact transfers more kinetic energy to the samples than 45◦ and therefore causes more damage and has a more significant effect.

Converesely, for sandstone, bullet type has a more significant effect than angle (*P* value: 0.03). This is thought to be because lead-cored bullets often result in virtually no cratering in sandstone samples, as the soft lead deforms on impact with the hard/high compressive strength sandstone, whilst steel cored bullets are able to penetrate the stone, excavating an impact crater and resulting in hardness reduction (figure 5.13).

One limestone sample is worth noting individually due to the nature of the damage it sustained. CHCL_31 was impacted at 45◦ with 5.54 x 45mm ammunition and was the only sample that lost material from sides other than the impact surface (in this instance material was lost from side 2 (figure 5.15).

Figure 5.15: *The damage to side 1 and side 2 caused by 45◦ impact into sample CHCL_31 by 5.56 x 45mm ammunition.*

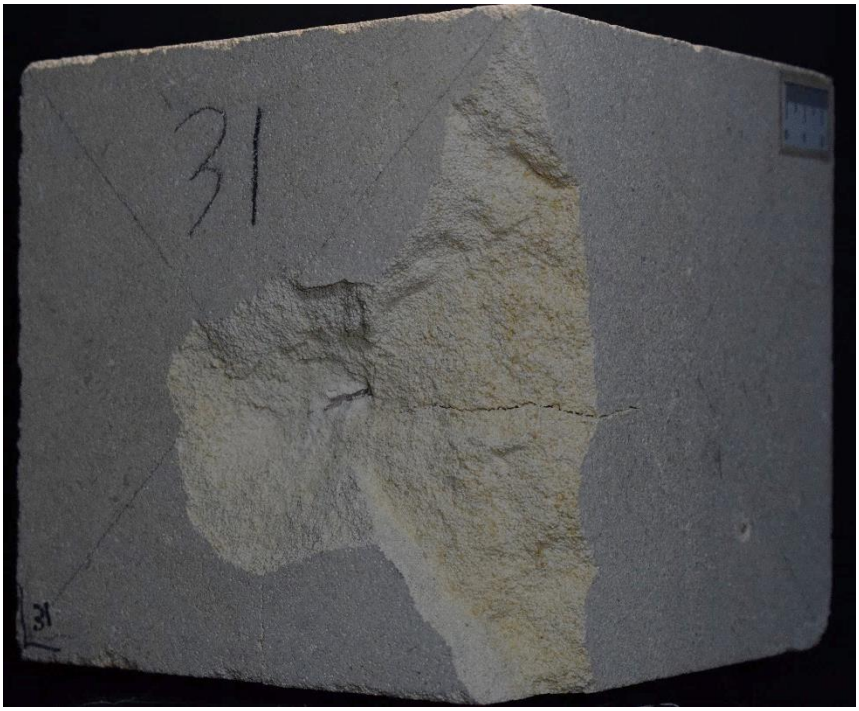

As a result of the wider spread of material loss caused by the 45◦ impact, CHCL_31 sees a decrease in average hardness much higher than other samples impacted at 45◦ (figure 5.16). This suggests that under certain conditions, the trajectory of a 45◦ impact is able to exploit existing defects in a target block to cause damage on surfaces other than the target face. In this instance, 45◦ impact can cause greatly increased weakening that is comparable to 90◦ impact (-4.2% for this sample vs -2.5% for 45° impact average). This is an important finding because it supports findings in chapter 3 which tentatively suggested that under certain circumstances 45◦ impact can result in greater damage than 90◦ due to the wider area of damage. Whilst the example of CHCL_31 does not directly demonstrate this (figure 5.16), it shows that under conditions where 45◦ leads to material loss on non-impact faces, damage and hardness loss is substantially increased relative to oblique impacts where no damage is experienced on non-impact faces.

Figure 5.16: *Demonstrating that CHCL_31 experienced hardness loss after 45◦ substantially higher than other impacts under the same conditions, believed to be due to the loss of material on non-impact surfaces. N.B. CHCL_31 does not have a standard error bar as it is not possible to calculate standard error for relative change on a single sample.*

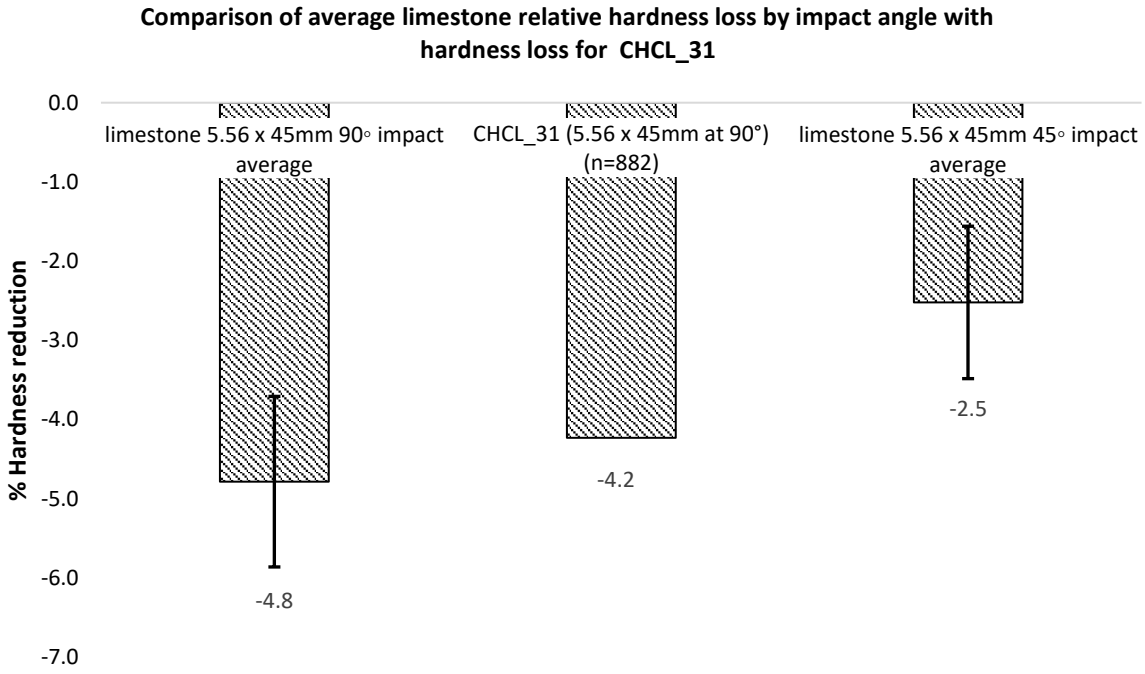

It was hypothesised that it may be possible to detect any surface defects in a sample that may be exploited by subsequent oblique impact using pre-shot hardness survey data. If the cells that were excavated/removed from sample CHCL_31 during the oblique impact process were found to have a lower-initial hardness it may suggest that surface hardness survey can predict areas most at risk from oblique impact. However, when the 21 right-hand cells of the impact face were analysed for pre-shot hardness, it was found to be almost identical to the average un-shot hardness of the Cotswold Hill Cream limestone samples (CHCL 31 removed cells = 379, n = 21 Leeb, unshot cells average = 380 Leeb, n = 10854).

Finally, the previously described phenomenon of compaction of the stone matrix at the point of ballistic impact was explored by comparing the hardness of the cell containing the impact point compared to the average hardness of the surrounding 8 cells of the impact crater (figure 5.17).

Figure 5.17: *Showing sampling of the central impact point (red star) and surrounding 8 cells (dashed black line).*

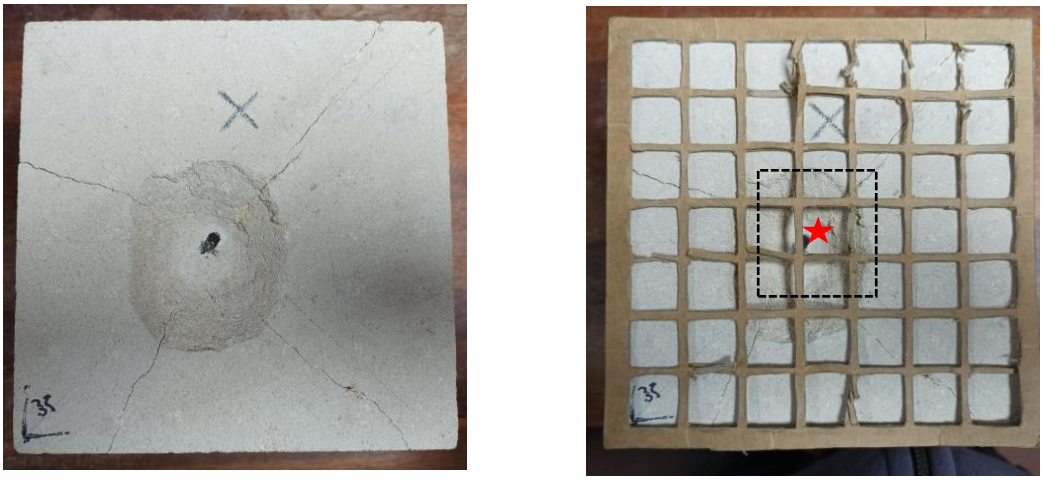

This analysis was performed for each of the 12 samples impacted at 90◦, as many of the impacts at 45◦ have irregularly shaped impact craters inappropriate for this analysis. The results are presented in figure 5.18.

Figure 5.18: *A comparison of the hardness of impact point and surrounding cells for all samples impacted at 90°. Projectiles used in each impact are listed in table 5.6. Error bars are the standard error of the mean for the given data set.*

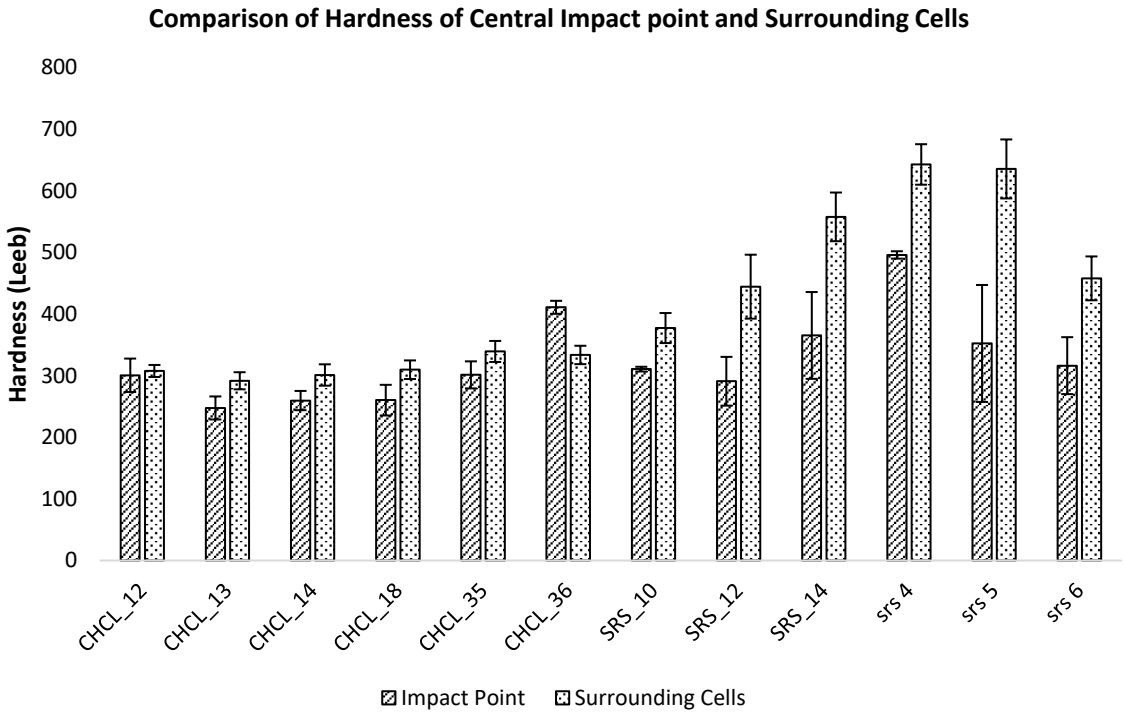

Figure 5.18 shows that for every individual sample except CHCL_36, the central impact point has a lower hardness than the surrounding cells. This suggests that previous findings of compaction at the impact point are not a universal rule, and that in many instances the impact point is substantially weaker than the surrounding surface. This disparity with previous findings may be the result of the different lithologies used in previous studies that reached this conclusion (see chapter 2) or the different projectiles used in published works that found a hardening effect (Mol *et al*, 2017, Mol, Gomez-Heras, 2019). Therefore, whilst this study, which uses a greater number of samples than previous work, found no evidence of compaction at the point of ballistic impact resulting in increased hardness, this does not preclude the phenomenon happening under different parameters. Furthermore, as detailed in the following section, permeability analysis of these samples does suggest that compaction at the impact point can reduce permeability compared to the surrounding impact crater for limestone samples (see figure 5.22).

Further spatial analyses for the hardness data were undertaken using the techniques described in section 5.1.3.4 to create a colour-coded distribution of hardness loss across the impact faces under each impact condition. The results are presented in figures 5.18 and 5.19:

Figure 5.19: *Spatial distribution of hardness loss data for each combination of impact conditions at 90°. Hardness values are in leebs. Weakest cells are red, hardest cells are green.*

Limestone, 5.56 x 45mm, 90° impact

0	13	-8	1	-24	-32	-13
0	-44	-38	8	-20	-20	-6
-25	-49	-38	-61	-54	7	-1
-114	-47	-76	-53	-53	0	30
-31	-19	-93	-21	4	-17	-3
-38	-56	-85	-113	-76	-29	3
-27	-73	-49	-73	-29	-71	1

Limestone, 7.62 x 39mm, 90° impact

-40	-32	-54	-57	-42	-63	-13
-17	-44	-46	-50	-79	-36	3
-17	-22	-62	-65	-99	-10	-1
-12	-11	-95	-108	-102	-24	-65
-2	-24	-12	-78	-70	-15	-1
-27	-33	-30	-67	0	-10	-7
-3	-8	-16	-41	-11	-19	-6

: Impact crater centre

Sandstone, 7.62 x 39mm, 90° impact

-156	-5	-69	-40	-50	12	-53
-8	-8	3	-36	-74	-126	-40
-202	-52	-29	-73	-119	-76	-73
-95	-31	-84	-92	-104	-32	-110
-62	-117	15	-311	-148	-35	-104
-20	-43	-124	-61	-172	-38	-64
-57	-45	-99	-124	-56	-55	-62

Sandstone, 5.56 x 45mm, 90° impact

-217	-45	-150	-148	-58	-67	-101
-105	-192	-122	-148	-127	-9	-41
-299	-279	-273	-241	-189	-42	-55
-290	-284	-295	-377	-166	-113	-123
-233	-232	-235	-278	-99	-22	-61
-208	-149	-97	-83	-89	-40	-59
-143	-69	-108	-116	-81	-54	-46

As might be expected, the hardness data distribution mapping shows that the greatest density of weakened cells is often found at the impact centre and surrounding cells. This is consistent with the findings in chapter 2 and figure 5.19 which demonstrate that after ballistic impact the area that experiences greatest weakening is the impact crater which is weaker than un-cratered portions of the impact face. The data hardness for sandstone samples impacted with 5.56 x 45mm ammunition at 90° shows a greater weakening of the right-hand side. This is believed to be due to the impact induced fracture network exploitation of lithological defects such as bedding planes. This is discussed more in section 5.2.3.2 and illustrated in figure 5.24.

Figure 5.20: *Spatial distribution of hardness loss data for each combination of impact conditions at 45°. Hardness values are in leebs. Weakest cells are red, hardest cells are green.*

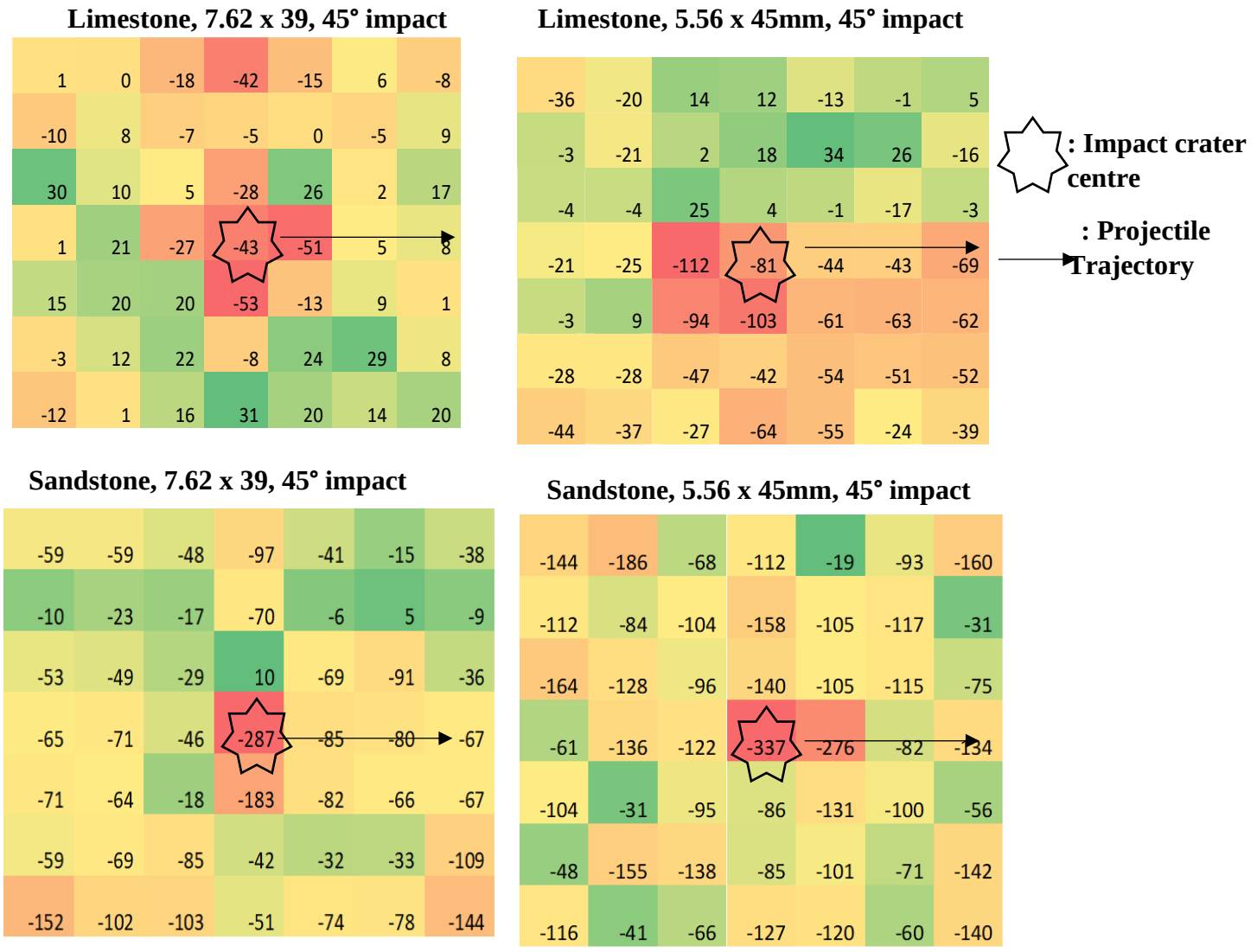

It was hypothesised that cells on the right of the impact face, which are along the trajectory of the 45° impact would be weaker than those on the left of the sample. However, figure 5.20 shows that this trend does not appear to be consistently evident for 45° impacts, with the right-hand side cells having broadly similar values to the left-hand cells. Based on figure 5.20, there is no evidence to suggest that oblique introduces asymmetry into the spread of hardness reduction across the impact face. Therefore, surveying regimes and conservation interventions should consider the whole impact face to be equally at risk after oblique impact in a conflict setting.

Figure 5.21: *Images showing that 5.56x45mm projectile impact at 45° excavate a longer, deeper crater across the sample than 7.69 x 39mm ammunition, damaging a wider area. Note the lead smearing (dark area) in the impact crater at the centre of the impact crater in the 7.62 x 39mm impact crater*

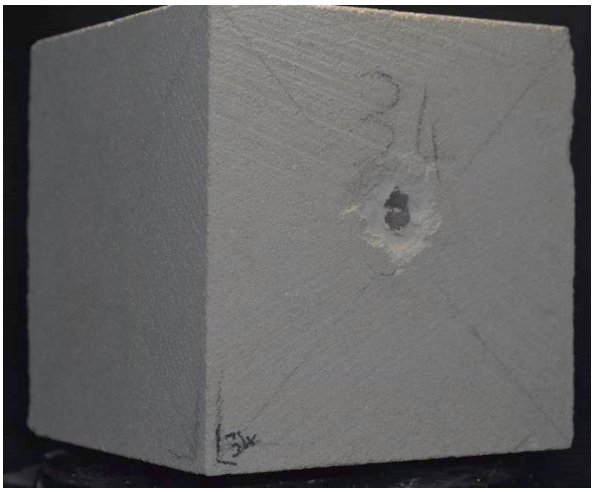

5.2.3.2: Permeability Results

As was the case for hardness loss, permeability increase was higher on the impact face than on non-impact faces for all shooting conditions and lithologies (figure 5.23).

Figure 5.23: *Charts showing permeability by sample surface and impact angle for both lithologies. Error bars are the standard error of the mean for the given data set.*

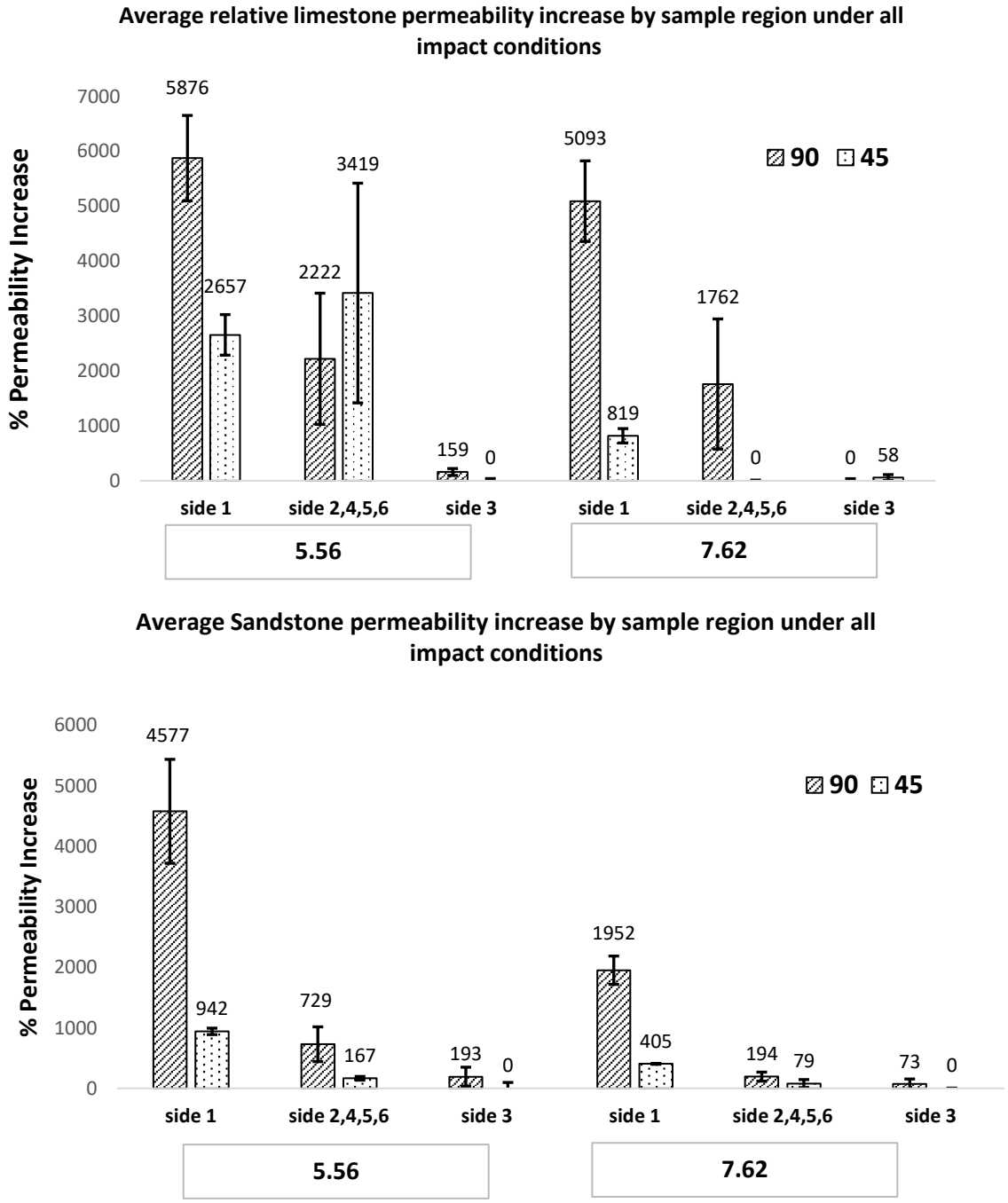

The fact that permeability increase is highest on the impact face is hypothesised to be because the impact face exhibits multiple spoke-like fractures emanating from the impact crater, whilst non-impact faces only exhibit surface fracture when fractures initiated at the impact crater are able to exploit sample defects to cause fracturing on non-impact surfaces. This means that all fractures on non-impact faces are initiated at the impact crater on the target face. This phenomenon was observed in many samples and shown in figure 5.24:

Figure 5.24: *Images showing preferential fracturing along defects in samples CHCL_36 and SRS_10 on Side 4 compared to side 2.*

CHCL_36 Side 4

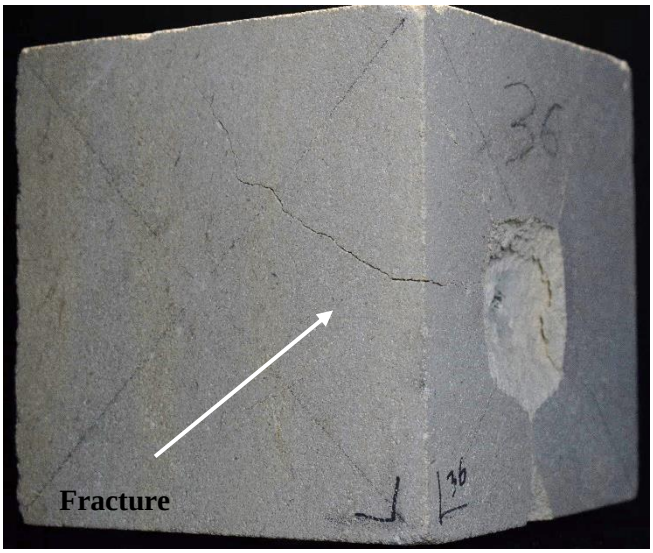

CHCL_36 Side 2

SRS_10 Side 4

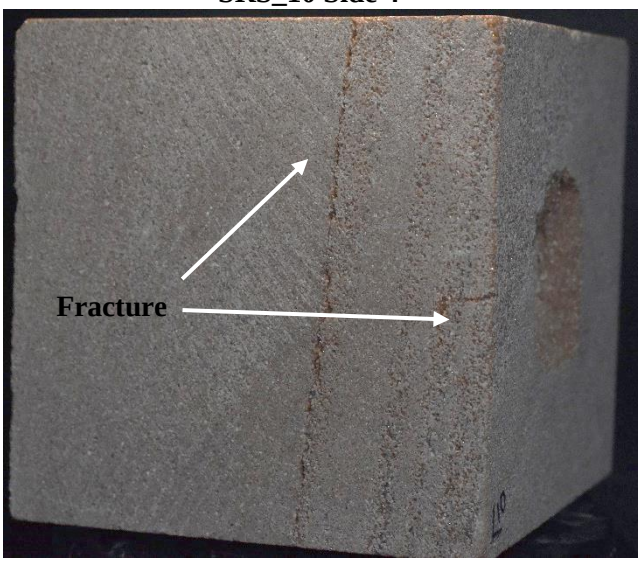

SRS_10 Side 2

These findings suggest that increases in permeability will likely be greatest on the impact face, as this is the case for all impact conditions except for 5.56 x 45mm impact into limestone at 45°. In this instance, the increase in permeability is higher than that on the impact face due to the removal of material and large surface fracture created on side 2 of sample CHCL_31, as discussed previously and shown in figure 5.24. Increases to permeability on those sides adjoining the impact surface are likely to be controlled by random defects in the individual blocks themselves which will be exploited by fractures propagating from the impact face as shown in figure 5.24. This is further evidence for the hypothesis described in section 5.2.2.3 that permeability is controlled by visible surface fractures propagating from the impact face. To test this hypothesis, each of the samples was visually assessed for visible surface fractures on non-impact faces propagating from the impact face. The number of non-impact faces with visible fracture networks was then plotted against the average permeability of the sides outside of the impact face. This is shown in figure 5.25:

Figure 5.25: *Average permeability of non-impact surfaces by number of non-impact faces with visible surface fracture. Limestone samples- A, Sandstone Samples- B:*

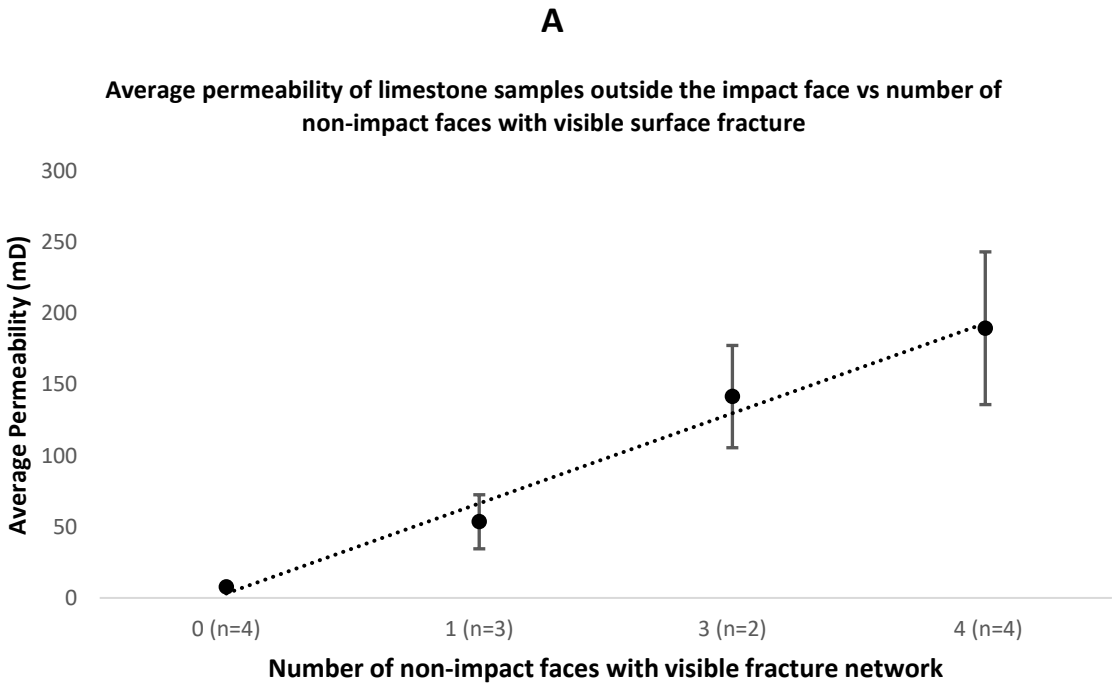

B

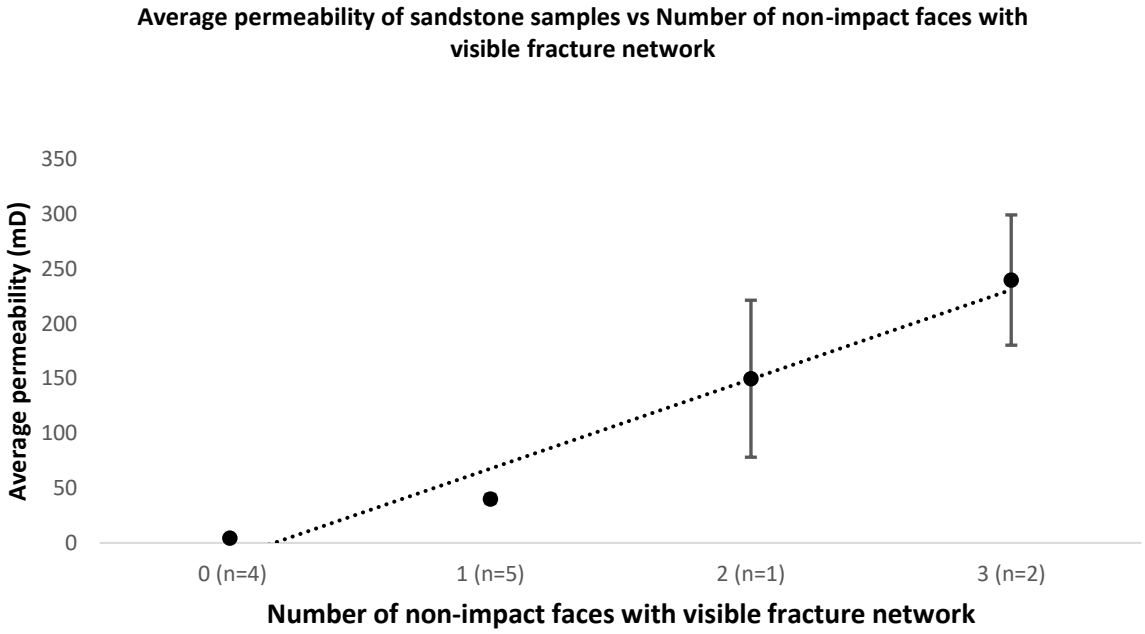

Figure 5.25 Shows that for samples with no fractures on non-impact faces, the permeability outside of the impact face is comparable to the control permeability of non-shot samples (limestone-7.8mD, control: 5.4mD sandstone-4.3 mD, control: 10.1mD). Conversely, for both lithologies, samples with three non-impact faces displaying surface fracture, permeability is in the region of 200mD and thus far higher than non-fractured control stone. This supports the hypothesis that permeability on non-impact faces is controlled by fractures initiated at the impact face. Finally, the permeability of side 3 sees no increase in permeability in three of the four impact conditions shown in figure 5.23, echoing the results of the surface hardness survey in determining that the surface opposite the impact face is usually least at risk of deterioration in the aftermath of ballistic impact.

Therefore, based on the results presented in figures 5.23 and 5.25, both in future conservation work and in the future experimental work of this PhD, intensive permeability survey should be targeted at the impact face, whilst permeability survey with less sampling points can be deployed on non-impact faces. This will allow monitoring of permeability changes due to weathering effects outside of the impact face, whilst still ensuring that data collection is rapid enough to be deployed in field setting. Intensive sampling of the impact face will ensure that high quality data is available for the areas of stone most likely to see a substantial change in

permeability due to impact induced fracturing, and permeability changes in the fracture network initiated at the impact face can be monitored.

It is worth noting that the spatial methods used to understand hardness data distribution in figure 5.20, which involve the aggregation of many data points for a given cell across multiple replicate samples, would likely not be appropriate for understanding distribution of fracture networks and associated permeability changes. This is because surface fractures that greatly increase permeability for individual cells are randomly distributed across sample faces based on lithological defects, and aggregating permeability data caused by these random fracture patterns is unlikely to yield useful spatial information.

ANOVA tests were conducted across both lithology types by ballistic variable (angle of impact and projectile) to determine which variables had statistically significant effects on permeability increase on the target face (where permeability increase was most pronounced) when altered. The results of these ANOVA tests for mean hardness loss are shown in table 5.9:

Table 5.9: *Results of ANOVA tests grouped by target lithology to determine which ballistic variables have a significant effect on relative permeability increase on impact face. Limestone: A. Sandstone: B.*

A

Tests of Between-Subjects Effects

Source	Type III Sum of Squares	df	Mean Square	F	Sig.
Corrected Model	21588711.68[a]	3	7196237.225	4.588	.038
Intercept	51114593.841	1	51114593.841	32.591	<.001
Bullet	3281560.870	1	3281560.870	2.092	.186
Angle	18306788.741	1	18306788.741	11.672	.009
Bullet * Angle	362.064	1	362.064	.000	.988
Error	12547008.984	8	1568376.123		
Total	85250314.500	12			
Corrected Total	34135720.659	11			

a. R Squared = .632 (Adjusted R Squared = .495)

B

Tests of Between-Subjects Effects

Source	Type III Sum of Squares	df	Mean Square	F	Sig.
Corrected Model	6777556.079[a]	3	2259185.360	2.685	.117
Intercept	12421285.355	1	12421285.355	14.764	.005
Bullet	2015249.084	1	2015249.084	2.395	.160
Angle	3879143.415	1	3879143.415	4.611	.064
Bullet * Angle	883163.580	1	883163.580	1.050	.336
Error	6730422.259	8	841302.782		
Total	25929263.693	12			
Corrected Total	13507978.338	11			

a. R Squared = .502 (Adjusted R Squared = .315)

As with hardness loss, for limestone samples, impact angle has a more significant effect than bullet type. Again, this is thought to be because because the limestone is weak enough that impact by either projectile causes fracturing and increased permeability.

However, 90◦ impact transfers more kinetic energy to the samples than 45◦, resulting in higher wave pressures that result in denser fracture network, in keeping with the findings from chapter 4.

Similarly, for sandstone samples, angle has a more significant effect (at 10% significance level) than bullet type. A possible explanation for this is that at 90◦ impact, fractures radiate in a spoke like fashion from the impact crater, resulting in greater fracturing across target surface than 45◦ impact which only "scrapes" the target surface. Therefore, even with steel-cored 5.56 x 45mm projectiles, which are more able to penetrate the sandstone samples, 45◦ may only result in a small increase in permeability. Therefore, impact angle has the most significant effect on increase in permeability.

As with the hardness survey, to determine the presence or absence of compaction at the impact point, the average permeability of the central impact point was compared with that of the 9 surrounding cells. As discussed in relation to figure 5.18, this analysis was conducted on the 12 samples that were shot at 90° because the irregularly shaped asymmetrical craters created by 45° impact were not appropriate for this analysis. The results are presented in figure 5.26:

Figure 5.26: *A comparison of the permeability of impact point and surrounding cells after 90° impact by lithology. Error bars are the standard error of the mean for each of the data sets listed.*

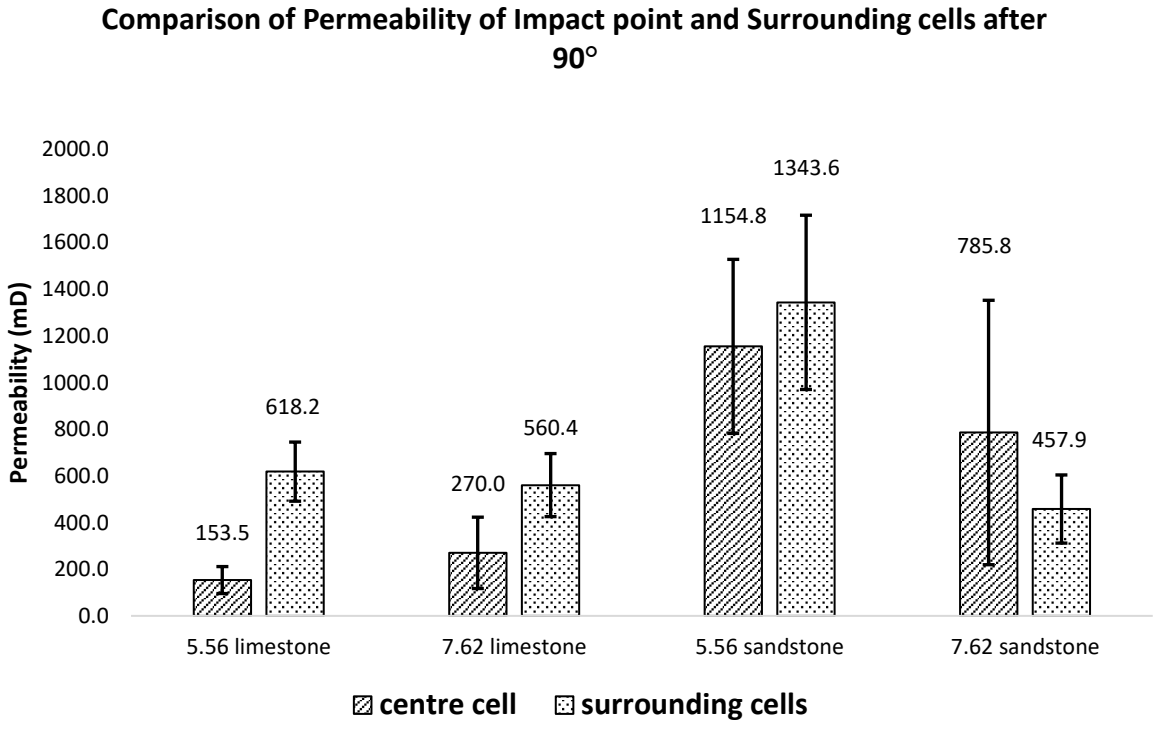

Unlike the results for surface hardness, there was a clear distinction between the two lithologies. For the limestone samples, the central impact point saw a much lower increase in permeability than surrounding cells, with no overlap between standard errors. This was not the case for sandstone samples, as after impact by 7.62 x 39mm projectiles, the increase in permeability is greater for surrounding cells, but within margins of error represented by the error bars, and after 5.56 x 45mm impact, the reverse is true with the centre cell most permeable, although still within margins of error. This distinction is believed to be a result of the matrix properties of the two stone types. Whilst the limestone samples consist of friable ooids which are crushed and easily compacted by the projectile impact, resulting in the permeability of central impact point being lower than surrounding un-crushed cells, the silicate crystals of the sandstone samples are not as easily compacted and therefore do not see lower permeability for the central cells after direct impact. This again highlights the importance of understanding lithological properties of damaged stone when seeking to understand the damage profiles caused by ballistic impact. This data also suggests that whilst compaction of the matrix may not be detectable using rebound hardness survey (figure 5.18), limestone samples may be compacted more at the centre of the impact crater than in the wider impact crater, and that this is detectable through permeability survey, highlighting the validity of employing multiple methods for assessing damage distribution on heritage surfaces in a field setting to ensure a holistic understanding of likely deterioration patterns, as compaction of the rock matrix at the impact centre may result in altered moisture flow and weathering behaviour as previously discussed (Mol *et al*, 2017).

5.1.3.3: UPV Results:

Figures 5.26 and table 5.10 show the results of UPV analysis by specific shooting parameters and the ANOVA analysis of individual variables.

Figure 5.27: *The effects of shooting conditions on decrease in average UPV. Error bars are the standard error of the mean for the given data set.*

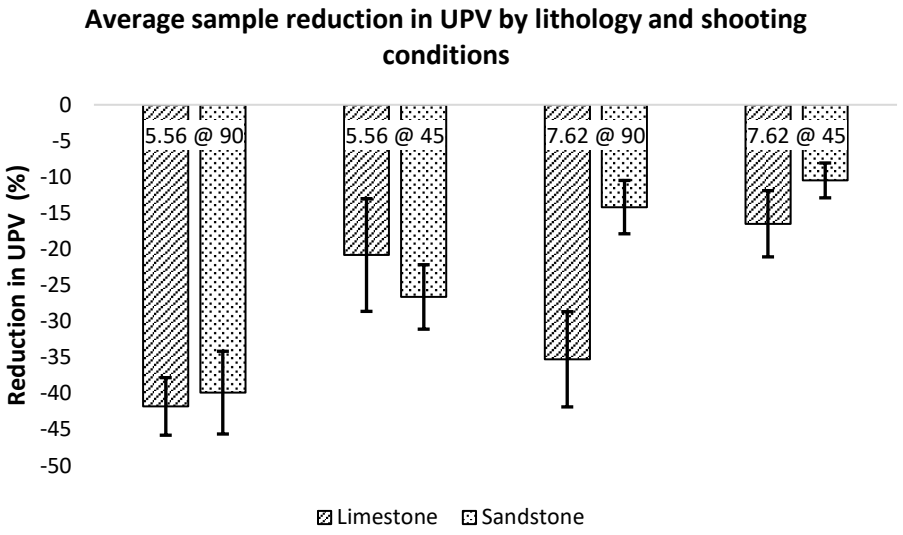

Table 5.10: *Results of ANOVA tests grouped by target lithology to determine which ballistic variables have a significant effect on average UPV decrease. Limestone: A. Sandstone: B.*

A

Source	Type III Sum of Squares	df	Mean Square	F	Sig.
Corrected Model	1277.775[a]	3	425.925	8.111	.008
Intercept	9809.147	1	9809.147	186.788	<.001
Bullet	88.458	1	88.458	1.684	.231
Angle	1185.683	1	1185.683	22.578	.001
Bullet * Angle	3.633	1	3.633	.069	.799
Error	420.119	8	52.515		
Total	11507.041	12			
Corrected Total	1697.894	11			

a. R Squared = .753 (Adjusted R Squared = .660)

B

Tests of Between-Subjects Effects

Dependent Variable: Hardness_Loss

Source	Type III Sum of Squares	df	Mean Square	F	Sig.
Corrected Model	1597.867[a]	3	532.622	36.017	<.001
Intercept	6233.429	1	6233.429	421.513	<.001
Bullet	1313.607	1	1313.607	88.828	<.001
Angle	215.729	1	215.729	14.588	.005
Bullet * Angle	68.531	1	68.531	4.634	.064
Error	118.306	8	14.788		
Total	7949.602	12			
Corrected Total	1716.173	11			

a. R Squared = .931 (Adjusted R Squared = .905)

The UPV results in figure 5.27 are in agreement with the results already presented with respect to changes in hardness and permeability. Impact by 5.56 x 45mm at 90◦ results in the largest reduction in UPV whilst 7.62 x 39mm impact at 45◦ causes the lowest reduction. This indicates that impact at 90◦ by 5.56 x 45mm ammunition causes substantially more internal fracturing of the impacted samples than an impact at 45◦ by 7.62 x 39mm ammunition, which in turn will correspond to greater risk of future deterioration.

For limestone samples, impact angle has a more significant effect than bullet type, again this is thought to be because because the limestone is weak enough that impact by either projectile causes internal fracturing and resulting reduction in UPV. However, 90◦ impact transfers more kinetic energy to the samples than 45◦, resulting in higher wave pressures that result in denser fracture network, in keeping with the UPV findings from chapter 4.

For sandstone samples, both bullet and angle have a significant effect (.0.05). For the harder sandstone samples which are more easily penetrated by steel-cored 5.56 x 45mm ammunition than lead-cored 7.62 x 39mm ammunition, this is to be expected; a harder bullet impacting at 90◦ will transfer more kinetic energy, creating higher stress wave pressures and thus result in more internal fracturing of the sample.

5.2.3.4: Photogrammetry analysis results, Changes to surface area and volume

Results of photogrammetric analysis of the area of the impact crater are shown in figure 5. 28.. The results demonstrate that 5.56 x 45mm ammunition creates a larger damaged area on average. 5.56 x 45mm ammunition at 45◦ creates the largest average crater but this is a result of the very large damaged area (108cm^2) created on sample CHCL_31 (figure 5.14). As a result of this large damaged area on one sample, the results for impacts at 45◦ are highly variable (as seen in the error bars) and should be treated with some caution, but do support the hypothesis put forward in chapter 4 that 45◦ has the potential to cause damage over a larger area than 90◦. Although this is not the case for most impacts generated in these experiments, it demonstrates the importance of determining whether an oblique impact has caused damage and material loss to non-impact faces when assessing risk to heritage buildings in a field setting.

Figure 5.28: *The effects of shooting conditions on average impact crater area. Error bars are the standard error of the mean for the given data set.*

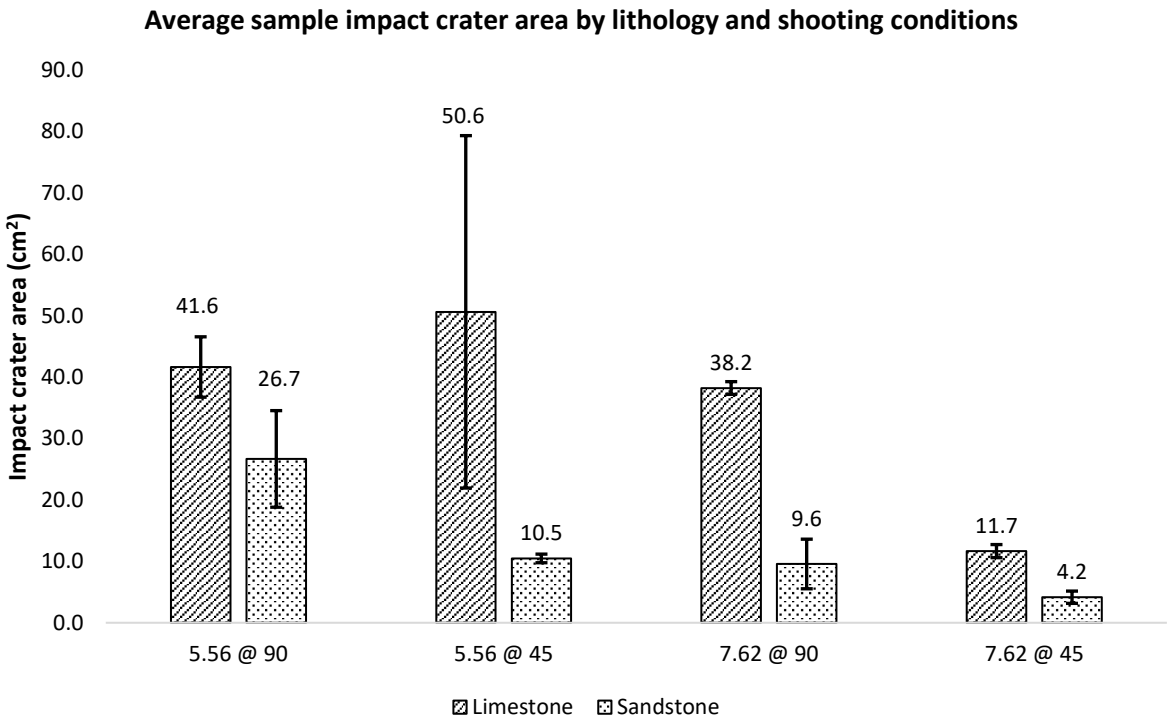

Table 5.11: *Results of ANOVA tests grouped by target lithology to determine which ballistic variables have a significant effect on impact crater area. Limestone: A. Sandstone: B.*

A

Tests of Between-Subjects Effects

Source	Type III Sum of Squares	df	Mean Square	F	Sig.
Corrected Model	2526.468[a]	3	842.156	1.322	.333
Intercept	15157.724	1	15157.724	23.790	.001
Bullet	1347.404	1	1347.404	2.115	.184
Angle	231.831	1	231.831	.364	.563
Bullet * Angle	947.233	1	947.233	1.487	.257
Error	5097.096	8	637.137		
Total	22781.288	12			
Corrected Total	7623.564	11			

a. R Squared = .331 (Adjusted R Squared = .081)

B

Tests of Between-Subjects Effects

Dependent Variable: Hardness_Loss

Source	Type III Sum of Squares	df	Mean Square	F	Sig.
Corrected Model	849.106[a]	3	283.035	4.740	.035
Intercept	1942.148	1	1942.148	32.522	<.001
Bullet	411.472	1	411.472	6.890	.030
Angle	350.393	1	350.393	5.867	.042
Bullet * Angle	87.242	1	87.242	1.461	.261
Error	477.746	8	59.718		
Total	3269.001	12			
Corrected Total	1326.853	11			

a. R Squared = .640 (Adjusted R Squared = .505)

Results of the ANOVA analysis suggest that for limestone samples, neither variable seems to have a significant effect, suggesting that impact under any condition will result in substantial impact cratering in this lithology, as demonstrated by the data presented in figure 5.28, with similar impact crater sizes for limestone samples impacted under a variety of impact conditions (5.56 @ 90: 41.6cm^2, 5.56 @ 45: 50.6 cm^2, 7.62 @ 90: 38.2cm^2). It is hypothesised that the size of impact crater in limestone due to ballistic impact is more likely

to be controlled by random defects in the sample itself such as bioclastic inclusions which introduce large areas of inhomogeneity in the matrix (Building Research Establishment, 1999a).

However, for sandstone samples, where 7.62 x 39mm projectiles cause very little cratering (see figure 5.13), both variables are significant. This is consistent with expectations as 90◦ impact transfers more kinetic energy to the samples than 45◦, resulting in higher wave pressures that eject more material and excavate a larger impact crater (section 1.4).

Finally, it was hypothesised that the area of an impact crater may be a useful proxy measurement for other damage parameters, such as increase in permeability or decreases in surface hardness. This is because a larger impact crater indicates that more kinetic energy has been transferred to a block of a given lithology, and therefore more fracturing may have occurred across the sample which would increase permeability and lower hardness. It is self-evident that a larger impact crater with associated fracture networks and matrix disaggregation will result in a higher permeability and lower surface hardness than a smaller impact crater on the impacted face. That is to say that it is self-evident that impact crater size will be correlated with permeability increased on the impact face, and therefore the relationship was tested for the average of all the samples' surfaces. To test this, calculated impact crater area was plotted against relative increase in permeability and relative decrease in surface hardness. The results are shown in figures 5.29 and 5.30.

Figure 5.29: *Decrease in Hardness across whole sample plotted against Impact crater area.*

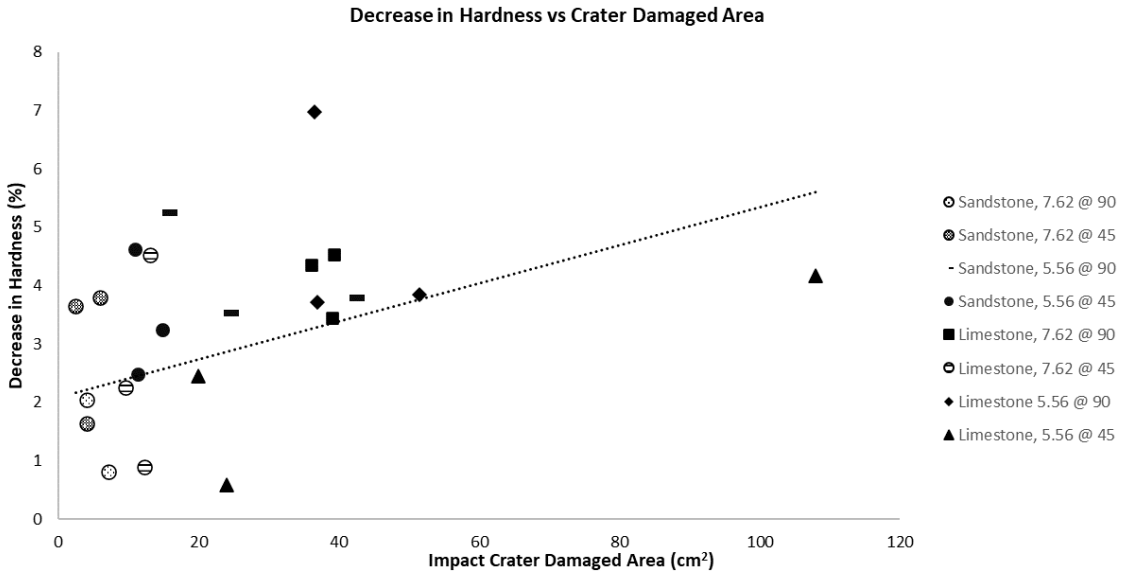

Figure 5.30: *Increase in Permeability across whole sample plotted against Impact crater area.*

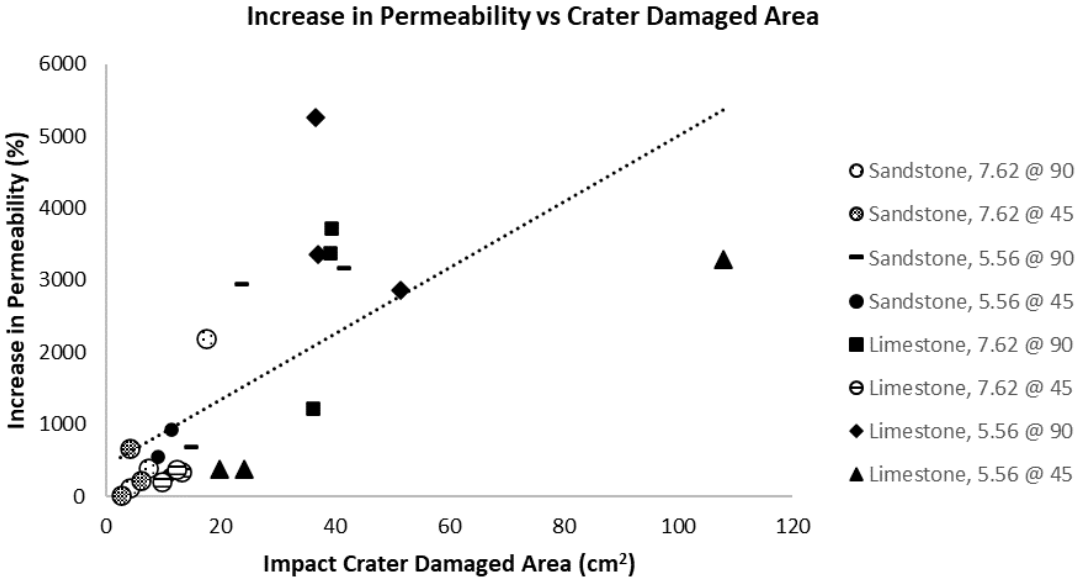

Figure 5.29 shows that there is only a weak, but significant (correlation between reductions in hardness and impact crater area (correlation coefficient = 0.39 significance level 10 %, p = 0.058). However, the association between increase in permeability and impact crater area is considerably stronger and also statistically significant (figure 5.30, correlation coefficient 0.68, p = 0.00024). This is likely due to a large impact crater being associated with a wider surface fracture network which is detectable through permeability survey. This finding is

supported by work by Ahrens *et al,* (2002) who noted that the depth/extent of fracture damage is proportional to the size of the impact crater. This finding is also consistent with the finding in chapter 2 that the size of ballistic damage area is correlated with increases in permeability (figure 3.17). This raises the prospect that future risk assessments of stone-built heritage damaged in conflict could us measurements of impact crater area as a quick and efficient way of estimating the increased permeability of a given damaged site, and thus its elevated risk of future deterioration caused by ingress of weathering agents. Figure 5.30 is also further evidence that permeability is controlled by visible surface damage and fracture propagating from the impact face, as discussed in section 5.2.3.2.

5.2.4: Discussion of significance of results

The results presented here have clearly demonstrated that the ballistic parameters under which a block is impacted alter the levels of damage, as determined through a variety of measurements, and that the results are consistent across all these measurements. For almost all the techniques used (hardness survey, permeability survey, and UPV analysis). 5.56 x 45mm impact at 90◦ was found to cause the greatest damage, with the greatest damage invariably occurring on the impact face for hardness and permeability surveys. This is shown by the fact that these shooting parameters have the highest loss of hardness (figure 5.13), highest increase in permeability due to surface fracturing (figure 5.23), and highest reduction in UPV due to internal fracturing (figure 5.27). 5.56 x 45mm impact also caused the greatest loss of volume and area of impact crater at 45◦ due to the large damaged area created on sample CHCL_31 (figure 5.15).

By separating the variables of impact angle and ammunition type using ANOVA analysis, it was determined that the most important variable varied by greatly by lithology and across the metrics used to assess damage. To summarise this, a table was created to show which variables were found to be significant under which conditions:

Table 5.12: *Showing which ballistic variables were found to have a significant effect on the various metrics of damage on the impact face. An "x" indicates that the given variable has a significant effect under the shooting conditions given for the given metric.*

		Angle	Bullet
Hardness Loss	Limestone	x (p = 0.02	
	Sandstone		x (p = 0.03)
Permeability Increase	Limestone	x (p = 0.009)	
	Sandstone	x p = (0.064)	
UPV Decrease	Limestone	x (p = 0.001)	
	Sandstone	x (p = <0.005)	x (p = 0.005)
Impact crater area	Limestone		
	Sandstone	x (p = 0.03)	x (p = 0.042)

Broadly speaking, angle was found to be the most important variable for impacts into limestone, because limestone was substantially damaged by both projectile types, whilst the harder sandstone was much less damaged by lead cored 7.62 x 39mm ammunition and therefore ammunition type became the most significant variable for this lithology.

When combined with the results from section 5.1, which found that lithologies with low stress wave impedance (limestone) suffer far more damage under the same impact conditions as lithologies with high stress wave impedance the results presented in section 5.2 allow the construction of a simple qualitative risk index. The reasoning for the relative weighting of the factors in this risk matrix is outline below:

- Lithology and its interaction with stress waves generated through impact should have greatest weighting- it results in wildly different sample damage and controls which variables are most important. The response of a given lithology to ballistic impact is controlled by its stress wave impedance, which is dictated by properties such as density, porosity and compressive strength as outlined by Zhang, Hou and Aladejare (2020).

- Impact angle should be considered the next most important factor- it is most often a significant variable in the ANOVAs conducted above, and in a worst-case scenario of a weak lithology it has a greater influence than bullet type (see ANOVA's for limestone above).

- Bullet type is least important because these other variables are weighted higher.

The risk index details the broad categories of ballistic impact and determines relative risk. This is modelled on the qualitative indices detailed in section 1.12, and partially fulfils Research Objective IV of this thesis by creating a risk index for the damage caused in the immediate aftermath of ballistic impact. The proposed index is shown below:

Table 5.13: *Proposed risk index for ballistic damage to stone. This is an example with a hypothetical steel projectile impacting a high wave impedance rock at a normal angle.*

			Score
Target lithology	High Wave Impedance	0	0
	Low Wave Impedance	3	
Impact Angle	Oblique	0	2
	Normal	2	
Projectile construction	Lead	0	1
	Steel	1	
			Total
			3

Total Score

6:	Very High Risk
5:	High Risk
3-4:	Moderate Risk
0-2:	Low Risk

For each of the conditions of impact positively identified, conservation experts in the field would give a corresponding score in the right-hand column, which is left blank. The total score across the variables determines the risk for a given damaged heritage monument.

The numerical values for risk are designed to give those impacts with a higher number of risk factors and those impacts with the risk factors with the greatest weighting according to the rational laid out above a higher score. The weighted scale of 0-3 for the individual risk factors, and the assigning of numerical values to qualitative factors of a ballistic impact, such as projectile construction, is inspired by the structure of risk matrices already used in the conservation of stone heritage, such as the Rock Art Stability Index (Dorn *et al,* 2008). Specifically, the number of categories is dictated by the number of risk variables (lithology, impact angle, projectile construction) and the weight given to each category is dictated by the relative risk posed by the presence of that variable (i.e., as discussed, a weak target lithology is a bigger risk factor than projectile construction). Furthermore, in keeping with Dorn *et al,* (2008) a 0 is assigned to those risk factors which are not present at the site. In this way, the risk index proposed here follows similar numerical reasoning to risk indices for at-risk heritage stone already accepted in published literature (Dorn *et al,* 2008 Fitzner, Heinrichs and La Bouchardiere, 2002).

In a field setting, conservation experts would be trained to determine the stress wave impedance of a target lithology using reference data for relevant lithologies on compressive and tensile strength, porosity and density of stone, and combine this with data obtained in the field on likely ammunition types used and angles of impact based on crater morphology (i.e. oblique angles are often elongated, see figure 5.21). Work on comprehensive data bases of geotechnical data for stone types of particular heritage significance has already been discussed Cooper *et al* (2013), and such resources could be integrated into conservation responses to armed conflicts. This would be a quick and effective way of determining likely risk to damaged heritage buildings, and could be supplemented with targeted field measurements of rebound hardness and permeability to confirm likely areas of elevated risk of future deterioration due to weathering etc. In an instance where a variable such as projectile construction is unknown, the cautionary principle should be employed, and the highest possible score should be allocated for that variable. It is worth nothing that this risk matrix will be further refined to include results and findings from weathering experiments in future chapters of this thesis to construct a matrix that considers weathering factors in a field setting as well.

The distribution of damage to samples analysed in figures 5.13 and 5.23 illustrates that surfaces opposite the impact face usually experiences the least damage, due to wave attenuation increasing with distance resulting in reduced damage further from the impact point (Mitani, 2003, Kato *et al*, 2001). However, figure 5.13 suggests that oblique angle may result in increased weakening on this surface under certain circumstances, and therefore conservation professionals in a field setting should seek to determine angle of impact where possible and employ appropriate sampling regimes. It should be noted, that as described by Gault (1973), the closer to normal the impact, the more kinetic energy is imparted to the target. Therefore, impacts at angles greater than 45° may result in more damage than was observed in this study, and this could be the focus of future research in this field and refinement of the risk matrix.

Another useful outcome of these results is the likely correlation between impact crater area and the increase in permeability across the sample as a whole. This finding could be deployed in the field by conservation experts using rapid measurements of crater areas collected via non-destructive photogrammetry. This data could then be used to identify damaged areas most likely to have increased permeability and risk of exacerbated weathering. Photogrammetry analyses of the geometry of cavernous weathering features such as tafoni is already used in conservation science for rock art sites and could easily be adapted for recording ballistic impact craters (Sampietro-Vattuone, Pena-Monne, 2021). Furthermore, the Excel based approach has proven to be an effective way of understanding hardness data spatially (figures 5.11, 5.20) and could therefore be used to rapidly assess damage distribution by in-field conservation professionals in order to quickly identify specific portions of damaged stone most weakened by impact and in need of targeted intervention. Analysis of the distribution of surface fractures and associated increases in permeability on non-impact faces has further contributed to the development of effective field methods for studying ballistic damage by showing that permeability survey should target the impact face of the damaged stone to understand the fracture network that propagates to other faces. On non-impact faces it will be sufficient to reduce sampling points to monitor changes in permeability caused by weathering processes whilst also ensuring that data collection is not so time intensive as to be ineffective.

Finally, the results of this section appear to show that compaction of the stone matrix does not invariably lead to raised hardness at the centre of the impact crater relative to the surrounding area, and that under certain parameters this does not occur. However,

permeability results from the limestone samples do suggest that compaction of the limestone matrix by ballistic impact leads to a reduction in permeability at the centre of the impact crater relative to the surrounding area. This compaction and reduction of permeability at the central impact point could affect weathering behaviour by altering moisture flow patterns in the limestone samples, as outline by Mol *et al* (2017).

5.2.5: Conclusions

The results of this set of experiments have shown categorically that lithology, angle of impact and impacting ammunition type are critical in determining the levels of damage sustained by stone undergoing ballistic impact. Target lithology is less damaged when it has higher wave impedance (controlled by density, porosity, tensile strength and compressive strength). Projectiles constructed from harder materials are more likely to penetrate the target stone and cause more damage, and 90◦ impacts cause higher strains to the target surface and result in greater impact than oblique impacts.

These findings have implications for the identification and treatment of stone-built heritage damaged by ballistic impact and have been used to construct a simple risk matrix which will allow for rapid assessment of areas of risk in the field. Furthermore, this chapter has served to work towards fulfilling Research Objective II and IV of this thesis:

Research Objective II: *To use the methods developed under Research Objective I to compare and isolate the effects of changing calibre, angle of impact and target stone type on the damage caused by ballistic impact.*

Research Objective IV: *To use statistical analysis of results from weathering experiments on stone samples impacted under differing ballistic conditions to construct a risk index that can be used to assess the level of risk to damaged stone based on information on target lithology, ammunition, impact angle.*

Chapter 6

Effects of ballistic variables on weathering deterioration to target stone

Chapter 6 Overview

Chapter 6 aims and hypotheses

To assess the effects of changing the following variables on the extent of weathering deterioration following ballistic impact into stone:

- Lithology
- Ammunition
- Angle of Impact

It was hypothesised that the greater damage caused to samples by 5.56 x 45mm impact at 90° described in chapter 5 would result in larger and more connected fracture networks throughout the samples that results in increased weathering deterioration due to greater moisture mobility and salt crystallisation levels. It was also hypothesised that limestone samples, which were more damaged than sandstone samples in chapter 5, would exhibit greater weathering deterioration for the same reasons.

Chapter 6 methods

The shot samples from chapter 5 were artificially weathered using a weathering regime designed to simulate haloclasty weathering by NaCl in an arid environment. The effect of impact angle and ammunition type on deterioration was then investigated using measurements of rebound hardness, permeability and ultrasonic velocity. Photogrammetric models were also created for each sample after weathering to assess volume change due to matrix loss and efflorescence.

Chapter 6 principal findings

As in chapter 5, findings suggest that the single most important variable is the target lithology, with limestone samples exhibiting greater loss of hardness than sandstone samples and greater increases in permeability. Results also suggest that ballistic impact and associated fracture network around the impact crater may act to concentrate weathering damage on the

impact face, resulting in lower weathering deterioration on non-impact surfaces for certain lithologies. Finally, results show that impacts at 90◦ result in greater weathering deterioration than impacts at 45◦. Analysis of these variables and their effects on damage sustained were used to further refine the risk matrix developed in chapter 5 to take account of the effects of haloclasty weathering after ballistic impact.

6.1: Introduction

As discussed in all the previous chapters of this thesis, and demonstrated experimentally in chapters 3 and 4, it is believed that the fracture networks induced in stone by ballistic damage influence and exacerbate the weathering deterioration experienced by stone after impact. The experimental work of this chapter was therefore conceived in order to elucidate how the ballistic variables explored in chapter 5 (lithology, projectile, impact angle) influenced the patterns of weathering deterioration following ballistic impact. The aim was to identify the extent to which individual impact variables and combinations of impact variables contribute to the subsequent weathering deterioration of stone so that the risk matrix outlined in chapter 5 could be updated to include weathering risks to stone-built heritage damaged in conflicts. This would fulfil Research Objective IV outlined in chapter 1, and ultimately could be used by conservation professionals in a field setting to assess and mitigate long-term deterioration risks confronting conflict damaged heritage sites.

6.2: Methods

6.2.1: The weathering regime

To ensure that the weathering regime reflected real-world conditions as closely as possible, temperature data was obtained from a heritage site in a MENA region damaged by armed conflict; the Roman amphitheatre at Sabratha. The site history and the field investigations at Sabratha are the subject of chapter 7 of this project, forming a field-based assessment of the validity of the conclusions and methods developed throughout the experimental sections of this PhD. As such, the methods deployed, including those for temperature monitoring, are discussed in greater detail there. Temperature data was obtained from thirty locations around the site over a 72-hour period in July 2021 using Ibutton temperature sensors collecting data every 15 minutes (see appendix B). temperature data for summer was used to construct the

heating regime because higher temperatures will facilitate greater haloclasty weathering through greater evaporation of saline water precipitating greater volumes of salt on the samples.

The data from the sensor with the maximum diurnal temperature fluctuation was used as the basis for the weathering regime to simulate the effects of salt weathering on conflict damaged heritage stone in a highly exposed MENA region (i.e., without shading to protect from temperature fluctuation). This data was used to create the following heating and cooling regime:

Figure 6.1: *24-hour heating cycle of the simulated weathering regime*

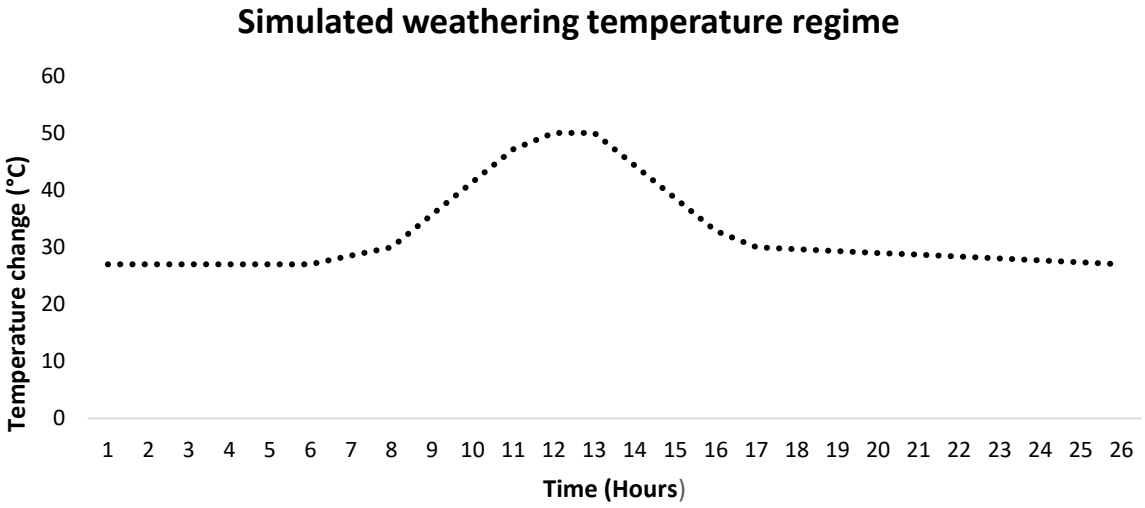

Using this heating regime, all of the shot samples from chapter 5 as well as three un-shot control samples of both lithologies were artificially weathered in an Atlas SC1000 Environmental test chamber. Samples were placed in trays with Saturated NaCl solution at their base, and temperature was set at 54% relative humidity, which is the relative humidity of the Sabratha site in July as reported by Abdalahh (2011). The saline solution was topped up at the beginning of each 24-hour cycle, and the regime was continued for 340 hours (two weeks). This is a sufficient period to simulate salt weathering deterioration in heritage stones over a long period in a "real-world" scenario, given the presence of abundant saline solution in the laboratory environment, as demonstrated by Aly *et al*, (2015). Samples were placed in the environmental cabinet in the same orientation as when they were shot (i.e. side 6 facing downwards).

6.2.2: Data collection

After weathering, photogrammetry was undertaken using the same methods outlined in chapters 3 and 5 to assess change in sample volume due to efflorescence of NaCl crystals. After photogrammetry was complete, efflorescence was removed by brushing so that the properties of the stone surface could be assessed.

Hardness survey and UPV analysis were undertaken on the cleaned sample using the same sampling regimes outlined in section 5.2.2.3.

Section 5.2.3.2 demonstrated that permeability survey in a field setting could be expedited by intensive sampling on the impact face, which is the initiation point of surface fracture networks which cause large increase in permeability. Therefore, a permeability regime was used which would most closely mirror that advised for rapid assessment in a field setting. All of the 49 cells of the impact face were sampled for permeability, as outlined in section 5.2.2.3. On non-impact faces, six cells were sampled that would intersect with the sampling regime previously used in chapter 5 (figure 5). In this way, increases in permeability on non-impact faces after weathering compared to shooting could be monitored. This permeability regime would provide 79 for each sample, and a statistically significant number of data points for non-impact faces (30 non-impact face data points for each sample, 90 data points across the triplicate samples of each combination of lithology, projectile and impact region).

Figure 6.2: *The sampling regime for permeability survey on non-impact faces of weathered samples*

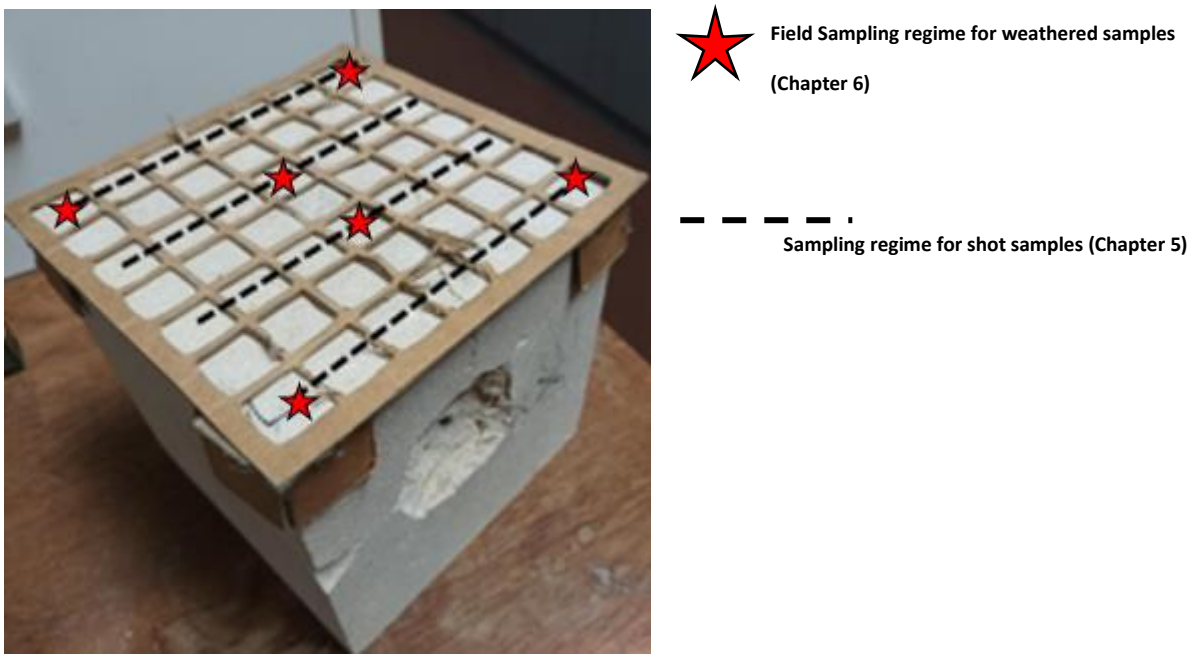

6.3: Results and interpretation

6.3.1: Hardness results

The impact face of the six samples used in chapter 5 to determine how lithology affects the damage of ballistic impact were compared again after weathering. Figure 6.3 shows that overall, haloclasty weathering has produced greater loss of hardness than shooting alone, and sandstone samples see a lesser reduction in hardness across both shooting and weathering, as was hypothesised (limestone: - 22% sandstone: -14%).

Figure 6.3: *Relative change in hardness for samples shot with 7. 62 x 39mm ammunition at 200m after shooting and weathering compared to intact hardness. N.B. samples do not have a standard error bar as it is not possible to calculate standard error for relative change on a single sample.*

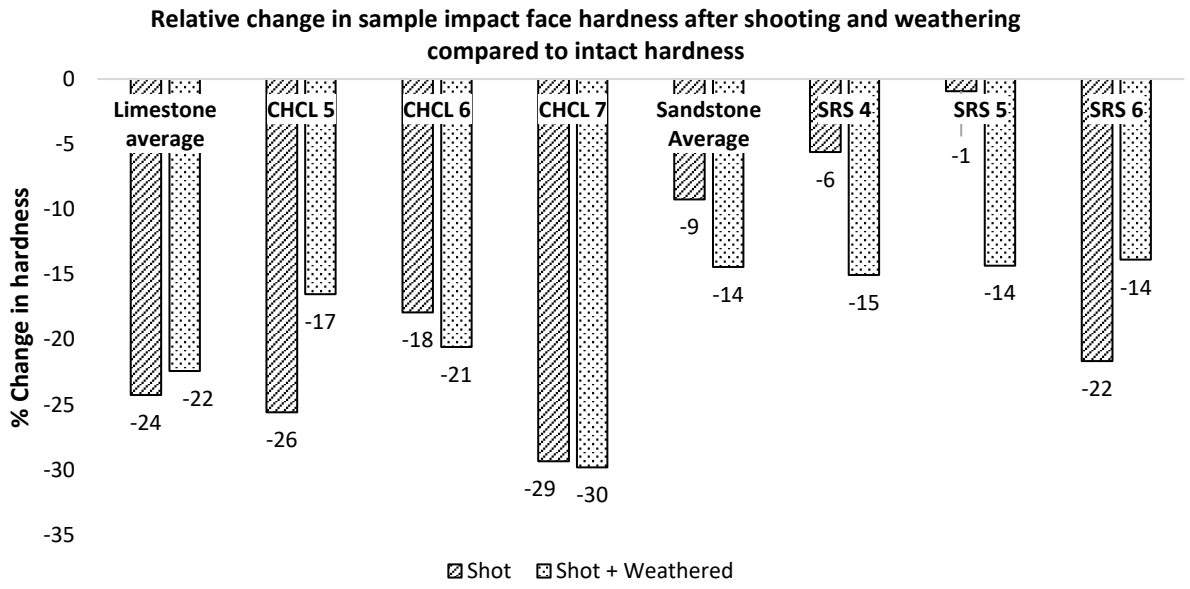

However, both samples CHCL 5 and SRS 6 see a net increase in hardness after weathering compared to their shot hardness (CHCL 5: +9%, SRS 6: + 8%). These two samples were also the samples that experienced the greatest loss of hardness of their respective lithologies after shooting, as shown in figure 6.3, with SRS 6 undergoing a much greater loss of hardness after shooting than samples SRS 5 and SRS 6 (-22% reduction in hardness of SRS 6 after shooting vs average sandstone reduction of -14%). It is hypothesised that for these samples, the initial

ballistic impact led to severe disaggregation of the sample surface, and that the weathering process then led to the removal and/or consolidation of this disaggregated surface, resulting in a net increase in hardness after weathering when compared with the shot stone.

This hypothesised removal of stone material weakened by ballistic impact due to weathering processes was supported by field observations discussed in section 3.4.1. Published work has also demonstrated that weakened stone matrix is removed due to weathering processes, both in field studies (Knight and Burningham, 2020) and in laboratory experiments (Porter *et al*, 2010). In both studies, the removal of weakened surface material from the stone surface resulted in increased hardness measurements. Furthermore, the ability of salt weathering to contribute to the removal of weakened matrix material from rock surfaces has been demonstrated by Mottershead and Pye (1989, 1994). Given these findings in other works, it is plausible that haloclasty processes are responsible for removing enough weakened material from the samples most severely damaged by the initial ballistic impact to cause a relative increase in hardness after weathering.

It is also possible that for some samples, hardness is increased due to deposition of salt crystals in ballistic fracture networks increasing compressive strength. NaCl crystals filling and sealing fractures in rock has been observed experimentally by Renard *et al* (2009), whilst increases to compressive strength (which is correlated with surface hardness as shown by Aoki and Matsukura, 2008) was observed by Manohar *et al* (2020) in measurements of NaCl weathered heritage stone as well and in laboratory experiments by Zheng *et al*, (2015). If NaCl crystallisation within fracture networks is the cause of the increase in hardness of these samples, it appears to be the result of random defects/fracture networks in the weathered stone, as the majority of samples exhibit hardness loss after weathering, and therefore is likely not a consistent behaviour after ballistic impact.

As discussed in section 5.1.2.1 and 5.1.4, the massive loss of material from limestone samples shot at a range of 200m prevented any data collection from non-impact faces. Therefore, to analyse data on the effects of weathering on non-impact faces we must consider the cratered samples discussed in section 5.1.2.1. The hardness loss from each sample surface for these samples is presented in figure 6.4, again grouping the surfaces by impact face, impact face adjacent, and opposite the impact face, as discussed in section 5.2.3.1

Figure 6.4: *Charts showing decrease in surface hardness by sample surface and impact angle for both lithologies. Error bars are the standard error of the mean for the given data set.*

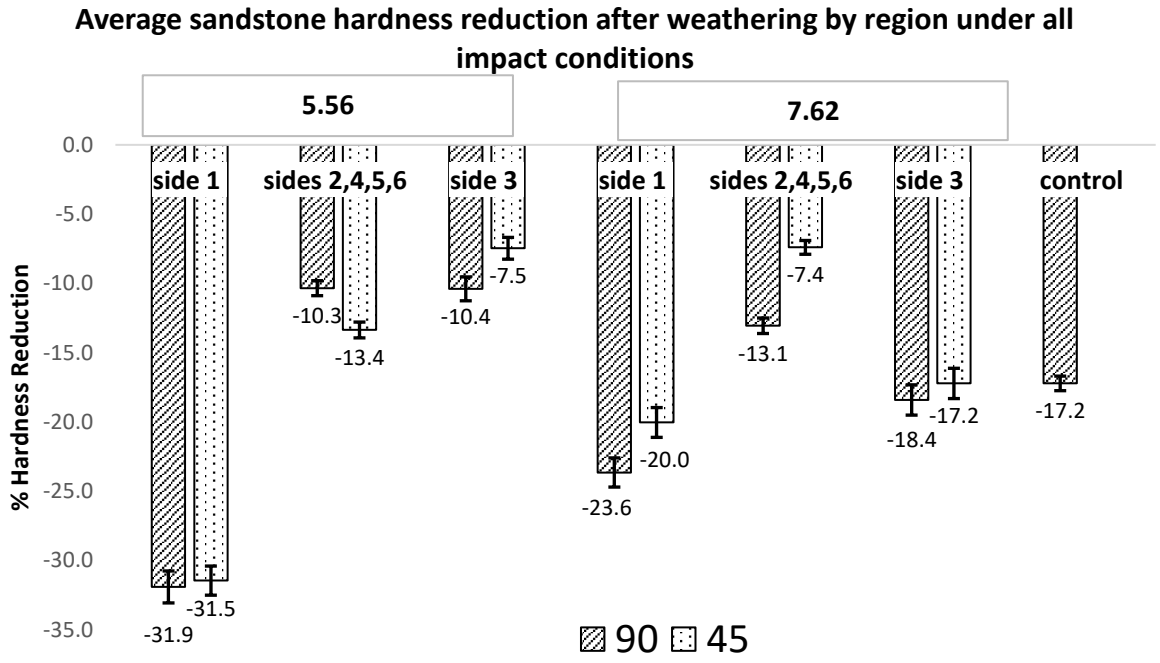

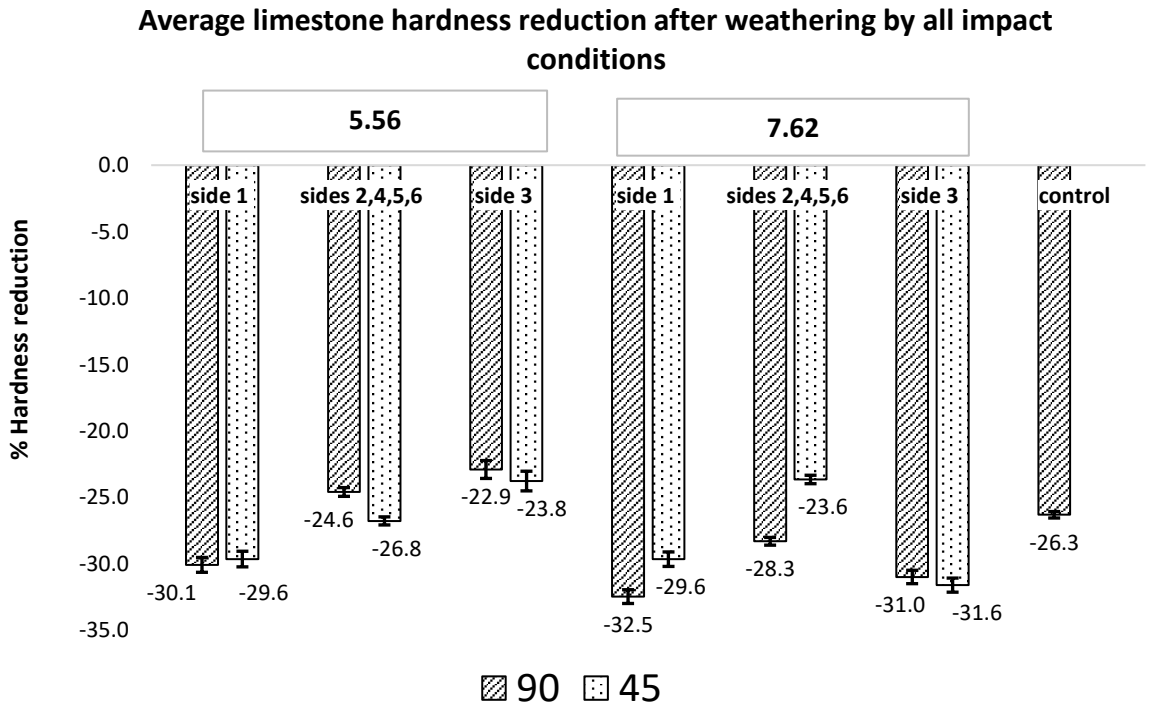

As figure 6.4 shows, hardness loss after weathering is most pronounced on the impact face as opposed to non-impact faces for both lithologies under most impact conditions and is considerably higher than hardness loss in the control samples, suggesting that ballistic impact exacerbates weathering deterioration on the impact face.

Interestingly, on non-impact faces hardness loss after weathering is often less than the un-shot control samples (e.g. limestone control hardness loss is -26.3%, side 3 of limestone samples shot by 5.56 x 45mm sees a hardness loss of -22.9%). This suggests that the fracture network induced by ballistic impact may not increase weathering deterioration in all areas of the affected sample but concentrate it on the impact face. This is hypothesised to be due to the fracture network that propagates from the impact crater facilitating the transport of moisture and salt to the impact face preferentially and thus diverting it from the non-impact faces. The exception to these observations is limestone samples shot by 7.62 x 39mm ammunition at 45°. These impact conditions see a slightly larger hardness loss on side 3 than the impact face (-31.6% vs -29.6% for the impact face). Given that these shooting conditions also induced the smallest loss of hardness of any impact on the impact face after the initial shooting (only -1% compared to intact hardness, see figure 5.13) this anomaly is hypothesised to be due to an insufficient fracture network induced on the impact face to cause exacerbated deterioration on this surface after weathering. This would explain both the small reduction in hardness after shooting and the anomalous hardness loss after weathering.

Evidence supporting the interpretation that fracture networks induced by ballistic impact act to concentrate weathering deterioration on the impact face is provided by laboratory studies undertaken by McCabe *et al* (2010), which demonstrated that pre-existing fracture networks in stone caused by fire fatiguing and detected using UPV techniques were exploited by subsequent salt weathering to exacerbate deterioration and weakening. Preferential exploitation of fracture networks by NaCl crystallisation was also demonstrated experimentally by Renard *et al* (2009), who used microscopy of stone samples with induced fracture networks and subjected to NaCl weathering to demonstrate how the salt crystallisation process propagates a network of secondary fractures which further weaken the stone. The findings of these studies support the hypothesis that the fracture networks induced by the ballistic impact at the impact face are subsequently exploited by NaCl crystallisation to cause the most severe weakening and hardness reduction on the impact face of the sample. This hypothesis has been further supported by recent experimental findings from Campbell *et al* (2022), which used thin section microscopy to show that after ballistic impact, the area

around the impact crater on the impact face experiences the most intense fracturing and will thus be most susceptible to subsequent exploitation and weakening by salt crystallisation.

Given that hardness loss due to weathering is focussed at the impact face, the effect of combinations of ballistic variables on the impact face across all of the samples was analysed using ANOVA.

Table 6.1: *Results of ANOVA tests grouped by target lithology to determine which ballistic variables have a significant effect on relative hardness loss on impact face after weathering. Limestone: A. Sandstone: B.*

A

Tests of Between-Subjects Effects

Source	Type III Sum of Squares	df	Mean Square	F	Sig.
Corrected Model	180.258[a]	3	60.086	1.727	.239
Intercept	10134.636	1	10134.636	291.272	<.001
Bullet	53.040	1	53.040	1.524	.252
Angle	84.128	1	84.128	2.418	.159
Bullet * Angle	43.090	1	43.090	1.238	.298
Error	278.355	8	34.794		
Total	10593.250	12			
Corrected Total	458.613	11			

a. R Squared = .393 (Adjusted R Squared = .165)

B

Tests of Between-Subjects Effects

Source	Type III Sum of Squares	df	Mean Square	F	Sig.
Corrected Model	254.378[a]	3	84.793	1.905	.207
Intercept	5803.731	1	5803.731	130.373	<.001
Bullet	222.617	1	222.617	5.001	.056
Angle	31.177	1	31.177	.700	.427
Bullet * Angle	.584	1	.584	.013	.912
Error	356.130	8	44.516		
Total	6414.239	12			
Corrected Total	610.508	11			

a. R Squared = .417 (Adjusted R Squared = .198)

The ANOVA analysis in table 6.1 suggests that for limestone samples neither ballistic variable seems to have a significant effect on hardness loss due to weathering, but figure 6.4 shows that shot sample impact faces see greater reduction in hardness after weathering than un-shot control samples. This suggests that ballistic impact leads to exacerbated weathering on the impact face, as demonstrated in the results presented above, but no individual variable is worse than another because for limestone samples any impact is sufficient to create a fracture network that will exacerbate weathering on the impact face. This is consistent with the large impact craters shown in figure 5.4, and in keeping with the findings of Ahrens *et al,* (2002) which demonstrated that larger impact craters are associated with larger fracture networks.

Conversely for sandstone samples, bullet type has a more significant effect than angle (10% significance level p=0.056). This is because lead-cored bullets often result in little fracturing on target surface, resulting in less saline solution migrating to impact face and therefore less weathering deterioration for these sandstone samples than those impacted with steel-cored ammunition.

To further understand the hardness loss on the impact face due to weathering spatially, the hardness loss of each cell after weathering compared with the shot hardness was plotted using the methods outlined in section 5.1.3.4. In order to understand the role of the impact crater in influencing changes in hardness after weathering, the average hardness loss for the central 9 cells was calculated and compared with the outer 21 cells. The results are presented in figure 6.5 and table 6.2:

Figure 6.5: Example *Spatial distribution of impact face plotting showing central 9 cells and outer 21 cells. NB; to aid interpretation, the full results of these analyses are presented in table 6.2 rather than showing each plot separately.*

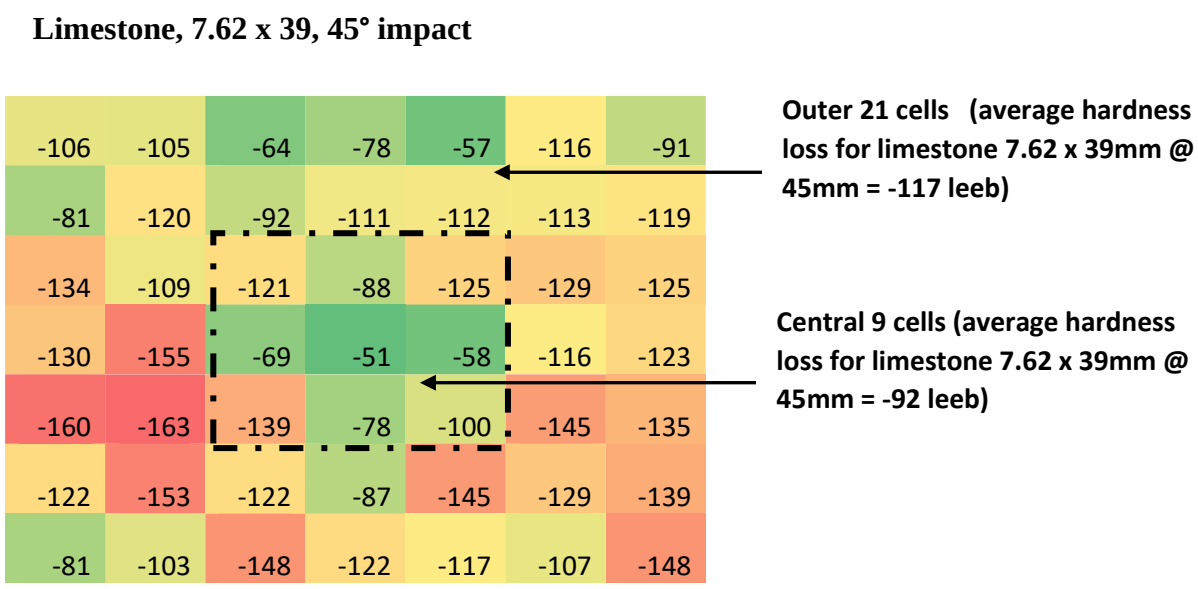

Table 6.2: *Data on hardness loss spatial distribution on impact face under all impact conditions*

Impact Condition	**Inner Cells Loss of Hardness (Leeb)**	**Outer Cells Loss of Hardness (Leeb)**
Limestone, 5.56 @ 90	-46	-87
Limestone, 7.62 @ 90	-35	-100
Limestone, 5.56 @ 45	-68	-87
Limestone, 7.62 @ 45	-92	-118
Limestone Control	-123	-119
Sandstone, 5.56 @ 90	-103	-74
Sandstone,7.62 @ 90	-148	-79
Sandstone, 5.56 @ 45	-133	-102
Sandstone 7.62 @ 45	-130	-63
Sandstone control	-120	-144

The results shown in table 6.2 reveal a distinct difference between the two lithologies. For all limestone samples, the inner cells, closest to the impact crater, see a lower reduction in hardness after weathering than the outer cells, and the difference between the two is much more pronounced for shot samples than for the un-shot control samples. This suggests that the impact crater influences the distribution of hardness loss after weathering. For sandstone samples, the inverse is true, with the cells closes to the impact crater seeing a much larger loss of hardness than outlying cells. The reason for the differing behaviour between the two samples is likely to be the fact that the limestone impact crater has already undergone a large reduction in hardness, and therefore is pre-weakened via the crack softening discussed in section 1.5, meaning that it is less weakened by the subsequent weathering action. This hypothesis is supported by the JH-2 model of fracture weakening validated by Ai and Ahrens (2006). Pre-weakening induced by ballistic impact is also consistent with the observation in chapter 2.4.1 that ballistic impact can act to cause weakening and matrix disaggregation similar to weathering processes but acting instantaneously. In this conception, the impact crater experiences less weakening due to weathering because it is effectively "pre-weathered" relative to the surrounding, un-damaged cells.

Conversely, sandstone samples have smaller, less weakened impact craters after shooting (as shown in figure 5.13) and therefore the inner cells are more susceptible to weakening by subsequent weathering which is focussed in the area of the impact crater by fracture networks that act to channel weathering agents to the impact face and impact crater as outlined above in relation to figure 6.4.

6.3.2: Permeability results

After weathering, the two lithologies showed differing behaviour in changes to permeability, as shown in figure 6.6:

Figure 6.6: *Changes in permeability for samples shot at 90◦ with 7.62 x 39mm ammunition. Error bars are the standard error of the mean for the given data set.*

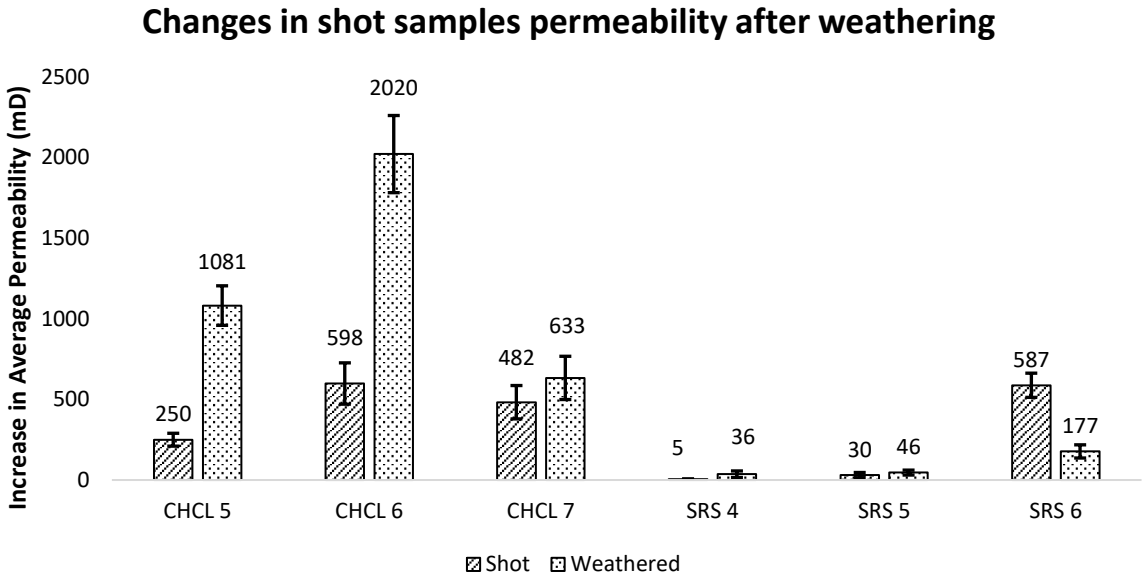

Limestone samples all showed large increases in permeability after weathering compared to shooting alone, whilst the sandstone samples showed negligible increases in permeability, or a notable decrease in permeability in the instance of SRS 6 of -410 mD. This trend was also observed across all of the cratered samples (table 6.2), with the twelve sandstone samples exhibiting an average 51% reduction in permeability across all surfaces after weathering compared with shooting, and the limestone samples seeing a 30% increase. The differing permeability behaviour of the two lithologies can be understood through their geo-technical properties.

Table 6.3: *Descriptive statistics for permeability changes after weathering of cratered samples*

Limestone	Average	n	Maximum	Minimum	Range	Standard Deviation	Standard Error
Intact	5.39	1470.00	88.93	0.01	88.92	8.50	0.22
Shot	156.42	943.00	5900.00	0.00	5900.00	498.69	16.21
Weathered	226.08	943.00	3800.00	0.19	3799.81	395.96	12.91
Sandstone	Average	n	Maximum	Minimum	Range	Standard Deviation	Standard Error
Intact	10.11	1470.00	761.00	0.01	1469.99	53.52	1.40
Shot	142.38	948.00	6000.00	0.03	950.97	528.27	17.13
Weathered	69.33	948.00	2100.00	0.00	948.00	187.17	6.08

As described by Renard *et al* (2009), and Viles and Goudie (2007), the ability of salt crystallisation to propagate a fracture network within a given rock is dictated by whether the crystallisation pressure of the crystals within the rock pores exceeds the tensile strength of the rock. When this occurs the rock matrix fails, and the rock is able to propagate. When the fracture propagates, the permeability of the rock will increase, as observed in field studies which have demonstrated the enhancement of permeability by weathering induced feedback loops Worthington *et al*, (2016). As shown by Campbell *et al*, (2022) Stoneraise red sandstone has a tensile strength more than double that of Cotswold Hill sandstone (5Mpa for Stoneraise red vs 2.2Mpa for Cotswold Hill). Therefore, given the mechanisms outlined in the literature above, it seems likely that the limestone increases in permeability due to salt crystallisation pressures able to propagate fracture networks within the stone, whilst the sandstone reduces in permeability because its tensile strength is greater than the crystallisation pressure of the salt crystals. This means that NaCl crystals only fill the pore spaces and fracture networks, rather than propagating them, which reduces the permeability of the samples.

The increase in permeability for the limestone samples is in contrast to the decrease in Cotswold Hill Cream limestone samples' permeability observed in chapter 2. This disparity is believed to have been caused by this experimental work weathering the samples for twice as long as earlier experimental work, allowing more cycles of salt crystallisation that caused a

greater extent of secondary fracturing caused by salt crystallisation pressure overcoming the rocks tensile strength. Evidence supporting this is given by Buj *et al* (2011), who describe how salt crystallisation can result in lower permeability values in the short term due to salt crystals sealing surface pores, but that over time repeated weathering cycles and associated salt crystallisations will produce microfracture networks that result in an increased permeability.

Given the finding that sandstone permeability is not increased by the weathering processes, further analysis was focussed on the permeability of limestone samples after weathering.

To ascertain which areas of the limestone samples were most adversely affected by the feed-back loop, permeability data relative to intact permeability for the cratered samples was plotted by region:

Figure 6.7: *Charts showing increase in permeability by sample surface and impact angle for both lithologies. Error bars are the standard error of the mean for the given data set.*

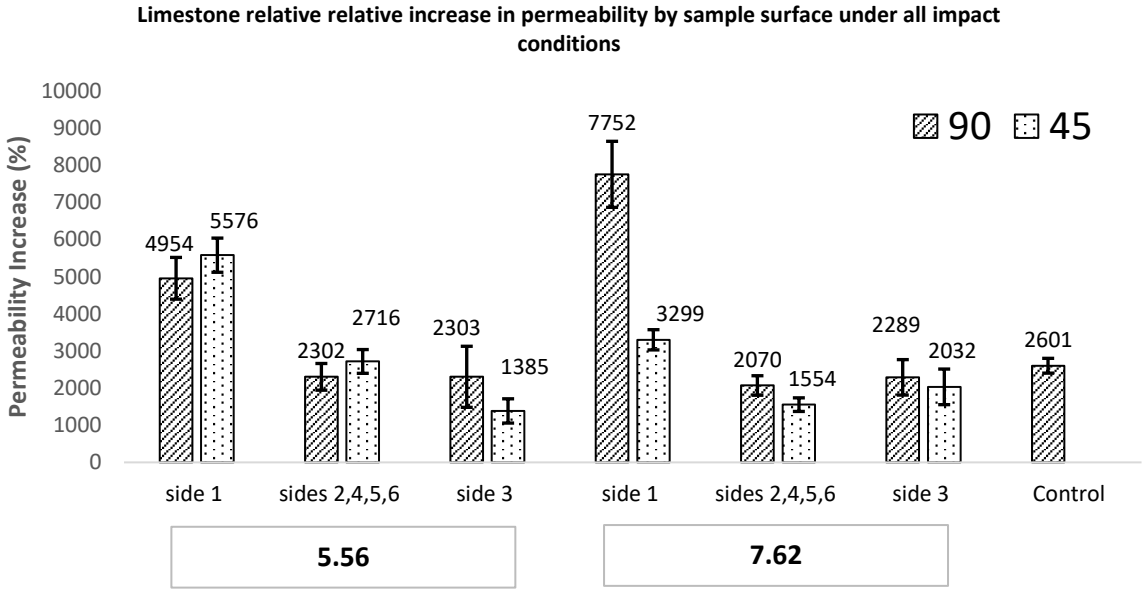

As figure 6.7 shows, and in keeping with all previous findings, the highest increase of permeability for limestone samples is consistently found on the impact face, with all other sample surfaces showing permeability increases comparable with or below that of the un-shot control sample (2601%). This is further evidence that the fracture network induced in the impact face acts to channel weathering agents to the impact crater and impact face, where the feedback loop previously discussed exacerbates increases in permeability.

To test this hypothesis, further analysis was undertaken to compare the impact point (where the fracture network is initiated) with the rest of the impact face and wider sample surfaces, as shown in figure 6.8.

Figure 6.8: *Increases in permeability of cratered limestone samples by region. Error bars are the standard error of the mean for the given data set.*

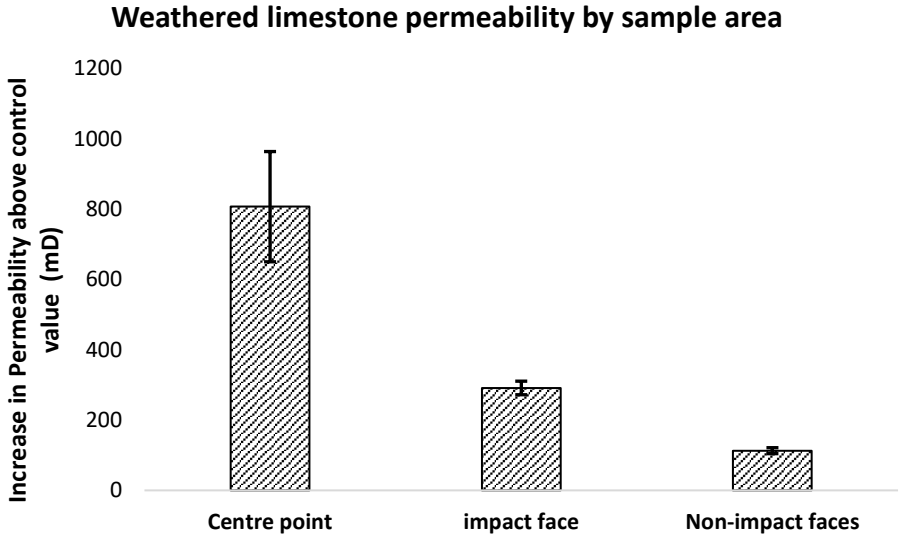

The centre of the impact crater sees the greatest increase in permeability after weathering, supporting the suggestion in section 6.3.1 that fracture networks connected to the impact crater facilitate the movement of weathering agents and that they are likely to concentrate in this area, resulting in a larger increase in permeability and an exacerbated feed-back loop. As discussed previously in relation to figure 6.4, fracture networks likely to be exacerbated by salt crystallisation have been shown to be densest around the area of the impact crater (Campbell *et al*, 2022) and such fracture networks are known to cause accelerated weakening when exploited by salt crystallisation that result in fracture propagating feed-back loops (Renard *et al*, 2009, McCabe, 2010, Navarre-Sitchler *et al*, 2013, 2015). Figure 6.7 also validates the suggestion put forward in the findings of chapter 5 and in section 6.2.2 that permeability increases are smallest on non-impact faces and that intensive monitoring should be focussed on the impact face when seeking to understand and mitigate weathering deterioration caused by ballistic damage in a field setting.

Finally, the same spatial analysis conducted for hardness loss after weathering presented in figure 6.9 and table 6.2 was conducted for permeability across the limestone samples' impact faces. The results are presented in table 6.4.

Table 6.4: *Data on permeability increase distribution on impact face under all impact conditions.*

Impact Condition	**Inner Cells increase in permeability (mD)**	**Outer Cells increase in permeability (mD)**
Limestone, 5.56 @ 90	444	221
Limestone, 7.62 @ 90	1176	242
Limestone, 5.56 @ 45	618	312
Limestone, 7.62 @ 45	285	147
Limestone Control	146	171

The data presented in table 6.4 shows that the inner cells of each limestone impact condition see a greater increase in permeability than the outer cells. In some instances, the increase of the inner cells is almost 500% greater than the increase for the outer cells (242mD for outer cells vs 1176 mD for inner cells of samples shot with 5.56 x 45mm ammunition at 90°). This is in contrast to the control sample, where the increase between inner and outer cells is only 25mD. This is hypothesised to be the result of the weakening caused by the fracturing induced by ballistic impact, which lowers the strength of the stone matrix, meaning that it is easier for salt crystals to create crystallisation pressures in excess of the tensile strength of the sample pores and thus expand fracture networks and increase permeability. This is in keeping with the findings of research discussed previously. (Renard *et al,* 2009, Viles and Goudie, 2007). It is worth noting that this is the opposite of the hardness spatial distribution results presented in table 6.2, where the outer cells of the limestone samples were found to be more weakened by the weathering process than the already weakened inner cells closer to the impact crater. This suggests that areas of hardness loss and areas of increased permeability will not necessarily correspond spatially, as was also found to be the case in the results presented in the spatial plots of data in chapter 2, where permeability increases correlated strongly with visible surface fractures whilst hardness loss did not always correspond with the same areas (figure 2.14, 2.16). This shows the importance of deploying a suite of methods

to fully understand areas of potential deterioration when dealing with monuments damaged by ballistic impact and at risk of haloclasty weathering processes.

ANOVA analysis of individual variables for the impact face of cratered limestone samples suggested neither ballistic variable has a significant effect on permeability increases after weathering. Coupled with the fact that permeability increase is lower for un-shot weathered limestone control samples than for shot limestone samples impact face (figure 6.7) this suggests that ballistic impact causes exacerbated preferential weathering of fracture networks that leads to the feed-back loops of permeability increase discussed in the paragraphs above, but that neither ballistic variable has a significant controlling effect on this phenomenon. This is consistent with the results of chapter 4, agreeing with the conclusion in section 4.5 that there is no "worst case scenario" in terms of impact angle when considering weathering damage to this lithology after ballistic impact.

Table 6.5: *Results of ANOVA tests to determine which ballistic variables have a significant effect on relative permeability increase on cratered limestone samples' impact face after weathering.*

Tests of Between-Subjects Effects

Dependent Variable: Hardness_Loss

Source	Type III Sum of Squares	df	Mean Square	F	Sig.
Corrected Model	89022.029[a]	3	29674.010	1.822	.221
Intercept	1018507.559	1	1018507.559	62.535	<.001
Bullet	592.545	1	592.545	.036	.853
Angle	32103.124	1	32103.124	1.971	.198
Bullet * Angle	56326.360	1	56326.360	3.458	.100
Error	130295.597	8	16286.950		
Total	1237825.185	12			
Corrected Total	219317.626	11			

.

6.3.2: Photogrammetry results

Some samples showed significant accumulation of efflorescence after the weathering cycles (figure 6.9). To determine where the volume of efflorescence deposited on the samples' surface could be used to predict mechanical degradation, correlation coefficients were calculated across the volume of efflorescence detected using photogrammetry and measurements for both lithologies for impact crater area, hardness loss and permeability across the whole surface of the samples (as the efflorescences were across all sample surfaces). As shown in table 6.6, none of these variables were found to have a correlation with the volume of efflorescence correlation coefficient < 0.3. Therefore, it is not believed that photogrammetric analysis of efflorescence volume should be used as a method of assessing potential mechanical degradation of heritage stone damaged by ballistic impact.

Figure 6.9: *Un-textured image from the photogrammetric model of sample SRS 16, showing the substantial efflorescence accumulated on the sample surface after the weathering cycles*

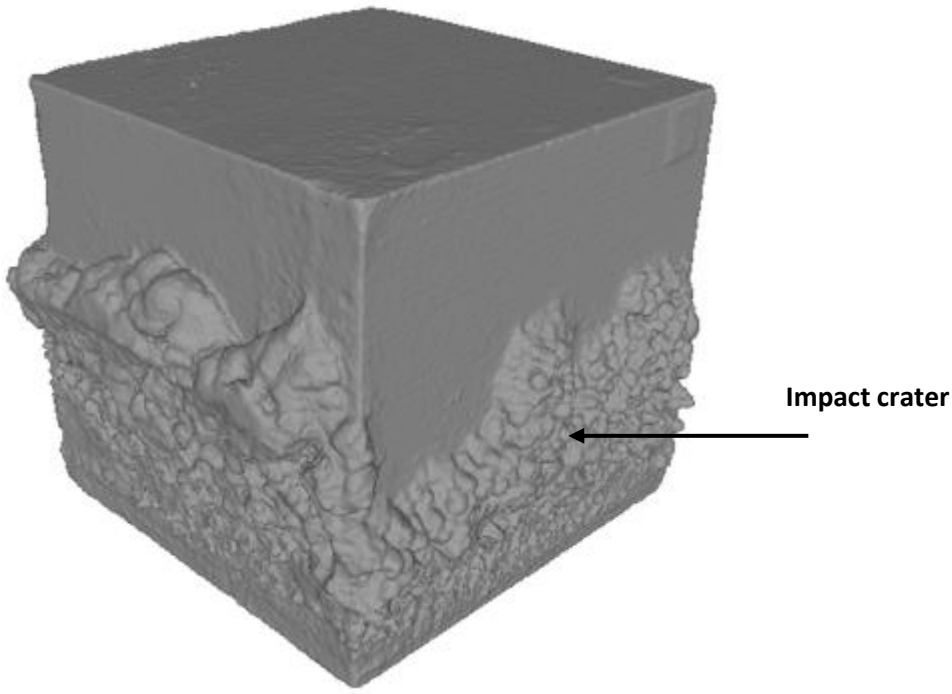

Table 6.6: *Data on the calculated correlation coefficient between sample efflorescence volume and various mechanical properties. Note that Efflorescence volume does not appear to be correlated with any of the listed properties.*

	Correlation coefficient (Impact crater area vs efflorescence volume)	**Correlation coefficient (Relative Hardness Loss vs efflorescence volume)**	**Correlation coefficient (Permeability vs efflorescence volume)**
Sandstone	-0.06	-0.10	-0.09
Limestone	-0.06	-0.05	-0.04

Although large efflorescences which increased the volume of the samples were present after completion of the weathering cycles (figure 6.12), after these efflorescences had been removed, there was no significant loss of volume from the samples that might be expected to be caused by salt crystallisation causing substantial internal fracturing and corresponding detachment of noticeable volumes of stone. Given that the salt used in these experiments was NaCl this observation is consistent with the findings of Goudie *et al* (1970) and Manohar *et al,* (2020), both of which fond little substantial volume reduction in samples weathered with NaCl. as well as the results from chapter 4 of this research (see figures 4.15, 4.16). To illustrate the lack in volume change, the average % change in volume for both litholoies under each shooting condition is shown in table 6.7, which shows that no combination of shooting conditions produced samples with changes in volume in excess of the 0.3% error associated with photogrammetry (section 4.4.2), whilst figure 6.10 visually illustrates the lack of any substantial loss of volume between samples after shooting and after the weathering cycles.

Table 6.7: *Changes in sample volume after weathering cycles. Note that no shooting conditions across either lithology result in a change of volume in excess of the 0.3% error associated with photogrammetry measurements of volume.*

Lithology	**Shooting Condition**	**Change in Volume (%)**
Limestone	5.56 @ 90◦	-0.05
	5.56 @ 45◦	-0.19
	7.62 @ 90◦	-0.05
	7. 62 @ 45◦	-0.12
Sandstone	5.56 @ 90◦	-0.18
	5.56 @ 45◦	-0.28
	7.62 @ 90◦	0.04
	7. 62 @ 45◦	0.13

Figure 6.10: *Photogrammetry images of samples SRS 5 and CHCL 14 after shooting (A) and after completing the weathering cycles (B). Note the lack of any substantial reduction in volume for either sample.*

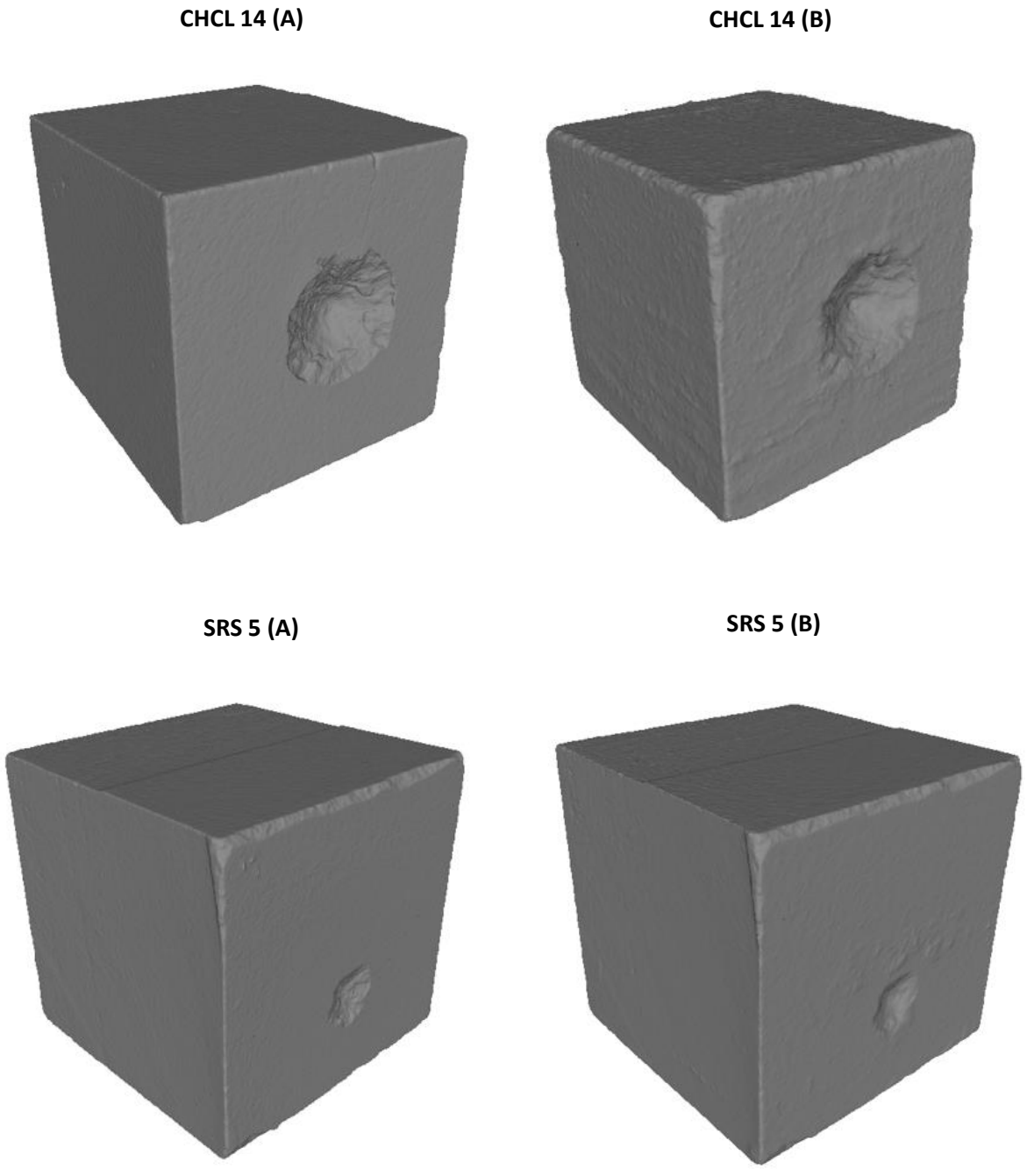

As discussed in section 5.2.3.4 and shown in figures 5.29 and 5.30, impact crater area is correlated with hardness loss and permeability increase across all samples surfaces immediately after a ballistic impact. This correlation was tested again after weathering (for the average of all sample surfaces rather than the impact face alone for the reasons discussed previously in relation to figure 5.29). As only limestone samples increased in permeability after weathering only these samples were tested, and it was found that after weathering, the area of the impact crater is still correlated with permeability (correlation coefficient 0.66, p = 0.018):

Figure 6.11: *Impact crater area vs average permeability of all sample sides of cratered limestone samples after weathering.*

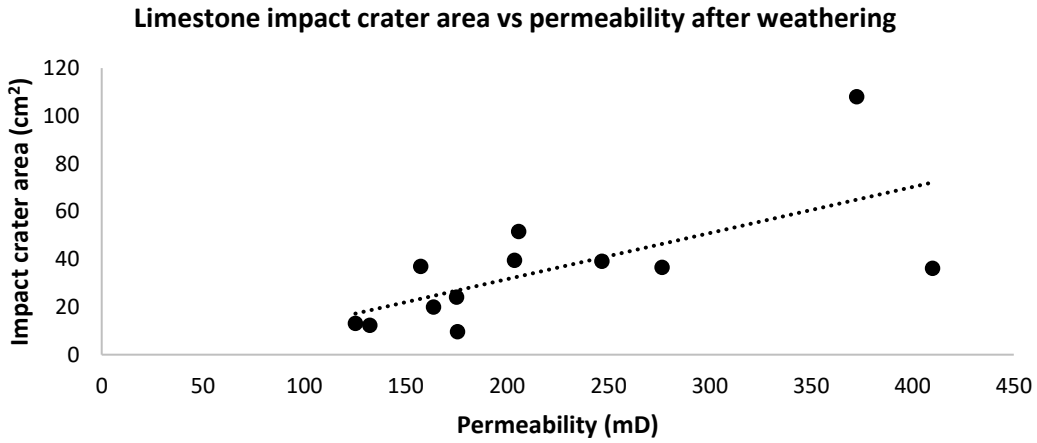

This finding is supported by work by Ahrens *et al,* (2002) who noted that the depth/extent of fracture damage is proportional to the size of the impact crater. As described previously, a denser fracture network will result in a higher permeability after weathering due to salt crystallisation exploiting and extending existing fracture networks (Renard *et* al, 2009). Therefore, figure 6.11 demonstrates that data collected on impact craters through photogrammetry could be a useful tool in predicting which areas of stone damaged by ballistic impact are likely to be most adversely affected by subsequent weathering deterioration, in particular the increase in permeability caused by salt crystallisation exploitation of fracture networks and the feedback loops of increasing fracture density that this causes discussed in detail above. No correlation was found between relative hardness reduction after weathering across wider sample surfaces and impact crater area (correlation coefficient for limestone sample: 0.19 sandstone samples: 0.09). Therefore, whilst impact crater area may be useful in predicting the permeability increase in stone after weathering due

to the salt crystallisation feedback loops discussed previously, it does not appear to be a useful metric for predicting hardness reductions across the wider sample surface.

6.3.3: UPV results

As observed in chapter 4, the weathered samples saw an average increase in UPV due to salt crystals filling pores and fractures, increasing sample density and therefore ultrasonic pulse velocity. Across both lithologies the average increase in UPV compared to shot samples was 21% (see appendix A, table 3). Because the increase in UPV is known to be caused by the uptake of salt crystals into rock pores and fractures (and associated increase in density, see Aly, 2016), it was hypothesised that those samples that saw a higher increase in UPV would undergo more intense haloclasty weathering and therefore see a greater decrease in surface hardness due to weathering. As shown in figure 6.13, analysis seems to confirm this, as decrease in surface hardness shows a correlation with increase in UPV after weathering (correlation coefficient -0.58):

Figure 6.12: *Sample decrease in surface hardness after weathering vs increase in UPV after weathering*

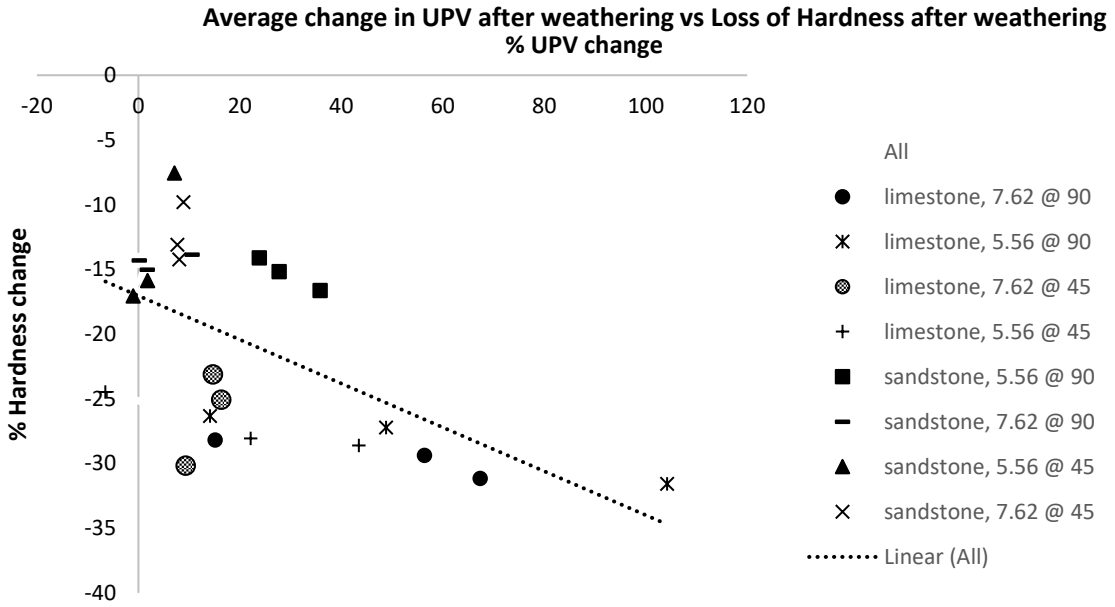

The fact that increase in UPV can be used to identify stone that has increased in density due to salt crystallisation, as well as the correlation of UPV measurements with decreased surface hardness due to haloclasty suggest that this could be an effective method for identifying damaged stone at risk of weathering deterioration in a heritage setting, which in turn could be priorities for conservation intervention.

6.4: Discussion of significance of results

Most significantly, the hardness results presented in section 6.3.1 demonstrate that ballistic impact worsens weathering weakening on impacted surfaces compared to un-shot control samples (figure 6.4). It is also clear that the same variables that determine weakening in the immediate aftermath of ballistic impact also exacerbate weakening of the impact surface due to weathering. That is to say that the weaker limestone is more severely weathered than the sandstone (figure 6.3) and steel-cored projectile contribute to greater weakening of sandstone samples after weathering subsequent to ballistic impact than is the case for lead-cored projectile (table 6.1). It should be noted these observations are only true of the target impact surface, and non-impacted surfaces do not see the same levels of deterioration after weathering (figure 6.4). As outlined in section 6.3.1 it is believed that fracture networks caused by ballistic impact act to concentrate weathering deterioration on the impact surface due to the likelihood that fracture networks around the impact crater will be exploited by feed-back loops of fracture propagating salt crystallisation, as this is consistent with the findings of other works (Campbell *et al*, 2022, Renard *et al*, 2009). This is in keeping with observations in chapter 4 that the impact face experiences the most weakening after ballistic impact and weathering (figure 4.25).

To take account of these observations in the risk matrix first described and justified in chapter 5, two additional criteria have been added: whether or not haloclasty weathering is present at a damaged heritage site (as evidenced by the presence of visible efflorescence) and if efflorescence is in and around the impact crater. If both of these are true, then based on the results presented in this chapter, there is a high chance that this area will be at greater risk of deterioration than other, unimpacted stone at a given heritage site.

These new criteria are weighted above ballistic variables because un-shot weathered samples see a reduction in hardness higher than samples that have only been shot and not weathered (figures 5.13 and 6.5, hardness reduction after shooting for both lithologies c.10%, hardness

reduction for both lithologies after un-shot samples weathered c.24%). Target lithology remains the most important variable as results in section 6.3.2 demonstrate that lithology controls weathering behaviour such as feedback loops of increasing permeability, and that the same properties which produce high wave impedance (i.e compressive/tensile strength) will also govern resistance to secondary fracturing produced by salt crystallisation pressure exploiting fracture networks initiated by ballistic impact (Renard *et al*, 2009, Viles and Goudie, 2007). The numerical values for risk are designed to give those impacts with a higher number of risk factors and those impacts with the risk factors with the greatest weighting a high score. As discussed in section 5.2.4, the numerical reasoning for the weighting of the variables in the risk index is underpinned by existing risk quantification systems for heritage stone in published literature. To re-iterate, the revised matrix takes inspiration from existing risk matrices for assessing weathering risk to heritage stone such as the Rock Art Stability Index, which like the risk matrix outlined below, assigns a 0 value to weathering risks not visibly present at the site, and aggregates various risk factors to give an overall risk score to an affected site (Dorn *et al*, 2008). The revised risk matrix is presented below.

Table 6.8: *Proposed risk index for ballistic damage to stone including both ballistic parameters and weathering risks.*

			Score
Target lithology	High Wave Impedance	0	
	Low Wave Impedance	6	
Efflorescence visible in impact crater?	No	0	
	Yes	5	
Known sources of weathering salts at site (e.g. coastal)?	No	0	
	Yes	4	
Impact Angle	Oblique	0	
	Normal	3	
Projectile construction	Lead	0	
	Steel	2	
			Total:

Total Score

20:	Very High Risk
>10:	High Risk
≥5:	Moderate Risk
<5:	Low Risk

In relation to the permeability results presented in section 6.3.2, which showed limestone sample increasing in permeability whilst sandstone samples decreased, existing literature (McCabe *et al*, 2010 Renard *et al*, 2009 Navarre-Sitchler *et al,* 2013, 2015, Worthington *et al* 2016) suggests that this disparity is due to differing tensile strengths. The limestone has a lower tensile strength which can be overcome by the crystallisation pressure of the NaCl, which propagates the fracture network in the sample and increases the overall permeability, creating the feedback loops of increasing permeability already discussed. This is an important finding because it suggests that in a field context, small scale sampling of the tensile strength of lithologies known to be used in heritage buildings could be utilised to inform which lithologies and sites are most at risk of rapid deterioration caused by such salt weathering driven deterioration feed-back loops.

Finally, both photogrammetry analysis of impact crater area and UPV analysis have been shown in this chapter to have potential to predict geotechnical parameters of weathered stone, chiefly increases in permeability and decreases in surface hardness due to uptake of saline groundwater. This suggests that these would be effective field methods for assessing weathering risk to heritage sites that have experienced ballistic damage.

6.5: Conclusions

Most significantly for the goal of this project, this chapter has allowed the successful completion of Research Objective V, facilitating the creation of a risk matrix which identifies heritage stone most at risk of exacerbated weakening due to a number of variables including lithology, ammunition it was impacted with, impact angle and presence or absence of certain weathering conditions. This was achieved through the completion of Research Objective III:

To assess the effects of arid environment weathering processes (haloclasty, moisture, temperature change) on the deterioration of stone after ballistic impact and investigate the interaction between ballistic impact and subsequent weathering processes.

Finally, the risk matrix is based on methods that are field appropriate, as outlined in Research Objective I, and has further highlighted the utility of methods such as photogrammetry and UPV analysis by demonstrating their potential uses in identifying weathering risks.

Chapter 7

Field testing of Surveying Techniques in a Recent Conflict Context

Chapter 7 aims

To apply the techniques developed in chapters 2-5 to a heritage monument recently damaged by small arms fire in an arid setting and exposed to weathering by saline water. The use of Equotip rebound hardness survey and Protimeter Survey for moisture/salt content to survey the Sabratha World Heritage Site would determine whether the interplay between the mechanical degradation caused by ballistic impact could be shown to interact with the processes present at the site (salt, moisture, temperature fluctuations). This would fulfil Research Objective 5 by ground truthing the laboratory based observations that weathering processes can be exacerbated by ballistic impact. Furthermore, this fieldwork would determine whether the methods and risk matrix developed throughout the course of the PhD project are suitable for identifying areas of increased risk on damaged monuments and targeting conservation strategies appropriately.

Chapter 7 methods

Through collaboration with colleagues on the Sabratha Heritage Protection Project (SHPP), based in the U.K. and Libya, a training programme was developed that allowed Libya-based conservation experts to capture photogrammetry data of the Sabratha Roman Amphitheatre. This photogrammetry data was then used by colleagues in the SHPP to create a 3D photogrammetric model. This model was used to identify ballistic damage caused by armed clashes around the port of Sabratha in 2016. Having identified all obvious impact craters visible on the model, a survey regime for Equotip rebound hardness survey and protimeter survey were developed that gathered characteristic data from across the different areas of the site. This allowed for a comparative analysis of the data based on the different areas of the amphitheatre and their likely exposure to weathering processes. Data on diurnal temperature variations at various points around the site was also gathered using Ibutton temperature sensors.

Chapter 7 principal findings

Analysis of the data suggests that there is interplay between ballistic damage and weathering processes that causes greater degradation to impacted surfaces more exposed to weathering risks due to their location at the site. Impact craters closer to sources of salt contamination from coastal sea spray are also exposed to greater diurnal temperature fluctuations due to the relative position of the sun. This appears to have caused greater accumulation and mobility of saline water in these regions and contributed to an increased loss of hardness in these areas than in other areas of the site protected from saline sea spray and solar heating. The identification of these trends using surface hardness survey and protimeter analysis provide preliminary evidence that these techniques are well suited to identifying areas of heritage sites most at risk of degradation due to weathering by haloclasty in the aftermath of ballistic damage. This validates the use of these methods in a field context. Data obtained from impacts into differing target materials (stone and restored plaster) also support findings from chapters 5 and 6 that target material is a key determinant of damage sustained after ballistic impact. Finally, the use of the risk matrix on two real-world impacts with some known impact conditions and known values for hardness loss validates the risk matrix, successfully identifying the impact most at risk.

7.1: Introduction

As discussed in section 1.15, this PhD project is oriented towards developing methods that can be used by conservation experts in a field setting to assess conflict damage to built heritage. Therefore, it is important that the methods used in this research are field-appropriate. Chapter 3 demonstrated that these methods can be useful in determining the interplay between ballistic damage and weathering processes on historic impacts over 80 years old. However, it has not yet been determined whether they would be able to discern areas most at risk after recent ballistic damage. Therefore, a project was conceived to train colleagues at the Department of Antiquities in Libya to collect data on ballistic impacts at the Sabratha World heritage Site, which was damaged during armed clashes in 2016. This would also allow for the assessment of the feasibility of applying these techniques across the conservation community amongst colleagues who have not used these kinds of techniques before. Due to constraints in shipping equipment to Libya, it was decided that the survey would consist of measurements of surface rebound hardness, masonry moisture content and temperature variation across the site to determine the likely effects of weathering processes on mechanical degradation. It was not possible to ship the necessary equipment to Sabratha to allow for a permeability survey, and therefore this method was excluded from this fieldwork.

7.2 Background to the site

7.2.1: History of the Site

The settlement of Sabratha has a history extending far back into antiquity. It began as a Phoencian trading post, with the first textual sources mentioning the site dating from the 4th century BC (Leone, 2012). In the centuries after the Punic wars, the site came under the control of the Romans, and it was during the 2nd Century that the city was expanded and the amphitheatre constructed (Bomgardner, 2018). By the 11th century, the city was abandoned, and the amphitheatre subsequently fell into ruin (ICOMOS, 1982). The current amphitheatre is a reconstruction utilising original stones excavated by an Italian archaeological team in the 1930's. Recovered decorative reliefs and carvings were used in the reconstruction of the scaenae frons (the decorated architectural background to the theatre stage), and the site has subsequently been recognised as a uniquely well-preserved example of a decorated Roman amphitheatre (Lopez 2017). The significance of the Archaeological Site of Sabratha was further cemented when the area was inscribed as a UNESCO world heritage site in 1982.

During the second Libyan civil war (2014-2016) there were clashes for the control of the strategically important port of Sabratha and the amphitheatre, which is only 200m south of the coast suffered a great deal of ballistic damage from both small arms fire and larger weapons such as Rocket Propelled Grenades (RPG's) (Aboub, 2018). The widespread and easily visible nature of this damage across the amphitheatre made this monument the obvious choice when planning a survey to assess the validity of field-based measurements in assessing the potential deterioration risks at the Sabratha archaeological site.

7.2.2 Site Layout

The amphitheatre lies approximately 200m south of the Mediterranean coast, and north of the modern town of Sabratha, which is 70km west of Tripoli.

Figure 7.1: *The location of the Sabratha amphitheatre on the Mediterranean coast (adapted from www.google.com/maps)*

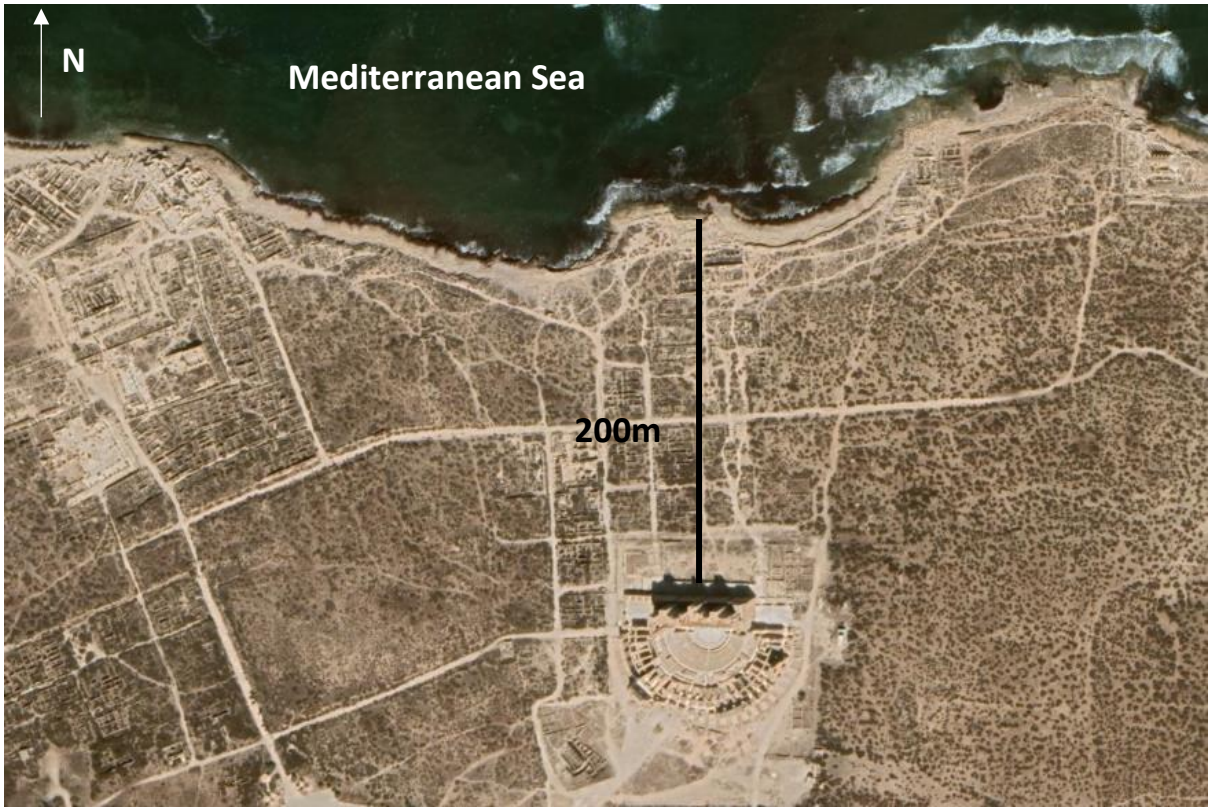

Using images captured by a drone with a pre-programmed flight path, a 3D model of the amphitheatre was created by Patrica Voke, a member of the Sabratha Heritage Protection programme. Using this model, different areas of the amphitheatre were assigned group names, to allow for quick referencing of the location of impact clusters:

Figure 7.2: *The names used to designate regions of the amphitheatre where ballistic impact clusters were identified. (Adapted from www.bing.com/maps)*

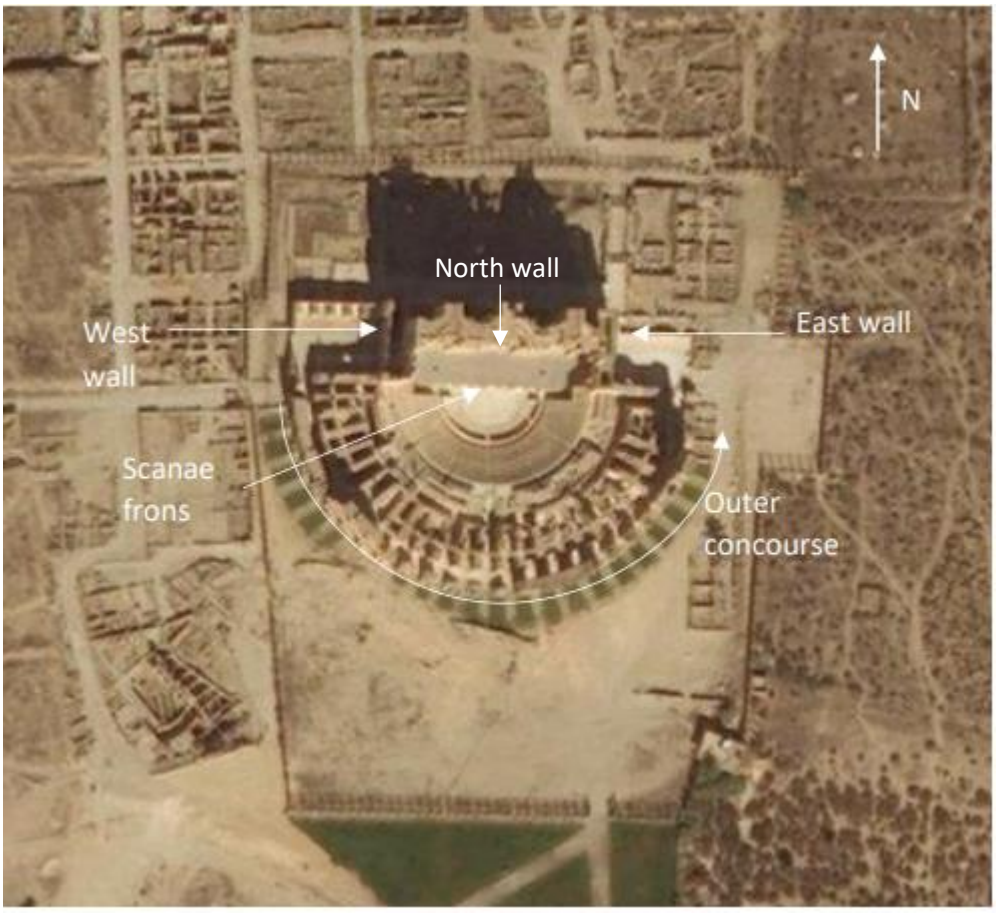

7.2.3: *Description of Ballistic Damage at the Site*

The 3D model was used by the author to visually assess each area of the site for ballistic damage, and several regions of the theatre were identified as featuring high-density clusters of impact craters. To identify areas of likely ballistic damage, the model and associated images were examined for areas of the monument with characteristic features of a ballistic impact into stone. These features include a central hemispherical crater area, radial fractures surrounding the impact area, discolouration of the stone surface due to exposure of underlying un-weathered stone and clustering of impacts due to concentrated bursts of small-arms fire.

Figure 7.3: *Impact crater and radial fracturing typical of ballistic impact (A), and examples of this type of crater on the Sabratha amphitheatre (B). (Adapted from Polanskey and Ahrens, 1990).*

A

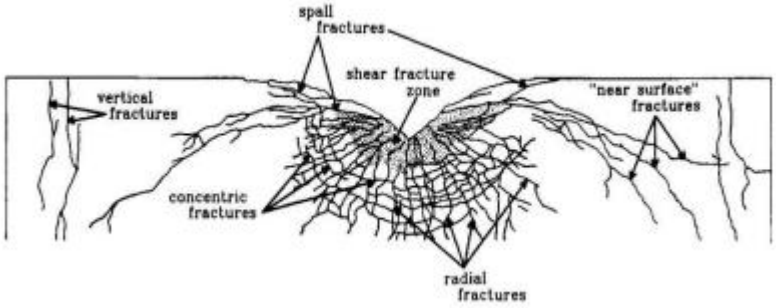

B

It is note-worthy that no impacts were detected on the north wall, to the rear of the scaenae frons facing the coast. This clustering of impacts allows a tentative reconstruction of some of the fighting that took place in and around the theatre, with incoming fire being directed toward fighters embedded at the top of the scaenae frons facing broadly southward, and returning fire causing damage to the inner portion of the outer concourse:

Figure 7.4: *A diagram showing reconstructed exchanges of small arms fire around the amphitheatre. Adapted from Caputo, 1959.*

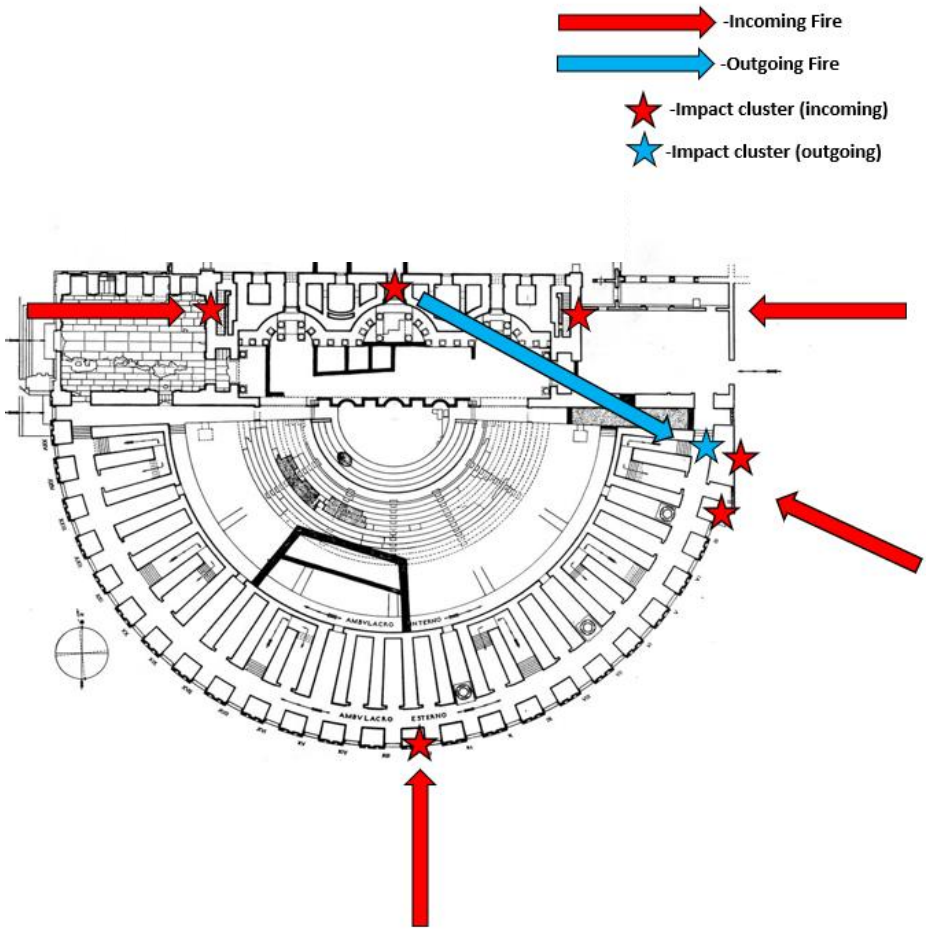

Images of the 4 impact cluster areas used to create the recording sheets are shown below, in total, some 157 probable ballistic impact craters were identified across these clusters.

Figure 7.5: *Images showing the location of every identified impact by impact cluster. Impacts in green are impacts that were surveyed for hardness data, areas in pink are areas surveyed for control data (see section 7.3.1).*

East Wall cluster

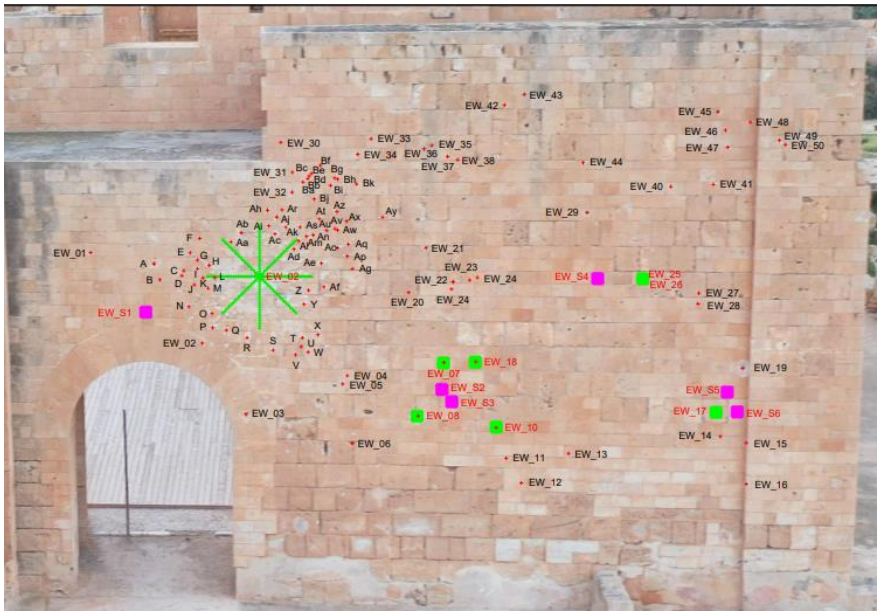

West Wall cluster

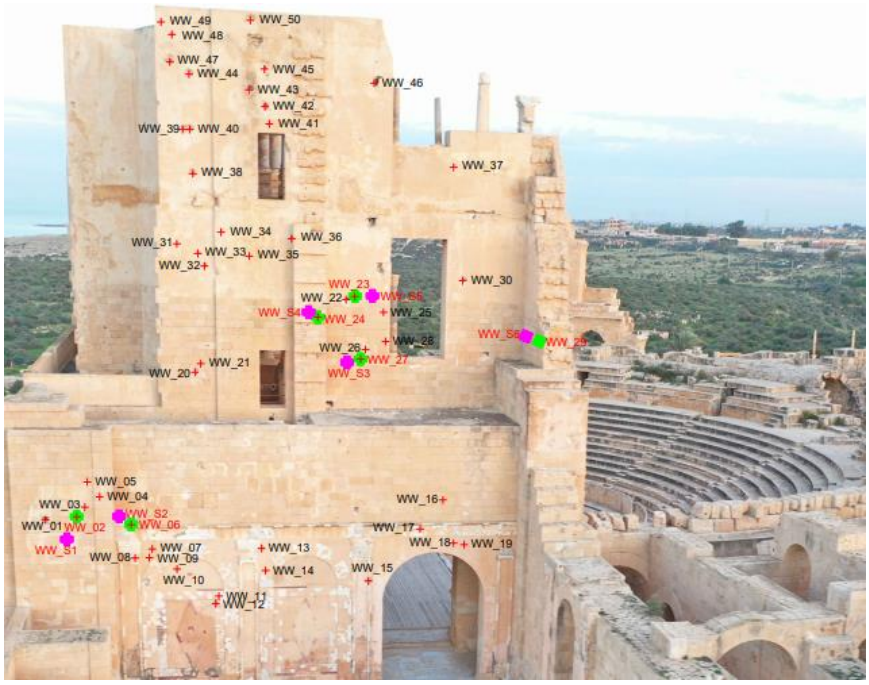

Outer Concourse cluster (facing north-west)

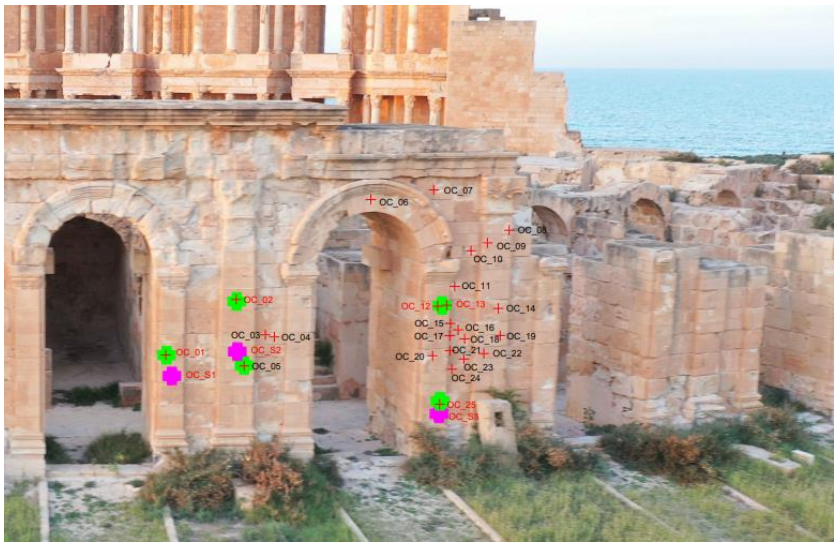

Outer Concourse cluster (facing west)

scaenae frons cluster

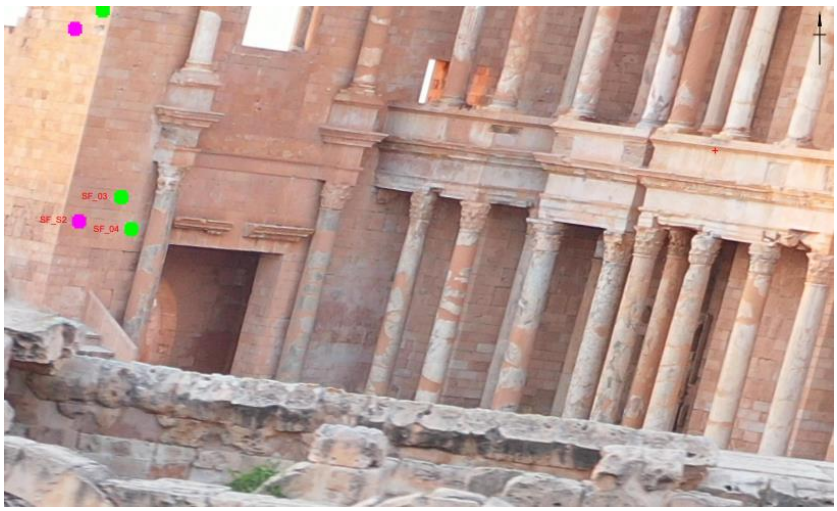

7.2.4: Description of Weathering Risks at the Site

The monuments at Sabratha are primarily constructed from Gargaresh calcarenite, a bioclastic quaternary limestone with low compressive strength (5.6) Mpa, high carbonate content (>90%) and moderate to high porosity (9-17%). (El-Shahat, Minas, Khomiara, 2014, Abdalahh, 2011). Large pores in excess of 0.1mm allow rapid entry of water into the rock, and thus present a risk of weathering deterioration even prior to the introduction of ballistic fracture networks. In addition to the risks associated with the properties of the stone itself, investigations of weathering processes at the site have revealed blackening of stone surfaces associated with biofilm colonisation, whilst the primary cause of weathering deterioration has been identified as mechanical degradation occurring from crystallization of salts from saline sea-spray (figure 7.6) *(Ibid.).* High absolute temperatures at the site, as well as wide temperature fluctuations are likely to exacerbate salt weathering by aiding capillary rise and causing repeated precipitations of salt crystals (Abdalahh, 2011).

Figure 7.6: *A clear example of a ballistic impact crater present on the amphitheatre site (impact point WW_29) alongside obvious alveolar weathering of the stone surface arising from salt crystallisation processes. This image demonstrates why ballistic impacts are likely to exacerbate existing structural degradation.*

7.3 Methods

7.3.1: Rebound hardness survey

Once all identifiable impacts had been recorded as described in section 7.2.3, the 22 impacts that were accessible for Equotip hardness testing were identified by the author and incorporated into recording sheets created by Patricia Voke to allow project colleagues in the field, Mahmoud Hadia and Ahmed Masoud, to easily locate the areas to be sampled for Equotip surface hardness survey.

The recording sheets also included diagrams of the sampling grid to be overlaid over the impact craters that would facilitate hardness testing. Most of the craters were overlaid with a 18cm x 18cm 10x10 grid of 100 points with 2cm between sampling points. Colleagues in the field used chalk and pencil to mark the sampling grid over the impact craters. Three hardness measurements were taken from each of the 100 points using an Equotip Bambino 2 Hardness

tester that was calibrated on a type D test block (figure 7.7, 7.8). This instrument is a smaller version of the Equotip device used in chapters 2-6.

In addition to ballistic impact caused by small arms fire such as assault rifles, the survey also identified a large radial pattern of damage characteristic of a High Explosive Anti-Tank (HEAT) munition such as an RPG. This was also incorporated into the survey of the site using a "cross-hairs" sampling regime made up of four 2m intersecting sampling lines each including 20 sampling points at 10cm intervals (figures 7.9, 7.10).

In addition to the impact craters, 19 control regions of intact wall close to each impact crater were sampled in order to be able to determine the hardness of the walls prior to impact in each distinct area of the site. These control regions were given an "S" designation for "sample", e.g. "WWS_01" and were sampled using the 18cm^2 grid detailed above.

The data gathered in this way was transferred to the author, and all data analysis undertaken in this chapter is the work of the author.

Figure 7.7: *An example of the recording sheet showing the locations of impacts on the east wall of the Sabratha amphitheatre. Impacts that were selected for surface hardness survey are highlighted in green, control regions are highlighted in pink. The green cross hairs pattern labelled EW_02 is the RPG impact discussed previously.*

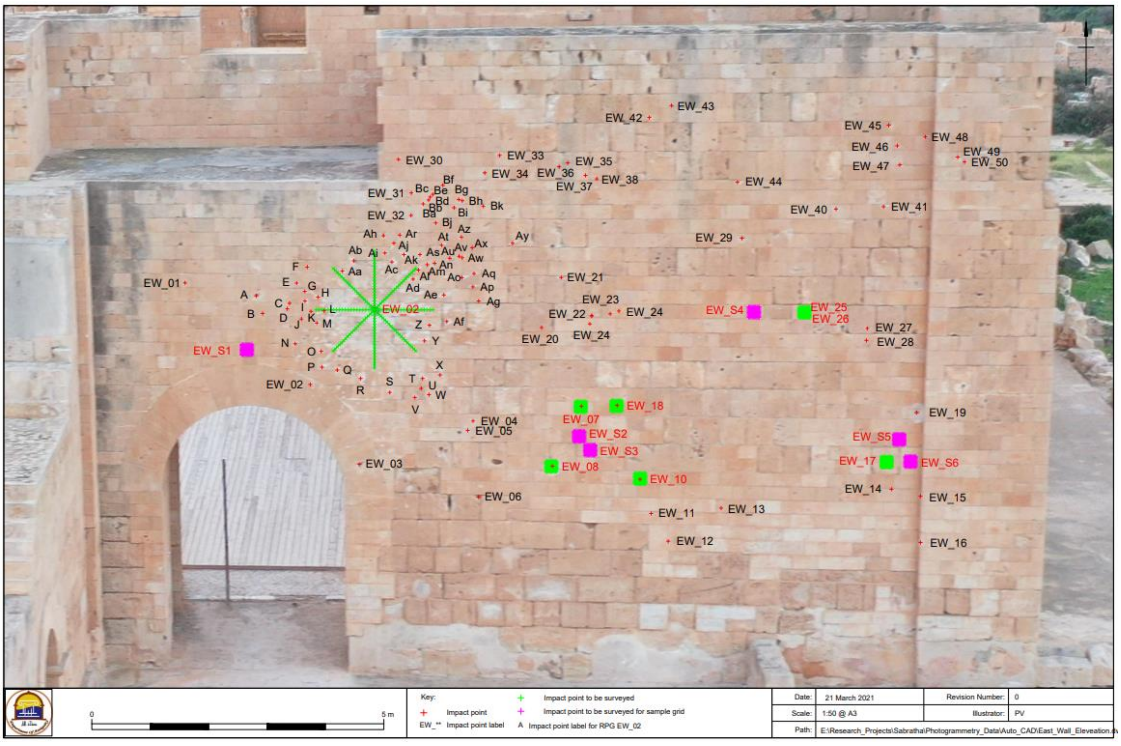

Figure 7.8: *A pencil sampling grid ion the amphitheatre wall and data Equotip data collection in progress.*

Figure 7.9: *A recording sheet showing close up images of an impact crater, sampling grid, and sampling grid over intact control stone on the West wall of the amphitheatre.*

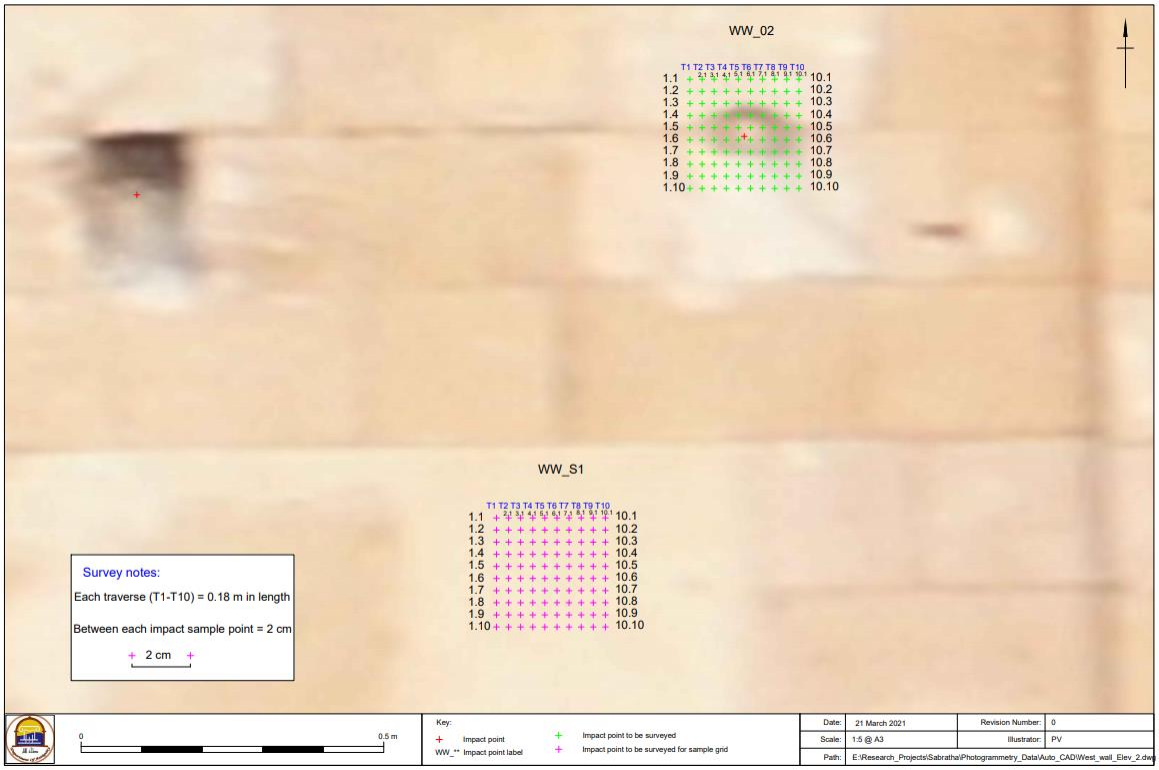

Figure 7.10: *A comparison between the RPG impact on the East wall of the amphitheatre (A) (B) and HEAT warhead impact into an armoured vehicle from the Vietnam war. Adapted from Bryla and Starry, 1979.*

7.3.2: Protimeter Data Collection

In addition to the aesthetic deterioration that small arms cause to heritage stone, research has demonstrated that ballistic impact weakens the stone's exterior and increases its permeability through the creation of fracture networks (Gilbert *et al*, 2019). This allows the ingress of weathering agents such as moisture and dissolved salts, exacerbating weathering processes such as haloclasty. The Sabratha amphitheatre is particularly likely to be affected by this, as it is close to the coast, and therefore likely to be affected by salt weathering from sea spray similar to the salt weathering caused by saline water seen at other heritage sites in arid regions in North Africa (Mahmoud, Kantaranis, Stratis, 2010).

To determine the extent of moisture and salt contamination present at the site likely to exacerbate damage caused by ballistic impact, a Protimeter Digital Mini moisture meter was used, as described in chapter 3. To ensure Protimeter data was gathered from the different regions of the site, 22 vertical sampling transects were placed around the perimeter of the amphitheatre. These transects consisted of three metre vertical lines from the base of the monument (where groundwater moisture contamination might be expected to be highest). The moisture content was sampled every 30cm along these transects, giving ten sampling points per transect.

Figure 7.11: *An aerial view of the location of Protimeter sampling transects around the perimeter of the amphitheatre. Adapted from Caputo, 1959.*

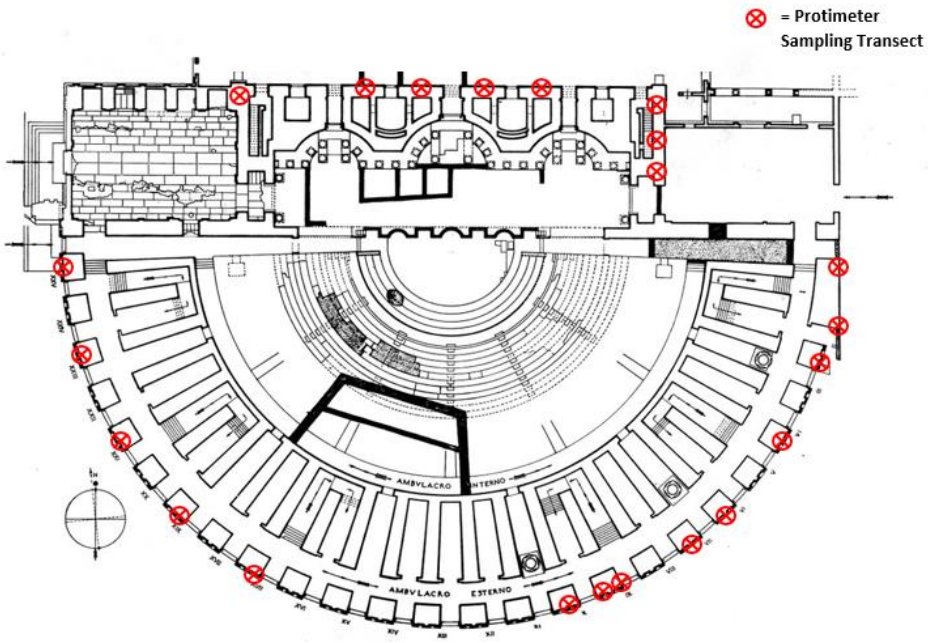

7.3.3: Temperature Data Collection

Temperature is a key metric in determining likely weathering damage to ballistic impact craters, because large temperature fluctuations will facilitate capillary transport of saline water (Karagiannis *et al*, 2016). Temperature cycles will also cause salt crystals to precipitate in masonry fracture networks and pores exerting internal crystallization pressure and causing further weathering deterioration (Shahidzadeh, Desarnaud, 2012). Temperature data was collected using Ibutton Thermachron Sensors. 30 of these sensors were placed around the site in order to see localised temperature variations as well as the average temperature cycle across the whole site (See Appendix B for sensor locations). Each sensor logged the temperature at 15-minute intervals for 70 hours, beginning at 13.30 on 27/07/2021.

Taken as a whole, the use of surface hardness survey, and protimeter survey (both methods used in previous chapters) in an arid setting with risk of exacerbated haloclasty weathering was designed to test the methods developed in previous chapters on a heritage site in an arid MENA region subjected to recent armed conflict. This is in contrast to chapter 3, which only tested methods on 80-year-old impacts in a boreal climate (Portsmouth, U.K.).

7.4: Results and interpretation

7.4.1: Hardness Survey Results

One of the most important findings from the surface hardness survey is that across all of the sampled areas, the portions of the amphitheatre exhibiting ballistic impact are of substantially lower surface hardness than the intact control regions. This indicates that impacted regions of the theatre have been weakened by projectile impact and could be at risk of accelerated future deterioration due to chemical weathering processes by salt and moisture. There is also a risk of mechanical degradation due to abrasion of the increased surface area of the impact crater by aeolian processes (Coombes *et al*, 2013). The average hardness of the intact regions of the amphitheatre was 262 leeb, whilst impacted regions had an average hardness of 233 leeb, which represents a hardness reduction of 12%, as seen in figure 7.12. This suggests that impact craters are weaker than the intact material of the amphitheatre and should be considered when planning future conservation work.

Figure 7.12: *A comparison of the surface hardness of intact control regions of the amphitheatre and impacted regions. Error bars are the standard error of the mean for the given data set.*

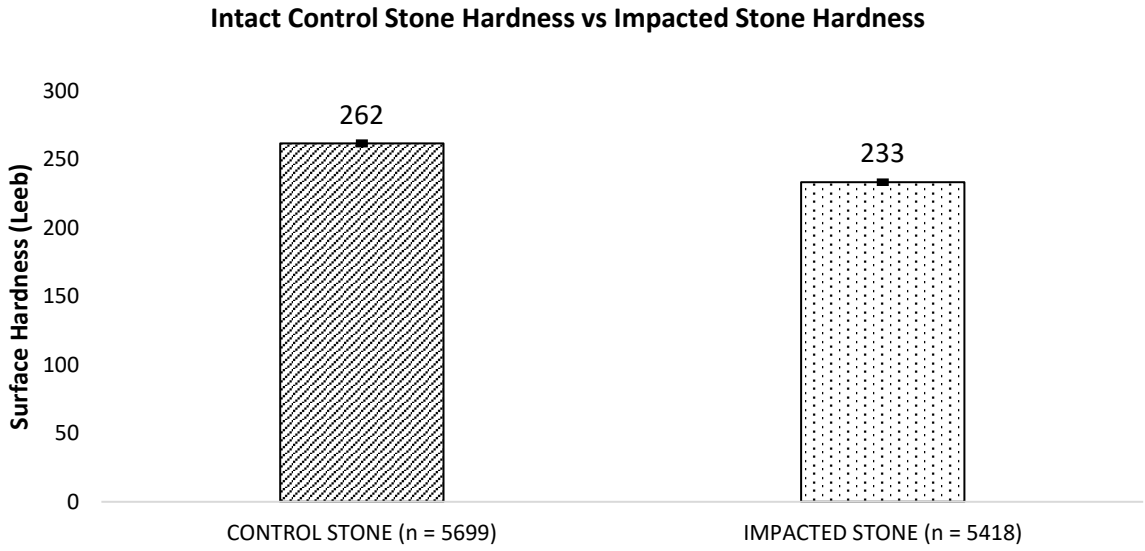

As outlined in chapters 2 and 5, previous studies into ballistic impact into stone have identified the presence of a central region of rock matrix compaction immediately around the impact point that experiences a lesser reduction in hardness than the wider impact crater surface (Mol *et al*, 2017 Gilbert, *et al*, 2019 Gilbert *et al*, 2020). To determine whether the centre of impact craters at Sabratha were less weakened than surrounding crater, the four central sampling points of each impact crater were analysed and averaged (figure 7.13, figure 7.14).

Figure 7.13: *The location of sampling points in the centre of the impact crater and the surrounding sampling points.*

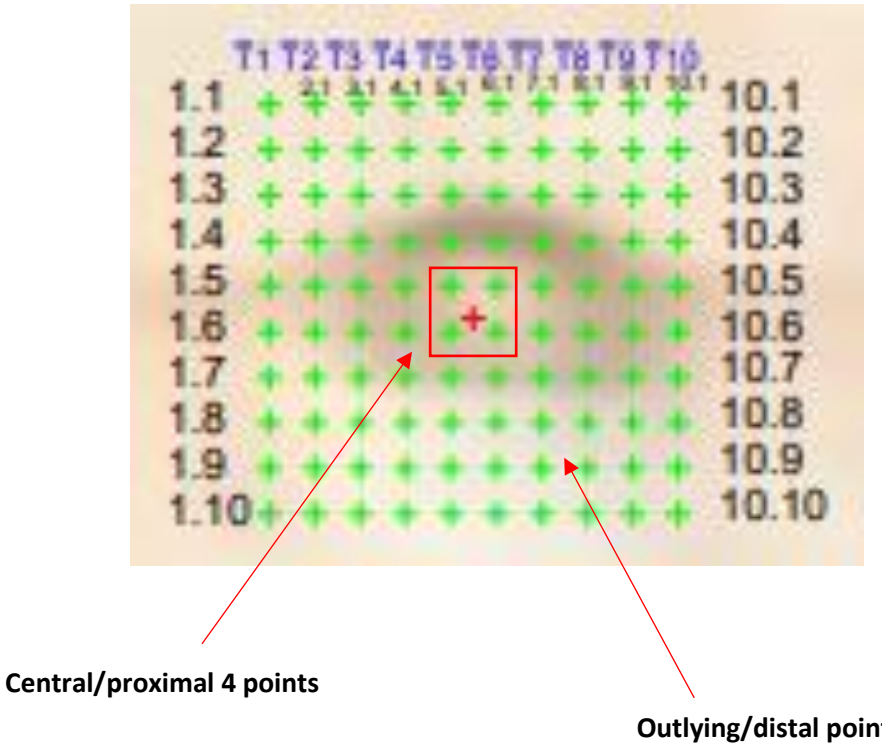

Figure 7.14: *A comparison of the average hardness of central imp-act crater points and outlying points.*

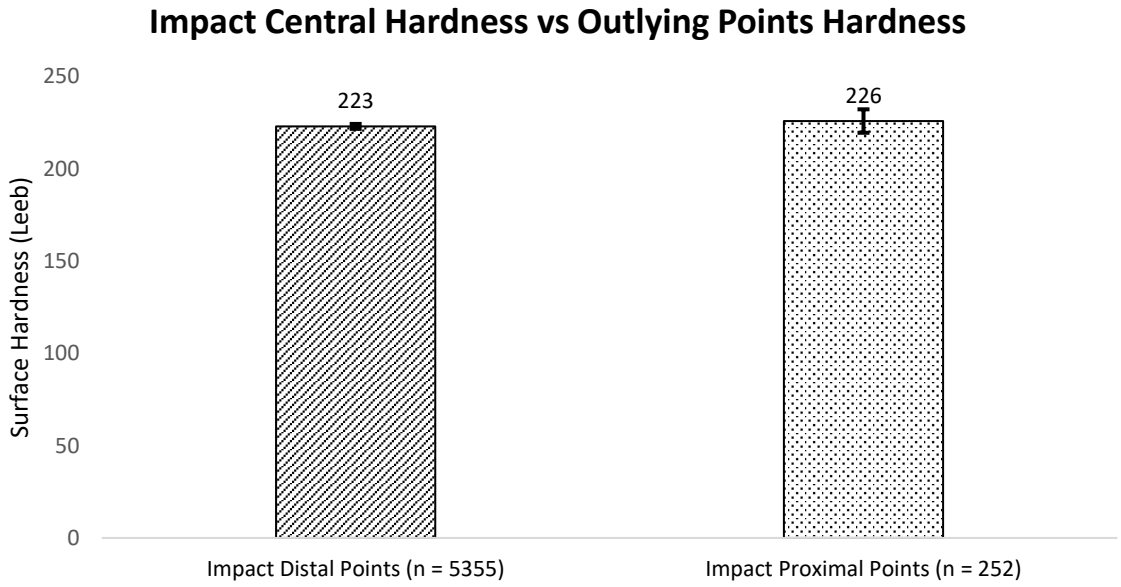

As seen in figure 7.14, central points of the impact crater are marginally harder (3 leeb/1.3%) than areas in the centre of the impact crater. This suggests that the findings of previous laboratory studies (chapter 2, chapter 3, Mol *et al*, 2017) that have shown hardening at the impact crater centre due to rock matrix compaction hold true in a "real-world" field setting. Although this is not in keeping with the results from chapter 5, which showed no hardening at the impact crater centre, this discrepancy supports the hypothesis put forward in section 5.2.3.1 that the presence or lack of hardening at the impact crater following ballistic impact is dependent on parameters such as target lithology and ammunition type.

In determining the effects of ballistic damage at the Sabratha site, it was necessary to determine which overall areas and specific craters were most weakened by the projectile impacts. To do this, the % hardness reduction of each impact crater was calculated by comparing its average hardness with the average hardness of the nearest control sample grid from of intact stone. The relative hardness reduction for all individual impact craters were then plotted in figure 7.15:

Figure 7.15: *Relative hardness reduction of each of the individual impact craters. N.B. samples do not have a standard error bar as it is not possible to calculate standard error for relative change on a single sample.*

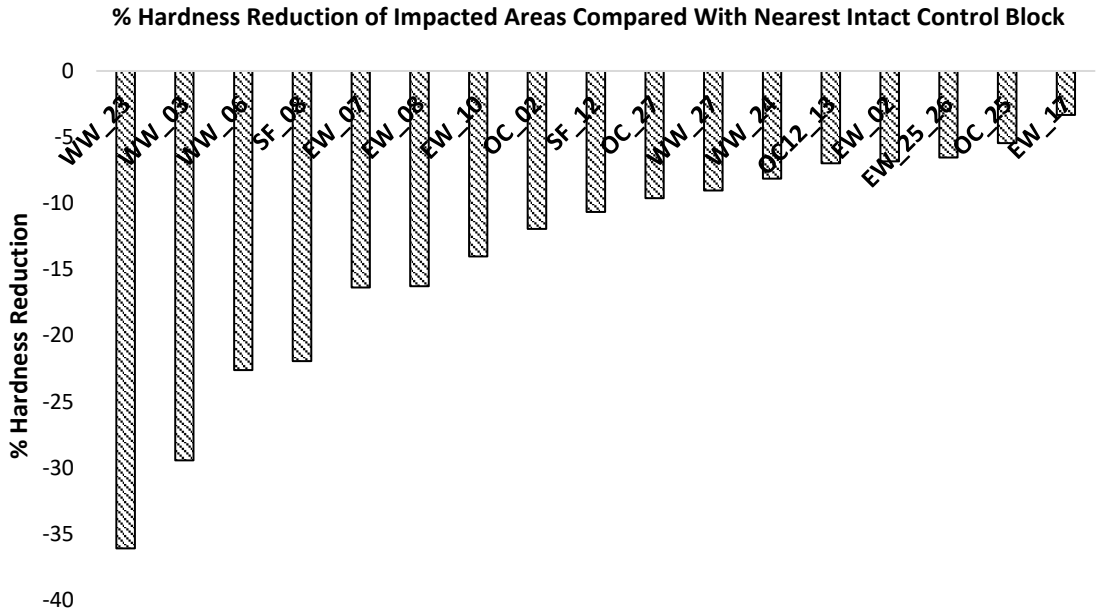

As seen in figure 7.15, WW_23 experiences the greatest reduction in hardness (-36.1%). The reason for this is believed to be that WW_23 is the only impact recorded present in the restored plaster section of the western wall (figure 7.16). This plaster is likely to be rigid, friable and with a lower compressive strength than the limestone of the amphitheatre walls. Therefore, it seems likely that impacts into this plastered section will lead to the greatest weakening. It should be noted that less data is available for WW_23 than for other craters (n =165 vs n = 300 for other craters). This discrepancy is due to the irregular surface being impossible to sample in places, so this conclusion should be treated with caution.

Figure 7.16: *The location of impact WW_23 into restored plaster*

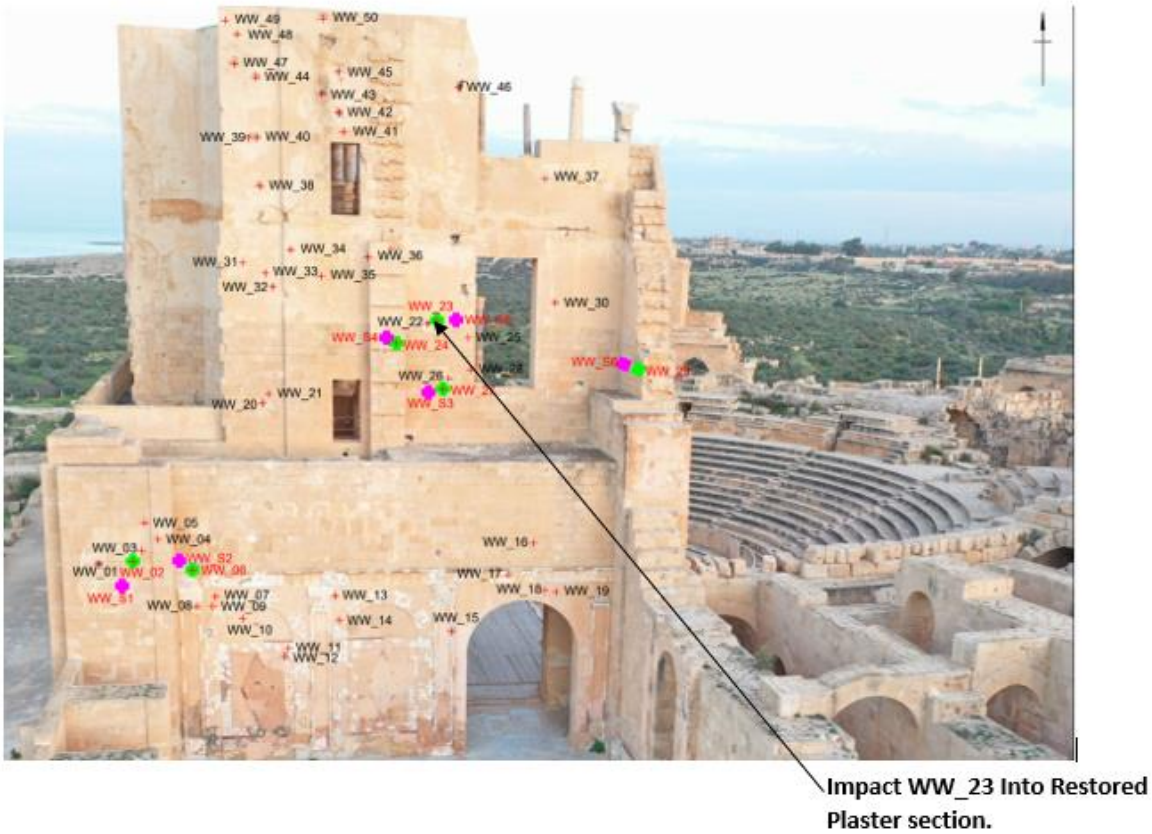

Also of interest is that the RPG Impact (EW_02) sees a lesser strength reduction than many other areas (-6.8%). This is thought to be because the radial scarring seen around the RPG hit is perpendicular to the wall surface and the direction of the RPG travel. This would mean that the shrapnel that caused that scarring "scraped" along the wall at an oblique angle, causing less of the kinetic energy of the shrapnel to be delivered to the wall, and thus resulting in a smaller reduction in hardness and corresponding weakening. This supports the findings of chapter 5 that angled impact results in less weakening than direct impact. However, the central block of the RPG hit has clearly been completely penetrated (figure 7.17), and although surrounding areas may have not been significantly weakened, this block is likely to be at risk of exacerbated further deterioration and structural weakening due to the large amount of material that has been removed/destroyed. Furthermore, the RPG hit has arguably caused the greatest spread of aesthetic deterioration at the site, as the radial scarring around the impact covers a large area (figure 7.7, figure 7.18).

Figure 7.18: *Radial scarring around the RPG Hit perpendicular to the central hole indicating the direction of travel of the RPG.*

Finally, in order to inform future conservation and restoration efforts at the site, it was decided to determine which region of the theatre was most damaged by the ballistic impacts.

The hardness data for the intact control blocks in each area containing a significant number of impact craters was compared with the hardness data for the impacted areas to calculate an average reduction in surface strength by each region of the theatre:

Figure 7.19: *Average reduction in surface hardness of impact craters by region*

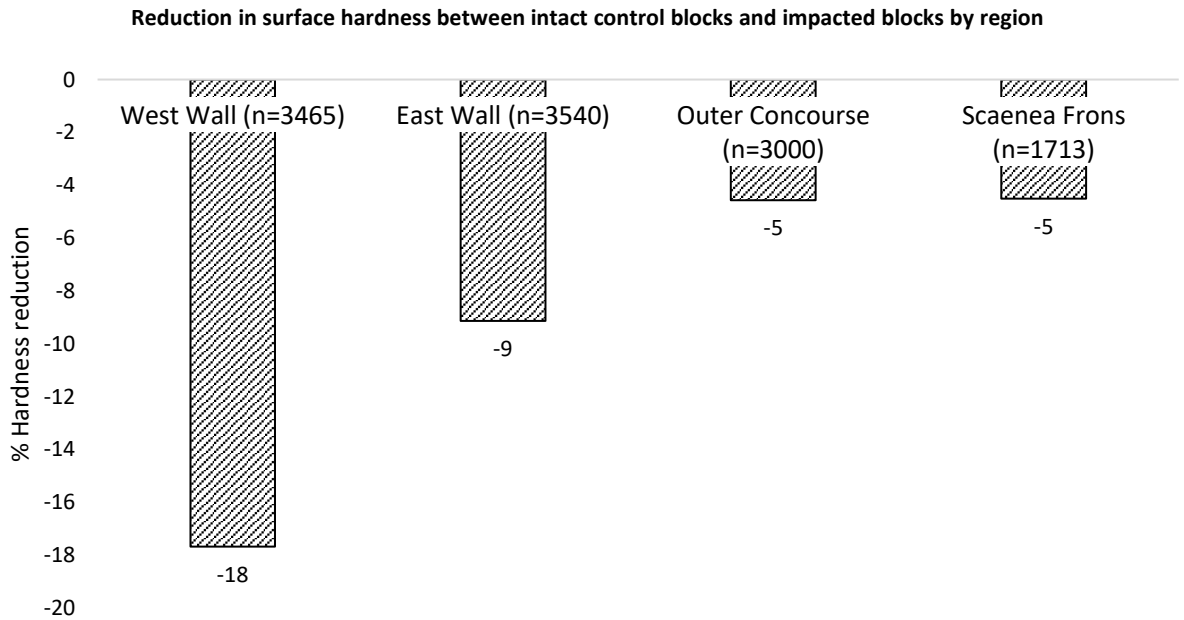

Figure 7.19 shows that the western wall appears to have undergone the greatest loss of hardness. This weakening is likely to be a result of the extensive restoration work in this region of the theatre, with widespread use of friable brittle plaster across the surface. This is notable because it supports the findings presented in chapter 5 that the variable most important in determining damage to heritage monuments damaged by ballistic damage is the target material/lithology. It also seems likely that the weakening in this region has been exacerbated by weathering action due to higher diurnal temperature fluctuations and exposure to saline sea spray. This is discussed in the following section.

7.4.2: Temperature results

Figure 7.20 shows the average temperature fluctuation of all 26 sensors across the site, as well as the fluctuations for IB 10, which showed the greatest overall temperature range (17◦C), and IB 5, which showed the lowest variation (9◦C).

Figure 7.20: *Average temperature variation over all sensors, and lowest and highest individual sensor variation*

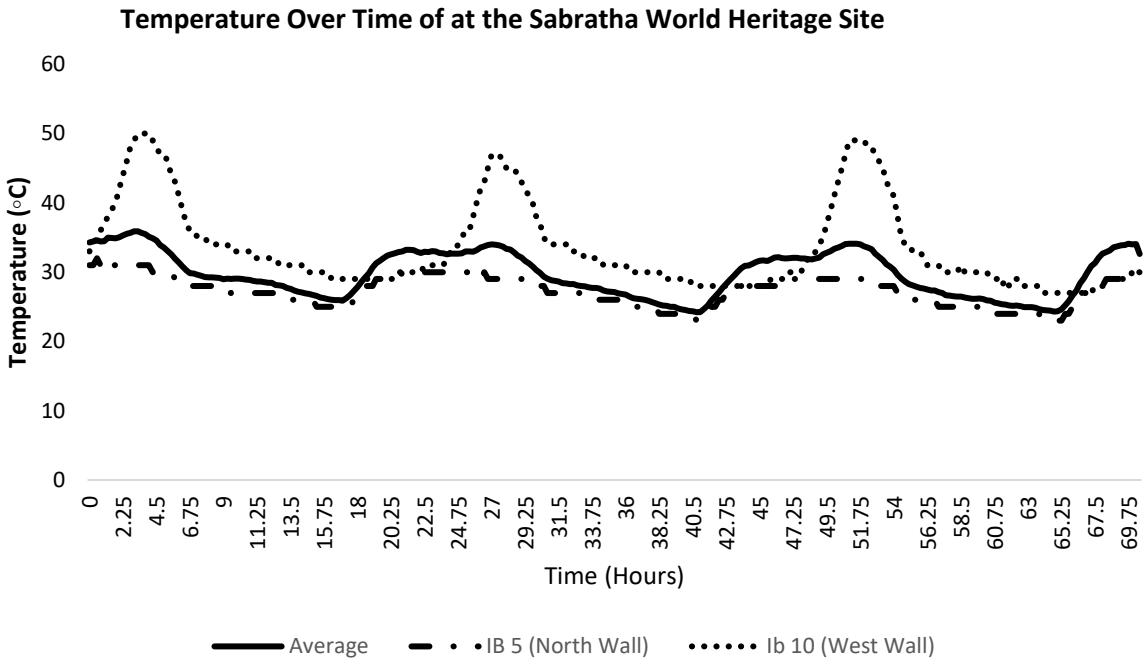

Figure 7.21 shows the locations of sensors IB 10 and IB 5. IB 5 is on the northern wall of the theatre. Using the sun plotting tool available at sunearthtools.com, it can be shown that the north wall, and sensor IB 5 never experiences direct sunlight on the dates for which data was collected. Therefore, it is unsurprising that IB 5 experiences little temperature variations as it is consistently in shadow.

Conversely, sensor IB 10 which was on a thin portion of the western wall, and therefore the east facing portion of this wall experiences direct sunlight until 12:00, at which point the west facing portion of the wall experiences direct insolation (figure 7.22). Given that this thin section of wall is likely to be exposed to sunlight throughout the day it is likely to see the greatest heating, this is supported by the Ibutton temperature data, which shows that IB 10 placed on this section of wall experiences the highest temperature variation.

Figure 7.21: *Locations of temperature sensors (North Wall) IB 5 and IB 10 (West wall).*

Figure 7.22: *Plot of the sun's course relative to the centre of the Sabratha amphitheatre on 27/07/2021 with location of sensors. Adapted from sunearthtools.com.*

North facing location of IB 5 in shadow zone- low temperature variation

West facing location of IB 10, constant west wall on both sides of thin wall, high temperature variation.

When analysing the ballistic damage and its interactions with potential weathering action, it was necessary to plot the average temperature variation of sensors by the various theatre areas. As see in figure 7.23, the east and west walls have much larger temperature variations than the scaenae frons and outer concourse. This supports the previous suggestion that east-west oriented surfaces experience much higher temperature variations than surfaces aligned north-south, as seen in figure 7.23.

Figure 7.23: *Average temperature variation across different regions of the amphitheatre.*

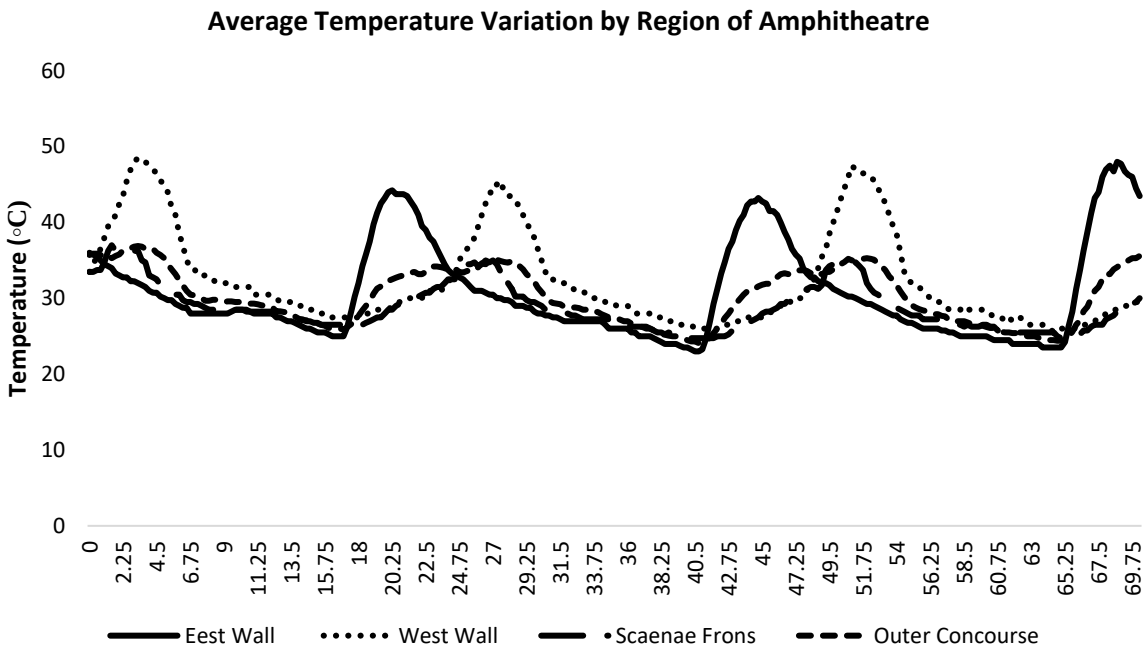

It is also noteworthy that the surfaces that experience the lowest temperature variation (the scaenae frons and outer concourse), also experience the lowest reduction in relative surface hardness of impact craters, as seen in figure 7.19. This is evidence that weathering action, which can be exacerbated by wide temperature fluctuations as previously discussed, may be causing enhanced hardness loss and weakening on the east and west walls when compared with the scaenae frons and outer concourse. This hypothesis is also supported by protimeter data indicating the presence of moisture and salt contamination at various points around the site.

7.4.3: Protimeter results

Results from the protimeter transects are shown in figure 7.24 and suggest that transect 8 has the highest overall WME, suggesting the highest contamination by salt and moisture. The lowest moisture and salt content is found on transect 14. These results are notable, because they correspond well with the distance of the transects to the most likely source of moisture/salt contamination, the sea. Transect 8 is on the west wall, and directly exposed to saline sea spray. Transect 14 is on the opposite side of the theatre, and thus sheltered from the coast, and likely to experience less contamination by saline spray, this can be seen in figure 7.25.

Figure 7.24: *Showing WME of individual transects, indicating salt/moisture contamination levels.*

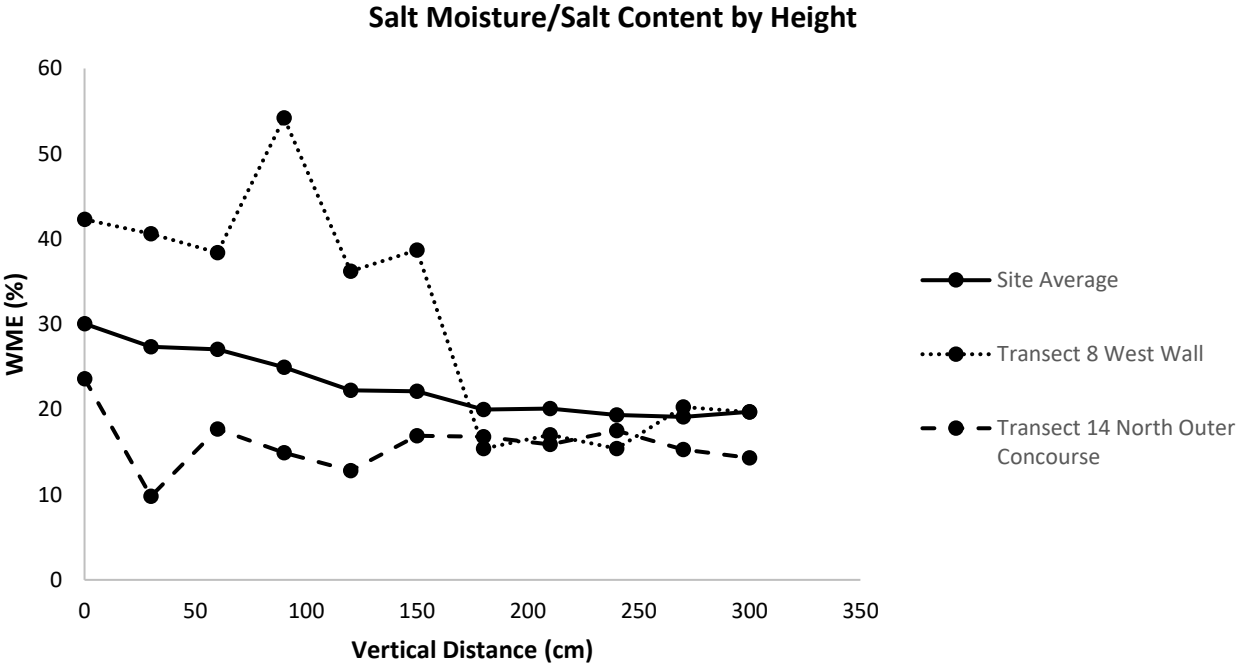

Figure 7.25: *Demonstrating that transect 8 which has the highest WME is directly exposed to sea spray from the coast, whilst transect 14 is well sheltered from any potential contamination by sea spray.*

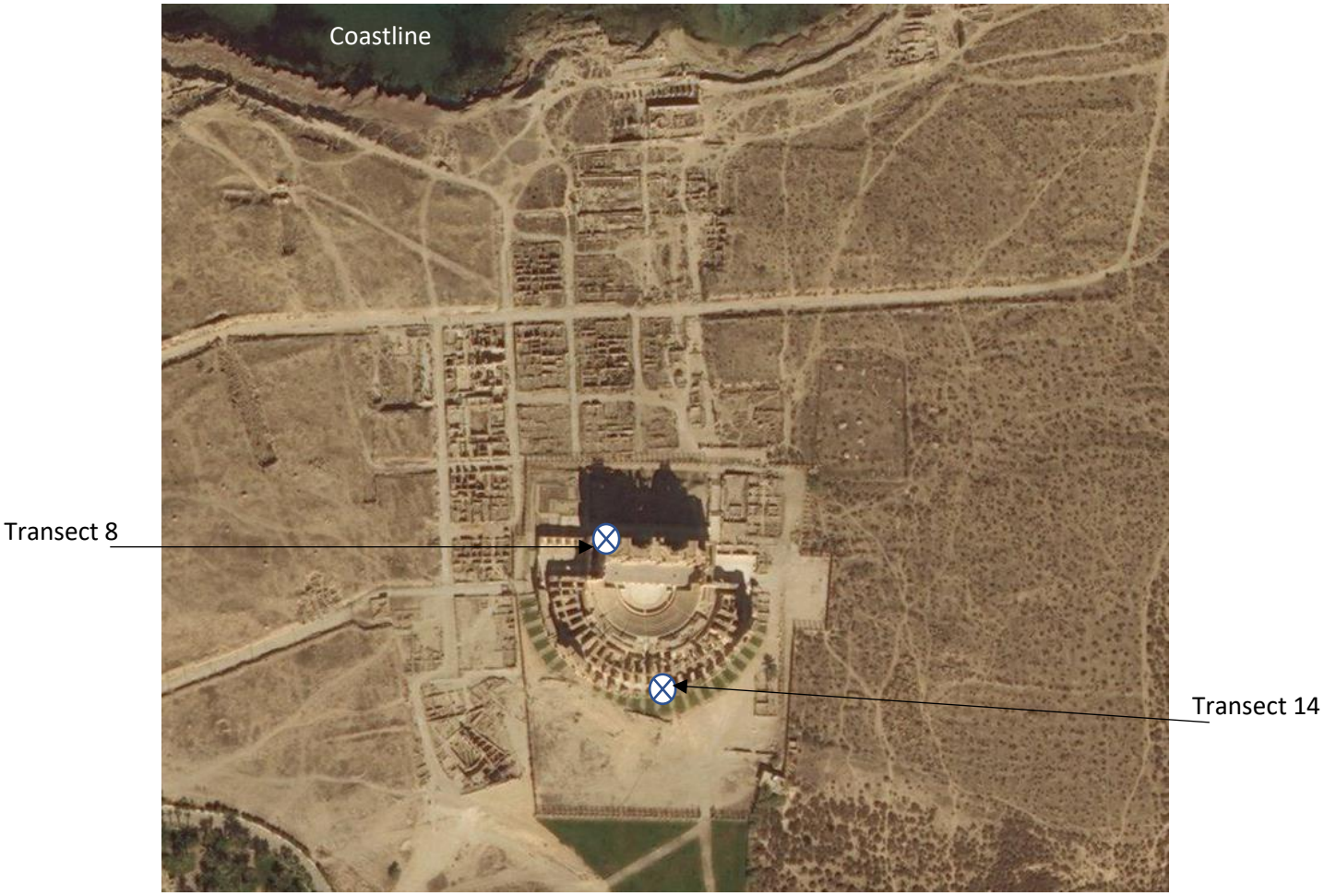

This trend is mirrored over the site as a whole. Transects present on the main theatre building (transects 1-9) have consistently higher WME readings than the transects on the outer concourse (transects 9-22) as shown in figure 7.26. This is because the transects on the theatre are more directly exposed to saline spray contamination from the coast than transects on the outer concourse which are sheltered from this contaimination.

Figure 7.26: *Average WME readings from the exposed theatre transects and the sheltered outer concourse transetcs.*

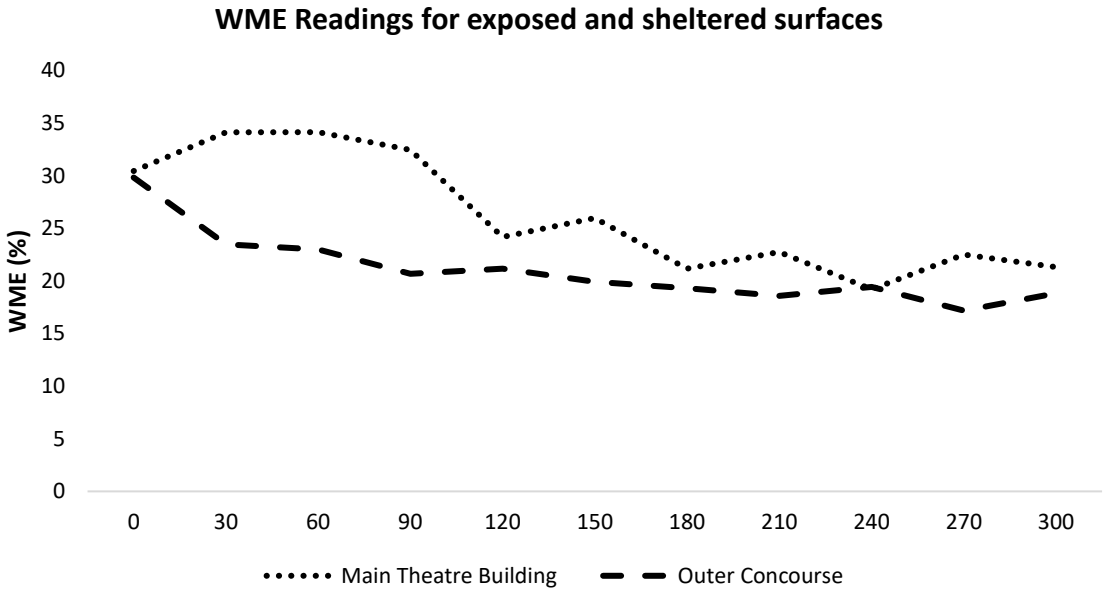

The data presented in figure 7.26 is further evidence that the hardness loss of a given impact crater is affected by weathering action. The outer concourse shows less salt and moisture contamination than transects on the main theatre building and experiences a lower loss of hardness than areas of the theatre directly exposed to sea spray, as seen in figure 7.19. This suggests that hardness reductions are more severe in areas exposed to weathering by sea spray. Protimeter readings were not possible on the sheltered scaenae frons due to its uneven wall topography and decorative columns etc. Therefore, data for this area is not included in figure 7.26, but the fact that this area is completely sheltered from exposure to the coast would suggest that there is comparatively little salt/moisture contamination in this area. This agrees well with the small hardness reduction of impacts in the scaenae frons region seen in figure 7.19.

7.5: Discussion of significance of results

Taken as a whole, the results from the Sabratha heritage protection project present a compelling narrative. The identification of impact clusters on southward facing portions of the structure as well as the interior of the outer concourse allow the reconstruction of probable exchanges of fire during the fighting around the theatre (figure 7.11). As a whole, areas of the amphitheatre exhibiting ballistic impact craters are weaker than unimpacted regions, and therefore this damage should be considered for targeted intervention when planning future conservation work at the site.

The hardness readings allow us to identify that the western and eastern wall of the structure have been most weakened by the small arms fire, whilst the impacts on the outer concourse and scaenae frons have caused comparatively little weakening (figure 7.19). The hardness loss on the western wall is particularly pronounced, probably due to the presence of impact craters in plaster material used in restoration work. Therefore, future interventions may wish to target the western and eastern walls as a priority, especially as the RPG impact to the eastern wall has caused massive damage to the central block and widespread aesthetic damage, although outlying areas of the RPG impact seem to have experienced relatively little weakening (figure 7.15, figure 7.18).

Weathering action seems to have played a role in the exacerbated hardness loss of impacts on the east and west walls of the main theatre building. These surfaces are directly exposed to saline sea spray from the nearby coast, and also experience much greater temperature fluctuations due to their east-west orientation. Conversely, the scaenae frons and outer concourse experience less direct solar heating and are sheltered from sea spray. This has led to less weathering action through capillary driven penetration of saline water and resulted in less surface hardness loss in the impact craters on these surfaces. This connection between solar heating, ingress of saline water and weathering deterioration of impact craters shows strong agreement with the results discussed in section 3.4.4 and strengthen the conclusions of that chapter, as well as the argument that ballistic impact acts to exacerbate weathering deterioration.

It is also possible to assess the validity of the risk matrix using two impacts at the Sabratha site. Consider impact WW_23, the impact which sees the greatest loss of hardness, and impact EW_02, the RPG impact area which sees surprisingly little reduction in strength. Below are the known risk factors for each of these two impacts:

Table 7.1: *Known risk factors for impacts WW_23 and EW_02*

Impact	lithology/material and wave impedance?	Efflorescence Visible at impact site?	Known sources of weathering salts at site (e.g. coastal)?	Impact Angle?	Projectile Construction?
WW_23	Plaster (relatively low wave impedance	No	Yes	Normal	Unknown
EW_02	Stone (relatively high wave impedance)	No	Yes	Oblique (shrapnel ricocheting along target surface, see figure 7.18)	Unknown

Using the risk matrix conceived in chapter 7 we can compare the scores of these two impacts. As noted (Santa Cruz Astorqui *et al*, 2023) building plaster is a porous material that will have a lower density and therefore wave impedance than the dense limestone used to construct the theatre, therefore WW_23 scores 6 in this category and EW_02 scores 0. No efflorescence was observed in either crater, scoring both impacts 0 for this criteria. Both impacts are found on a monument near the coast where salt presence is known to be an issue, as demonstrated by elevated protimeter readings on portions of the site (see figure 7.26) and therefore both impacts receive 4 in this category. The hemispherical nature of impact WW_23 suggests a 90° impact (3), whilst the HEAT warhead which caused the radial, elongated scarring of impact EW_02 is observably oblique (0). Finally, the metal of both projectiles is unknown, and therefore the cautionary principle is applied and both impacts are given a 2. These scores are shown in the context of the refined risk matrix in table 7.2:

Table 7.2: *Risk comparison of impacts WW_23 and EW_02*

WW_23:

			Score
Target lithology	High Wave Impedance	0	6
	Low Wave Impedance	6	
Efflorescence visible in impact crater?	No	0	0
	Yes	5	
Known sources of weathering salts at site (e.g. coastal)?	No	0	4
	Yes	4	
Impact Angle	Oblique	0	3
	Normal	3	
Projectile construction	Lead	0	2
	Steel	2	
			Total: **15**

EW_02:

			Score
Target lithology	High Wave Impedance	0	0
	Low Wave Impedance	6	
Efflorescence visible in impact crater?	No	0	0
	Yes	5	
Known sources of weathering salts at site (e.g. coastal)?	No	0	4
	Yes	4	
Impact Angle	Oblique	0	
	Normal	3	
Projectile construction	Lead	0	2
	Steel	2	
			Total: **6**

Total Score

20:	Very High Risk
>10:	High Risk
≥5:	Moderate Risk
<5:	Low Risk

WW_23 score: 15 (high risk)

EW_02 score: 6 (moderate risk)

As is demonstrated, the risk matrix identifies impact WW_23 as significantly higher risk than EW_02, which is consistent with the known results for hardness loss for these two impacts shown in figure 7.15, with WW_23 seeing a reduction in hardness of -36.1%, compared to –6.8% for impact EW_02. This therefore validates the construction of the risk matrix, demonstrating its ability to identify those impacts most at risk, even in spite of the arguably more spectacular visual damage caused by the RPG hit that created impact EW_02.

7.6: Conclusions

This chapter was a success in fulfilling its stated aims. The work presented here has demonstrated that techniques developed in a laboratory setting and fieldwork on historic impacts could be used to identify modern ballistic damage at risk of further deterioration. The particular observations and risks identified using these methods in a field setting are outlined below, demonstrating the ability of these techniques to highlight specific areas at increased risk, and what hose risk factors are:

- Regions that have undergone ballistic impact are weaker than those that have not. Therefore, impact craters should be considered as particularly vulnerable to increase future deterioration when planning conservation work.

- The east and west walls have been most weakened by ballistic impact as measured by surface hardness loss. These surfaces see the highest temperature fluctuations due to solar action, as well as the highest moisture and salt content. Therefore, their exacerbated weakening is likely due to increased weathering action. Future conservation and restoration efforts may be best targeted at these portions of the main theatre building.

- The outer concourse and scaenae frons have been less weakened by comparison and experience lower temperature fluctuations and are less exposed to saline spray contamination from the coast.

- The impact that sees the greatest weakening is WW_23 which is an impact into a plastered region of the west wall. It seems likely that plastered regions are most at risk from ballistic impact due to the weak and brittle nature of this material. Given that many impacts on the theatre's west wall are into this plaster material (figure 7.16), this information may prove useful when prioritising conservation and preservation work. It also supports findings in chapter 5 that the mechanical properties of the target lithology/material are critical in controlling damage levels and hardness loss.

Finally, the fieldwork at Sabratha was able to fulfil Research Objective V by ground-truthing the laboratory-based findings of the risk of exacerbated deterioration of impact craters exposed to ingress of saline groundwater in wide-temperature fluctuation arid environments. The Sabratha study also confirmed the findings of chapter 5 that target lithology/material is a key factor in controlling damage levels after ballistic damage, which is a core aspect of the risk matrix detailed in chapters 5 and 6. The risk matrix was then applied to two impacts at the site with a known differences in risk factors (target lithology/material wave impedance and impact angle) and successfully identified the impact with the greatest reduction in hardness, thereby validating the risk factors used in the risk matrix and its formulation. Further testing and refinement of the risk matrix could be achieved in future work by identifying sites with known projectile construction and efflorescence visible inside the impact craters, as it was not possible to identify these risk factors at the Sabratha site.

Chapter 8
Conclusions

8.1 Discussion of key project findings

In order to provide a comprehensive overview of the findings of this PhD project and how the research developed, the outcomes of each chapter have been separated according to the various methods used throughout the project.

8.1.1: Surface hardness survey findings

Chapter 2 served as a pilot study to develop and test an effective method for collecting and analysing surface hardness data from stone damaged by ballistic impact. As outlined in sections 2.4.1 and 2.5.1, the surface hardness survey using the Equotip rebound device was able to demonstrate a statistically significant difference between intact control stone and the damaged areas of the impacted sample. Furthermore, the survey was able to demonstrate a statistically significant difference between the areas of the sample directly damaged by the impact (i.e. the impact crater/shattered surface) and non-impacted sides/surfaces of the sample. This was an early indicator of the ability of surface hardness survey to identify areas of heritage stone weakened by ballistic impact, and therefore the potential efficacy of this method in identifying and triaging heritage assets most at risk in a post-conflict environment. Limitations to this method identified in chapter 2 are that heat-mapping of the hardness survey data suggests that weakened areas of stone often do not correspond to areas of visible surface fracture (figure 2.14). This suggests that other surveying methods (e.g. permeability survey) would be required to identify areas of surface fracture induced by ballistic impact which are likely to be exploited and exacerbated by weathering subsequent to ballistic damage. Chapter 2 also provided limited support for the crushing and compaction of the stone matrix at the impact crater centre hypothesised by Mol *et al,* (2017) by demonstrating that the centre point of the impact crater had a higher hardness than the wider damaged surface, which is consistent with hardening caused by compaction as observed by Aoki and Matsukura, (2007). If this phenomenon could be demonstrated to be a consistent feature of ballistic impact into rock, it could have implications for weathering behaviour of the impacted stone, as crushing of the matrix in particular areas of the impact crater will affect moisture flow and accumulation in this area (Mol *et al,* 2017).

Having demonstrated the potential for hardness survey to identify areas of ballistic damage in a field setting, chapter 3 aimed to test this technique in a field setting where heritage stone damaged by ballistic impact has subsequently been exposed to salt-weathering. Surface

hardness survey was deployed across the impact craters and unimpacted stone inside the Royal Garrison Church, Portsmouth, which has been highly exposed to salt weathering processes due to its lack of roofing and coastal location providing a constant source of saline sea spray. The hardness results from this field study showed that after an extended period of weathering (C. 80 years in the case of the church) weathering of the impact craters has been sufficient to remove any material initially weakened by the ballistic impact, resulting in impact craters and intact column surfaces not having a statistically significant difference in hardness (figure 3.13). This is consistent with the findings of Mottershead and Pye (1989, 1994) that showed that weakened surface material is often removed from weathered rock by the haloclasty process. In addition to this, hardness survey in chapter 3 showed that column sides without any ballistic impact were significantly harder than those that had sustained ballistic impact (figure 3.12), suggesting that the introduction of fracture networks precipitated by ballistic impact allows more severe weathering induced weakening in impacted columns than unimpacted columns due to the connectivity of fracture networks. This hypothesis is supported by the diagrams presented in figures 3.20-3.11 and 3.24-3.36. Section 3.4.4 showed that hardness data can be highly useful in detecting variation in weathering induced weakening associated with spatial variation in exposure to weathering agents. Those columns which were most exposed to weathering processes due to a lack of roofing or accumulation of moisture associated with solar heating exhibited lower hardness. These weathering processes are also likely to be the cause of the probable gypsum crusts accumulating in impact craters shown in figure 3.31 (Rodriguez-Navarro and Sebastian, 1996, Török, 1996, Montana *et al*, 2008). Principally then, hardness survey results presented in chapter 3 served to illustrate the potential efficacy of the technique in analysing the relationships between ballistic impact craters and fracture networks and spatial variation in exposure to weathering processes, and how ballistic impact contributes to these weathering processes in a field setting.

Chapter 4 sought to determine the ability of hardness survey to assess differences in surface hardness profiles caused by two of the key parameters considered as part of this PhD project; changing impact angle and the presence of haloclasty weathering processes. Hardness data for Cotswold Hill Cream Limestone samples impacted at 90° suggested that normal impact results in greater weakening of the impact face (figure 4.24). Hardness measurements obtained from the centre of the impact crater after 90° impact were higher than those obtained from peripheral areas of the impact crater, which is consistent with the findings of chapter 1,

and again provides limited evidence to support the hypothesis of matrix compaction at the point of direct bullet impact (figure 4.27). For both impact angles (90° and 45°), samples were found to be substantially reduced in hardness after weathering, with large reductions in hardness for both samples occurring on the impact face, whilst side 3 (the antipode of the impact face) saw the lowest reduction in hardness both after impact and after weathering (figures 4.24, 4.25). This suggests that ballistic impact causes the greatest fracturing around the impact crater on the impact face, due to the high stress wave pressures at the impact point (Campbell *et al*, 2022). This dense fracture network surrounding the impact crater can then be exploited by saline solution during the weathering cycles, leading to higher levels of salt crystallisation and associated micro-fracturing, which causes greater weakening and loss of hardness on the impact face after weathering (Renard *et al*, 2009). Finally, chapter 4 served to highlight the need for a greater number of samples in subsequent experiments of this project to determine whether phenomena such as the apparent greater loss of hardness across the wider sample surface outside of the impact face for 45° could be replicated with a greater number of samples or was an artefact of random inhomogeneities in the small sample size used in this experiment.

Chapter 5 employed the lessons learned in chapter 4, utilising a greater number of samples across two different lithologies, whilst also investigating how bullet type/construction and impact angle affected the loss of hardness after ballistic impact. As shown in section 5.1, lithology is key in determining the hardness loss of stone due to ballistic impact. Sandstone samples, with a greater compressive strength (which is correlated with rebound surface hardness as described by Aoki and Matsukura, 2008) saw substantially less hardness loss than limestone samples (figure 5.9), suggesting that hardness could provide a rapid and non-invasive method of assessing which heritage buildings are most at risk from ballistic impact in a field setting. Chapter 5 supported the findings of chapter 4 by confirming that for both impact angles and both lithologies hardness loss was greatest on the impact face (figure 5.12), which is due to the dense fracture network initiated at the impact crater as discussed previously. Finally, throughout the ANOVA analysis performed in chapter 5, detailed statistical analysis of surface hardness survey results demonstrated the utility of this technique in determining which parameters (impact angle and bullet type) resulted in significant weakening for each of the lithologies. This contributed to the creation of a data-driven risk matrix that can be used to identify and triage regions of heritage stone most weakened in the aftermath of ballistic impact (table 5.13). Analysis of the hardness results in

chapter 5 found no evidence of the matrix compaction at the point of impact observed in chapters 2 and 4, which may suggest that this phenomenon is not a consistent behaviour of stone after ballistic impact, but rather a product of individual impacts and arising from a confluence of target lithology, impact angle and projectile type. Limited evidence of this compaction phenomenon occurring for limestone samples after 90◦ impact is provided by permeability data as discussed in section 8.1.2 below.

Chapter 6 continued the analysis of the larger data set analysed in chapter 5, having subjected these samples to an intensive weathering regime. Hardness results confirmed the preliminary findings of chapter 4, that the fracture network initiated on the impact face by the projectile allows the accumulation of saline solution in the area around the impact crater, causing the impact face to experience the greatest loss of hardness after weathering for both lithologies at each impact angle/ bullet type (figure 6.4). As in chapter 5, chapter 6 showed that lithology is a key determinant of the degree of weakening after impact, with limestone samples seeing greater loss of hardness than sandstone samples (figure 6.3). This is because the limestone samples have a low enough tensile strength that fracture networks initiated by the ballistic impact can be exploited and extended by salt crystallisation with pressure in excess of the tensile strength of the rock (Viles, Goudie, 2007). The hardness results in chapter 6 were subject to the same statistical ANOVA testing that was used in Chapter 5, allowing the identification of the ballistic parameters contribute to the most severe weathering weakening for each of the variables. This allowed the refinement of the risk matrix first devised in chapter 5 to include weathering risks likely to be present at arid MENA heritage sites (table 6.8).

Chapter 7 served as the culmination of the project, deploying the hardness surveying techniques developed in previous chapters to a heritage site recently damaged by ballistic impact and exposed to haloclasty weathering risks. The hardness survey encompassed the perimeter of the Sabratha Roman amphitheatre World Heritage Site and allowed the identification of those regions of the site most weakened after ballistic impact. Results demonstrate both that impacted regions of stone were weaker than unimpacted regions of stone (figure 7.12) and that some areas of the site had experienced greater loss of hardness after ballistic impact than others (figure 7.19). Analysis of weathering risks associated with higher temperature variation and exposure to contaminated saline water presented in figures 7.20-7.26 suggest that the impact craters that have experienced greatest loss of hardness are those most likely to experience repeated cycles of salt crystallisation caused by ingress of

saline moisture and higher diurnal temperature variation. The risk matrix was tested on two impacts at the Sabratha site, and successfully distinguished the impact crater at greatest risk, as defined by the greatest reduction in surface hardness, demonstrating the validity of the risk matrix constructed using the findings of the previous chapters. Taken together, the hardness results presented in chapter 7 validate the premise of this project by showing that ballistic impact acts to exacerbate weathering weakening of heritage stone in arid MENA regions, and that the regions most at risk after ballistic impact can be identified and ultimately prioritised for conservation intervention using the risk matrix designed over the course of this project.

8.1.2: Permeability findings

The permeability results presented in chapter 2 provided preliminary evidence of the efficacy of permeability survey as a technique for identifying areas of deterioration and susceptibility to subsequent weathering in stone damaged by ballistic impact. Figure 2.12 shows both that the impacted stone sample has a higher permeability than unimpacted stone, and that the impact face and impact crater see the highest increase in permeability, due to the dense fracture network initiated at the impact crater raising the permeability most in the area around this point. This is consistent with the results of the hardness survey, which consistently found that damage and weakening to impacted samples was most intense on the impact face of samples, as discussed in section 8.1.1 above, and confirmed by Osinski *et al,* (2020). In addition to demonstrating the ability of ballistic impact to increase permeability in impacted stone, detailed mapping of the permeability survey in chapter 2 also showed that the areas of greatest increase in surface permeability were associated with visible surface fracturing (figure 2.14), which suggests that rapid in-situ visual assessment of heritage stone damaged by ballistic impact could quickly assess highly fractured stone which is most susceptible to the ingress of weathering agents, allowing rapid allocation of conservation resources. One limiting aspect of permeability survey discovered in chapter 2 was the highly time-intensive nature of the technique. It was determined that it would be necessary to develop a more targeted approach than surveying the entire surface of an area of heritage stone damaged by ballistic impact, as such an approach would likely not be compatible with the time constraints often associated with a field setting.

To further assess how well-suited permeability survey was to use in-situ in a heritage setting, chapter 3 sought to deploy the technique to impact craters and unimpacted stone inside the

Royal Garrison Church, Portsmouth. Results showed both that impact craters had significantly greater permeability than un-impacted areas of the church's columns (figure 3.14), and also that intact region of columns without impact craters were less permeable than those that exhibited impact crater (figure 3.15). The relationship between ballistic damage and increased column permeability was further supported by the demonstration that column permeability outside of the impact crater was correlated with distance from the explosive device which was the source of ballistic damage (figure 3.17). The findings presented in figure 3.14-3.17 illustrated the ability of ballistic impact to create interconnected fracture networks across an affected surface, which was then mapped and visually demonstrated in figures 3.18-3.22. These interconnected fracture networks can then be more easily exploited by weathering agents, ultimately contributing to greater weakening across the affected surface, as demonstrated through hardness survey and discussed in section 8.1.1 and shown experimentally by McCabe *et al,* (2010). Therefore, the permeability results presented in chapter 3 demonstrated both that this technique was appropriate for a field-setting, and that it was highly useful in understanding the role that ballistic damaged played in creating fracture networks that were then exploited by weathering agents such as saline water to exacerbate haloclasty weakening on surfaces affected by ballistic impact.

Chapter 4 provided a preliminary insight into the permeability behaviour of stone samples damaged by ballistic impact after weathering, and with varied impact angle. Permeability data from the impact craters of the two samples provides further limited evidence of the compaction of stone matrix after 90◦, which is not believed to occur after oblique impact of 45◦ (section 4.4.6.1). The difference in crater permeabilities before and after weathering for the two samples presented in table 4.10 provides preliminary evidence of the importance of impact angle in controlling mechanical responses of impacted stone, with direct impact crater increasing in permeability after weathering, whilst oblique impact crater exhibits a decrease in permeability after weathering. This disparity is believed to be the result of differing compaction behaviours of the two samples due to ballistic impact, as outlined in section 4.10. Outside of the impact crater. Permeability data agreed with the hardness findings discussed in chapter 4 and section 8.1.1 in showing that 90◦ impact resulted in much greater fracture damage, and corresponding increase in permeability, than 45◦ impact. Outside of the impacted face, the limited data which was collected for sample surfaces 2-6 was found to be highly variable and skewed by high permeability readings from individual cells. This was an indication that the attempt to find a faster permeability sampling regime which would be

appropriate for a field setting suffered from having a limited sample set of two. Chapter 4 therefore served to highlight the requirement for a larger number of replicate samples in future experiments in order to obtain useful data sets.

Using a larger number of samples, chapter 5 utilised permeability survey to highlight the parameters which were most significant in controlling fracture damage immediately after ballistic impact. Results agreed with the findings of hardness survey in showing that lithology was the most important variable in determining fracture induced increases in permeability, with the weaker limestone samples seeing substantially larger increases in permeability after impact than sandstone samples impacted under equivalent conditions (figure 5.9). This is consistent with known mechanics of rock fracture, whereby stone with a lower tensile strength will experience more fracturing due to stress waves with peak pressures in excess of the rock's tensile strength (Ai, 2006). Furthermore, permeability results in chapter 5 confirmed the findings of chapter 4, that the impact face is most severely fractured after ballistic impact (figure 5.23) and also demonstrated that fractures on non-impact faces were initiated and spread from the impact crater (figure 5.24, 5.20). Therefore, given the issues with the time-intensive nature of permeability survey, the results in chapter 5 were used to determine that the most efficient method for in-situ sampling of permeability of damaged heritage stone is to target intensive sampling on the impact face, where fracture damage is likely to be most intense and ingress of weathering agents presents the greatest risk. Unlike the results of hardness survey, permeability data from the 12 limestone samples impacted at 90◦ does suggest that the impact point experiences matrix compaction at the point of ballistic impact, resulting in a lower permeability than the surrounding impact crater (figure 5.26). This phenomenon was not present in sandstone samples, which again suggests that matrix compaction may only occur under certain conditions of lithology, impact angle and projectile type. Finally, the permeability results were analysed using ANOVA to determine which ballistic parameters (impact angle, projectile type) had the greatest influence on permeability changes after impact due to fracturing. The results of these ANOVA were then used in conjunction with the hardness findings discussed in section 8.1.1 to construct the risk matrix presented in table 5.13.

Chapter 6 completed the permeability work of this project by subjecting the samples shot in chapter 5 to intensive weathering regimes and analysing the effects on permeability. Principally, the results demonstrated that lithology is the key determinant of permeability both before and after weathering, as limestone samples saw an increase in permeability due to

weathering, whilst sandstone samples saw a decrease. This is believed to be due to the differing tensile strengths of the two lithologies, with salt crystallisation pressures able to exceed the tensile strength of the limestone and increase permeability through secondary fracturing, a phenomenon that does not occur for the sandstone samples due to a higher tensile strength (Renard *et al,* 2009, Viles and Goudie, 2007). The increases in permeability after weathering were focussed on the impact face, suggesting that the denser fracture network created on the impact face after ballistic impact (as demonstrated in chapter 5) acted to accumulate salt crystallisation weathering in this region, supporting the findings of chapter 3 which showed that impact craters and their associated fracture networks accumulate weathering agents that exacerbate deterioration (figure 3.31). The permeability results in chapter 5, coupled with published literature (McCabe *et al*, 2010 Renard *et al*, 2009 Navarre-Sitchler *et al,* 2013, 2015, Worthington *et al* 2016) illustrated that fracture networks first precipitate by ballistic impact can be exploited by haloclasty processes to create feed-back loops which expand fracture networks in certain lithologies and thus increase permeability and ultimately weaken the affected stone. This finding was then used to refine the risk matrix to highlight the risk of further deterioration by weathering to heritage stone damaged by ballistic impact (table 6.8).

8.1.3: Photogrammetry findings

The results of photogrammetric analysis presented in chapter 4 demonstrate that the method can detect small relative changes in the volume of impacted stone (< 2%, figure 4.13, table 4.4). The results presented here also demonstrate that 90° impact causes a greater loss of volume than 45° impact, which is consistent with the hardness and permeability findings presented above which suggest that direct impact causes more damage than oblique impact across every metric used to measure deterioration. This finding is also consistent with work by Gault (1973), which found that the mass of material ejected by the impact decreases with more oblique impact angles, as less kinetic energy is available to excavate the impact crater when the projectile ricochets off the target surface. Photogrammetry also proved useful in quantifying the volume of salt crystals precipitated on sample surfaces after weathering (figure 4.13), and was able to demonstrate that despite reductions in sample hardness, neither sample had experienced a substantial loss of volume due to haloclasty weathering, which is in keeping with previous studies that have found that NaCl weathering does not cause break down of rock to the point of disintegration and volume loss (Goudie *at al,* 1970, Manohar *et al,* 2020).

In addition to supporting the findings of chapter 4 by demonstrating that NaCl weathering produces hardness reduction without volume loss, Photogrammetry results in chapters 5 and 6 expanded on those in chapter 4 by attempting to correlate measurements of impact crater area with other indicators of stone deterioration and susceptibility to weathering agents. Impact crater has been shown to be correlated with the overall increase of permeability of shot samples and with the loss of hardness across the sample surface (figures 5.29, 5.30). The correlation of impact crater with permeability is also evident for limestone samples after weathering, suggesting that the size of the impact crater and corresponding fracture network controls the extent of weathering induced fracturing feed-back loops (Navarre-Sitchler *et al,* 2013). As with hardness and permeability results discussed above, photogrammetry data shows that lithology is a critical variable in controlling the level of damage sustained by shot stone, with limestone samples exhibiting substantially larger impact craters than sandstone samples (figure 5.5, figure 5.28). This finding was used to inform the increased weighting given to the target lithology in the creation of the risk matrix presented in tables 5.14 and 6.5. ANOVA analysis of photogrammetric data showed that impact angle and projectile construction also have a significant effect on the size of impact crater in sandstone samples but not limestone samples, (table 5.11), a finding that again highlights the importance of lithology in controlling response to ballistic impact. Taken together, these results suggest that in-situ collection of photogrammetric data that can then be used to quantify the frequency and scale of ballistic impact at a given heritage site could be a rapid and non-destructive method for assessing damaged sites likely to be at risk of exacerbated deterioration in the aftermath of conflict damage.

8.1.4: UPV findings

UPV analysis was conducted in chapters 4, 5 and 6, with results remaining consistent throughout. Analysis of the data shows that 90° creates a denser fracture network than 45° impact that limestone samples suffer more internal fracturing than sandstone samples, and that steel cored projectiles cause more fracturing than lead (figures 4.21, 5.27). These results are in keeping with those for hardness and permeability survey, as well as photogrammetry, which also demonstrate these parameters to control the damage received by impacted stone. These findings are further supported by the ANOVA analysis of their significance presented in table 5.10.

Chapters 4 and 6 also demonstrated that the exploitation of fracture networks by ingress of saline moisture and precipitation of salt crystals within pore spaces and fracture networks can be detected using UPV (figure 4.21, section 6.3.3.) This precipitation of salt crystals in the fracture network is known to contribute to exacerbated weakening through extension of internal fracture networks (Renard *et al*, 2009) and the ability of UPV to detect this phenomenon was demonstrated in figure 6.13, which shows that UPV is correlated with loss of hardness in weathered samples. Therefore, UPV data collected in a field setting for a given lithology from areas of differing exposure to likely ingress of salts could be used to infer the amount of salt crystallisation present within the damaged stone, and therefore used as a rapid means of assessing probably risk of future deterioration.

8.2: Assessment of progress towards project aims

In order to assess the overall impact of this project it is necessary to review the research questions outlined in section 1.14 and assess whether the objectives created to answer these questions have been completed. The ways in which each chapter contributed to these objectives are laid out below:

Research Objective I: To develop field appropriate non-destructive methods to assess exterior and interior damage to limestone and sandstone arising from military projectile damage (7.62 x 39mm and 5.56 x 45mm).

Research Objective 1 was partially completed in chapter 2, which demonstrated that Equotip rebound survey and permeability survey were effective at assessing ballistic impact's effect on the mechanical properties of target zone. This work was continued through chapter 4 and 5, which added further analytical techniques for assessing damage to stone, namely UPV analysis of internal fracture networks, photogrammetry techniques for analysing spatial data on the area and volume parameters of ballistic damage and protimeter based methods for detecting ingress of weathering agents. The fact that these methods are appropriate for a field setting and are non-destructive has been shown through their deployment in field-based studies in chapters 3 and 7.

Research Objective II: To use the methods developed under Research Objective I to compare and isolate the effects of changing calibre, angle of impact and target stone type on the damage caused by ballistic impact before weathering. This will determine which variables have the greatest effect on damage levels prior to weathering.

This Research Objective was begun with the pilot study in chapter 4, which began to explore the links between ballistic impact angle and subsequent damage due to weathering and continued in chapter 5 and 6. The results of chapter 5 and 6 suggest the single most important variable is the target lithology, which caused the largest variability in target damage both before and after weathering. Stone with geotechnical properties that result in lower wave attenuation (lower density, lower compressive strength, higher porosity) experience much higher damage after ballistic impact due to fracturing and ejection of matrix material. The denser fracture network resulting from impact into this stone also results in a greater degree of deterioration after haloclasty weathering.

In terms of ballistic variables, the results show that steel cored ammunition is more damaging to the target than lead cored ammunition, and 90◦ impact is more damaging that 45◦. Angle of impact can lead to complex damage patterns in some instances, as results in chapter 4 and 5 show that in instances where 45◦ impact causes damage and loss of material to non-impact faces damage across the wider stone surface can result in greater deterioration than 90◦ impact.

The completion of these Research Objectives allows research question 1 to be answered:

Research Question 1: *"How does modern military ammunition affect the investigated stone types in the immediate aftermath of an impact?"*

The results of this project show that impact by modern military ammunition causes mechanical degradation of impacted stone after impact, as measured by decreased surface hardness and increased fracture density. Ultimately, this exacerbates weathering deterioration subsequent to impact, particularly on the impact face. Mechanical properties of the target stone are the most important factor in controlling damage, whilst projectile construction and angle of impact are also important variables.

Research Objective III: To assess the effects of arid environment weathering processes (haloclasty, moisture, temperature change) on the deterioration of stone after ballistic impact and investigate the interaction between ballistic impact and subsequent weathering processes to determine if weathering processes exacerbate damage initiated by ballistic impact.

The effects of weathering on ballistic impact were explored both through experimental work (chapters 4 and 6) and in two field studies (chapters 3 and 7). Universally, haloclasty weathering acts to lower the surface hardness of the impact face of stone subject to ballistic impact, and to a greater extent than un-shot control stone (chapter 6). However, weathering behaviour of impact craters is strongly influenced by the location of a crater at a given heritage site. The fieldwork in chapters 3 and 7 showed that proximity to sources of weathering agents such as saline sea spray, as well as orientation of the crater relative to solar heating are also crucial in controlling presence and mobility of weathering agents and resulting weathering and loss of hardness at impact craters. Chapter 6 showed that changes in permeability after weathering are controlled by the lithological properties of the stone, with some lithologies decreasing in permeability after shooting due to filling of pores and fractures, whilst others appear to undergo feedback loops of increasing permeability. This is an important finding that shows that in a field setting the lithology of any heritage monument must be considered before conservation interventions are undertaken. The completion of Research Objective III allowed research question 2 to be answered:

Research Question 2: *"How do weathering processes affect the degradation of impacted stone?"*

Broadly speaking, weathering processes exacerbate the mechanical deterioration of impacted stone. The location of the impact crater relative to sources of weathering agents and solar radiation are key determinates of weathering deterioration in a field setting.

Research Objective IV: To use statistical analysis of results from weathering experiments on stone samples impacted under differing ballistic and weathering conditions to construct a risk index that can be used to assess the level of risk to damaged stone based on information on target lithology, ammunition, impact angle and weathering conditions.

Research Objective IV was completed across chapters 5 and 6, which undertook detailed analysis of each of the ballistic impact variables both after impact and after weathering and analysed the data using statistical methods to determine which variables contributed most to deterioration of the stone. This analysis was then used to construct a weighted risk matrix in chapters 5 and 6.

Research Objective V: To "ground truth" the laboratory based methods that the risk matrix is based on through fieldwork. This will involve identifying and exploring links between weathering risks and exacerbated deterioration of ballistic impacts to ensure that observed links between ballistic damage and weathering behaviours are applicable to real-world situations and can be identified in a field setting using the methods developed in this project.

Research Objective V was completed across chapters 3 and 7, which demonstrated that the laboratory observation of increased deterioration of ballistic impacts due to haloclasty weathering processes was identifiable in a field context using the methods developed in this project.

Research Question 3: *"How do lithology, ballistic impact and weathering conditions combine to deteriorate stone, and which combinations are the most damaging?"*

The most damaging combination of variables is 90◦ impact by steel-cored projectiles into stone with low wave attenuation and exacerbated by proximity to sources of saline water and sources of heat such as sunlight.

Therefore, this project has successfully completed all the Research Objectives, and in doing so answered the research questions.

8.3: Significance of Research

As stated in section 1.14, the ultimate application of this research was to:

"Develop a risk indexing system and field methodologies that can be used by conservation teams in the field to triage conflict-damaged heritage monuments most in need of conservation intervention".

This aim has demonstrably been achieved, with the completion of a risk matrix that considers a number of deterioration risks, and methodologies that have been successfully deployed in two field studies. Significantly, the work at Sabratha, and the validation of the risk matrix and methods for identifying impacts at risk, resulted in a report on areas of highest risk, which has been passed to the Department of Antiquities and is being used to inform planned conservation and restoration work in the aftermath of fighting at the site. This demonstrates that the methods developed in this project have real-world applications. The other significance of the Sabratha field study is that the methods were deployed by colleagues in the field after training from the author, which demonstrates that the methods developed here can be successfully taught (even remotely and internationally) and then used by heritage and conservation professionals. This is important in bridging the gap between research output and real-world applications. The project has also successfully applied a suite of novel methods for in-situ, non-destructive data collection on heritage sites at risk after armed conflict. To the knowledge of the author, many of these techniques, which include rebound surface hardness survey, permeability survey, protimeter analysis and photogrammetry have not been used in the assessment of conflict damage and associated weathering risk in modern conflict context before, and therefore represent an original methodological contribution to the field of conservation science.

Furthermore, as outlined in chapter 1, prior to this project, very little published work had considered the effects of ballistic impact by military ammunition on stone, and no known previous work has demonstrated the interplay between haloclasty weathering processes and impact induced damage which acts to exacerbate stone deterioration caused by these weathering processes. This project has clearly demonstrated that ballistic impact does indeed worsen weathering deterioration of impacted heritage stone, particularly on the impact surface, through both laboratory experiments and fieldwork. Results arising from this project have expanded the published work in this field, considering both the macroscopic and microscopic effects of ballistic impact on sedimentary stones. These publications have

contributed to the advancement of materials science and ballistics, as well as the conservation science field. Details of the publications arising directly from this project or making use of results obtained through the work of this project are given below:

Gilbert, O. Mol, L. Campbell, O. Blenkinsop, T. (2019). Permeability and surface hardness surveying of stone damaged by ballistic impact. *Heritage*, *2*(2), pp.1369-1389.

Gilbert, O., Mol, L., Campbell, O., and Blenkinsop, T. (2020). The influence of angle of ballistic impact on stone weathering. In *Proceedings of the 14th International Congress on the Deterioration and Conservation of Stone, Göttingen, Germany* (pp. 309-315).

Campbell, O., Blenkinsop, T., Gilbert, O., and Mol, L. (2022). Bullet impacts in building stone excavate approximately conical craters, with dimensions that are controlled by target material. *Scientific reports*, *12*(1), 1-11.

Campbell, O. Blenkinsop, T. Gilbert, O. Mol, L. (2021). Surface and subsurface damage caused by bullet impacts into sandstone. *Geosciences*, *11*(9), pp.395.

Campbell, O., Blenkinsop, T., Gilbert, O., and Mol, L. (2022). Surface damage from perpendicular and oblique bullet impacts in stone., *Royal Society Open Science*, 9(220029)

8.4: Further Work

This project has been principally concerned with the development of methods and theory that are applicable to a field setting. Therefore, further work should be focussed on refining these field methods further. For instance, due to time constraints in both field studies of this project, it was not possible to test UPV methods on ballistic impact in the field, this could be remedied with further field studies.

Furthermore, if field sites could be identified that featured impacts arising from a range of known weapons and known impact angles, such as the field site in Madrid identified by Mol and Gomez-Heras (2018), then it would be possible to empirically test these components of the risk matrix in a field setting.

As discussed in section 5.2.4, to make full use of the risk matrix, it would be necessary to compile a data base of heritage stones and their mechanical properties, in order to predict both their response to ballistic damage through wave attenuation, as well as subsequent weathering deterioration. Similarly, a database of ammunition used by various militaries and paramilitary groups that was available to conservation professionals could be used in conjunction with the risk matrix developed in this project to allow in field- assessment of likely projectile responsible for ballistic damage to heritage monuments based on the known combatants in a given field setting. As highlighted in section 5.2.4, the risk matrix could be further refined by analysing a greater number of impact angles for oblique impacts, both above and below 45°. Whilst the work of Gault (1973) has shown that impact angles closer to 90° will result in greater kinetic energy imparted to the target, and more mechanical damage, the relationship between a variety of impact angles, corresponding levels of fracture damage, and subsequent weathering deterioration is yet to be explored.

The reliability of the risk matrix could be enhanced with expert statistical analysis to use the different significance levels detected for each variable in the ANOVA analyses presented in chapters 5 and 6 to weight the risk associated with each variable in a more nuanced way. That is to say it may allow for a risk matrix that more accurately reflects risk in a quantitative manner than the current scale which descends from 6 to 2 using a simplistic hierarchy. Greater statistical analysis with a greater number of lithologies and shooting conditions could even allow specific continuous numeric values to be given to continuous data for variables such as wave impedance and impact angle rather than binary cut offs such as high/low and

normal/oblique. For instance, an impact angle of 72° could be given a specific higher score than an impact angle of 43, but lower than an impact angle of 80°.

Finally, this project was narrowly focussed on certain weathering conditions found in arid MENA regions, and the two most common ammunition types found in modern conflicts. Conflict damage to heritage monuments has been occurring recently in non-arid environments, such as the conflict in Ukraine (Niesel, 2014), and there are a myriad of ammunition types used by modern militaries, with the U.S. army currently looking to replace its standard 5.56 x 45mm cartridge with an updated and more powerful 6.8mm projectile (Dimitrov, 2021). Therefore, an expansion of this work to consider other weathering conditions, salts, and projectile types would increase the applicability of the methods and theories outlined in this project.

Appendix A: Descriptive statistics for Chapter 5 Data (Cratered samples)

Table 1: *Hardness data*

	n	Mean	Maximum	Minimum	Range	Standard Deviation	Standard Error
Limestone un-shot samples	10584	380.6	605	200	405	40.9	0.4
Limestone samples shot	10569	369.1	627	200	427	46.8	0.0
Limestone samples shot + weathered	10569	275.0	469	200	269	49.2	0.5
Limestone control samples	2646	371.7	536	207	329	42.5	0.8
Limestone control samples weathered	2646	277.8	429	200	229	47.2	0.9
Sandstone un-shot samples	10584	697.0	905	208	697	114.4	1.1
Sandstone samples shot	10584	675.1	902	175	727	117.1	1.1
Sandstone samples shot + weathered	10584	600.7	895	200	695	163.9	1.6
Sandstone control samples	2646	707.6	903	245	658	98.0	1.9
Sandstone control samples weathered	2646	578.6	866	200	666	188.7	3.7

Table 2: *Permeability data*

	n	Mean	Maximum	Minimum	range	Standard Deviation	Standard Error
Limestone samples shot	948	156.42	5900	0.00	5900.00	498.69	16.20
Limestone samples shot + weathered	948	223.50	3800	0.19	3799.81	391.99	12.73
Limestone control samples	224	5.99	89	0.01	88.92	9.14	0.61
Limestone control samples weathered	224	140.44	985	0.19	984.71	165.66	11.07
Sandstone samples shot	951	142.38	6000	0.03	5999.97	528.27	17.13
Sandstone samples shot + weathered	951	64.69	2100	0.00	2100.00	187.17	6.07
Sandstone control samples	224	13.27	761	0.01	760.99	66.97	4.47
Sandstone control samples weathered	224	30.59	1345	0.02	1344.98	110.14	7.36

Table 3: *UPV Data*

	n	Mean	Maximum	Minimum	Range	Standard Deviation	Standard Error
Limestone un-shot samples	36	568.8	727	465	262	37.7	6.3
Limestone samples shot	36	412.1	757	198	559	127.9	21.3
Limestone samples shot + weathered	36	509.8	782	340	442	112.0	18.7
Limestone control samples	9	547.6	575	434	141	50.2	16.7
Limestone control samples weathered	9	518.4	596	357	239	73.4	24.5
Sandstone un-shot samples	36	833.0	883	545	338	78.5	13.1
Sandstone samples shot	36	610.4	828	287	541	136.9	22.8
Sandstone samples shot + weathered	36	739.3	1382	282	1100	235.1	39.2
Sandstone control samples	9	868.3	885	853	32	10.2	3.4
Sandstone control samples weathered	9	748.9	999	400	599	165.5	55.2

Appendix B: Locations of Ibutton temperature sensors around the Sabratha amphitheatre site

East wall:

North Wall:

West Wall:

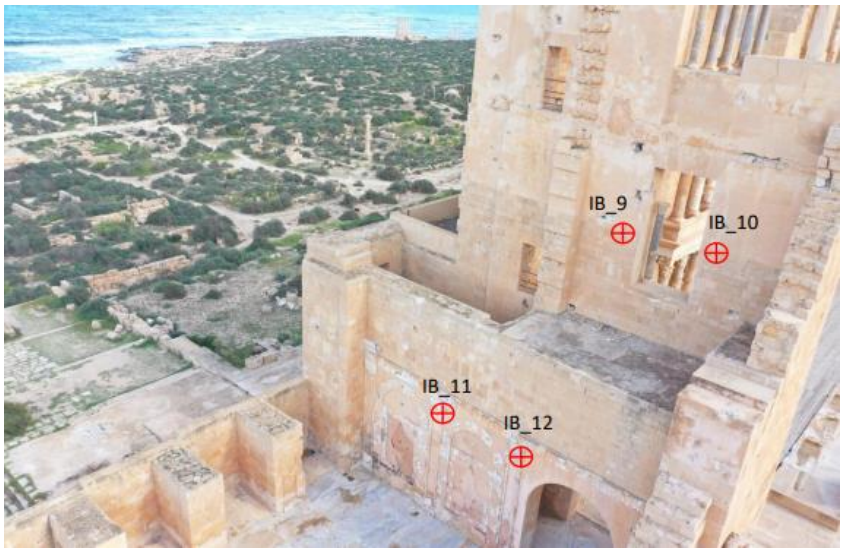

Outer Concourse:

scaenae frons and Amphitheatre Centre

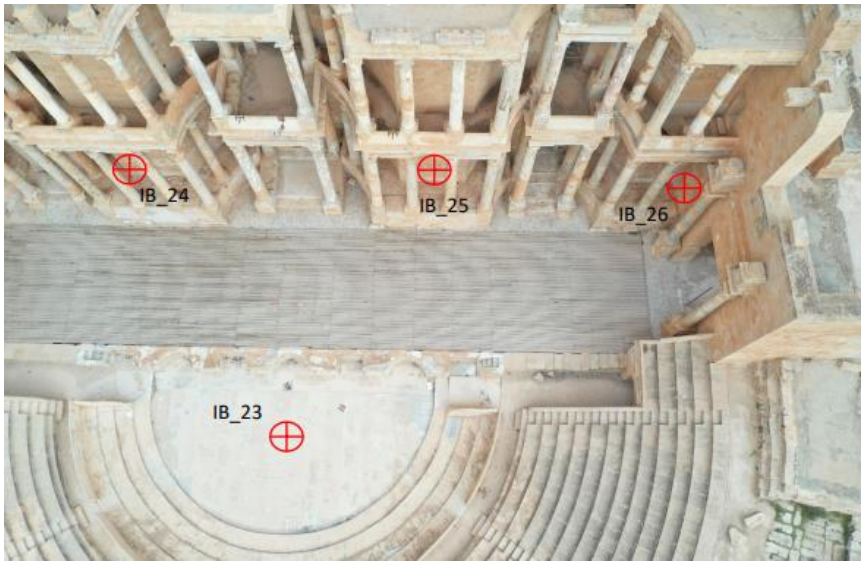


IB_27


IB_28
IB_29


IB_30

References

Abdalahh, M (2011). "Impact of coastal environmental conditions on building materials of The Roman Theater at the archaeological site of Sabratha, Libya." حولية الاتحاد العام للآثاريين العرب) 1414) pp.288-323.

Aboub, M. A. (2018). Sustainable development of the city of Sabratha in Libya–strategy and possibilities. *Sociološki diskurs*, 8(16), pp.53-75.

Adamczyk, K. Premont-Schwarz, M. Pines, D. Pnes, E. Nibbering, E. (2009) Real Time Observation of Carbonic Acid Formation in Aqueous Solution, *Science*, 326(5960) pp.1690-1694.

Ahmed, A. A., and and Fogg, G. E. (2014). The impact of groundwater and agricultural expansion on the archaeological sites at Luxor, Egypt. *Journal of African Earth Sciences*, 95, 93-104.

Ahmed, E. S., and and Hassan, A. S. (2018). The impact of the extreme Air temperatures on the characteristics of Iraq weather. *Iraqi Journal of Science*, 59(2C), 1139-1145.

Ahmed, H. Török, A. Locsei, J. (2006). Performance of some commercial consolidating agents on porous limestones from Egypt. In: Fort, R. de Buergo, A. Gomez-Heras, M. eds., *Proceedings of the International Heritage, Weathering and Conservation Conference*, Madrid, Spain, 21-24 June, 2006, pp.735-740.

Ai, H. (2006) Shock-Induced Damage in Rocks: Application to Impact Cratering, PhD, California Institute of Technology.

Ai, H. Ahrens, T. (2014) Dynamic tensile strength of terrestrial rocks and application to impact cratering, *Meteoritics and and Science*, 39(2), pp. 233-246.

Ahrens, T. J., Xia, K., and Coker, D. (2002, July). Depth of cracking beneath impact craters: New constraint for impact velocity. *AIP Conference Proceedings* (Vol. 620, No. 1, pp. 1393-1396). American Institute of Physics.

Aly, N. Gomez-Heras, M. Hamed, A. Alvarez de Buergo, M. Soliman, F. (2015) The influence of temperature in a capillary imbibition salt weathering simulation test on Mokattam limestone, *Materiales de construccion*, 65(317), pp.1-10.

Aly, N., Hamed, A., Gómez Heras, M., Benavente, D., and and Álvarez de Buergo, M. (2016). The effect of salt crystallisation on the mechanical properties of limestone: statistical correlation between non-destructive and destructive techniques, *Science and Art, A Future for Stone*, Proceedings of the 13th International Congress on the Deterioration and Conservation of Stone, 6th-10th September, 2016, Paisley, Scotland.

Antoun, T. Curran, D. Razorenov, S. Seaman, L., Gennady, K, Utkin, A. (2002). *Spall Fracture*, Springer Science and Business Media

Antoun, T. Glenn, L. Walton, O. Goldstein, P. Lomov, I. Liu, B. (2006) Simulation of hypervelocity penetration in limestone, *International Journal of Impact Engineering*, 33(1-12), pp.45-52

Aoki, H. and Matsukura, Y., (2008) Estimating the unconfined compressive strength of intact rocks from Equotip hardness. *Bulletin of Engineering Geology and the Environment*, 67(1), pp.23-29.

Aoki, H. Matsukura, Y. (2007). A new technique for non-destructive field measurement of rock-surface strength: an application of the Equotip hardness tester to weathering studies. *Earth Surface Processes and Landforms* 32, 1759–1769

Architecture Today (2018) Stabilised Ruin, Architecture Today, online article available at: http://www.architecturetoday.co.uk/stabilised-ruin/ (accessed 08/07/2019)

Aydin, A. (2009) ISRM Suggested method for determination of the Schmidt hammer rebound hardness: Revised version. International Journal of Rock Mechanics and and Mining Sciences, 46, pp. 627-634.

Azam, I. (2001) Gypsum/anhydrite: Some engineering problems, *Bulletin of Engineering Geology and the Environment*, 60(3), pp.227-230

Bader, N. (2014a) Honeycomb Weathering of Limestone Buildings in The Archaeological Sites of Leptis Magna (Libya): Causes, Processes and Damages, *International Journal of Conservation Science*, 5(2), pp.189-202

Bader, N. (2014b) The deterioration problems of the wall reliefs of Komir Temple, Esna, Egypt, *Mediterranean Archaeology and Archeometry*, 14(1), pp.201-209

Baumann, R. Engelhardt, B. Matheson, (2010) Research Note: Hail to the Chief: assessing th economic impact of presidential inaugurations on the Washington, DC, local economy, *Tourism Economics*, 2010, 16(4), pp.1081-1087

Becherini, F. Cassar, J. Galea, M. Bernardi, A. (2016) Evaluation of the shelters over the prehistoric Megalithic Temples of Malta: environmental considerations, *Environmental Earth Sciences*, 75(14) pp.1-13.

Benavente, D. Sanchez-Moral, S. Fernandez-Cortes, A. Canaveras, C. Elez, J. Saiz-Jimenez, C. (2011) Salt damage and microclimate in the Postiumius Tomb, Roman Necropolis of Carmona, Spain, *Environmental Earth Sciences*, 63(7-8), pp.1529-1543

Berenfeld, M. L. (2015, January). Planning for permanent emergency:" Triage" as a strategy for managing cultural resources threatened by climate change. In *The George Wright Forum* (Vol. 32, No. 1, pp. 5-12). George Wright Society.

Bevan, J. Savage, D. (1989) The effect of organic acids on the dissolution of K-feldspar under conditions relevant to burial diagenesis, *Mineralogical Magazine*, 53, pp.415-425

Billi, A. Valle, A. Brilli, M. Faccenna, C. Funiciello, R. (2007) Fracture controlled fluid circulation and dissolutional weathering in sinkhole- prone carbonate rocks from central Italy, *Journal of Structural Geology*, 29(3), pp.385-395

Björn, H., Lundqvist, C., and and Hjelmström, P. (1954). A photogrammetric method of measuring the volume of facial swellings. *Journal of Dental Research*, 33(3), pp.295-308

Blackett-Ord Conservation Engineering (2014) Structural Inspection of Church of St Luke Berry Street Liverpool L1 4JA, Liverpool City Council.

Bomgardner, D. L. (2018). Plotting a course through the 'Arab Spring': restudying the Sabratha amphitheatre in the context of those of Africa Proconsularis *Journal of Roman Archaeology*, *31*, pp.859-875.

Bonazza, A. Sabbioni, C. Messina, P. Guaraldi, C. De Nuntiis, P. (2009) Climate change impact: Mapping thermal stress on Carrara marble in Europe, *Science of the Total Environment*, 407, pp.4506-4512

Borvik, T. Dey, S. Olovsson, L. (2015) Penetration of granular materials by small-arms bullets, *International Journal of Impact Engineering*, 75(2015) pp.123-139

Bradley, S. Middleton, S. (1988) A study of Deterioration of Egyptian Limestone Sculpture, *Journal of the American Institute for Conservation*, 27(2), pp. 64-86

Bruning, T., Webster, S., and and Teet, R. (2022). The Equotip hardness method for spatial geotechnical assessment of a Northparkes Mine block cave. *Caving 2022: Fifth International Conference on Block and Sublevel Caving*

Bryla, E. A., and and Starry, D. A. (1979). Mounted Combat In Vietnam. *Naval War College Review*, 32(7), pp.22.

Building Research Establishment (1999a) *Technical data sheet Cotswold Hill Quarry Cream (Bed 1)*, Building Research Establishment, available at: https://projects.bre.co.uk/ConDiv/stonelist/cotswoldc.html (Accessed 21/04/2020)

Building Research Establishment (1999) *Technical data sheet Stoneraise Red Sandstone*, Building Research Establishment, available from: https://projects.bre.co.uk/condiv/stonelist/stoneraise.html (Accessed 21/04/2020)

Buj, O., Gisbert, J., McKinley, J. M., and and Smith, B. (2011). Spatial characterization of salt accumulation in early stage limestone weathering using probe permeametry. *Earth Surface Processes and Landforms*, *36*(3), pp.383-394.

Butler, D. (1975) An analytical study of projectile penetration into rock, U.S. Department of Commerce, National Technical Information Service

Campbell, O., Blenkinsop, T., Gilbert, O., and and Mol, L. (2022). Bullet impacts in building stone excavate approximately conical craters, with dimensions that are controlled by target material. *Scientific reports*, *12*(1), pp.1-11.

Caputo, G. (1959) Il teatro di Sabratha e l'architettura teatrale Africana, *Monografie di Archeologia Libica,* Vol. 6, L'Erma di Bretschneider.

Carlucci, D. Jacobson, S. (2013) Ballistics: Theory and Design of Guns and Ammunition, Second Edition, CRC Press, pp.4-5

Çelik, M. Y., and Aygün, A. (2019). The effect of salt crystallization on degradation of volcanic building stones by sodium sulfates and sodium chlorides. *Bulletin of Engineering Geology and the Environment*, 78(5), 3509-3529.

Charola, A. (2000) Salts in the deterioration of porous materials: An overview, *Journal of the American Institute for Conservation*, 39(3), pp.327-343

Champion, S. (2020) Email to Oscar Gilbert, 02 March.

Cheon, J. Choi, Y. (2016) Effect of Projectile Incident Angle on Penetration of Steel Plates, *International Journal of Precision Engineering and Manufacturing*, 17(12), pp.1721-1727

Cheng, Y., Song, Z., Jin, J., Wang, J., and and Wang, T. (2019). Experimental study on stress wave attenuation and energy dissipation of sandstone under full deformation condition. *Arabian Journal of Geosciences*, *12*(23), pp.1-14.

Christensen, M. (2003) Water Treatment Third Edition, American Water Works Association, pp.273

Chrysostomoua, C. Z., Hadjimitsisa, D. G., Agapioua, A., Lysandrou, V., Themistocleous, K., and and Demetriadou, C. (2010). Application of non-destructive techniques in assessing the quality of stone building materials in cultural heritage structures in Cyprus: Use of ultrasonic and 3D laser scanning integrated approach for diagnostic tests. *Digital Heritage*, 269.

Cimini, A., Bedini, G., and and Moresi, M. (2021). Rough Beer Filterability in Industrial Powder-Filters and Lab-Scale Dead-End and Crossflow Filtration Apparatuses. *Chemical Engineering Transactions*, 87, pp.247-252.

Collins, G. S. (2014). Numerical simulations of impact crater formation with dilatancy. *Journal of Geophysical Research: Planets*, *119*(12), pp.2600-2619

Conca, J. Rossman, G. (1985) Core Softening in Cavernously Weathered Tonalite, *The Journal of Geology*, 93(1), pp.59-73

Concu, G., De Nicolo, B., and and Valdes, M. (2014). Prediction of building limestone physical and mechanical properties by means of ultrasonic P-wave velocity. *The Scientific World Journal*, *2014*.

Cooke, R. (1978) Laboratory Simulation of Salt Weathering Processes in Arid Environments, *Earth Surface Processes*, 4(4), pp.347-359

Cooke, R. Warren, A. Goudie, A. (2006) Desert Morphology, CRC Press, pp.23-45

Coombes, M. A., Feal-Pérez, A., Naylor, L. A., and Wilhelm, K. (2013). A non-destructive tool for detecting changes in the hardness of engineering materials: Application of the Equotip durometer in the coastal zone. *Engineering Geology*, *167*, p.14

Cooper, B. J., Marker, B. R., and and Thomas, I. A. (2013). *Towards international designation of a heritage dimension stone* (Vol. 548, pp. 329-335). Trans Tech Publications Ltd.

Crundwell, F. (2017) On the Mechanism of the Dissolution of Quartz and Silica in Aqueous Solutions, ACS Omega, 2(3), pp.1116-1127

Cunliffe, E. Fox, P. Stone, P. (2018) The Protection of Cultural Property in the Event of Armed Conflict: Unnecessary Distraction or Mission-Relevant Priority?, *NATO Open Publications,* 2(4) pp.1-19

Curless, B. (1999) From range scans to 3D models, *ACM SIGGRAPH Computer Graphics*, 33(4), pp.38-41

Danti, M. (2015) Ground-Based Observations of Cultural Heritage Incidents in Syria and Iraq, *Near Eastern Archaeology*, 78(3), pp.132-141

Delmonaco, G. Margottini, C. and and Spizzichino, D. (2013),Slope dynamics, monitoring and geological conservation of the Siq of Petra (Jordan). *Geotechnical engineering for the preservation of monuments and historic sites. Taylor and and Francis Group, London*, 325-334.

De Kock, T., Dewanckele, J., Boone, M., De Schutter, G., Jacobs, P., and and Cnudde, V. (2014). Replacement stones for Lede stone in Belgian historical monuments. *Geological Society, London, Special Publications*, *391*(1), pp.31-46.

Departments of the Army and Air force (1953) *"Technical Manual 9-1985-2 German Explosive Ordnance (Bombs, Fuzes, Rockets, Land Mines, Grenades and Igniters,* United States Government Printing Office

Desarnaud, J. Bonn, D. Shahidzadeh, N. (2016) The pressure induced by salt crystallization in confinement, *Scientific Reports*, 6:30856

Desarnaud, J., Kiriyama, K., Bicer Simsir, B., Wilhelm, K., and and Viles, H. (2019). A laboratory study of Equotip surface hardness measurements on a range of sandstones: What influences the values and what do they mean?. *Earth Surface Processes and Landforms*, *44*(7), pp.1419-1429.

Dimitrov, M. (2021). Analysis on the next generation assault rifles and ammunition designed for the US Army. *Problemy Mechatroniki: uzbrojenie, lotnictwo, inżynieria bezpieczeństwa*, *12*.

Dorn, R. Mahaney, W. Krinsley, D. (2017) Case Hardening: Turning Weathering Rinds into Protective Shells, *Elements*, 13(3) pp.165-169

Dorn, R. I., Whitley, D. S., Villa Cerveny, N., Gordon, S. J., Allen, C. D., and and Gutbrod, E. (2008). The Rock Art Stability Index: A new strategy for maximizing the sustainability of rock art. *Heritage Management*, *1*(1), 37-70.

Duda, M. Renner, J. (2013) The weakening of water on the brittle failure strength of sandstone, *Geophysical Journal International*, 192(3), pp.1091-1108

Duperret, A. Taibi, S. Mortimore, R. Daigenault, M. (2005) Effect of groundwater and sea weathering cycles on the strength of chalk rock from unstable cliffs of NW France, *Engineering Geology*, 78(3-4) pp.321-343

Ehlen, J. (1999) Fracture characteristics in weathered granites, *Geomorphology*, 31, pp.29-45

Eklund, S. (2008) *Stone Weathering in the Monastic Building Complex on Mountain of St Aaron in Petra, Jordan*, MA, University of Helsinki.

El Azhari, H., and and El Hassani, I. E. E. A. (2013). Effect of the number and orientation of fractures on the P-wave velocity diminution: application on the building stones of the Rabat area (Morocco), *Geomaterials*, 3(3), pp.1-11

El-Azabi, M. (2006) Sedimentological Characteristics, Palaeoenvironments and Cyclostratigraphy of the Middle Eocene Sequences in Gabal El-Ramiliya, Maadi-Sukhna Stretch, North Eastern Desert, Egypt, *Proceedings of the 8th International Conference on the Geology of the Arab World*, Cairo, Egypt, 2006, pp.459-484

El Fadli, K. I., Cerveny, R. S., Burt, C. C., Eden, P., Parker, D., Brunet, M., ... and Pace, M. B. (2013). World Meteorological Organization assessment of the purported world record 58 C temperature extreme at El Azizia, Libya (13 September 1922). *Bulletin of the American Meteorological Society*, *94*(2), 199-204.

Elgohary, M. (2008) Air pollution and Aspects of stone degradation "Umayyed Liwan - Amman Citadel as a Case Study", *Journal of applied sciences research*, 4(6), pp.669-682

El-Nahhas, F., Mostafa, A. R., and and Abdel Tawab, S. (1990, December). Geotechnical characteristics of limestone formations of Gebel Mokattam area. In *Proceedings of the First Alexandria Conference on Structural and Geotechnical Engineering, Alexandria, Egypt* (pp. 1-3).

El-Shahat, A., Minas, H., and and Khomiara, S. (2014). Weathering of Calcarenite Monuments at Roman and Byzantine Archaeological Sites at Sabratha, Northwestern Libya: A Pilot Study. *African Archaeological Review*, *31*(1), 45-58.

English Heritage (1995) English Heritage Battlefield Report: Worcester 1651, English Heritage, p.8

English Heritage (2004) *Heritage Unlocked*, English Heritage

Eppes, M. McFadden, L. Wegmann, K. Scuderi, L. (2010) Cracks in desert pavement rocks: Further insights into mechanical weathering by directional insolation, *Geomorphology*, 123(1-2), pp.97-108

Erhhart, T. (2009) Increasing Small Arms Lethality in Afghanistan: Taking Back the Infantry Half-Kilometre, School of Advanced military Studies United States Army Command and General Staff College Fort Leavenworth, Kansas

Erkman,J. Christensen, B. Fowles, G. (1966). Attenuation of stress waves in solids. Sanford Research institute.

Espinosa-Marzal, R. Franke, L. Deckelmann, G. (2007) Predicting efflorescence and subflorescences of salts, *Materials Research Society Symposium Proceedings*, 1047, pp.1-11

Fahmy, A., Molina-Piernas, E., Martínez-López, J., Machev, P., and and Domínguez-Bella, S. (2022). Coastal Environment Impact on the Construction Materials of Anfushi's Necropolis (Pharos's Island) in Alexandria, Egypt. *Minerals*, *12*(10), 1235.

Fang, Q. Zhang, J. (2014) 3D numerical modelling of projectile penetration into rock-rubble overlays accounting for random distribution of rock-rubble. *International Journal of Impact Engineering*, 63, pp.118-128

Farkas, O. Siegesmund, S. Licha, T. Török, Á. (2018). Geochemical and mineralogical composition of black weathering crusts on limestones from seven different European countries. *Environmental earth sciences*, *77*(5), pp.1-20.

Fawaz, Z., Zheng, W., and and Behdinan, K. (2004). Numerical simulation of normal and oblique ballistic impact on ceramic composite armours. *Composite Structures*, *63*(3-4), 387-395.

Fernando, P. Mohotti, D., Remennikov, A., Hazell, P., Wang, H., Amin, A. (2020). Experimental, numerical and analytical study on the stress wave propagation through impedance-graded multi-metallic systems. *International Journal of Mechanical Sciences*, 105621.

Filomena, C. Hornung, J. Stollhofen, H. (2014) Assessing accuracy of gas-driven permeability measurements: a comparative study of diverse Hassler-cell and probe permeameter devices, Solid Earth, 5, pp.1-11

Fitzner, B. Heinrichs, K. La Bouchardiere, D. (2002) Limestone Weathering of historical monuments in Cairo, Egypt, *Geological Society London Special Publications*, 205, pp.217-239

Flatt, R. J., Caruso, F., Sanchez, A. M. A., and Scherer, G. W. (2014). Chemo-mechanics of salt damage in stone. *Nature communications*, *5*(1), 4823.

Flood, F. (2002) Between Cult and Culture: Bamiyan, Islamic Iconoclasm, and the Museum, *The Art Bulletin*, 84(4), pp. 641-659

Forquin, P., and Hild, F. (2010). A probabilistic damage model of the dynamic fragmentation process in brittle materials. *Advances in applied mechanics*, *44*, 1-72.

Franchi, R. Savelli, D. Colosi, F. Drapp, P. Gabrielli, R. Moretti, E. Peloso, D. (2009) Memorie Descrittive della Carta *geologica d'Italia*, 83, pp.77-90

Freire-Lista, D. M., and and Fort, R. (2017). Exfoliation microcracks in building granite. Implications for anisotropy. *Engineering Geology*, pp.220, 85-93.

French, B. (1998) Traces of Catastrophe, A handbook of Shock Metamorphic Effects in terrestrial Meteorite Impact Structures, Lunar and Planetary Institute, pp.17-28

Gault, D. E. (1973). Displaced mass, depth, diameter, and effects of oblique trajectories for impact craters formed in dense crystalline rocks. *The Moon*, 6(1-2), pp.32-44.

Gilbert, O. Mol, L. Campbell, O. Blenkinsop, T. (2019) Permeability and Surface Hardness Surveying of Stone Damaged by Ballistic Impact, *Heritage*, 2(2), pp.1369-1389

Gilbert, O.; Mol, L.; Campbell, O.; Blenkinsop, T. (2020) The influence of angle of ballistic impact on stone weathering. In *Proceedings of the 14th International Congress on the Deterioration and Conservation of Stone*, Göttingen, Germany, 7–12 September 2020; pp. 309–313.

Giustetto, R. Moschella, E. Cristellotti, M. Costa, E. (2017) Deterioration of building materials and artworks in the 'Santa Maria della Stella' church, Saluzzo (Italy): Causes of decay and possible remedies, *Studies in Conservation*, 62(2017), pp.474-493

Gomez-Heras, M. McCabe, S. (2015) Weathering of stone-built heritage: A lens through which to read the Anthropocene, Anthropocene, 11(2015), pp.1-13

Goudie, A. (2009) The Nature of the Environment, John Wiley and and Sons, pp.412-413

Goudie, A., Cooke, R., and and Evans, I. (1970). Experimental investigation of rock weathering by salts. *Area*, *2*(4), pp.42-48.

Goudie, A. Cooke, R. Salt Weathering Simulation. Some Comments (1983), Geografiska Annaler. Series A, *Physical Geography*, 65(3/4), pp.296-298

Grieve, R. Langenhorst, F. Stoffler, D. (1996) Shock metamorphism of quarts in nature and experiment: II. Significance in geoscience, *Meteoritics and and Planetary Science*, 31, pp.6-35

Grover, D., Savidge, C. R., Townsend, L., Rosario, O., Hu, L. B., Rizzo, D. M., and and Dewoolkar, M. M. (2016). Surface permeability of natural and engineered porous building materials. *Construction and Building Materials*, *112*, 1088-1100.

Grujicic, M. Bell, W. Pandurangan, B. Cheeseman, B. Fountzoulas, C. Patel, P. Templetn, D. Bishnoi, K. (2011) The effect of high-pressure densification on ballistic-penetration resistance of a soda-lime glass. *Journal of Materials Design and Applications*, 225(4), pp.298-315

Grussenmeyer, P., Al Khalil, O. (2017). From metric image archives to point cloud reconstruction: Case study of the great Mosque of Aleppo in Syria. *International Archives of the Photogrammetry, Remote Sensing and and Spatial Information Sciences*, 42.

Güldemeister, N., Wünnemann, K., and and Poelchau, M. H. (2015). Scaling impact crater dimensions in cohesive rock by numerical modeling and laboratory experiments. *Geological Society of America Special Papers*, *518*, 17-29.

Hall, K., Arocena, J. M., Boelhouwers, J., and and Liping, Z. (2005). The influence of aspect on the biological weathering of granites: observations from the Kunlun Mountains, China. *Geomorphology*, 67(1-2), pp.171-188.

Hall, Meiklejohn, I. Arocena, J. (2007), The thermal responses of rock art pigments: Implications for rock art weathering in southern Africa, *Geomorphology*, 91(1-2), pp.132-145

Hall, C. M., and Page, S. (2012). *Tourism in south and southeast Asia*. Routledge.

Hamed, A. Aly, N. Gomez-Heras, M. Alvarez de Buergo, M. (2015) New experimental method to study the combined effect of temperature and salt weathering, *Geological Society*, 416, pp.229-239

Hampshire Telegraph and Post (1945) *Night of Terror in 1941 Jan. 10 Fire Blitz*. The Hampshire Telegraph and Post (1945)

Harrel, J. Storemyr, P. (2009) Ancient Egyptian quarries- an illustrated overview, QuarryScapes: ancient stone quarry landscapes in the Eastern Mediterranean, *Geological Survey of Norway Special Publication* 12 pp.7–50.

Harrell, J. A. (2012). Building stones. *UCLA Encyclopedia of Egyptology*, 1(1).

Heinrichs, K., and and Fitzner, B. (2000). Lithotypes of rock-carved monuments in Petra, Jordan: classification and petrographical properties. *Annual of the Department of Antiquities*

of Jordan, 44, pp.283-312

Historic England (2020) *Royal Garrison Church,* Available at: https://historicengland.org.uk/listing/the-list/listentry/1245790?section=official-listing-contributions-banner Accessed: 07/01/2022

Hoerle, S. (2006) Rock temperatures as an indicator of weathering processes affecting rock art, *Earth Surface Processes and Landforms*, 31, pp.383-389

Hofman, J. Travnickova, E. Andel, P. (2012) Road salts effects on soil chemical and microbial properties at grassland and forest site in protected natural areas, *Plant Soil and Environment*, 58(6), pp.282-288

Holmes, T. R. H., Crow, W. T., Hain, C., Anderson, M. C., and and Kustas, W. P. (2015). Diurnal temperature cycle as observed by thermal infrared and microwave radiometers. *Remote Sensing of Environment*, 158, pp.110-125.

Holynska, B. Gilewicz-Wolter, Ostachowicz, B. Bielewski, M. Streli, C. Wobrauschek, P. (2003) Study of the deterioration of sandstone due to acid rain and humid SO2 gas, *X-Ray Spectrometry*, 33(5), pp.342-348

Housen, K. R., and and Holsapple, K. A. (2011). Ejecta from impact craters. *Icarus*, *211*(1), pp.856-875.

Hubner, C. and Kaatze, U. (2016) *Electromagnetic Moisture Measurement Principles and Applications,* Universitatsverlag Gottingen, pp.33-38

ICOMOS, International Council on Monuments and Sites, (1982) *Nomination: Archaeological Site of Sabratha*, ICOMOS, 1982.

Imperato, J. Sanchez, L. (2009) Ballistics, In: Harwood-Nuss' Clinical Practice of Emergency Medicine, Lippincott Williams and and Wilkins, p.321

Imperial War Museum (2020) *Tikka M55 Sniper Rifle,* Available at: https://www.iwm.org.uk/collections/item/object/30031273 Accessed: 04/01/2022

Inkpen, R. (2003). The whole building and patterns of degradation. *The effects of air pollution on the built environment. Imperial College Press, London*, pp.393-422.

Jankowski, S. (1990) Warsaw: Destruction, Secret Town Planning, 1939-44 and Postwar Reconstruction, In: Diefendorf, P. ed. (1990) Rebuilding Europe's Bombed Cities, Palgrave Macmillan, pp. 77-93

Jenzen-Jones, N. R. Global Development and Production of Self-loading Service Rifles. Small Arms Survey, 2017

Johnson, G. Beissel, S. Holmquist, T. Frew, D. (1998) Computed radial stresses in a concrete target penetrated by a steel projectile. *Transactions on the Built Environment*, 32, pp.1-14

Johnson, G. Holmquist, T. (1999) Response of boron carbide subjected to large strains, high strain rates, and high pressures, *Journal of Applied Physics*, 85(8060).

Jones, O. (1972). Metal response under explosive loading (No. SC-DC-721202; CONF-720303-2). Sandia National Lab.(SNL-NM), Albuquerque, NM (United States).

Jutla, R. (2016) The Evolution of the Golden Temple of Amristar into a Major Sikh Pilgrimage Centre, *Geosciences*, 2(3), pp. 259-272

Karagiannis, N. Karoglou, M. Bakolas, A. Moropoulou, A. (2016) Effect of temperature on water capillary rise coefficient of building materials, *Building and Environment*, 106, pp.402-408

Karp, A. (2018) Estimating Global Military-Owned Firearms Numbers, Small Arms Survey Briefing Paper, June 2018, p.4

Kato, M., Higa, M., Shirai, K., Iijima, Y. I., Kiyono, T., Nakazawa, S., and and Arakawa, M. (2001). Shock pressure attenuation in water ice at a pressure below 1 GPa. *Journal of Geophysical Research: Planets*, *106*(E8), pp.17567-17578.

Kenkmann, T. Wunnemann, K. Deutsch, A. Poelchau, M. Schafer, F. Thoma, K. (2011) Impactcratering in sandstone: The MEMIN pilot study on the effect of pore water, *Meteoritics and and Planetary Science*. 46(6), pp.890-902

Khan, M.A., Wang, Y., Cheng, H., Yasin, G., Malik, A., Nazeer, F., Ahmad, T., Kamran, M. and Afifi, M.A. (2020) Microstructure evolution of an artificially aged Al-Zn-Mg-Cu alloy subjected to soft-and hard-steel core projectiles. *Journal of Materials Research and Technology*, *9*(5), pp.11980-11992.

Kiwara-Wilson, S. (2013) Restituting Colonial Plunder: The Case for the Benin Bronzes and Ivories, *DePaul Journal of Art, Technology and and Intellectual Property Law*, 23(2), pp.375-425

Klimchouk, A. (1996) The Dissolution and Conversion of Gypsum and Anhydrite, *International Journal of Speleology*, 25(3-4), pp.21-36

Kloppmann, W. Bromblet, P. Vallet, Verges-Belmin, V. Rolland, O. Guerrot, C. Gosslin, C. (2011) *Science of the Total Environment*, 409, pp.1658-1669

Knight, J., and Burningham, H. (2020). What Controls Bedrock Shore Platform Hardness? A Field Study from South Africa. *Journal of Coastal Research*, *95*(SI), pp.537-541.

Kolsky, H. (1963). *Stress waves in solids* (Vol. 1098). Courier Corporation.

Krenn, P. Kaluas, P. Hall, B. (1995) Material Culture and Military History: Test-Firing Early Modern Small Arms, *Material Culture Review*, 42, pp.101-109

Krinsley, D. Digregorio, B. Dorn, R. Razink, J. Fisher, R. (2017) Mn-Fe-enhancing budding bacteria in century-old rock varnish, Erie barge canal, New York, *Journal of Geology*, 125(3) pp.317-336

Kubeyev, A. (2013). Impact of multi-set fracture pattern on the effective permeability of fractured porous media. *Journal of Petroleum Science and Engineering*, *112*, pp.161-169.

Kumano, A. Goldsmith, W. (1995) Projectile Impact on Soft Porous Rock, *Rock Mechanics*, 15(3) pp.113-132.

Kumar, P. S., and Kring, D. A. (2008). Impact fracturing and structural modification of sedimentary rocks at Meteor Crater, Arizona. *Journal of Geophysical Research: Planets*, *113*(E9).

Labadi, S. (2007), Representations of the nation and cultural diversity in discourses on World Heritage. *Journal of social archaeology*, 7(2), pp.147-170.

Lambert, S. Rockwell, C. (2012) Protecting Cultural Heritage in Times of Conflict, International Centre for the Study of the Preservation and Restoration of Cultural Property (ICCROM). Rome, Italy, pp.1-16

Lamur, A. Kendrick, J. Eggertsson, G. Wall, R. Ashworth, J. Lavallee, Y. (2017) The permeability of fractured rock in pressurised volcanic geothermal systems, *Scientific Reports*, 7(6173), pp.1-9

Leary, P. Pogacnik, J. Malin, P. (2012) Fractures ~ Porosity → Connectivity~ permeability → EGS Flow Stimulation, *GRC Transactions*, 36, pp.499-506

Lebedeva, M. I., and and Brantley, S. L. (2017). Weathering and erosion of fractured bedrock systems. *Earth Surface Processes and Landforms*, *42*(13), pp.2090-2108.

Leone, A. (2013). Sabratha. *The Encyclopaedia of Ancient History*.

Leucci, G, De Giorgi, L. (2006) Experimental studies on the effects of fracture on the P and S wave velocity propagation in sedimentary rock ("Calcarenite del Salento"). *Engineering Geology*, 84(3-4), 130-142.

López, M. (2017). The Relief Decorations of the Ancient Roman Theater: The Case of Sabratha. *Music in Art*, *42*(1-2), pp.17-31.

Li, X., Tao, M., Wu, C., Du, K., and and Wu, Q. (2017). Spalling strength of rock under different static pre-confining pressures. *International Journal of Impact Engineering*, *99*, 69-74.

Lin, M. Jeng, F. Tsai, L. Huang, T. (2005) Wetting weakening of tertiary sandstones-Microscopic mechanism, *Environmental Geology*, 48(2) pp.265-275

Liszka, K. (2017). Egyptian or Nubian? Dry-Stone Architecture at Wadi el-Hudi, Wadi es-Sebua, and the Eastern Desert. *The Journal of Egyptian Archaeology*, 103(1), pp.35-51.

Lohmann, D. Kropp, A. (2011) 'Master, look at the size of those stones! Look at the size of those buildings!' Analogies in Construction Techniques Between the Temples at Heliopolis (Baalbek) and Jerusalem, *Levant*, 43(1), 38-50

López, M. I. R. (2017). The Relief Decorations of the Ancient Roman Theater: The Case of Sabratha. *Music in Art*, *42*(1-2), 17-31

López-Arce, P., Varas-Muriel, M. J., Fernández-Revuelta, B., De Buergo, M. Á., Fort, R., and Pérez-Soba, C. (2010). Artificial weathering of Spanish granites subjected to salt crystallization tests: surface roughness quantification. *Catena*, 83(2-3), 170-185

Luck, E. (2018) Cultural Genocide and the Protection of Cultural Heritage, J Paul Getty Trust *Occasional Papers In Cultural Heritage Policy*, Number 2, 2018.

Ludovico-Marques, M., and and Chastre, C. (2012). Effect of salt crystallization ageing on the compressive behaviour of sandstone blocks in historical buildings. *Engineering Failure Analysis*, *26*, pp.247-257.

Ma, G. An, X. (2008) Numerical simulation of blasting-induced rock fractures, International *Journal of Rock Mechanics and Mining Sciences*, 45(6), pp.966-975.

Macaluso, T. Sauro, U. (1996) Weathering Crust and Karren on Exposed Gypsum Surfaces, *International Journal of Speleology,* 3-4, pp.115-126

Mahmoud, H. Kantiranis, N. Stratis, J. (2010) Salt damage on the wall paintings of the festival temple of Thutmosis III, Karnak temples complex, Upper Egypt. A case study, *International Journal of Conservation Science*, 1(3), pp.133-142

Manes, A. Serpellini, F. Pagani, M. Saponara, M. Giglio, M. (2014) Perforation and penetration of aluminium target plates by armour piercing bullets, *International Journal of Impact Engineering*, 69, pp.39-54

Manohar, S., Bala, K., Santhanam, M., and and Menon, A. (2020). Characteristics and deterioration mechanisms in coral stones used in a historical monument in a saline environment. *Construction and Building Material*s, 241

Marszalek, M. Alexandrowicz, Z. Rzepa, G. (2014) Composition of weathering crusts on sandstones from natural outcrops and architectonic elements in an urban environment, *Environmental Science and Pollution Research International*, 21(6) pp.14023-14036

Martínez-Garrido, M. I., Fort, R., Gómez-Heras, M., Valles-Iriso, J., and and Varas-Muriel, M. J. (2018). A comprehensive study for moisture control in cultural heritage using non-destructive techniques. *Journal of Applied Geophysics*, *155*, pp.36-52.

Matsukura, Y. Tanaka, Y. (2000). Effect of rock hardness and moisture content on tafoni weathering in the granite of Mount Doeg-Sung, Korea. *Geografiska Annaler: Series A*,

Physical Geography, *82*(1), pp.59-67.

Maurer, W. C., and and Rinehart, J. S. (1960). Impact crater formation in rock. *Journal of applied physics*, *31*(7), pp.1247-1252.

May, E., Papida, S., and and Abdulla, H. (2003). Consequences of microbe-biofilm-salt interactions for stone integrity in monuments. *Art, biology, and conservation: biodeterioration of works of art*, pp.452-471.

McCabe, S., Smith, B. J., and and Warke, P. A. (2010). Exploitation of inherited weakness in fire-damaged building sandstone: the 'fatiguing'of 'shocked'stone. *Engineering Geology*, *115*(3-4), pp.217-225.

McFadden, L. D., Eppes, M. C., Gillespie, A. R., and Hallet, B. (2005). Physical weathering in arid landscapes due to diurnal variation in the direction of solar heating. *Geological Society of America Bulletin*, *117*(1-2), 161-173.

McFadden, L. Eppes, M. Gillespie, A. Hallet, B. (2005) Physical weathering in arid landscape due to diurnal variation in the direction of solar heating, *Geological Society of America Bulletin*, 117(1), pp.161-173

McGreevy, J. Smith, B. (1982) Salt Weathering in Hot Deserts: Observations on the Design of Simulation Experiments, Geografiska Annaler: Series A, *Physical Geography*, 64(3/4), pp.161-170

McKinley, J. M., and and Warke, P. A. (2007). Controls on permeability: implications for stone weathering. *Geological Society, London, Special Publications*, 271(1), pp.225-236.

McPhee, C. Arthur, K. (1991) Klinkenberg Permeability Measurements: Problems and Practical Solutions. *Reviewed Proceedings of the Second Society of Core Analysts European Core Analysis Symposium*, London, UK, 20-22 May 1991

Melosh, H. J. (2013). The contact and compression stage of impact cratering. *Impact Cratering: processes and products*, 2013, pp.32-42.

Melosh, H. J., and and Ivanov, B. A. (1999). Impact crater collapse. *Annu. Rev. Earth Planet. Sci*, *27*, pp.385-415.

Menéndez, B. (2018). Estimators of the impact of climate change in salt weathering of cultural heritage. *Geosciences*, 8(11), pp.401.

Menéndez, B., Petráňová, V. (2016) Effect of mixed vs single brine composition on salt weathering in porous carbonate building stones for different environmental conditions *Engineering Geology* 210, pp.124-139.

Met Office (2022) *Solent MSRC,* Available at: https://www.metoffice.gov.uk/research/climate/maps-and-data/uk-climate-averages/gcp1h90k5, Accessed: 07/11/2022

Mertz, J. D., Colas, E., Yahmed, A. B., and and Lenormand, R. (2016). Assesment of a non-destructive and portable mini permeameter based on a pulse decay flow applied to historical surfaces of porous materials. *Science and art: A future for stone*, 415.

Miao, T. Yu, B. Duan, Y. Fang, Q. (2015) A fractal analysis of permeability for fractured rocks, *International Journal of Heat and Mass Transfer*,81, pp.75-80

Micallef, A. (2003) Salt migration by capillary action through lithic arenite sandstone as controlled by solution concentration and drying rate, MSc, University of Oxford

Michette, M. (2021) Integrating non-destructive techniques into the scientifically robust assessment of vulnerable historic masonry: Case studies on Reigate Stone, *Journal of Building Survey, Appraisal and and Valuation*, 10(3), pp.242-256.

Middendorf, B., Knöfel, D. (1998). Gypsum and lime mortars of historic German brick buildings. In: Baer, N. Fitz, S. Livingston, R. eds, *Conservation of Historic Brick Structures*', Routledge, pp.197-208.

Migoń, P., and and Goudie, A. (2014). Sandstone Geomorphology of South-West Jordan, Middle East, *QUAESTIONES GEOGRAPHICAE*, 33(3). pp.123-130

Mitani, N. K. (2003). Numerical simulations of shock attenuation in solids and reevaluation of scaling law. *Journal of Geophysical Research: Planets*, *108*(E1).

Moffet, M. Fazio, M. Wodehouse, L. (2003) *A World History of Architecture*, Laurence King Publishing, pp.9-14

Mol, L. (2014) Investigations into the relationship between changes in internal moisture regimes and rock surface deterioration in cavernous sandstone features, *Earth Surface Processes and Landforms*, 39(7), pp.914-927

Mol, L. Gomez-Heras, L. (2018) Bullet Impacts and built heritage damage 1640-193, *Heritage Science*, 6(35)

Mol, L. Gomez-Heras, M. Brassey, C. Green, O. Blenkinsop, T. (2017) The benefit of a tough skin: bullet holes, weathering and the preservation of heritage, *Royal Society Open Science*, 4:160335

Mol, L. Viles, H. (2010) Geoelectric investigations into sandstone moisture regimes: Implications for rock weathering and the deterioration of San Rock Art in the Golden Gate Reserve, South Africa, *Geomorphology*, 118(3-4), pp.280-287

Mol, L. Viles, H. (2011) The role of rock surface hardness and internal moisture in tafoni development in sandstone, *Earth Surface Processes and Landforms*, 37(3), pp.301-314

Montana, G. Randazzo, L. Oddo, I. Valenza, M. (2008) The growth of "black crusts" on calcerous building stone in Palermo (Sicily): a first appraisal of anthropogenic and natural sulphur sources, *Environmental Geology*, 56, pp.367-380

Mottershead, D. N. (1989). Rates and patterns of bedrock denudation by coastal salt spray weathering: a seven-year record. *Earth Surface Processes and Landforms*, *14*(5), pp.383-398.

Mottershead, D. N., and and Pye, K. (1994). Tafoni on coastal slopes, South Devon, UK. *Earth Surface Processes and Landforms*, *19*(6), pp.543-563.

Mtani, I. W. (2016). *Salt Deterioration of Historic Mortars in Tropical Climate: Analysis and Characterisation: Case Studies from Tanzania* (Vol. 26). Kassel university press GmbH.

Nakazawa, S., Watanabe, S., Iijima, Y., and and Kato, M. (2002). Experimental investigation of stress wave attenuation in basalt. *Icarus*, *156*(2), 539-550.

Navarre-Sitchler, A. Brantley, S. Rother, G. (2015) How Porosity Increases During Incipient Weathering of Crystalline Silicate Rocks, *Reviews in Mineralogy and Geochemistry*, 80, pp.331-354

Navarre-Sitchler, A. Cole, D. Rother, G. Jin, L. Buss, H. Brantley, S. (2013) Porosity and surface area evolution during weathering of two igneous rocks, *Geochimica et Cosmochimica Acta*, 109, pp.400-413

New England Research Inc. (2015) *TinyPerm 3 Portable Handheld Permeameter Instruction Manual 1.1*, New England Research, Vermont, USA.

Nguyen, T. Cheung, C. (2014) The classification of heritage tourists: a case of Hue City, Vietnam, *Journal of Heritage Tourism*, 9(1), pp.35-50

Nguyen, T. Shu, M. Huang, Y. Hsu, B. (2013) Accurate forecasting models in predicting the inbound tourism demand in Vietnam, *Journal of Statistics and Management Systems*, 16(1), pp. 25-43

Nia, S. F., and and Jessen, K. (2015). Theoretical analysis of capillary rise in porous media. *Transport in Porous Media*, *110*(1), pp.141-155.

Niesel, Z. (2014) "Collateral Damage: Protecting Cultural Heritage in Crimea and Eastern Ukraine." *Wake Forest Law Review Online* 4 (25).

Nobili, A., Radi, E., and and Lanzoni, L. (2017). Flexural edge waves generated by steady-state propagation of a loaded rectilinear crack in an elastically supported thin plate. *Proceedings of the Royal Society A: Mathematical, Physical and Engineering Sciences*, 473(2204), 20170265.

Noiriel, C. Renard, F. Doan, M. Gratier, J. (2010) Intense fracturing and fracture sealing induced by mineral growth in porous rocks, *Chemical Geology*, 269, pp.197-209
Nord, A. Tronner, K. (1995) Effect of acid rain on sandstone: The Royal Palace and the Riddarholm church, Stockholm, *Water, Air, and Soil Pollution*, 85(4), pp.2719-2724.

Norris, A. N., Krylov, V. V., and Abrahams, I. D. (2000). Flexural edge waves and

Comments on “A new bending wave solution for the classical plate equation”[J. Acoust. Soc. Am. 104, 2220–2222 (1998)]. *The Journal of the Acoustical Society of America*, *107*(3), pp.1781-1784.

Nugent, M. Brantley, S. Pantano, C. Maurice, P. (1998) The influence of natural mineral coatings on feldspar weathering, *Nature,* 395, pp.588-591

O’Hare, G. Sweeney, J. Wilby, R. (2014) Weather, Climate and Climate Change: Human Perspectives, Routledge, pp.322

Ohnaka, M. (1973) The Quantitative Effect of Hydrostatic Confining Pressure on the Compressive Strength of Crystalline Rocks, Journal of Physics of the Earth, 21, pp.125-140

Okai, R. (2016). Effects of Grain Angle on Reproducibility and Accurate Measurement of Moisture Content of Wood Samples Using a Pin-Style Moisture Meter. *Journal of Environmental Science and Engineering*, pp.139-145.

Okubo, C. H., and and Schultz, R. A. (2007). Compactional deformation bands in Wingate Sandstone; additional evidence of an impact origin for Upheaval Dome, Utah. *Earth and Planetary Science Letters*, 256(1-2), pp.169-181.

Osinski, G. R., Cockell, C. S., Pontefract, A., and Sapers, H. M. (2020). The role of meteorite impacts in the origin of life. *Astrobiology*, *20*(9), pp.1121-1149.

Oyer, H. (1999) The 1954 Hague Convention for the Protection of Cultural Property in the Event of Armed Conflict - Is It Working - A Case Study: The Persian Gulf War Experience, *Columbia VLA Journal of Law and and the Arts*, 23, pp.49-67

Paniconi, C., Khlaifi, I., Lecca, G., Giacomelli, A., and and Tarhouni, J. (2001). Modeling and analysis of seawater intrusion in the coastal aquifer of eastern Cap-Bon, Tunisia. *Transport in porous media*, 43(1), 3-28.

Paradise, T. (2014) Analysis of sandstone deterioration on petroglyphs, architecture, inscriptions, and dressed surfaces across Wadi Rum, Jordan, Desert and Man, *Proceedings of the second international multidisciplinary conference*, Wadi Rum-Amman, Jordan, March 4-7, 2014

Park, H. Shin, G. (2009) Geotechnical and geological properties of Mokattam limestones: Implications for conservation strategies for ancient Egyptian stone monuments, *Engineering Geology*, 104(3-4), pp.190-199

Parsons, N. (2016) Iconoclasm: The Struggle for Ownership of Symbolic History, *Hungarian Review*, 7(5), pp.105-115.

Perry, J. (2019). Climate change adaptation in natural world heritage sites: A triage approach. *Climate*, *7*(9), p.105

Pikirayi, I., Sulas, F., Musindo, T. T., Chimwanda, A., Chikumbirike, J., Mtetwa, E., ... and and Sagiya, M. E. (2016). Great Zimbabwe's water. Wiley Interdisciplinary Reviews: Water, 3(2), pp.195-210.

Pinker, R. Sun, D. , Miller, M. Robinson, G. (2007) Diurnal cycle of land surface temperature in a desert encroachment zone as observed from satellites, *Geophysical Research Letters*, 34(11), pp.1-5

Polanskey, C. Ahrens, T. (1990) Impact Spallation Experiments: Fracture Patterns and Spall Velocities, *Icarus*, 87, pp.140-155

Pope, G. Dorn, R. Dixon, J. (1995) A new conceptual model for understanding geographical variations in weathering, *Annals of the Association of American Geographers*, 85(1), pp.38-64

Porter, N. J., Trenhaile, A. S., Prestanski, K., and and Kanyaya, J. I. (2010). Patterns of surface downwearing on shore platforms in eastern Canada. *Earth Surface Processes and Landforms*, *35*(15), pp.1793-1810.

Potter, R. Clynne, M. (1978) Solubility of highly soluble salts in aqueous media- part 1, NaCI, KCI, CaCI2, Na2S02 , and K2S04, Solubilities to 100°C, *Journal of Research of the U.S. Geological Survey*, 6(6), pp. 701-705

Proceq (2017a) *Equotip* 550 *Operating Instructions*, Proceq, Switzerland

Proceq, (2019) *Equotip Application Booklet, Portable Hardness Testing Leeb, Portable Rockwell and UCI*, Proceq, Switzerland.

Proceq (2017b) *Proceq Pundit Operating Instructions,* Proceq, Switzerland

Pulte, A. (2013). Views from the Cathedral: Blindfolds, Color-Blindness and Other Problems with Justice's Visual Acuity. *Journal of Jurisprudence*, 20, 399.

Quinault, R. (1992) Westminster and the Victorian Constitution, *Transactions of the Royal Historical Society*, 2(1992), pp.79-104

Renard, F., Noiriel, C., Doan, M., and and Gratier, J. (2009, December). Intense fracturing and fracture sealing induced by mineral growth in porous rocks: the force of crystallization. In *AGU Fall Meeting Abstracts* (Vol. 2009, pp. T43A-2048).

Ringl, C., Bringa, E. M., Bertoldi, D. S., and Urbassek, H. M. (2012). Collisions of porous clusters: a granular-mechanics study of compaction and fragmentation. *The Astrophysical Journal*, *752*(2), 151

Rodriguez-Navarro, C. Doehne, E. (1999) Salt Weathering: Influence of evaporation rate, supersaturation and crystallization pattern, *Earth Surface Processes and Landforms*, 24(3), pp.191-209

Rodriguez-Navarro, C., and and Sebastian, E. (1996). Role of particulate matter from vehicle exhaust on porous building stones (limestone) sulfation. *Science of the total*

environment, *187*(2), 79-91.

Rodríguez-Rellán, C. (2016). Variability of the rebound hardness as a proxy for detecting the levels of continuity and isotropy in archaeological quartz. *Quaternary International*, 424, pp.191-211.

Rosen, F. (2017) NATO and Cultural Property, Embracing New Challenges in the Era of Identity Wars, Nordic Centre for Cultural Heritage and and Armed Conflict, Copenhagen, Denmark

Rothert, E. Eggers, T. Cassar, J. Ruedrich, J. Fitzner, B. Siegesmund, S. (2007). Stone properties and weathering induced by salt crystallization of Maltese Globigerina Limestone. *Geological Society, London, Special Publications*, *271*(1), 189-198.

Rottman, G. L. (2011). *The AK-47: Kalashnikov-series assault rifles*. Bloomsbury Publishing.

Rubin, A. E., and Swindle, T. D. (2011). Flattened chondrules in the LAP 04581 LL5 chondrite: Evidence for an oblique impact into LL3 material and subsequent collisional heating. *Meteoritics and Planetary Science*, *46*(4), pp.587-600

Russel, B. (2013) Gazetteer of Stone Quarries in the Roman World, Oxford University, version 1.0., Available at: oxrep.classics.ox.ac.uk/databases/stone_quarries_database/

Sabbioni, C., Bonazza, A., Zamagni, J., Ghedini, N., Grossi, C. M., and Brimblecombe, P. (2004). The Tower of London: A case study on stone damage in an urban area. *Air Pollution and Cultural Heritage. London: AA Balkema*, pp.57-62.

Santa Cruz Astorqui, J., del Río Merino, M., Villoria Saez, P., & Porras-Amores, C. (2017). Analysis of the relationship between density and mechanical strength of lightened gypsums: proposal for a coefficient of lightening. *Advances in Materials Science and Engineering*, *2017*.

Santo, A. P., Agostini, B., Garzonio, C. A., Pecchioni, E., and Salvatici, T. (2022). Decay Process of Serpentinite: The Case of the San Giovanni Baptistery (Florence, Italy) Pavement. *Applied Sciences*, *12*(2), p.861

Sampietro-Vattuone, M. M., and and Peña-Monné, J. L. (2021). Application of 2D/3D models and alteration mapping for detecting deterioration processes in rock art heritage (Cerro Colorado, Argentina): A methodological proposal. *Journal of Cultural Heritage*, 51, 157-165.

Santo, Alba Patrizia, Beatrice Agostini, Carlo Alberto Garzonio, Elena Pecchioni, and Teresa Salvatici. "Decay Process of Serpentinite: The Case of the San Giovanni Baptistery (Florence, Italy) Pavement." *Applied Sciences* 12(2) pp.861-874

Taylor, F. (2011) *Dresden, Tuesday 13 February 1945*, Bloomsbury

Sawangsuriya, A. (2012). Wave propagation methods for determining stiffness of geomaterials. In: Giovine, P. ed., *Wave processes in classical and new solids*, IntechOpen, pp.157-200

Scherer, G. (2002) Factors Affecting Crystallization Pressure, International RILEM TC 186-ISA Workshop on Internal Sulfate Attack and Delayed Ettringite Formation, 4-6 September 2002, Villars, Switzerland

Schultz, P. H. (1996). Effect of impact angle on vaporization. *Journal of Geophysical Research: Planets*, *101*(E9), pp.21117-21136.

Shahidzadeh, N. Desarnaud, J. (2012) Damage in porous media: role of the kinetics of salt (re)crystallization, *The European Physical Journal, Applied Physics*, 60(2), pp.1-7

Shakoor A. Barefield, E. (2009) Relationship between unconfined compressive strength and degree of saturation for selected sandstones, *Environmental and Engineering Geoscience*, 15(1), pp.29-40

Shiels, D. (2006) The Potential for Conflict Archaeology in the Republic of Ireland, *Journal of Conflict Archaeology*, 2(1) pp.169-187

Shimmon, R. (2004), The International Committee of the Blue Shield 1998–2004: An Overview, *Alexandria*, 16(3), pp.133-141.

Siegfried, R. Simmons, G. Richter, D. Horz, F. (1977) Microfractures produced by a laboratory scale hypervelocity impact into granite, Proceedings of the 8th Lunar Science Conference, Houston, Texas, USA, March 14-18th 1977, pp. 1249-1270

Siekman, M. W., Anderson, D. A., and Boyce, A. S. (2010). SPECTRUM Small-Arms Ammunition Production and Acquisition: Too Many Eggs in One Basket?. *Army Sustainment*, *42*(5), p.60.

Singer, A. Stoffers, P. (1980) Clay mineral diagenesis in two East African Lake Sediments, *Clay Minerals*, 15, pp.291-307

Sivan, O., Yechieli, Y., Herut, B., and and Lazar, B. (2005). Geochemical evolution and timescale of seawater intrusion into the coastal aquifer of Israel. *Geochimica et Cosmochimica Acta*, *69(3), 579-592*.

Summers, G. D. (2001). Keykavus Kale and associated remains on the Kerkenes Dağ in Cappadocia, central Turkey. *Anatolia antiqua. Eski Anadolu*, 9(1), pp.39-60.

Smith, B. McGreevy, J. (1983) A Simulation of Salt Weathering in Hot Deserts, *Physical Geography*, 65(1-2), pp.127-133

Smith, M. K., and Richards, G. (Eds.). (2013). *The Routledge handbook of cultural tourism*. Routledge.

Smith, B. Whalley, W. (1988) A note on the characteristics and possible origins of desert

varnishes from southeast Morocco, *Earth Surface Processes and Landforms*, 13(3), pp.251-258

Sperling, C. H. B., and and Cooke, R. U. (1985). Laboratory simulation of rock weathering by salt crystallization and hydration processes in hot, arid environments. *Earth Surface Processes and Landforms*, *10*(6), 541-555.

Stoffler, D. Langenhorst, F. (1993) Shock Metamorphism of Quartz Grains in Nature and Experiment I. Basic Observation and theory. *Meteoritics*, 29, pp.155-181

Su, Y. Lin, H. (2013) Analysis of international tourist arrivals worldwide: The role of world heritage sites, *Tourism Management*, 40, pp.46-58

Tahan, L. (2007) Lebanon Cultural Heritage Threatened by the War in Lebanon. In: Reinhold-Verlag ed. (2007), Heritage at Risk, ICOMOS World Report 2006/2007 On Monuments and Sites in Danger, p.107

Tandon, A. (2018) First Aid to Cultural Heritage in Times of Crisis Handbook, International Centre for the Study of the Preservation and Restoration of Cultural Property (ICCROM), Rome, Italy

Tedeschi, W. Remo, J. Schulze, J. Young, R. (1995) Experimental Hypervelocity Impact effects on Simulated Planetesimal Materials, *International Journal of Impact Engineering*, 17(4-6), pp.837-848

Thoma, K. Hornemann, U. Sauer, M. Schneider, E. (2005) Stress waves—Phenomenology, experimental, and numerical simulation, *Meteoritics and and Planetary Science*, 40, pp. 1283–1298

Thornbush, M. Viles, H. (2006) Simulation of the dissolution of weathered versus unweathered limestone in carbonic acid solutions of varying strength, *Earth Surface Processes and Landforms*, 32(6), pp.841-852

Trudgill, S. Viles, H. Inkpen, R. Moses, C. Gosling, W. Yates, T. Collier, P. Smith, D. Cooke, R. (2001) Twenty-year weathering remeasurements at St Paul's Cathedral, London, *Earth Surface Processes and Landforms*, 26(10)

Török, A. (2007), Morphology and detachment mechanism of weathering crusts of porous limestone in the urban environment of Budapest, *Central European Geology*, pp.225-240,50(3), pp.225-240

Török, Á., and and Vásárhelyi, B. (2010). The influence of fabric and water content on selected rock mechanical parameters of travertine, examples from Hungary. *Engineering Geology*, 115(3-4), pp. 237-245.

Tsui, N. Flatt, R. Scherer, G. (2003), Crystallization damage by sodium sulfate, *Journal of Cultural Heritage*, 4(2003), pp.109-115

Turkington, A. V., and Paradise, T. R. (2005). Sandstone weathering: a century of research

and innovation. *Geomorphology*, *67*(1-2), pp.229-253.

Turkington, A.V. Smith, B. (2000) Observations of three-dimensional salt distribution in building sandstone. *Earth Surface Processes and Landforms*, 25, pp. 1317–1332.

United Nations. (2011). International Ammunition Technical Guidelines

Van der Plas, (2004), New Fund for Emergency Aid to Culture: Cultural Emergency Response, Alexandria, 16(3), pp.159-169.

Vaughn, D. (2005) Arid Climates. In: Oliver J.E. (eds) Encyclopedia of World Climatology, Springer, pp.85-89

Verwaal, W., and Mulder, A. (1993, December). Estimating rock strength with the Equotip hardness tester. In *International Journal of Rock Mechanics and Mining Sciences and Geomechanics Abstracts* (Vol. 30, No. 6, pp. 659-662). Elsevier Science.

Veran-Tissoires, S. Prat, M. (2014) Evaporation of a sodium chloride solution from a saturated porous medium with efflorescence formation, *Journal of Fluid Mechanics*, 749, pp.701-749

Vickers, A. J. (2005). Parametric versus non-parametric statistics in the analysis of randomized trials with non-normally distributed data. *BMC medical research methodology*, *5*(1), 1-12.

Viles, H. Goudie, A.(2004) Biofilms and Case Hardening on Sandstones from Al-Quwayra, Jordan, *Earth Surface Processes and Landforms*, 29(12), pp.1473-1485

Viles, H. A., and Goudie, A. S. (2007). Rapid salt weathering in the coastal Namib desert: Implications for landscape development. *Geomorphology*, *85*(1-2), pp.49-62.

Viles, H. Goudie, A. Grab, S. Lalley, J. (2011) The use of the schmidt hammer and equotip for rock hardness assessment in geomorphology and heritage science: A comparative analysis. *Earth Surface Processes and Landforms*, 36, pp.320–333

Vlasic, M. Turku, H. (2016) 'Blood Antiquities': Protecting Cultural Heritage beyond Criminalization, *Journal of International Criminal Justice*, 14(5), pp. 1175-1197

Walker, P. J., and and Dickens, J. G. (1995). Stability of medieval dry-stone walls in Zimbabwe. Geotechnique, 45(1), pp.141-147.

Wang, J. Yin, Y. Luo, C. (2018) Johnson-Holmquist-II (JH-2) Constitutive Model for Rock Materials: Parameter Determination and Application in Tunnel Smooth Blasting, *Applied Sciences*, 8(1675), pp.1-23

Wang, Z. L., and Konietzky, H. (2009). Modelling of blast-induced fractures in jointed rock masses. *Engineering Fracture Mechanics*, *76*(12), pp.1945-1955.

Wang, Y., Lin, H., Zhao, Y., Li, X., Guo, P., and and Liu, Y. (2019). Analysis of fracturing characteristics of unconfined rock plate under edge-on impact loading. *European Journal of*

Environmental and Civil Engineering, pp.1-16.

Waragai, T., and and Hiki, Y. (2019). Influence of microclimate on the directional dependence of sandstone pillar weathering in Angkor Wat temple, Cambodia. *Progress in Earth and Planetary Science*, *6*(1), pp.10.

Warke, P. A., Smith, B. J., and and Lehane, E. (2011). Micro-environmental change as a trigger for granite decay in offshore Irish lighthouses: implications for the long-term preservation of operational historic buildings. *Environmental Earth Sciences*, 63(7-8), 1415-1431.

Weinhaus, F. Devarajan, V. (1997) "Texture mapping 3D models of real-world scenes." *ACM Computing Surveys (CSUR)* 29(4), pp.325-365.

Weiss, T. Connelly, N. (2017) Cultural Cleansing and Mass Atrocities Protecting Cultural Heritage in Armed Conflict Zones, J. *Paul Getty Trust Occasional Papers in Cultural Heritage Policy*, Number 1, 2017

Weiss, T. Siegesmund, S. Kirchner, D. Sippel, J. (2004) Insolation weathering and hygric dilatation: two competitive factors in stone degradation, *Environmental Geology*, 46(3-4), pp.402-413

Wen, Y., Xu, C., Jin, Y., Batra, R. C. (2017). Rifle bullet penetration into ballistic gelatin. *Journal of the mechanical behavior of biomedical materials*, *67*, pp.40-50.

Wheida, E., and and Verhoeven, R. (2006). Review and assessment of water resources in Libya. *Water international*, *31*(3), pp.295-309.

Wiebe, R. Gaddy, V. (1940) The Solubility of Carbon Dioxide in Water at Various Temperatures from 12 to 40° and at Pressures to 500 Atmospheres. Critical Phenomena, *Journal of the American Chemical Society*, 62(4) pp.815-817

Wijesuriya, G. (2000) Conserving the Temple of the Tooth Relic, Sri Lanka, *Public Archaeology*, 1(2), pp.99-108

Wilhelm, K., Viles, H., and Burke, Ó. (2016). Low impact surface hardness testing (Equotip) on porous surfaces–advances in methodology with implications for rock weathering and stone deterioration research. *Earth Surface Processes and Landforms*, *41*(8), 1027-1038.

Woo, C. (1991) Sorting Out the Victims: Triage and Cultural Resources. *CRM Bulletin*

World Travel and and Tourism Council (2019) Travel and Tourism Economic Impact 2019, World Travel and and Tourism Council, pp.1-13

Worthington, S. Davies, G. Alexander, C. (2016) Enhancement of bedrock permeability by weathering, *Earth-Science Reviews*, 160, pp.188-202

Wright, G. R. H. (1998). Two notes on funerary monuments at Petra. *East and West*, *48*(1/2), 153-165

Wright, H. (1873) *The Story of the 'Domus Dei' of Portsmouth, commonly called the Royal Garrison Church,* James Parker and and Co.

Wust, R. Schluchter, C. (2000) The origin of soluble salts in rocks of the Thebes Mountains, Egypt: The damage potential to ancient Egyptian wall art, *Journal of Archaeological Sciences*, 27(12), pp.1161-1172

Xu, H., Zhou, W., Xie, R., Da, L., Xiao, C., Shan, Y., and and Zhang, H. (2016). Characterization of rock mechanical properties using lab tests and numerical interpretation model of well logs. *Mathematical Problems in Engineering*, *2016*.

Yarwood, J. (2003) Cultural Warfare, *Art, Antiquity and Law*, 8(2), pp.191-200

Yilmaz, H. M. (2010). Close range photogrammetry in volume computing. *Experimental Techniques*, *34*, 48-54.

Yilmaz, H. Yakar, M. Ildiz, F. (2008) Digital photogrammetry in obtaining of 3D model data of irregular small objects, *The International Archives of the Photogrammetry, Remote Sensing and Spatial Information Sciences*, 37, pp. 125-130.

Young, R. Frowell, R. (1974) Assessing rock discontinuities. *Tunnels and and Tunnelling International,*10, 45–48

Young, R., Young, A., Young, R., and Young, A. (1992). Chemical Weathering and Cavernous Weathering. *Sandstone Landforms*, pp.61-80.

Yu, J. Chen, X. Li, H. Zhou, J. Cai, Y. (2015) Effect of Freeze-Thaw Cycles on Mechanical Properties and Permeability of Red Sandstone under Triaxial Compression, *Journal of Material Science*, pp.218-231

Xu, H., Zhou, W., Xie, R., Da, L., Xiao, C., Shan, Y., and Zhang, H. (2016). Characterization of rock mechanical properties using lab tests and numerical interpretation model of well logs. *Mathematical Problems in Engineering*, *2016*.

Zaradona, J. Abarran-Torres, C. Isakhan, B. (2017) Digitally Mediated Iconoclasm: the Islamic State and the war on Cultural Heritage, *International Journal of Heritage Studies*. 24(4), pp.649-671.

Zhang, Z. X., Hou, D. F., and and Aladejare, A. (2020). Empirical equations between characteristic impedance and mechanical properties of rocks. *Journal of Rock Mechanics and Geotechnical Engineering*, *12*(5), 975-983.

Zielińska, M., and and Rucka, M. (2018). Non-destructive assessment of masonry pillars using ultrasonic tomography. *Materials*, 11(12), 2543.

Zheng, H., Feng, X. T., and and Jiang, Q. (2015). The influence of NaCl crystallization on the long-term mechanical behavior of sandstone. *Rock Mechanics and Rock Engineering*, *48*(1), pp.33-51.

Zumdahl, S. (1996) Basic Chemistry, D.C. Heath, pp. 193